

First-Principles Density Functional Theory Study of Novel Materials for Solar Energy Conversion and Environment Applications

Submitted by **Habib Ullah** to the University of Exeter

as a thesis for the degree of

Doctor of Philosophy in Renewable Energy

In March 2018

This thesis is available for Library use on the understanding that it is copyright material and that no quotation from the thesis may be published without proper acknowledgement.

I certify that all material in this thesis which is not my own work has been identified and that no material has previously been submitted and approved for the award of a degree by this or any other University.

Signature:

DEDICATION

*This humble work is dedicated to
My Beloved Mother BBG, Father
(Muhammad Ishaq), daughter
(Quratulain Khan) and Wife
(Salma Bibi)*

ABSTRACT

To design an efficient solar energy conversion device, theoretical input is extremely important to provide the basic guideline for experimental scientists, to fabricate the most efficient, cheap, and stable device with less efforts. This desire can be made possible if computational scientist use a proper theoretical protocol, design an energy material, then the experimentalist will only invest weeks or months on the synthetic effort. This thesis highlights my recent efforts in this direction.

Monoclinic BiVO_4 is has been using as a photocatalyst due to its stability, cheap, easily synthesizable, narrow band gap and ideal VB (-6.80 eV vs vacuum) but inappropriate CB (-4.56 eV vs vacuum) edge position, responsible for its low efficiency. We have carried out a comprehensive experimental and periodic density functional theory (DFT) simulations of the pristine, Oxygen defective (O_v), Se doped monoclinic BiVO_4 and heterojunction with Selenium (Se-BiVO_4), to improve not only its CB edge position but photocatalytic and charge carrier properties. It is found that O_v (1% Oxygen vacancy) and mild doped BiVO_4 (1 to 2% Se) are thermodynamically stable, have ideal band edges ~ -4.30 eV, band gaps (~ 1.96 eV), and small effective masses of electrons and holes. We have also investigated the contribution of Se to higher performance by effecting morphology, light absorption and charge transfer properties in heterojunction. Finally, it is found that Se makes a direct Z-scheme (band alignments) with BiVO_4 where the photoexcited electron of BiVO_4 recombine with the VB of Se, consequences electron-hole separation at Se and BiVO_4 , respectively, as a result, enhanced photocurrent is obtained.

Theoretical study of β -TaON in the form of primitive unit cell, supercell and its N, Ta, and O terminated surfaces are carried out with the help of periodic DFT. Optical and electronic properties of all these different species are simulated, which predict TaON as the best candidate for photocatalytic water splitting contrast to their Ta₂O₅ and Ta₃N₅ counterparts. The calculated bandgap, valence band, and conduction band edge positions predict that β -TaON should be an efficient photoanodic material. The valence band is made up of N 2p orbitals with a minor contribution from O 2p, while the conduction band is made up of Ta 5d. Turning to thin films, the valence band maximum; VBM (−6.4 eV vs. vacuum) and the conduction band minimum; CBM (−3.3 eV vs. vacuum) of (010)-O terminated surface are respectively well below and above the redox potentials of water as required for photocatalysis. Charge carriers have smaller effective masses than in the (001)-N terminated film (VBM −5.8 and CBM −3.7 eV vs. vacuum). However, due to wide band gap (3.0 eV) of (010)-O terminated surface, it cannot absorb visible wavelengths. On the other hand, the (001)-N terminated TaON thin film has a smaller band gap in the visible region (2.1 eV) but the bands are not aligned to the redox potential of water. Possibly a mixed phase material would produce an efficient photoanode for solar water splitting, where one phase performs the oxidation and the other reduction.

Computational study of an optically transparent, near-infrared-absorbing low energy gap conjugated polymer, donor–acceptor–donor (**D-A-D**) with promising attributes for photovoltaic application is reported herein. The **D** and **A** moiety on the polymeric backbone have been found to be responsible for tuning the band gap, optical gap, open circuit (V_{oc}) and short-circuit current

density (J_{sc}) in the polymers solar cells (PSC). Reduction in the band gap, high charge transformation, and enhanced visible light absorption in the **D-A-D** system is because of strong overlapping of molecular orbitals of **D** and **A**. In addition, the enhanced planarity and weak steric hindrance between adjacent units of **D-A-D**, resulted in red-shifting of its onset of absorption. Finally, PSC properties of the designed **D-A-D** was modeled in the bulk heterojunction solar cell, which gives theoretical V_{oc} of about 1.02 eV.

DFT study has been carried out to design a new *All-Solid-State* dye-sensitized solar cell (SDSC), by applying a donor-acceptor conjugated polymer instead of liquid electrolyte. The typical redox mediator (I^1-/I^3-) is replaced with a narrow band gap, hole transporting material (HTM). A unique “upstairs” like band energy diagram is created by packing N3 between HTM and TiO_2 . Our theoretical simulations prove that the proposed configuration will be highly efficient as the HOMO level of HTM is 1.19 eV above the HOMO of sensitizer (dye); providing an efficient pathway for charge transfer. High short-circuit current density and power conversion efficiency is promised from the strong overlapping of molecular orbitals of HTM and sensitizer. A low reorganization energy of 0.21 eV and exciton binding energy of 0.55 eV, confirm the high efficiency of HTM.

Theoretical and experimental studies of a series of four porphyrin-furan dyads were designed and synthesized, having anchoring groups, either at *meso*-phenyl or pyrrole- β position of a zinc porphyrin based on donor- π -acceptor (D- π -A) approach. The porphyrin macrocycle acts as donor, furan hetero cycle acts as π -spacer and either cyanoacetic acid or malonic acid group acts as acceptor. Optical bandgap, natural bonding, and molecular bonding orbital

(HOMO–LUMO) analysis confirm the high efficiency pyrrole- β substituted zinc porphyrins contrast to *meso*-phenyl dyads.

DFT study of polypyrrole-TiO₂ composites has been carried out to explore their optical, electronic and charge transfer properties for the development of an efficient photocatalyst. Titanium dioxide (Ti₁₆O₃₂) was interacted with a range of pyrrole (Py) oligomers to predict the optimum composition of nPy-TiO₂ composite with suitable band structure for efficient photocatalytic properties. The study has revealed that Py-Ti₁₆O₃₂ composites have narrow band gap and better visible light absorption capability compared to individual constituents. A red-shifting in λ_{\max} , narrowing band gap, and strong intermolecular interaction energy (-41 to -72 kcal/mol) of nPy-Ti₁₆O₃₂ composites confirm the existence of strong covalent type interactions. Electron–hole transferring phenomena are simulated with natural bonding orbital analysis where Py oligomers found as donor and Ti₁₆O₃₂ as an acceptor in nPy-Ti₁₆O₃₂ composites.

Sensitivity and selectivity of polypyrrole (PPy) towards NH₃, CO₂ and CO have been studied at DFT. PPy oligomers are used both, in the doped (PPy⁺) and neutral (PPy) form, for their sensing abilities to realize the best state for gas sensing. Interaction energies and amount of charges (NBO and Mulliken charge analysis) are simulated which reveal the sensing ability of PPy towards these gases. PPy, both in doped and neutral state, is more sensitive to NH₃ compared to CO₂ and CO. More interestingly, NH₃ causes doping of PPy and de-doping of PPy⁺, providing evidence that PPy/PPy⁺ is an excellent sensor for NH₃ gas. UV-vis and UV-vis-near-IR spectra of nPy, nPy⁺, and nPy/nPy⁺-X complexes demonstrate strong interaction of PPy/PPy⁺ with these atmospheric gases.

The applications of graphene (GR) and its derivatives in the field of composite materials for solar energy conversion, energy storage, environment purification and biosensor applications have been reviewed. The vast coverage of advancements in environmental applications of GR-based materials for photocatalytic degradation of organic pollutants, gas sensing and removal of heavy metal ions is presented. Additionally, the presences of graphene composites in the bio-sensing field have been also discussed in this review.

Acknowledgements

All the gratitude is to Almighty **ALLAH**, the Most Gracious and Merciful. O my **ALLAH** please guide me to act upon on the Golden principle of Islam, practiced by our Holy Prophet **Muhammad** (SAW), and do not make me the source of anyone's pain.

I am very thankful to my supervisor Dr. Asif Ali Tahir, whose continued support and guidance put me able to complete this challenging task. Particularly, I appreciate his endless patience which helped me discover my own eccentricities. Apart from Ph.D, I have been blessed to be surrounded by Asif and his family.

Throughout my Ph.D, I have been facing different situations; awesome, pleasant, bad, worse, and painful. I was lucky to had Exeter Ph.D studentship and then its proper use in right time and place. Exeter may also proud on me and my achievements, during these three and half years. I cannot forget my great and beloved mother BBG (RIP), an inspiration of my life; who passed away during the first year of my Ph.D. I am also thankful to all my family members for their help, love and prayer during my education, especially my father Muhammad Ishaq, and brothers Shakir Ullah, Safi Ullah, Zakir Ullah, beloved wife Salma Bibi and daughter Quratulain Khan.

Greatly acknowledged are Prof. Tapas K. Mallick (second supervisor), Dr. Steven Hepplestone (third supervisor), Prof. Neil Allan (Bristol University), Prof. Smagul Zh. Karazhanov (IFE, Oslo Norway), Dr. Senthilarasu Sundram, and

Dr. Khurshid Ayub (M.Phil co-supervisor) towards my guiding in Ph.D research, of which I had lots of problems and no experience.

I want to extend special thanks to Prof. Alessandro Troisi, Bristol University, for his guidance of Quantum Espresso and the provision of lab facilities. I am thankful to Prof. Smagul Zh. Karazhanov of IFE—Institut for Energiteknikk, Oslo Norway, who has helped me in learning the VASP software. I also appreciate the helpful discussion of Dr. Sergio C. Espindola (Bristol University).

I am thankful to all my colleagues and friends to have their friendship, Nazmi Sellami, Abusara, Rashid, Walid, Imran, Muhammad Sajid, Hassan Bag, Hameed, Bandar, Idress, Prabhu, Kun, Lal bahadar, Rudhra Bhai, Meena, Rupesh, and Sabir Hussain.

I highly acknowledge Dr. Andrew Cowley for his time, during the installation of Quantum Espresso, Crystal 14, and Quantum wise ATK on the Carson cluster (ESI, University of Exeter) as without him, the work would not have been obtained.

Table of Contents

Abstract.....	3
Acknowledgements.....	8
List of Figures.....	13
Abbreviations, Symbols and Nomenclature.....	17
List of Accompanying Material.....	19
CHAPTER 1: Introduction.....	27
1.1. Aims and Objectives of Research.....	29
1.2. Research Methodology.....	30
1.2.1. First-Principles Density Functional Theory (DFT)	30
1.2.1.1. Time-Dependent Density Functional Theory (TD-DFT)	30
1.2.1.2. Periodic DFT Methods for Metal Oxides.....	30
1.2.1.3. Bulk, Slab, O Defective, and Se Doped BiVO ₄	31
1.2.1.4. Electronic Properties and Effective Masses of Charge Carriers.....	32
1.2.1.5. Surface Formation Energy	33
1.2.1.6. Bulk, Slab, and Water Interacted TaON Systems.....	33
1.2.1.7. DFT Methods for Molecular Systems.....	34
1.2.1.8. Computational Study of Polymer Solar Cell.....	34
1.2.1.9. Theoretical Performance of Polymer Solar Cell	35
1.2.1.10. Polaron, Bi-polaron, and Exciton Binding Energy.....	36
1.2.1.11. Partial Charge Difference Analysis.....	37
1.2.1.12. Theoretical Simulations for Dye-Sensitized Solar Cell.....	38
1.3. Contribution of the Papers in the Field.....	39
1.4. Outline of Thesis.....	40
1.5. Novel Materials and Solar Energy Conversion.....	43

1.5.1. Energy Conversion	43
1.5.1.1. Photocatalysis.....	44
1.5.1.2. Photovoltaic.....	45
1.5.1.3. Dye-Sensitized Solar Cell	46
1.5.2. Novel Energy Materials.....	48
1.5.2.1. Metal Oxides	49
1.5.2.2. Oxynitrides	50
1.5.2.3. Conducting Polymers	51
1.5.2.4. Lead Halide Perovskites	53
1.5.2.5. Heterostructure Semiconducting Materials	54
1.6. Environmental Applications	58
1.7. Conclusions	59
CHAPTER 2: BiVO₄ for Photoelectrochemical Solar Water Splitting	62
2.1. Introduction.....	62
2.2. Pristine, Oxygen Defective, and Se-Doped BiVO ₄ for Solar Water Splitting	63
2.3. Se and BiVO ₄ Heterostructure for Photocatalysis.....	69
2.4. g-C ₃ N ₄ and BiVO ₄ Heterostructure for Solar Water Splitting.....	72
2.5. Summary.....	76
CHAPTER 3: Oxynitrides and Their Surfaces for Photocatalysis.....	78
3.1. Electronic Properties of Bulk TaON.....	78
3.2. Surface Effect of TaON on Water Oxidation.....	79
3.3. Electronic Properties of N Terminated TaON(001).....	80
3.4. Electronic and Properties of O terminated TaON(010).....	81
3.5. Summary.....	83

CHAPTER 4: Donor-Acceptor Polymers for Organic Solar Cells.....	84
4.1. Background and Challenges of Donor-Acceptor Polymer.....	84
4.2. Results and Discussion	85
4.3. Summary.....	94
CHAPTER 5: All-Solid-State Dye-Sensitized Solar Cell.....	96
5.1. Traditional DSSC vs Solid-State DSSC.....	96
5.2. Solid-State DSSC.....	96
5.3. Zinc Porphyrin Based DSSC	102
5.4. Summary.....	105
CHAPTER 6: Polymers and Their Composites for the Environmental Applications.....	106
6.1. Polypyrrole/TiO ₂ Composites for Pollutants Degradation.....	106
6.2. Polypyrrole Gas Sensors.....	114
6.3. Graphene and their Derivatives Gas Sensors.....	120
6.4. Summary.....	122
CHAPTER 7: Conclusions and Future Work.....	125
7.1. Conclusions	125
7.2. Recommendations for Future Work	129
Bibliography.....	130
Appendix	156

List of Figures

Figure 1: Applications of energy materials for solar energy conversion and environment.....	28
Figure 2. Photosynthesis in plants; a process by which green plants [having Chlorophyll (a) and (b)] use sunlight to produce Energy (glucose) from carbon dioxide and water.	43
Figure 3. VBM and CBM positions of selected semiconductors at pH 0 with respect to vacuum and normal hydrogen electrode (NHE) levels (in unit of eV): The redox potential of water is shown in blue solid and doted lines [1].....	45
Figure 4. Supposed device structure of the inverted organic solar cell along with energy band diagram of D-A-D and other species [2].	46
Figure 5. Schematic representation of various processes occurring in DSSCs upon sunlight irradiation. Photoexcitation of dye molecules upon absorption of photons [3].....	47
Figure 6. Different types of COPs and their copolymers.	52
Figure 7. Crystal Structure of a typically lead halide perovskite- $\text{CH}_3\text{NH}_3\text{PbX}_3$	54
Figure 8. Energy level diagram of Se-bulk and $\text{BiVO}_4(001)$ heterostructure, making direct Z-scheme.	55
Figure 9: Schematic representation of different band alignments for high PEC performance.	56
Figure 10. Tetrahedral and dodecahedra geometries of VO_4 (a) and BiO_8 (b) in BiVO_4 (c).	63
Figure 11. Band Structure and PDOS plot of $\text{BiVO}_4(001)$; the Fermi energy is set to zero.	64

Figure 12. Band Structure and PDOS plot of $O_v\text{-BiVO}_4(001)$; the Fermi energy is set to zero.....	66
Figure 13. PDOS plot of (a) 3Se and (b) $4\text{Se_BiVO}_4(001)$; the Fermi energy is set to zero.....	67
Figure 14. Relaxed structure of (a) $\text{BiVO}_4(001)\text{@H}_2\text{O}$, (b) $O_v\text{-BiVO}_4(001)\text{@H}_2\text{O}$, (c) $1\text{Se_BiVO}_4(001)\text{@H}_2\text{O}$, and (d) water.	67
Figure 15. Band structure and PDOS of $1\text{Se_BiVO}_4(001)\text{@H}_2\text{O}$; the Fermi energy is set to zero.	69
Figure 16: Valence and Conduction DOS of $\text{BiVO}_4(001)$, Fermi level is set to zero.....	70
Figure 17. Energy level diagram of the simulated Se-bulk and $\text{BiVO}_4(001)$	71
Figure 18. Relaxed geometries of (a) $g\text{-C}_3\text{N}_4$, (b) $\text{BiVO}_4(001)$ and (c) $g\text{-C}_3\text{N}_4/\text{BiVO}_4$ (having lattice mismatch of 0.02%).....	72
Figure 19. Simulated band structures of (a) $\text{BiVO}_4(001)$ slab, (b) $g\text{-C}_3\text{N}_4$, and (c) $g\text{-C}_3\text{N}_4/\text{BiVO}_4$ heterojunction; the Fermi energy is set to zero.	73
Figure 20. Partial density of states plots of (a) $\text{BiVO}_4(001)$, (b) $g\text{-C}_3\text{N}_4$, and (c) $g\text{-C}_3\text{N}_4/\text{BiVO}_4$ heterojunction. The vertical dashed lines represent the work function and the energy is in eV versus vacuum.	74
Figure 21. Energy level diagram of these three constituents and averaged electron density difference ($\Delta\rho$) along the Z-direction for $g\text{-C}_3\text{N}_4/\text{BiVO}_4$. The green and yellow shaded areas indicate electron accumulation and donation, respectively.....	76
Figure 22. Band Structure of the $2\times 2\times 2$ supercell of TaON; the Fermi Energy is set to zero.	78

Figure 23. Optimized Crystal structure of unit cell (a), supercell (b), N-terminated (c), and O-terminated (d) slab of TaON.	79
Figure 24. PDOS of N-TaON(001), (a) and N-TaON(001)@H ₂ O, (b); the Fermi energy is set to zero.	80
Figure 25. PDOS of O-TaON(010), (a) and O-TaON(010)@H ₂ O, (b); Fermi energy is set to zero.	82
Figure 26. Comparative band structure of O terminated TaON(010) and TaON(010)@H ₂ O; Fermi energy is set to zero.	82
Figure 27. Energy level diagram and schematic representation of O and N terminated TaON.	83
Figure 28. Optimized geometric structures of D (a), A (b) and D-A-D (c).....	85
Figure 29. Contours of the HOMO and LUMO of D (a), A (b) and D-A-D (c)....	86
Figure 30. Orbital correlation diagram for D , D-A-D , and A	87
Figure 31. Energy level diagram of the neutral, mono, and di-cationic state of D	88
Figure 32. Energy level diagram of the neutral, mono, and di-cationic state of D-A-D	89
Figure 33. UV-vis Spectra of A , D , and D-A-D at B3LYP/6-31G**.....	91
Figure 34. UV-Vis Spectra along with Optical band gaps of Neutral, Mono, and Di-Cationic states of D-A-D at B3LYP/6-31G**.....	93
Figure 35. Optimized Geometric Structure of HTM along with side view.....	97
Figure 36. Energy level diagram of HTM.	97
Figure 37. UV-vis Spectra of BSD, EDOS, and HTM at CAM-B3LYP/LanL2DZ.	100

Figure 38. Optimized Geometric Structure of the HTM-N3-TiO ₂ system; for simplicity reason, some of the hydrogen atoms are omitted.....	101
Figure 39. Contours of HOMO and LUMO of Zn Porphyrin-Furan dyes.....	102
Figure 40. Contours of Occupied and Unoccupied NBO of Zn Porphyrin-Furan dyes.....	103
Figure 41. TD-DFT simulated UV-vis spectra of Zn Porphyrin-Furan dyes...	104
Figure 42. Optimized Geometric Structure of Ti ₁₆ O ₃₂ and Ti ₂₈ O ₅₆ clusters...	107
Figure 43. Optimized Geometric Structure of 7Py-Ti ₁₆ O ₃₂	107
Figure 44. Contours of the HOMO and LUMO of Ti ₁₆ O ₃₂	110
Figure 45. Density of states plots of Ti ₁₆ O ₃₂ , nPy and nPy-Ti ₁₆ O ₃₂ bounded complexes.....	112
Figure 46. First allowed electronic excitation energy of nPy and nPy-Ti ₁₆ O ₃₂ composites.....	113
Figure 47. Reference optimized geometric structure of 5Py ⁺ -X (X=NH ₃ , CO ₂ , and CO).....	115
Figure 48: Frontier Molecular Orbitals of 3Py/3Py ⁺ and 3Py/3Py ⁺ -X (X = NH ₃ , CO ₂ , CO(1) and CO(2)), Using B3LYP/6-31G (d) and UB3LYP/6-31G (d) Level of Theory.	118
Figure 49. UV-Vis/UV-Vis-near-IR of 3Py (red), 3Py-NH ₃ (blue), 3Py ⁺ (green), and 3Py ⁺ -NH ₃ (black).	119
Figure. 50. Illustration of photocatalytic process of degradation in pollutants in TiO ₂	121

Abbreviations, Symbols, and Nomenclature

A	Acceptor
B3LYP	Becke, 3-Parameter, Lee Yang-Parr
BiVO ₄	Bismuth Vanadate
COPs	Conjugated Organic Polymer
CO ₂	Carbon Dioxide
CO	Carbon Monoxide
CBM	Conduction Band Minimum
CH ₃ NH ₃ PbX ₃	Methyl Ammonium Led Halide
DFT	Density Functional Theory
D-A-D	Donor-Acceptor-Donor
D	Donor
DSSC	Dye-Sensitized Solar Cell
DOS	Density of State
EA	Electron Affinity
E _b	Exciton Binding Energy
FF	Fill Factor
GR	Graphene
g-C ₃ N ₄	Graphitic Carbon Nitride
HTM	Hole Transporting Material
HOMO	Highest Occupied Molecular Orbital
IP	Ionization Potential
J _{sc}	Short-Circuit Current Density
LanL2DZ	Los Alamos National Laboratory 2-Double Z
LUMO	Lowest Unoccupied Molecular Orbital

N3	Cis-bis(isothiocyanato)bis(2,2'-bipyridyl-4,4'-dicarboxylato)ruthenium(II)
NH ₃	Ammonia
Ov	Oxygen Vacancy
PBC	Periodic Boundary Condition
PEC	Photoelectrochemical
PCE	Power Conversion Efficiency
PSC	Polymer Solar Cell
PPy	Polypyrrole
PANI	Polyaniline
PCBM	Phenyl-C61-Butyric Acid Methyl Ester
ΔQ_H	Partial Charge Difference
RHE	Reference Hydrogen Electrode
SDSC	Solid-State Dye Sensitized Solar Cell
Se	Selenium
TD-DFT	Time Dependent-DFT
TaON	Tantalum Oxynitride
TiO ₂	Titanium Dioxide
UV-Vis	Ultra-Violet and Visible
VBM	Valence Band Maximum
V _{oc}	Open Circuit Voltage
λ_{max}	Maximum Wavelength
η_{CT}	Charge Transportation Efficiency
Δp	Electron Density Difference

List of Accompanying Material

In the Appendix the following published and submitted articles are given.

Journal Papers Published:

Article 1.

H. Ullah, A. A. Tahir, T. K. Mallick, "Structural and electronic properties of oxygen defective and Se-doped p-type BiVO₄(001) thin film for the applications of photocatalysis." *Appl. Catal., B: Environ.*, vol. 224, pp. 895-903, May. 2018.

The idea of this work was proposed by the first author and then the theoretical simulations were performed. The paper was written under the guidance of supervisors. All authors contributed to the discussion and reviewed the paper.

Article 2.

S. N. F. M. Nasir, H. Ullah, M. Ebadi, A. A. Tahir, J. S. Sagu, M. A. Mat Teridi, "New insights into Se/BiVO₄ heterostructure for photoelectrochemical water splitting: A combined experimental and dft study." *J. Phys. Chem. C*. vol. 121, pp. 6218-6228, Feb. 2017.

The idea of this work was proposed by the second and last authors and the experimental work was performed by first author under the guidance of last author. The theoretical work was designed and carried out by second author. Initially, the paper was written by first author under the guidance of supervisors. Finally, the paper was modified, corrected and finalized by second author, under the supervision of supervisors.

Article 3.

J. Safaei, H. Ullah, N. A. Mohamed, M. F. M. Noh, M. F. Soh, A. A. Tahir, N. A. Ludin, M. A. Ibrahim, W. N. R. W. Isahak, M. A. M. Teridi, "Enhanced photoelectrochemical performance of Z-scheme g-C₃N₄/BiVO₄ photocatalyst." *Appl. Catal., B: Environ.*, vol. 234, pp. 296-310, Oct. 2018.

The idea of this manuscript was initiated by second and ninth author. The experimental work was performed by first author under the supervision of second and ninth author. All the theoretical simulations were carried out by second author along with their writeup. The paper was proofread by second and rest of authors. All authors contributed to the discussion and reviewed the paper.

Article 4.

H. Ullah, A. A. Tahir, S. Bibi, T. K. Mallick, S. Z. Karazhanov, "Electronic properties of β -TaON and its surfaces for solar water splitting." *Appl. Catal., B: Environ.*, vol. 229, pp. 24-31, Aug. 2018.

The idea of this work was proposed by first author under the supervision of second author. The calculations of this work were carried out by first author under the supervision of last author. The paper was written by first author and checked by third author. The work was finalized under the supervision of supervisors. All authors contributed to the discussion and reviewed the paper.

Article 5.

H. Ullah, S. Bibi, A. A. Tahir, T. K. Mallick, "Density functional theory study of selenium-substituted low-bandgap donor-acceptor-donor polymer." *J. Phys. Chem. C*. vol. 120, pp. 27200–27211, Nov. 2016.

The idea of this work was proposed by first author under the supervision of third author. The calculations for this work were performed and analyzed by first author. The paper was written by first author and checked by second author. The final draft was corrected by third and fourth authors.

Article 6.

H. Ullah, S. Bibi, A. A. Tahir, T. K. Mallick, "Donor-acceptor polymer for the design of all-solid-state dye-sensitized solar cells." *J. Alloys Compd.*, vol. 696, pp. 914-922, Mar. 2017.

The material design and solid-state DSSC idea was proposed by first author under the supervision of third author. All the calculations for this manuscript were carried out by first author. The paper writing was completed by first author and checked by second author. The work was proofread by third and fourth authors.

Article 7.

V. K. Narra, H. Ullah, V. K. Singh, L. Giribabu, S. Senthilarasu, S. Z. Karazhanov, A. A. Tahir, T. K. Mallick, H. M. Upadhyaya, "D- π -A system based on zinc porphyrin dyes for dye-sensitized solar cells: Combined experimental and DFT-TDDFT study." *Polyhedron*. vol. 100, pp. 313-320, Nov. 2015.

Initially, the idea of this work was proposed by first author under the supervision of supervisors. Second author had been asked to perform theoretical simulations for the already experimental work. All the theoretical simulations and their writeup were carried out by second author. The paper was re-modified by first author under the supervision of supervisors.

Article 8.

H. Ullah, A. A. Tahir, T. K. Mallick, "Polypyrrole/TiO₂ composites for the application of photocatalysis." *Sens. Actuators, B: Chem.*, vol. 241, pp. 1161-1169, Mar. 2017.

The initial concept was conceived by first and second authors. All the theoretical simulations were performed and evaluated by first author. The work was performed and written by the author under the guidance of the supervisors. All authors contributed to the discussion and reviewed the paper.

Article 9.

S. Bibi, H. Ullah, S. M. Ahmad, A.-u.-H. Ali Shah, S. Bilal, A. A. Tahir, K. Ayub, "Molecular and electronic structure elucidation of polypyrrole gas sensors." *J. Phys. Chem. C*. vol. 119, pp. 15994-16003, Jun. 2015.

The idea of this work was proposed by first and second authors and the calculations were performed by first author under the guidance of second author. The paper was written by first and third author under the guidance of

second author. Finally, the manuscript was checked and corrected by the rest of authors.

Article 10.

A. Ali Tahir, H. Ullah, P. Sudhagar, M. Asri Mat Teridi, A. Devadoss, S. Sundaram, "The application of graphene and its derivatives to energy conversion, storage, and environmental and biosensing devices." *The Chemical Record*. vol. 16, pp. 1591-1634, Jun. 2016.

The concept of this review was conceived jointly between the first, second, third, fourth, fifth, and sixth authors. The work was jointly written by all these authors, while the format and references issues were performed by second author under the guidance of supervisors.

Other co-authored papers

Article 11.

M. Kamran, H. Ullah, A. S. Anwar-ul-Haq, S. Bilal, A. A. Tahir, K. Ayub, "Combined experimental and theoretical study of poly (aniline-co-pyrrole) oligomer." *Polymer*. vol. 72, pp. 30-39, Aug. 2015.

The idea of this manuscript was given by second author. The experimental work was performed by first author under the guidance of second author. The

theoretical simulations and paper writeup were carried out by second author. The manuscript was finalized under the supervision of rest of authors.

Article 12.

H. Ullah, "Inter-molecular interaction in polypyrrole/TiO₂: A DFT study." *J. Alloys Compd.*, vol. 692, pp. 140-148, Jan. 2017.

The idea, simulations setup and manuscript writeup was conceived by first author. This work belonged to author previous and part time research.

Article 13.

B. Y. Alfaifi, H. Ullah, S. Alfaifi, A. A. Tahir, T. K. Mallick, "Photoelectrochemical solar water splitting: From basic principles to advanced devices." *Veruscript Funct. Nanomater.*, vol. 2, pp. 1-26, Feb. 2018.

This review was proposed by fourth author and performed by first and second authors. All authors contributed to the discussion and reviewed.

Article 14.

R. Ullah, H. Ullah, S. Bilal, K. Ali, "Oligomeric synthesis and density functional theory of leucoemeraldine base form of polyaniline." *J. Mol. Struct.*, vol. 1127, pp. 734-741, Jan. 2017.

The idea of this work was proposed by second author and the first author had been asked to perform the experimental work. All the theoretical simulations

were performed by second author. The paper was written by first and second author under the supervision of supervisors. All authors contributed to the discussion and reviewed the paper.

Article 15.

Z. Ullah, A. Rauf, M. Yaseen, W. Hassan, M. Tariq, K. Ayub, A. A. Tahir, H. Ullah, "Density functional theory and phytochemical study of 8-hydroxyisodiospyrin." *J. Mol. Struc.*, vol. 1095, pp. 69-78, 2015.

The idea of this work was jointly proposed by second and last author. The experimental and theoretical simulations were performed by first author under the supervisor of last author. The paper was written by first author under the guidance of last author. All authors have given final proof to it.

Article 16.

Z. Ullah, A. Rauf, M. Tariq, A. A. Tahir, K. Ayub, H. Ullah, "Phytochemical, spectroscopic and density functional theory study of diospyrin, and non-bonding interactions of diospyrin with atmospheric gases." *Spectrochim. Acta, Part A*. vol. 141, pp. 71-79, Apr. 2015.

This work was initially proposed by second and last author. The experimental and theoretical simulations were performed by first author under the guidance of second and last authors. All authors have helped in the writup of this manuscript.

Article 17.

Hyeong Pil Kim, Anil Kanwat, Habib Ullah, D.G, Xiuling Li, Jeongmo Kim, W. J. Silva, F.K. Schneider, Abd. Rashid bin Mohd Yusoff, Jin Jang, Deji Akinwande, A. A. Tahir, and Mohammad Khaja Nazeeruddin. “*Improving Charge Transport and Stability of Perovskite Thin Film Transistors by Crosslinking with Diethyl-(12-phosphonododecyl)phosphonate*” Ready to submit **Nature Chemistry**.
2018.

The idea of this work was proposed by first and third authors under the supervision of eighth author. A.R.B.M.Y., W.J.D.S., F.K.S. and J.J. developed the basic concept and coordinated the project. A.R.B.M.Y., A.K., H.P.K. and J.K. fabricated, characterized, optimized transistors performance and carried out the all characterizations and measurements. W.J.D.S. and F.K.S. performed simulation works and carried out all analysis. H.U. performed and write the DFT section under the supervision of M.A.M.T and A.A.T. A.R.B.M.Y., W.J.D.S., M.A.M.T., H.U., J.J. and M.K.N. wrote the initial draft of the manuscript. All authors contributed to the discussion and reviewed the paper.

CHAPTER 1: Introduction

Clean energy and a sustainable environment are grand challenges that the world is facing which can be addressed by converting solar energy into transportable and storable fuels. This solar energy conversion can be either performed by photovoltaic or photocatalytic technique. In photovoltaic solar cell, when sunlight shines on a suitable semiconductor, it produces photoexcitation which directly generates electric current. On the other hand, when sunlight irradiates on an ideal photocatalyst, its ground state electrons jump to excited state which produce holes. Alternatively, these holes and electrons cause photo-oxidation and reduction of water, produces O_2 and H_2 .

Chemical fuels such as hydrogen, produced from renewable resources (water and sunlight) and chemicals i.e., methanol, ethanol, methane and syngas by reduction of CO_2 back to fuel can make solar energy highly distributable, from small to large-scale applications. Currently, most developed renewable energy sources are based on electricity generation or thermal energy and cannot fulfill the energy transportation and storage demand. Therefore, the conversion of solar energy into electricity or chemical fuels as a vital future energy carrier is the main challenge and technical advancement is required to overcome this to provide clean energy to the world (see Fig 1). The main scientific and technological challenges for efficient solar energy conversion, energy storage, and environment applications are the stability, durability, and performance of low-cost functional materials.

Solar energy harvesting via photovoltaic effect is one the challenging tasks to current renewable energy scientists. Researchers are struggling for designing a cheap, liable, elastic, and environmental friendly optoelectronic device with

high efficiency [4-7]. Silicon-based materials are ideal in the current solar cells technology but having a high cost, high operation temperature; limits its portability and versatility [8]. A step toward the development of low-cost, environmentally friendly, easily synthesizable, flexible and efficient material for solar cells lead scientists to the use of conjugated organic polymers (COPs). COPs are emerging as promising materials due to their stability, low-cost processing and ability to form tunable and robust structures. Four prominent generations of COPs are being explored by scientists, which has application in the field of solar to power energy conversion [9-13].

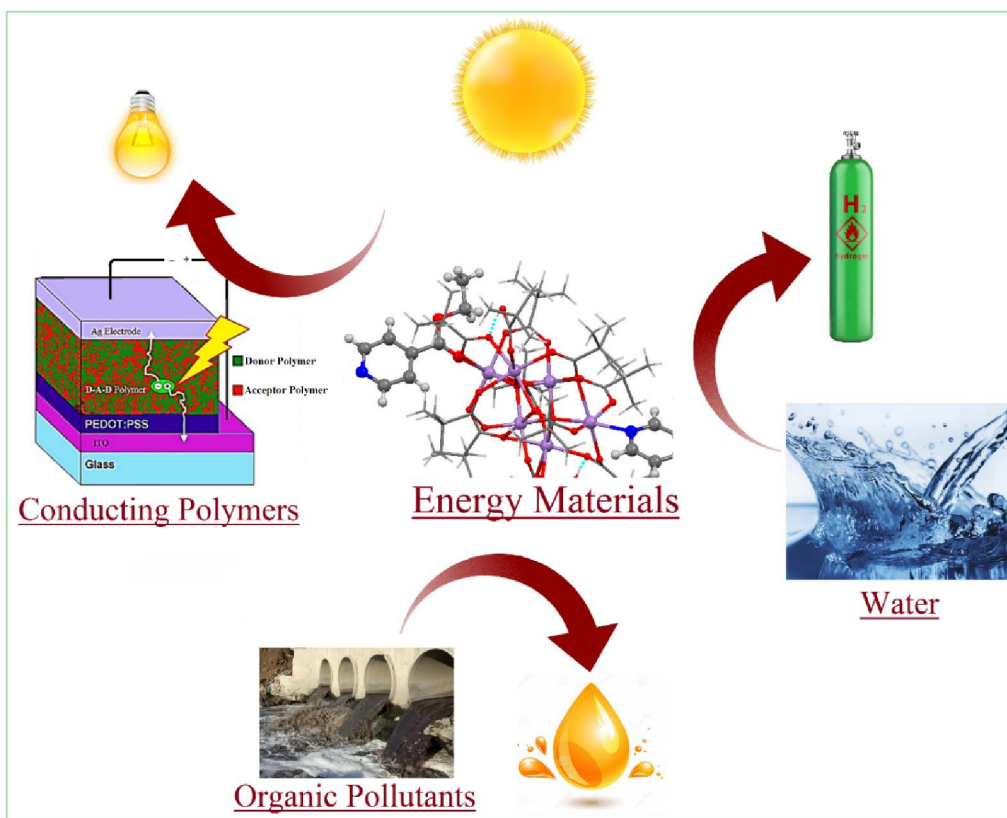


Figure 1: Applications of energy materials for solar energy conversion and environment.

1.1. Aims and Objectives of Research

- Solid state DFT simulations of metal oxides will be performed to understand the PEC water splitting mechanism.
- Reviewing the available literature of energy materials such as metal oxides, conducting polymers, and composite materials; disseminating the technology into its multiple constituents and identifying routes to designing higher performing photocatalytic and photovoltaic solar cells.
- Computational simulations, using first principal Density Functional Theory to design suitable materials based on their electronic structure properties such as surface formations energy, density of state (DOS), band structure, effective masses of electron and hole, electron-phonon coupling, charge transferring, re-organization energy, open-circuit voltage, interaction energy, molecular orbitals, and UV/Vis-near-IR spectroscopy.
- To model and suggest such a polymer (combination of donor and acceptor moieties) that can be used in the bulk heterojunction; organic solar cell, having enhanced V_{OC} , J_{SC} , and fill factor (FF). Finally, how theoretical investigation will minimize the synthetic effort for the future experimentalists.
- Surface and interface engineering of earth-abundant electroactive materials through doping, vacancy, and heterostructure formation (with other electroactive materials) to improve charge carrier separation for the overall solar cell performance.

1.2. Research Methodology

Literature of the already reported photocatalysts and organic photovoltaic cells are studied to understand the scientific problem in detail. After pointing out the drawbacks/faults in the existing materials, different first-principles method's softwares were comprehensively reviewed. Different important simulating tools of the systems were identified and verified.

1.2.1. First-Principles Density Functional Theory (DFT)

In computational materials science, first principles DFT calculations can easily predict and calculate the behavior of material on the basis of quantum mechanical considerations. Modern DFT techniques can evaluate the electronic structure from a potential, acting on the system's electrons. This DFT potential is the sum of external potentials (V_{ext}), determined solely by the structure and the elemental composition of the system, and an effective potential (V_{eff}), denotes inter-electronic interactions. So, super-cell of a material with n electrons can be studied as a set of n one-electron Schrödinger like equations, which are also known as Kohn–Sham equations [14].

1.2.1.1. Time-dependent Density Functional Theory (TD-DFT)

TD-DFT is a quantum mechanical theory which investigate the properties and dynamics of many-body systems in the presence of time-dependent potentials, such as electric or magnetic fields. TD-DFT calculations can incorporate environmental effects and quickly give best quantitative fit to UV–vis spectra (excitation energy) of polymeric species, especially using hybrid functionals (B3LYP). So, UV–vis, UV–vis-near IR spectra, polaron, bipolaron, exciton

binding energy (E_b), and optical gap are simulated with TD-B3LYP/6-31G** level of theory.

1.2.1.2. Periodic DFT Methods for Metal Oxides.

First principle periodic boundary DFT simulations are carried out, using Quantum ESPRESSO [15] and QuantumWise-ATK [16] while the results are visualized on VESTA [17] and vnl 2017.0 [18]. Generalized gradient approximation (GGA) at Perdew-Burke-Ernzerhof (PBE) exchange-correlation functional is used for the structural and energy optimization [19]. The local density approximation (LDA) method is found to be superior in reproducing the experimental data of BiVO_4 , compared to pure GGA and meta GGA (MGGA). A 5x5x1 Monkhorst-Pack k-grid and energy cutoff of 100 Ry is employed for the geometry relaxation and self-consistent (SCF) simulations of BiVO_4 ; consisting of 96 atoms. The Broyden-Fletcher-Goldfarb-Shanno algorithm (BFGS) is used for the structural relaxation [20].

1.2.1.3. Bulk, Slab, O Defective, and Se Doped- BiVO_4 .

The experimentally observed crystallographic file of BiVO_4 ; clinobisvanite structure is used as such which has Hall symmetry space group of I2/b with lattice parameters of $a = 5.147 \text{ \AA}$, $b = 5.147 \text{ \AA}$, $c = 11.7216 \text{ \AA}$, and $\gamma = 90^\circ$ [21]. As an input structure for the calculations; the 24 atoms primitive unit cell and its 2x2x2 supercell along with (001) direction with 10 \AA vacuum, is considered as a model for the periodic boundary condition (PBC) DFT simulations. Generally, it is believed that clinobisvanite monoclinic BiVO_4 exists in (001) orientation so, that is why the (001) slab is opted for the theoretical simulations to represent its experimental thin film [22]. Moreover, the unreconstructed (001)

termination possesses low surface energy and as a result, represents the most probable surface termination [22]. Stability of these different slabs are confirmed from their positive formation energy and electrostatic potential.

1.2.1.4. Electronic Properties and Effective Masses of Charge carriers

A 5x5x5 Monkhorst-Pack k-grid with the same energy cutoff is used for the non-SCF part to get the density of states (DOS) and partial DOS (PDOS), band structure and effective masses of photogenerated electrons and holes. The DFT occupied and unoccupied DOS are considered as the VB and CB edges, respectively; separated by an energy equal to the known optical band gap.[23] The band structure simulations were performed along the appropriate direction of the Brillouin zone. Meta-GGA is used for the band gap simulations of TaON in the Truhlar Blaha exchange functional and the correlation functional of Perdew-Zunger (LDA) in the form of TB09LDA [24]. The effective masses of the photogenerated electrons (m_e^*) and holes (m_h^*) along the suitable directions of k-points are calculated by fitting parabolic approximation around the bottom of the CBM or the top of the VBM, respectively; using equation 1.

$$m^* = \hbar^2 (d^2 E/dk^2)^{-1} \quad (1)$$

where \hbar is the reduced Planck constant, E is the energy of an electron at wave vector k in the same band (VBM or CBM). To acquire the validity of the parabolic approximation within the specified space, the region for parabolic fitting is controlled by an energy difference of 1 meV along a particular direction around the VBM or CBM.

1.2.1.5. Surface Formation Energy

As we know, that if the surface formation energy is in negative, then its mean that the material should dissociate, i.e. the crystal should disperse into the surrounding medium. For all of the slabs discussed, we got positive surface formation energy, which confirmed their thermodynamically stability.

The surface formation energy of pristine and Se-doped BiVO₄(001) slabs are calculated using equation 2, while that of O defective BiVO₄(001) is calculated with the help of equation 3.

$$E_{\text{surf}} = \frac{1}{2A} (E_{\text{slab}} - NE_{\text{bulk}}) \quad (2)$$

$$E_{\text{vf}} = E_{\text{slab}} + N_{\text{vac}} \times 1/2E_{\text{O}_2} - E_{\text{slab(st)}} \quad (3)$$

In eq 2, A is the cross-sectional area of slab, E_{slab} is the ground state total energy of slab, NE_{bulk} represents number of bulk in the slab. In eq 3, E_{vf} is the vacancy formation energy, N_{vac} , number of vacancy, E_{O_2} , energy of oxygen molecule and $E_{\text{slab(st)}}$ is the total energy of stoichiometric slab.

1.2.1.6. Bulk, Slab, and water interacted TaON Surfaces

On the other hand, β -TaON has a monoclinic structure in the $P 2_1/C$ space group [25]. The primitive unit cell contains 12 atoms and the initial crystal structure parameters in our calculations are taken from experimental data [26]. After optimizing the lattice parameters of the unit cell, a (2x2x2) supercell was constructed. (100), (010) and (001) slabs for each O, N, and Ta atoms were built by cleaving appropriately the 2x2 supercell of TaON. For the slab model calculations of surface energies and band edge positions, the thickness of the slabs were four primitive unit cells of TaON (5 Å thick having 48 atoms), to ensure that the center of the slab can be regarded as the bulk phase.

1.2.1.7. DFT Methods for Molecular Systems

Molecular DFT simulations of the donor, acceptor, and their combinations have been carried out on Gaussian 09 [27] while visualizations are achieved on *Gabedit* [28] and *GaussView*. [29] Electronic structure properties of different oligomers and their co-oligomeric combination are carried out with the help of density functional theory (DFT) at hybrid functional of the B3LYP/6-31G** level of theory. The oligomeric chain length is optimized to accurately represent their polymeric nature. From computational and accuracy point of view, TD-DFT is optimistic between semi-empirical and wave function approaches [30-32]. TD-DFT calculations can incorporate environmental effects and quickly give best quantitative fit to UV-vis spectra (excitation energy) of these species, especially using hybrid functionals (B3LYP) [32-34]. In the case of approximate DFT, negative orbital energies (HOMO and LUMO) do not give accurate ionization potentials (IP) and electron affinities (EA), but the deviation is about 1 eV. Since the error is method dependent and consistent for all oligomers, orbital energies can be still used to examine trends consistently. Our simulated results have also a nice correlation with the experimental data, so, that is why the current level of theory is employed for the rest of simulations [35,36].

1.2.1.8. Computational Study of Polymer Solar Cell

Key parameters of the photovoltaic system such as reorganization energy (λ), Polaron, Bi-polaron, UV-Vis spectra, and exciton binding energy (E_b) are also simulated with the said level of theory. Reorganization energy (λ) is directly associated with the geometrical distortion of a chemical substance when it changes from neutral to cationic state. The internal reorganization energy of **A**,

D and **D-A-D** are simulated, using the adiabatic potential energy surface method with equation 4 (Table 2).

$$\lambda = \lambda_1 + \lambda_2 = (E_0^* - E) + (E_+^* - E_+) \quad (4)$$

The E_0 and E_+ are the energies of neutral and cationic species in their lowest energy geometries and E_0^* and E_+^* represent the energy of a neutral molecule at the geometry of charged molecule and charged molecule at the geometry of the neutral molecule.

We have simulated the exciton binding energy (E_b) from the energy difference of neutral exciton and the two free charge carriers, using an expression such as $E_b = E_{\text{Band gap}} - E_{\text{Optical gap}}$.

The stability, perturbation in electroactivity and conductivity upon mixing of donor and acceptor species are estimated from the energy of HOMO, LUMO, and band gap. The electrons and holes carrying nature are simulated from the reorganization energy and also from the contours of HOMO and LUMO, respectively. UV-vis, UV-Vis-Near IR spectra and an optical gap of the **D-A-D** are simulated, using TD-B3LYP/6-31G** level of theory.

1.2.1.9. Theoretical Performance of Polymer Solar Cell

To get the high efficiency of bulk heterojunction (BHJ) polymer solar cell, scientists are struggling to achieve higher (i) short-circuit current density (J_{sc}) (ii) open circuit voltage (V_{oc}) (iii) and a high fill factor (FF). The efficiency of a PSC can be obtained using equation 5 [7],

$$\eta = \frac{V_{oc} J_{sc} FF}{P_{in}} \times 100 \quad (5)$$

where η is efficiency and P_{in} is the power density of incident light.

The J_{sc} has an inverse relation with the band gap value in PSC; lower the band gap much higher will be the short-circuit current density and vice versa. So, narrow band gap polymer can harvest sufficient amount of sunlight and lead to enhanced J_{sc} . Furthermore, J_{sc} is also dependent on the LUMO energy levels of the hole transporting material (here **D-A-D**) and acceptor (PCBM) in the PSC device. If the difference is more than 0.3 eV (equation 3), then the device will result in high J_{sc} , and this energy difference can also be correlated with charge transport (η_{CT}) within PSC. The smaller-scale phase separation creates larger area of interfaces where charge separation can take place. A large energy difference between the LUMO of **D-A-D** (donor) and the LUMO of PCBM (acceptor) is required for ultrafast photoinduced electron transfer [37]. The next important parameter of the PSC is the V_{oc} , which can be tuned/enhanced by lowering down the HOMO level of the polymer in the BHJ. Theoretically, the V_{oc} of PSCs can be estimated from the orbital difference of **D-A-D** (HOMO) and PCBM (LUMO), using equation 6 [7].

$$V_{oc} = e^{-1} \times (|E_{HOMO}^{Donor}| - |E_{LUMO}^{Acceptor}| - 0.3 \text{ eV}) \quad (6)$$

Where e^{-} is the elementary charge, E is the energy level and 0.3 eV is an empirical value for efficient charge separation (minimum difference of the LUMOs of donor and acceptor). The final crucial parameter in getting the high efficiency of PSC is the FF, which is simply a ratio between the maximum obtainable power and the product of V_{oc} and J_{sc} .

1.2.1.10. Polaron, Bi-polaron, and Exciton Binding Energy

It is generally believed that PSCs require well-controlled movement of charges for efficient photon conversion [38]. In conjugated polymers, usually polaronic and bi-polaronic states appear within the parent band gap [39] upon doping with

appropriate doping agents. These are the key tools for charge storage and charge transportation in COPs. Charge and the associated distortion along the backbone of COP create either polaron or bi-polaron. Single charge and the associated distortion are termed as polaron (delocalized state), denoted as E_p while a pair of charges and their distortion in the polymeric body is regarded as bi-polaron. Bi-polarons states are comparatively stable, localized and less electroactive to that of polarons. Donation of charge by a particular conjugated system is followed by intra-molecular relaxation which can be precisely called as polaronic effect. Polaron-binding energy can be easily obtained from the reorganization energy (λ) using an expression such as $E_p = (1/2 \lambda)$. On the other hand, exciton binding energy or an electron–hole binding energy is the amount of that barrier (coulombic energy) with which the lowest unoccupied orbital accepts an extra electron and left behind the occupied orbital as degenerate. We have simulated the exciton binding energy (E_b) from the energy difference of neutral exciton and the two free charge carriers, using an expression such as $E_b = E_{\text{Band gap}} - E_{\text{Optical gap}}$.

1.2.1.11. Partial Charge Difference Analysis

Partial charge difference on the conjugated backbone of HTM is simulated by using equation 7. NBO charge on a particular atom in the neutral as well as in the cationic state is considered for the charge transferring phenomena in HTM. Partial charge difference analysis of HTM predicts that H and Se atoms are responsible for the charge donation.

$$\Delta Q_X = \sum Q_{X_i^+} - \sum Q_{X_i^0} \quad (7)$$

Where ΔQ is a charge on particular X atom, either in cationic (X^+) or neutral state (X^0).

1.2.1.12. Theoretical simulations for Dye-Sensitized Solar Cell

Prior to property simulations of the interacting systems such as N3-HTM, N3-TiO₂, and HTM-N3-TiO₂; the DFT method was confirmed through correlation of the HTM simulated HOMO, LUMO and band gaps with experimental data (see Article 6) [35,36]. Hybrid functional such as B3LYP has been successfully applied for this type of polymers and has been found to be superior over other functionals [36,40-42]. In the case of inter-molecular study of the proposed model, N3 was sandwiched between TiO₂ and HTM and then optimized at B3LYP functional with LanL2DZ basis set. The interaction energy of these three components is simulated with the help of inter-molecular energy simulation as explained elsewhere [43-47]. The quantitative and qualitative behavior of charge transferring phenomena of the entitled complexes are simulated at natural bonding orbital (NBO) analysis. The prediction of stability, electroactivity, conductivity and donor/acceptor nature are estimated from ionization energy (IP), electron affinity (EA), and band gap analysis. UV-vis spectra and Δ SCF energy gap (optical gap) were simulated in a solvent medium such as chlorobenzene, using a conductor like polarized continuum model (CPCM) at TD-B3LYP/LanL2DZ level which unveils our results regarding the optical and electrical properties.

1.3. Contribution of the papers in the field

- Substitution of O with Se atom (1-4% doping), result a stable *p*-type Se/BiVO₄ thin film which improve the overall photocatalytic efficiency.
- The importance of direct Z-scheme heterostructure, made of Se and BiVO₄ for the photoelectrochemical water splitting.
- g-C₃N₄/BiVO₄ heterostructure for the enhanced photoelectrochemical performance.
- Predicting the suitable surfaces of β -TaON from periodic density functional theory for solar water splitting.
- The concept of selenium-substituted low-bandgap donor-acceptor-donor polymer for high-performance polymer solar cell.
- The effect of solid-state electrolyte in the dye-sensitized solar cells.
- Designing composites material (organic polymer and metal oxides) for the application of photocatalysis and gas sensing.

1.4. Outline of the thesis

Chapter 1 introduces the importance and varieties of solar energy conversion and its basic understanding along with inherent problems. Different simulating techniques and the main findings of article 1 and 10, explaining photocatalytic water splitting, organic solar cell, dye-sensitized solar cell, and gas sensing applications are briefly summarized. This section also describes the novel energy materials and their applications.

Chapter 2 explains the structural and electronic properties of BiVO₄ ultra-thin film. Monoclinic BiVO₄ is has been using as a photocatalyst but due to its inappropriate CB (-4.56 eV vs vacuum) edge position, it has low efficiency. DFT simulations are performed for the pristine, Oxygen defective (O_v), Se doped monoclinic BiVO₄, and heterojunction with Selenium (Se-BiVO₄), to improve the photocatalytic and charge carrier properties. Different doping ratios of Se are employed to find the most suitable and thermodynamically stable BiVO₄ derivatives with an ideal band edges, band gap, and small effective masses of electrons and holes. Finally, our theoretical simulations are counterchecked by our Malaysian collaborative [48] through spectroscopic and photoelectrochemical characterization. Overall, it is found that Se either in the doped (Se@BiVO₄ with doping ratio of about 1-2%) or heterostructure (Se/BiVO₄), result an efficient photocatalyst. In nutshell, this chapter summarize the work of article 1-3 [1,48,49].

Chapter 3 highlights the different characteristic surfaces of an oxynitrides materials such as β -TaON. Although, this material has been using as a

photoanode material in the field of photocatalysis, but the overall performance is very low. Through periodic DFT modeling of its N, Ta, and O terminated surfaces, we found that a mixed phase material [(010)-O and (001)-N terminated] would produce an efficient photoanode for solar water splitting, where one phase performs the oxidation and the other reduction. This chapter summarizes the results from the article 4 [50].

Chapter 4 demonstrates the concept of organic solar cell, made from donor-acceptor-donor polymer. This unique combination of polymer has an optically transparent, near-infrared-absorbing low energy gap with promising attributes for photovoltaic application. Moreover, the polymeric backbone tunes the band gap, optical gap, open circuit (V_{oc}) and short-circuit current density (J_{sc}) in the polymers solar cells. Different characteristic parameters of organic solar cell are theoretically investigated. Moreover, we proposed a bulk heterojunction solar cell, which gives theoretical open circuit voltage of about 1.02 eV. Our theoretical investigation will minimize the synthetic effort of the experimentalist. This chapter describes the results of article 5 [2].

Chapter 5 gives a thorough example of the comprehensive experimental and theoretical investigation of Zinc porphyrin dyes for dye-sensitized solar cell (DSSC). The experimental work of this work was performed by our Indian collaboratives [51]. Moreover, we also propose the design of solid-state DSSC and then its comparison with the traditional liquid electrolyte based DSSC. Although, we have highly efficient DSSCs, but they are facing long-term performance and durability problems which are because of the liquid

electrolytes; causes serious problems such as electrode corrosion and electrolyte leakage. In this solid-state DSSC, we replace the liquid electrolyte with an efficient donor-acceptor-donor polymer. This chapter summarizes the results from the articles 6 and 7 [3,51].

Chapter 6 introduces and summarize the results from the articles 8-10; detailing the sensing behavior and hazardous pollutants degradation. We have designed and proposed a photocatalyst, made of polypyrrole and TiO_2 (composite). The composite materials has an ideal properties to be used for organic pollutants degradation. The stability and suitability of the results materials is confirmed from different theoretical simulations. Moreover, we also predict that polypyrrole can be used as gas sensor for different hazardous gases; either in the laboratory, home or industry. This work was carried out with our Pakistani collaborative [44]. Finally, the last part of this chapter is devoted to the environmental and biosensing applications of graphene and its derivatives [44,52,53].

Chapter 7 describes the conclusion of all the work published and gives recommendations for future work. This chapter also lists the author's contribution to all the articles as well as other related work

1.5. Novel Materials and Solar Energy Conversion

1.5.1. Energy Conversion

The idea of solar energy conversion comes from the photosynthesis in plants. In this process, green plants convert light energy into chemical energy (fuel) via photosynthetic reaction as shown in Fig 2. Solar energy is an alternative to fossil fuels, which convert photons into electricity, fuel, and heat. Moreover, this technology covers light-harvesting technologies such as traditional photovoltaic devices, emerging photovoltaics, solar fuel generation via electrolysis, artificial photosynthesis and other photocatalytic techniques [54]. In this work, the energy conversion has been carried out by photocatalytic and photovoltaic (including dye-sensitized solar cell) process.

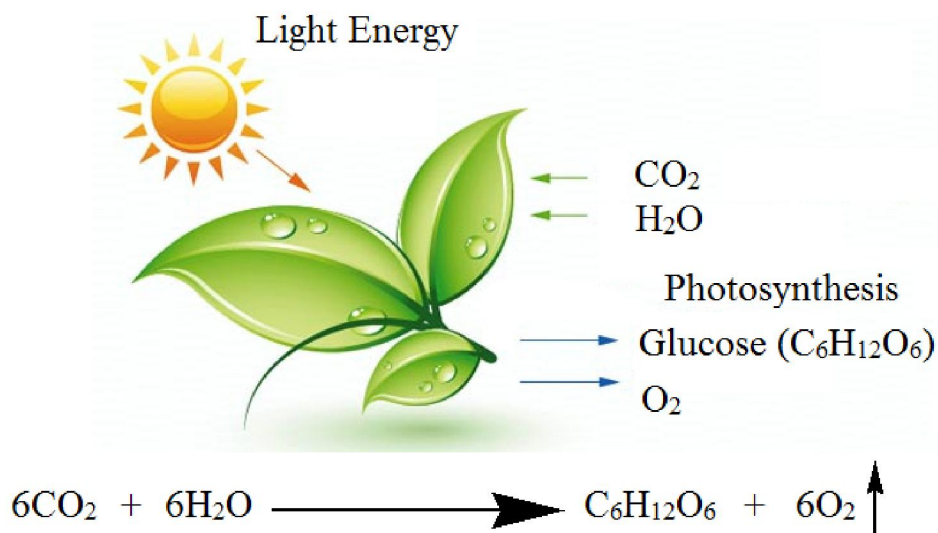
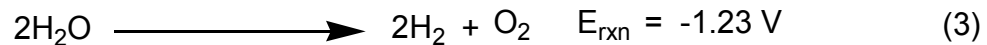
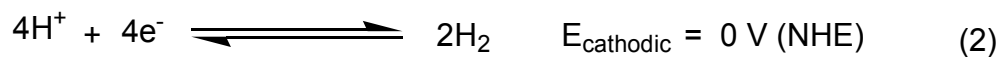
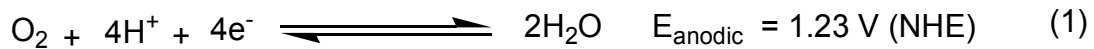


Figure 2. Photosynthesis in plants; a process by which green plants [having Chlorophyll (a) and (b)] use sunlight to produce Energy (glucose) from carbon dioxide and water.

1.5.1.1. Photocatalysis

Solar energy harnessing via photoelectrochemical (PEC) water splitting, using transition metal oxides, is a direct chemical energy conversion and storage technique. Since the discovery of the first photocatalytic water splitting experiment, range of transition metal oxides have been employing to produce solar fuel [55]. An ideal photocatalyst must have valance band (VB) and conduction band (CB), which straddle the redox potentials of photocatalytic reaction, and must have high stability, availability, and narrow band gap which can efficiently absorb the visible part of sun light [56,57].



To date, the current focus semiconductors/photocatalysts are Fe_2O_3 , LaFeO_3 , TaON , LaCrO_3 , LaCoO_3 , TiO_2 , BiVO_4 , ZnS , ZnO_2 , Bi_2WO_6 , SrTiO_3 , BiOX (Cl, Br, I), and etc. Some of these semiconductors have ideal band edges position but they are either unstable or having large band gaps, while some of them are narrow band gap but one of the band edges (either VB or CB) is situated at improper band edge energy (Fig 3) [58]. So, the redox reaction cannot be completed without the external bias potential (see reactions 1-3). Band structure engineering is one of the excellent strategies to tailor the band edges and band gaps of these semiconductors, through doping process.

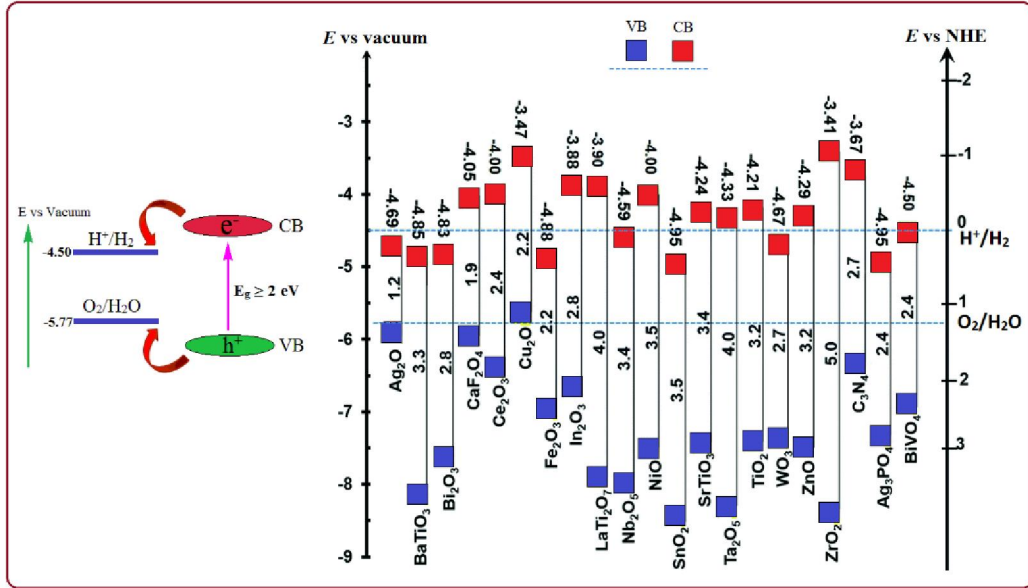


Figure 3. VBM and CBM positions of selected semiconductors at pH 0 with respect to vacuum and normal hydrogen electrode (NHE) levels (in unit of eV): The redox potential of water is shown in blue solid and dotted lines [1].

1.5.1.2. Photovoltaic

The conversion of sunlight (photons) directly into electricity is called photovoltaic (PV) effect, the name comes from the conversion of photons to voltage. Scientists are struggling to design a cheap, liable, elastic, and environmental friendly optoelectronic devices with high efficiency [4-7]. As we know, silicon-based materials are ideal in the current solar cells technology but having a high cost, high operation temperature; limits its portability and versatility [8]. A step toward the development of low-cost, environmentally friendly, easily synthesizable, flexible and efficient material for solar cells lead scientists to the use of conjugated organic polymers (COPs) [7,59]. COPs are emerging as promising materials due to their stability, low-cost processing and ability to form tunable and robust structures. Four prominent generations of

COPs are being explored by scientists, which has application in the field of solar to power energy conversion [9-13].

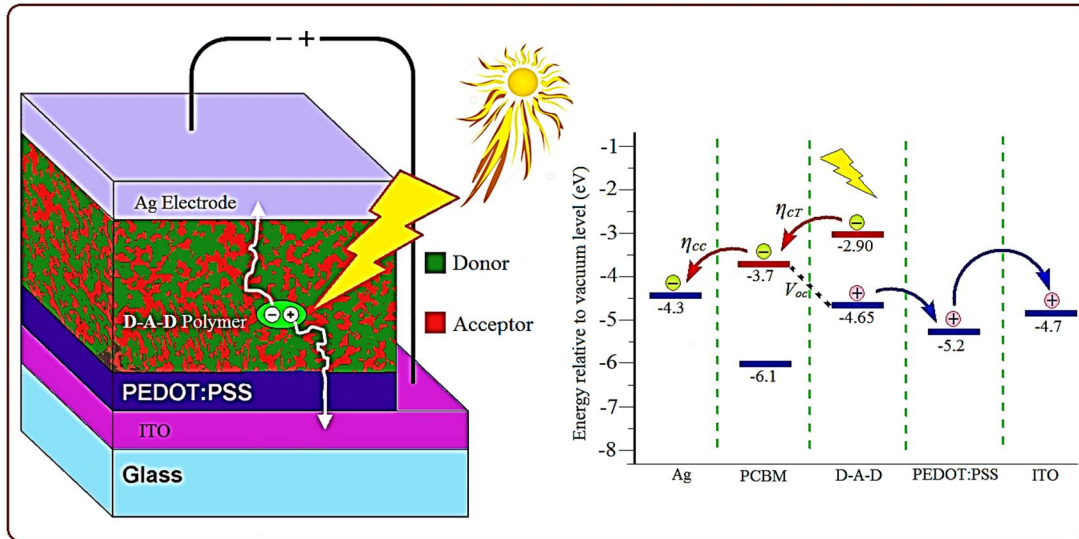


Figure 4. Supposed device structure of the inverted organic solar cell along with energy band diagram of **D-A-D** and other species [2].

COPs have tunable band gap where one can precisely tune the desired band gap, HOMO, and LUMO energy levels during the synthesis, which directly affect the open circuit voltage (V_{oc}), charge transport (η_{cT}) and short-circuit current density (J_{sc}) in the polymer solar cell (PSC) [7]. Generally, polymer with a band gap of more than 4 eV is considered to be insulator while the underneath represents semiconducting nature [60]. Since the discovery of the conducting nature of polyacetylene (PA), researchers are working to minimize this band gap. Many efforts are reported in this regards which are either, co-polymerization, composites, nanoparticles, and donor-acceptor co-polymerization [61].

1.5.1.3. Dye-Sensitized Solar Cell

When Sun strikes the earth for an hour, if that energy is properly harvest then it can fulfill whole the world energy demand for a year, but unfortunately, we are

not able to harvest it properly [62,63]. Solar energy technology in the market is mostly Silicon-based photovoltaic cells, which is a promising renewable energy technique for [64]. Silicon-based solar cells are ideal but having a high cost and high operation temperature limits its portability and versatility, so, it is an urgent need to replace Si with a better and efficient material for photovoltaic applications. Thin film solar technology based on CdTe, *p*-GaAs/*n*-GaAs, and ZnO/CdS/CuInSe₂ etc., exhibiting ~ 20% efficiency, however, this is more expensive and having elements which are not earth abundance and toxic for environment [65].

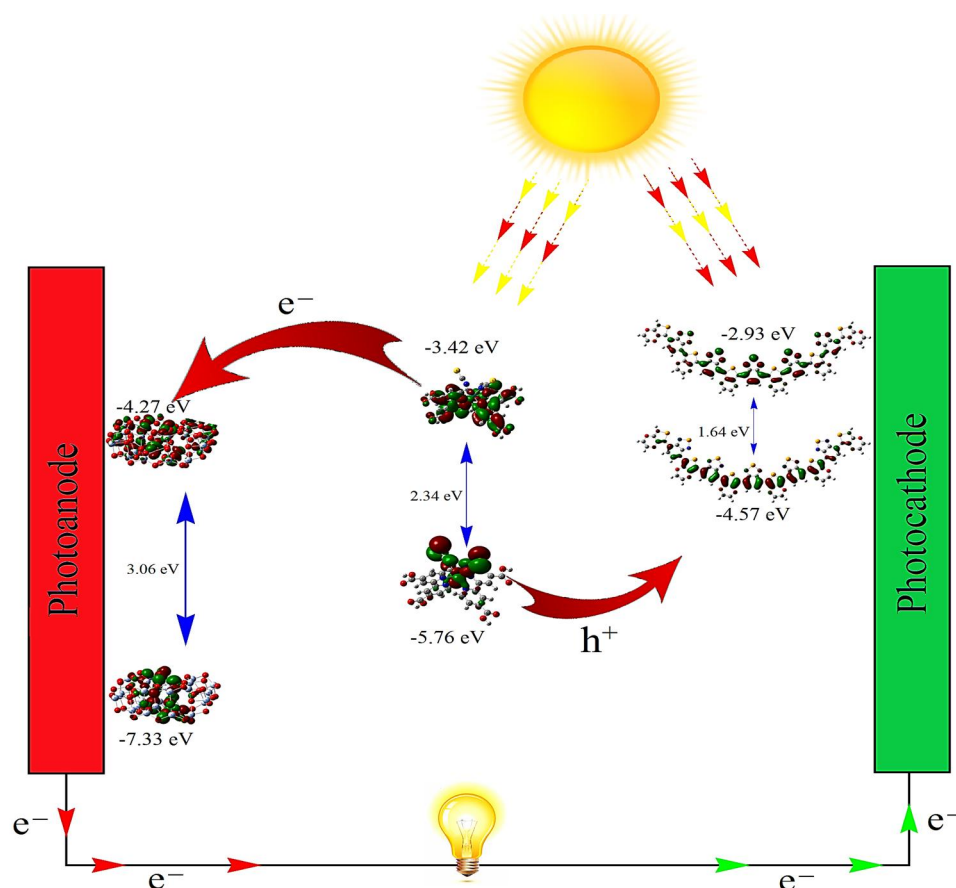


Figure 5. Schematic representation of various processes occurring in DSSCs upon sunlight irradiation. Photoexcitation of dye molecules upon absorption of the photons [3].

Dye-sensitized solar cell (DSSC) is considered as the best way forward to fulfill our energy requirements due to its low-cost, easy fabrication and environmentally friendly [66]. A basic DSSC consists of molecular dye, adsorbed on a mesoporous wide band gap semiconductor oxide (frequently TiO_2), a redox couple (I^-/I_3^-) usually liquid electrolyte and a *p*-type hole collector/counter electrode [51,67]. The dye molecule (photosensitizer) absorbs light and injects its excited electrons into the conduction band of TiO_2 and becomes oxidized. The redox electrolyte acts as an intermediate to transfer holes from dye to counter electrode for regeneration of dye [68-70]. Although, highly efficient DSSCs have been reported but they are facing long-term performance and durability problems which stem from liquid electrolytes; the I^-/I_3^- redox couple, leads to serious problems such as electrode corrosion and electrolyte leakage [71-73]. The crucial solution would be the purely solid-state cells, given the expected issues of any liquid electrolyte, such as leakage, heavyweight and complex chemistry.

1.5.2. Novel Energy Materials

As discussed in the previous section, solar energy can either be harvested by photoelectrochemical or photovoltaic process. The ideal materials must have an ideal band structure which can absorb the visible portion of sunlight, highly efficient, earth abundant, environmental friendly, low cost, easily synthesizable, and stable towards corrosion. Since the discovery of Fujishima and Honda, various semiconductors have been investigated to produce hydrogen as a solar fuel from water, using a visible spectrum of sunlight. However, development of suitable and sustainable semiconductor materials as efficient photoelectrode remains a challenge. A metal oxide such as TiO_2 has band edge positions that

straddle the standard electrochemical potential of $E^\circ(\text{H}^+/\text{H}_2)$ and $E^\circ(\text{O}_2/\text{H}_2\text{O})$, but its large band gap (absorb the UV part of the solar spectrum) accounts for 4 % of the solar irradiance. Although, CdS and CdSe having small band gap and suitable band edge positions but they are not stable under water photooxidation conditions [74,75]. The stable semiconductors such as Fe_2O_3 , WO_3 , and BiVO_4 have been explored for the water splitting application over the last few years [76-82]. Among them, Fe_2O_3 is the most widely studied material for H_2 production. However, the conduction band edge of Fe_2O_3 is too low for spontaneous water photoreduction [83]. As a result, complete water splitting with Fe_2O_3 requires large external bias. While WO_3 having a band gap energy of 2.7 eV limits the theoretical solar-to-hydrogen (STH) efficiency to ca. 4.5% [78]. Donor-acceptor polymer approach can efficiently tune the HOMO-LUMO levels and optical band gap. However, the processes are not so simple, requires a lot of efforts to get insight into the underlying phenomenon [84]. The combination of the donor (electron donating species) and acceptor moieties (electron withdrawing) in a copolymer can tune the optical gap and efficiently harness the solar energy influx which is consequently responsible for the increase of J_{sc} . This would not simply solve our problem but band gap engineering of a polymer can lead to increase the V_{oc} , followed by efficient exciton dissociation in the PSC [85].

1.5.2.1. Metal Oxides

The main scientific and technological challenges for efficient solar energy conversion, energy storage, and environment applications are the stability, durability, and performance of low-cost functional materials. Despite the work of last four decades, since the first demonstration of solar water splitting using

TiO₂ electrode, the optimal materials remain to be discovered. Many semiconductor materials have been extensively investigated, including metal oxides (TiO₂, ZnO, WO₃, α -Fe₂O₃, BiVO₄), metal chalcogenides (CdS, CdSe), metal nitrides (Ta₃N₅) and oxynitrides (TaON) [86,87]. Most of the stable oxide such as SnO₂, Ta₂O₅, TiO₂, and ZnO are only photoactive in UV region due to their wide bandgap, which limits absorption of sunlight. While small bandgap metal oxides such as α -Fe₂O₃, can harvest maximum solar spectrum but its conduction band potential is more positive than the water and CO₂ reduction potential. Moreover, most of these metal oxides are oxygen evolving and *n*-type, which cannot split water to generate hydrogen or photoreduce CO₂ back to fuel. Similarly, metal chalcogenides i.e., CdS and CdSe have ideal band structures for spontaneous water splitting but are highly unstable in aqueous photooxidation conditions. These factors emphasize a pressing need to research not only in the field of material design, discovery, and development but also on the architecture-controlled fabrication of new and existing materials

1.5.2.2. Oxynitrides

Oxynitrides have recently attracted much attention while transition metal oxide semiconductors are also suitable candidates as photocatalysts for storable fuels because of their low cost, nontoxicity, abundance, and high corrosion resistance [88-90], they have low efficiencies due to their poor carrier conductivity and generally have large bandgaps.[91] To reduce the band gap, many methods have been tried including defect formation and doping by cations and anion [92,93]. Incorporation of N is promising way as the N 2p states are energetically shallower than the deeper O 2p orbitals [94]. Generally, the CBM of a transition metal oxynitride is mainly formed from the empty metal

orbitals while the VBM of oxynitrides are shifted to more negative energy by N 2p mixed states [95,96]. Thus the band gaps of oxynitrides can be narrower than those of the corresponding metal oxides [93,94]. Recently, Cui *et al.* and Respinis *et al.* have comprehensively investigated the electronic structures and photocatalytic activities of tantalum-based compounds such as Ta₂O₅, TaON, Ta₃N₅, and shown that the TaON exhibit visible-light photocatalytic activity since they have smaller band gaps compared to common oxides.

Tantalum oxynitride (TaON) is one promising material as a photoanode for solar water splitting but works under external applied bias. Recently, it has been reported that suitable energy of valence and conduction band edges of TaON make it an electrode material for both water oxidation and reduction, and a narrow band gap of ~ 2.4 eV allows absorption of visible light [88,97,98]. However, the photocatalytic activity of TaON is still limited, due to self-deactivation upon irradiation, conversion of TaON to Ta₂O₅, high exciton binding energy, and ultra-fast electron-hole recombination [97,99].

1.5.2.3. Conducting Polymers

Conjugated organic polymers (COPs) are conducting due to delocalized π -molecular orbitals on the polymeric backbone [100]. The main advantage of conjugated organic polymers (COPs) over other materials (inorganic semiconductors) is their possibility of processing to form useful, tunable and robust structures. Polyaniline (PANI), polypyrrole (PPy), polythiophene (PT), polyacetylene (PA), polythiopene (PT), polyparaphenylene (PPP), polyparaphenyleneevenylene (PPV), poly(*o*-phenylenediamine) (POPD) and their copolymers are prominent examples of COPs (see Fig 1) [101,102]. Most of the COPs have non-linear response to electronic excitation but the induction

of doping/de-doping (injection of an electron and hole) on the conjugated chain can lead to a self-localized excited state (imprinted), suggesting opportunity for use in energy storage devices, electrocatalysis, smart windows, membrane gas separation, microwave screening, organic electrochemistry, microsystem technologies, electronic devices, bioelectrochemistry, photoelectrochemistry, electroanalysis, sensors, electrochromic displays, and anti-corrosion [103,104].

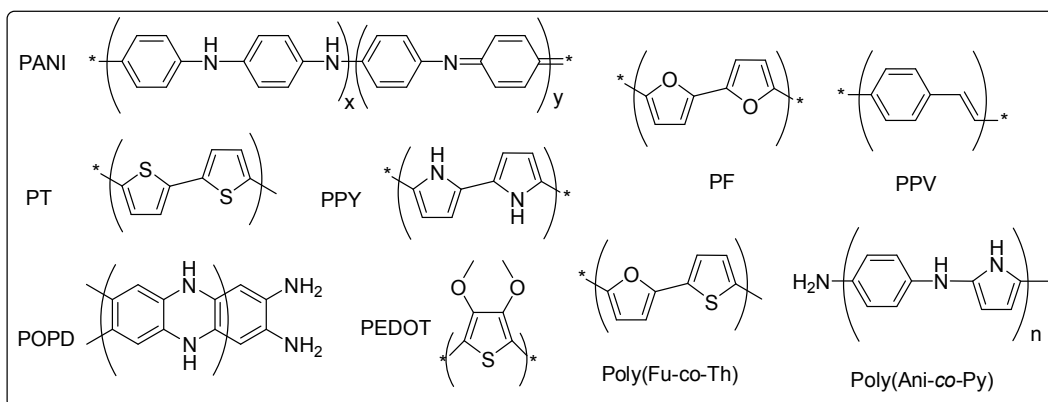


Figure 6. Different types of COPs and their copolymers.

Scientific community's interest is increasing day-by-day to explore novel materials, for high performance solid-state gas sensors [105]. Gas sensors have vital role in the home safety, environmental monitoring and chemical controlling, both in industries and laboratories [106]. The commonly available sensors include, metal oxide semiconductors (MOS), MOS field effect transistors, quartz crystal microbalance, surface acoustic wave, and COPs [107-109]. The metal oxide semiconductors (inorganic materials) gas sensors have low selectivity and operate at high temperature which increases power consumption, reduces sensor life and limits their portability [110], scientists are struggling to explore sensors which would be chemically miscellanies, stable, selective, highly sensitive, and have quick response mechanism [111]. COPs are superior gas sensors in contrast to their counterpart inorganic sensors,

having easy synthesis, chemical diversity, stability, selectivity, high sensitivity, and quick response mechanism even at room temperature operation [112].

COPs are emerging as promising materials due to their stability, low-cost processing and ability to form tunable and robust structures. Four prominent generations of COPs are being explored by scientists, which has application in the field of solar to power energy conversion [9-13].

COPs have tunable band gap where one can precisely tune the desired band gap, HOMO, and LUMO energy levels during the synthesis, which directly affect the open circuit voltage (V_{oc}), charge transport (η_{CT}) and short-circuit current density (J_{sc}) in the polymer solar cell (PSC) [7]. Generally, polymer with a band gap of more than 4 eV is considered to be insulator while the underneath represents semiconducting nature [60]. Since the discovery of the conducting nature of polyacetylene (PA), researchers are working to minimize this band gap [113]. Many efforts are reported in this regards which are either, co-polymerization, composites, nanoparticles, and donor-acceptor co-polymerization [61].

1.5.2.4. Lead Halide Perovskite

Methylammonium lead halides are hybrid solid compounds with perovskite type structure, having chemical formula of $\text{CH}_3\text{NH}_3\text{PbX}_3$; where X=I, Br or Cl (see Fig 5). These compounds have wide range of applications in solar cells, lasers, light-emitting diodes, photodetectors, radiation detectors, data storage, thin-film transistor, and hydrogen production [114]. $\text{CH}_3\text{NH}_3\text{PbX}_3$ perovskite-based solar cells are highly efficient due to their large power conversion efficiency (PCE) ~ 15% [114]. The ABX_3 hybrid perovskite has a versatile structure which can incorporate varieties of cations and anions, forming mixed perovskite. This

incorporation of different constituents change the physical and chemical properties, including crystal structure parameters, bandgaps, charge carrier, defect properties, phase stabilities, and moisture and thermal resistance [115]. Moreover, mixed perovskites solar cells such as lead halide perovskite $APbX_3$ [A = Cs (cesium), MA (CH_3NH_3 , methylammonium), and FA ($NH = CHNH_3$, formamidinium); X = Cl, Br, and I] have improved PCE $\sim 22.1\%$ [115].

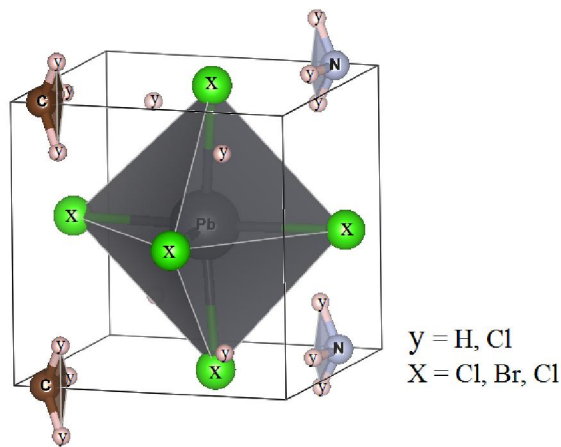


Figure 7. Crystal Structure of a typically lead halide perovskite - $CH_3NH_3PbX_3$

1.5.2.5. Heterostructure Semiconducting Materials

Generally, some metal oxides shows a low photocatalytic activity owing to poor charge-transport characteristics [78] and weak surface adsorption properties [116]. In addition, many attempts have been made to improve the poor photocatalytic activity of metal oxides such as $BiVO_4$ with an oxygen evolution catalyst such as cobalt-phosphate, iron oxyhydroxide [117] and cobalt-borate [118] is one of the options. Making a heterojunction between two dissimilar semiconductors is also an effective strategy to improve the electron-hole separation in $BiVO_4$.

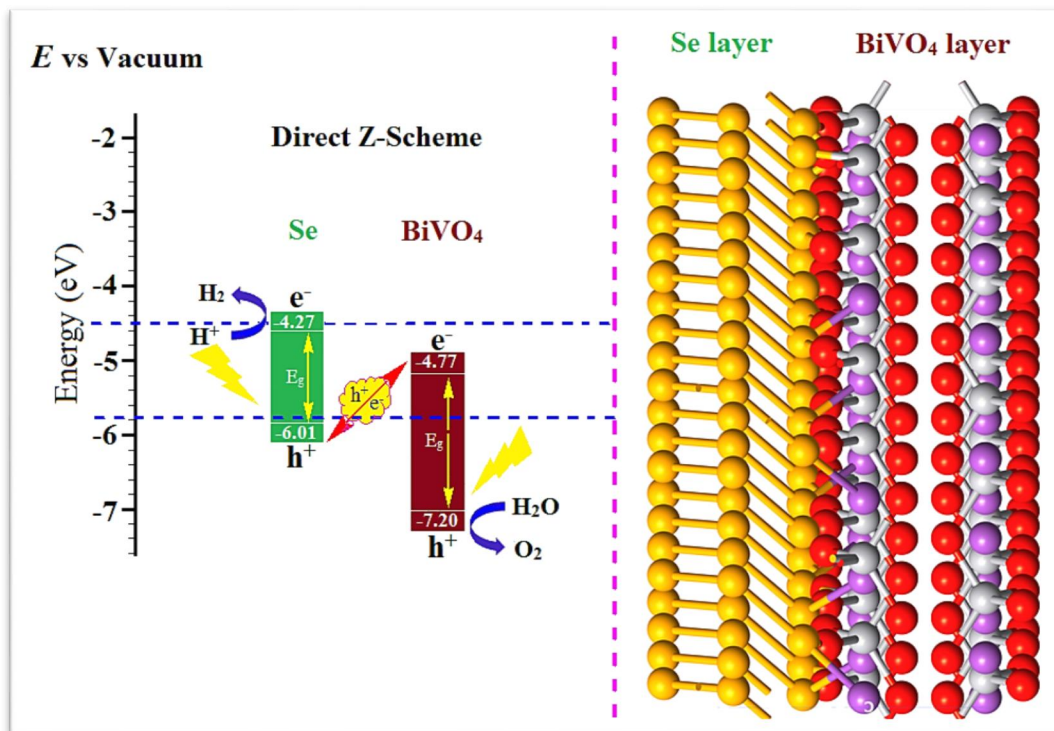


Figure 8. Energy level diagram of Se-bulk and BiVO₄(001) heterostructure, making direct Z-scheme.

Heterojunction has great benefit to PEC activities such as broadening the light absorption spectral, suppressing the charge recombination and enhancing charge separation [58]. Representative heterojunctions or band alignments of binary dissimilar semiconductors is shown in Fig 9. Type-I heterojunction (Fig. 9a), an extensively studied PEC water splitting techniques where a narrow band gap semiconductor (Fe₂O₃) is combined with wide band gap semiconductor such as TiO₂ [119]. In this combination, a complementary light absorption takes place and photocurrent improves by a consequence of facile electrons and hole transfer from the conduction and valence band of wide band gap semiconductor to small band gap material. In Type-II heterojunction (Fig. 9b), the relatively more negative potential (vs RHE) of the conduction and valence band of a narrow band gap of semiconductor (BiVO₄) is beneficial to

enable the efficient charge transfer [58] and high photocurrent density. Since the photo-excited electrons in BiVO_4 where the conduction band is located at more negative potential can easily transfer an electron to the conduction band of WO_3 that have the conduction band at positive potential (Fig. 9b), responsible for high photocurrent. And as a result, the holes from the valence band of WO_3 can be transferred to the valence band of BiVO_4 to oxidize H_2O and generate O_2 [79]. In Type III heterojunction, both narrow band gap semiconductors (each having either an ideal VB or CB) are combined to efficiently perform the photoelectrochemical water splitting (Fig 9c).

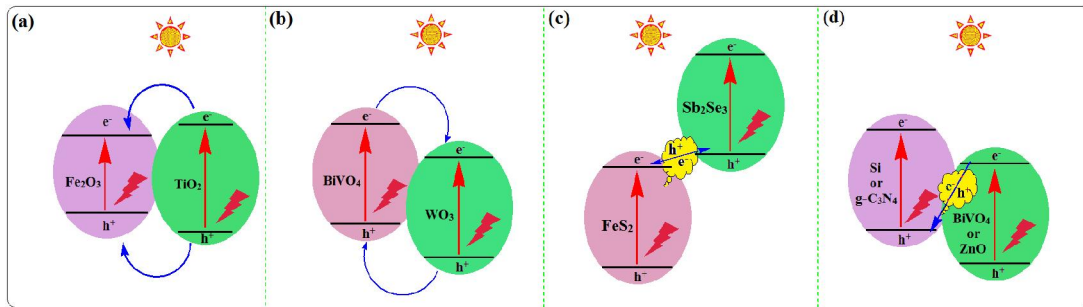


Figure 9: Schematic representation of different band alignments for high PEC performance.

The photogenerated electron at the CB of FeS_2 recombines with a hole at the VB of Sb_2Se_3 and consequences separation of electron and hole, responsible for high photocatalytic activity [120]. In Type IV band alignments (Fig 9d), electron-hole pairs separation occurs very easily due to the establishment of a direct Z-scheme in binary semiconductors. Since the photo-excited electrons at CB of wide band gap semiconductor (i.e., BiVO_4 or ZnO), located at more positive potential (vs RHE) would recombine with the holes of $g\text{-C}_3\text{N}_4$ that have the valence band at a more negative potential (Fig 9d). As a result of the aforementioned recombination, holes from the valence band of ZnO/BiVO_4 are

transferred into the electrolyte to oxidize $\text{H}_2\text{O} \rightarrow \text{O}_2$, whereas the electrons from the conduction band of g- C_3N_4 are transferred to the counter electrode which enhances the photocurrent [121]. Therefore, a proper band alignment of each semiconductor in all types of heterojunctions is necessary to develop a deeper understanding of the charge transport properties in water splitting process.

The Type-I and II heterojunction are widely reported compared to Type III and IV, where BiVO_4 is mixed with other materials [78,122,123]. From a thermodynamic point of view, the material used in place of g- C_3N_4 must have small band gap energy in case of Type IV heterojunction to favor the electrons excitation process. Graphitic carbon nitride; g- C_3N_4 ($E_g = 2.7$ eV) and Silicon, Si ($E_g = 1.1$ eV) are the most popular visible light absorbing semiconductor to be paired in various metal oxide for PEC cells [124-126]. The more negative conduction band potential of g- C_3N_4 and Si compared to that of BiVO_4 , facilitate the photogenerated electrons mobility to the external circuit due to high electron-hole pairs separation. Si-based materials are highly efficient in the solar cell technology, but they are too expensive to be used in PEC water splitting. The cost of a silicon wafer comprises the pure silicon cost, the crystallization cost, and the slicing cost [127]. Also, the fabrication of the Si-based device is more complex as it requires proper handling of fairly fragile Si wafer. These factors lead to a motivation in developing Si-free PEC cell with a potentially good absorber material which can be prepared by easy growth techniques to reduce cost production and achieve high charge transport characteristics in the heterojunction (Type-IV heterojunction).

1.6. Environmental Applications

Nanostructured TiO₂ is one of the most investigated photoactive materials due to its excellent electronic structure and high stability to photocorrosion under redox conditions [128-130]. TiO₂ has drawn much attention due to its potential applications in solar energy conversion (such as photocatalytic water splitting and dye-sensitized solar cell), environmental cleaning (photocatalytic degradation of pollutants, self-cleaning, and water purification), and bio-sensing [131-134]. The solar energy conversion and photocatalytic efficiency of TiO₂ is limited due to its wide band gap (3.20 eV), as it can only absorb UV region of the solar spectrum [135]. Along with wide band gap, TiO₂ also suffer from high charge recombination rate (photogenerated electron-hole pair) which hindered the photocatalytic activity [136]. Strategies such as noble metal deposition as co-catalyst, metal or non-metal doping and photosensitization have been adopted to tailor band gap and enhance the charge transport properties to improve the photocatalytic performance of TiO₂ [137,138]. Recently, it has been found that composite of metal oxide and COP into intimate contact on both physical and electronic levels have significantly improved solar energy conversion and photocatalytic performance compared to metal oxide or COP individually [139]. Moreover, an increasing interest is found on the fabrication of COP-TiO₂ nanocomposites for photocatalytic degradation of environmental pollutants as well as water splitting to generate hydrogen [140,141].

Recently, interest of the scientific community has increased in the application of COPs in high performance solid state gas sensor devices. Gas sensors are very important in the environmental monitoring, home safety and chemical controlling (both in the industries and laboratories). The most frequently

reported sensors are metal oxide semiconductors [142], quartz crystal microbalance [143], surface acoustic wave [144], field effect transistor [145], and conducting polymers (CPs). The metal oxide semiconductors (inorganic materials) gas sensors work on the principle of change in conductivity upon interaction with gas molecules, but they suffer from low selectivity (specific target gases). Moreover, high operation temperature leads to increased power consumption which reduces sensor life and limits the portability. In order to overcome these issues, research is directed to explore sensors which are stable, selective, high sensitive, and have quick response mechanism. COPs have found a worth place as room temperature gas sensors. Several reports have shown that COPs are sensitive to a wide range of gases, vapors, metals and volatile organic solvents. COPs-based sensors are also superior to other sensors because of their chemical diversity, stability, selectivity, high sensitivity, and quick response mechanism [112].

1.7. Conclusions

This chapter is focused on the challenges and opportunities in the area of solar cell technology (photovoltaic and photocatalytic) and clean environment. The current developments in the field are reviewed along with different types of technologies. Theoretical methodologies for the current work are comprehensively summarized in this chapter. Past, present and future aspects of solar energy conversion techniques such as photocatalysis's, photovoltaics, and dye-sensitized solar cells are described. The challenging materials of the field are discussed in detail. To investigate the gap between research and the industry is very important, to identify and understand the task. The performance of a chemical material strongly depends on several parameters including,

bandgap, optical absorption, stability, heat dissipation, precision manufacturing and accurate tracking. Moreover, we also highlighted how the earth abundant low-cost, easily synthesizable, environment friendly materials can lower down the cost of the device, through doping, heterostructure formation, and defect formation. Vast coverage of advancements in environmental applications of graphene-based materials for photocatalytic degradation of organic pollutants, gas sensing and removal of heavy metal ions are also reviewed. Additionally, the presences of graphene composites in the bio-sensing field have been discussed. We concluded the review with remarks on the challenges, prospective and further development of graphene-based materials in the exciting field of energy, environment, and bioscience.

Se and BiVO₄ form a direct Z-scheme like heterojunction, where an enhanced PEC activity is observed in case of heterojunction, compared to their individual constituents (Se and BiVO₄). The enhanced PEC properties of Se/BiVO₄ is due to the presence of Se layer, acts as a hole trapping agent, light absorber, and improves the charge separation in the resulted film. The results prove that Se/BiVO₄ heterostructure is a potential candidate for PEC water splitting, confirmed by DFT simulations.

In summary, the oxygen and nitrogen terminated TaON along (010) and (001), respectively has good stability and sensitivity towards water molecule. Moreover, O terminated TaON has ideal band edge positions while N terminated has strong ability towards visible light absorption, so a mixed phase would result an efficient photoanode for water splitting. Furthermore, the development of effective dopants will be very crucial in improving the transport

properties of the surface of TaON to further reduce the masses of photogenerated electrons and holes for high charge mobility rate.

The g-C₃N₄ and BiVO₄ form a van der Waals type heterojunction, where an internal electric field facilitated the separation of electron/hole pair at the g-C₃N₄/BiVO₄ interface which further restrain the carrier recombination. In this combination, the photogenerated electrons from CB of g-C₃N₄ directly reduce water and produce H₂ while holes at VB of BiVO₄ directly oxidize water and results O₂. On the other hand, electrons from CB of BiVO₄ recombine with the holes from the VB of g-C₃N₄.

CHAPTER 2: BiVO₄ for Photoelectrochemical Solar Water Splitting

2.1. Introduction

Bismuth vanadate (BiVO₄) is a promising photocatalyst for solar energy conversion due to its nontoxic, low-cost, photostable, and eco-friendly nature. Generally, BiVO₄ has three different crystalline polymorphs: orthorhombic pucherite, tetragonal dreyerite, and monoclinic clinobisvanite [146]. These different polymorphs have different properties as the photocatalytic activity is strongly influenced by the crystal structure. For instance, the tetragonal BiVO₄ possesses a band gap of 2.9 eV and mainly absorbs UV region, while the monoclinic clinobisvanite (m-BiVO₄) exhibits a much higher photocatalytic activity due to its ideal band gap (2.4–2.5 eV) which absorb the UV and visible regions of the electromagnetic spectrum, having an ideal valence band edge position for driving water oxidation [147]. However, it has been recently reported that m-BiVO₄, an *n*-type semiconductor [148], exhibits poor photocatalytic property which is stem to low mobility of the photogenerated charge carriers (electron–hole pairs), positive potential of CB (vs NHE) and high charge recombination rates which significantly limit its practical applications. The photocatalytic activity of m-BiVO₄ can be tuned either with metal or non-metal doping, semi-conductor recombination (heterojunction formation), depositing the co-catalysts, defect formation (oxygen vacancy creation), and crystal-facet control or morphological modification.

Moreover, it is important to investigate/design an efficient dopant for BiVO₄, which not only keeps its monoclinic crystal structure but to slow down the charge recombination rate and more negative CB (vs NHE) edge position. The monoclinic clinobisvanite structure of BiVO₄, consists of rows of isolated [VO₄]

tetrahedra which are separated by the dodecahedral coordinated Bi atoms to form $[\text{BiO}_8]$ with eight O atoms (Fig 10).

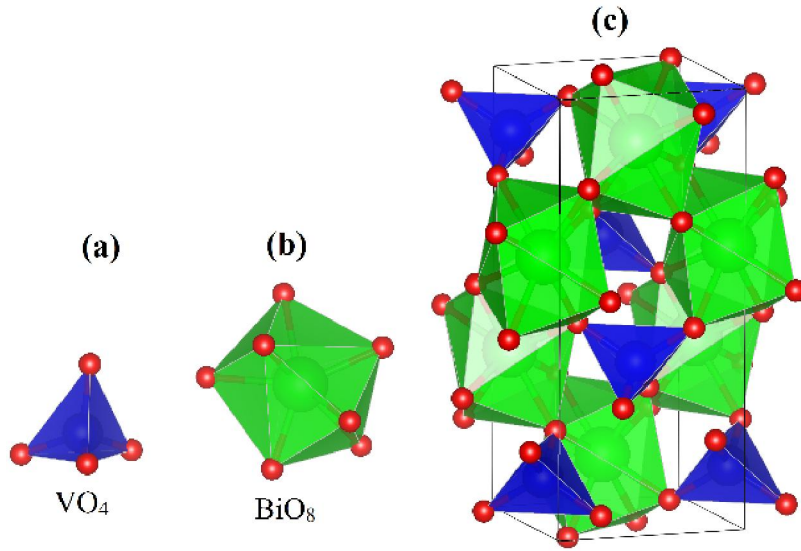


Figure 10. Tetrahedral and dodecahedra geometries of VO_4 (a) and BiO_8 (b) in BiVO_4 (c).

In order to improve the overall photocatalytic activity of $m\text{-BiVO}_4$ (simply denoted as BiVO_4), different doping agents have been applied; these doping agents have either substituted the (I) V or (II) Bi atoms but no one has paid attention to substitute the (III) O site of BiVO_4 . In this work, we investigated the effect of Oxygen vacancy and Se-dopant for the geometrical structure and corresponding photocatalytic activity of BiVO_4 .

2.2. Pristine, Oxygen Defective, and Se-Doped BiVO_4 for Solar Water Splitting

The removal of an oxygen atom, and Se dopant on the tetrahedral or dodecahedra geometries of monoclinic clinobisvanite is investigated from the resulting relaxed geometries, where the bond distances between V—O and Bi—O decrease; considering the case of O_v and Se-doped $\text{BiVO}_4(001)$. When the Se dopant ratio is increased from 2 to 3 or 4, it distorted the geometries of

parent $\text{BiVO}_4(001)$, discussed in Article 1. However, in case of 1-2% doping ratios, the resulted geometries were quite compact and similar to parent $\text{BiVO}_4(001)$.

Electronic properties of $\text{BiVO}_4(001)$ surface: As discussed in our previous report [48], that the monoclinic clinobisvanite phase exhibits a much higher photocatalytic activity compared to its other polymorphs due to its favourable band gap (2.4–2.5 eV) in the visible region of electromagnetic spectrum and a valence band position suitable for driving water oxidation [147].

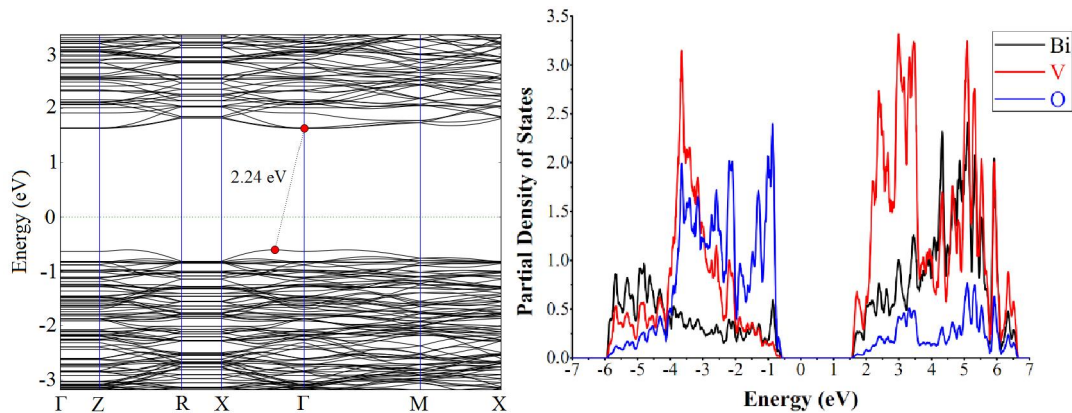


Figure 11. Band Structure and PDOS plot of $\text{BiVO}_4(001)$; the Fermi energy is set to zero (Article 1).

The electronic properties such as DOS/PDOS and band structure of $\text{BiVO}_4(001)$ are given in Fig 11, where its band gap is 2.24 eV. This band gap along the k-points direction of Γ , Z, R, X, and M, is about 0.16 eV smaller than that of experimental but it is expected from LDA [149], which underestimate the band gap. Furthermore, the simulated band edge energies (VBM \sim -6.80 and CBM \sim -4.56 eV at vacuum level) of BiVO_4 indicate that its CBM need to be engineered for high PEC performance (see Table 1).

TABLE 1: Fermi energy, % doping, VBM, CBM, Band Gap, and Effective Masses of Photogenerated Electrons and Holes, Estimated from the calculated Band Structure along the suitable direction.

<i>Species</i>	<i>Fermi Energy</i>	<i>% Doping</i>	<i>m_e[*]/m₀</i>	<i>m_h[*]/m₀</i>	<i>VBM</i>	<i>CBM</i>	<i>Band gap</i>
BiVO ₄ (001)	-6.18	Pure	0.09	0.28	-6.80	-4.56	2.24
O _v _BiVO ₄	-4.28	1.0	0.19	0.18	-6.29	-4.33	1.96
1Se_BiVO ₄ (001)	-5.17	1.04	0.09	0.02	-5.80	-4.41	1.39
2Se_BiVO ₄ (001)	-5.19	2.08	0.04	0.31	-5.81	-4.08	1.73
3Se_BiVO ₄ (001)	-4.93	3.0	0.65	2.02	-5.47	-4.39	1.08
4Se_BiVO ₄ (001)	-4.73	4.16	0.01	0.24	-5.38	-4.14	1.24

Electronic properties of Oxygen vacancy BiVO₄(001) Surface: The VB and CB orbitals distributions of 1% O_v_BiVO₄(001) are almost similar to that of parent slab, however, the Fermi energy merge in the CB which is due to the extra electron(s) of the O_v, as can be seen from Fig 12. It is also reported that monoclinic BiVO₄ is normally an intrinsic *n*-type semiconductor [150]. In this case, the electrons (0.19 m_e) are said to be the "majority carriers" for current flow (behave as an *n*-type semiconductor) while the effective mass of holes is 0.18 m_e. Overall, small effective masses of electrons and holes are estimated from the CBM and VBM of O_v_BiVO₄(001) compared to that of parent slab. Moreover, electron doping (Oxygen vacancy creation) of BiVO₄ has not only reduced its band gap but shift the CB to more positive potential (vs vacuum) as can be seen from Table 1.

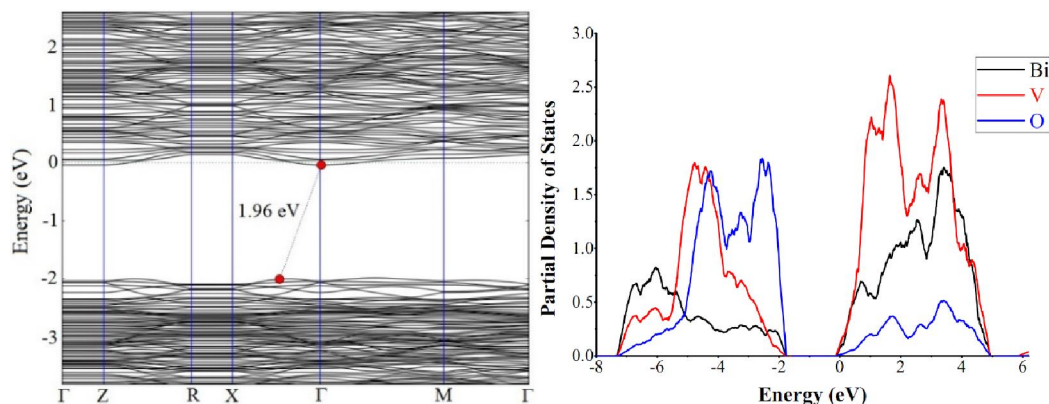


Figure 12. Band Structure and PDOS plot of $O_v\text{-BiVO}_4(001)$; the Fermi energy is set to zero (Article 1).

Electronic properties of Se-Doped $\text{BiVO}_4(001)$ Surfaces: Oxygen atom(s) is substituted with Se in $\text{BiVO}_4(001)$, from 1-4 % dopant ratios, denoted as 1Se, 2Se, 3Se and 4Se_ $\text{BiVO}_4(001)$, given in Article 1. Se has not only reduced the band gap of parent BiVO_4 , but changed both the VB and CB, to -5.80 eV and -4.41 eV (vs vacuum), respectively. Compared to parent $\text{BiVO}_4(001)$, 1Se_ $\text{BiVO}_4(001)$ has an ideal CBM position which is well above the redox potential of water, responsible for water reduction. Se is a *p*-type dopant, which has produced some flat bands in the VB of parent $\text{BiVO}_4(001)$, however, it has significantly reduced the effective masses of electrons and holes (Table 1). Moreover, 1Se_ $\text{BiVO}_4(001)$ can be used as a best photocatalyst for solar water splitting due to its ideal band edges positions, narrow band gap, and small effective masses of charge carriers (*vide infra*). Both the 1 and 2% Se doped $\text{BiVO}_4(001)$ have almost similar photocatalytic characteristics and can be used for efficient water splitting, especially for water reduction. The effect of 3 and 4% Se on $\text{BiVO}_4(001)$ and their band gap and effective masses of charge carriers are contrast to that of 1 and 2%, as can be seen from Table 1 and Fig 13. The VBM and CBM of 3Se_ $\text{BiVO}_4(001)$ are -5.47 and -4.39 eV while that of

4Se_BiVO₄(001) are -5.38 and -4.14 eV, respectively. For the effective masses of charge carriers of these two systems, see Table 1.

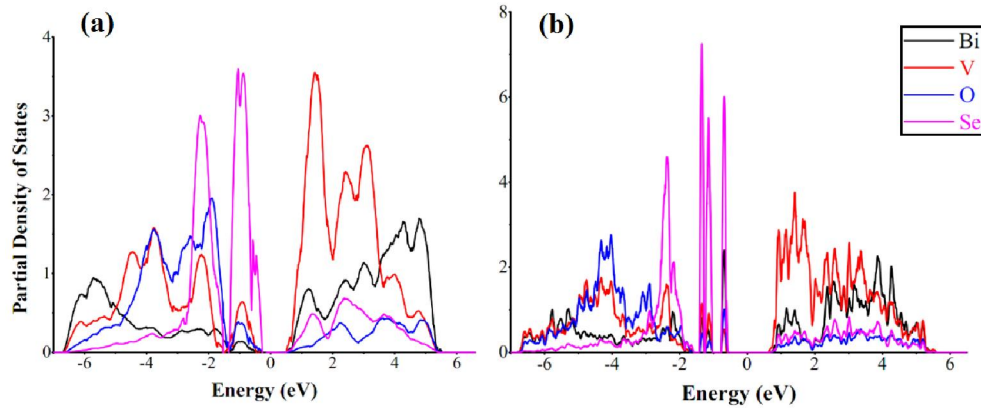


Figure 13. PDOS plot of (a) 3Se and (b) 4Se_BiVO₄(001); the Fermi energy is set to zero (Article 1).

Comparative analysis of the Oxygen defective and Se doped (1-4%) BiVO₄(001), led us to conclude that both the defective and mild (1 and 2%) Se-Doped BiVO₄(001) are best candidates for photocatalytic water splitting, based on their simulated VB, CB, Bandgap and effective masses of charge carriers.

Pristine BiVO₄(001)@H₂O: In case of BiVO₄(001)@H₂O, one of the water molecules is more attracted towards the surface via O—Bi and two H—O bondings, having distances of 2.45 and 1.62 Å, respectively (Table 2).

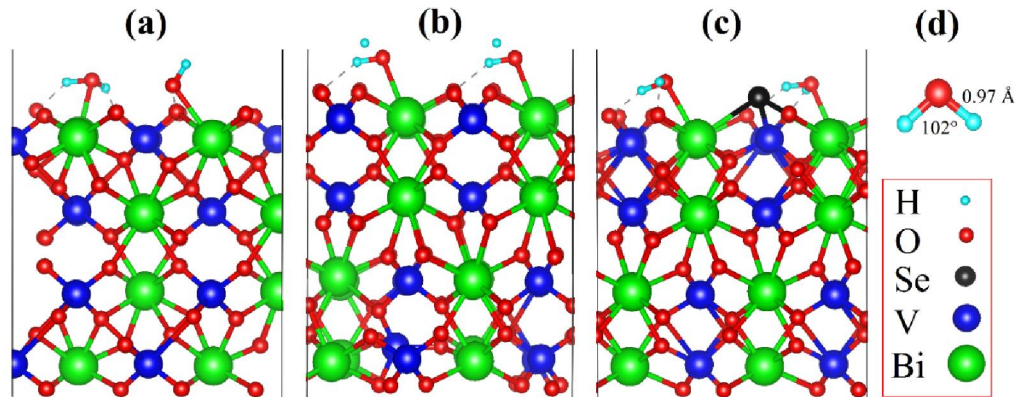


Figure 14. Relaxed structure of (a) BiVO₄(001)@H₂O, (b) O_v-BiVO₄(001)@H₂O, (c) 1Se_BiVO₄(001)@H₂O, and (d) water (Article 1).

Hydrogen atoms of water molecules make a strong hydrogen bonding with the surface O atoms of BiVO₄(001). The per-water molecular adsorption energy is -38.28 kcal/mol, responsible for H₂O splitting over (001) surface of BiVO₄.

Comparative analysis of the data of Table 2 and Fig 14 led us to conclude that the water has moved the VB of pristine BiVO₄(001) from -6.80 to -5.96 eV and CB from -4.56 to -4.22 eV, at vacuum level.

TABLE 2: Inter-bond distance, Water Adsorption Energy (E_{ad}), and Bandgaps of Water Adsorbed-BiVO₄(001), O_v, and 1Se_BiVO₄(001) Systems.

Species	$H_{(water)}-O_{(surface)}$ (Å)	$Bi_{(surface)}-O_{(water)}$ (Å)	E_{ad} (kcal/mol)	Band gap
BiVO ₄ (001)@H ₂ O	1.62	2.45	-38.28	1.74
O _v _BiVO ₄ @H ₂ O	1.75	2.51	-50.85	2.28
1Se_BiVO ₄ @H ₂ O	1.59	2.45	-40.24	1.35

Oxygen Defective BiVO₄(001)@H₂O: This defective surface has strong attraction for water molecules as can be observed from its adsorption energy (-50.85 kcal/mol). However, the inter-bond distances of H—O and Bi—O are longer compared to that of pristine@H₂O system.

1% Se-Doped-BiVO₄(001)@H₂O: Finally, the water adsorption on the 1Se_BiVO₄(001) surface is investigated, where its optimized parameters are given in Table 2 and electronic properties in Fig 14. The simulated water adsorption energy (-40.24 kcal/mol) led us to conclude that 1% Se doped BiVO₄(001) can be easily used an efficient photocatalytic material. Both the VB and CB are slightly moved from its parental position, which has decreased the overall band gap, from 1.39 to 1.35 eV as can be seen from Fig 15 and Table 2.

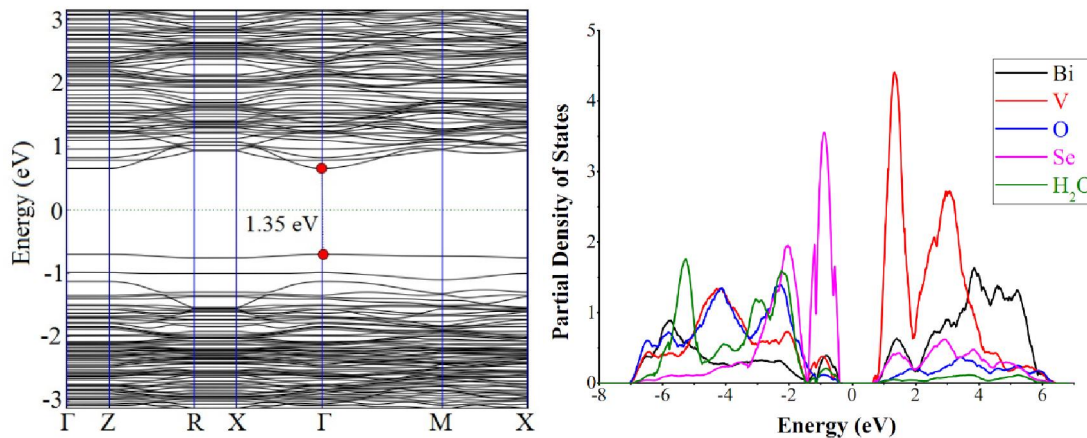


Figure 15. Band structure and PDOS of 1Se_BiVO₄(001)@H₂O; the Fermi energy is set to zero (Article 1).

2.3. Se and BiVO₄ Heterostructure for Photocatalysis

The performance of BiVO₄ (photoanode) is improved through combining with an n-type Selenium (Se), to build band alignments as that of direct Z-scheme (Fig 9d). Due to small band gap of Se, it has high light absorption efficiency [151] and can be combined with BiVO₄ to further improve the light harvesting ability. Therefore, when Se is coupled with a larger band gap semiconductor (in Type-IV heterojunction), the charge recombination of the photogenerated electron-hole pair can be reduced and also suppresses the Se layer photocorrosion. Since very limited information is available regarding Se-based PEC water splitting, hence, this work is a step forward to provide a new direction to replace a traditional visible-light photoabsorber *i.e* Si with Se. The fundamental electronic structure of the monoclinic clinobisvanite BiVO₄ are rarely considered for the water splitting, so, its theoretical investigations along with experimental study might provide rational answers to comprehend the optical and electronic-relationship. Finally, these findings will be useful to get an insight to design an appropriate approach for improved PEC performance.

Electronic and Optical Properties of BiVO₄: Basically, BiVO₄ exists in three different crystalline polymorphs; orthorhombic pucherite, tetragonal dreyerite, and monoclinic clinobisvanite [152]. The photocatalytic activity and surface reaction is highly dependent on phase and crystal orientation of semiconductor oxide [153-155]. For instance, the tetragonal BiVO₄ possesses a band gap of 2.9 eV and mainly absorbs UV light, while the monoclinic clinobisvanite phase exhibits a much higher photocatalytic activity due to its favorable band gap (2.4–2.5 eV) in the visible region of the electromagnetic spectrum (shows both visible light and UV absorption), and a valence band position suitable for driving water oxidation under illumination [147].

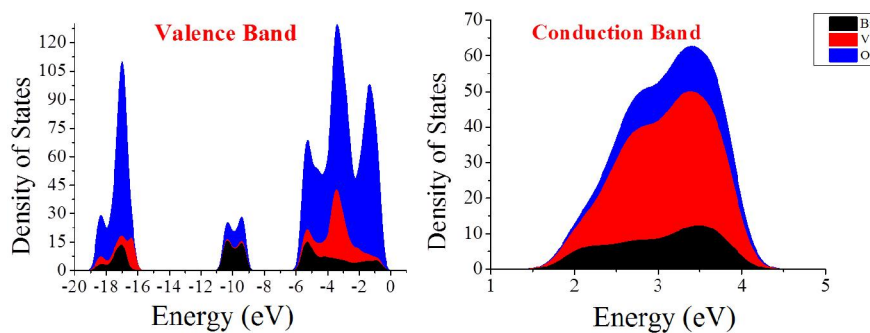


Figure 16: Valence and Conduction DOS of BiVO₄(001), Fermi level is set to zero (Article 2).

Band structure of the BiVO₄(001) along the k-points direction of Γ , Z, R, X, and M is given in Article 2. An indirect band gap of 2.25 eV is simulated which is in good agreement with the experimental and recently theoretical reported data [147]. At the Fermi energy of -5.73 eV, the vacuum phase VBM and CBM are ca. -6.38 and -4.13 eV, respectively, see Table 3 and Fig 16. These simulated band edge energies indicate that BiVO₄ can be used as a photocatalytic material for redox reactions, such as water splitting but need modification for high PEC performance.

Table 3: Band gap and effective masses of photogenerated electrons and holes, estimated from the calculated band structure along the suitable direction.

<i>Experimental</i>	<i>Theoretical</i>	<i>Direction Brillouin zone</i>	<i>in</i>	<i>m_e^*/m_0</i>	<i>m_h^*/m_0</i>	<i>Band gap</i>
BiVO ₄ (Film)		Indirect				2.43
	BiVO ₄ (001)	X→Γ		1.93	0.45	2.25
Se Bulk		Direct				1.74
	Se Bulk	Γ→Γ				1.60

The simulated values of the effective masses of photogenerated electrons and holes of the BiVO₄(001) slab are 0.45 and 1.93 m_e , respectively. Lighter mass of charge carriers the faster will be their movements at the interface [156,157]. As shown in Fig 17, the Se/BiVO₄ form a direct Z-scheme like heterojunction, where the enhanced photocurrent activities are because of Se layer. When light shines on Se/BiVO₄ heterostructure, the photogenerated electron of BiVO₄ in its CB recombine with a hole at VB of Se, consequences free electrons and at CB of Se case substential increase in photocurrent as observed experimentally. This electron/hole recombination and separation create a direct Z-scheme like structure where the free electron at negative potential (CB) of Se is responsible for the enhancement of photocurrent (Fig 17).

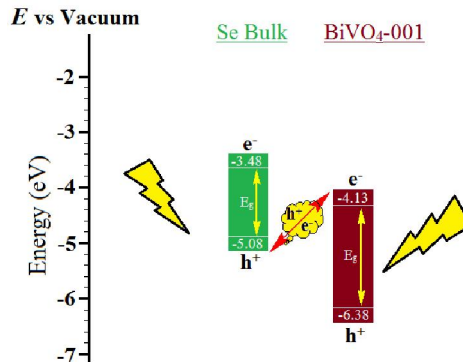


Figure 17. Energy level diagram of the simulated Se-bulk and BiVO₄(001).

2.4. g-C₃N₄ and BiVO₄ Heterostructure for Solar Water Splitting

Electronic properties of BiVO₄(001), g-C₃N₄, and g-C₃N₄/BiVO₄(001):

Periodic DFT calculations are carried out for BiVO₄(001), g-C₃N₄, and g-C₃N₄/BiVO₄(001) heterostructure. Moreover, TiO₂/BiVO₄(001) heterojunction has larger lattice mismatch (7.3 %) compared to g-C₃N₄/BiVO₄ (0.02 %). The optimized structures and lattice parameters of monolayer g-C₃N₄, bulk g-C₃N₄, BiVO₄, BiVO₄(001), and g-C₃N₄/BiVO₄(001) are given in Fig 18. There was almost no lattice mismatch (0.02 %) in the heterojunction of g-C₃N₄/BiVO₄(001), because of the similar surface areas of BiVO₄(001) and monolayer g-C₃N₄. Hereafter, the g-C₃N₄/BiVO₄(001) will be denoted as g-C₃N₄/BiVO₄. Moreover, the calculated adsorption energy of g-C₃N₄ nanosheet over the BiVO₄(001) is -0.68 eV which also confirm the thermodynamic stability of g-C₃N₄/BiVO₄ heterojunction.

The energy bands of single layer g-C₃N₄, BiVO₄(001), and g-C₃N₄/BiVO₄ systems are depicted in Fig 19.

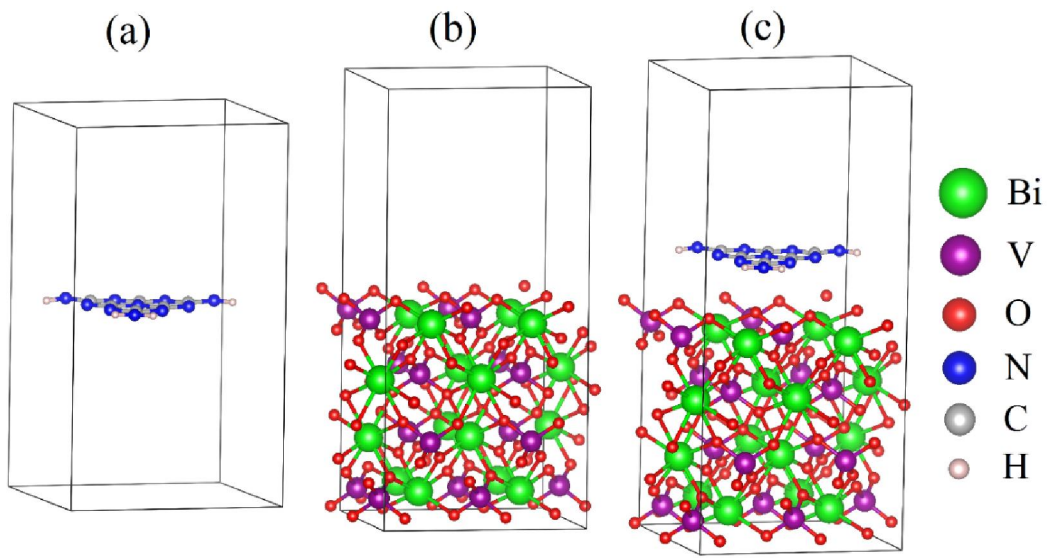


Figure 18. Relaxed geometries of (a) gC₃N₄, (b) BiVO₄(001) and (c) g-C₃N₄/BiVO₄ (having lattice mismatch of 0.02%).

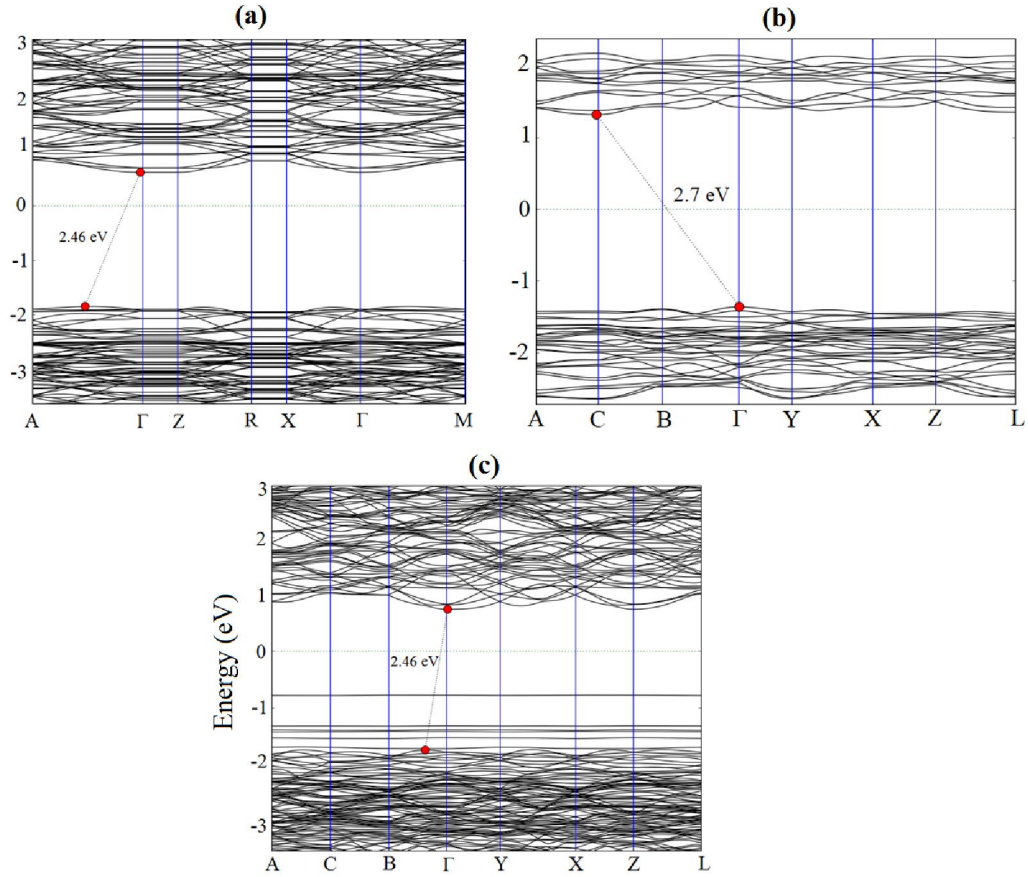


Figure 19. Simulated band structures of (a) BiVO₄(001) slab, (b) g-C₃N₄, and (c) g-C₃N₄/BiVO₄ heterojunction; the Fermi energy is set to zero.

On the other hand, monolayer g-C₃N₄ has also an indirect band gap (2.70 eV) where the valence band maximum (VBM) is located at Γ point and the conduction band minimum (CBM) is at C point (Fig 19b). The g-C₃N₄/BiVO₄ heterostructure has an indirect gap (2.46 eV), and the VBM is located between B and Γ points, whereas the CBM is at Γ point (see Fig 19c). Upon interaction of g-C₃N₄ with BiVO₄(001), flat bands are produced in the VB of the resulted heterojunction. Using meta-GGA, the simulated values of the effective masses of photogenerated electrons and holes of the BiVO₄ slab are 0.02 and 0.01 m_e , respectively (Table 4). These masses are comparatively lower than that of our previous report which were calculated at LDA method [48,158]. Although, pristine BiVO₄ has lighter effective masses of photocarriers; responsible for

high carrier mobilities but its VBM is situated at more positive potential (vs vacuum) than the reduction potential of water.

Table 4: Work function, VBM, and CBM at vacuum level, Band Gap (in unit of eV), and Effective Masses of Photogenerated Electrons and Holes; Estimated from the calculated Band Structure along the suitable direction.

<i>Species</i>	<i>Work function</i>	m_e^*/m_0 (m_e)	m_h^*/m_0 (m_e)	<i>VBM</i>	<i>CBM</i>	<i>Bandgap</i>
BiVO ₄ (001)	5.18	0.02	0.01	-7.03	-4.57	2.46
g-C ₃ N ₄	4.38	0.12	0.44	-5.74	-3.07	2.70
g-C ₃ N ₄ /BiVO ₄	4.43	0.01	0.10	-6.16	-3.70	2.46

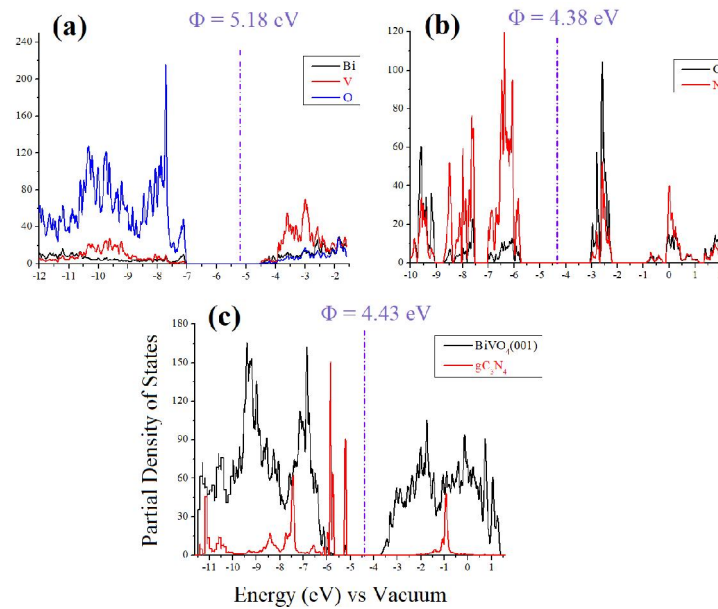


Figure 20. Partial density of states plots of (a) BiVO₄(001), (b) g-C₃N₄, and (c) g-C₃N₄/BiVO₄ heterojunction. The vertical dashed lines represent the work function and the energy is in eV versus vacuum.

In order to understand the contribution of individual species (atoms), responsible for VBM and CBM; the partial density of state (PDOS) of these three constituents are calculated which are shown in Fig 20a-c. The VBM and

CBM of monolayer g-C₃N₄, BiVO₄(001), and g-C₃N₄/BiVO₄ heterojunction were simulated from the DOS calculations.

As can be seen from Table 4 and Fig 21, the VBM of BiVO₄(001) is higher than that of g-C₃N₄, whereas the CBM of g-C₃N₄ is lower than that of BiVO₄(001). In the resulted heterojunction, both the Fermi energy and the band edge positions are between that of g-C₃N₄ and BiVO₄(001). As shown clearly in Fig 21, the VB and CB of heterojunction are shifted downward compared to g-C₃N₄, while these bands are shifted upward when compared to BiVO₄(001). Moreover, this change in the VB, CB, and Fermi energy result an internal electric field in the heterojunction; responsible for the enhanced photogenerated electrons. The photogenerated electrons from CB of g-C₃N₄ directly reduce water and produce H₂ while holes at VB of BiVO₄ directly oxidize water and results O₂. On the other hand, electrons from CB of BiVO₄ recombine with the holes from the VB of g-C₃N₄. Upon making a heterojunction, both Fermi level and the CB and VB of the resulted g-C₃N₄/BiVO₄ heterostructure are at different positions compared to that of their constituents. In summary, we can see that the g-C₃N₄/BiVO₄ heterojunction is a Type-II band alignment structure which has lighter effective masses of electrons (0.01 m_e) and holes (0.10 m_e); responsible for high photocatalytic activities. The green and yellow shaded areas represent charge accumulation and depletion, respectively. As shown in Fig 21 and Table 4, the work function of BiVO₄ surface (5.18 eV) is higher than that of monolayer g-C₃N₄ (4.38 eV), which causes the charge to move from g-C₃N₄ to BiVO₄ until the Fermi energy of these two constituents are aligned.

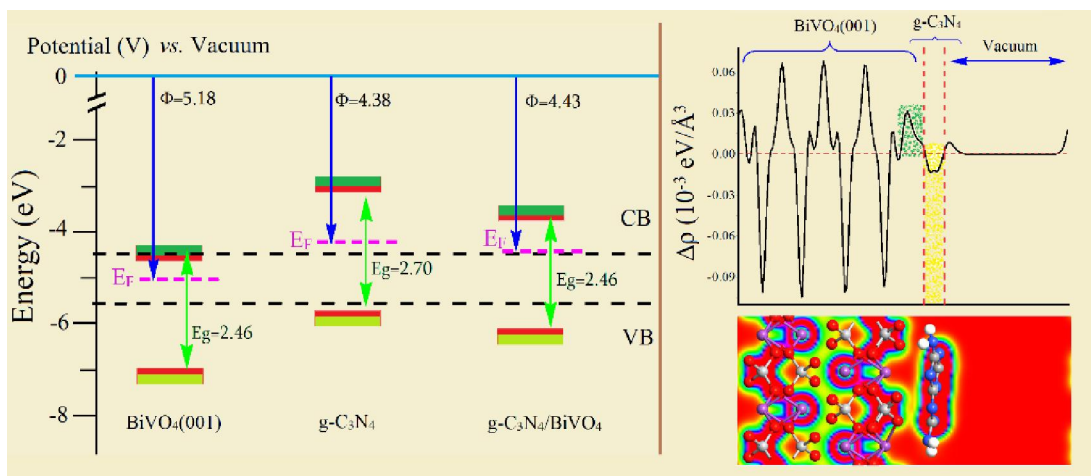


Figure 21. Energy level diagram of these three constituents and averaged electron density difference ($\Delta\rho$) along the Z-direction for g-C₃N₄/BiVO₄. The green and yellow shaded areas indicate electron accumulation and donation, respectively.

2.5. Summary

In summary, although pristine BiVO₄ is a good photocatalyst for water splitting, having narrow bandgap and VB edge position, but inappropriate CB potential, reduces its hydrogen evaluation efficiency. This comprehensive theoretical simulation predicts that both the Oxygen defective and mild doped (1 or 2 % Se) BiVO₄ have not only changed the band edges positions (well above and below the redox potential of water) but reduced the bandgap as well, results a champion photocatalyst for water splitting (Article 1).

We also tried Se and BiVO₄ heterojunction, which form a direct Z-scheme like heterojunction of; having improved PEC performance. DFT simulations are carried out for the BiVO₄ and Se to simulate their band gap, and band edge positions in the proposed heterojunction band diagram. The PEC properties of Se/BiVO₄ indicate that the increment in performance is due to the presence of Se layer which acts as a hole trapping agent, light absorber, and improves the

charge separation in the resulted film. The Se/BiVO₄ has 1.5 times higher photocurrent density than that of BiVO₄ due to higher surface area, small grain size, high roughness, efficient charge separation and minimum charge recombination rate (Article 2).

Heterojunction of g-C₃N₄/BiVO₄ were designed and which has higher photocurrent compared to that of TiO₂/BiVO₄, which consequences the superiority of g-C₃N₄ over TiO₂. The higher reducing capability of g-C₃N₄ is because of its more negative situated conduction band and enhanced photogenerated electrons, larger surface roughness, and higher charge carrier density. The simulated results confirmed that g-C₃N₄ and BiVO₄ has formed a van der Waals type heterojunction, where an internal electric field facilitated the separation of electron/hole pair at the g-C₃N₄/BiVO₄ interface which further restrain the carrier recombination. In brief, the construction of Z-scheme based g-C₃N₄ based PEC device was successfully illustrated in this paper and there is great promises for further explorations and research (Article 3).

CHAPTER 3: Oxynitrides and Their Surfaces for Photocatalysis

In this chapter, we employ first principle periodic density functional theory (DFT) simulations to examine the optical and electronic properties of β -TaON. TaON exists in three different polymorphs, a hexagonal α -TaON phase, monoclinic β -TaON, and a metastable γ -TaON phase [159,160]. We consider bulk β -TaON and its six different slabs such as (001)-N, (010)-N, (001)-O, (010)-O, (001)-Ta, and (010)-Ta. Among all these slabs, the (010)-O and (001)-N terminated surfaces were found to be suitable ultra-thin films for solar water splitting applications.

3.1. Electronic Properties of Bulk TaON

At meta-GGA, the band structures and DOS/PDOS are calculated from the optimized crystal structures, details of these properties are given in Article 4.

Band structures of the TaON bulk is given in Fig 22. TaON has an indirect band gap (2.42 eV) which changes to direct (2.44 eV), considering the supercell (2x2x2) as can be seen from its band structure (Fig 22).

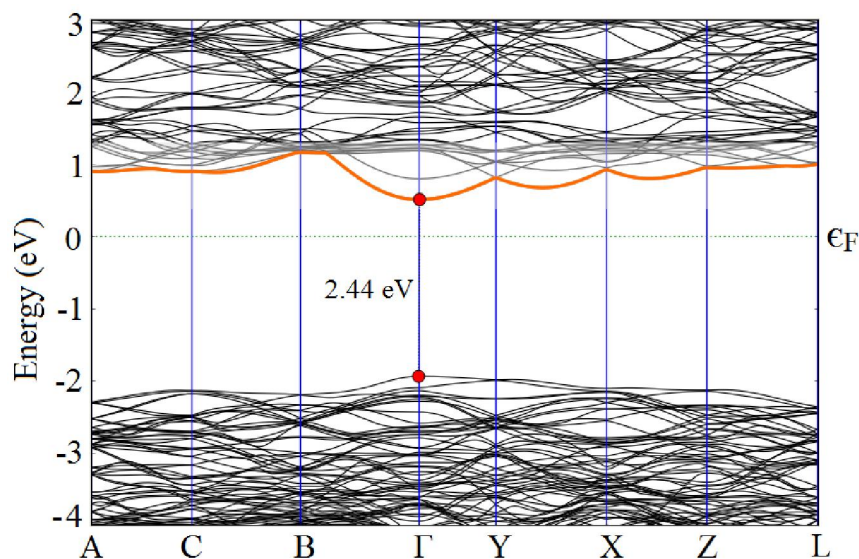


Figure 22. Band Structure of the 2x2x2 supercell of TaON; the Fermi Energy is set to zero (Article 4).

At the Fermi energy of 4.60 eV, the vacuum phase VBM and CBM values are ca. -6.54 and -4.10 eV, respectively. Both the VBM and CBM are well below and above the redox potential of water (Fig 3).

3.2. Surface Effect of TaON on Water Oxidation

Geometries of unit cell, supercell, and slabs are optimized prior to their electronic and optical properties simulation. The crystal structure of unit cell is compared with the available crystallographic parameters of TaON (Fig 23). PBE/GGA reproduces the experimental data accordingly as explained in Article 4 [26]. The cohesive formation energy of Ta, at GGA/PBE using DZP basis set is 10 eV/atom and has nice correlation with the experimental reported one (8.10 eV/atom) [161]. The simulated cohesive formation energy of O and N are 3.7 and 3.1 eV/atom while their experimental values are 2.60 and 4.91 eV/atom, respectively [161]. The calculated band edge, band gap and formation energy of these six different slabs are listed in Table S4 of Article 4, where the (010)-O and (001)-N terminated surfaces have suitable VB, CB, band gap and formation energies, to be used for water splitting applications.

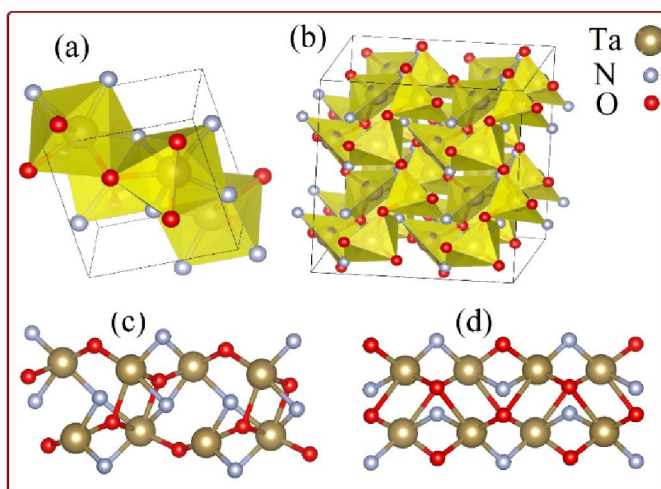


Figure 23. Optimized Crystal structure of unit cell (a), supercell (b), N-terminated (c), and O-terminated (d) slab of TaON (Article 4).

3.3. Electronic Properties of N Terminated TaON(001)

The simulated PDOS of the N terminated TaON(001) surface is given in Fig 24, where the VBM and CBM positions are located at -0.61 and +1.50 eV, respectively. Again, the CBM is made of Ta atom but at a higher potential (2.46 eV compared to 1.50 eV) and with minor contribution of anti-bonding orbitals of O and N atoms (Fig 24b). Hydrogen of water has slight contribution in the lower energy region of VBM as can be seen from Fig 24b. At vacuum phase, the VBM and CBM of N terminated TaON(001) are situated ca. -5.77 and -3.66 eV, respectively (Table 5).

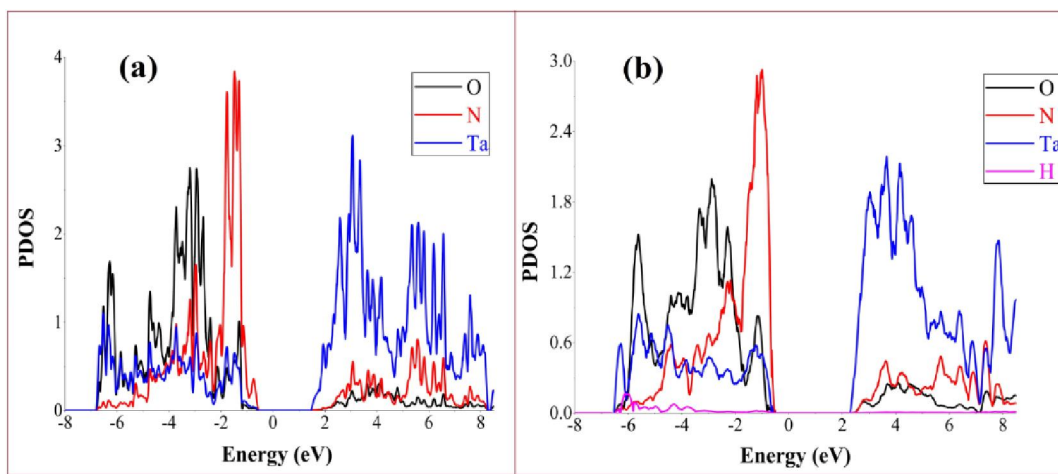


Figure 24. PDOS of N_TaON(001), (a) and N_TaON(001)@H₂O, (b); the Fermi energy is set to zero (Article 4).

The simulated band structure of pristine N terminated TaON(001) is given in Fig 5, having band gap of 2.11 eV. Upon adsorption of water molecule, its band gap elongates to 3.09 eV which is due to the reduction nature of H₂O. This band gap difference of 0.98 eV is because of the shifting of CBM towards more positive potential (2.46 eV).

Table 5: Fermi Energy level, VBM, and CBM at vacuum level, Band Gap (in unit of eV), Effective Masses of Photogenerated Electrons and Holes; Estimated from the calculated Band Structure along the suitable direction.

<i>Species</i>	<i>Surface atoms</i>	<i>Fermi level</i>	m_e^*/m_0 (m_e)	m_h^*/m_0 (m_e)	<i>VBM</i>	<i>CBM</i>	<i>Band gap</i>
TaON	Bulk	-4.60	0.85	0.82	-6.54	-4.10	2.44
TaON(001)	N	-5.16	0.81	3.99	-5.77	-3.66	2.11
TaON(001)@H ₂ O	~	-5.01	1.49	3.46	-5.64	-2.55	3.09
TaON(010)	O	-5.78	0.67	1.63	-6.36	-3.34	3.02
TaON(010)@H ₂ O	~	-4.83	0.72	1.64	-5.42	-2.24	3.18

To further elaborate the interaction of water molecule on the N terminated TaON(001) surface, UV-Vis absorption spectra are simulated. Pristine N-TaON(001) give rise to λ_{max} of 442 nm which became blue shifted (367 nm) when water is adsorbed. In summary, N-TaON(001) surface has good interaction ability towards H₂O besides its non-suitable VBM position (-5.77 eV vs vacuum).

3.4. Electronic and Properties of O terminated TaON(010)

The PDOS of O terminated TaON(010) is given in Figure 25a, where the VBM and CBM are located at -0.58 and 2.44 eV, respectively (at Fermi energy of 5.78 eV). The PDOS of O-TaON(010) depicts that the VBM is located at -0.58 eV (-6.36 eV vs vacuum), having major contribution of N 2p along with minor participation of Ta 5d, and O 2p orbitals (Fig 25a). The CB of O-TaON(010) is situated (-3.34 eV vs vacuum) at well above the redox CBM level of water (Fig 3).

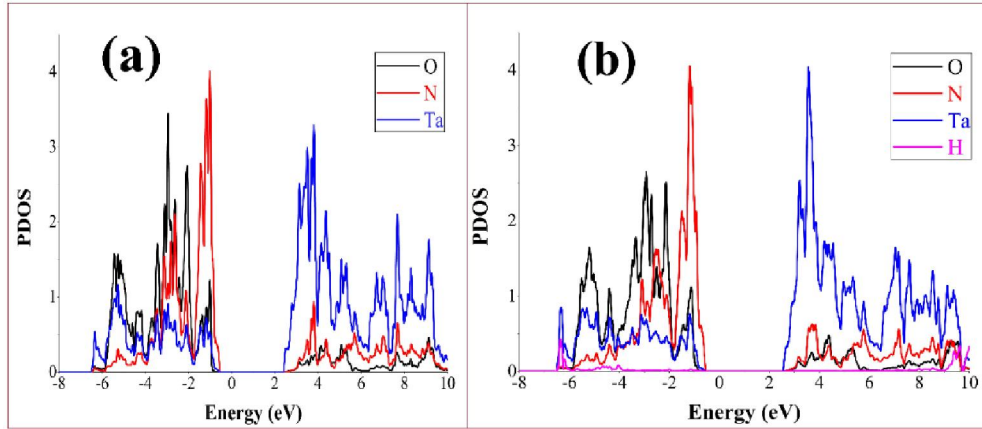


Figure 25. PDOS of O_TaON(010), (a) and O_TaON(010)@H₂O, (b); Fermi energy is set to zero (Article 4).

The CBM of O_TaON(010) moved from 2.44 to 2.59 eV when water molecule is adsorbed on its surface, as can be clearly seen from their comparative band structures (Fig 26). So, the band gap of O_TaON(010) increases from 3.02 to 3.18 eV upon adsorption of H₂O. Furthermore, to check the photocatalytic efficiency, the effective masses of electrons and holes of parent O_TaON(010) are 0.67 and 1.63 m_e , respectively which increase when water is adsorbed, as can be seen from Table 5.

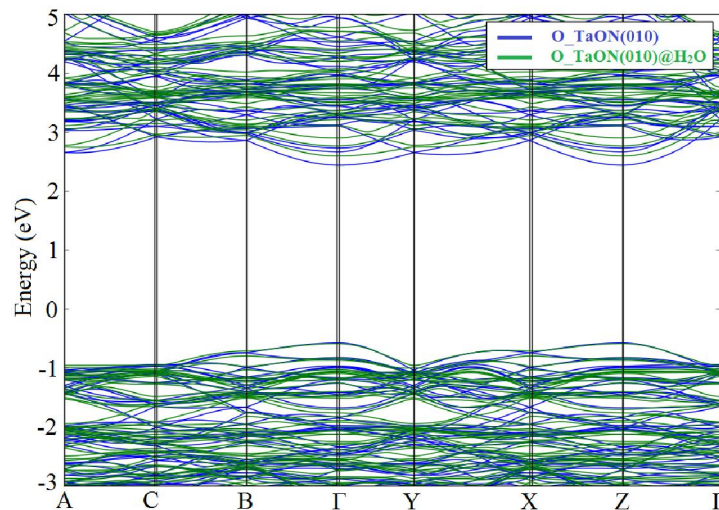


Figure 26. Comparative band structure of O terminated TaON(010) and TaON(010)@H₂O; Fermi energy is set to zero (Article 4).

A blue-shifting in λ_{\max} is observed when H_2O is presents on the surface of $\text{O}_\text{-TaON}(010)$. Water molecule has shifted the λ_{\max} of $\text{O}_\text{-TaON}(010)$ from 368 to 332 nm which consequences its good adsorption capability. Moreover, this shifting in λ_{\max} (36 nm) strongly corroborates the previous characterizations such as effective masses of charge carriers and VBM and CBM positions. An adsorption energy of -148 kJ mol^{-1} in $\text{O}_\text{-TaON}(010)@\text{H}_2\text{O}$ system; shows high dissociative adsorption. Furthermore, this non-covalent interaction can also be seen from the electron localization function plots, given in Fig 11 of Article 4.

3.5. Summary

We investigate the electronic and optical properties and photocarrier mobility of bulk β -TaON which predict TaON is a better candidate for photocatalytic water splitting than either Ta_2O_5 or Ta_3N_5 . In summary, the oxygen and nitrogen terminated TaON along (010) and (001), respectively has good stability and sensitivity towards water molecule. Moreover, O terminated TaON has ideal band edge positions while N terminated has strong ability towards visible light absorption, so a mixed phase would result an efficient photoanode for water splitting.

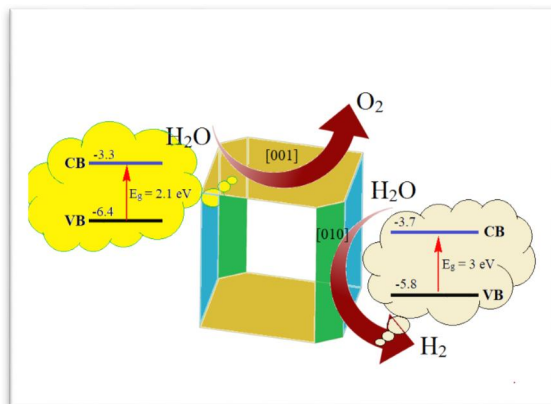


Figure 27. Energy level diagram and schematic representation of O and N terminated TaON (Article 4).

CHAPTER 4: Donor-Acceptor Polymers for Organic Solar Cells

4.1. Background and Challenges of Donor-Acceptor Polymer

One of the major issues with PSCs are their low efficiency in the photovoltaic devices which links to the incident photon to electron conversion. To date, the power conversion efficiency (PCE) of PSC has been enhanced up to 13.2% [162,163], means still large efforts are being required of making it acceptable all over the world. As explained elsewhere [7], the conduction mechanism of the PSC is also different from that of inorganic semiconductors. Other problem associated with the PSC is large exciton binding energy which requires the high energy of dissociation into electron and hole and thus results in less efficiency of the organic based PSC [84]. Finally, COPs used in the PSC should have the ability to absorb the visible part of the solar spectrum (narrow band gap) and a well below HOMO energy level compared to the LUMO of Phenyl-C₆₁-butyric acid methyl ester (PCBM), used in the bulk heterojunction.

COPs monomers such as 3,4-ethylenedioxythiophene (EDOT) and 3,4-ethylenedioxysephenophene (EDOS) are working as a donor while 2,1,3-benzothiadizole (BOD) and 2,1,3-benzoselenadiazole (BSD) moieties act as an acceptor in the donor-acceptor combination. Synthetic mechanism and electropolymerization of EDOS into poly 3,4-ethylenedioxysephenophene (PEDOS) are given in Fig S1 and S2, respectively while that of poly 3,4-ethylenedioxythiophene (PEDOT), poly 2,1,3-benzoselenadiazole (PBSD), and poly 2,1,3-benzothiadizole (PBOD) can be found elsewhere [35].

The purpose of this work is to design and suggest such a polymer that can be used in the bulk heterojunction (organic solar cell), having enhanced V_{oc} , J_{sc} , and fill factor (FF) [164]. In this work, we used different conjugated organic

monomer having donors and acceptors nature which can give rise to a low band gap polymer with desired bandwidth positions.

4.2. Results and Discussion

Optimized Geometries: Planarity in molecular geometry and the corresponding π -electrons conjugation over the backbone play an important role in the visible light absorption of a chemical substance. Optimized molecular and crystal structure of **D-A-D** are given Article 5. An ideal 180° dihedral (Table 6) of the **D-A-D** shows that combination of donor and acceptor moieties has planarized the geometry of the resulting polymer via establishing a delocalized π -electronic cloud density over the backbone. The out of the plane behavior of the benzo selenadiazole rings in the polymeric body may be responsible for the high resistance in delocalization of the electron cloud density (Fig 28).

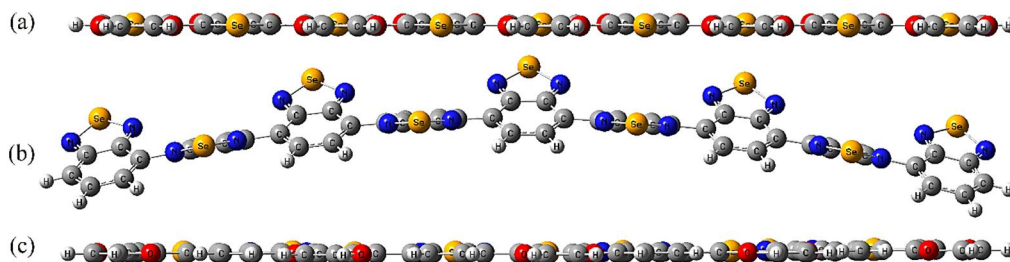


Figure 28. Optimized geometric structures of **D** (a), **A** (b) and **D-A-D** (c) (Article 5).

Table 6: Dihedral angles between the neighboring rings of **D**, **A**, and **D-A-D**.

#	Φ_1	Φ_2	Φ_3	Φ_4	Φ_5	Φ_6	Φ_7	Φ_8
D	179	180	179	179	179	179	180	179
A	146	148	147	149	147	149	147	148
D-A-D	180	180	180	180	180	180	180	180

Electronic Prosperities: Comparative analysis of the data of Table 7 and a visual look of the contours of HOMO and LUMO (Fig 29) predict that excited state properties in **D-A-D** are optimum compared to their individuals' **D** and **A** species. The data shown in Table 7 are specifically for the nine repeating units, however, rest of oligomeric species are given in the Supporting Information. Variation in characteristic properties is very common in short oligomers, but beyond the seven or eight repeating units, they remain almost constant. The purpose of other repeating units is to provide a range of entities which may be useful as a guideline for other experimentalists, as short oligomers are more electroactive but tricky to synthesize.

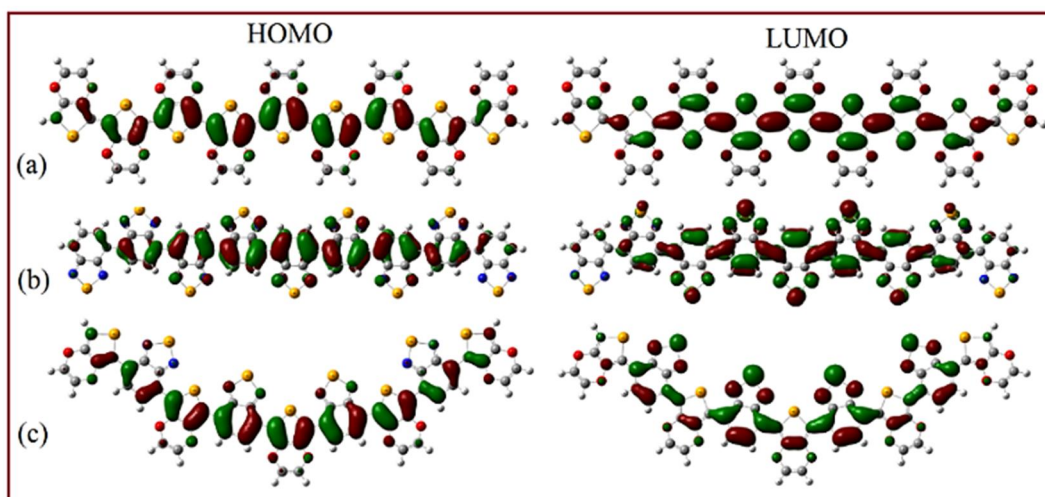


Figure 29. Contours of the HOMO and LUMO of **D** (a), **A** (b) and **D-A-D** (c) (Article 5).

The electrical band gap (estimated from the HOMO-LUMO difference) of the isolated **D** (2.42 eV) and **A** (2.22 eV) provide the evidence of their absorption in the green region of visible spectrum. Prominent near-IR absorption (red regions of the visible spectrum) by the **D-A-D** can be correlated with its band gap of 1.75 eV. Simulated band gaps of the **D**, **A**, and **D-A-D** are comparatively shown in Fig 30. The band structure of **D-A-D** is also obtained from the PBC

simulations and has a good correlation with the molecular one, given in Article 5. The purpose of the PBC simulated band gap of **D-A-D** is to clarify and confirm our level of theory used.

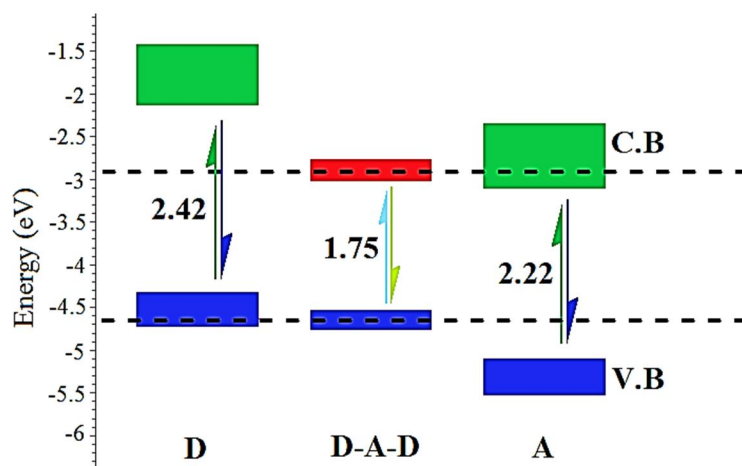


Figure 30. Orbital correlation diagram for **D**, **D-A-D**, and **A** (Article 5).

Table 7. HOMO, LUMO, Band gap, optical gap, Exciton binding and Reorganization energy in eV of the studied species at B3LYP/6-31G** level of theory.

#	HOMO	LUMO	Band gap	Optical gap	E_b	λ
D	-4.44	-2.02	2.42	2.04	0.38	0.22
A	-5.22	-2.99	2.22	1.85	0.37	0.16
D-A-D	-4.65	-2.90	1.75	1.46	0.29	0.20

Reorganization Energy: Comparative analysis of the reorganization energies of these three-different species (Table 7) led us to conclude that geometrical distortion in **A** is quite easy but on the other hand its exciton binding (0.37 eV) is higher because of its electron accepting nature. So, **D-A-D** has an optimum reorganization energy compared to the isolated **D**, and **A** but a much lower E_b (0.29 eV) which ultimately easily separate the electron-hole pair upon visible

light irradiation. So, it is verified that **D-A-D** has better hole transferability due to lower reorganization energy which may be correlated to its fully planar geometrical structure with an ideal dihedral of 180°.

Polaron, Bi-polaron, and Exciton Binding Energy: Molecular orbital energy diagram of the neutral, cationic and di-cationic states of **D** is depicted in Fig 31, where orbital transition along with energy is clearly shown. Band gap and exciton binding energy of **D** in its neutral state are 2.42 and 0.38 eV, respectively. Mono-cationic state in the unrestricted formalism and in the absence of counter-ion is considered to efficiently explore the polaronic effect. Removal of an electron from the oligomeric backbone of **D** induces an extra band within its parental band gap, regarded as inter-band. Mono-cationic state not only reduces the band gap (2.23 or 2.15 eV) of parent **D** by lowering down the HOMO and LUMO energy levels but also increases the delocalization over the polymeric backbone.

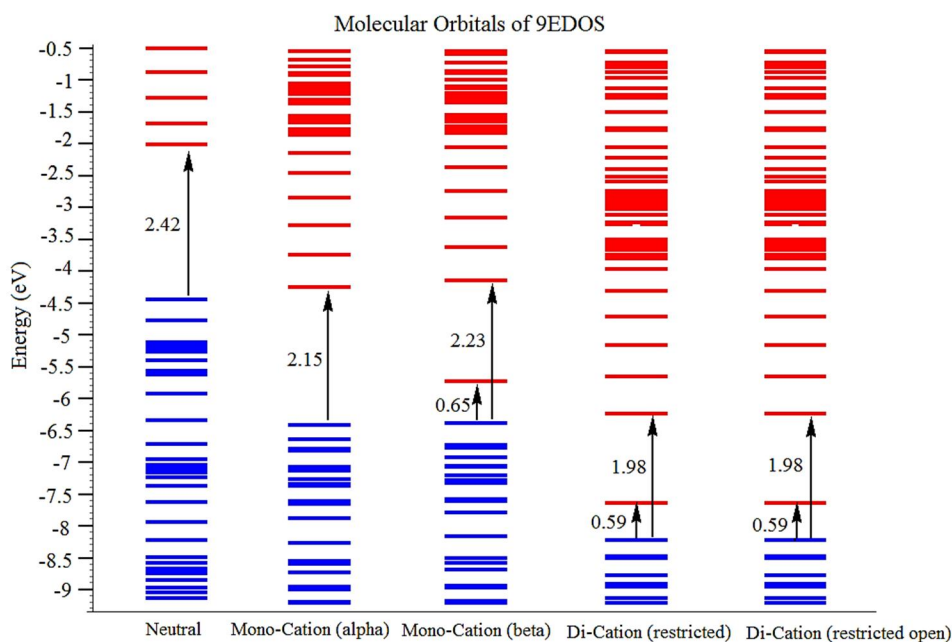


Figure 31. Energy level diagram of the neutral, mono, and di-cationic state of **D** (Article 5).

The delocalization over the oligomeric body of mono-cationic state can be seen from the non-degenerate molecular orbitals, termed as Alpha and Beta (Fig 31) or polaron. Di-cationic state of **D** creates a bi-polaronic state as can be seen from its degenerate frontier molecular orbitals (Fig 31). This degenerate state in the highly cationic state is not only responsible for reducing the band gap but promotes stability compared to that of the polaronic state.

A similar trend in the molecular orbital distribution of **A** is observed upon making its cationic and di-cationic states, as shown in Article 5. Band gap of the acceptor species in the neutral state is found to be 2.22 eV while the coulombic force which holds the electron-hole pair is 0.37 eV.

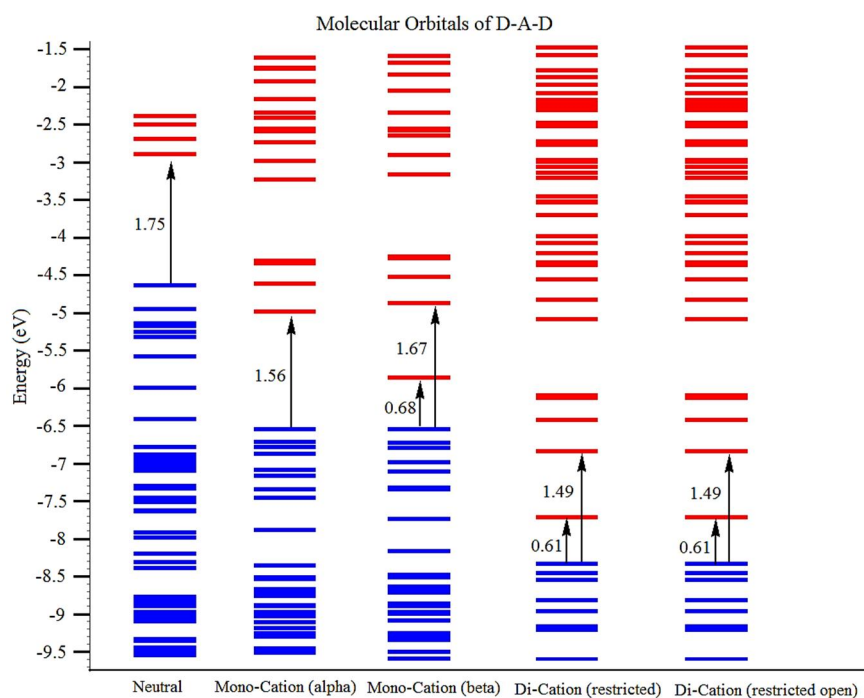


Figure 32. Energy level diagram of the neutral, mono, and di-cationic state of **D-A-D** (Article 5).

The combination of the **D** and **A** moieties in the oligomeric form such as **D-A-D** has much stretched down the HOMO and LUMO energy levels which result in a band gap of 1.75 eV (Fig 32). Keeping in mind the exciton binding energies

of **D** and **A**, this donor-acceptor combination has considerably lowered down the E_b (0.29 eV). So, this lower exciton binding energy and narrow band gap are clear indications for the charge separation (electron-hole pair) at the donor-acceptor interface (here acceptor is the PCBM in the PSC device) and high short-circuit current density, respectively (*vide infra*). The simulated narrow band gap (1.75 eV) of the **D-A-D** has a good correlation with the experiment, which strongly validates the level of theory, we used [35]. The stability of bi-polaron over the polaron is due to these degenerate molecular orbitals. Moreover, restricted and unrestricted formalism has a similar effect in the di-cationic states.

UV-Vis and UV-Vis-Near-IR Absorption Spectral Analysis: UV-Vis and UV-Vis-Near-IR absorption spectra of the **D**, **A**, and **D-A-D** along with their corresponding mono and di-cationic states are simulated at TD-DFT. The UV-Vis spectra of the neutral state of **D** (see Article 5) show two distinct peaks at ca. 608 and 440 nm and arises from $\pi \rightarrow \pi^*$ and HOMO-1 to LUMO-1 transition, respectively. The effect of cationic and di-cationic is investigated in the absence of counter-ion; where the mono-cation induces polaron and deficiency of two electrons create a bi-polaron state. For detail see the discussion in Article 5. In summary, a well-doped state of the **D** can also give desirable efficiency if used in the BHJ of the PSC (*vide supra*). UV-Vis spectra of **A** give rise to a strong absorption band peak which is peaked at 669 nm and is termed as the first allowed $\pi \rightarrow \pi^*$ transition, capable of red light absorption of the solar spectrum, shown in Article 5. For the polaronic and bipolaronic states, see discussion of Article 5.

Comparative UV-Vis spectra of **D**, **A**, and **D-A-D** are given in Figure 33, where the maximum absorption band peaks are peaked at 608, 669 and 847 nm, respectively. These bands can also be regarded as the first allowed maximum electronic excitation (the one with higher oscillator strength) in the visible region and are due to $\pi \rightarrow \pi^*$ transitions (Table 8). The absorption band peak at ca. 847 nm in **D-A-D** is a strong evidence of its efficient absorption in the visible region and responsible for charge transferring ability as well. Moreover, this simulated λ_{\max} has a strong correlation with the already experimental observed UV-Vis spectra (843 nm) [35] which also supports and confirmed the level of theory used. Furthermore, it can be concluded that this wide range of the visible light absorption in the **D-A-D** is responsible for higher efficiency, compared to that of their individual counterparts. From Fig 33, it is evident that how the Donor and Acceptor moieties in the form of **D-A-D**, increase the visible light absorption in a particular polymer.

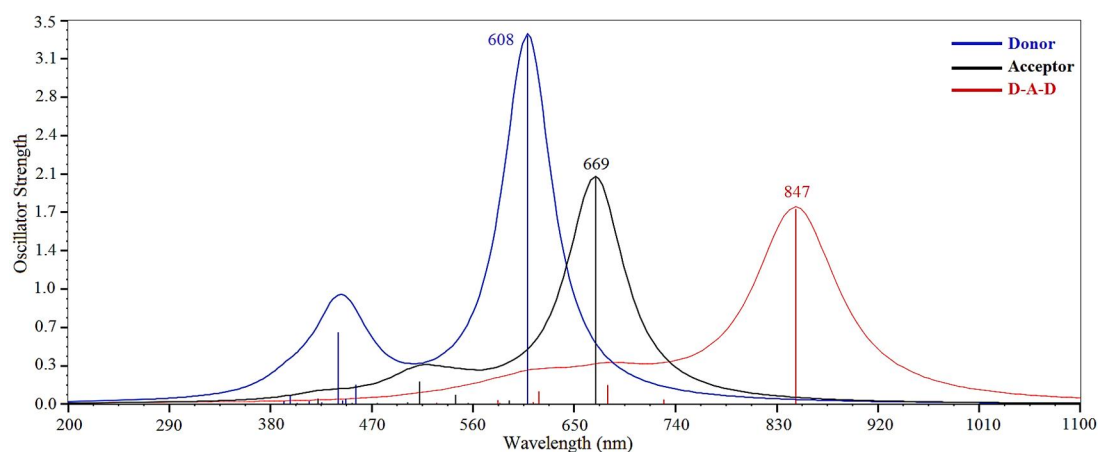


Figure 33. UV-vis Spectra of **A**, **D**, and **D-A-D** at B3LYP/6-31G** (Article 5).

As discussed above, a reduction in the optical band gap of the resulted polymer along with wide UV-Vis absorption is achieved through a mutual overlapping of the molecular orbitals of donor and acceptor. The UV-vis spectra of **D-A-D** has

three distinct absorptions; two small peaks in the visible and a broad one near the IR region, which is an indication of its efficient light-harvesting ability. Furthermore, we also predicted the polaron and bi-polaron states in the extended conjugation of **D-A-D**, which is given in Figure 34.

Table 8: First three vertical allowed transitions along with f and MO transition.

Species	Excited Energy (eV)	λ (nm)	f	Electronic Transition
D	1	608	3.35	HOMO→LUMO
	2	456	0.17	HOMO _{.3} →LUMO
	3	440	0.65	HOMO _{.1} →LUMO ₁
A	1	669	2.06	HOMO→LUMO
	2	544	0.08	HOMO→LUMO ₂
	3	512	0.20	HOMO _{.1} →LUMO ₁
D-A-D	1	847	1.78	HOMO→LUMO
	2	680	0.17	HOMO _{.1} →LUMO
	3	618	0.12	HOMO _{.1} →LUMO ₁

Once again, a similar trend is observed in the case of **D-A-D**, upon creation of polaronic and bi-polaronic states. Optical band gap of the parent **D-A-D** is 1.46 eV, which reduces to 1.10 eV in the mono-cationic state. The optical band gap of the bi-polaronic state is about 1.12 eV which is because of the $\pi \rightarrow \pi^*$ transition. Unlike the **D**, and **A**, UV-Vis-Near-IR spectra of the di-cationic state is ideal and transparent in the whole region of the solar spectrum. Additionally, two extra low energy band peaks, located at 1501 and 2277 nm strengthen the absorption ability of **D-A-D** in the bi-polaronic state. These near-IR absorptions arise from the electronic transition of $\sigma \rightarrow \pi^*$ orbitals.

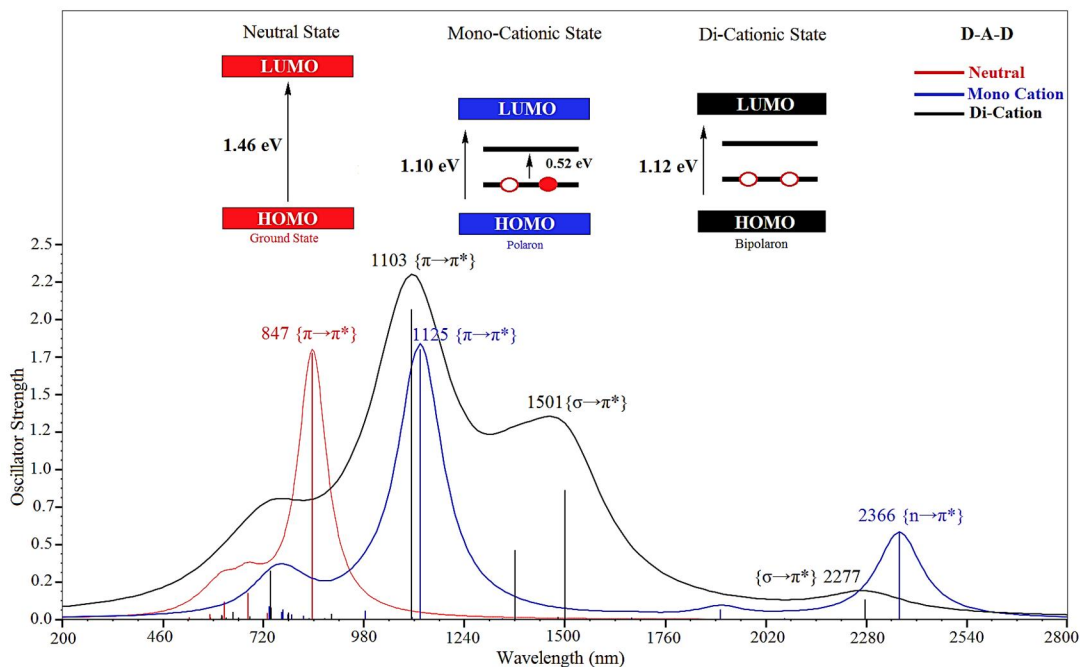


Figure 34. UV-Vis Spectra along with Optical band gaps of Neutral, Mono, and Di-Cationic states of **D-A-D** at B3LYP/6-31G** (Article 5).

Theoretical Performance of Polymer Solar Cells: The photovoltaic properties of **D-A-D** in the PSC device such as V_{oc} and charge transport are simulated which are listed in Table 9. Different HOMO and LUMO energy levels of the fullerenes derivatives are reported (Table 9), however, few of them are considered with our investigated **D-A-D** polymer. From Table 9, it can be analyzed that the V_{oc} of the PSC has a direct relation with the LUMO energy level of PCBM, higher the LUMO level results in large V_{oc} . A PC₆₁BM [165] with LUMO energy level of -3.63 eV, produces V_{oc} of 1.02 eV with our designed **D-A-D**, however, this voltage drops down to 0.65 eV when PC₇₁BM [166] is used (LUMO, -4.0 eV). Comparative analysis of the data of Table 9 led us to predict that an average open circuit voltage of roundabout 0.90 eV can be achieved, using **D-A-D** as donor material in the BHJ solar cell devices. Compared to individual **D** and **A** conformer, the resulted constituent has planner geometry

so, a high FF is expected and the narrow optical band gap (1.46 eV) and electrical band gap (1.75 eV) are responsible for high J_{sc} (*vide supra*).

Table 9. HOMO, LUMO of fullerene derivatives and open circuit voltage (V_{oc}) and $LUMO^{Donor} - LUMO^{Acceptor}$ energy difference (L-L) of **D-A-D**; all values are in eV.

#	Species	HOMO	LUMO	V_{oc}	L-L
1	PC ₆₁ BM[165]	-6.10	-3.63	1.02	0.73
2	PC ₆₁ BM[167]	-6.10	-3.70	0.95	0.80
3	IC ₆₀ BA[166]	-5.80	-3.70	0.95	0.80
4	IC ₆₀ BA[168]	-5.85	-3.74	0.91	0.84
5	IC ₆₀ MA[168]	-5.91	-3.86	0.79	0.90
6	PC ₆₀ BM[169]	-5.93	-3.91	0.74	1.01
7	PC ₇₀ BM[170]	-5.87	-3.91	0.74	1.01
8	PC ₇₀ BM[171]	-6.0	-4.0	0.65	1.10
9	PC ₇₁ BM[166]	-6.0	-4.0	0.65	1.10
10	PC ₆₁ BM[172]	-6.2	-4.10	0.55	1.20

4.3. Summary

DFT and TD-DFT at hybrid functional, to assess the nature and electronic properties of a near-infrared-absorbing, low energy gap conjugated polymer; donor–acceptor–donor (**D-A-D**). The **D-A-D** is consisting of 2,1,3-benzosele-nadiazole (**A**) as acceptor and 3,4-ethylenedioxy-selenophene (**D**) as donor fragments. The **D** and **A** moieties in the polymeric backbone have been found to be responsible for reducing the band gap, open circuit (V_{oc}) and increasing short-circuit current density (J_{sc}) in polymers solar cells (PSC). Our theoretical studies revealed that charge transportation efficiency (η_{CT}), V_{oc} , J_{sc} and, in turn,

device performance, are influenced by electronic energy level alignment at interfaces. A lower HOMO energy level (-4.65 eV) of designed **D-A-D** is responsible for increasing the ambient stability during device operation and results in high V_{oc} of 1.02 eV. Furthermore, it is found that donor-acceptor combination has a key role in charge separation, weak steric hindrance, and molecular architecture (planarity of the polymeric backbone) which directly influences the charge transport compared to that of counterpart homopolymers (either **D** or **A**). Reduction in the band gap, high charge transformation, and enhanced visible light absorption in **D-A-D** system is because of strong overlapping of the frontier molecular orbitals of the **D** and **A**.

CHAPTER 5: All-Solid-State Dye-Sensitized Solar Cell

5.1. Traditional DSSC vs Solid-State DSSC

As discussed in chapter 1, DSSC is consist of molecular dye, adsorbed on a mesoporous wide band gap semiconductor oxide (frequently TiO_2), a redox couple (I^-/I_3^-) usually liquid electrolyte and a p -type hole collector/counter electrode. The dye molecule (photosensitizer) absorb light and injects its excited electrons into the conduction band of TiO_2 and become oxidized. The redox electrolyte act as an intermediate to transfer hole from dye to counter electrode for regeneration of dye. So, if we replace this liquid electrolyte with solid state material, then the overall efficiency of the device increases.

5.2. Solid-State Dye-Sensitized Solar Cell

Cluster of titanium dioxide [$(\text{TiO}_2)_{28}$] is used as a representative of the [101] surface of anatase [12,13,173-175]. The major part of this work is devoted to the hole transporting material (HTM), its applicability in SDSC and the corresponding efficiency. However, HTM interaction with dye, N3- TiO_2 , and HTM-N3- TiO_2 systems are also highlighted. Charge transferring phenomena, electron-hole exchange and band edge positions of these systems are simulated and discussed in their respective parts.

Geometrical and Electronic Properties of HTM: The optimized geometric structure of HTM is given in Fig 35, where an ideal dihedral angle of 180° is because of donor and acceptor moieties; which has planarized the geometry of the resulting polymer through establishing a delocalized π -electronic cloud density over its polymeric backbone.

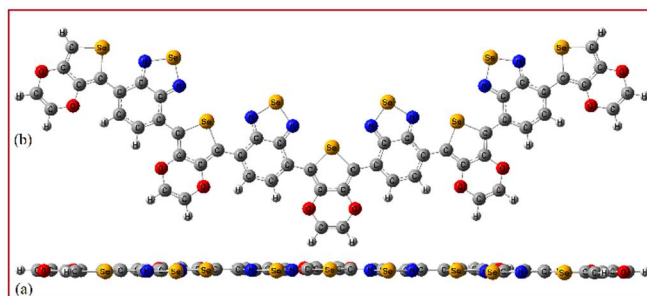


Figure 35. Optimized Geometric Structure of HTM along with side view (Article 6).

Both the HOMO and LUMO of HTM are fully covered by electronic cloud density (see Article 6), a clear indication of the free availability of π -electrons in the HTM (Fig. 36). Moreover, this molecular orbital overlapping (delocalized π -electrons in HTM) of the C, H, O, N, and Se atoms provides an easy pathway for the movement of free electrons which make it as a donor species (hole donor) in the bulk heterojunction solar cell.

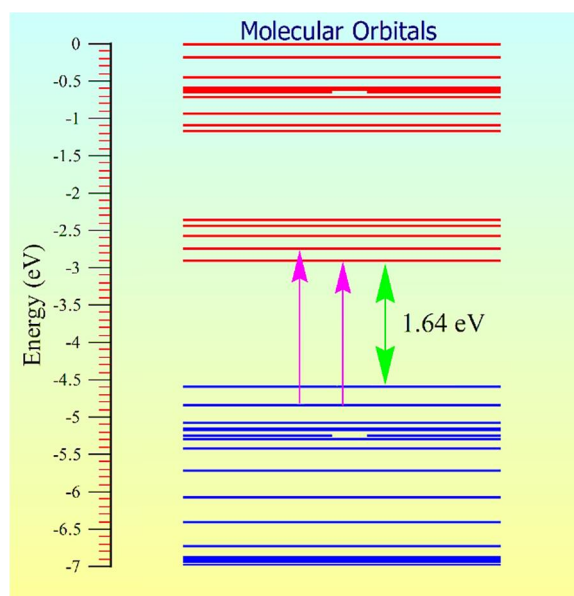


Figure 36. Energy level diagram of HTM (Article 6).

Reorganization Energy (λ) of HTM: Comparative analysis of the reorganization energy of HTM with the already reported hole transporting materials [176-178], shows that our proposed HTM has better hole transfer

ability due to lower reorganization energy. This low reorganization energy of HTM can also be correlated to its fully planar geometrical structure, where an ideal dihedral of 180° is present.

Polaron and Exciton Binding Energy of HTM: The intra-molecular charge transfer (E_b) in HTM has a binding energy of 0.55 eV. A lower E_b is responsible for the charge separation (prevent electron/hole recombination) and high charge carrier mobility in a solar cell. Furthermore, binding energy can also be used for the determination of short-circuit current density in a solar cell; lower exciton binding energy of a HTM is responsible for its higher short-circuit current density and vice versa.

Partial Charge Difference Analysis: The partial charge difference of the atoms involved in HTM backbone is given in Table 10, which demonstrates that the ΔQ_H value is slightly larger than ΔQ_{Se} to about 0.05 e^- . Comparative analysis of the data of Table 10 led us to conclude that Se and H atoms are mainly involved for the charge transfer in HTM, however, H atom plays a significant role compared to Se atom. The partial charge difference of ΔQ_H is 0.296 e^- while that of ΔQ_{Se} is 0.24 e^- . Partial charge difference values for N, O, and C are 0.026, 0.054 and 0 e^- , respectively.

Table 10: Partial Charge Difference Analysis of HTM

Species	Cation	Neutral	Difference
Se	7.084	6.844	0.24
N	-5.552	-5.578	0.026
O	-5.520	-5.574	0.054
C	0.126	0.126	0
H	4.868	4.572	0.296

UV-vis Absorption Spectra of HTM: The first allowed maximum electronic excitation energy of HTM (λ_{\max}) at ca. 925 nm has strong evidence to be an efficient charge transporting material, as it can easily absorb in the visible region. The effect of the alternating donor and acceptor moieties in the polymeric backbone is found in the form of visible light absorption as can be seen from Fig 37. It is observed that the contribution of HOMO-LUMO transition decreases and new absorption from HOMO-1→LUMO+1, HOMO-2-LUMO, and HOMO-LUMO+2 excitations start to contribute (given in Article 6). The strong transition (the one with high oscillator strength) of HTM in the visible region corresponds to the transitions from HOMO to LUMO (Table 11).

Table 11. Excitation Energy, HOMO, LUMO, Band gap, optical gap, Exciton Binding Energy (E_b) and reorganization energy in eV of HTM (in solvent), N3, and TiO_2 .

<i>Species</i>	<i>HOMO</i>	<i>LUMO</i>	<i>Band gap</i>	<i>Optical gap</i>	λ (eV)	<i>Orbital Transition</i>	E_b (eV)
HTM	-4.57	-2.93	1.64	1.34	0.21	H→L	0.55
TiO₂	-7.33	-4.27	3.06	2.62		H→L	
N3	-5.76	-3.42	2.34	2.27		H ₂ →L	

The UV-vis spectra of HTM has three absorptions band peaks; two in the visible and one near to the IR region of the spectrum, which is an indication of its efficient light-harvesting ability. Charge-transfer character occurs at the lower energy part of UV-vis absorption and a low-lying wide conduction band (Fig 3) [179].

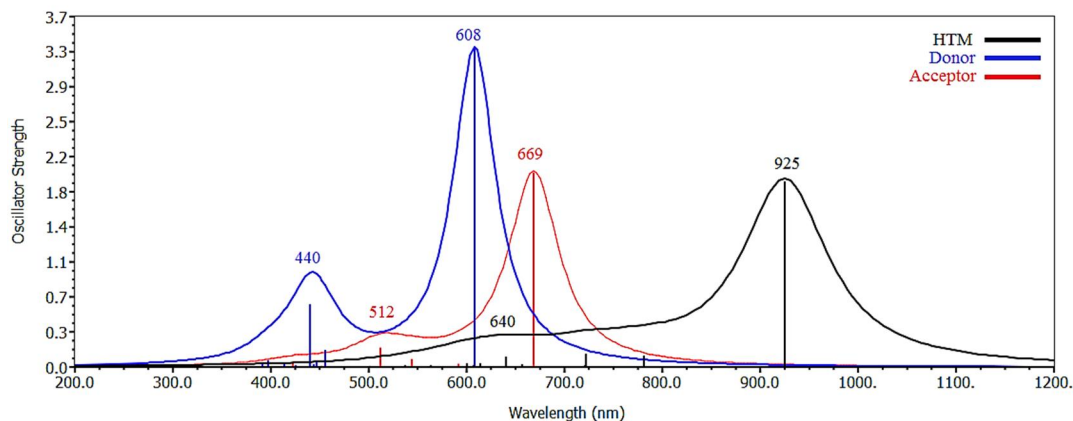


Figure 37. UV-vis Spectra of BSD, EDOS, and HTM at CAM-B3LYP/LanL2DZ (Article 6).

HTM and N3 Interacting System. A non-dissociative but quite strong interaction is found between N3 and HTM, which is due to the establishment of non-covalent bonding. The carboxylic anchoring groups of N3 establishes non-covalent bonding with the N and Se of HTM, which is a clear evidence of their strong interaction. The inter-molecular electrostatic energy of this interaction is -8.72 kcal/mol, which further confirms the evidence of charge transferring between HTM and N3. The higher electronic cloud density at LUMO compared to that of HOMO shows that the charge injection is favored from HTM to dye and prevents charge recombination in the dye molecule (Table 11). The HOMO and LUMO of HTM in the HTM-N3 system indicates how the transformation of π -electrons towards N3 is achieved (see Article 6). The high IP (4.57 eV) of HTM which 1.19 eV above the HOMO of dye is responsible for the hole exchange as well as high chemical stability toward oxidation. According to NBO charge analysis, HTM and N3 share about 0.184 e^- of electronic cloud density.

N3 and TiO₂ Interacting System: The estimated open circuit voltage of this solar cell is 1.49 eV which is simulated from the difference of the quasi-Fermi levels of the TiO₂ and the HOMO energy level of N3 (Table 11).

HTM, N3, and TiO₂ Interacting System. The HTM-N3-TiO₂ complex is optimized with LanL2DZ pseudopotential, using hybrid functional of DFT such as B3LYP (Fig 38). On the electrostatic energy surface, both dissociative and non-dissociative strong interactions are found among these three components as can be seen from Fig 38. The interaction of N3 with TiO₂ is dissociative where oxygen atoms of the carboxylic groups make covalent bonds with the Ti atom of TiO₂.

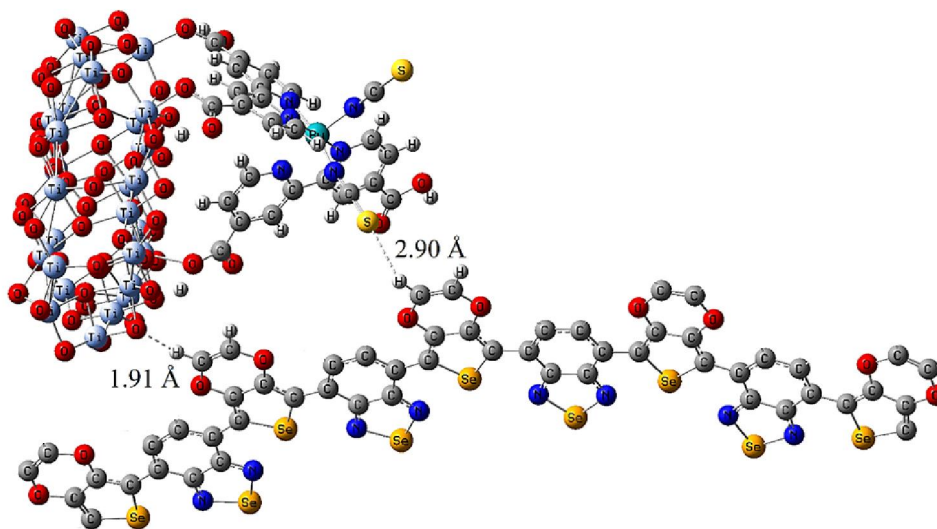


Figure 38. Optimized Geometric Structure of the HTM-N3-TiO₂ system; for simplicity reason, some of the hydrogen atoms are omitted (Article 6).

However, the HTM and N3 interaction is non-dissociative but quite strong, due to the establishment of Hydrogen bonding (Se---H). The HOMO and LUMO results are also inconsistent with the previous results. Based on these simulations, we can say that when light shines on the proposed configuration, the delocalized π -electrons of N3 would become activated and move to TiO₂ and ultimately would regenerate itself by sharing an electron from the HOMO of HTM. In summary, if the proposed configuration of SDSC is exposed to light; the excited electrons of both dye and HTM become delocalize and move from

the dye to nonporous TiO₂ and consequently the oxidized dye would be regenerated from the HTM via exchanging of the electron.

5.3. Zinc Porphyrin Based DSSC

Theoretical simulations are carried out for the synthesized porphyrin-based sensitizers, having a furan hetero aromatic ring between the porphyrin macrocycle and anchoring group either at *meso*-phenyl or at pyrrole- β position of porphyrin. The experimental effort was performed by our Indian collaborative as mention in Chapter 1 (Article 7). The porphyrin macrocycle acts as donor, furan hertero cycle acts as π -spacer and either cyanoacetic acid or malonic acid group acts as acceptor. Comprehensive details of these dyes are given in Article 7.

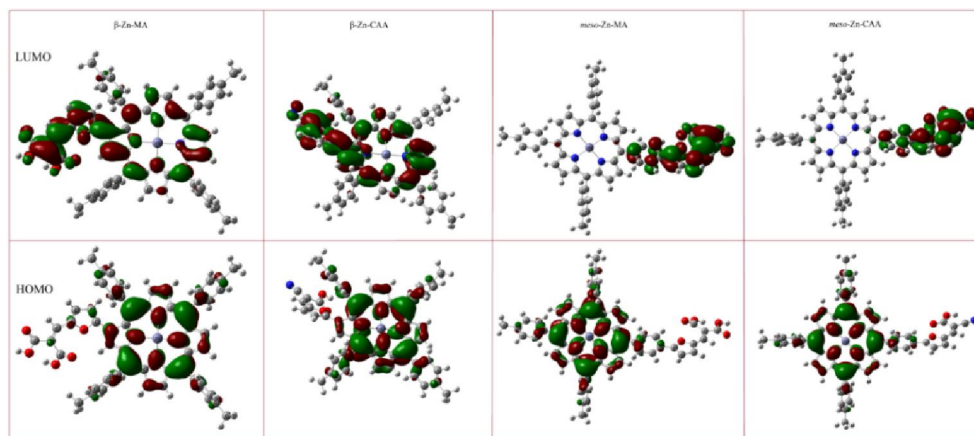


Figure 39. Contours of HOMO and LUMO of Zn Porphyrin-Furan dyes (Article 7).

The theoretical predicted frontier molecular and NBO contours of these dyes are shown in Fig 39 and 40, where topmost HOMO is strongly contributed by the N 2p states and the lowest LOMO is strongly contributed by C 2p-like states slightly hybridized with O 2p and C 2p states. Most contribution to the highest HOMO and lowest LUMO states are coming from p electrons whereas

contribution from s-electrons is modest. Since the p - p electrons transitions are not allowed, very strong absorption of sunlight by the molecule is not expected.

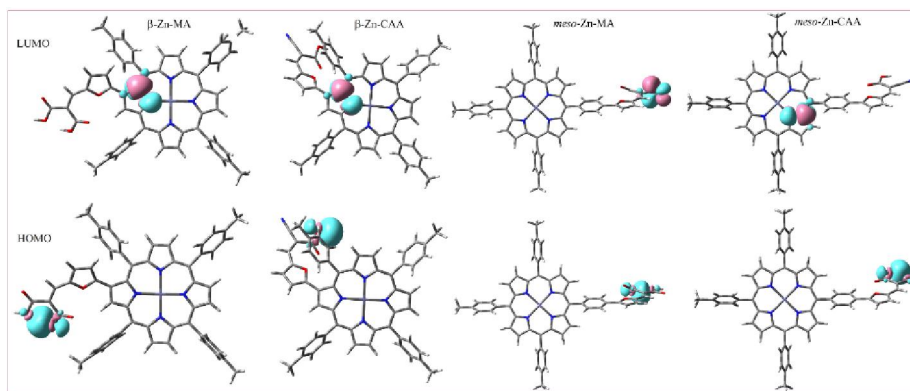


Figure 40. Contours of Occupied and Unoccupied NBO of Zn Porphyrin-Furan dyes (Article 7).

The electron localization function for the dyes can be found from Fig 40. Analysis shows that the electrons are distributed around the ring, so the dye molecules can be oxidized. Highest electronic cloud density on the HOMO at anchoring sites of these dyes clearly predict that charge injection is favoured while the lowest one on the LUMO shows that charge recombination is prevented. From the NBO contours of all these dyes (Fig 40), it is evident that except the *meso*-Zn-MA, the rest of them have good electron donating ability.

TABLE 12. TD-DFT calculated electronic excitations (λ_{max}) and Optical gap of Zn Porphyrin-Furan dyes

<i>Species</i>	<i>Maximum Excitation</i>	<i>Oscillator Strength</i>	<i>Electronic Transition</i>	<i>Optical Gap (eV)</i>
β -Zn-MA	617	0.13	$\pi \rightarrow \pi^*$	2.00
β -Zn-CAA	609	0.11	$\pi \rightarrow \pi^*$	2.03
<i>meso</i> -Zn-MA	585	0.22	$\pi \rightarrow \pi^*$	2.11
<i>meso</i> -Zn-CAA	611	0.22	$\pi \rightarrow \pi^*$	2.02

The electronic absorption spectra of these porphyrin-based sensitizers were recorded in THF solution, which are given in Fig 41. The wavelengths of maximum absorbance (λ_{max}) values of these porphyrin-furan conjugates are obtained from UV-Vis studies which are summarized in Table 12.

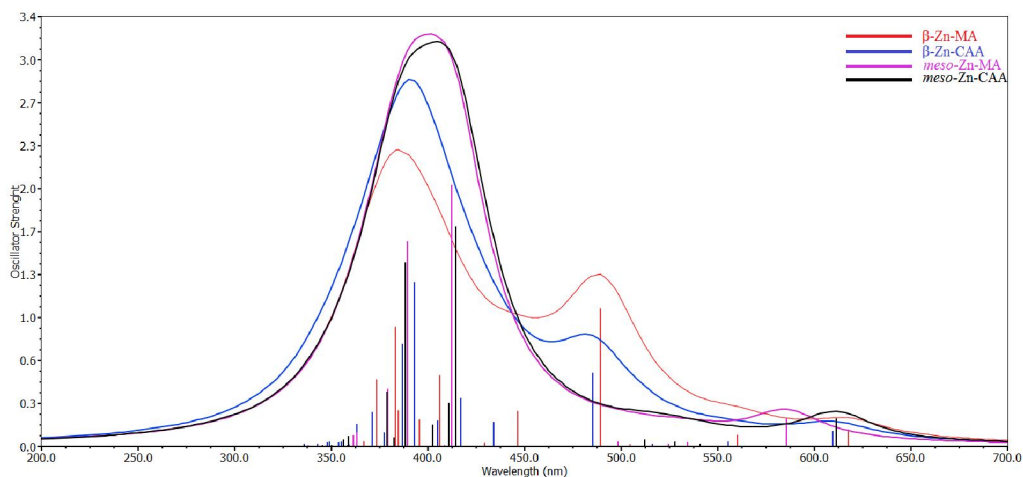


Figure 41. TD-DFT simulated UV-vis spectra of Zn Porphyrin-Furan dyes (Article 7).

The absorption spectra of these porphyrin-furan conjugates in THF solution shows an intense soret band between 420-430 nm and two less intense Q-bands between 500 to 625 nm due to $\pi-\pi^*$ absorption of the conjugated macrocycle. We also simulated the singlet excited state (optical band gap) energy at Δ SCF method, which has excellent matching as can be seen from Table 12 and Article 7. The simulated optical band gap of β -Zn-MA is 2.0, β -Zn-CAA has 2.03, *meso*-Zn-MA has 2.11 and *meso*-Zn-CAA has 2.02 eV.

5.4. Summary

We have carried out structural, electronic, optical, and charge-transport properties of a donor-acceptor-donor polymer; a Hole transporting material (HTM), N3 and TiO₂ for the design of an efficient SDSC. We proposed an ideal setup for an SDSC, where the HTM, N3, and TiO₂ are chosen, based on their upstairs like energy levels (band edge positions); having a difference of at least 0.50 eV. Our theoretical simulations prove that if we shine a light on the proposed setup, the electron would move from the dye to TiO₂ and from HTM to dye, to be regenerate. The theoretical open-circuit voltage of about 1.49 eV is responsible for high quantum yield.

Moreover, we have carried out comprehensive theoretical and experimental studies of porphyrin–furan conjugates, in which anchoring group either at meso-phenyl or at pyrrole-β position of a zinc porphyrin based on donor-π-acceptor approach. The dyads were tested in dye sensitized solar cells using I⁻/I₃⁻ redox couple. Both theory and experiment strongly corroborate each other, however, the overall efficiency of these sensitizers is very low, which need to be improved.

CHAPTER 6: Polymers and Their Composites for the Environmental Applications

6.1. Polypyrrole/TiO₂ Composites for Pollutants Degradation

Although, experimental study of PPy-TiO₂ as a photocatalyst is reported but facing lower photocatalytic efficiency which is due to lack of theoretical investigation [180-183]. The fully explored theoretical insight of optical, electronic structure, surface interactions, electroactivity and charge transfer mechanism between PPy and TiO₂ is essential to tailor and improve photocatalytic activity of PPy-TiO₂ nanocomposite. Detailed theoretical investigation of charge transfer mechanism between nPy and TiO₂ (molecular cluster; Ti₁₆O₃₂) in a connected junction such as nPy-TiO₂ nanocomposite. The present article is focused on the investigation of important photocatalytic parameters such as (i) interaction of Ti₁₆O₃₂ with PPy oligomers to find out electron-hole transformation, (ii) band structure alteration, (iii) charge transport (NBO) (vi) optimisation of oligomeric length of Py for efficient performance and (v) structure-property relationship. The study is aimed to provide a better understanding of the electronic structure of nPy-Ti₁₆O₃₂ nanocomposite and will open new direction to synthesize an efficient nPy-TiO₂ nanocomposite photocatalyst with the optimized composition for visible light photocatalysis. Moreover, this work will also inspire computational scientists to explore structural property relationship of other COP- metal oxide nanocomposites.

Results and Discussion: Based on band gap simulation and computational point of view, it is evident that Ti₁₆O₃₂ (band gap 3.06 eV) is a better

representative of bulk anatase (Fig 42). The current study is focused on $\text{Ti}_{16}\text{O}_{32}$ and their interaction with different Py oligomers.

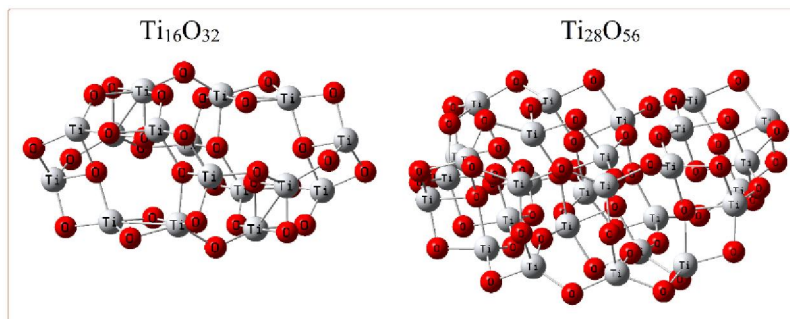


Figure 42. Optimized Geometric Structure of $\text{Ti}_{16}\text{O}_{32}$ and $\text{Ti}_{28}\text{O}_{56}$ clusters.

During the optimization, $\text{Ti}_{16}\text{O}_{32}$ circulated and finally attached at the middle of nPy oligomer by establishing strong non-covalent bonds with H and C atoms of Py. The interaction of $\text{Ti}_{16}\text{O}_{32}$ with nPy oligomers, results distortion in nPy geometries (Fig 43), which is a direct consequence of their strong orbital overlapping.

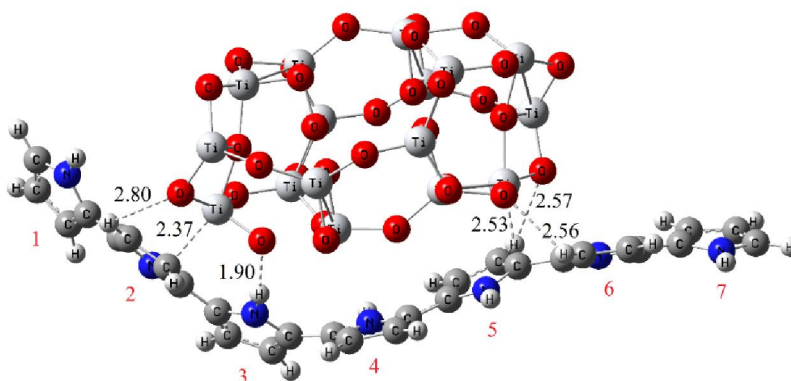


Figure 43. Optimized Geometric Structure of $7\text{Py-Ti}_{16}\text{O}_{32}$ (Article 8).

Six different types of inter-molecular interactions are observed in the case of the $7\text{Py-Ti}_{16}\text{O}_{32}$ system; where Ti and O of $\text{Ti}_{16}\text{O}_{32}$ have made the strong

electrostatic type of bonding with the C and H atoms of 7Py; ranging at ca. 1.90 to 2.80 Å. In all these composites, Ti atom of $\text{Ti}_{16}\text{O}_{32}$ makes an inter-molecular electrostatic bond with C of nPy and a Hydrogen bond between the O of $\text{Ti}_{16}\text{O}_{32}$ and H atoms of nPy. The O---H inter-molecular bonds in the studied systems are strong bonds and can be regarded as covalent bonding. On the other hand, simulated Ti---C bond distances in the range of 2.30-2.70 Å confirm the formation of a strong electrostatic interaction. Jeffery et al. have reported that 2.2-2.5 Å of hydrogen bonding will be "strong, mostly covalent", 2.5-3.2 Å as "moderate, mostly electrostatic" while 3.2-4.0 Å as "weak, mostly electrostatic" along with following bond energies, -40 to -14, -15 to -4, and <-4 kcal/mol, respectively [184]. Comparative analysis of simulated inter-molecular bonding led us to conclude that $\text{Ti}_{16}\text{O}_{32}$ make a strong composite with Py oligomers.

Interaction Energy in nPy-Ti₁₆O₃₂ Composites: $\text{Ti}_{16}\text{O}_{32}$ and PPy oligomers have a good interaction which is mostly covalent and electrostatic, simulated from interaction energy (ΔE_{int}) and geometrical counterpoise corrected ($\Delta E_{\text{gCP-D3}}$) methods (Table 13). The $\Delta E_{\text{gCP-D3}}$ method is employed to minimize the geometrical and dispersion factors. The result of this inter-molecular interaction energy proved that a very strong interaction is present in nPy and $\text{Ti}_{16}\text{O}_{32}$ species. In the 3Py- $\text{Ti}_{16}\text{O}_{32}$ composite, the ΔE_{int} is -42.54 kcal/mol while this interaction energy is simulated to be -54.09 kcal/mol with $\Delta E_{\text{gCP-D3}}$ method which is 11.55 kcal/mol higher than the ΔE_{int} method. A comparatively weak inter-molecular force is present in 5Py- $\text{Ti}_{16}\text{O}_{32}$ for which these energies are; -34.22 kcal/mol based on ΔE_{int} and -47.50 kcal/mol based on $\Delta E_{\text{gCP-D3}}$. This decrement in inter-molecular interaction energy is due to its geometrical shape

compared to the 3Py-Ti₁₆O₃₂ composite. With chain length elongation, a slight difference in ΔE_{int} is observed as can be seen from data in Table 13.

Table 13: Inter-molecular interaction energy (ΔE_{int}), geometrical counterpoise corrected energy (ΔE_{gCP-D3}), in kcal/mol), and NBO charges analysis of nPy-Ti₁₆O₃₂.

<i>Species</i>	ΔE_{int}	ΔE_{gCP-D3}	Q_{NBO}
3Py-Ti ₁₆ O ₃₂	-42.54	-54.09	0.409
5Py-Ti ₁₆ O ₃₂	-34.22	-47.50	0.469
7Py-Ti ₁₆ O ₃₂	-41.10	-72.47	0.709
9Py-Ti ₁₆ O ₃₂	-41.47	-68.21	0.599

In the case of 7Py-Ti₁₆O₃₂, this inter-molecular non-bonding energy is about -41.10 kcal/mol, based on ΔE_{int} while -72.47 kcal/mol based on ΔE_{gCP-D3} . This highest interaction energy (ΔE_{gCP-D3}) in 7Py-Ti₁₆O₃₂ can be attributed to the suitable oligomeric length of PPy. Moreover, strong interaction of 7Py-Ti₁₆O₃₂ can be correlated to the fully relaxed geometric structure, which allows 7Py to wrap around Ti₁₆O₃₂ cluster much effectively compared to other compositions of nPy-Ti₁₆O₃₂. A similar but less pronounced trend is observed in 9Py-Ti₁₆O₃₂ composite, where the ΔE_{int} and ΔE_{gCP-D3} are -41.47 and -68.21 kcal/mol, respectively. Comparative analysis of the interaction energy of 7Py-Ti₁₆O₃₂ and 9Py-Ti₁₆O₃₂ indicate that 7Py make stronger nanocomposite.

Natural Bonding Orbital Analysis: In connection with previous sections, Ti₁₆O₃₂ interacts with nPy oligomers through strong hydrogen (mostly covalent) and electrostatic (Ti---C). The analysis of NBO simulation indicates that Ti---C

bond is the main charge transferring paths in all nPy-Ti₁₆O₃₂ composites. The net charge transfer in all nPy-Ti₁₆O₃₂ composites is comprehensively listed Article 8.

Electronic Properties Simulation: The electronic properties such as IP, EA, HOMO, LUMO, ESP, DOS and band gap of isolated as well as nPy-Ti₁₆O₃₂ composites was estimated at B3LYP/LanL2DZ level. The Δ SCF and negative of HOMO orbital energies are almost similar, especially for long chain systems. The IP energy is estimated from the negative of HOMO while the EA is obtained from negative of LUMO, using Koopman's theorem. Higher the EA and IP values of a chemical substance, greater will be its electroactivity and stability. The HOMO and LUMO energies (band edge positions) of isolated Ti₁₆O₃₂ are listed 14 and in Fig 44.

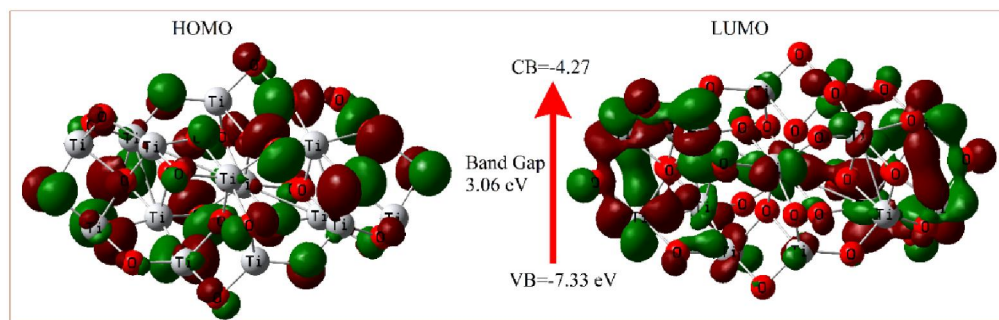


Figure 44. Contours of the HOMO and LUMO of Ti₁₆O₃₂ (Article 8).

Our simulated band gap value for Ti₁₆O₃₂ is 3.06 eV at B3LYP/LanL2DZ level, which is close to that of the observed data (3.20 eV) [185].

Ionization Potential: Interaction of Ti₁₆O₃₂ with nPy increases the IP of nPy oligomers indicating the increased stability of the resulted composite. Higher the IP more will be the stability of a chemical substance. In case of 3Py-Ti₁₆O₃₂

composite, the increase in IP is about 0.96 eV which consequently narrow its band gap from 4.27 to 2.12 eV. A similar trend is observed in rest of the nPy oligomers in nPy-Ti₁₆O₃ composites, except 9Py-Ti₁₆O₃ composite, where negligible change (IP value) has been observed which can be attributed to lower interaction ability of their molecular orbitals.

Electron Affinities: EA is estimated from the negative of LUMO, which found to be increasing in nPy oligomers upon interacting with Ti₁₆O₃₂. A substantial shift in LUMO to narrow the band gap is observed in nPy-Ti₁₆O₃₂ bounded species compared to individual Ti₁₆O₃₂ and nPy.

Band Gap and Molecular Orbitals Energy: The band gap of nPy oligomers become narrow upon interaction with Ti₁₆O₃₂, which is an evidence of their excellent electroactive property in the resulted composite (Table 14).

TABLE 14: Molecular Orbital Energy, Band Gap (in eV) and Dipole moment (Debye) of nPy and nPy- Ti₁₆O₃₂ composites

<i>Species</i>	<i>HOMO</i>	<i>LUMO</i>	<i>Dipole moment</i>	<i>Band Gap</i>
Ti ₁₆ O ₃₂	-7.33	-4.27	0.0007	3.06
3Py	-4.71	-0.44	1.56	4.27
3Py-Ti ₁₆ O ₃₂	-5.67	-2.12	13.63	2.55
5Py	-4.45	-0.76	1.08	3.69
5Py-Ti ₁₆ O ₃₂	-5.04	-3.53	10.89	1.51
7Py	-4.34	-0.91	0.58	3.43
7Py-Ti ₁₆ O ₃₂	-5.24	-3.37	9.97	1.87
9Py	-4.28	-0.98	0.07	3.30
9Py-Ti ₁₆ O ₃₂	-4.42	-3.68	8.75	0.74

It can be easily predicted from the data that molecular orbitals of $\text{Ti}_{16}\text{O}_{32}$ strongly interact with the HOMO/LUMO of nPy through establishing strong covalent types of bonding (Table 14). The strong covalent type of bonding indicate the stability of nPy- $\text{Ti}_{16}\text{O}_{32}$ composites which have an intermediate band gap and highest dipole moment. Moreover, narrowing band gap, have also a direct relationship with chain length elongation of Py as obvious from Fig 45.

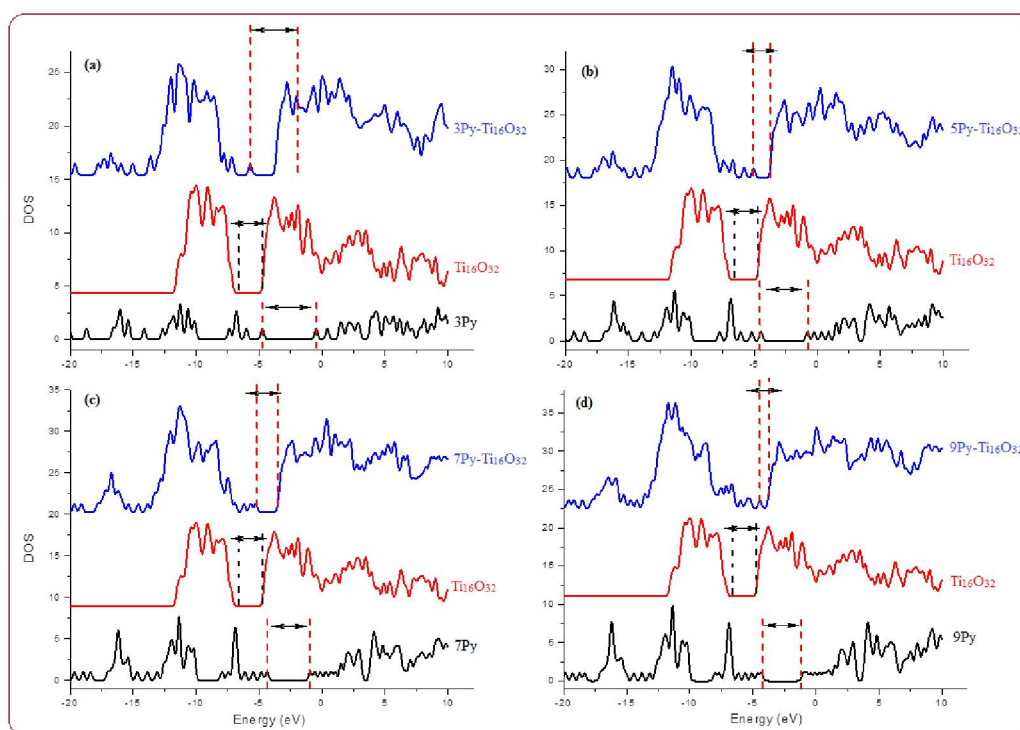


Figure 45. Density of states plots of $\text{Ti}_{16}\text{O}_{32}$, nPy and nPy- $\text{Ti}_{16}\text{O}_{32}$ bounded complexes (Article 8).

$\text{Ti}_{16}\text{O}_{32}$ reduces the HOMO of 5Py from -4.45 to -5.04 eV (actually increase in negative charge), LUMO from -0.76 to -3.53 eV and band gap from 3.69 to 1.51 eV. Similar, but more pronounced reduction in these values can be seen in 7Py- $\text{Ti}_{16}\text{O}_{32}$, 0.90 eV in HOMO, 2.46 eV in LUMO, and a reduction of 1.56 eV in its band gap. Electronic cloud densities of the contours of HOMO and LUMO of 9Py- $\text{Ti}_{16}\text{O}_{32}$ compared to that of 9Py are enhanced to about 0.14 eV and 2.70

eV, respectively. While their dipole moment and band gap change from 0.07 to 8.75 Debye and 3.30 to 0.74 eV, respectively.

So, from experimental point view, we don't need to synthesize an infinite chain length of PPy, the routine oligomer (up to 6 or 8 repeating units) will be a best fit for the commercially available TiO₂ (anatase). Furthermore, the study also provides insight into improving the band structure, charge transport and determination of physical and chemical bonding between nPy and TiO₂ species.

UV-vis Study: The first allowed electronic excitation energies are correlated with the experimentally observed λ_{\max} , which are listed in Figure 46 and Table 15. Three prominent band peaks are found in the UV-vis spectra of nPy oligomers where the high wavelengths one is referred as λ_{\max} ; the transition of an electron from valence to conduction band. Interaction of Ti₁₆O₃₂ with nPy oligomers (Fig 46) cause a red-shifting in the λ_{\max} of nPy. This red-shifting in λ_{\max} of all nPy oligomers illustrates the *n*-type doping nature of Ti₁₆O₃₂.

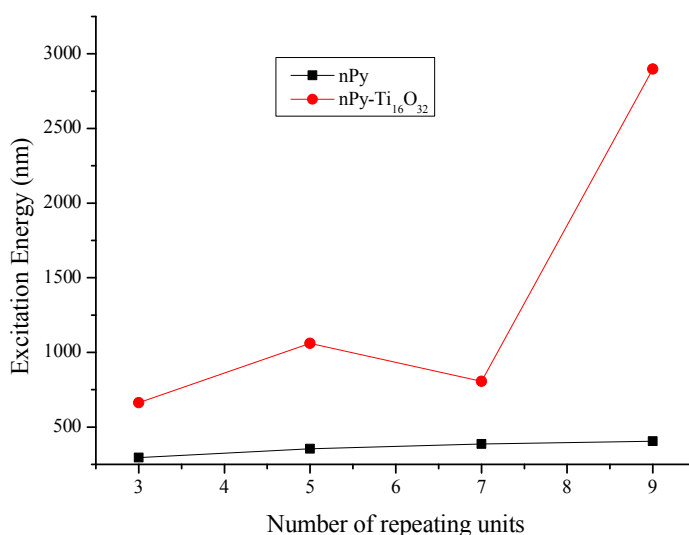


Figure 46. First allowed electronic excitation energy of nPy and nPy-Ti₁₆O₃₂ composites (Article 8).

In the case of 3Py, the excitation energy of $\pi \rightarrow \pi^*$ transition increased from 296 to 663 nm in the resulted composite (3Py-Ti₁₆O₃₂), which evidences the establishment of strong bonding. As shown in Table 6, Ti₁₆O₃₂ increases the first allowed electronic excitation energy of 5Py to about 707, 420 in 7Py, and 2493 nm in 9Py. This substantial increase can be attributed to improved conductivity/delocalization of the composites compared to isolated nPy oligomers (*vide infra*).

The individual Ti₁₆O₃₂ and nPy oligomers are unable to absorb in the visible range, however, nPy-Ti₁₆O₃₂ composites have excellent absorption capability in the visible region due to a substantial decrease in the band gap. The red-shifting from the ultraviolet to visible elucidates/evidences the excellent photovoltaic and photocatalytic activity of nPy-Ti₁₆O₃₂ composites over their individual constituents.

6.2. Polypyrrole Gas Sensors

PPy is a promising candidate for gas sensing applications due to its ease of synthesis, high redox properties, tunable nature [45], stability either in the neutral or doped form, and good electrical conductivity. Changes in electrical conductivity of PPy can easily be observed, upon interaction with various volatile organic and inorganic analytes. Several reports are presented in this regard, where change in conductivity of PPy is measured upon exposure to different gases such O₂, NO₂, CO, CO₂ and NH₃. Blance *et al* [186] reported NH₃ gas sensing properties of PPy upon exposure to a mixture of O₂, NO₂, and NH₃. On the other hand, Lui *et al.* [187] fabricated a CO gas sensor by growing a PPy film through electropolymerization. A gas sensors for CO₂, based on PPy film is also reported [188] showing the interactive ability of PPy, but not counter

checked by theory. Among other fascinating properties, the ability of PPy to form covalent bonding with inorganic substances like diamond, make it a valuable material for molecularly imprinted sensors [189].

In this work, sensing mechanism of both, cationic and neutral, forms of different oligomers of PPy are investigated with the help of electronic structure theory simulations. The interaction of different analytes such as NH₃, CO₂, and CO on the surface of PPy (nPy/nPy⁺) are considered for the sensitivity (Fig 47).

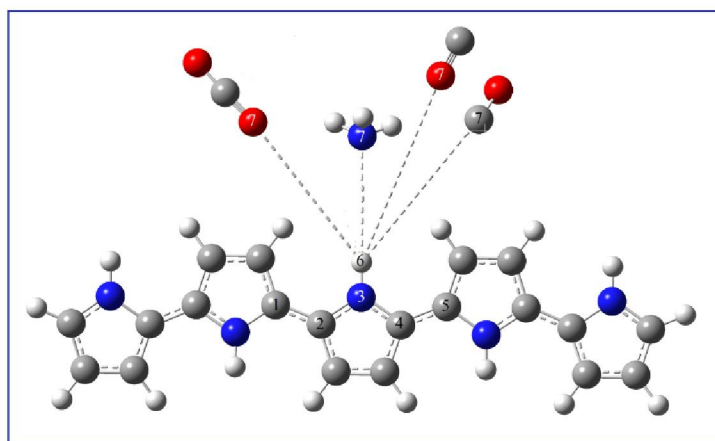


Figure 47. Reference optimized geometric structure of 5Py⁺-X (X=NH₃, CO₂, CO) (Article 9).

Inter-molecular bond length: The inter-molecular non-bonding distance, $d_{H6...X7}$ between nPy and NH₃ is about 1.94 Å for all oligomers. Inter-molecular non-bonding interaction analyses led us to conclude that NH₃ and PPy oligomers have strong interaction compared to nPy-CO₂ and nPy-CO complexes. The doped form of PPy have smaller inter-molecular distance with NH₃, compared to the neutral form. It is found from the inter-molecular bond distance analysis that PPy (both doped and neutral form) shows excellent response towards ammonia, compared to that of carbon dioxide and carbon monoxide. It means that PPy is more responsive and selective towards ammonia gas in presence of CO₂ and CO.

Intra-molecular bond length: Results of the intra-molecular bond distance analysis are also in good agreement with inter-molecular bond distances; higher sensitivity and selectivity of PPy with NH₃.

Table 3. ΔE_{int} , $\Delta E_{int,CP}$, Q_{NBO} and $Q_{Mulliken}$ of nPy^+-X ($X=NH_3$, CO_2 , and CO), ($n=3, 5, 7$, and 9) Using UB3LYP/6-31G (d) level of theory.

Species	ΔE_{int}	$\Delta E_{int,CP}$	Q_{NBO}	$Q_{Mulliken}$
3Py⁺-NH₃	-16.69	-15.62	-0.071	-0.080
5Py⁺-NH₃	-14.68	-13.74	-0.061	-0.070
7Py⁺-NH₃	-13.74	-12.80	-0.060	-0.068
9Py⁺-NH₃	-13.05	-12.11	-0.057	-0.065
∞Py⁺-NH₃	-10.74	-9.69		
3Py⁺-CO₂	-5.08	-4.58	-0.018	-0.045
5Py⁺-CO₂	-4.27	-4.10	-0.015	-0.038
7Py⁺-CO₂	-3.95	-3.45	-0.013	-0.037
9Py⁺-CO₂	-3.64	-3.50	-0.013	-0.035
∞Py⁺-CO₂	-2.78	-2.41		
3Py⁺-CO(1)	-4.46	-3.22	-0.030	-0.056
5Py⁺-CO(1)	-4.02	-3.01	-0.026	-0.050
7Py⁺-CO(1)	-3.70	-2.61	-0.024	-0.047
9Py⁺-CO(1)	-3.51	-2.31	-0.023	-0.045
∞Py⁺-CO(1)	-2.63	-0.80		
3Py⁺-CO(2)	-3.20	-1.76	-0.015	-0.039
5Py⁺-CO(2)	-2.70	-1.50	-0.012	-0.033
7Py⁺-CO(2)	-2.51	-1.19	-0.011	-0.033
9Py⁺-CO(2)	-2.32	-1.02	-0.010	-0.030
∞Py⁺-CO(2)	-1.81	-0.07		

Bond angle and Dihedral angle: Both, inter- and intra-molecular bond distances, angles and torsional angles are found disturbed after interacting with analytes, so, it is proved that both nPy and nPy⁺ have sensing ability with these gases; however, it is more sensitive to NH₃. Interaction of 9Py/Py⁺ with mixture of three gases attached in the trimer (NH₃, CO₂ and CO) are also performed to check the selectivity phenomena more accurately.

Interaction Energy Analysis: Greater this interaction energy, greater will be response of the nPy/nPy⁺ towards analytes. The calculated interaction energies are also counterpoise corrected. Counterpoise corrected energy method removes the error arising from the use of finite basis sets. Adsorbent species (PPy/PPy⁺ in this case) interacts with analytes and become stable due to these interaction energies. The complexes are stable either because of hydrogen bond or weak dipole-induced-dipole, or ion-dipole interaction with adsorbate (NH₃, CO₂, CO). Simple and BSSE interaction energies of PPy/PPy⁺ with these different analytes are listed in Table 3 and Article 9. Comparative analysis of the above results illustrates that PPy oligomers either in the doped and neutral state, are sensitive and selective towards NH₃. The interaction energy analysis also supports the experimental evidences of high sensitivity of PPy towards NH₃ gas.

Charges Analysis: Interaction between two or more species is often associated with charge transfer. Charge transfer alters the electronic and structural properties of these interacting species. The sensing capability and therefore, selectivity of PPy oligomers (doped and neutral forms) towards NH₃, CO₂, and CO can be well understood through amount of charge transfer between the oligomer and analyte. Charge analyses predict that PPy is more

sensitive and selective towards NH_3 , amongst CO_2 , CO and NH_3 . NH_3 causes doping in $n\text{Py}$ and de-doping in $n\text{Py}^+$ oligomers, establishing hydrogen and ion-electrostatic bonding, respectively. PPy, doped or neutral, shows high response towards ammonia.

Frontier Molecular orbital and Band gap analysis: Sensing properties of a substance are also greatly dependent on the interaction of molecular orbitals of oligomer with analyte. Molecular orbitals of sensing material, particularly HOMO and LUMO get perturbed after interaction with analyte. Contours of the HOMO and LUMO of isolated $n\text{Py}/n\text{Py}^+$ and analyte bounded complexes are given in Figures 48.

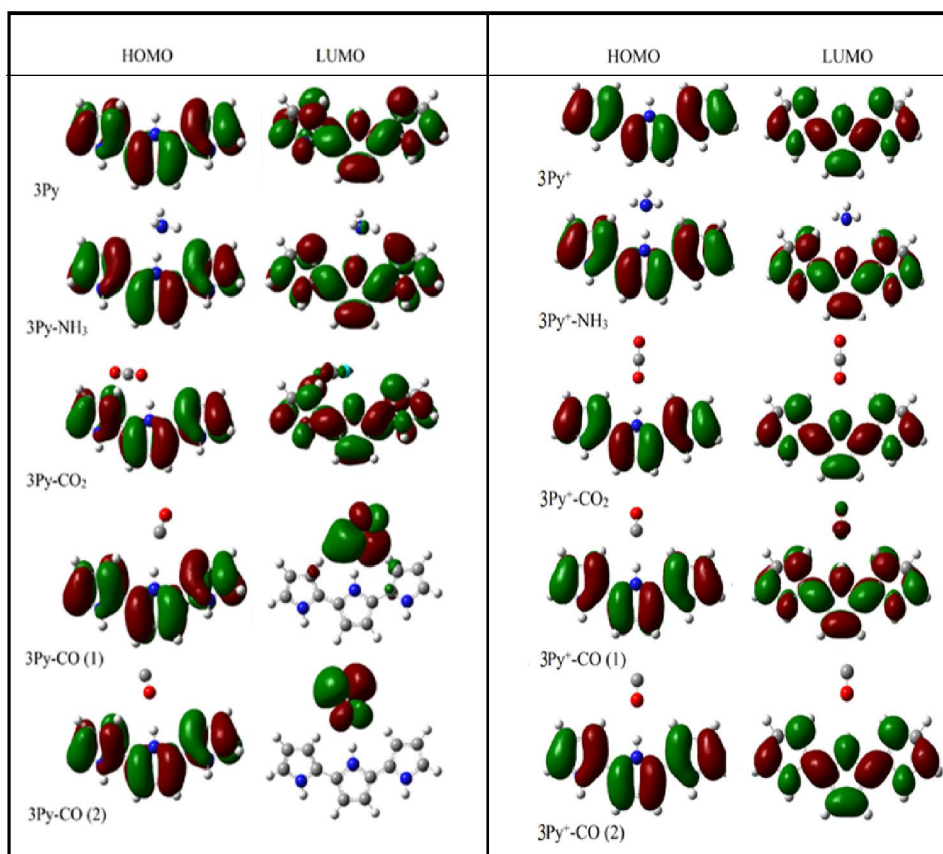


Figure 48: Frontier Molecular Orbitals of $3\text{Py}/3\text{Py}^+$ and $3\text{Py}/3\text{Py}^+-\text{X}$ ($\text{X} = \text{NH}_3$, CO_2 , $\text{CO}(1)$ and $\text{CO}(2)$), Using B3LYP/6-31G (d) and UB3LYP/6-31G (d) Level of Theory (Article 9).

Overall, NH_3 donates electronic cloud density and causes de-doping of nPy^+ oligomers while CO_2 has less effective interaction on large oligomer. Interaction of CO with nPy^+ also follows the same trend as for nPy , however, the overall interaction is very small.

UV-vis/UV-vis-Near-IR spectroscopic analysis: UV-Vis spectra of nPy/nPy^+ and $\text{nPy}/\text{nPy}^+-\text{X}$ complexes can be found from Article 9, while that of $3\text{Py}/\text{Py}^+$ and their complexes are given in Fig 49. A peak in the near-IR region can be observed in the doped form of nPy (nPy^+) and their analyte bound complexes, besides the three main peaks.

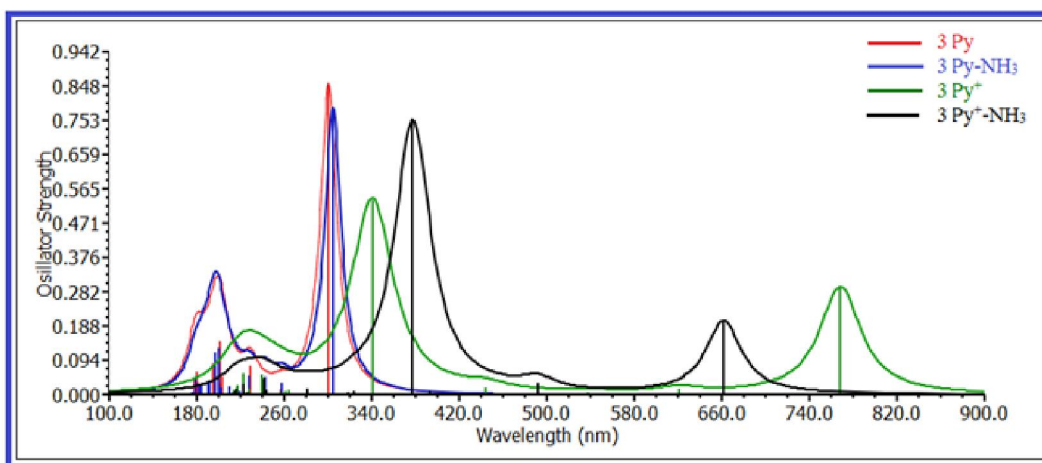


Figure 49. UV-Vis/UV-Vis-near-IR of 3Py (red), $3\text{Py}-\text{NH}_3$ (blue), 3Py^+ (green), and $3\text{Py}^+-\text{NH}_3$ (black) (Article 9).

UV-vis spectrum of nPy^+ shifts to low energy (compared to nPy) band peak in the near-IR region which clearly shows the doping phenomenon of nPy . NH_3 decrease the doping intensity of nPy^+ by transferring electronic charge density, therefore, it causes a blue shift in the low energy band peak. CO_2 and CO also show similar but less pronounced effect, compared to NH_3 , on interaction with nPy/nPy^+ . The peaks shifting are less pronounced as compared to NH_3 ; depicting more sensitivity of PPy/PPy^+ towards NH_3 .

6.3. Graphene and their Derivatives Gas Sensors

The main challenges for scientific and technological research for solar energy conversion, energy storage and environment are the stability, durability, and performance of low cost functional materials. The discoveries of sp² hybridized carbon nanomaterials such as buckminsterfullerene, carbon nanotubes and GR have revolutionized the research directions in the fields of physics, material science, chemistry, and life sciences [190-193]. The progress made in GR-based materials for energy and environmental applications has been discussed in several reviews articles with either focus on specific materials or general preparation methods and functionalization.

Environmental applications of GR molecules: The effect of globalisation and industrialisation increased the amount of contamination in soil and water. This leads to severe environmental problems and health issues. The wastewater industrial plants generate increasing amounts of environmental concerns through enormous amounts of wastewater production. This contains toxic organic compounds which includes organic dyes, phenols, biphenyls, pesticides, fertilizers, hydrocarbons, plasticizers, detergents, oils, greases, pharmaceuticals, proteins, carbohydrates, etc.[194]. GR has been used as a remediation agent, widely in the adsorption and photocatalytic approach. Adsorption is a surface phenomenon which depends on many factors such as nature of adsorbate and adsorbant and their physical characteristics, i.e temperature, pH, concentration of pollutants, contact time, particle size, and temperature [195]. The photocatalytic approach involves light induced photochemical reactions due to the unique electronic band structure of the semiconducting materials involved in the reaction process.

Photocatalytic degradation of Pollutant: The photocatalytic action requires the catalytic species to be active with respect to the illumination of light on the semiconductor surface. The following steps are involved in the process of photocatalytic degradation of pollutants, as shown in Fig. 50 (here TiO_2 semiconductor is used as a photocatalytic materials)

- The excitation of electron from valence band to conduction band, when TiO_2 absorbs energy equal to or larger than the band gap.
- The excitation of these electrons results in the generation of “holes” (electron vacancy) in the valence band.
- The results of excitation will also generate oxidizing and reducing agents.
- The holes (h^+) reacts with water and generate highly active hydroxyl radical ($\text{OH}\cdot$) that can act as powerful oxidant.
- The hydroxyl radicals can react with organic pollutants to degrade or oxidize them to form CO_2 and H_2O .

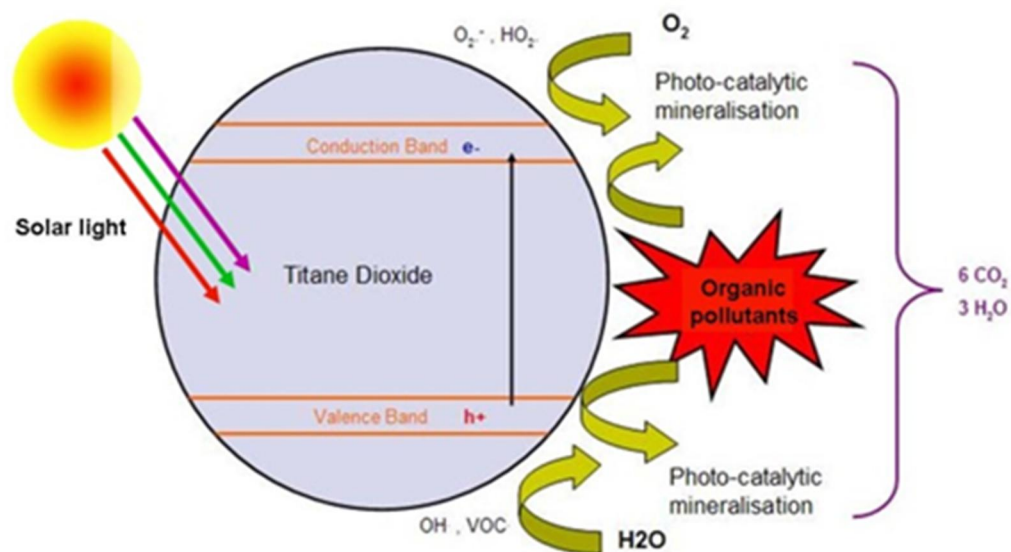


Figure. 50. Illustration of photocatalytic process of degradation in pollutants in TiO_2 (Article 10).

Gas Sensor Applications: The extensive application of graphene in a gas sensor is due to the large specific surface area that can adsorb gas molecules on the surface. The gas sensitivity of graphene comes from, large specific areas which enable graphene to provide the largest sensing area per unit volume, strong covalent interactions between surface atoms, and adsorbates and high carrier mobility. The interaction between gas molecules and graphene atoms perturbs the graphene electronic system which can be monitored with external electronic components.[196] Interestingly, graphene has low electrical noise due to its high quality crystal lattice arrangements that makes it capable of screening more charge fluctuation. The ability of charge fluctuation screening in graphene provides a noticeable change in the conductance. Graphene has been able to detect the CO₂, CO, NO, NH₃, SO₂, H₂, Cl₂, and NO₂ and organic vapours includes acetone, benzene, and toluene.[197-201] The limit of gas detection, as low as parts per billion graphene, has been prepared as single layer graphene using mechanical exfoliation,[202] adhesive tape methods, and mechanical exfoliated graphene[197] for NO₂ detection. In other studies, RGO was applied to detect chemical warfare agents, NO₂, NH₃ and Cl₂ at low ppm.

Heavy metal ion detection and removal: Environmental contaminations are often from toxic heavy metal ions and other pollutants. Usually heavy metal ions, such as arsenic (As), antimony (Sb), cadmium (Cd), chromium (Cr), lead (Pb), mercury (Hg), and zinc (Zn) are hazardous to human health when consumed in excess amount or over longer periods of contact. Heavy metal ions commonly lead to mental confusion, acute pains in joints and muscles, short-term memory loss, food intolerances/ allergies, headaches, gastrointestinal upsets, etc.[203] However, each element is responsible for

some serious health issues which are related to the nervous system, cardiovascular system, kidneys, and even reproductive system.[203] In recent years, there has been a lot of interest in using carbon related materials for the detection and removal of toxic and harmful substances from the environment, especially from water and air.

Biosensing applications: Biosensors utilize biological or molecular recognizers and transducers to register a specific biomolecular interaction and/or the amount of target analyst. The development of simple, sensitive, and low-cost biosensing platforms with high selectivity is critical in bioanalysis. The excellent physiochemical characteristics render GR and its derivatives as excellent transducing element in bioanalysis [204,205]. For example, the existence of π -rich conjugation domains in GR facilitates the interaction between the single stranded DNA molecules through π - π stacking interactions.[204,205] Also, extensive efforts have been made in analyzing the nano-bio interface of GR, and its derivatives, with various biomolecules. It is shown that under a favorable environment, the immobilization of enzymes on GR, and its derivatives, improves enzyme stability and specificity together with prolonged enzyme functionality.[206,207].

6.4. Summary

DFT of pyrrole-Ti₁₆O₃₂ bounded systems are carried out to find their interaction to tailor the best composite for the photodegradation of environmental pollutants and solar water splitting. So, after confirming the composite formation, band gap narrowing, and better visible light absorption capability is observed compared to their individual nPy and Ti₁₆O₃₂ constituents. Moreover, UV-vis spectra of these composites predict the visible light absorption

compared to nPy and $Ti_{16}O_{32}$. Electron-hole transferring define Py oligomers as a donor and $Ti_{16}O_{32}$ cluster as an acceptor in the resulted composites.

DFT study of nPy/nPy⁺ (where n=3, 5, 7, 9) and their complexes with NH₃, CO₂ and CO are carried out to analyze the sensitivity and selectivity of PPy, both in neutral and doped form. Comparative results of interaction energy of neutral and doped form of PPy reveal greater response for the doped form towards different analytes. It is also indicated from interaction energy that PPy shows more response to CO₂ than CO. Frontier molecular orbitals energies of nPy-X and nPy⁺-X, before and after sensing, confirm that NH₃ perturbed the orbital energy of PPy to greater extent than the perturbation caused by CO₂, CO(2) and CO(1). In neutral forms, red shifting in UV-Vis spectra are observed upon interacting with NH₃, CO₂, CO(1) and CO(2), which confirm the doping process. In conclusion, PPy (both the nPy and nPy⁺) has greater response/selectivity with NH₃, in presence of CO₂ and CO gases.

Graphene with its unique 2D structure and excellent electrical, thermal, mechanical, and optical properties has attracted tremendous multidisciplinary research interest since its discovery in 2004. In this updated review, we explored and summarized the exciting recent progress on the use of GR and its derivatives for PEC, photocatalytic water splitting, photocatalytic conversion for fuels, photovoltaic, and application in supercapacitors, batteries, fuel cell, degradation of pollutants, gas sensors, heavy metal removal, and as biosensing applications.

CHAPTER 7: Conclusions and Future Work

7.1. Conclusions

It is observed that, although pristine BiVO_4 is a good photocatalyst for water splitting but, their Oxygen defective and mild doped (1 or 2 % Se) BiVO_4 are much efficient; having reduced bandgap and ideal VB and CB for water reduction and oxidation, respectively. Se and BiVO_4 heterojunction is also investigated, which form a direct Z-scheme like heterojunction of; having improved PEC performance. DFT simulations are carried out for the BiVO_4 and Se to simulate their band gap, and band edge positions in the proposed heterojunction band diagram. The PEC properties of Se/BiVO_4 indicate that the increment in performance is due to the presence of Se layer which acts as a hole trapping agent, light absorber, and improves the charge separation in the resulted film. The Se/BiVO_4 has 1.5 times higher photocurrent density than that of BiVO_4 due to higher surface area, small grain size, high roughness, efficient charge separation and minimum charge recombination rate.

Moreover, heterojunction of $\text{g-C}_3\text{N}_4/\text{BiVO}_4$ were designed and which has higher photocurrent compared to that of $\text{TiO}_2/\text{BiVO}_4$, which consequences the superiority of $\text{g-C}_3\text{N}_4$ over TiO_2 . The higher reducing capability of $\text{g-C}_3\text{N}_4$ is because of its more negative situated conduction band and enhanced photogenerated electrons, larger surface roughness, and higher charge carrier density. The simulated results confirmed that $\text{g-C}_3\text{N}_4$ and BiVO_4 has formed a van der Waals type heterojunction, where an internal electric field facilitated the separation of electron/hole pair at the $\text{g-C}_3\text{N}_4/\text{BiVO}_4$ interface which further restrain the carrier recombination. In brief, the construction of Z-scheme based

g-C₃N₄ based PEC device was successfully illustrated in this paper and there is great promises for further explorations and research.

The electronic and optical properties and photocarrier mobility of bulk β -TaON which predict TaON is a better candidate for photocatalytic water splitting than either Ta₂O₅ or Ta₃N₅. In summary, the oxygen and nitrogen terminated TaON along (010) and (001), respectively has good stability and sensitivity towards water molecule. Moreover, O terminated TaON has ideal band edge positions while N terminated has strong ability towards visible light absorption, so a mixed phase would result an efficient photoanode for water splitting.

DFT and TD-DFT at hybrid functional, to assess the nature and electronic properties of a near-infrared-absorbing, low energy gap conjugated polymer; donor-acceptor-donor (**D-A-D**). The **D-A-D** is consisting of 2,1,3-benzosele-nadiazole (**A**) as acceptor and 3,4-ethylenedioxy-selenophene (**D**) as donor fragments. The **D** and **A** moieties in the polymeric backbone have been found to be responsible for reducing the band gap, open circuit (*V_{oc}*) and increasing short-circuit current density (*J_{sc}*) in polymers solar cells (PSC). Our theoretical studies revealed that charge transportation efficiency (η_{CT}), *V_{oc}*, *J_{sc}* and, in turn, device performance, are influenced by electronic energy level alignment at interfaces. A lower HOMO energy level (-4.65 eV) of designed **D-A-D** is responsible for increasing the ambient stability during device operation and results in high *V_{oc}* of 1.02 eV. Furthermore, it is found that donor-acceptor combination has a key role in charge separation, weak steric hindrance, and molecular architecture (planarity of the polymeric backbone) which directly influences the charge transport compared to that of counterpart homopolymers (either **D** or **A**). Reduction in the band gap, high charge transformation, and

enhanced visible light absorption in **D-A-D** system is because of strong overlapping of the frontier molecular orbitals of the **D** and **A**.

We have carried out structural, electronic, optical, and charge-transport properties of a donor-acceptor-donor polymer; a Hole transporting material (HTM), N3 and TiO₂ for the design of an efficient SDSC. We proposed an ideal setup for an SDSC, where the HTM, N3, and TiO₂ are chosen, based on their upstairs like energy levels (band edge positions); having a difference of at least 0.50 eV. Our theoretical simulations prove that if we shine a light on the proposed setup, the electron would move from the dye to TiO₂ and from HTM to dye, to be regenerate. The theoretical open-circuit voltage of about 1.49 eV is responsible for high quantum yield.

Comprehensive theoretical and experimental studies of porphyrin–furan conjugates are carried out, in which anchoring group either at meso-phenyl or at pyrrole-β position of a zinc porphyrin based on donor-π-acceptor approach. The dyads were tested in dye sensitized solar cells using I⁻/I₃⁻ redox couple. Both theory and experiment strongly corroborate each other, however, the overall efficiency of these sensitizers is very low, which need to be improved.

DFT of pyrrole-Ti₁₆O₃₂ bounded systems are carried out to find their interaction to tailor the best composite for the photodegradation of environmental pollutants and solar water splitting. So, after confirming the composite formation, band gap narrowing, and better visible light absorption capability is observed compared to their individual nPy and Ti₁₆O₃₂ constituents. Moreover, UV-vis spectra of these composites predict the visible light absorption compared to nPy and Ti₁₆O₃₂. Electron-hole transferring define Py oligomers as a donor and Ti₁₆O₃₂ cluster as an acceptor in the resulted composites.

DFT study of nPy/nPy⁺ (where n=3, 5, 7, 9) and their complexes with NH₃, CO₂ and CO are carried out to analyze the sensitivity and selectivity of PPy, both in neutral and doped form. Comparative results of interaction energy of neutral and doped form of PPy reveal greater response for the doped form towards different analytes. It is also indicated from interaction energy that PPy shows more response to CO₂ than CO. Frontier molecular orbitals energies of nPy-X and nPy⁺-X, before and after sensing, confirm that NH₃ perturbed the orbital energy of PPy to greater extent than the perturbation caused by CO₂, CO(2) and CO(1). In neutral forms, red shifting in UV-Vis spectra are observed upon interacting with NH₃, CO₂, CO(1) and CO(2), which confirm the doping process. In conclusion, PPy (both the nPy and nPy⁺) has greater response/selectivity with NH₃, in presence of CO₂ and CO gases.

Graphene with its unique 2D structure and excellent electrical, thermal, mechanical, and optical properties has attracted tremendous multidisciplinary research interest since its discovery in 2004. In this updated review, we explored and summarized the exciting recent progress on the use of GR and its derivatives for PEC, photocatalytic water splitting, photocatalytic conversion for fuels, photovoltaic, and application in supercapacitors, batteries, fuel cell, degradation of pollutants, gas sensors, heavy metal removal, and as biosensing applications

7.2. Recommendations for Future Work

- These PBC simulations will minimize the synthetic effort in the designing and fabrication of efficient devices; solar energy conversion and pollutants degradations.
- We used Se as dopant agent for BiVO_4 , other efficient dopants such as N, Ar, Te, P, Ca, etc may also be tried.
- Nano-sized thin film study can accurately represent the experimental effort compared to that of Ultra-thin film.
- Designing Bifunctional electrocatalyst for Oxygen Evolution Reaction (OER) and Hydrogen Evolution Reaction (HER).
- Theoretical Mechanistic study of OER and HER over the surface of catalyst.
- Complex interface study of the materials used in this work, will further improve the overall efficiency.
- Molecular Dynamic, electron phonon coupling, thermal transport and I-V curve simulations are future research highlights.
- Molecular Dynamic and Density Functional Theory study of 2D materials such as Graphene, 2D layer Metal Oxides and their complex interfaces are very crucial for high performance photovoltaic and photocatalytic solar cell.
- These tools will be very essential to explore in terms of knowing underlying mechanism of charge carrier transport, surface reconstruction, kinetics of reactions etc.

Bibliography

- [1] H. Ullah, A. A. Tahir, T. K. Mallick, "Structural and electronic properties of oxygen defective and Se-doped p-type BiVO₄(001) thin film for the applications of photocatalysis." *Appl. Catal., B: Environ.*, vol. 224, pp. 895-903, 2018.
- [2] H. Ullah, S. Bibi, A. A. Tahir, T. K. Mallick, "Density functional theory study of selenium-substituted low-bandgap donor–acceptor–donor polymer." *J. Phys. Chem. C*. vol. 120, pp. 27200-27211, 2016.
- [3] H. Ullah, S. Bibi, A. A. Tahir, T. K. Mallick, "Donor-acceptor polymer for the design of all-solid-state dye-sensitized solar cells." *J. Alloys Compd.*, vol. 696, pp. 914-922, 2017.
- [4] J. Wolf, M. Babics, K. Wang, Q. Saleem, R. Z. Liang, M. R. Hansen, P. M. Beaujuge, "Benzo[1,2-b:4,5-b']dithiophene-pyrido[3,4-b] pyrazine small-molecule donors for bulk heterojunction solar cells." *Chem. Mater.*, vol. 28, pp. 2058-2066, 2016.
- [5] M. Wang, D. Cai, Z. Yin, S. C. Chen, C. F. Du, Q. Zheng, "Asymmetric-indenothiophene-based copolymers for bulk heterojunction solar cells with 9.14% efficiency." *Adv. Mater.*, vol. 28, pp. 3359-3365, 2016.
- [6] M. Scharber, N. Sariciftci, "Efficiency of bulk-heterojunction organic solar cells." *Prog. Polym. Sci.*, vol. 38, pp. 1929-1940, 2013.
- [7] G. Li, R. Zhu, Y. Yang, "Polymer solar cells." *Nat. Photon.*, vol. 6, pp. 153-161, 2012.
- [8] M. A. Green, K. Emery, Y. Hishikawa, W. Warta, E. D. Dunlop, "Solar cell efficiency tables (version 45)." *Prog. Photovoltaics Res. Appl.*, vol. 23, pp. 1-9, 2015.

- [9] A. J. Heeger, "Semiconducting and metallic polymers: The fourth generation of polymeric materials (nobel lecture)." *Angew. Chem. Inter. Ed.*, vol. 40, pp. 2591-2611, 2001.
- [10] A. J. Heeger, "Semiconducting and metallic polymers: The fourth generation of polymeric materials." *J. Phys. Chem. B.* vol. 105, pp. 8475-8491, 2001.
- [11] A. Facchetti, " π -conjugated polymers for organic electronics and photovoltaic cell applications." *Chem. Mater.*, vol. 23, pp. 733-758, 2010.
- [12] H. Ullah, A. A. Tahir, T. K. Mallick, "Polypyrrole/TiO₂ composites for the application of photocatalysis." *Sens. Actuators, B.* vol., pp. 2016.
- [13] H. Ullah, "Inter-molecular interaction in polypyrrole/TiO₂: A DFT study." *J. Alloys Compd.*, vol. 692, pp. 140-148, 2017.
- [14] D. A. Hanaor, M. H. Assadi, S. Li, A. Yu, C. C. Sorrell, "Ab initio study of phase stability in doped TiO₂." *Comput. Mechan.*, vol. 50, pp. 185-194, 2012.
- [15] P. Giannozzi, S. Baroni, N. Bonini, M. Calandra, R. Car, C. Cavazzoni, D. Ceresoli, G. L. Chiarotti, M. Cococcioni, I. Dabo, "Quantum espresso: A modular and open-source software project for quantum simulations of materials." *J. Phys: Cond. Matter.* vol. 21, pp. 395502, 2009.
- [16] S. Le, T. Jiang, Q. Zhao, X. Liu, Y. Li, B. Fang, M. Gong, "Cu-doped mesoporous graphitic carbon nitride for enhanced visible-light driven photocatalysis." *RSC Adv.*, vol. 6, pp. 38811-38819, 2016.
- [17] K. Momma, F. Izumi, "An integrated three-dimensional visualization system vesta using wxwidgets." *Commision Crystallogr. Comput., IUCr Newslett.* vol., pp. 106-119, 2006.

- [18] J. Jiang, J. Yu, S. Cao, "Au/PtO nanoparticle-modified gC₃N₄ for plasmon-enhanced photocatalytic hydrogen evolution under visible light." *J. Colloid Interf. Sci.*, vol. 461, pp. 56-63, 2016.
- [19] A. H. Larsen, M. Vanin, J. J. Mortensen, K. S. Thygesen, K. W. Jacobsen, "Localized atomic basis set in the projector augmented wave method." *Phys. Rev. B*. vol. 80, pp. 195112, 2009.
- [20] W. H. Press *Numerical recipes 3rd edition: The art of scientific computing*; Cambridge university press, 2007.
- [21] A. Sleight, H.-Y. Chen, A. Ferretti, D. Cox, "Crystal growth and structure of BiVO₄." *Materials Research Bulletin*. vol. 14, pp. 1571-1581, 1979.
- [22] G. Xi, J. Ye, "Synthesis of bismuth vanadate nanoplates with exposed {001} facets and enhanced visible-light photocatalytic properties." *Chem. Commun.*, vol. 46, pp. 1893-1895, 2010.
- [23] J. Endres, D. A. Egger, M. Kulbak, R. A. Kerner, L. Zhao, S. H. Silver, G. Hodes, B. P. Rand, D. Cahen, L. Kronik, "Valence and conduction band densities of states of metal halide perovskites: A combined experimental–theoretical study." *J. Phys. Chem. Lett.*, vol. 7, pp. 2722-2729, 2016.
- [24] J. Hafner, "Materials simulations using VASP—A quantum perspective to materials science." *Comput. Phys. Commun.*. vol. 177, pp. 6-13, 2007.
- [25] S. Yoon, A. E. Maegli, S. K. Matam, M. Trottmann, T. Hisatomi, C. M. Leroy, M. Grätzel, S. Pokrant, A. Weidenkaff, "The influence of the ammonolysis temperature on the photocatalytic activity of β-TaON." *Int. J. Photoenergy*. vol. 2013, pp. 2013.

- [26] D. Armytage, B. Fender, "Anion ordering in NaON: A powder neutron-diffraction investigation." *Acta Crystallogr., Sect. B: Crystallogr. Crystal Chem.*, vol. 30, pp. 809-812, 1974.
- [27] M. J. T. Frisch, G. W.; Schlegel, H. B.; Scuseria, G. E.; Robb, M. A.; Cheeseman, J. R.; Scalmani, G.; Barone, V.; Mennucci, B.; Petersson, G. A.; et al. *Gaussian 09*, Revision D. 01; Gaussian, Inc.: Wallingford, CT, 2013.
- [28] A. R. Allouche Gabedit, <http://gabedit.sourceforge.net>, 2011.
- [29] R. Dennington, T. Keith, J. G. Millam, "Version 5.0. 8." *Semichem Inc., Shawnee Mission KS*. vol., pp. 2008.
- [30] D. Jacquemin, V. Wathelet, E. A. Perpète, C. Adamo, "Extensive TD-DFT benchmark: Singlet-excited states of organic molecules." *J. Chem. Theo. Comput.*, vol. 5, pp. 2420-2435, 2009.
- [31] O. Cramariuc, T. I. Hukka, T. T. Rantala, H. Lemmetyinen, "TD-DFT description of photoabsorption and electron transfer in a covalently bonded porphyrin-fullerene dyad." *J. Phys. Chem. A*. vol. 110, pp. 12470-12476, 2006.
- [32] H. Sun, J. Autschbach, "Electronic energy gaps for π -conjugated oligomers and polymers calculated with density functional theory." *J. Chem. Theo. Comput.*, vol. 10, pp. 1035-1047, 2014.
- [33] D. Jacquemin, E. A. Perpète, G. E. Scuseria, I. Ciofini, C. Adamo, "TD-DFT performance for the visible absorption spectra of organic dyes: Conventional versus long-range hybrids." *J. Chem. Theo. Comput.*, vol. 4, pp. 123-135, 2008.
- [34] E. Berardo, H.-S. Hu, S. A. Shevlin, S. M. Woodley, K. Kowalski, M. A. Zwijnenburg, "Modeling excited states in TiO₂ nanoparticles: On the accuracy of a TD-DFT based description." *J. Chem. Theo. Comput.*, vol. 10, pp. 1189-1199, 2014.

- [35] E. Poverenov, N. Zamoshchik, A. Patra, Y. Ridelman, M. Bendikov, "Unusual doping of donor–acceptor-type conjugated polymers using lewis acids." *J. Am. Chem. Soc.*, vol. 136, pp. 5138-5149, 2014.
- [36] A. Patra, Y. H. Wijsboom, S. S. Zade, M. Li, Y. Sheynin, G. Leitus, M. Bendikov, "Poly(3, 4-ethylenedioxy-selenophene)." *J. Am. Chem. Soc.*, vol. 130, pp. 6734-6736, 2008.
- [37] S. H. Park, A. Roy, S. Beaupre, S. Cho, N. Coates, J. S. Moon, D. Moses, M. Leclerc, K. Lee, A. J. Heeger, "Bulk heterojunction solar cells with internal quantum efficiency approaching 100%." *Nat. Photon.*, vol. 3, pp. 297-302, 2009.
- [38] V. Coropceanu, J. Cornil, D. A. da Silva Filho, Y. Olivier, R. Silbey, J.-L. Brédas, "Charge transport in organic semiconductors." *Chem. Rev.*, vol. 107, pp. 926-952, 2007.
- [39] Y. Okawa, M. Akai-Kasaya, Y. Kuwahara, S. K. Mandal, M. Aono, "Controlled chain polymerisation and chemical soldering for single-molecule electronics." *Nanoscale*. vol. 4, pp. 3013-3028, 2012.
- [40] A. Patra, V. Agrawal, R. Bhargav, D. Bhardwaj, S. Chand, Y. Sheynin, M. Bendikov, "Metal free conducting PEDOS, PEDOT, and their analogues via an unusual bromine-catalyzed polymerization." *Macromolecules*. vol. 48, pp. 8760-8764, 2015.
- [41] A. Patra, M. Bendikov, S. Chand, "Poly(3, 4-ethylenedioxy-selenophene) and its derivatives: Novel organic electronic materials." *Acc. Chem. Res.*, vol. 47, pp. 1465-1474, 2014.
- [42] M. Li, Y. Sheynin, A. Patra, M. Bendikov, "Tuning the electrochromic properties of poly (alkyl-3, 4-ethylenedioxy-selenophenes) having high contrast ratio and coloration efficiency." *Chem. Mater.*, vol. 21, pp. 2482-2488, 2009.

- [43] H. Ullah, A. A. Shah, S. Bilal, K. Ayub, "DFT study of polyaniline NH₃, CO₂, and CO gas sensors: Comparison with recent experimental data." *J. Phys. Chem. C*. vol. 117, pp. 23701-23711, 2013.
- [44] S. Bibi, H. Ullah, S. M. Ahmad, A. A. Shah, S. Bilal, A. A. Tahir, K. Ayub, "Molecular and electronic structure elucidation of polypyrrole gas sensors." *J. Phys. Chem. C*. vol. 119, pp. 15994-16003, 2015.
- [45] H. Ullah, A.-u.-H. A. Shah, S. Bilal, K. Ayub, "Doping and dedoping processes of polypyrrole: DFT study with hybrid functionals." *J. Phys. Chem. C*. vol. 118, pp. 17819-17830, 2014.
- [46] H. Ullah, K. Ayub, Z. Ullah, M. Hanif, R. Nawaz, S. Bilal, "Theoretical insight of polypyrrole ammonia gas sensor." *Synth. Met.*, vol. 172, pp. 14-20, 2013.
- [47] Z. Ullah, A. Rauf, M. Yaseen, W. Hassan, M. Tariq, K. Ayub, A. A. Tahir, H. Ullah, "Density functional theory and phytochemical study of 8-hydroxyisodiospyrin." *J. Mol. Struct.*, vol. 1095, pp. 69-78, 2015.
- [48] S. N. F. M. Nasir, H. Ullah, M. Ebadi, A. A. Tahir, J. S. Sagu, M. A. Mat Teridi, "New insights into Se/BiVO₄ heterostructure for photoelectrochemical water splitting: A combined experimental and dft study." *J. Phys. Chem. C*. vol. 121, pp. 6218-6228, 2017.
- [49] J. Safaei, H. Ullah, N. A. Mohamed, M. F. M. Noh, M. F. Soh, A. A. Tahir, N. A. Ludin, M. A. Ibrahim, W. N. R. W. Isahak, M. A. M. Teridi, "Enhanced photoelectrochemical performance of Z-scheme gC₃N₄/BiVO₄ photocatalyst." *Appl. Catal. B: Environ.* vol. 234, pp. 296-310, 2018.
- [50] H. Ullah, A. A. Tahir, S. Bibi, T. K. Mallick, S. Z. Karazhanov, "Electronic properties of β -TaON and its surfaces for solar water splitting." *Appl. Catal., B: Environ.*, vol. 229, pp. 24-31, 2018.

- [51] V. K. Narra, H. Ullah, V. K. Singh, L. Giribabu, S. Senthilarasu, S. Z. Karazhanov, A. A. Tahir, T. K. Mallick, H. M. Upadhyaya, "D- π -A system based on Zinc porphyrin dyes for dye-sensitized solar cells: Combined experimental and DFT-TDDFT study." *Polyhedron*. vol. 100, pp. 313-320, 2015.
- [52] H. Ullah, A. A. Tahir, T. K. Mallick, "Polypyrrole/TiO₂ composites for the application of photocatalysis." *Sens. Actuators, B: Chem.*, vol. 241, pp. 1161-1169, 2017.
- [53] A. Ali Tahir, H. Ullah, P. Sudhagar, M. Asri Mat Teridi, A. Devadoss, S. Sundaram, "The application of graphene and its derivatives to energy conversion, storage, and environmental and biosensing devices." *Chem. Rec.*, vol. 16, pp. 1591-1634, 2016.
- [54] C. S. Ponseca Jr, P. Chábera, J. Uhlig, P. Persson, V. Sundström, "Ultrafast electron dynamics in solar energy conversion." *Chem. Rev.*, vol. 117, pp. 10940-11024, 2017.
- [55] A. Fujishima, "Electrochemical photolysis of water at a semiconductor electrode." *Nature*. vol. 238, pp. 37-38, 1972.
- [56] M. G. Walter, E. L. Warren, J. R. McKone, S. W. Boettcher, Q. Mi, E. A. Santori, N. S. Lewis, "Solar water splitting cells." *Chem. Rev.*, vol. 110, pp. 6446-6473, 2010.
- [57] T. Hisatomi, J. Kubota, K. Domen, "Recent advances in semiconductors for photocatalytic and photoelectrochemical water splitting." *Chem. Soc. Rev.*, vol. 43, pp. 7520-7535, 2014.
- [58] J. Li, N. Wu, "Semiconductor-based photocatalysts and photoelectrochemical cells for solar fuel generation: A review." *Catal. Sci. Technol.*, vol. 5, pp. 1360-1384, 2015.

- [59] M. C. Scharber, D. Mühlbacher, M. Koppe, P. Denk, C. Waldauf, A. J. Heeger, C. J. Brabec, "Design rules for donors in bulk-heterojunction solar cells—towards 10% energy-conversion efficiency." *Adv. Mater.*, vol. 18, pp. 789-794, 2006.
- [60] U. Salzner, "Quantitatively correct UV-vis spectrum of ferrocene with TDB3LYP." *J. Chem. Theo. Comput.*, vol. 9, pp. 4064-4073, 2013.
- [61] K. Müllen, W. Pisula, "Donor–acceptor polymers." *J. Am. Chem. Soc.*, vol. 137, pp. 9503-9505, 2015.
- [62] J. D. Servaites, B. M. Savoie, J. B. Brink, T. J. Marks, M. A. Ratner, "Modeling geminate pair dissociation in organic solar cells: High power conversion efficiencies achieved with moderate optical bandgaps." *Energy & Env. Sci.*, vol. 5, pp. 8343-8350, 2012.
- [63] J. Twidell, T. Weir *Renewable energy resources*; Routledge, 2015.
- [64] A. Colli, "Failure mode and effect analysis for photovoltaic systems." *Renew. Sustain. Energy Rev.*, vol. 50, pp. 804-809, 2015.
- [65] M. A. Mughal, R. Engelken, R. Sharma, "Progress in indium (iii) sulfide (In_2S_3) buffer layer deposition techniques for CIS, CIGS, and CdTe-based thin film solar cells." *Solar Energy*. vol. 120, pp. 131-146, 2015.
- [66] M. Grätzel, "Dye-sensitized solar cells." *J. Photochem. Photobio. C: Photochem. Rev.*, vol. 4, pp. 145-153, 2003.
- [67] M. Grätzel, "Dye-sensitized solar cells." *J. Photochem. Photobio. C: Photochem. Rev.*. vol. 4, pp. 145-153, 2003.
- [68] S.-H. Liu, H. Fu, Y.-M. Cheng, K.-L. Wu, S.-T. Ho, Y. Chi, P.-T. Chou, "Theoretical study of N749 dyes anchoring on the $(\text{TiO}_2)_{28}$ surface in dsscs and

their electronic absorption properties." *J. Phys. Chem. C.* vol. 116, pp. 16338-16345, 2012.

[69] M. Zhou, J. Bao, Y. Xu, J. Zhang, J. Xie, M. Guan, C. Wang, L. Wen, Y. Lei, Y. Xie, "Photoelectrodes based upon Mo:BiVO₄ inverse opals for photoelectrochemical water splitting." *ACS Nano.* vol. 8, pp. 7088-7098, 2014.

[70] D. Moia, U. B. Cappel, T. Leijtens, X. Li, A. M. Telford, H. J. Snaith, B. C. O'Regan, J. Nelson, P. R. Barnes, "The role of hole transport between dyes in solid-state dye-sensitized solar cells." *J. Phys. Chem. C.* vol. 119, pp. 18975-18985, 2015.

[71] X.-L. He, G.-J. Yang, C.-J. Li, M. Liu, S.-Q. Fan, "Failure mechanism for flexible dye-sensitized solar cells under repeated outward bending: Cracking and spalling off of nano-porous titanium dioxide film." *J. Power Sour.*, vol. 280, pp. 182-189, 2015.

[72] M. G. Lobello, S. Fantacci, F. De Angelis, "Computational spectroscopy characterization of the species involved in dye oxidation and regeneration processes in dye-sensitized solar cells." *J. Phys. Chem. C.* vol. 115, pp. 18863-18872, 2011.

[73] S. Fantacci, F. De Angelis, M. K. Nazeeruddin, M. Grätzel, "Electronic and optical properties of the spiro-metad hole conductor in its neutral and oxidized forms: A dft/tddft investigation." *J. Phys. Chem. C.* vol. 115, pp. 23126-23133, 2011.

[74] R. Williams, "Becquerel photovoltaic effect in binary compounds." *J. Chem. Phys.*, vol. 32, pp. 1505-1514, 1960.

[75] A. B. Ellis, S. W. Kaiser, J. M. Bolts, M. S. Wrighton, "Study of n-type semiconducting cadmium chalcogenide-based photoelectrochemical cells

employing polychalcogenide electrolytes." *J. Am. Chem. Soc.*, vol. 99, pp. 2839-2848, 1977.

[76] S. D. Tilley, M. Cornuz, K. Sivula, M. Grätzel, "Light-induced water splitting with hematite: Improved nanostructure and iridium oxide catalysis." *Angew. Chem. Int. Ed.*, vol. 122, pp. 6549-6552, 2010.

[77] K. Sayama, A. Nomura, Z. Zou, R. Abe, Y. Abe, H. Arakawa, "Photoelectrochemical decomposition of water on nanocrystalline BiVO₄ film electrodes under visible light." *Chem. Commun.*, vol., pp. 2908-2909, 2003.

[78] S. J. Hong, S. Lee, J. S. Jang, J. S. Lee, "Heterojunction BiVO₄/WO₃ electrodes for enhanced photoactivity of water oxidation." *Energy & Envir. Sci.*, vol. 4, pp. 1781-1787, 2011.

[79] J. Su, L. Guo, N. Bao, C. A. Grimes, "Nanostructured WO₃/BiVO₄ heterojunction films for efficient photoelectrochemical water splitting." *Nano Lett.*, vol. 11, pp. 1928-1933, 2011.

[80] R. Saito, Y. Miseki, K. Sayama, "Highly efficient photoelectrochemical water splitting using a thin film photoanode of BiVO₄/SnO₂/WO₃ multi-composite in a carbonate electrolyte." *Chem. Commun.*, vol. 48, pp. 3833-3835, 2012.

[81] A. Fujishima, K. Honda, "TiO₂ photoelectrochemistry and photocatalysis." *Nature*. vol. 238, pp. 37-38, 1972.

[82] R. Saito, Y. Miseki, K. Sayama, "Photoanode characteristics of multi-layer composite BiVO₄ thin film in a concentrated carbonate electrolyte solution for water splitting." *J. Photochem. Photobiol A: Chem.*, vol. 258, pp. 51-60, 2013.

[83] J. Krysa, M. Zlamal, S. Kment, M. Brunclikova, Z. Hubicka, "TiO₂ and Fe₂O₃ films for photoelectrochemical water splitting." *Molecules*. vol. 20, pp. 1046-1058, 2015.

- [84] J.-L. Brédas, J. E. Norton, J. Cornil, V. Coropceanu, "Molecular understanding of organic solar cells: The challenges." *Acc. Chem. Res.*, vol. 42, pp. 1691-1699, 2009.
- [85] Y. Ogawa, M. S. White, L. Sun, M. C. Scharber, N. S. Sariciftci, T. Yoshida, "Substrate-oriented nanorod scaffolds in polymer–fullerene bulk heterojunction solar cells." *Chem. Phys. Chem.*, vol. 15, pp. 1070-1075, 2014.
- [86] D. Kang, T. W. Kim, S. R. Kubota, A. C. Cardiel, H. G. Cha, K.-S. Choi, "Electrochemical synthesis of photoelectrodes and catalysts for use in solar water splitting." *Chem. Rev.*, vol. 115, pp. 12839-12887, 2015.
- [87] Z. Zou, J. Ye, K. Sayama, H. Arakawa, "Direct splitting of water under visible light irradiation with an oxide semiconductor photocatalyst." *Nature*. vol. 414, pp. 625, 2001.
- [88] C. Zhen, R. Chen, L. Wang, G. Liu, H.-M. Cheng, "Tantalum (oxy) nitride based photoanodes for solar-driven water oxidation." *J. Mater. Chem. A*. vol., pp. 2016.
- [89] S. S. Gujral, A. N. Simonov, M. Higashi, X.-Y. Fang, R. Abe, L. Spiccia, "Highly dispersed cobalt oxide on TaON as efficient photoanodes for long-term solar water splitting." *ACS Catal.* vol. 6, pp. 3404-3417, 2016.
- [90] Z. Zhao, Z. Wang, J. Bao In *Nanomaterials for sustainable energy*; Springer: 2016, p 445-470.
- [91] G. Hitoki, T. Takata, J. N. Kondo, M. Hara, H. Kobayashi, K. Domen, "An oxynitride, TaON, as an efficient water oxidation photocatalyst under visible light irradiation ($\lambda \leq 500$ nm)." *Chem. Commun.* vol., pp. 1698-1699, 2002.
- [92] T. Lüdtkke, A. Schmidt, C. Göbel, A. Fischer, N. Becker, C. Reimann, T. Bredow, R. Dronskowski, M. Lerch, "Synthesis and crystal structure of δ -TaON,

a metastable polymorph of tantalum oxide nitride." *Inorg. Chem.* vol. 53, pp. 11691-11698, 2014.

[93] M. de Respinis, M. Fravventura, F. F. Abdi, H. Schreuders, T. J. Savenije, W. A. Smith, B. Dam, R. van de Krol, "Oxynitrogenography: Controlled synthesis of single-phase tantalum oxynitride photoabsorbers." *Chem. Mater.* vol. 27, pp. 7091-7099, 2015.

[94] N. K. Allam, B. S. Shaheen, A. M. Hafez, "Layered tantalum oxynitride nanorod array carpets for efficient photoelectrochemical conversion of solar energy: Experimental and dft insights." *ACS Appl. Mater. & Interf.* vol. 6, pp. 4609-4615, 2014.

[95] S. Balaz, S. H. Porter, P. M. Woodward, L. J. Brillson, "Electronic structure of tantalum oxynitride perovskite photocatalysts." *Chem. Mater.* vol. 25, pp. 3337-3343, 2013.

[96] R. Sasaki, K. Maeda, Y. Kako, K. Domen, "Preparation of calcium tantalum oxynitride from layered oxide precursors to improve photocatalytic activity for hydrogen evolution under visible light." *Appl. Catal. B: Environ.* vol. 128, pp. 72-76, 2012.

[97] P. Carvalho, J. Borges, M. Rodrigues, N. Barradas, E. Alves, J. Espinós, A. González-Elipe, L. Cunha, L. Marques, M. Vasilevskiy, "Optical properties of zirconium oxynitride films: The effect of composition, electronic and crystalline structures." *Applied Surface Science.* vol. 358, pp. 660-669, 2015.

[98] W.-J. Chun, A. Ishikawa, H. Fujisawa, T. Takata, J. N. Kondo, M. Hara, M. Kawai, Y. Matsumoto, K. Domen, "Conduction and valence band positions of Ta_2O_5 , TaON , and Ta_3N_5 by UPS and electrochemical methods." *J. Phys. Chem. B.* vol. 107, pp. 1798-1803, 2003.

- [99] C. Taviot-Guého, J. Cellier, A. Bousquet, E. Tomasella, "Multiphase structure of tantalum oxynitride TaO_xN_y thin films deposited by reactive magnetron sputtering." *J. Phys. Chem. C*. vol. 119, pp. 23559-23571, 2015.
- [100] G. Gustafsson, Y. Cao, G. Treacy, F. Klavetter, N. Colaneri, A. Heeger, "Flexible light-emitting diodes made from soluble conducting polymers." *Nature*. vol. 357, pp. 477-479, 1992.
- [101] R. Friend, R. Gymer, A. Holmes, J. Burroughes, R. Marks, C. Taliani, D. Bradley, D. Dos Santos, J. Bredas, M. Lögdlund, "Electroluminescence in conjugated polymers." *Nature*. vol. 397, pp. 121-128, 1999.
- [102] J. Janata, M. Josowicz, "Conducting polymers in electronic chemical sensors." *Nat. Mater.*, vol. 2, pp. 19-24, 2003.
- [103] H. Sirringhaus, P. Brown, R. Friend, M. M. Nielsen, K. Bechgaard, B. Langeveld-Voss, A. Spiering, R. A. Janssen, E. Meijer, P. Herwig, "Two-dimensional charge transport in self-organized, high-mobility conjugated polymers." *Nature*. vol. 401, pp. 685-688, 1999.
- [104] A. G. MacDiarmid, "“Synthetic metals”: A novel role for organic polymers (nobel lecture)." *Angew. Chem. Inter. Ed.*, vol. 40, pp. 2581-2590, 2001.
- [105] J. Kong, N. R. Franklin, C. Zhou, M. G. Chapline, S. Peng, K. Cho, H. Dai, "Nanotube molecular wires as chemical sensors." *Science*. vol. 287, pp. 622-625, 2000.
- [106] J. Huang, S. Virji, B. H. Weiller, R. B. Kaner, "Polyaniline nanofibers: Facile synthesis and chemical sensors." *J. Am. Chem. Soc.*, vol. 125, pp. 314-315, 2003.

- [107] K. J. Albert, N. S. Lewis, C. L. Schauer, G. A. Sotzing, S. E. Stitzel, T. P. Vaid, D. R. Walt, "Cross-reactive chemical sensors arrays." *Chem. Rev.* vol. 100, pp. 2595-2626, 2000.
- [108] H. Bai, G. Shi, "Gas sensors based on conducting polymers." *Sensors*. vol. 7, pp. 267-307, 2007.
- [109] M. Penza, G. Cassano, P. Aversa, F. Antolini, A. Cusano, A. Cutolo, M. Giordano, L. Nicolais, "Alcohol detection using carbon nanotubes acoustic and optical sensors." *Appl. Phys. Lett.*, vol. 85, pp. 2379, 2004.
- [110] H. Ullah, A. A. Shah, S. Bilal, K. Ayub, "Dft study of polyaniline nh₃, co₂, and co gas sensors: Comparison with recent experimental data." *J. Phys. Chem. C*. vol. 117, pp. 23701-23711, 2013.
- [111] H. Ullah, K. Ayub, Z. Ullah, M. Hanif, R. Nawaz, A. A. Shah, S. Bilal, "Theoretical insight of polypyrrole ammonia gas sensor." *Synth. Met.*, vol. 172, pp. 14-20, 2013.
- [112] M. M. Rahman, A. Ahammad, J. H. Jin, S. J. Ahn, J. J. Lee, "A comprehensive review of glucose biosensors based on nanostructured metal-oxides." *Sensors*. vol. 10, pp. 4855-4886, 2010.
- [113] O. V. Mikhnenko, H. Azimi, M. Scharber, M. Morana, P. W. Blom, M. A. Loi, "Exciton diffusion length in narrow bandgap polymers." *Energy Environ. Sci.*, vol. 5, pp. 6960-6965, 2012.
- [114] V. Gonzalez-Pedro, E. J. Juarez-Perez, W.-S. Arsyad, E. M. Barea, F. Fabregat-Santiago, I. Mora-Sero, J. Bisquert, "General working principles of ch₃nh₃pbx₃ perovskite solar cells." *Nano Lett.*, vol. 14, pp. 888-893, 2014.

- [115] J. W. Xiao, L. Liu, D. Zhang, N. De Marco, J. W. Lee, O. Lin, Q. Chen, Y. Yang, "The emergence of the mixed perovskites and their applications as solar cells." *Adv. Energy Mater.*, vol., pp. 2017.
- [116] W. Yao, H. Iwai, J. Ye, "Effects of molybdenum substitution on the photocatalytic behavior of BiVO₄." *Dalton Trans.*, vol., pp. 1426-1430, 2008.
- [117] J. A. Seabold, K.-S. Choi, "Efficient and stable photo-oxidation of water by a bismuth vanadate photoanode coupled with an iron oxyhydroxide oxygen evolution catalyst." *J. Am. Chem. Soc.*, vol. 134, pp. 2186-2192, 2012.
- [118] C. Ding, J. Shi, D. Wang, Z. Wang, N. Wang, G. Liu, F. Xiong, C. Li, "Visible light driven overall water splitting using cocatalyst/BiVO₄ photoanode with minimized bias." *Phys. Chem. Chem. Phys.*, vol. 15, pp. 4589-4595, 2013.
- [119] Z. Lou, F. Li, J. Deng, L. Wang, T. Zhang, "Branch-like hierarchical heterostructure (α -Fe₂O₃/TiO₂): A novel sensing material for trimethylamine gas sensor." *ACS Appl. Mater. Interfac.*, vol. 5, pp. 12310-12316, 2013.
- [120] X. An, T. Li, B. Wen, J. Tang, Z. Hu, L. M. Liu, J. Qu, C. Huang, H. Liu, "New insights into defect-mediated heterostructures for photoelectrochemical water splitting." *Adv. Energy Mater.*, vol., pp. 2016.
- [121] F. Dong, Z. Zhao, T. Xiong, Z. Ni, W. Zhang, Y. Sun, W.-K. Ho, "In situ construction of g-C₃N₄/g-C₃N₄ metal-free heterojunction for enhanced visible-light photocatalysis." *ACS Appl. Mater. Interfac.*, vol. 5, pp. 11392-11401, 2013.
- [122] M. G. Mali, H. Yoon, M.-w. Kim, M. T. Swihart, S. S. Al-Deyab, S. S. Yoon, "Electrosprayed heterojunction WO₃/BiVO₄ films with nanotextured pillar structure for enhanced photoelectrochemical water splitting." *Appl. Phys. Lett.*, vol. 106, pp. 151603, 2015.

- [123] Y. Pihosh, I. Turkevych, K. Mawatari, J. Uemura, Y. Kazoe, S. Kosar, K. Makita, T. Sugaya, T. Matsui, D. Fujita, "Photocatalytic generation of hydrogen by core-shell $\text{WO}_3/\text{BiVO}_4$ nanorods with ultimate water splitting efficiency." *Sci. Rep.*, vol. 5, pp. 2015.
- [124] H. Jung, S. Y. Chae, C. Shin, B. K. Min, O.-S. Joo, Y. J. Hwang, "Effect of the $\text{Si}/\text{TiO}_2/\text{BiVO}_4$ heterojunction on the onset potential of photocurrents for solar water oxidation." *ACS Appl. Mater. Interfaces*. vol. 7, pp. 5788-5796, 2015.
- [125] H. Yu, S. Chen, X. Quan, H. Zhao, Y. Zhang, "Silicon nanowire/ TiO_2 heterojunction arrays for effective photoelectrocatalysis under simulated solar light irradiation." *Appl. Catal. B-Environ.* vol. 90, pp. 242-248, 2009.
- [126] Y. J. Hwang, A. Boukai, P. Yang, "High density n-Si/n- TiO_2 core/shell nanowire arrays with enhanced photoactivity." *Nano Lett.*, vol. 9, pp. 410-415, 2008.
- [127] K. Catchpole, M. Mc Cann, A. Blakers, K. Weber In *Proceedings 16th European Photovoltaic Solar Energy Conference 2000*, p 1165-1168.
- [128] S. Cherian, C. C. Wamser, "Adsorption and photoactivity of tetra (4-carboxyphenyl) porphyrin (TCPP) on nanoparticulate TiO_2 ." *J. Phys. Chem. B*. vol. 104, pp. 3624-3629, 2000.
- [129] Y.-G. Kim, J. Walker, L. A. Samuelson, J. Kumar, "Efficient light harvesting polymers for nanocrystalline TiO_2 photovoltaic cells." *Nano Lett.*, vol. 3, pp. 523-525, 2003.
- [130] I. Robel, V. Subramanian, M. Kuno, P. V. Kamat, "Quantum dot solar cells. Harvesting light energy with cdse nanocrystals molecularly linked to mesoscopic TiO_2 films." *J. Am. Chem. Soc.*, vol. 128, pp. 2385-2393, 2006.

- [131] Y.-Y. Song, F. Schmidt-Stein, S. Bauer, P. Schmuki, "Amphiphilic TiO₂ nanotube arrays: An actively controllable drug delivery system." *J. Am. Chem. Soc.*, vol. 131, pp. 4230-4232, 2009.
- [132] K. Woan, G. Pyrgiotakis, W. Sigmund, "Photocatalytic carbon-nanotube-TiO₂ composites." *Adv. Mater.*, vol. 21, pp. 2233-2239, 2009.
- [133] V. Chabot, D. Higgins, A. Yu, X. Xiao, Z. Chen, J. Zhang, "A review of graphene and graphene oxide sponge: Material synthesis and applications to energy and the environment." *Energy & Environ. Sci.* vol. 7, pp. 1564-1596, 2014.
- [134] D. Wen, S. Guo, J. Zhai, L. Deng, W. Ren, S. Dong, "Pt nanoparticles supported on TiO₂ colloidal spheres with nanoporous surface: Preparation and use as an enhancing material for biosensing applications." *J. Phys. Chem. C.* vol. 113, pp. 13023-13028, 2009.
- [135] S. Banerjee, S. C. Pillai, P. Falaras, K. E. O'Shea, J. A. Byrne, D. D. Dionysiou, "New insights into the mechanism of visible light photocatalysis." *J. Phys. Chem. Lett.*, vol. 5, pp. 2543-2554, 2014.
- [136] N. Serpone, "Is the band gap of pristine TiO₂ narrowed by anion- and cation-doping of titanium dioxide in second-generation photocatalysts?" *J. Phys. Chem. B.* vol. 110, pp. 24287-24293, 2006.
- [137] X. Chen, S. Shen, L. Guo, S. S. Mao, "Semiconductor-based photocatalytic hydrogen generation." *Chem. Rev.*, vol. 110, pp. 6503-6570, 2010.
- [138] H.-i. Kim, J. Kim, W. Kim, W. Choi, "Enhanced photocatalytic and photoelectrochemical activity in the ternary hybrid of CdS/TiO₂/WO₃ through the cascaded electron transfer." *J. Phys. Chem. C.* vol. 115, pp. 9797-9805, 2011.

- [139] C. Janaky, N. R. de Tacconi, W. Chanmanee, K. Rajeshwar, "Bringing conjugated polymers and oxide nanoarchitectures into intimate contact: Light-induced electrodeposition of polypyrrole and polyaniline on nanoporous WO_3 or TiO_2 nanotube array." *J. Phys. Chem. C*. vol. 116, pp. 19145-19155, 2012.
- [140] R. J. Nussbaumer, W. R. Caseri, P. Smith, T. Tervoort, "Polymer- TiO_2 nanocomposites: A route towards visually transparent broadband UV filters and high refractive index materials." *Macromol. Mater. Eng.*, vol. 288, pp. 44-49, 2003.
- [141] W. Feng, E. Sun, A. Fujii, H. Wu, K. Niihara, K. Yoshino, "Synthesis and characterization of photoconducting polyaniline- TiO_2 nanocomposite." *Bull. Chem. Soc. Jpn.*, vol. 73, pp. 2627-2633, 2000.
- [142] G. Korotcenkov, "Metal oxides for solid-state gas sensors: What determines our choice?," *Materials Science and Engineering: B*. vol. 139, pp. 1-23, 2007.
- [143] L. Bao, L. Deng, L. Nie, S. Yao, W. Wei, "Determination of microorganisms with a quartz crystal microbalance sensor." *Anal. Chim. Acta*. vol. 319, pp. 97-101, 1996.
- [144] J. W. Grate, "Acoustic wave microsensor arrays for vapor sensing." *Chem. Rev.*, vol. 100, pp. 2627-2648, 2000.
- [145] K. Natori, "Ballistic metal-oxide-semiconductor field effect transistor." *J. Appl. Phys.*, vol. 76, pp. 4879-4890, 1994.
- [146] M. D. Rossell, P. Agrawal, A. Borgschulte, C. c. Hébert, D. Passerone, R. Erni, "Direct evidence of surface reduction in monoclinic BiVO_4 ." *Chem. Mater.* vol. 27, pp. 3593-3600, 2015.

- [147] H. S. Park, K. E. Kweon, H. Ye, E. Paek, G. S. Hwang, A. J. Bard, "Factors in the metal doping of BiVO₄ for improved photoelectrocatalytic activity as studied by scanning electrochemical microscopy and first-principles density-functional calculation." *J. Phys. Chem. C*. vol. 115, pp. 17870-17879, 2011.
- [148] M. Long, W. Cai, H. Kisch, "Visible light induced photoelectrochemical properties of n-BiVO₄ and n-BiVO₄/p-Co₃O₄." *J. Phys. Chem. C*. vol. 112, pp. 548-554, 2008.
- [149] F. Tran, P. Blaha, "Accurate band gaps of semiconductors and insulators with a semilocal exchange-correlation potential." *Phys. Rev. Lett.*, vol. 102, pp. 226401, 2009.
- [150] Z. He, Y. Shi, C. Gao, L. Wen, J. Chen, S. Song, "BiOCl/BiVO₄ p-n heterojunction with enhanced photocatalytic activity under visible-light irradiation." *J. Phys. Chem. C*. vol. 118, pp. 389-398, 2013.
- [151] M. Ebadi, M. Y. Sulaiman, M. A. Mat-Teridi, W. J. Basirun, M. A. Golsefidi, K. Sopian, A. Sateei, R. Z. Mehrabian, "Efficient photo-electrochemical performance using CuO-based electrodes in aqua medium." *J. Appl. Electrochem.*, vol. 46, pp. 645-653, 2016.
- [152] M. D. Rossell, P. Agrawal, A. Borgschulte, C. c. Hébert, D. Passerone, R. Erni, "Direct evidence of surface reduction in monoclinic BiVO₄." *Chem. Mater.*, vol. 27, pp. 3593-3600, 2015.
- [153] B. J. Morgan, G. W. Watson, "A density functional theory+U study of oxygen vacancy formation at the (110), (100), (101), and (001) surfaces of rutile TiO₂." *J. Phys. Chem. C*. vol. 113, pp. 7322-7328, 2009.

- [154] J. Pan, G. Liu, G. Q. M. Lu, H. M. Cheng, "On the true photoreactivity order of {001}, {010}, and {101} facets of anatase TiO₂ crystals." *Angew. Chem. Inter. Ed.*, vol. 50, pp. 2133-2137, 2011.
- [155] M. Batzill, "Fundamental aspects of surface engineering of transition metal oxide photocatalysts." *Energy & Environ. Sci.*, vol. 4, pp. 3275-3286, 2011.
- [156] G. Giorgi, J.-I. Fujisawa, H. Segawa, K. Yamashita, "Small photocarrier effective masses featuring ambipolar transport in methylammonium lead iodide perovskite: A density functional analysis." *J. Phys. Chem. Lett.*, vol. 4, pp. 4213-4216, 2013.
- [157] J. Zhang, S. Wageh, A. Al-Ghamdi, J. Yu, "New understanding on the different photocatalytic activity of wurtzite and zinc-blende cds." *Appl. Catal. B: Environ.*, vol. 192, pp. 101-107, 2016.
- [158] H. Ullah, A. A. Tahir, T. K. Mallick, "Structural and electronic properties of oxygen defective and Se-doped p-type BiVO₄(001) thin film for the applications of photocatalysis." *Appl. Catal. B: Environ.*, vol. 224, pp. 895-903, 2018.
- [159] H. Wolff, T. Bredow, M. Lerch, H. Schilling, E. Irran, A. Stork, R. Dronskowski, "A first-principles study of the electronic and structural properties of γ -taon." *J. Phys. Chem. A*, vol. 111, pp. 2745-2749, 2007.
- [160] H. Schilling, A. Stork, E. Irran, H. Wolff, T. Bredow, R. Dronskowski, M. Lerch, " Γ -taon: A metastable polymorph of tantalum oxynitride." *Angew. Chem. Inter. Ed.*, vol. 46, pp. 2931-2934, 2007.
- [161] C. Kittel *Introduction to solid state physics*; Wiley, 2005.

- [162] M. C. Scharber, "On the efficiency limit of conjugated polymer: Fullerene-based bulk heterojunction solar cells." *Adv. Mater.*, vol. 28, pp. 1994-2001, 2016.
- [163] H. Tan, A. Furlan, W. Li, K. Arapov, R. Santbergen, M. M. Wienk, M. Zeman, A. H. Smets, R. A. Janssen, "Highly efficient hybrid polymer and amorphous silicon multijunction solar cells with effective optical management." *Adv. Mater.*, vol. 28, pp. 2170-2177, 2016.
- [164] S.-O. Kim, Y.-S. Kim, H.-J. Yun, I. Kang, Y. Yoon, N. Shin, H. J. Son, H. Kim, M. J. Ko, B. Kim, "N-octyl-2, 7-dithia-5-azacyclopenta [a] pentalene-4, 6-dione-based low band gap polymers for efficient solar cells." *Macromolecules*, vol. 46, pp. 3861-3869, 2013.
- [165] S. Ayachi, A. Mabrouk, K. Alimi, M. Bouachrine *Photophysical properties of two new donor-acceptor conjugated copolymers and their model compounds: Applications in polymer light emitting diodes (PLEDS) and polymer photovoltaic cells (PPCS)*; INTECH Open Access Publisher, 2012.
- [166] L. Dou, J. You, J. Yang, C.-C. Chen, Y. He, S. Murase, T. Moriarty, K. Emery, G. Li, Y. Yang, "Tandem polymer solar cells featuring a spectrally matched low-bandgap polymer." *Nat. Photon.*, vol. 6, pp. 180-185, 2012.
- [167] L. Li, Y. Huang, J. Peng, Y. Cao, X. Peng, "Enhanced performance of solution-processed solar cells based on porphyrin small molecules with a diketopyrrolopyrrole acceptor unit and a pyridine additive." *J. Mater. Chem. A*, vol. 1, pp. 2144-2150, 2013.
- [168] Y. He, H.-Y. Chen, J. Hou, Y. Li, "Indene-C₆₀ bisadduct: A new acceptor for high-performance polymer solar cells." *J. Am. Chem. Soc.*, vol. 132, pp. 1377-1382, 2010.

- [169] J. Hou, X. Guo In *Organic solar cells*; Springer: 2013, p 17-42.
- [170] F. Wang, B. Zhang, Q. Li, Z. Shi, L. Yu, H. Liu, Y. Wang, S. Dai, Z. a. Tan, Y. Li, "Management of the light distribution within the photoactive layer for high performance conventional and inverted polymer solar cells." *J. Mater. Chem. A*. vol., pp. 2016.
- [171] Y. M. Yang, W. Chen, L. Dou, W.-H. Chang, H.-S. Duan, B. Bob, G. Li, Y. Yang, "High-performance multiple-donor bulk heterojunction solar cells." *Nat. Photon.*, vol. 9, pp. 190-198, 2015.
- [172] H. Cheun, J. Kim, Y. Zhou, Y. Fang, A. Dindar, J. Shim, C. Fuentes-Hernandez, K. H. Sandhage, B. Kippelen, "Inverted polymer solar cells with amorphous indium zinc oxide as the electron-collecting electrode." *Opt. Express*. vol. 18, pp. A506-A512, 2010.
- [173] F. Nunzi, S. Agrawal, A. Selloni, F. De Angelis, "Structural and electronic properties of photoexcited TiO₂ nanoparticles from first principles." *J. Chem. Theo. Comput.*, vol. 11, pp. 635-645, 2015.
- [174] M. Pastore, F. De Angelis, "First-principles modeling of a dye-sensitized TiO₂/IrO₂ photoanode for water oxidation." *J. Am. Chem. Soc.*, vol. 137, pp. 5798-5809, 2015.
- [175] E. Ronca, G. Marotta, M. Pastore, F. De Angelis, "Effect of sensitizer structure and TiO₂ protonation on charge generation in dye-sensitized solar cells." *J. Phys. Chem. C*. vol. 118, pp. 16927-16940, 2014.
- [176] Y. A. Duan, Y. Geng, H. B. Li, J. L. Jin, Y. Wu, Z. M. Su, "Theoretical characterization and design of small molecule donor material containing naphthodithiophene central unit for efficient organic solar cells." *J. Comput. Chem.*, vol. 34, pp. 1611-1619, 2013.

- [177] D. Alberga, G. F. Mangiatordi, F. Labat, I. Ciofini, O. Nicolotti, G. Lattanzi, C. Adamo, "Theoretical investigation of hole transporter materials for energy devices." *J. Phys. Chem. C*. vol. 119, pp. 23890-23898, 2015.
- [178] C. Risko, G. Kushto, Z. Kafafi, J.-L. Brédas, "Electronic properties of silole-based organic semiconductors." *J. Chem. Phys.*, vol. 121, pp. 18, 2004.
- [179] U. Salzner, "Electronic structure of conducting organic polymers: Insights from time-dependent density functional theory." *Wiley Interdisciplinary Reviews: Comput. Mol. Sci.* vol. 4, pp. 601-622, 2014.
- [180] X. C. Li, J. S. Sun, G. H. He, G. L. Jiang, Y. Tan, B. Xue, "Macroporous polypyrrole-TiO₂ composites with improved photoactivity and electrochemical sensitivity." *J. Colloid Interf. Sci.*, vol. 411, pp. 34-40, 2013.
- [181] J. B. Zhu, X. Zhao, M. L. Xiao, L. Liang, C. P. Liu, J. H. Liao, W. Xing, "The construction of nitrogen-doped graphitized carbon-TiO₂ composite to improve the electrocatalyst for methanol oxidation." *Carbon*. vol. 72, pp. 114-124, 2014.
- [182] J. J. Li, J. T. Feng, W. Yan, "Excellent adsorption and desorption characteristics of polypyrrole/TiO₂ composite for methylene blue." *Appl. Surf. Sci.*, vol. 279, pp. 400-408, 2013.
- [183] F. Deng, L. J. Min, X. B. Luo, S. L. Wu, S. L. Luo, "Visible-light photocatalytic degradation performances and thermal stability due to the synergetic effect of TiO₂ with conductive copolymers of polyaniline and polypyrrole." *Nanoscale*. vol. 5, pp. 8703-8710, 2013.
- [184] G. A. Jeffrey *An introduction to hydrogen bonding*; Oxford university press New York, 1997; Vol. 12.

- [185] D. O. Scanlon, C. W. Dunnill, J. Buckeridge, S. A. Shevlin, A. J. Logsdail, S. M. Woodley, C. R. A. Catlow, M. J. Powell, R. G. Palgrave, I. P. Parkin, "Band alignment of rutile and anatase TiO₂." *Nat. Mater.*, vol. 12, pp. 798-801, 2013.
- [186] J. Blanc, N. Derouiche, A. El Hadri, J. Germain, C. Maleysson, H. Robert, "Study of the action of gases on a polypyrrole film." *Sens. Actuators, B: Chem.* vol. 1, pp. 130-133, 1990.
- [187] D. Liu, J. Aguilar-Hernandez, K. Potje-Kamloth, H. Liess, "A new carbon monoxide sensor using a polypyrrole film grown on an interdigital-capacitor substrate." *Sens. Actuators, B: Chem.* vol. 41, pp. 203-206, 1997.
- [188] S. Waghuley, S. Yenorkar, S. Yawale, S. Yawale, "Application of chemically synthesized conducting polymer-polypyrrole as a carbon dioxide gas sensor." *Sens. Actuators, B: Chem.* vol. 128, pp. 366-373, 2008.
- [189] V. Ratautaite, S. D. Janssens, K. Haenen, M. Nesládek, A. Ramanaviciene, I. Baleviciute, A. Ramanavicius, "Molecularly imprinted polypyrrole based impedimetric sensor for theophylline determination." *Electroch. Acta.* vol. 130, pp. 361-367, 2014.
- [190] M. J. Allen, V. C. Tung, R. B. Kaner, "Honeycomb carbon: A review of graphene." *Chem. Rev.* vol. 110, pp. 132-145, 2009.
- [191] C. N. R. Rao, A. K. Sood, K. S. Subrahmanyam, A. Govindaraj, "Graphene: The new two-dimensional nanomaterial." *Angew. Chem. Inter. Ed.* vol. 48, pp. 7752-7777, 2009.
- [192] H. Chang, H. Wu, "Graphene-based nanomaterials: Synthesis, properties, and optical and optoelectronic applications." *Adv. Funct. Mater.* vol. 23, pp. 1984-1997, 2013.

- [193] K. Yang, L. Feng, X. Shi, Z. Liu, "Nano-graphene in biomedicine: Theranostic applications." *Chem. Soc. Rev.* vol. 42, pp. 530-547, 2013.
- [194] M. A. Imran Ali, Tabrez A. Khan, "Low cost adsorbents for the removal of organic pollutants from wastewater." *J. Environ. Manag.* vol. 113, pp. 170–183, 2012.
- [195] A. Dabrowski, "Adsorption — from theory to practice." *Adv. Colloid Interf. Sci.* vol. 93, pp. 135-224, 2001.
- [196] G. Shi, "Graphene-based gas sensors." *J. Mater. Chem. A.* vol. 1, pp. 10078, 2013.
- [197] A. K. G. F. Schedin, S. V. Morozov, E. W. Hill, P. Blake, M. I. Katsnelson & K. S. Novoselov, "Detection of individual gas molecules adsorbed on graphene." *Nat. Mater.* vol. 6, pp. 652-659, 2007.
- [198] F. K. P. Jeremy T. Robinson, Eric S. Snow, Zhongqing Wei and Paul E. Sheehan, "Reduced graphene oxide molecular sensors." *Nano Lett.* vol. 8, pp. 3137-3140, 2008.
- [199] S. P. S. Vineet Dua, Srikanth Ammu, Srikanth Rao Agnihotra, Sujit Jain, Kyle E. Roberts, Sungjin Park, Rodney S. Ruoff and Sanjeev K. Manohar, "All-organic vapor sensor using inkjet-printed reduced graphene oxide." *Angew. Chem. Inter. Ed.* vol. 49, pp. 2154-2157, 2010.
- [200] Y.-K. H. Tae Hee Han, Alvin T. L. Tan, Vinayak P. Dravid, and Jiaying Huang, "Steam etched porous graphene oxide network for chemical sensing." *J. Am. Chem. Soc.* vol. 133, pp. 5264–5267, 2011.
- [201] H. Wu, "Graphene-based nanocomposites: Preparation, functionalization, and energy and environmental applications." *Energy Environ. Sci.* vol. 6, pp. 3483-3507, 2013.

- [202] A. K. G. K. S. Novoselov, S. V. Morozov, D. Jiang, Y. Zhang, S. V. Dubonos, I. V. Grigorieva, A. A. Firsov, "Electric field effect in atomically thin carbon films." *Science*. vol. 306, pp. 666-669 2004.
- [203] X.-H. Z. Jin-Gang Yu, Lin-Yan Yu, Fei-Peng Jiao, Jian-Hui Jiang , Xiao-Qing Chen, "Removal, recovery and enrichment of metals from aqueous solutions using carbon nanotubes." *J. Radioanal. Nuclear Chem*. vol. 299, pp. 1155–1163, 2014.
- [204] N. Varghese, U. Mogera, A. Govindaraj, A. Das, P. K. Maiti, A. K. Sood, C. N. R. Rao, "Binding of DNA nucleobases and nucleosides with graphene." *ChemPhysChem*. vol. 10, pp. 206-210, 2009.
- [205] C.-H. Lu, H.-H. Yang, C.-L. Zhu, X. Chen, G.-N. Chen, "A graphene platform for sensing biomolecules." *Angew. Chem. Inter. Ed*. vol. 48, pp. 4785-4787, 2009.
- [206] H. Liu, C.-A. Tao, Z. Hu, S. Zhang, J. Wang, Y. Zhan, "An electrochemical glucose biosensor based on graphene composites: Use of dopamine as reducing monomer and as site for covalent immobilization of enzyme." *RSC Adv*. vol. 4, pp. 43624-43629, 2014.
- [207] S. Alwarappan, C. Liu, A. Kumar, C.-Z. Li, "Enzyme-doped graphene nanosheets for enhanced glucose biosensing." *J. Phys. Chem. C*. vol. 114, pp. 12920-12924, 2010.

Appendix

[Article 1]

H. Ullah, A. A. Tahir, T. K. Mallick, "Structural and electronic properties of oxygen defective and Se-doped p-type BiVO₄(001) thin film for the applications of photocatalysis." *Appl. Catal., B: Environ.*, vol. 224, pp. 895-903, May. 2018.



Research paper

Structural and electronic properties of oxygen defective and Se-doped *p*-type BiVO₄(001) thin film for the applications of photocatalysis

Habib Ullah*, Asif A. Tahir*, Tapas K. Mallick

Environment and Sustainability Institute (ESI), University of Exeter, Penryn Campus, Penryn, Cornwall TR10 9FE, United Kingdom

ARTICLE INFO

Keywords:

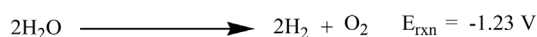
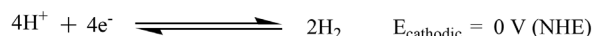
Se-doped BiVO₄
p-type semiconductor
 Charge carriers
 Water splitting

ABSTRACT

Monoclinic BiVO₄ is being used as a photocatalyst due to its stability, cost-effectiveness, ease of synthesis, and narrow band gap. Although, the valence band maximum, VBM (~ -6.80 eV vs vacuum) of BiVO₄ is well below the redox potential of water but having less positive conduction band minimum, CBM (-4.56 eV vs vacuum), responsible for its low efficiency. We have carried out a comprehensive periodic density functional theory (DFT) simulations for the pristine, Oxygen defective (O_v) and Se doped BiVO₄, to engineer not only its CB edge position but the overall photocatalytic and charge carrier properties. Our theoretical method has nicely reproduced the experimental data of pristine BiVO₄, which encouraged us to elaborate further its O_v and Se-doped characteristics. It is found that both the O_v (1% Oxygen vacancy) and Se-doped BiVO₄ (1–2% Se) have ideal band edges, band gaps, and small effective masses of electrons and holes, responsible for high photocatalytic activities. Moreover, Se-doped BiVO₄ behave as *p*-type semiconductor. Finally, the photocatalytic water-splitting behaviour of the selected surfaces were counterchecked with water interaction, where the strong water adsorption energy of about ~ -38 to -50 kcal/mol, confirms and predicts their higher efficiencies compared to that of parent BiVO₄.

1. Introduction

Solar energy harnessing via photoelectrochemical (PEC) water splitting, using transition metal oxides, is a direct chemical energy conversion and storage technique. Since the discovery of the first photocatalytic water splitting experiment, a range of transition metal oxides have been employed to produce solar fuel [1]. An ideal photocatalyst must have valance band (VB) and conduction band (CB), which straddle the redox potentials of photocatalytic reaction, and must have high stability, availability, and narrow band gap which can absorb efficiently the visible part of sun light [2,3].



To date, the current focus semiconductors/photocatalysts are Fe₂O₃, LaFeO₃, TaON, LaCrO₃, LaCoO₃, TiO₂, BiVO₄, ZnS, ZnO₂, Bi₂WO₆, SrTiO₃, BiOX (Cl, Br, I), and etc. Some of these semiconductors have ideal band edges position but they are either unstable or having large

band gaps, while some of them are narrow band gap but one of the band edges (either VB or CB) is situated at improper band edge energy (see Scheme S1) [4]. So, the redox reaction cannot be completed without the external bias potential (see reactions 1–3). Band structure engineering is one of the excellent strategies to tailor the band edges and band gaps of these semiconductors, through doping process [5–7].

Bismuth vanadate (BiVO₄) is a promising photocatalyst for solar energy conversion due to its nontoxic, low-cost, photostable, and eco-friendly nature. Generally, BiVO₄ has three different crystalline polymorphs: orthorhombic pucherite, tetragonal dreyerite, and monoclinic clinobisvanite [8]. These different polymorphs have different properties as the photocatalytic activity is strongly influenced by the crystal structure. For instance, the tetragonal BiVO₄ possesses a band gap of 2.9 eV and mainly absorbs UV region, while the monoclinic clinobisvanite (m-BiVO₄) exhibits a much higher photocatalytic activity due to its ideal band gap (2.4–2.5 eV) which absorb the UV and visible regions of the electromagnetic spectrum, having an ideal valence band edge position for driving water oxidation [9]. However, it has been recently reported that m-BiVO₄, an *n*-type semiconductor [10], exhibits poor photocatalytic property which is stem to low mobility of the photogenerated charge carriers (electron–hole pairs), positive potential of CB (vs NHE) and high charge recombination rates which

* Corresponding author.

E-mail addresses: hu203@exeter.ac.uk, habib_chemist@yahoo.com (H. Ullah), A.Tahir@exeter.ac.uk (A.A. Tahir).

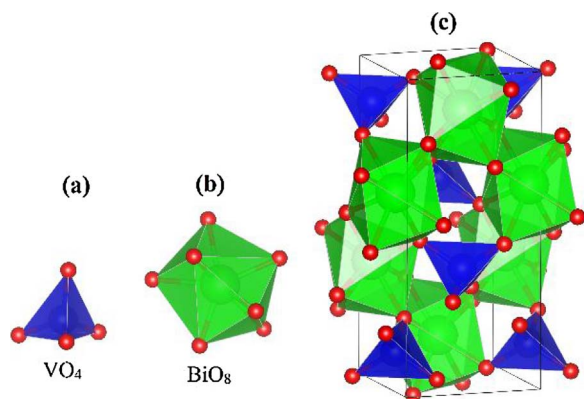


Fig. 1. Tetrahedral and dodecahedra geometries of VO_4 (a) and BiO_8 (b) in BiVO_4 (c).

significantly limit its practical applications. The photocatalytic activity of *m*- BiVO_4 can be tuned either with metal or non-metal doping, semiconductor recombination (heterojunction formation), depositing the co-catalysts, defect formation (oxygen vacancy creation), and crystal-facet control or morphological modification.

Moreover, it is important to investigate/design an efficient dopant for BiVO_4 , which not only keeps its monoclinic crystal structure but to slow down the charge recombination rate and more negative CB (vs NHE) edge position. The monoclinic clinobisvanite structure of BiVO_4 , consists of rows of isolated $[\text{VO}_4]$ tetrahedra which are separated by the dodecahedral coordinated Bi atoms to form $[\text{BiO}_8]$ with eight O atoms (Fig. 1).

In order to improve the overall photocatalytic activity of *m*- BiVO_4 (simply denoted as BiVO_4), different doping agents have been applied; these doping agents have either substituted the (I) V or (II) Bi atoms but no one has paid attention to substitute the (III) O site of BiVO_4 . The previous literature of different doping agents [11–18], used for BiVO_4 can be summarized as!

(I). Doping of BiVO_4 at the V-sites is very common but due to different valence states of the dopant, a distortion in the $[\text{VO}_4]$ tetrahedral chains cause phase transition from the parental monoclinic to tetragonal structure (Fig. 1). This distortion of $[\text{VO}_4]$ tetrahedron chains in BiVO_4 , plays a negative impact on the photocatalytic water-splitting, to generate H_2 gas. On the other hand, monoclinic BiVO_4 exhibits weak hole localization and is very helpful for water-splitting reaction. So, to keep the $[\text{VO}_4]$ tetrahedral in the monoclinic structure of BiVO_4 , Luo et al. have reported that ion doping with higher valence states such as Mo^{6+} and W^{6+} , to substitute V in BiVO_4 , not only keep the parental geometry but also enhanced its photocatalytic activity [19].

(II). Another useful dopant agent which keeps the tetrahedral geometrical part of $[\text{VO}_4]$ is Ce^{3+} , which substitutes the Bi^{3+} sites in BiVO_4 . Ce^{3+} is a trivalent cation and has similar ionic radius to that of Bi^{3+} , substitutes the Bi-sites and not the V-sites (V^{5+}). Z. Jiang et al. have investigated that Ce^{3+} ions doped- BiVO_4 (Ce-BiVO_4) do not distort either the octahedral and dodecahedral geometries but act as trapping agent for the photogenerated holes which is responsible for the higher photocatalytic water oxidation activity compared to that of pristine one [20].

(III). No one has paid attention to substitute the O-sites in BiVO_4 , and we believe that its substitution with di-anionic species such as selenium (Se^{2-}), with appropriate amount of doping ratio, will not disturb both the $[\text{VO}_4]$ and $[\text{BiO}_8]$ geometries. Furthermore, Se^{2-} would have dual attachment in the BiVO_4 , coordinated with Bi on one hand and with V on the other side.

In this work, we investigated the effect of Oxygen vacancy and Se-dopant for the geometrical structure and corresponding photocatalytic activity of BiVO_4 .

2. Computational methodology

First principle periodic boundary density functional theory (DFT) simulations are carried out, using Quantum ESPRESSO [21] and QuantumWise-ATK [22] while the results are visualized on VESTA [23] and vnl 2017.0 [24]. The experimentally observed crystallographic file of BiVO_4 ; clinobisvanite structure is used as such which has Hall symmetry space group of I2/b with lattice parameters of $a = 5.147 \text{ \AA}$, $b = 5.147 \text{ \AA}$, $c = 11.7216 \text{ \AA}$, and $\gamma = 90^\circ$ (See Fig. 1) [25]. Generalized gradient approximation (GGA) at Perdew-Burke-Ernzerhof (PBE) exchange-correlation functional is used for the structural and energy optimization [26]. As an input structure for the calculations; the 24 atoms primitive unit cell and its $2 \times 2 \times 2$ supercell along with (001) direction with 10 \AA vacuum, is considered as a model for the periodic boundary condition (PBC) DFT simulations. The local density approximation (LDA) method is found to be superior in reproducing the experimental data of BiVO_4 , compared to pure GGA and meta GGA (MGGA). The detailed comparison of these methods is given in Supporting Information (Fig. S1 and S3). Generally, it is believed that clinobisvanite monoclinic BiVO_4 exists in (001) orientation so, that is why the (001) slab is opted for the theoretical simulations to represent its experimental thin film [27]. Moreover, the unreconstructed (001) termination possesses low surface energy and as a result represents the most probable surface termination [27]. Stability of these different slabs are confirmed from their positive formation energy and electrostatic potential; details of surface formation energy is given in Table S1 and Fig. S4-10 of the Supporting Information. A $5 \times 5 \times 1$ Monkhorst-Pack k-grid and energy cutoff of 100 Ry is employed for the geometry relaxation and self-consistent (SCF) simulations of BiVO_4 ; consisting of 96 atoms. The Broyden-Fletcher-Goldfarb-Shanno algorithm (BFGS) is used for the structural relaxation [28]. A $5 \times 5 \times 5$ Monkhorst-Pack k-grid with the same energy cutoff is used for the non-SCF part to get the density of states (DOS) and partial DOS (PDOS). The band structure simulations were performed along the direction of Γ , Z, R, X, and M of the Brillouin zone. The valence electron configurations considered are: $5d^{10} 6s^2 6p^3$ for Bi; $3p^6 3d^3 4s^2$ for V; $2s^2 2p^4$ for O, $1s^2$ for H, and $4s^2 4p^4 3d^{10}$ for Se atom.

3. Results and discussion

3.1. Optimized structures of pristine, oxygen defective, and Se-Doped $\text{BiVO}_4(001)$

The removal of an oxygen atom, and Se dopant on the tetrahedral or dodecahedra geometries of monoclinic clinobisvanite is investigated from the resulting relaxed geometries. Optimized structures of these different species of BiVO_4 are given in Fig. 2, where the bond distances between V–O and Bi–O decrease; considering the case of O_v and Se-doped $\text{BiVO}_4(001)$. When the Se dopant ratio is increased from 2 to 3 or 4, it distorted the geometries of parent $\text{BiVO}_4(001)$ as can be seen from Fig. 2. However, in case of 1–2% doping ratios, the resulted geometries were quite compact and similar to parent $\text{BiVO}_4(001)$.

3.2. Electronic properties

3.2.1. Electronic properties of $\text{BiVO}_4(001)$ surface

As discussed in our previous report [29], that the monoclinic clinobisvanite phase exhibits a much higher photocatalytic activity compared to its other polymorphs due to its favourable band gap (2.4–2.5 eV) in the visible region of electromagnetic spectrum and a valence band position suitable for driving water oxidation [9].

The electronic properties such as DOS/PDOS and band structure of $\text{BiVO}_4(001)$ are given in Fig. 3, where its band gap is 2.24 eV. This band gap is about 0.16 eV smaller than that of experimental but it is expected from LDA [30], which underestimate the band gap. However, it has nicely reproduced both the VB and CB edge positions of pristine

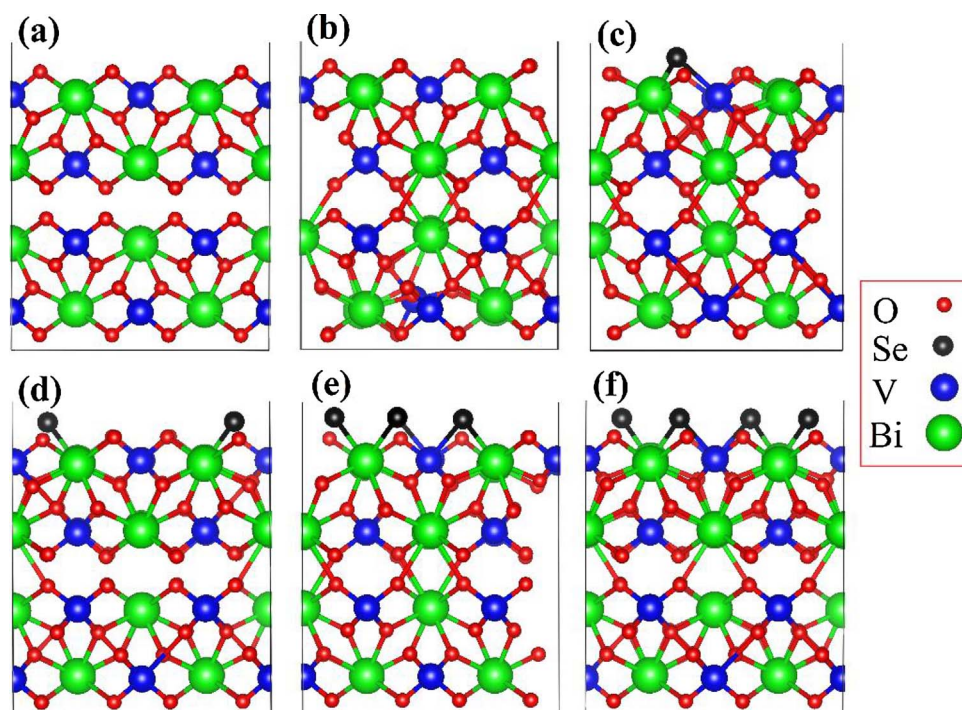


Fig. 2. Relaxed structures of (a) $\text{BiVO}_4(001)$, (b) Ov, (c) 1%, (d) 2%, (e) 3%, and (f) 4% Se doped $\text{BiVO}_4(001)$.

$\text{BiVO}_4(001)$; ca. at -6.80 eV and -4.56 eV (vs vacuum), respectively. Analysis of the PDOS led us to conclude that orbitals of O atoms are responsible for developing valence band edge, however, the conduction band edge is that of V atoms. Contribution of the s, p, and d orbitals of Bi, V, and O, in making the band gap and edge positions are given in Fig. S11 of the Supporting Information. The s and p orbitals of Bi atoms constitute VB and CB edge of Bi, 3d orbitals of V are responsible for its VB and CB while in case of O, 2p orbitals have a major role in developing their band edge positions. Band structure of the $\text{BiVO}_4(001)$ along the k-points direction of Γ , Z, R, X, and M is given in Fig. 3, where an indirect band gap of 2.24 eV has good agreement with the experimental and recently theoretical reported data [9]. Furthermore, the simulated band edge energies (VBM ~ -6.80 and CBM ~ -4.56 eV at vacuum level) of BiVO_4 indicate that its CBM need to be engineered for high PEC performance. The effective masses of the photogenerated electrons (m_e^*) and holes (m_h^*) along the $X \rightarrow \Gamma$ directions of k-points are calculated by fitting parabolic approximation around the bottom of the CBM or the top of the VBM, respectively; using Eq. (1) (Table 1):

$$m^* = \hbar^2 (d^2 E/dk^2)^{-1} \quad (1)$$

where \hbar is the reduced Planck constant, E is the energy of an electron at wave vector k in the same band (VBM or CBM). The simulated values of the effective masses of photogenerated electrons and holes of the $\text{BiVO}_4(001)$ are 0.09 and 0.28 m_e , respectively.

The integrated local DOS (ILDOS) of $\text{BiVO}_4(001)$ within various energetic windows of the VBM, CBM, band gap, and electrostatic potential (ESP) are presented in Fig. 4. The ILDOS at the CBM (0–1.6 eV), as well as a cross section of the ILDOS through the (001) plane highlights the primary contribution from V orbitals which can be found from Fig. 3 and Fig. S11. Localization of CBM electrons is because of the poor hybridization of V neighbouring orbitals as can be seen from Figs. 3, 4 and S11. The poor photoelectrochemical performance BiVO_4 thin film can be correlated with poor hole mobility (effective mass of hole $\sim 0.28 m_e$) rather than electron, which limits photocarrier transport and charge extraction. The self-trapping and small electron polaron formation in this material is due to the localization of photogenerated hole. Pristine $\text{BiVO}_4(001)$ is an *n*-type semiconductor where the electrons play an important role in the photocatalytic reaction. This statement also corroborate the already reported work of A. Rettie et al. [31] So, the relative delocalized orbitals at CBM compared to VBM (Fig. 3) confirmed that majority of hole, limit the charge transport in

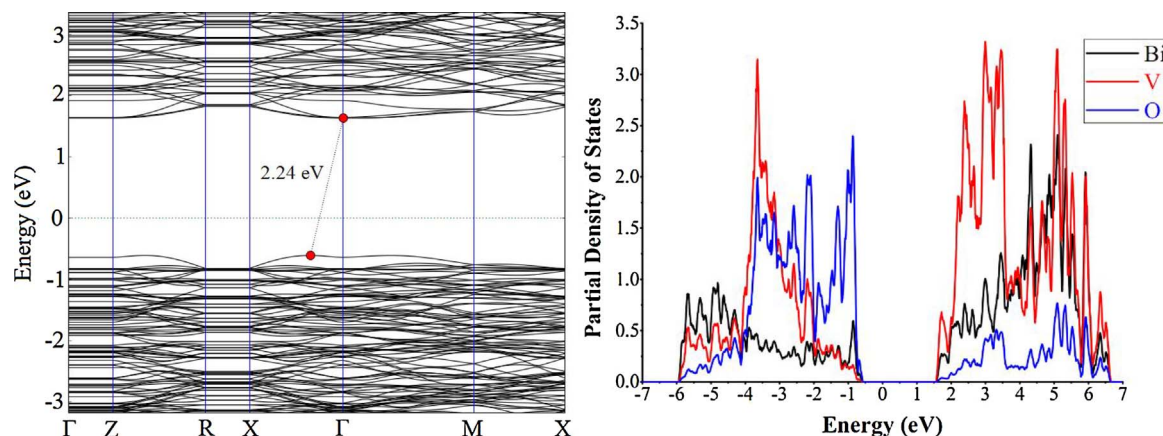


Fig. 3. Band Structure and PDOS plot of $\text{BiVO}_4(001)$; the Fermi energy is set to zero.

Table 1

Fermi energy, % doping, VBM, CBM, Band Gap, and Effective Masses of Photogenerated Electrons and Holes, Estimated from the calculated Band Structure along the suitable direction.

Species	Fermi Energy	% Doping	m_e^*/m_0	m_h^*/m_0	VBM	CBM	Band gap
BiVO ₄ (001)	−6.18	Pure	0.09	0.28	−6.80	−4.56	2.24
O _v -BiVO ₄	−4.28	1.0	0.19	0.18	−6.29	−4.33	1.96
1Se-BiVO ₄ (001)	−5.17	1.04	0.09	0.02	−5.80	−4.41	1.39
2Se-BiVO ₄ (001)	−5.19	2.08	0.04	0.31	−5.81	−4.08	1.73
3Se-BiVO ₄ (001)	−4.93	3.0	0.65	2.02	−5.47	−4.39	1.08
4Se-BiVO ₄ (001)	−4.73	4.16	0.01	0.24	−5.38	−4.14	1.24

this material.

3.3. Electronic properties of oxygen vacancy BiVO₄(001) surface

In order to understand the effect of oxygen vacancy (O_v) on the photoelectrochemical performance of BiVO₄, 1% O_v-BiVO₄(001) is employed for DFT simulations. The VB and CB orbitals distributions are almost similar to that of parent slab, however, the Fermi energy merge in the CB which is due to the extra electron(s) of the O_v, as can be seen from Fig. 5. It is also reported that monoclinic BiVO₄ is normally an intrinsic *n*-type semiconductor [32]. The contribution of V, Bi, and O orbitals are comparatively given in Fig. S12 of the Supporting Information. In this case, the electrons (0.19 *m_e*) are said to be the “majority carriers” for current flow (behave as an *n*-type semiconductor) while the effective mass of holes is 0.18 *m_e*. Overall, small effective masses of electrons and holes are estimated from the CBM and VBM of O_v-BiVO₄(001) compared to that of parent slab. At vacuum level, the CBM and VBM are −6.29 and −4.33 eV, which are well above and below the redox potential of water, respectively (Table 1). Moreover, electron doping (Oxygen vacancy creation) of BiVO₄ has not

only reduced its band gap, but shift the CB to more positive potential (vs vacuum) as can be seen from Table 1.

3.4. Electronic properties of Se-Doped BiVO₄(001) surfaces

In order to improve the photocatalytic performance of BiVO₄, Se is incorporated in the form of different dopant concentrations. Oxygen atom(s) is substituted with Se in BiVO₄(001), from 1 to 4% dopant ratios, denoted as 1Se, 2Se, 3Se and 4Se-BiVO₄(001). 1% Se-doped has excellently improved the visible light absorption of BiVO₄(001) as can be seen from its band gap reduction, from 2.24 to 1.39 eV (Fig. 6 and Table 1). Moreover, *p* orbitals of Se constitute the VB of 1Se-BiVO₄(001), as can be seen from its PDOS plot (Fig. 6). The individual PDOS plots of Bi, V, O, and Se are shown in Fig. S13 of the Supporting Information. Se has not only reduced the band gap of parent BiVO₄, but changed both the VB and CB, to −5.80 eV and −4.41 eV (vs vacuum), respectively. Compared to parent BiVO₄(001), 1Se-BiVO₄(001) has an ideal CBM position which is well above the redox potential of water, responsible for water reduction. Se is a *p*-type dopant, which has produced some flat bands in the VB of parent BiVO₄(001), however, it has

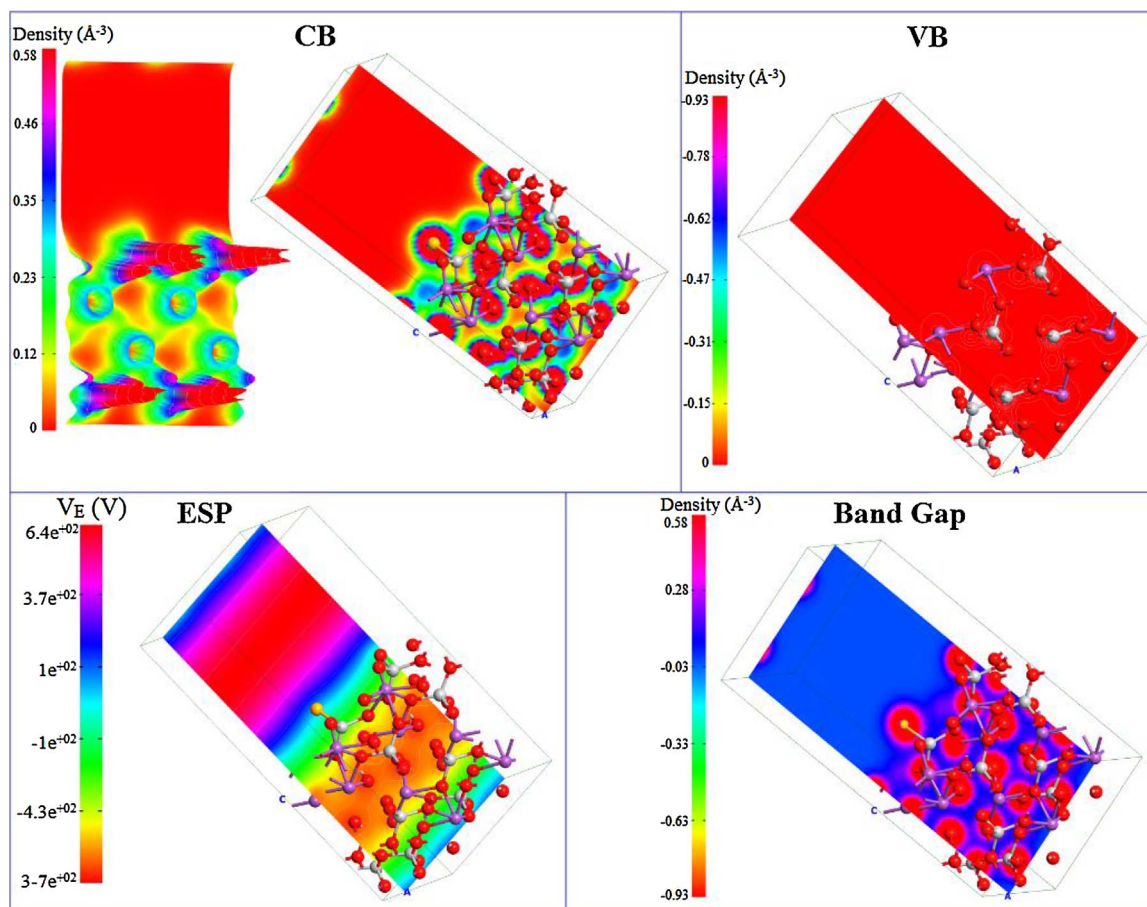


Fig. 4. Integrated local density of states of CBM, VBM, Band gap and ESP of BiVO₄(001).

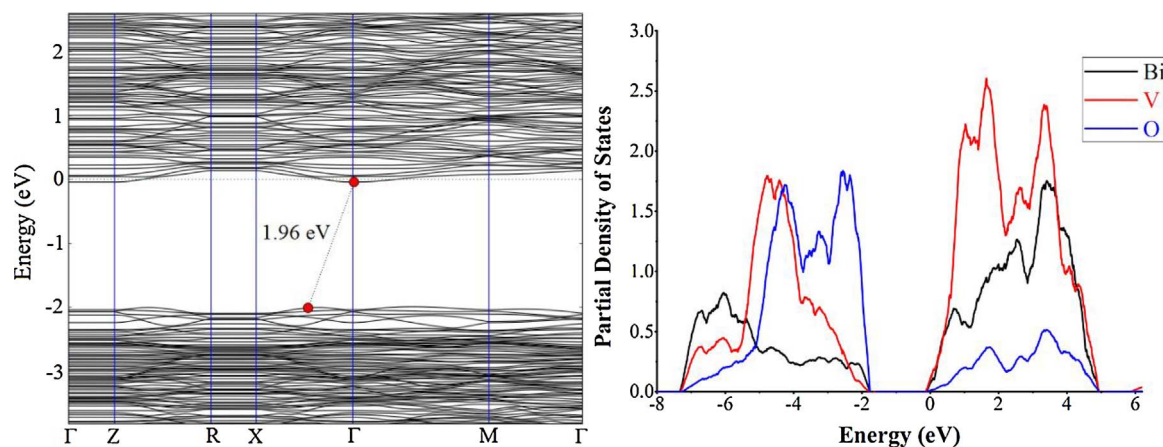


Fig. 5. Band Structure and PDOS plot of $O_v\text{-BiVO}_4(001)$; the Fermi energy is set to zero.

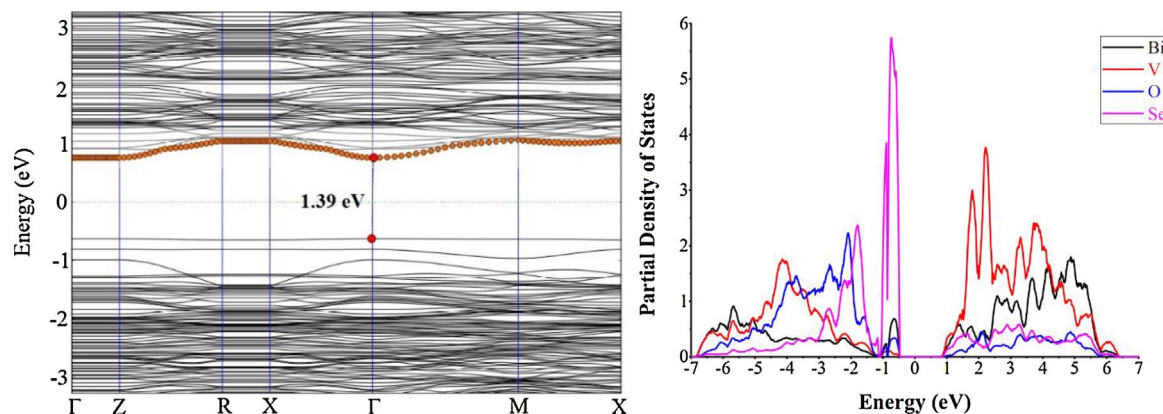


Fig. 6. Band structure and PDOS of 1% $\text{Se-BiVO}_4(001)$; the Fermi energy is set to zero.

significantly reduced the effective masses of electrons and holes (Table 1). The effective masses of these photocarriers are $0.09 m_e$ for electron and $0.02 m_e$ of hole (Note: for the effective masses of hole, we considered the third band, below the VBM). On the other hand, flat band of VB produces an effective mass of holes of about $7.12 m_e$, which are responsible for stationary holes. In summary, the high DOS in the VB Fermi level shift towards CB is clear evidence of the *p*-type nature of $1\text{Se-BiVO}_4(001)$. Moreover, $1\text{Se-BiVO}_4(001)$ can be used as a best photocatalyst for solar water splitting due to its ideal band edges positions, narrow band gap, and small effective masses of charge carriers (*vide infra*).

In the searching of an optimum dopant ratio of Se, to design an efficient photocatalyst, we also considered the $2\text{Se-BiVO}_4(001)$ system. The simulated band structure and PDOS of $2\text{Se-BiVO}_4(001)$ are given in Fig. 7, while its comparative PDOS plot for Bi, V, O, and Se atoms are given in Fig. S14 of the Supporting Information. Again, the VB and CB are made of Se and V atoms, respectively. The VB and CB of $2\text{Se-BiVO}_4(001)$ are situated at -5.81 and -4.08 eV (at vacuum), respectively which result band gap of 1.73 eV. Moreover, the simulated effective masses of electrons and holes are $0.04 m_e$ and $0.31 m_e$, respectively, which predict high carrier mobility and charge separation rate. Very similar to $1\text{Se-BiVO}_4(001)$, $2\text{Se-BiVO}_4(001)$ also behave as a *p*-type semiconductor as can be seen from its band structure and PDOS plot. So, both the 1 and 2% Se doped $\text{BiVO}_4(001)$ have almost similar photocatalytic characteristics and can be used for efficient water splitting, especially for water reduction.

The effect of 3 and 4% Se on $\text{BiVO}_4(001)$ and their band gap and effective masses of charge carriers are contrast to that of 1 and 2%, as can be seen from Table 1 and Fig. 8. For simplicity reason, the band gap and orbitals contribution of Bi, V, O, and Se of 3 and 4% Se-doped

$\text{BiVO}_4(001)$ are given in Fig. S15-S18 of the Supporting Information. Although, this higher doping concentration has well reduced the bandgap of parent $\text{BiVO}_4(001)$, 1.08 eV for 3 and 1.24 eV for 4% Se, but on the other hand it has sufficiently increased the VB and CB values (vs vacuum). The CBM positions of both these systems is well above the redox potential of water (vs vacuum) but the VBM is not able to perform the oxidation of water, to complete the overall water splitting reaction. The VBM and CBM of $3\text{Se-BiVO}_4(001)$ are -5.47 and -4.39 eV while that of $4\text{Se-BiVO}_4(001)$ are -5.38 and -4.14 eV, respectively. For the effective masses of charge carriers of these two systems, see Table 1.

Comparative analysis of the Oxygen defective and Se doped (1 and 2%) $\text{BiVO}_4(001)$, led us to conclude that both the defective and mild (1 and 2%) Se-Doped $\text{BiVO}_4(001)$ are best candidates for photocatalytic water splitting, based on their simulated VB, CB, Bandgap and effective masses of charge carriers.

3.5. Adsorption of water on pristine, oxygen defective, and 1% Se doped $\text{BiVO}_4(001)$

In order to elaborate the photocatalytic performance of the titled species, we adsorb water molecules on the surface of pristine, O_v - and $1\text{Se-BiVO}_4(001)$, see Fig. 9 for their relaxed structures. Two molecules of water are adsorbed on each of these surfaces, optimized and followed by electronic properties simulations such as bandgap, band edge and effective masses of charge carriers. The adsorption energy of water molecules is simulated with the help of Eq. (1), by subtracting the energies of the optimized water molecule and adsorbent bare slab (E_{slab}) from the optimized water-slab complex (slab@water), using Eq. (1).

$$\Delta E_{\text{ad}} = E_{\text{slab@water}} - (E_{\text{water}} + E_{\text{slab}}) \quad (1)$$

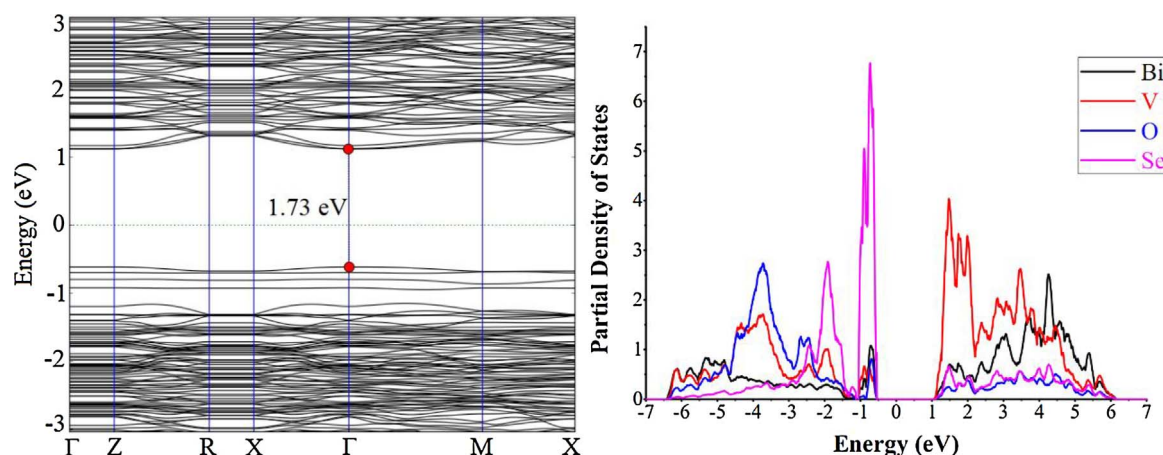


Fig. 7. Band Structure and PDOS plot of 2% Se-BiVO₄(001); the Fermi energy is set to zero.

3.6. Pristine BiVO₄(001)@H₂O

In case of BiVO₄(001)@H₂O, one of the water molecules is more attracted towards the surface via O–Bi and two H–O bondings, having distances of 2.45 and 1.62 Å, respectively (Table 2).

Hydrogen atoms of water molecules make a strong hydrogen bonding with the surface O atoms of BiVO₄(001), consequences the water splitting ability of pristine BiVO₄. The parent H–O bond distances (0.97 Å) and H–O–H angle (102°) of water molecule enlarged to 1 Å and 110.41°, respectively when H₂O is adsorbed on the (001) surface of BiVO₄. The per-water molecular adsorption energy is –38.28 kcal/mol, responsible for H₂O splitting over (001) surface of BiVO₄. Moreover, the negative ΔE_{ad} value indicates an exothermic adsorption process.

The electronic band structure and PDOS plot of BiVO₄(001)@H₂O are given in Fig. 10, where the band gap of parent BiVO₄(001) is reduced to 1.74 eV upon adsorption of water molecules. So, the bandgap reduction of 0.48 eV confirm the water affinity of BiVO₄ towards its (001) surface. From the band structure and PDOS (Fig. 10) of BiVO₄(001)@H₂O system, it can be concluded that the VB orbital of water molecules has strong hybridization with the VB of BiVO₄(001). Comparative analysis of the data of Table 1 and Fig. 10, led us to conclude that the water has moved the VB of pristine BiVO₄(001) from –6.80 to –5.96 eV and CB from –4.56 to –4.22 eV, at vacuum level. The individual PDOS plots of Bi, V, O, and H₂O is given in Fig. S19 of the Supporting Information. In summary, the strong adsorption energy, perturbation in both inter, and intra-bond distances of water and

BiVO₄(001), confirmed and validate the already experimental photocatalytic ability of BiVO₄ [33,34].

3.7. Oxygen defective BiVO₄(001)@H₂O

As discussed earlier, the Oxygen defective BiVO₄(001) has ideal band edge positions (well above and below the redox potential of water) and narrow band gap to be used as photocatalyst for water splitting. This defective surface has strong attraction for water molecules as can be observed from its adsorption energy (–50.85 kcal/mol). However, the inter-bond distances of H–O and Bi–O are longer compared to that of pristine@H₂O system. The reason behind this is, the more electropositive nature of O_v-BiVO₄(001) surface (especially O and Bi atoms), results weak hydrogen and electrostatic type of bondings (Table 2). In O_v-BiVO₄(001), the H–O bond distances of water molecules elongate to 0.99 Å, which result its further dissociation, as can be seen from Fig. 9b. The inter-bond distances such as the H–O (H of water and O of surface) are became enlarged which can be regarded to the cationic nature of O defective surface of BiVO₄(001).

Upon adsorption of water molecules on the Oxygen defective surface, the band gap of the resulted specie increases from 1.96 to 2.28 eV, as can be seen from Fig. 11 and Table 1 and 2. This 0.32 eV bandgap enlargement is due to the shifting of CB, which is about 0.38 eV compared to parent slab as can be seen from the PDOS of O_v-BiVO₄(001). Contrast to BiVO₄(001)@H₂O system, here water molecules has sufficiently changed the energy of CB of O_v-BiVO₄(001). The strong interaction of water with the O defective surface can be analysed from its

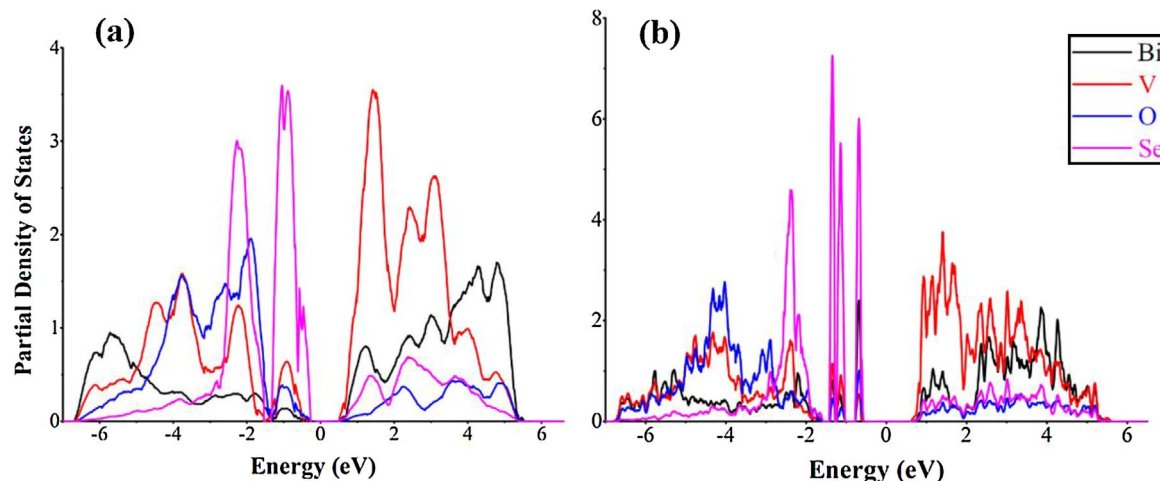


Fig. 8. PDOS plot of (a) 3Se and (b) 4Se-BiVO₄(001); the Fermi energy is set to zero.

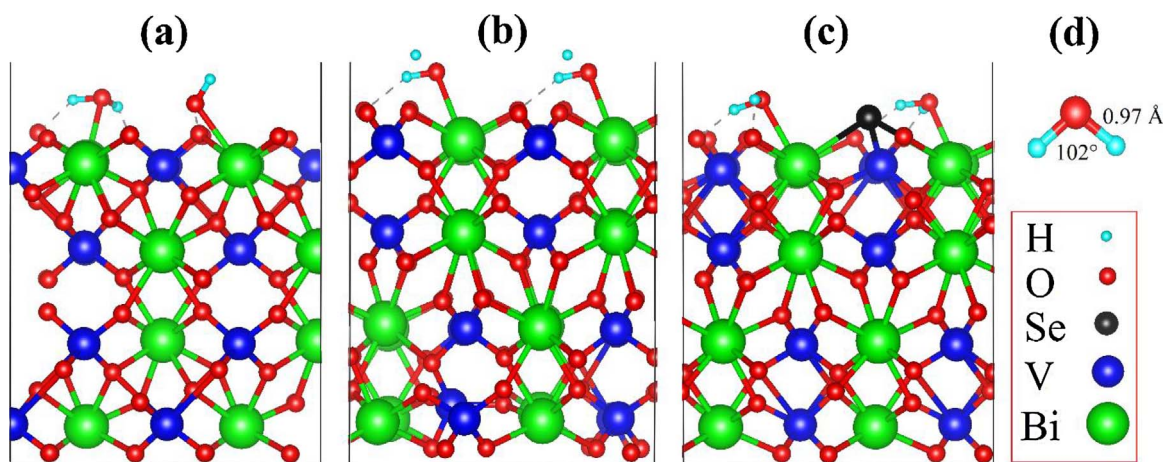


Fig. 9. Relaxed structure of (a) $\text{BiVO}_4(001)@H_2O$, (b) $O_v\text{-BiVO}_4(001)@H_2O$, (c) $1\text{Se-BiVO}_4(001)@H_2O$, and (d) water.

Table 2
Inter-bond distance, Water Adsorption Energy (E_{ad}), and Bandgaps of Water Adsorbed- $\text{BiVO}_4(001)$, Ov, and $1\text{Se-BiVO}_4(001)$ Systems.

Species	$H_{(water)}-O_{(surface)}$ (Å)	$Bi_{(surface)}-O_{(water)}$ (Å)	E_{ad} (kcal/mol)	Band gap
$\text{BiVO}_4(001)@H_2O$	1.62	2.45	-38.28	1.74
$O_v\text{-BiVO}_4@H_2O$	1.75	2.51	-50.85	2.28
$1\text{Se-BiVO}_4@H_2O$	1.59	2.45	-40.24	1.35

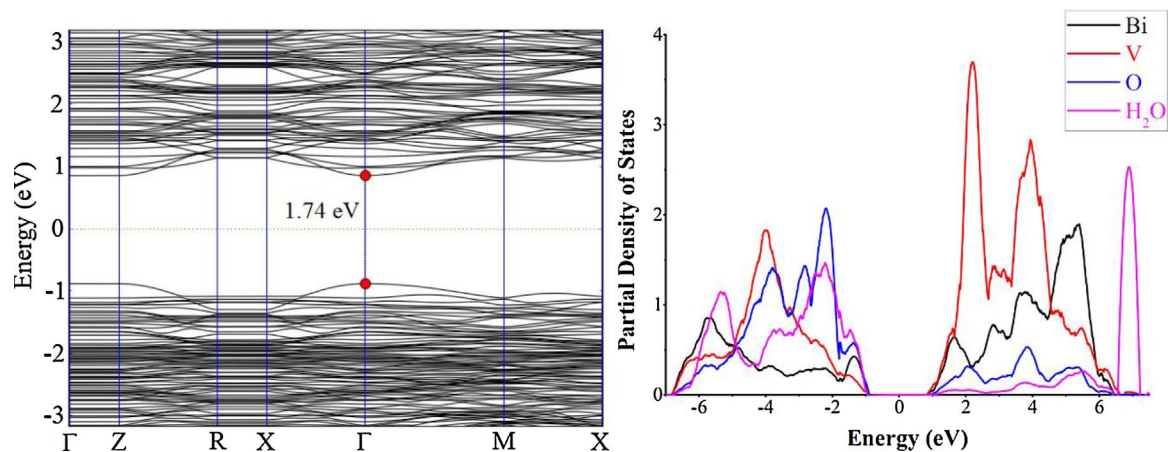


Fig. 10. Band Structure and PDOS plot of $\text{BiVO}_4\text{-}001@H_2O$; the Fermi energy is set to zero.

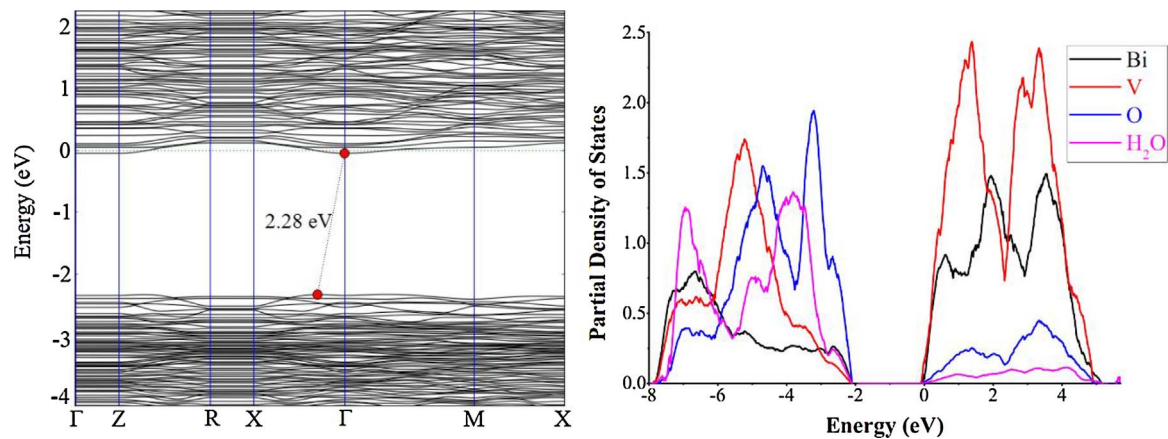


Fig. 11. Band structure and PDOS of $O_{vac}\text{-BiVO}_4(001)@H_2O$; the Fermi energy is set to zero.

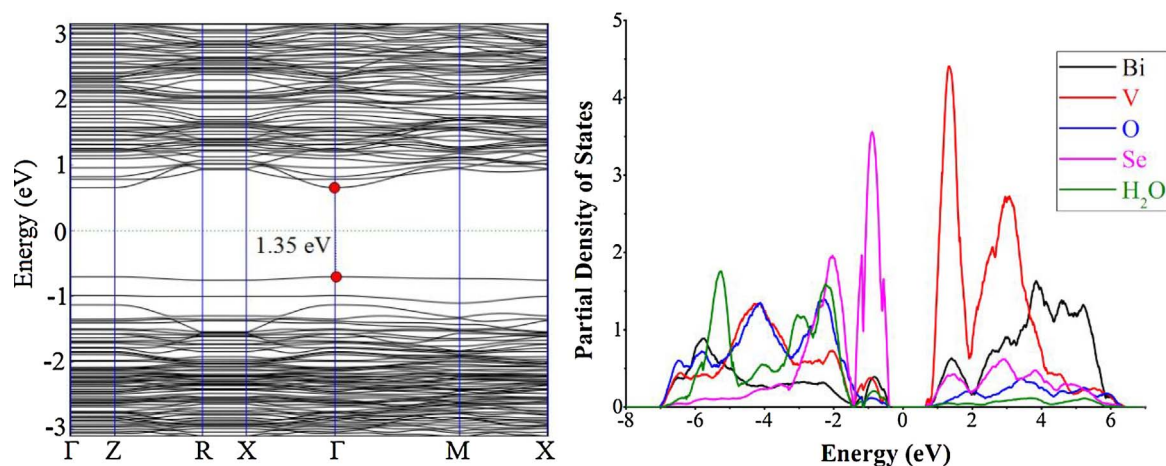


Fig. 12. Band structure and PDOS of 1Se_{BiVO}₄(001)@H₂O; the Fermi energy is set to zero.

highest adsorption energy (−50.85 kcal/mol) and orbital overlapping, especially in the VB of O_v-BiVO₄(001)@H₂O system (Fig. 11). The individual PDOS plots of Bi, V, O, and H₂O are given in Fig. S20 of the Supporting Information.

3.8. 1% Se-Doped-BiVO₄(001)@H₂O

Finally, the water adsorption on the 1Se_{BiVO}₄(001) surface is investigated, where its optimized parameters are given in Table 2 and electronic properties in Fig. 12 and S21. The simulated water adsorption energy (−40.24 kcal/mol) led us to conclude that 1% Se doped BiVO₄(001) can be easily used as an efficient photocatalytic material. Furthermore, the inter-Hydrogen bonding and electrostatic bond distances are 1.59 and 2.45 Å, respectively, which confirm the enhanced catalytic ability of Se doped BiVO₄. Besides these geometric parameters, electronic properties of the resulting system are also affected, upon adsorption of water molecules. Both the VB and CB are slightly moved from its parental position, which has decreased the overall band gap, from 1.39 to 1.35 eV as can be seen from Fig. 12 and Table 2.

In summary, although pristine BiVO₄ is a good photocatalyst for water splitting, having narrow bandgap and VB edge position, but inappropriate CB potential, reduces its hydrogen evaluation efficiency. This comprehensive theoretical simulation predicts that both the Oxygen defective and mild doped (1 or 2% Se) BiVO₄ have not only changed the band edges positions (well above and below the redox potential of water) but reduced the bandgap as well, results a champion photocatalyst for water splitting.

4. Conclusion

We have carried out a comprehensive periodic density functional theory (DFT) simulations for the pristine, oxygen defective (O_v) and Se-doped BiVO₄(001), to improve its photocatalytic performance. BiVO₄ is a stable, cheap, easily synthesizable, having appropriate band gap and valence band (VB) edge position but less positive conduction band (CB) edge position (vs vacuum). Our theoretical simulations of BiVO₄(001) surface has nicely reproduced the experimental data which has validated and confirm the method used. Furthermore, it is found that O_v (1%), and Se-doped (1–2%) BiVO₄(001) have narrowed band gaps, small effective masses of electrons and holes, and well above and below CBM and VBM, respectively (in line with the redox potential of water). Moreover, Se-doped BiVO₄(001) behave as a *p*-type semiconductor, capable of H₂ production from water reduction. Finally, the selected surfaces were interacted with water molecules, to check their water absorption energy. The water adsorption energies vary as O_v-BiVO₄(001)@H₂O > 1Se_{BiVO}₄(001)@H₂O > BiVO₄(001)@H₂O. Although, Oxygen defective (1% O vacancy) BiVO₄(001) has narrow

band gap (1.96 eV), suitable redox potentials (VB −6.29 eV, CB −4.33 eV at vacuum level), and high-water adsorption energy but thermodynamically less stable compared to Se-doped BiVO₄(001). So, we conclude and predict that mild doped Se_{BiVO}₄(001) is not only stable but can efficiently absorb the visible part of sun light and split water into O₂ and H₂ without any external biased.

Acknowledgment

The financial support was provided by Engineering and Physical Science Research Council, UK (EPSRC) under the research grant No EP/P510956/1. We also acknowledge Dr Andrew Cowley (Computing Development Officer) for the assistance of supercomputing facilities of ESI Beowulf Cluster.

Appendix A. Supplementary data

Supplementary data associated with this article can be found, in the online version, at <http://dx.doi.org/10.1016/j.apcatb.2017.11.034>.

References

- [1] A. Fujishima, Electrochemical photolysis of water at a semiconductor electrode, *Nature* 238 (1972) 37–38.
- [2] M.G. Walter, E.L. Warren, J.R. McKone, S.W. Boettcher, Q. Mi, E.A. Santori, N.S. Lewis, Solar water splitting cells, *Chem. Rev.* 110 (2010) 6446–6473.
- [3] T. Hisatomi, J. Kubota, K. Domen, Recent advances in semiconductors for photocatalytic and photoelectrochemical water splitting, *Chem. Soc. Rev.* 43 (2014) 7520–7535.
- [4] J. Li, N. Wu, Semiconductor-based photocatalysts and photoelectrochemical cells for solar fuel generation: a review, *Catal. Sci. Technol.* 5 (2015) 1360–1384.
- [5] H. Ullah, Inter-molecular interaction in Polypyrrole/TiO₂: a DFT study *J. Alloys Compd.* 692 (2017) 140–148.
- [6] H. Ullah, A.A. Tahir, T.K. Mallick, Polypyrrole/TiO₂ composites for the application of photocatalysis, *Sens. Actuators B* 241 (2017) 1161–1169.
- [7] X. Jia, J. Cao, H. Lin, M. Zhang, X. Guo, S. Chen, Transforming type-I to type-II heterostructure photocatalyst via energy band engineering: a case study of I-BiOCl/I-BiOBr, *Appl. Catal. B: Environ.* 204 (2017) 505–514.
- [8] M.D. Rossell, P. Agrawal, A. Borgschulte, C. c. Hébert, D. Passerone, R. Erni, Direct evidence of surface reduction in monoclinic BiVO₄, *Chem. Mater.* 27 (2015) 3593–3600.
- [9] H.S. Park, K.E. Kweon, H. Ye, E. Paek, G.S. Hwang, A.J. Bard, Factors in the metal doping of BiVO₄ for improved photoelectrocatalytic activity as studied by scanning electrochemical microscopy and first-principles density-functional calculation, *J. Phys. Chem. C* 115 (2011) 17870–17879.
- [10] M. Long, W. Cai, H. Kisch, Visible light induced photoelectrochemical properties of *n*-BiVO₄ and *n*-BiVO₄/*p*-Co₃O₄, *J. Phys. Chem. C* 112 (2008) 548–554.
- [11] S.K. Cho, H.S. Park, H.C. Lee, K.M. Nam, A.J. Bard, Metal doping of BiVO₄ by composite electrodeposition with improved photoelectrochemical water oxidation, *J. Phys. Chem. C* 117 (2013) 23048–23056.
- [12] S.K. Pilli, T.E. Furtak, L.D. Brown, T.G. Deutsch, J.A. Turner, A.M. Herring, Cobalt-phosphate (Co-Pi) catalyst modified Mo-doped BiVO₄ photoelectrodes for solar water oxidation, *Energy Environ. Sci.* 4 (2011) 5028–5034.
- [13] X. Zhang, Y. Zhang, X. Quan, S. Chen, Preparation of Ag doped BiVO₄ film and its

- enhanced photoelectrocatalytic (PEC) ability of phenol degradation under visible light, *J. Hazard. Mater.* 167 (2009) 911–914.
- [14] C. Yin, S. Zhu, Z. Chen, W. Zhang, J. Gu, D. Zhang, One step fabrication of C-doped BiVO₄ with hierarchical structures for a high-performance photocatalyst under visible light irradiation, *J. Mater. Chem. A* 1 (2013) 8367–8378.
- [15] S. Obregón, G. Colón, Heterostructured Er³⁺ doped BiVO₄ with exceptional photocatalytic performance by cooperative electronic and luminescence sensitization mechanism, *Appl. Catal. B* 158 (2014) 242–249.
- [16] M. Wang, Q. Liu, Y. Che, L. Zhang, D. Zhang, Characterization and photocatalytic properties of N-doped BiVO₄ synthesized via a sol–gel method, *J. Alloys Compd.* 548 (2013) 70–76.
- [17] G. Tan, L. Zhang, H. Ren, J. Huang, W. Yang, A. Xia, Microwave hydrothermal synthesis of N-doped BiVO₄ nanoplates with exposed {040} facets and enhanced visible-light photocatalytic properties, *Ceram. Int.* 40 (2014) 9541–9547.
- [18] W.J. Jo, J.W. Jang, K. j. Kong, H.J. Kang, J.Y. Kim, H. Jun, K. Parmar, J.S. Lee, Phosphate doping into monoclinic BiVO₄ for enhanced photoelectrochemical water oxidation activity, *Angew. Chem. Int. Ed.* 51 (2012) 3147–3151.
- [19] W. Luo, J. Wang, X. Zhao, Z. Zhao, Z. Li, Z. Zou, Formation energy and photoelectrochemical properties of BiVO₄ after doping at Bi³⁺ or V⁵⁺ sites with higher valence metal ions, *Phys. Chem. Chem. Phys.* 15 (2013) 1006–1013.
- [20] Z. Jiang, Y. Liu, T. Jing, B. Huang, X. Zhang, X. Qin, Y. Dai, M.-H. Whangbo, Enhancing the photocatalytic activity of BiVO₄ for oxygen evolution by ce doping: Ce³⁺ ions as hole traps, *J. Phys. Chem. C* 120 (2016) 2058–2063.
- [21] P. Giannozzi, S. Baroni, N. Bonini, M. Calandra, R. Car, C. Cavazzoni, D. Ceresoli, G.L. Chiarotti, M. Cococcioni, I. Dabo, QUANTUM ESPRESSO: a modular and open-source software project for quantum simulations of materials, *J. Phys. Condens. Matter* 21 (2009) 395502.
- [22] Atomistix ToolKitversion. 0, QuantumWise A/S, 2017. (<https://quantumwise.com>).
- [23] K. Momma and F. Izumi, An integrated three-dimensional visualization system VESTA using wxWidgets Commision Crystallogr. Comput., *IUCr Newslett.* 2006, 106–119.
- [24] Virtual NanoLabversion.0, QuantumWise A/S, 2017 (<https://quantumwise.com>).
- [25] A. Sleight, H.-Y. Chen, A. Ferretti, D. Cox, Crystal growth and structure of BiVO₄, *Mater. Res. Bull.* 14 (1979) 1571–1581.
- [26] A.H. Larsen, M. Vanin, J.J. Mortensen, K.S. Thygesen, K.W. Jacobsen, Localized atomic basis set in the projector augmented wave method, *Phys. Rev. B* 80 (2009) 195112.
- [27] G. Xi, J. Ye, Synthesis of bismuth vanadate nanoplates with exposed {001} facets and enhanced visible-light photocatalytic properties, *Chem. Commun.* 46 (2010) 1893–1895.
- [28] W.H. Press, Numerical recipes, The Art of Scientific Computing, 3rd edition, Cambridge University Press, 2007.
- [29] S.N.F.M. Nasir, H. Ullah, M. Ebadi, A.A. Tahir, J.S. Sagu, M.A. Mat Teridi, New insights into Se/BiVO₄ heterostructure for photoelectrochemical water splitting: a combined experimental and DFT study, *J. Phys. Chem. C* 121 (2017) 6218–6228.
- [30] F. Tran, P. Blaha, Accurate band gaps of semiconductors and insulators with a semilocal exchange-correlation potential, *Phys. Rev. Lett.* 102 (2009) 226401.
- [31] A.J. Rettie, H.C. Lee, L.G. Marshall, J.-F. Lin, C. Capan, J. Lindemuth, J.S. McCloy, J. Zhou, A.J. Bard, C.B. Mullins, Combined charge carrier transport and photoelectrochemical characterization of BiVO₄ single crystals: intrinsic behavior of a complex metal oxide, *J. Am. Chem. Soc.* 135 (2013) 11389–11396.
- [32] Z. He, Y. Shi, C. Gao, L. Wen, J. Chen, S. Song, BiOCl/BiVO₄ p–n heterojunction with enhanced photocatalytic activity under visible-light irradiation, *J. Phys. Chem. C* 118 (2013) 389–398.
- [33] D. Wang, R. Li, J. Zhu, J. Shi, J. Han, X. Zong, C. Li, Photocatalytic water oxidation on BiVO₄ with the electrocatalyst as an oxidation cocatalyst: essential relations between electrocatalyst and photocatalyst, *J. Phys. Chem. C* 116 (2012) 5082–5089.
- [34] S. Sun, W. Wang, D. Li, L. Zhang, D. Jiang, Solar light driven pure water splitting on quantum sized BiVO₄ without any cocatalyst, *ACS Catal.* 4 (2014) 3498–3503.

[Article 2]

S. N. F. M. Nasir, H. Ullah, M. Ebadi, A. A. Tahir, J. S. Sagu, M. A. Mat Teridi,
"New insights into Se/BiVO₄ heterostructure for photoelectrochemical water
splitting: A combined experimental and dft study." *J. Phys. Chem. C.* vol. 121,
pp. 6218-6228, Feb. 2017.

New Insights into Se/BiVO₄ Heterostructure for Photoelectrochemical Water Splitting: A Combined Experimental and DFT Study

Siti Nur Farhana M. Nasir,[†] Habib Ullah,^{*,‡,§} Mehdi Ebadi,^{†,⊥} Asif A. Tahir,[‡] Jagdeep S. Sagu,[§] and Mohd Asri Mat Teridi^{*,†}

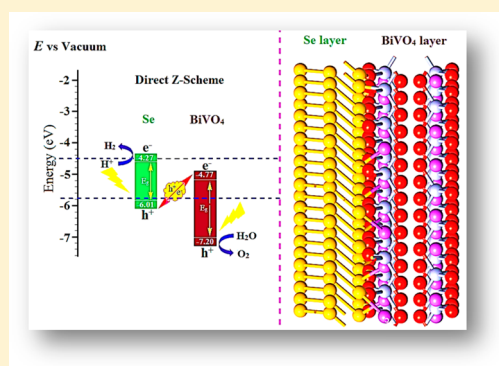
[†]Solar Energy Research Institute (SERI), National University of Malaysia, Bangi, Selangor 43600, Malaysia

[‡]Environment and Sustainability Institute (ESI), University of Exeter, Penryn Campus, Penryn, Cornwall TR10 9FE, United Kingdom

[§]Department of Chemistry, Loughborough University, Loughborough, Leicestershire LE11 3TU, United Kingdom

Supporting Information

ABSTRACT: Monoclinic clinobisvanite BiVO₄ is one of the most promising materials in the field of solar water splitting due to its band gap and suitable valence band maximum (VBM) position. We have carried out comprehensive experimental and periodic density functional theory (DFT) simulations of BiVO₄ heterojunction with selenium (Se-BiVO₄), to understand the nature of the heterojunction. We have also investigated the contribution of Se to higher performance by effecting morphology, light absorption, and charge transfer properties in heterojunction. Electronic properties simulations of BiVO₄ show that its VBM and conduction band minimum (CBM) are comprised of O 2p and V 3d orbitals, respectively. The Se/BiVO₄ heterojunction has boosted the photocurrent density by 3-fold from 0.7 to 2.2 mA cm⁻² at 1.3 V vs SCE. The electrochemical impedance and Mott–Schottky analysis result in favorable charge transfer characteristics, which account for the higher performance in Se/BiVO₄ as compared to the BiVO₄ and Se. Finally, spectroscopic, photoelectrochemical, and DFT show that Se makes a direct Z-scheme (band alignments) with BiVO₄ where the photoexcited electron of BiVO₄ recombines with the VB of Se, giving electron–hole separation at Se and BiVO₄, respectively; as a result, enhanced photocurrent is obtained.



1. INTRODUCTION

Hydrogen has long been identified as one of the most promising energy carriers,¹ which can be easily obtained from renewable resources (water and sunlight) through photoelectrochemical (PEC) water splitting.^{1–3} The bottleneck in realizing the concept practically has been the difficulty in identifying stable low-cost semiconductors that meet the thermodynamic and kinetic criteria for photoelectrolysis of water.¹ Suitable materials for PEC should be capable of absorbing maximum photons from the visible spectrum of sunlight and function as an effective catalyst for water splitting. Therefore, the semiconductor (electrode) must have band structure with band edge position above and below the redox potential of water, low electron affinity, good photocorrosion stability, and bandgap in the range of 1.8–2.2 eV for maximum solar to chemical energy conversion.⁴ Since the discovery of Fujishima and Honda,² various semiconductors have been investigated to produce hydrogen as a solar fuel from water, using a visible spectrum of sunlight. However, the development of suitable and sustainable semiconductor materials as efficient photoelectrode remains a challenge. A metal oxide such as TiO₂ has band edge positions that straddle the standard electrochemical potential of E°(H⁺/H₂) and E°(O₂/H₂O), but its

large band gap (absorbs the UV part of the solar spectrum) accounts for 4% of the solar irradiance. Although CdS and CdSe have a small band gap and suitable band edge positions, they are not stable under water photooxidation conditions.^{5,6} The stable semiconductors such as Fe₂O₃, WO₃, and BiVO₄ have been explored for the water splitting application over the past few years.^{2,7–12} Among them, Fe₂O₃ is the most widely studied material for H₂ production. However, the conduction band edge of Fe₂O₃ is too low for spontaneous water photoreduction.¹³ As a result, complete water splitting with Fe₂O₃ requires a large external bias. WO₃ having a band gap energy of 2.7 eV limits the theoretical solar-to-hydrogen (STH) efficiency to ca. 4.5%.⁹ Recently, it has been found that monoclinic clinobisvanite BiVO₄ with an ideal band gap with 2.4 eV¹⁴ for water splitting¹⁵ can absorb as much as 11% of the solar spectrum as compared to that of the 4% TiO₂.^{16–18} However, BiVO₄ usually shows a low photocatalytic activity due to poor charge-transport characteristics⁹ and weak surface adsorption properties.¹⁹ In addition, many attempts have been

Received: February 5, 2017

Revised: February 22, 2017

Published: February 24, 2017

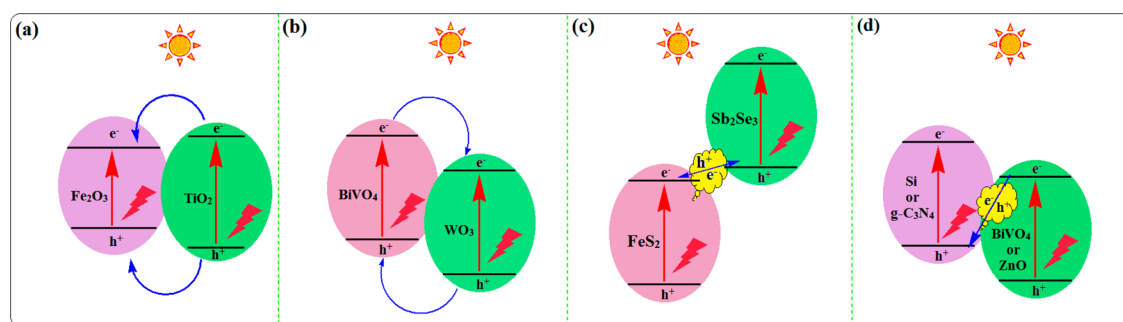


Figure 1. Schematic representation of different band alignments for high PEC performance.

made to improve the poor photocatalytic activity of BiVO_4 due to its more positive potential in thermodynamic level.²⁰ Coupling BiVO_4 with an oxygen evolution catalyst such as cobalt-phosphate,^{20–23} iron oxyhydroxide,²⁴ and cobalt-borate²⁵ is one of the options. Making a heterojunction between two dissimilar semiconductors is also an effective strategy to improve the electron–hole separation in BiVO_4 .^{2,7–12,20–23,26,27} Heterojunction has great benefit to PEC activities such as broadening the light absorption spectral, suppressing the charge recombination, and enhancing charge separation.²⁷ Representative heterojunctions or band alignments of binary dissimilar semiconductors are shown in Figure 1. Type-I heterojunction (Figure 1a) is an extensively studied PEC water splitting technique where a narrow band gap semiconductor (Fe_2O_3) is combined with wide band gap semiconductor such as TiO_2 .²⁸ In this combination, a complementary light absorption takes place, and photocurrent improves as a consequence of facile electrons and hole transfer from the conduction and valence band of wide band gap semiconductor to small band gap material. In Type-II heterojunction (Figure 1b), the relatively more negative potential (vs RHE) of the conduction and valence band of a narrow band gap of semiconductor (BiVO_4) is beneficial to enable the efficient charge transfer²⁷ and high photocurrent density. That the photoexcited electrons in BiVO_4 where the conduction band is located at more negative potential can easily transfer an electron to the conduction band of WO_3 that has the conduction band at positive potential (Figure 1b) is responsible for high photocurrent. As a result, the holes from the valence band of WO_3 can be transferred to the valence band of BiVO_4 to oxidize H_2O and generate O_2 .¹⁰ In Type-III heterojunction, both narrow band gap semiconductors (each having either an ideal VB or CB) are combined to efficiently perform the photoelectrochemical water splitting (Figure 1c). The photo-generated electron at the CB of FeS_2 recombines with a hole at the VB of Sb_2Se_3 and results in separation of electron and hole, responsible for high photocatalytic activity.²⁹ In Type-IV band alignments (Figure 1d), electron–hole pairs separation occurs very easily due to the establishment of a direct Z-scheme in binary semiconductors. Because the photoexcited electrons at CB of wide band gap semiconductor (i.e., BiVO_4 or ZnO) are located at a more positive potential (vs RHE), they would recombine with the holes of $\text{g-C}_3\text{N}_4$ that have the valence band at a more negative potential (Figure 1d). As a result of the aforementioned recombination, holes from the valence band of ZnO/BiVO_4 are transferred into the electrolyte to oxidize $\text{H}_2\text{O} \rightarrow \text{O}_2$, whereas the electrons from the conduction band of $\text{g-C}_3\text{N}_4$ are transferred to the counter electrode, which enhances the photocurrent.³⁰ Therefore, a proper band alignment of each

semiconductor in all types of heterojunctions is necessary to develop a deeper understanding of the charge-transport properties in the water splitting process.

The Types-I and -II heterojunctions are widely reported as compared to Types-III and -IV, where BiVO_4 is mixed with other materials.^{9,31,32} From a thermodynamic point of view, the material used in place of $\text{g-C}_3\text{N}_4$ must have a small band gap energy in case of Type-IV heterojunction to favor the electron excitation process. Graphitic carbon nitride, $\text{g-C}_3\text{N}_4$ ($E_g = 2.7$ eV), and silicon, Si ($E_g = 1.1$ eV), are the most popular visible light absorbing semiconductors to be paired in various metal oxide for PEC cells.^{33–35} The more negative conduction band potential of $\text{g-C}_3\text{N}_4$ and Si as compared to that of BiVO_4 facilitates the photogenerated electrons mobility to the external circuit due to high electron–hole pairs separation. Si-based materials are highly efficient in the solar cell technology, but they are too expensive to be used in PEC water splitting. The cost of a silicon wafer comprises the pure silicon cost, the crystallization cost, and the slicing cost.³⁶ Also, the fabrication of the Si-based device is more complex as it requires proper handling of fairly fragile Si wafer. These factors lead to a motivation in developing a Si-free PEC cell with a potentially good absorber material, which can be prepared by easy growth techniques to reduce cost production and achieve high charge-transport characteristics in the heterojunction (Type-IV heterojunction).

In this work, we demonstrate improved performance of a BiVO_4 (photoanode) through combining with an n-type selenium (Se), to build band alignments as that of direct Z-scheme (Figure 1d). Se has been extensively studied as a photoabsorber in thin film devices such as solar cells, photocatalyst, xerography, and rectifiers.^{37–39} Because of its small band gap, it has high light absorption efficiency⁴⁰ and can be combined with BiVO_4 to further improve the light harvesting ability. Moreover, Se has low surface states densities, large carrier lifetime,⁴¹ and a high conductivity ($1 \times 10^{-3} \text{ Sm}^{-1}$),⁴² which can affect the charge mobility. One disadvantage of Se is that it is more prone to photocorrosion by itself rather than their larger band gap counterparts. Therefore, when Se is coupled with a larger band gap semiconductor (in Type-IV heterojunction), the charge recombination of the photogenerated electron–hole pair can be reduced and also suppresses the Se layer photocorrosion. Because very limited information is available regarding Se-based PEC water splitting, hence, this work is a step forward to provide a new direction to replace a traditional visible-light photoabsorber, that is, Si with Se. The PEC performance of the Se/ BiVO_4 heterojunction has been discussed to prove that Se is a promising material to be used as a high-performance visible

light absorber in water splitting. Furthermore, periodic density functional (DFT) simulations are also carried out to counter-check the experimental data and elucidate the photocatalytic performance of Se, BiVO₄, and Se/BiVO₄. The fundamental electronic structure of the monoclinic clinobisvanite BiVO₄ is rarely considered for the water splitting, so its theoretical investigations along with experimental study might provide rational answers to comprehend the optical and electronic relationship. Finally, these findings will be useful to get an insight into designing an appropriate approach for improved PEC performance.

2. MATERIALS AND METHODS

2.1. Chemicals. All commercial chemicals were purchased from Sigma Aldrich and were used without any further purification. The chemicals used were bismuth nitrate pentahydrate, Bi(NO₃)₃·5H₂O, vanadium acetylacetonate, C₁₀H₁₄O₅V, sodium selenite, Na₂SeO₃, ethylene glycol, methanol, acetone, and isopropanol.

2.2. Synthesis of Se/BiVO₄ Photoanodes. Conductive fluorine-doped tin oxides (FTO TEC 18 Ω/cm², Pilkington)-coated glass was used as substrates. Before the deposition process, all substrates were cleaned with deionized water, followed by acetone and isopropanol for 15 min each, respectively, in the ultrasonic bath, and then dried. A potentiostat/galvanostat modulab solartron analytical was used for electrodeposition. A layer of Se was deposited galvanostatically at -20 mA vs SCE for 90 s in an aqueous solution containing 50 mM Na₂SeO₃ with an FTO working electrode, SCE reference electrode, and platinum counter electrode. The as-prepared Se layer was rinsed with deionized water and dried. In the next step, the BiVO₄ thin film was loaded on the Se layer by aerosol-assisted chemical vapor deposition (AACVD). The BiVO₄ precursor solution was prepared by dissolving 0.2 M Bi(NO₃)₃·5H₂O in ethylene glycol and 0.2 M C₁₀H₁₄O₅V in methanol as reported in our previous work.⁴³ The precursor solution was poured into a 20 mL round-bottom flask, which was converted to an aerosol by an ultrasonic dehumidifier and then transferred to the heated zone of a hot plate (where the Se-coated FTO sample was placed). The deposition of the BiVO₄ thin film was conducted for 90 min at ~450 °C in air.

2.3. Computational Methodology. First principle periodic DFT simulations were carried out with the help of Quantum ESPRESSO,⁴⁴ and the results were visualized with VESTA⁴⁵ and virtual nanolab (vnl 16.3).⁴⁶ The experimentally available crystallographic file of the BiVO₄, clinobisvanite structure, was used as such, which has Hall symmetry space group of *I2/b* with lattice parameters of *a* = 5.147 Å, *b* = 5.147 Å, *c* = 11.7216 Å, and $\gamma = 90^\circ$.⁴⁷ The bulk of Se with a space group of *P3₂21* having lattice parameters of *a* = 4.355 Å, *b* = 4.355 Å, *c* = 4.949 Å, $\alpha = 90^\circ$, and $\gamma = 120^\circ$ was used for simulations. The exchange and correlation potential was treated by the Perdew–Zunger, spin-unpolarized local density approximation (LDA). As an input structure for calculations, the 24 atoms unit cell with 2 × 2 × 2 supercell having [001] orientation and vacuum space of 10 Å was taken into account for the periodic boundary condition (PBC) DFT simulations. Mostly, clinobisvanite monoclinic BiVO₄ exists in [001] orientation, so that is why the [001] orientation is opted for theoretical simulations to represent the experimental thin film.⁴⁸ Moreover, the unreconstructed [001] termination possesses low surface energy and as a result represents the

most probable surface termination.⁴⁸ A 5 × 5 × 1 Monkhorst–Pack *k*-grid and energy cutoff of 100 Ry were employed for the geometry relaxation and self-consistent (SCF) simulations of BiVO₄, consisting of 96 atoms. The Broyden–Fletcher–Goldfarb–Shanno algorithm (BFGS) was used for the structural minimization.⁴⁹ A 5 × 5 × 5 Monkhorst–Pack *k*-grid with the same energy cutoff is used for the non-SCF part to get the density of states (DOS) and partial DOS (PDOS). The band structure simulations were performed along the direction of Γ , Z, R, X, and M of the Brillouin zone sampling. The valence electron configurations considered are 5d¹⁰6s²6p³ for Bi; 3p⁶3d³4s² for V; 2s²2p⁴ for O; and 4s²4p⁴3d¹⁰ for Se atom.

2.4. Characterizations. X-ray diffraction (XRD) measurements were conducted with Cu-X-ray in the 2 θ range from 20° to 60°. The morphologies and elemental mapping of the films were examined by field emission scanning microscopy (FESEM) and energy dispersive X-ray spectroscopy (EDX) on an FE-SEM SUPRA VP55. Optical characterizations were conducted by a UV–vis absorption spectrophotometer (PerkinElmer Lambda 950). The PEC measurements were recorded using a potentiostat/galvanostat Autolab PGSTAT 204, connected to the three-electrode configuration in a 0.5 M Na₂SO₄ electrolyte, an SCE (saturated KCl) as the reference electrode, and a platinum as the counter electrode in a quartz cell. Electrochemical impedance spectroscopy (EIS) and Nyquist plot were performed using the same experimental setup as the PEC measurements. The frequency was from 100 kHz to 100 mHz with 0.5 V applied bias under dark and simulated light conditions (light intensity of 100 mW cm⁻²). The illuminated area was 1.0 cm² for all experiments, and the observed spectra were fitted by using GPES software.

3. RESULTS AND DISCUSSION

3.1. Structural Analysis. The structural phase and purity of the as-synthesized BiVO₄ and Se/BiVO₄ films are shown in Figure 2. All of the diffraction peaks of Se/BiVO₄ were

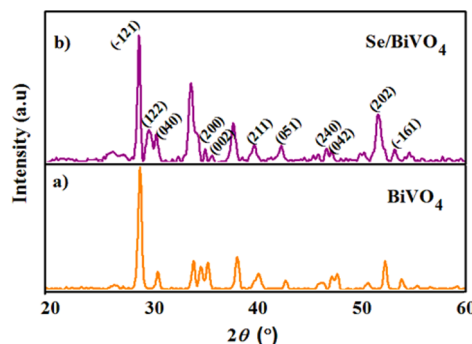


Figure 2. X-ray diffraction patterns of (a) BiVO₄ and (b) Se/BiVO₄.

identified to have a monoclinic clinobisvanite BiVO₄, which has good agreement with the standard JCPDS pattern (00-014-0688). The peaks exhibited from Se thin film appeared to have a monoclinic Se (JCPDS no. 00-054-0500) (Figure S1). No impurity phases are observed, which confirms the purity of deposited films. The narrow and sharp peaks from the XRD patterns of all samples indicate the high crystalline nature of the films. The peaks of BiVO₄ can clearly be seen at 2 θ = 28.82°, 30.55°, 34.50°, 35.22°, 39.78°, 42.47°, 46.71°, 47.31°, 50.32°, and 53.258°, which are assigned to the planes of (-121), (040),

(200), (002), (211), (051), (240), (042), (202), and (-161) , respectively. These BiVO_4 peaks are clearly visible in Se/BiVO_4 thin film followed by a small intensity Se peak at (122), while the rest of the Se peaks are diminished due to the growth of BiVO_4 on top of Se. Meanwhile, the deposition of BiVO_4 to form a heterojunction does not cause any changes in the crystal structure of Se and other electronic properties. The crystallite sizes calculated on the basis of t peaks at (122) for Se and (-121) for BiVO_4 in Se/BiVO_4 are 838.1 and 369.1 Å, respectively (Figure 2).

3.2. Morphology. Surface morphologies of Se, BiVO_4 , and Se/BiVO_4 thin films are characterized by FESEM analysis, which is presented in Figure 3. The surface morphology of Se

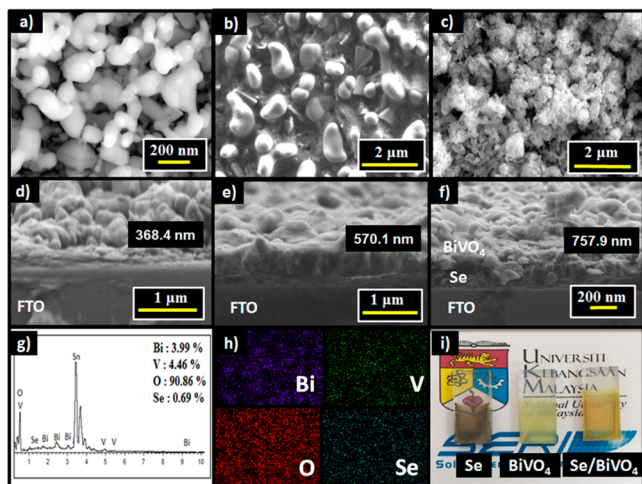


Figure 3. FESEM images and thickness of Se (a and d), BiVO_4 (b and e), and Se/BiVO_4 (c and f). The EDX spectrum (g) and elemental mapping (h) of Se/BiVO_4 , (i) the Se, BiVO_4 , and Se/BiVO_4 samples.

film has a dense sponge-like surface with particle diameter in the range of 217–392 nm on average and film thickness of 368 nm (Figure 3d). The morphology of BiVO_4 (Figure 3b) is comprised of a spherical particle bumpy surface with an average particle size and thickness (Figure 3e) of about 357–680 and 570 nm, respectively. The FESEM images of Se/BiVO_4 films showed a nanoporous structure with particles size smaller than those of Se and BiVO_4 as shown in Figure 3c. The porous structure proved beneficial to improve the electrode/electrolyte interfacial area, which ultimately increases the movement of the photogenerated charge carriers and reduces the charge recombination rate during the photo-oxidation reactions.⁵⁰ The reduction in particle size is consistent with the reduction of the grain size obtained from XRD. The film thickness of Se/BiVO_4 is increased to ~ 758 nm (Figure 3f). It is observed that the morphology of Se is denser than that of BiVO_4 . This feature is suitable for BiVO_4 to be deposited on top of the Se layer or in contact with the electrolyte in the heterojunction structure to increase the electrolyte/photoelectrode interfacial area (Figure S2a).⁵¹ The Se layer is placed on top of the BiVO_4 (forming the BiVO_4/Se heterojunction), along with compact morphology of Se, which may obstruct direct contact in the BiVO_4 layer into the electrolyte; the smaller band gap Se will also hinder light penetration to BiVO_4 as well as that Se is more prone to photocorrosion (Figure S2b). As a result, this may not only limit the catalytic reaction but also block some of the light penetration to the BiVO_4 film. A similar case is observed in the CdS/BiVO_4 electrode by Jiang et al.,⁵¹ where they compared

the influence of the light absorption on CdS/BiVO_4 and BiVO_4/CdS structures. In addition, the purity and elemental presence of the constituents in the heterojunction (Se/BiVO_4) electrode is confirmed through EDX and elemental mapping (Figure 3g and h). The EDX spectrum shows strong peaks for the Bi, V, O and a low level for the Se, while the rest of them belong to the FTO.

3.3. AFM. The 3D AFM images and surface roughness of Se, BiVO_4 , and Se/BiVO_4 films are shown in Figure 4 and Table 1.

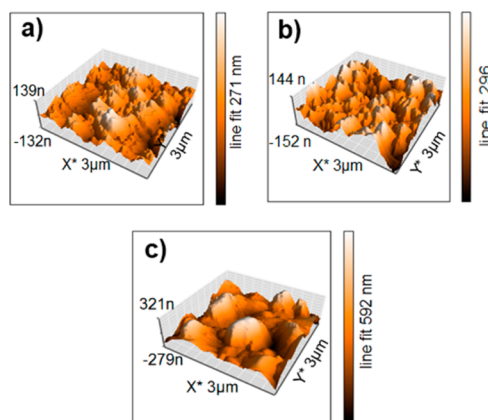


Figure 4. AFM images of (a) Se, (b) BiVO_4 , and (c) Se/BiVO_4 .

Table 1. Surface Roughness of Se, BiVO_4 , and Se/BiVO_4 Thin Film Photoanodes

sample	surface roughness (nm)
Se	32.71
BiVO_4	42.85
Se/BiVO_4	77.80

As expected, the Se/BiVO_4 film showed high surface roughness as compared to those of the Se and BiVO_4 films, which may be due to the formation of dual layers and thicker films in the heterojunction (Se/BiVO_4). Generally, high surface roughness and small grain size can significantly affect the PEC performance as more sites are exposed for the photocatalytic reactions.⁵² Moreover, it is believed that films with rough surface enhance the light scattering and improve the light absorption capability.

3.4. Optical Properties. The optical absorption spectra of these films are presented in Figure 5a, where the low absorption intensity of Se electrode is attributed due to its low thickness. As can be seen in Figure 3d, the substrate is not fully covered by Se particles, and in some part of the electrode, the FTO substrate can clearly be seen, responsible for the light scattering from FTO as compared to Se. The absorption intensity of Se/BiVO_4 was slightly enhanced to shorter wavelength when the BiVO_4 layer was coated on Se. This enhancement is because of the high absorption intensity of the BiVO_4 film, light scattering of porous, rougher surface, and thicker film of Se/BiVO_4 electrode. Moreover, the Se/BiVO_4 thin film is dark yellowish, which is almost similar to that of the BiVO_4 electrode (see samples shown in Figure 3i), which suggests that most of the light is absorbed by the BiVO_4 layer in the heterojunction (Se/BiVO_4). Therefore, the Se/BiVO_4 thin film electrode is more blue-shifted at a wavelength of ~ 470 – 500 nm ($\text{BiVO}_4 = 2.43$ eV) as compared to ~ 700 nm (Se = 1.74 eV). Because of these factors, Se/BiVO_4 electrode absorbs more visible light than that

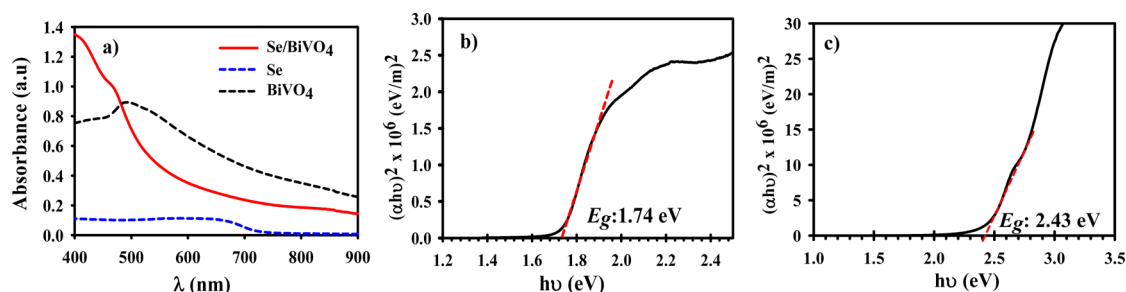


Figure 5. (a) UV–vis absorption spectra of the Se, BiVO₄, and Se/BiVO₄. Tauc plot of (b) Se and (c) Se/BiVO₄ thin films.

of either Se or BiVO₄. The optical band gap is calculated according to eq 1.⁵³

$$(\alpha h\nu)^n = A(h\nu - E_g) \quad (1)$$

where α is the absorption coefficient, ν is the incident light frequency, E_g is the band gap, and A is a constant. n depends on the characteristic of the transition in a semiconductor; for a direct transition, $n = 2$. The optical band gaps are evaluated from the relation of $(\alpha h\nu)^2$ versus photo energy ($h\nu$). The extrapolations of the Tauc plots on the x -intercept give the optical band gap of 2.43 eV for BiVO₄ (Figure S3)⁴³ and 1.74 eV for Se (Figure 5), which is also consistent with the recently reported work of Wang et al.⁵⁴

3.5. DFT Simulated Electronic and Optical Properties of BiVO₄. Basically, BiVO₄ exists in three different crystalline polymorphs: orthorhombic pucherite, tetragonal dreyerite, and monoclinic clinobisvanite.⁵⁵ The photocatalytic activity and surface reaction are highly dependent on phase and crystal orientation of semiconductor oxide.^{56–58} For instance, the tetragonal BiVO₄ possesses a band gap of 2.9 eV and mainly absorbs UV light, while the monoclinic clinobisvanite phase exhibits a much higher photocatalytic activity due to its favorable band gap (2.4–2.5 eV) in the visible region of the electromagnetic spectrum (shows both visible light and UV absorption), and a valence band position suitable for driving water oxidation under illumination.⁵⁹

The XRD analysis of our fabricated BiVO₄ films proves the formation of monoclinic clinobisvanite BiVO₄, so that is why we have considered the same structure to investigate its theoretical insight. To correlate the experimental thin film properties, the [001] phase (generally, the more stable) is employed for simulations (Figure 6).

Moreover, to analyze the electronic properties such as DOS/PDOS, and band structure, the positions of the valence band (VB) and conduction band (CB) are calculated from the optimized crystal structures. The DOS of BiVO₄(001) is simulated to find out its band gap and edge positions, which are given in Figure 7. The simulated band gap of BiVO₄-001 is 2.25 eV, which underestimates our experimental band gap (2.43 eV) to about 0.18 eV. This slight underestimation of the band gap is expected from the LDA method of DFT calculation.⁶⁰

To find the atomic and orbital contribution to form, valence, and conduction bands, the PDOS are simulated (Figure 8). In Figure 8a, the PDOS of BiVO₄(001) is shown, where the O atoms are responsible for the developing of valence band edge; however, the conduction band edge is populated by the atomic contribution of V atoms. Further details of the s, p, and d orbital contributions of Bi, V, and O are depicted in Figure 8b–d. The PDOS of Bi atoms show that s orbitals are involved in making the valence band edge of Bi, while its p orbitals are

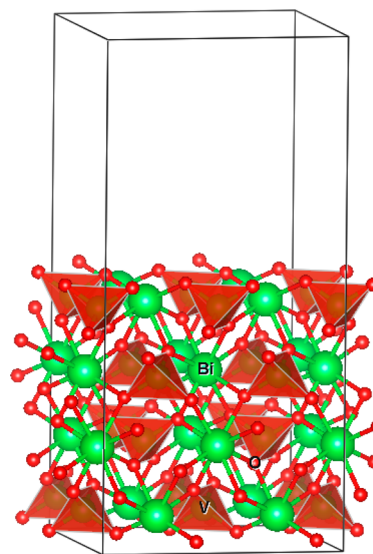


Figure 6. Optimized crystal structure of BiVO₄(001) slab.

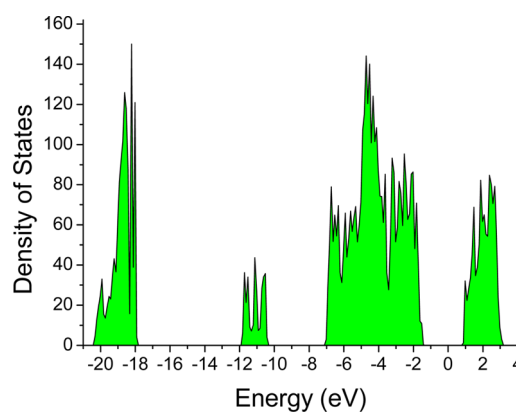


Figure 7. Total density of states of BiVO₄(001); the Fermi level is set to zero.

situated in the conduction band edge. Both the valence and the conduction bands of V atoms prominently consist of its 3d orbitals, while in case of O, 2p orbitals have a major role in developing their band edge positions.

The valence band electronic structure of BiVO₄(001) spread over the range from -0.65 to -19 eV can be distinguished into three major parts (vide infra). The upper portion of the region from -0.65 to -6 eV is clearly dominated by the 2p orbitals of O, while its lower portion is partially hybridized by the d and s orbitals of V and Bi, respectively. The middle portion (-9 to -11 eV) of the valence band is equally occupied by sp of O, pd of V, and sp orbitals of Bi. The region from -16 to -19 eV of

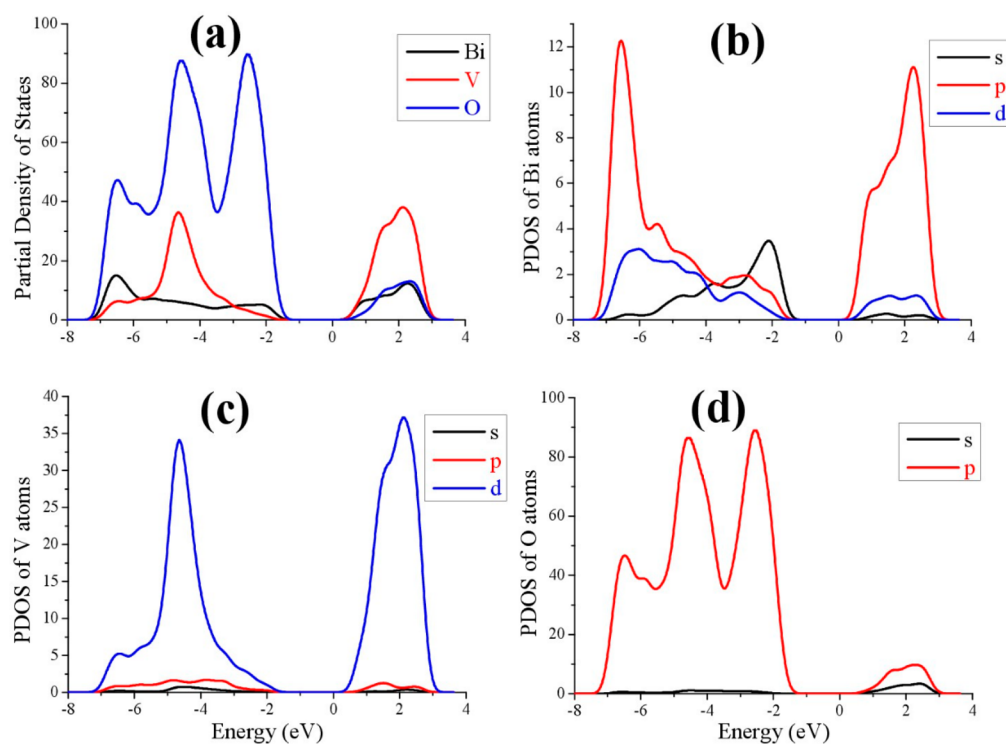


Figure 8. PDOS of $\text{BiVO}_4(001)$ (a), Bi (b), V (c), and O (d); Fermi level is set to zero.

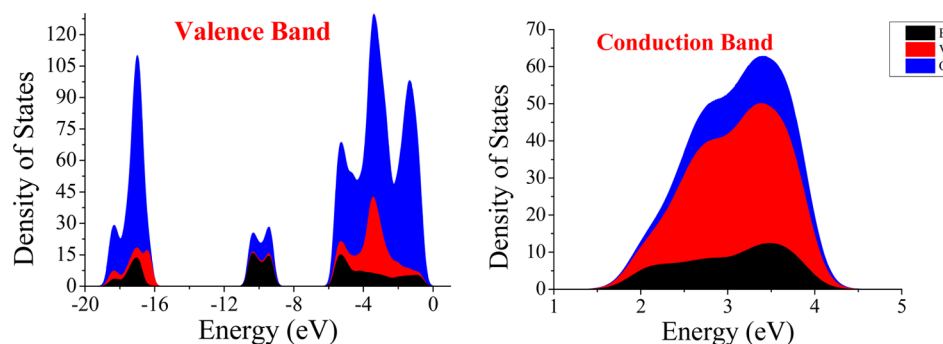


Figure 9. Valence and conduction DOS of $\text{BiVO}_4(001)$; Fermi level is set to zero.

the valence band is majorly contributed from the s orbital of O, and its lower part is constituted from the hybridized s, p, and d orbitals of Bi and V atoms. These orbitals have a major role in the developments of charge carriers and their effective masses.

The conduction-band electronic structure is situated in the range of 1.60–4.4 eV, where the CBM is occupied by the d orbitals of V with the contribution of the p orbitals of Bi. The major portion of the unoccupied state within the conduction band of BiVO_4 is almost equally populated through the mutual hybridization of Bi p and V d orbitals. From Figure 9, we can see that the antibonding orbitals of d and p of V and O are responsible for the effective masses of the electrons.

The band structure of the $\text{BiVO}_4(001)$ along the k -points direction of Γ , Z, R, X, and M is given in Figure 10. An indirect band gap of 2.25 eV is simulated, which is in good agreement with the experimental and recently theoretical reported data.⁵⁹ Furthermore, this indirect band gap is due to the electronic excitation from the $X \rightarrow \Gamma$, as is clearly shown Figure 10. Generally, in case of indirect band gap, the band edges are not aligned; thus the electron does not transit directly to the conduction band. In this process, both a photon and a phonon

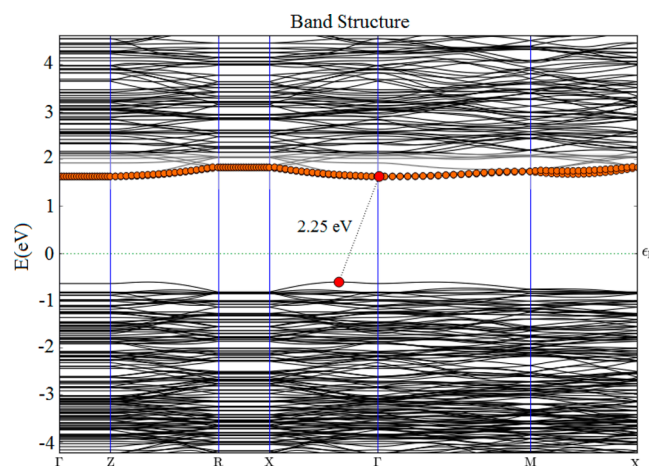


Figure 10. Band structure of the BiVO_4 along the $[001]$ direction; the Fermi level is set to zero.

are involved. That is why a new concept of the mixed phases of the BiVO_4 is reported, which can efficiently perform the water

splitting.⁶¹ At the Fermi energy of -5.73 eV, the vacuum phase VBM and CBM values are ca. -6.38 and -4.13 eV, respectively. These simulated band edge energies indicate that BiVO_4 can be used as a photocatalytic material for redox reactions, such as water splitting, but needs modification for high PEC performance. This statement clearly corroborates our photocatalytic activity (vide infra). The effective masses of the photogenerated electrons (m_e^*) and holes (m_h^*) along the $X \rightarrow \Gamma$ directions of k -points are calculated by fitting parabolic approximation around the bottom of the CBM or the top of the VBM, respectively; using eq 2 (Table 2):

$$m^* = \hbar^2(d^2E/dk^2)^{-1} \quad (2)$$

Table 2. Band Gap and Effective Masses of Photogenerated Electrons and Holes, Estimated from the Calculated Band Structure along the Suitable Direction

experimental	theoretical	direction in Brillouin zone	m_e^*/m_0	m_h^*/m_0	band gap
BiVO_4 (film)		indirect			2.43
	$\text{BiVO}_4(001)$	$X \rightarrow \Gamma$	1.93	0.45	2.25
Se bulk		direct			1.74
	Se bulk	$\Gamma \rightarrow \Gamma$			1.60

where \hbar is the reduced Planck constant, and E is the energy of an electron at wave vector k in the same band (VBM or CBM). To acquire the validity of the parabolic approximation within the specified space, the region for parabolic fitting is controlled by an energy difference of 1 meV along a particular direction around the VBM or CBM.

The effective masses of electrons and holes of the $\text{BiVO}_4(001)$ are calculated from the band structure as these photogenerated electrons and holes thermally relax to the bottom of the conduction band and the top of the valence band, respectively. The simulated values of the effective masses of photogenerated electrons and holes of the $\text{BiVO}_4(001)$ slab are 0.45 and 1.93 m_e , respectively. The lighter is the mass of charge carriers, the faster will be their movements at the interface.^{62,63} Moreover, the larger is the difference between the effective masses of electron and hole, the lower will their charge recombination. The lower photocatalytic activity of the

$\text{BiVO}_4(001)$ is because of their heavy charge carriers. Our experimental results also support this theoretical observation.

The band structure of Se bulk along with its crystal structure are given in Figure 11, where the simulated band gap of 1.60 eV in the $\Gamma \rightarrow \Gamma$ direction of the Brillouin zone has a nice correlation with our experimental value observed of 1.74 eV. The vacuum simulated VBM and CBM values of the Se bulk are ca. -5.08 and -3.48 eV, respectively, at the Fermi energy of 4.22 eV.

As shown in Figure S4, the Se/ BiVO_4 forms a direct Z-scheme-like heterojunction, where the enhanced photocurrent activities are because of the Se layer. When light shines on the Se/ BiVO_4 heterostructure, the photogenerated electron of BiVO_4 in its CB recombines with a hole at VB of Se; consequently, free electrons at CB of Se can substantially increase in photocurrent as observed experimentally. This electron/hole recombination and separation create a direct Z-scheme-like structure where the free electron at negative potential (CB) of Se is responsible for the enhancement of photocurrent (Figure S4).

3.6. Photoelectrochemical Properties. The results of photocurrent density measurements are presented in Figure 12,

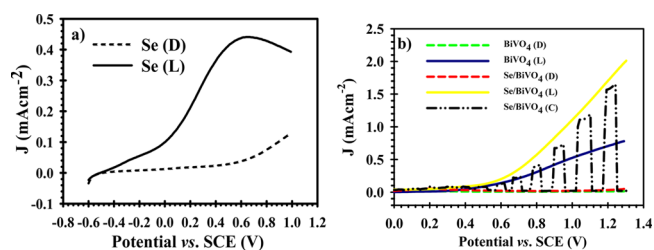


Figure 12. Photocurrent density of (a) Se and (b) Se/ BiVO_4 photoanodes under dark and light intensity of 100 mW cm^{-2} in $0.5 \text{ M Na}_2\text{SO}_4$.

which is also compared to our previous work.⁴³ The photocurrent density obtained by the samples increased with increasing applied voltage. All samples of Se, BiVO_4 , and Se/ BiVO_4 show very good response under illumination and represent anodic photocurrent patterns, which indicate that these electrodes have n-type semiconductor behavior. Moreover, the chopped photocurrent density–voltage shown in Figure 12b led us to conclude that the Se/ BiVO_4 photoanode is

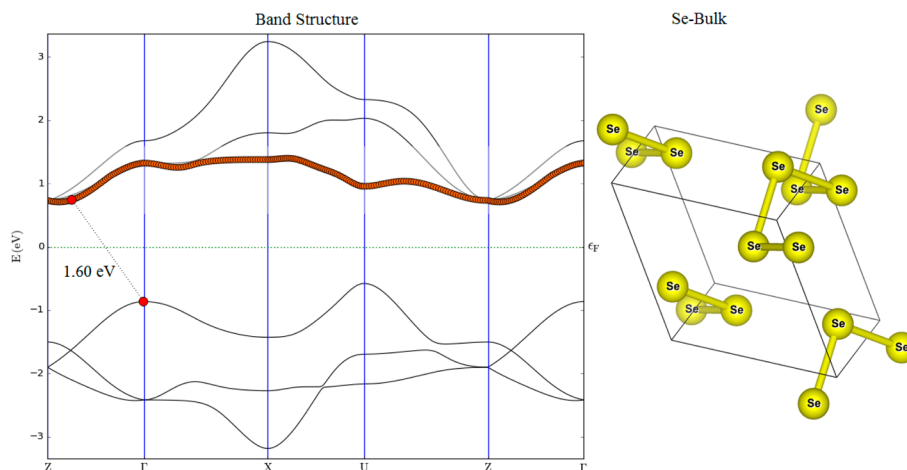


Figure 11. Band structure of the Se bulk, where the Fermi energy is set to zero.

photocatalytically active under illumination. The photocurrent density of Se/BiVO₄ increased up to 2.2 mA cm⁻² at 1.3 V vs SCE, much better than that of Se and BiVO₄. This enhanced photocurrent-density proves that Se could potentially be used in water splitting application as an efficient complementary light absorbing layer with other metal oxides. This photocurrent enhancement might also be attributed to better charge transfer in heterojunction as well as reduction of the grains and particles size, observed from XRD and FESEM analysis. In general, the small grain and particle size enlarge the surface area for reaction. Hence, more surface area is exposed to the electrode/electrolyte interface, which further promotes the photocatalytic process. Moreover, the porous structure of the Se/BiVO₄ film also widens the contact area between the Se/BiVO₄ photoanode and electrolyte. This feature provides more surface sites for reaction, reducing charge-transport distance and increasing the accumulation of photogenerated electrons.^{64–67}

To further support the PEC enhancement of Se/BiVO₄, EIS measurement was carried out. Figure 13a shows the Nyquist

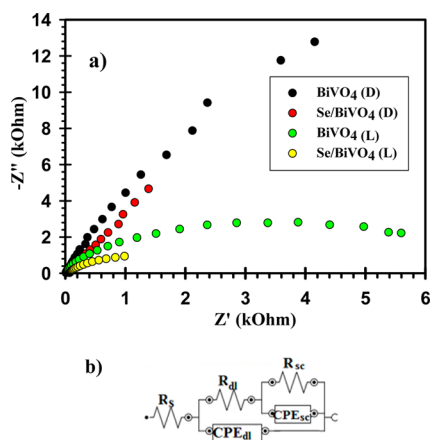


Figure 13. (a) The Nyquist plots and (b) equivalent circuit of BiVO₄ and Se/BiVO₄ photoanodes.

plots of BiVO₄ and Se/BiVO₄, measured in 0.5 M Na₂SO₄ at 100 kHz to 0.1 Hz in the presence and absence of light (100 mW cm⁻²) and 0.5 V applied potential vs SCE. It can be seen that the diameter of the curves diminished when the fabricated layers were exposed to light. The diameter of the curves is a function of overall charge transfer through the electrodes. To quantify the charge transfer resistance, the EIS data were fitted to the equivalent circuit shown in Figure 13b. The equivalent electrical circuit consists of two relaxation times, dark and light conditions. As observed in Figure 13a, both loops in the equivalent circuit are in a parallel configuration. The corresponding loop of the semiconductor ($R_{SC}||CPE_{SC}$) is in series with the interfacial resistance of the double layer/thin film (R_{dl}), and both of them are in parallel with the double layer capacitance (C_{dl}). For a more accurate representation of the capacitance behavior, the constant phase element (CPE) is used instead of a pure capacitor in the simulations. The impedance of a CPE (Z_{CPE}) for a nonideal circuit element is given in eq 3:

$$Z_{CPE} = \frac{1}{Q(j2\pi f)^n} \quad (3)$$

where f is applied frequency, j is imaginary number, $Q = C$ if the exponent $n = 1$, and $Q \neq C$ if the exponent $1 > n > 0$. It must be

noted that the capacitance behavior is approximated by Q , if the electrode surface is rough or when the dielectric property of the electrode components is heterogeneous.⁶⁸ The detailed corresponding electro-kinetic elements for the samples are tabulated in Table 3. It is found that the charge-transfer

Table 3. EIS Parameters from the Simulation of the Equivalent Circuit Model at 0.5 V versus SCE

electrode	R_s (Ω)	R_{dl} (k Ω)	C (μ F)	R_{SC} (k Ω)	Q (Y_0) (μ Mho)	n
BiVO ₄ (L)	15.50	1.91	18.70	5.56	33.81	0.62
BiVO ₄ (D)	21.90	47.44	14.02	97.74	30.30	0.83
Se/BiVO ₄ (L)	26.30	5.93	120.60	2.24	717.00	0.84
Se/BiVO ₄ (D)	24.60	1.81	164.40	18.25	148.50	0.88

resistance of the semiconductor (R_{SC}) is in the order of BiVO₄ > Se/BiVO₄ in both light and dark conditions. The photocurrent–voltage curve (Figure 12b) correlates with the EIS results. The smaller value of R_{SC} represents improved charge-transport characteristics, which provide a favorable environment for PEC reactions.⁶⁹

The stability of the Se/BiVO₄ electrode under chopped irradiation at 0.5 V vs SCE in 0.5 M Na₂SO₄ with an interval of 5 s is given in Figure S5. This potential was chosen because the photoelectrode has started to show response to light at ~ 0.40 V. As can be seen from Figure S5, the photocurrent of the BiVO₄ film is gradually decreased with increasing illumination time, which indicates the accumulation of photogenerated holes at the surface of BiVO₄. This accumulation of photogenerated holes is due to poor kinetics charge transfer. However, the photocurrent value of 0.15 mA cm⁻² remains constant up to 40 min for Se/BiVO₄ photoelectrode. This constant photocurrent value confirms the photostability of our heterojunction, which led us to conclude that the Se layer has improved the steady-state PEC performance of the BiVO₄ electrode. In the chopped stability plot, photocurrent spikes are observed, which indicate charge recombination. When the light is turned on, a sharp positive photocurrent spike is seen (which is termed as instantaneous hole current), which then decays to a steady-state current after recombination of holes and electrons.⁶⁹

Figure 14a and b shows the Mott–Schottky plot of Se and BiVO₄ electrodes that were measured in 0.5 M Na₂SO₄

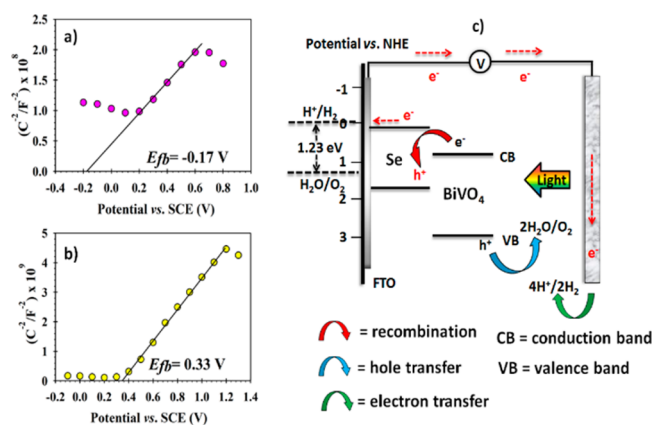


Figure 14. Mott–Schottky plots of (a) Se and (b) BiVO₄; (c) the alignment of the energy levels of heterojunction Se/BiVO₄.

electrolyte without illumination. The positive gradients of the Mott–Schottky plots indicate the n-type semiconducting nature in which electrons are the majority charge carriers. The flat band potential (E_{fb}) of the Se electrode is estimated to be -0.17 V vs SCE or equal to 0.074 V vs NHE, while the E_{fb} of BiVO_4 is 0.33 V vs SCE (0.57 V vs. NHE). At the vacuum level, the CBM of Se is ca. -4.51 eV, while that of BiVO_4 is -5.01 eV. By taking the E_g of the Se electrode from Figure 5b, the alignment of the energy levels for heterojunction Se/ BiVO_4 can thus be drawn in Figure 14c. Clearly, the valence band of Se is 1.814 V vs NHE (-6.25 eV at vacuum). In a dual-absorber system (complementary absorption of UV–vis), electrons in both Se and BiVO_4 are excited upon illumination. It can be further concluded that most of the incident light permeated through the BiVO_4 layer is absorbed by Se film. Because of the more negative potential of the conduction band of Se, photoelectrons at the conduction band of BiVO_4 recombined with holes at the valence band of Se, which reduced the recombination of photogenerated electron–hole pairs by Se itself. This process generates more photocurrent because photogenerated electrons in the conduction band of Se are impeded to recombine with its holes. Note that the high absorption intensity of the Se/ BiVO_4 electrode means more electron–hole pairs generation (Figure 5a), which does not contribute to the photo-oxidation process due to the thermodynamically forbidden hole transfer from Se to BiVO_4 (valence band Se located at more negative potential than valence band BiVO_4). However, this type of heterojunction had served as a center of charge recombination between holes in the valence band of Se and electrons from the conduction band of BiVO_4 . As a result, this facilitates the accumulation of photogenerated electrons in Se to the external circuit and generates high photocurrent. This type of heterojunction was said to have more efficient charge separation and photocatalytic activities.⁷⁰

4. CONCLUSION

We have successfully fabricated a direct Z-scheme-like heterojunction of Se and BiVO_4 (Se/ BiVO_4), as a thin film for the improved PEC performance. The thin film photoanodes are fully characterized by XRD, SEM, EDX, UV–vis band gap calculations, PEC, and electrochemical activity. Moreover, we also proposed a band structure diagram for our heterojunction, which is counterchecked by solid-state theoretical simulations. The as-prepared Se and BiVO_4 exhibit monoclinic and monoclinic clinobisvanite structures, respectively, and have low photocatalytic activities. An enhanced PEC activity is observed in case of heterojunction, as compared to their individual constituents (Se and BiVO_4). Density functional theory (DFT) simulations are carried out for the BiVO_4 and Se to simulate their band gap and band edge positions in the proposed heterojunction band diagram. The PEC properties of Se/ BiVO_4 indicate that the increment in performance is due to the presence of the Se layer, which acts as a hole trapping agent, light absorber, and improves the charge separation in the resulted film. The Se/ BiVO_4 has 1.5 times higher photocurrent density than that of BiVO_4 due to a higher surface area, small grain size, high roughness, efficient charge separation, and minimum charge recombination rate. Moreover, the existence of dual absorption layers of Se and BiVO_4 significantly increased the light absorption, which has ultimately promoted more charge generation. The results prove that the Se/ BiVO_4

heterostructure is a potential candidate for PEC water splitting, confirmed by DFT simulations.

■ ASSOCIATED CONTENT

Supporting Information

The Supporting Information is available free of charge on the ACS Publications website at DOI: 10.1021/acs.jpcc.7b01149.

Figures of the XRD of Se and BiVO_4 thin films (PDF)

■ AUTHOR INFORMATION

Corresponding Authors

*E-mail: hu203@exeter.ac.uk.

*E-mail: asri@ukm.edu.my.

ORCID

Habib Ullah: 0000-0001-9290-0265

Present Address

¹Department of Chemistry, Faculty of Sciences, Islamic Azad University-Gorgan Branch, Gorgan, Iran.

Notes

The authors declare no competing financial interest.

■ ACKNOWLEDGMENTS

We would like to thank the National University of Malaysia for the financial support from grant GUP-2016-089. H.U. acknowledges the NOTUR supercomputing facilities within the project nn4608k and the ESI Beowulf Cluster, University of Exeter, UK.

■ REFERENCES

- (1) Crabtree, G. W.; Dresselhaus, M. S.; Buchanan, M. V. The Hydrogen Economy. *Phys. Today* **2004**, *57*, 39–44.
- (2) Fujishima, A. Electrochemical Photolysis of Water at a Semiconductor Electrode. *Nature* **1972**, *238*, 37–38.
- (3) Chen, X.; Shen, S.; Guo, L.; Mao, S. S. Semiconductor-Based Photocatalytic Hydrogen Generation. *Chem. Rev.* **2010**, *110*, 6503–6570.
- (4) Grätzel, M. Photoelectrochemical Cells. *Nature* **2001**, *414*, 338–344.
- (5) Williams, R. Becquerel Photovoltaic Effect in Binary Compounds. *J. Chem. Phys.* **1960**, *32*, 1505–1514.
- (6) Ellis, A. B.; Kaiser, S. W.; Bolts, J. M.; Wrighton, M. S. Study of N-Type Semiconducting Cadmium Chalcogenide-Based Photoelectrochemical Cells Employing Polychalcogenide Electrolytes. *J. Am. Chem. Soc.* **1977**, *99*, 2839–2848.
- (7) Tilley, S. D.; Cornuz, M.; Sivula, K.; Grätzel, M. Light-Induced Water Splitting with Hematite: Improved Nanostructure and Iridium Oxide Catalysis. *Angew. Chem.* **2010**, *122*, 6549–6552.
- (8) Sayama, K.; Nomura, A.; Zou, Z.; Abe, R.; Abe, Y.; Arakawa, H. Photoelectrochemical Decomposition of Water on Nanocrystalline Bivo 4 Film Electrodes under Visible Light. *Chem. Commun.* **2003**, 2908–2909.
- (9) Hong, S. J.; Lee, S.; Jang, J. S.; Lee, J. S. Heterojunction $\text{BiVO}_4/\text{WO}_3$ Electrodes for Enhanced Photoactivity of Water Oxidation. *Energy Environ. Sci.* **2011**, *4*, 1781–1787.
- (10) Su, J.; Guo, L.; Bao, N.; Grimes, C. A. Nanostructured $\text{WO}_3/\text{BiVO}_4$ Heterojunction Films for Efficient Photoelectrochemical Water Splitting. *Nano Lett.* **2011**, *11*, 1928–1933.
- (11) Saito, R.; Miseki, Y.; Sayama, K. Highly Efficient Photoelectrochemical Water Splitting Using a Thin Film Photoanode of $\text{BiVO}_4/\text{SnO}_2/\text{WO}_3$ Multi-Composite in a Carbonate Electrolyte. *Chem. Commun.* **2012**, *48*, 3833–3835.
- (12) Saito, R.; Miseki, Y.; Sayama, K. Photoanode Characteristics of Multi-Layer Composite BiVO_4 Thin Film in a Concentrated

Carbonate Electrolyte Solution for Water Splitting. *J. Photochem. Photobiol.*, **A** **2013**, *258*, 51–60.

(13) Krysa, J.; Zlamal, M.; Kment, S.; Brunclikova, M.; Hubicka, Z. TiO_2 and Fe_2O_3 Films for Photoelectrochemical Water Splitting. *Molecules* **2015**, *20*, 1046–1058.

(14) Xie, B.; Zhang, H.; Cai, P.; Qiu, R.; Xiong, Y. Simultaneous Photocatalytic Reduction of Cr (VI) and Oxidation of Phenol over Monoclinic BiVO_4 under Visible Light Irradiation. *Chemosphere* **2006**, *63*, 956–963.

(15) Tokunaga, S.; Kato, H.; Kudo, A. Selective Preparation of Monoclinic and Tetragonal BiVO_4 with Scheelite Structure and Their Photocatalytic Properties. *Chem. Mater.* **2001**, *13*, 4624–4628.

(16) Abdi, F. F.; van de Krol, R. Nature and Light Dependence of Bulk Recombination in Co-Pi-Catalyzed BiVO_4 Photoanodes. *J. Phys. Chem. C* **2012**, *116*, 9398–9404.

(17) Iwase, A.; Yoshino, S.; Takayama, T.; Ng, Y. H.; Amal, R.; Kudo, A. Water Splitting and CO_2 Reduction under Visible Light Irradiation Using Z-Scheme Systems Consisting of Metal Sulfides, Coox-Loaded BiVO_4 , and a Reduced Graphene Oxide Electron Mediator. *J. Am. Chem. Soc.* **2016**, *138*, 10260–10264.

(18) Gu, S.; Li, W.; Bian, Y.; Wang, F.; Li, H.; Liu, X. Highly-Visible-Light Photocatalytic Performance Derived from a Lanthanide Self-Redox Cycle in $\text{Ln}_2\text{O}_3/\text{BiVO}_4$ (Ln: Sm, Eu, Tb) Redox Heterojunction. *J. Phys. Chem. C* **2016**, *120*, 19242–19251.

(19) Yao, W.; Iwai, H.; Ye, J. Effects of Molybdenum Substitution on the Photocatalytic Behavior of BiVO_4 . *Dalton Trans.* **2008**, 1426–1430.

(20) Abdi, F. F.; Firet, N.; van de Krol, R. Efficient BiVO_4 Thin Film Photoanodes Modified with Cobalt Phosphate Catalyst and W-Doping. *ChemCatChem* **2013**, *5*, 490–496.

(21) Jeong, H. W.; Jeon, T. H.; Jang, J. S.; Choi, W.; Park, H. Strategic Modification of BiVO_4 for Improving Photoelectrochemical Water Oxidation Performance. *J. Phys. Chem. C* **2013**, *117*, 9104–9112.

(22) Zhong, D. K.; Choi, S.; Gamelin, D. R. Near-Complete Suppression of Surface Recombination in Solar Photoelectrolysis by “Co-Pi” Catalyst-Modified BiVO_4 . *J. Am. Chem. Soc.* **2011**, *133*, 18370–18377.

(23) Jia, Q.; Iwashina, K.; Kudo, A. Facile Fabrication of an Efficient BiVO_4 Thin Film Electrode for Water Splitting under Visible Light Irradiation. *Proc. Natl. Acad. Sci. U. S. A.* **2012**, *109*, 11564–11569.

(24) Seabold, J. A.; Choi, K.-S. Efficient and Stable Photo-Oxidation of Water by a Bismuth Vanadate Photoanode Coupled with an Iron Oxyhydroxide Oxygen Evolution Catalyst. *J. Am. Chem. Soc.* **2012**, *134*, 2186–2192.

(25) Ding, C.; Shi, J.; Wang, D.; Wang, Z.; Wang, N.; Liu, G.; Xiong, F.; Li, C. Visible Light Driven Overall Water Splitting Using Cocatalyst/ BiVO_4 Photoanode with Minimized Bias. *Phys. Chem. Chem. Phys.* **2013**, *15*, 4589–4595.

(26) Chatchai, P.; Murakami, Y.; Kishioka, S.-y.; Nosaka, A.; Nosaka, Y. $\text{FTO}/\text{SnO}_2/\text{BiVO}_4$ Composite Photoelectrode for Water Oxidation under Visible Light Irradiation. *Electrochem. Solid-State Lett.* **2008**, *11*, H160–H163.

(27) Li, J.; Wu, N. Semiconductor-Based Photocatalysts and Photoelectrochemical Cells for Solar Fuel Generation: A Review. *Catal. Sci. Technol.* **2015**, *5*, 1360–1384.

(28) Lou, Z.; Li, F.; Deng, J.; Wang, L.; Zhang, T. Branch-Like Hierarchical Heterostructure ($\alpha\text{-Fe}_2\text{O}_3/\text{TiO}_2$): A Novel Sensing Material for Trimethylamine Gas Sensor. *ACS Appl. Mater. Interfaces* **2013**, *5*, 12310–12316.

(29) An, X.; Li, T.; Wen, B.; Tang, J.; Hu, Z.; Liu, L. M.; Qu, J.; Huang, C.; Liu, H. New Insights into Defect-Mediated Heterostructures for Photoelectrochemical Water Splitting. *Adv. Energy Mater.* **2016**, *6*, 1502268.

(30) Dong, F.; Zhao, Z.; Xiong, T.; Ni, Z.; Zhang, W.; Sun, Y.; Ho, W.-K. In Situ Construction of $\text{g-C}_3\text{N}_4/\text{g-C}_3\text{N}_4$ Metal-Free Heterojunction for Enhanced Visible-Light Photocatalysis. *ACS Appl. Mater. Interfaces* **2013**, *5*, 11392–11401.

(31) Mali, M. G.; Yoon, H.; Kim, M.-w.; Swihart, M. T.; Al-Deyab, S. S.; Yoon, S. S. Electrospayed Heterojunction $\text{WO}_3/\text{BiVO}_4$ Films with Nanotextured Pillar Structure for Enhanced Photoelectrochemical Water Splitting. *Appl. Phys. Lett.* **2015**, *106*, 151603.

(32) Pihosh, Y.; Turkevych, I.; Mawatari, K.; Uemura, J.; Kazoe, Y.; Kosar, S.; Makita, K.; Sugaya, T.; Matsui, T.; Fujita, D. Photocatalytic Generation of Hydrogen by Core-Shell $\text{WO}_3/\text{BiVO}_4$ Nanorods with Ultimate Water Splitting Efficiency. *Sci. Rep.* **2015**, *5*, 11141.

(33) Jung, H.; Chae, S. Y.; Shin, C.; Min, B. K.; Joo, O.-S.; Hwang, Y. J. Effect of the $\text{Si}/\text{TiO}_2/\text{BiVO}_4$ Heterojunction on the Onset Potential of Photocurrents for Solar Water Oxidation. *ACS Appl. Mater. Interfaces* **2015**, *7*, 5788–5796.

(34) Yu, H.; Chen, S.; Quan, X.; Zhao, H.; Zhang, Y. Silicon Nanowire/ TiO_2 Heterojunction Arrays for Effective Photoelectrocatalysis under Simulated Solar Light Irradiation. *Appl. Catal., B* **2009**, *90*, 242–248.

(35) Hwang, Y. J.; Boukai, A.; Yang, P. High Density n-Si/n- TiO_2 Core/Shell Nanowire Arrays with Enhanced Photoactivity. *Nano Lett.* **2008**, *9*, 410–415.

(36) Catchpole, K.; McCann, M.; Blakers, A.; Weber, K. *Proceedings 16th European Photovoltaic Solar Energy Conference*, 2000; pp 1165–1168.

(37) Nath, S.; Ghosh, S. K.; Panigahi, S. *Langmuir* **2004**, *20*, 7880.

(38) Yang, L.; Shen, Y.; Xie, A.; Liang, J.; Zhang, B. Synthesis of Se Nanoparticles by Using TSA Ion and Its Photocatalytic Application for Decolorization of Congo Red under UV Irradiation. *Mater. Res. Bull.* **2008**, *43*, 572–582.

(39) Johnson, J.; Saboungi, M.-L.; Thiyagarajan, P.; Csencsits, R.; Meisel, D. Selenium Nanoparticles: A Small-Angle Neutron Scattering Study. *J. Phys. Chem. B* **1999**, *103*, 59–63.

(40) Ebadi, M.; Sulaiman, M. Y.; Mat-Teridi, M. A.; Basirun, W. J.; Golsefidi, M. A.; Sopian, K.; Sateei, A.; Mehrabian, R. Z. Efficient Photo-Electrochemical Performance Using CuO -Based Electrodes in Aqua Medium. *J. Appl. Electrochem.* **2016**, *46*, 645–653.

(41) Ito, H.; Oka, M.; Ogino, T.; Takeda, A.; Mizushima, Y. Selenium Thin Film Solar Cell. *Jpn. J. Appl. Phys.* **1982**, *21*, 77.

(42) Luo, C.; Xu, Y.; Zhu, Y.; Liu, Y.; Zheng, S.; Liu, Y.; Langrock, A.; Wang, C. Selenium@ Mesoporous Carbon Composite with Superior Lithium and Sodium Storage Capacity. *ACS Nano* **2013**, *7*, 8003–8010.

(43) Mohd-Nasir, S.; Mat-Teridi, M.; Ebadi, M.; Sagu, J.; Sulaiman, M. Y.; Ludin, N. A.; Ibrahim, M. Influence of Ethylene Glycol on Efficient Photoelectrochemical Activity of BiVO_4 Photoanode Via AACVD. *Phys. Status Solidi A* **2015**, *212*, 2910–2914.

(44) Giannozzi, P.; Baroni, S.; Bonini, N.; Calandra, M.; Car, R.; Cavazzoni, C.; Ceresoli, D.; Chiarotti, G. L.; Cococcioni, M.; Dabo, I. Quantum Espresso: A Modular and Open-Source Software Project for Quantum Simulations of Materials. *J. Phys.: Condens. Matter* **2009**, *21*, 395502.

(45) Momma, K.; Izumi, F. An Integrated Three-Dimensional Visualization System Vesta Using Wxwidgets. *Commission Crystallogr. Comput., IUCr Newslett.* **2006**, 106–119.

(46) VirtualNanoLab. *QuantumWise A/S*; www.quantumwise.com, 2016; Vol. 3.

(47) Sleight, A.; Chen, H.-Y.; Ferretti, A.; Cox, D. Crystal Growth and Structure of BiVO_4 . *Mater. Res. Bull.* **1979**, *14*, 1571–1581.

(48) Xi, G.; Ye, J. Synthesis of Bismuth Vanadate Nanoplates with Exposed {001} Facets and Enhanced Visible-Light Photocatalytic Properties. *Chem. Commun.* **2010**, 46, 1893–1895.

(49) Press, W. H. Numerical Recipes. *The Art of Scientific Computing*, 3rd ed.; Cambridge University Press: New York, 2007.

(50) Pilli, S. K.; Janarthanan, R.; Deutsch, T. G.; Furtak, T. E.; Brown, L. D.; Turner, J. A.; Herring, A. M. Efficient Photoelectrochemical Water Oxidation over Cobalt-Phosphate (Co-Pi) Catalyst Modified $\text{BiVO}_4/\text{1D-WO}_3$ Heterojunction Electrodes. *Phys. Chem. Chem. Phys.* **2013**, *15*, 14723–14728.

(51) Jiang, J.; Wang, M.; Li, R.; Ma, L.; Guo, L. Fabricating CdS/BiVO_4 and BiVO_4/CdS Heterostructured Film Photoelectrodes for

Photoelectrochemical Applications. *Int. J. Hydrogen Energy* **2013**, *38*, 13069–13076.

(52) Najib áYahya, M. K.; áMohamad Sopian, N. W.; Ludin, N.; Adibábrahim, M.; Teridi, M. A. Heterojunction Cr₂O₃/CuO: Ni Photocathodes for Enhanced Photoelectrochemical Performance. *RSC Adv.* **2016**, *6*, 56885.

(53) Cooper, J. K.; Gul, S.; Toma, F. M.; Chen, L.; Liu, Y.-S.; Guo, J.; Ager, J. W.; Yano, J.; Sharp, I. D. Indirect Bandgap and Optical Properties of Monoclinic Bismuth Vanadate. *J. Phys. Chem. C* **2015**, *119*, 2969–2974.

(54) Wang, K.; Shi, Y.; Zhang, H.; Xing, Y.; Dong, Q.; Ma, T. Selenium as a Photoabsorber for Inorganic–Organic Hybrid Solar Cells. *Phys. Chem. Chem. Phys.* **2014**, *16*, 23316–23319.

(55) Rossell, M. D.; Agrawal, P.; Borgschulte, A.; Hébert, C.; Passerone, D.; Erni, R. Direct Evidence of Surface Reduction in Monoclinic Bivo₄. *Chem. Mater.* **2015**, *27*, 3593–3600.

(56) Morgan, B. J.; Watson, G. W. A Density Functional Theory+U Study of Oxygen Vacancy Formation at the (110),(100),(101), and (001) Surfaces of Rutile TiO₂. *J. Phys. Chem. C* **2009**, *113*, 7322–7328.

(57) Pan, J.; Liu, G.; Lu, G. Q. M.; Cheng, H. M. On the True Photoreactivity Order of {001},{010}, and {101} Facets of Anatase TiO₂ Crystals. *Angew. Chem., Int. Ed.* **2011**, *50*, 2133–2137.

(58) Batzill, M. Fundamental Aspects of Surface Engineering of Transition Metal Oxide Photocatalysts. *Energy Environ. Sci.* **2011**, *4*, 3275–3286.

(59) Park, H. S.; Kweon, K. E.; Ye, H.; Paek, E.; Hwang, G. S.; Bard, A. J. Factors in the Metal Doping of BiVO₄ for Improved Photoelectrocatalytic Activity as Studied by Scanning Electrochemical Microscopy and First-Principles Density-Functional Calculation. *J. Phys. Chem. C* **2011**, *115*, 17870–17879.

(60) Tran, F.; Blaha, P. Accurate Band Gaps of Semiconductors and Insulators with a Semilocal Exchange-Correlation Potential. *Phys. Rev. Lett.* **2009**, *102*, 226401.

(61) Tan, H. L.; Wen, X.; Amal, R.; Ng, Y. H. Bivo₄ {010} and {110} Relative Exposure Extent: Governing Factor of Surface Charge Population and Photocatalytic Activity. *J. Phys. Chem. Lett.* **2016**, *7*, 1400–1405.

(62) Giorgi, G.; Fujisawa, J.-I.; Segawa, H.; Yamashita, K. Small Photocarrier Effective Masses Featuring Ambipolar Transport in Methylammonium Lead Iodide Perovskite: A Density Functional Analysis. *J. Phys. Chem. Lett.* **2013**, *4*, 4213–4216.

(63) Zhang, J.; Wageh, S.; Al-Ghamdi, A.; Yu, J. New Understanding on the Different Photocatalytic Activity of Wurtzite and Zinc-Blende CdS. *Appl. Catal., B* **2016**, *192*, 101–107.

(64) Xu, C.; Shin, P.; Cao, L.; Gao, D. Preferential Growth of Long ZnO Nanowire Array and Its Application in Dye-Sensitized Solar Cells. *J. Phys. Chem. C* **2009**, *114*, 125–129.

(65) Shi, J.; Hara, Y.; Sun, C.; Anderson, M. A.; Wang, X. Three-Dimensional High-Density Hierarchical Nanowire Architecture for High-Performance Photoelectrochemical Electrodes. *Nano Lett.* **2011**, *11*, 3413–3419.

(66) Cho, I. S.; Chen, Z.; Forman, A. J.; Kim, D. R.; Rao, P. M.; Jaramillo, T. F.; Zheng, X. Branched TiO₂ Nanorods for Photoelectrochemical Hydrogen Production. *Nano Lett.* **2011**, *11*, 4978–4984.

(67) Xu, C.; Wu, J.; Desai, U. V.; Gao, D. Multilayer Assembly of Nanowire Arrays for Dye-Sensitized Solar Cells. *J. Am. Chem. Soc.* **2011**, *133*, 8122–8125.

(68) Chen, Z.; Dinh, H. N.; Miller, E. Photoelectrochemical Water Splitting. *SpringerBriefs in Energy, New York* **2013**, 49–61.

(69) Jo, W. J.; Jang, J. W.; Kong, K. j.; Kang, H. J.; Kim, J. Y.; Jun, H.; Parmar, K.; Lee, J. S. Phosphate Doping into Monoclinic Bivo₄ for Enhanced Photoelectrochemical Water Oxidation Activity. *Angew. Chem., Int. Ed.* **2012**, *51*, 3147–3151.

(70) Li, J.; Wu, N. Semiconductor-Based Photocatalysts and Photoelectrochemical Cells for Solar Fuel Generation: A Review. *Catal. Sci. Technol.* **2015**, *5*, 1360–1384.

[Article 3]

J. Safaei, H. Ullah, N. A. Mohamed, M. F. M. Noh, M. F. Soh, A. A. Tahir, N. A. Ludin, M. A. Ibrahim, W. N. R. W. Isahak, M. A. M. Teridi, "Enhanced photoelectrochemical performance of Z-scheme g-C₃N₄/BiVO₄ photocatalyst." *Appl. Catal., B: Environ.*, vol. 234, pp. 296-310, Oct. 2018.



Enhanced photoelectrochemical performance of Z-scheme g-C₃N₄/BiVO₄ photocatalyst

Javad Safaei^{a,*}, Habib Ullah^{b,*}, Nurul Aida Mohamed^a, Mohamad Firdaus Mohamad Noh^a, Mohd Fairus Soh^a, Asif A. Tahir^b, Norasikin Ahmad Ludin^a, Mohd Adib Ibrahim^a, Wan Nor Roslam Wan Isahak^c, Mohd Asri Mat Teridi^{a,*}

^a Solar Energy Research Institute, National University of Malaysia, 43600, Bangi, Selangor, Malaysia

^b Environment and Sustainability Institute, University of Exeter, Penryn Campus, Penryn, Cornwall, TR10 9FE, United Kingdom

^c Department of Chemical and Process Engineering, Faculty of Engineering and Build Environment, National University of Malaysia, 43600, Bangi, Selangor, Malaysia

ARTICLE INFO

Keywords:

Graphitic carbon nitride
Bismuth vanadate
Titanium dioxide
Z-Scheme

ABSTRACT

BiVO₄ is a considerably promising semiconductor for photoelectrochemical water splitting due to its stability, low cost and moderate band gap. In this research, g-C₃N₄ was proposed in Z-scheme configuration which boosted the performance of BiVO₄ up to four times. The experimental observations were counterchecked with Density Functional Theory (DFT) simulations. A TiO₂/BiVO₄ heterojunction was developed and its performance was compared with that of g-C₃N₄/BiVO₄. The photocurrent for g-C₃N₄/BiVO₄ was 0.42 mAcm⁻² at 1.23 V vs. RHE which was the highest among g-C₃N₄ based Z-scheme heterojunction devices. Lower charge transfer resistance, higher light absorption and more oxygen vacancy sites were observed for the g-C₃N₄ based heterojunction. The simulated results attested that g-C₃N₄ and BiVO₄ formed a van der Waals type heterojunction, where an internal electric field facilitated the separation of electron/hole pair at g-C₃N₄/BiVO₄ interface which further restrained the carrier recombination. Both the valence and conduction band edge positions of g-C₃N₄ and BiVO₄ changed with the Fermi energy level. The resulted heterojunction had small effective masses of electrons (0.01 m_e) and holes (0.10 m_e) with ideal band edge positions where both CBM and VBM were well above and below the redox potential of water.

1. Introduction

BiVO₄ has received extensive attention due to its moderate band gap, good stability and high activity for oxygen evolution which is a rate determining step in photoelectrochemical (PEC) water splitting [1]. It primarily exists in three different crystalline polymorphs, namely, orthorhombic pucherite, tetragonal dreyerite, and monoclinic clinobisvanite [2]. The photocatalytic activity and surface reaction is highly dependent on the phase and crystal orientation of a semiconductor oxide [3–5]. For instance, the tetragonal BiVO₄ possesses a band gap of 2.9 eV and predominantly absorbs UV light, while the monoclinic clinobisvanite phase exhibits a much higher photocatalytic activity due to its favourable band gap (2.4–2.5 eV) in the visible region [6]. Monoclinic clinobisvanite phase, however, has certain drawbacks such as low conduction band minimum position, poor charge transport properties and high recombination rate of photoelectrons, restraining its overall efficiency [7].

Numerous strategies have been adopted to enhance the performance

of BiVO₄. The enhancement can be obtained by doping or utilizing oxygen evolution reaction (OER) catalyst. Cobalt-phosphate, iron oxyhydroxide and nickel oxyhydroxide were introduced as OER catalyst to improve the surface kinetics [8–11] while tungsten and molybdenum were deployed to increase charge carrier densities [6,12–15]. Morphology control and facet modifications were utilized to investigate the charge separation and photocatalytic behaviour of BiVO₄ [16–21]. Zero-dimensional (0D) Quantum-sized BiVO₄ (5–20 nm) demonstrated higher PEC activities compared with those of nanoparticles (3D) ~200 nm due to their superior life time and elevated conduction band [16,17].

Another noteworthy strategy is to develop heterojunctions with the implementation of other types of semiconductors. The development of heterojunction with BiVO₄ suppresses its charge recombination by improving the charge transport properties. Furthermore, this strategy engenders the possibility of electronic band structure widening of BiVO₄ to undergo hydrogen evolution reaction (HER). It also broadens BiVO₄'s light absorption due to the implementation of diverse types of

* Corresponding authors.

E-mail addresses: javad.safaei@outlook.com (J. Safaei), hu203@exeter.ac.uk (H. Ullah), asri@ukm.edu.my (M.A. Mat Teridi).

materials with unidentical band gaps. Several types of heterojunctions can be constructed by employing two semiconductors, depending on their valence and conduction band edge positions. We have explained four diverse types of heterojunctions in our previous report [22]. Yet the application of type (II) heterojunction have been more prominent in previous researches, for the photogenerated electrons and holes in BiVO₄ tend to step down to a lower energy level of TiO₂ nanostructures or WO₃, contributing to HER on counter electrode and OER on BiVO₄ (Fig. S1) [9,22–29].

The graphitic carbon nitride (g-C₃N₄) has proved highly suitable for its oxygen and hydrogen evolution properties, moderate band gap of 2.7 eV, high photoelectrochemical and thermal stability, environmentally friendly properties, and its abundance in nature [30–32]. The more negative conduction band edge potential of g-C₃N₄, compared with the state of the art photocatalysts such as BiVO₄, TaON, WO₃, TiO₂, Fe₂O₃, ZnO, etc. enables it to form type (II) or Z-scheme heterojunction [33–35]. Despite its capability to absorb light in the visible range, the photocurrent of g-C₃N₄ is limited to only a few microamperes due to its high recombination rate of the photogenerated electron/hole pairs [33]. Although, the utilization of g-C₃N₄ as a hole extraction layer on top of TiO₂ [36] and ZnO [37] has proved successful, the development of thin film utilizing g-C₃N₄ as electron extraction layer is still in its preliminary stages.

If the host material, that is, the semiconductor deposited on FTO for two semiconductor heterojunction thin films in contact, has its conduction band above the water reduction potential and if the guest material has its valence band below the water oxidation potential, Z-scheme will be formed, leading to HER and OER at the counter electrode and guest material, respectively [22,38]. In order to obtain similar or higher order of PEC enhancement for BiVO₄, compared with TiO₂ or WO₃ nanostructures, one needs to employ semiconductors in Z-scheme with BiVO₄ due to its high efficiency in charge transportation and redox ability [33].

In our previous study, Selenium (Se) was deployed as a host material in Z-scheme to enhance the performance of BiVO₄ up to three times [22]. In another study by Wang et al. Z-scheme was constructed, using g-C₃N₄ and WO₃ (see Fig. 1) [38]. Even though Z-scheme provided a much higher boost for WO₃ compared with type (II) heterojunction, the overall performance of Z-scheme was still lower due to low photocurrent of planar WO₃ in relation to nanostructures such as WO₃ nanorods (WO₃-NRs) [27,38].

For BiVO₄, three methods of electrodeposition were developed, involving the intermediary phase of V₂O₅ that needed to be removed in 1 M KOH (~pH 13) aqueous solutions [10,39,40]. To fabricate heterojunctions with BiVO₄, using facile electrodeposition methods, the utilized semiconductor must be stable in strong basic/alkaline aqueous

solutions. The extensively deployed WO₃ limits the fabrication methods due to the instability of WO₃ in basic aqueous media. WO₃ forms sodium tungstate due to more stable phase of WO₄^{−2} in the pH of 8 and above (see Reaction (1)) [41]. It is necessary to mention that extremely thin layer of BiVO₄ (~40 nm) did not require basic/alkaline treatment [27], although this thickness is operational only on WO₃-NRs nanostructures which are costly to fabricate in comparison with planar structures [9,42].



The present research addresses two types of heterojunctions, comprised of g-C₃N₄/BiVO₄ and TiO₂/BiVO₄, where the former has superior efficiency. Various experimental methods have been utilized to investigate the performance of these heterojunctions. The experimental results, counterchecked with first principle density functional theory (DFT) simulations, confirmed that g-C₃N₄/BiVO₄ forms a van der Waals type heterojunction (Z-scheme), where an internal electric field facilitates the separation of electron–hole pair at the g-C₃N₄/BiVO₄ interface which further restrain the carrier recombination.

2. Methods

2.1. Synthesis of g-C₃N₄ thin film

Fluorine doped Tin Oxide (FTO TEC 8 Ω/cm², Pilkington) was deployed as substrate. Before deposition, FTO was respectively washed in acetone, ethanol and deionised water for ten minutes each, in ultrasonic bath, and dried with flow of nitrogen. The standard pyrolysis of urea was utilized to synthesize g-C₃N₄ in box furnace. Three grams of Urea (3 g; 99%, Aldrich), was poured in 50 ml alumina crucible with its lid on, with the temperature gradually rising to 520 °C in 15 min and remaining steady then for 15 min. Next the crucible was left in the furnace until it cooled down to the temperature of 400 °C before it was taken out of furnace and placed at room temperature. The obtained fine yellow powder (30–40 mg) was dispersed in deionised water and washed by centrifugation and ultrasonication three consecutive times to remove any extra organic compound. Then it was dried overnight at 100 °C in an oven and dispersed in methanol, deploying ultrasonic bath for 10 min with a concentration of 0.5 mg/ml. Before deposition of g-C₃N₄ thin film, the suspension was ultrasonicated for one minute to attain uniform suspension. For deposition of one-layer g-C₃N₄ [g-C₃N₄ (1 L)] thin film, 10 micro liter of the suspension was spun on the pre-cleaned FTO with speed of 2500 rpm, acceleration of 500 rpm/s and duration of 10 s. The g-C₃N₄ thin film was left at room temperature for five minutes to partially dry before performing another spin coating process for depositing second [g-C₃N₄ (2 L)] and third layer [g-C₃N₄

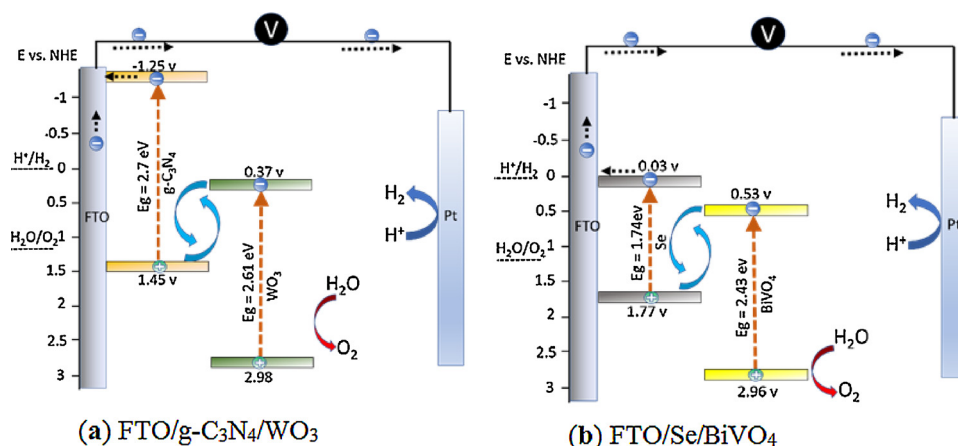


Fig. 1. Z-schemes, developed comprising g-C₃N₄/WO₃ (a) [38] and Se/BiVO₄ (b) [22]. In these heterojunction thin-film structures, the electrons from conduction band of g-C₃N₄ or Se directly contributed to HER while holes from valence band of WO₃ or BiVO₄ contributed to OER.

(3 L)]. Finally, g-C₃N₄ thin films were dried at 350 °C degrees on hot plate for 30 min.

2.2. Synthesis of TiO₂ thin film

TiO₂ thin film was fabricated by using commercial paste (18 NR-T, Dyesol) with three different concentrations of 5, 10 and 20 mg/mL in ethanol to deposit respectively different thickness of TiO₂ namely, TiO₂(A), TiO₂(B) and TiO₂(C) (See Supporting information Fig. S1 for TiO₂ nanoparticles). Subsequently, 10 μL of suspension was spun with speed of 2500 rpm, acceleration of 500 rpm/s with duration of 10 s. All TiO₂ thin films were annealed in a tube furnace at 500° for 2 h with a ramping rate of 0 °C/min.

2.3. Synthesis of BiVO₄, TiO₂/BiVO₄, and g-C₃N₄/BiVO₄ thin films

The electrodeposition method, developed by Seabold et al. [10] was used to synthesize BiVO₄ with a slight modification. Briefly, 10 mM bismuth nitrate pentahydrate of Bi(NO₃)₂·5H₂O (98%, Aldrich) and 35 mM vanadium oxide sulphate hydrate VSO₅·xH₂O (97%, Aldrich) were stirred in 1 M of nitric acid (68%, Aldrich) for 10 min. Then, sodium acetate (ACS Reag, Merck) was used to stabilize the solution to (PH ~ 5.1) and to (PH ~ 4.7) with a few drops of nitric acid. Electrodeposition process was carried out at 50° under a potential of 1.9 V vs. Ag/AgCl for 10 min, with FTO as working and platinum as counter electrode. After the electrodeposition, the blackish/yellowish samples, identified as Bi–V–O, were rinsed with DI water and left at room temperature to dry. Afterwards the samples were annealed in a tube furnace at

2.4. Characterizations

The electrochemical properties of the prepared samples were examined on Autolab potentiostat/galvanostat PGSTAT 204 at room temperature, utilizing three electrode configurations with Ag/AgCl (3 M NaCl) as reference electrode and 0.5 M Na₂SO₄ (PH ~ 7.0) as electrolyte. Potentials were converted to Reversible Hydrogen Electrode (RHE) by using Eq. (1).

$$E_{\text{RHE}} = E_{\text{Ag/AgCl}} + 0.059 \text{ pH} + E_{0 \text{ Ag/AgCl}} (0.1976) \quad (1)$$

Xenon lamp with 100 mW/cm² intensity was used as solar light simulator. The electrochemical fitting of Nyquist plots was analysed with the application of Nova Software. The optical properties of the samples were analysed by UV–vis absorption spectrophotometer, Perkin Elmer Lambda 950. The physical and morphological properties of samples were characterised with X-ray Diffraction (XRD), Field Emission Scanning Electron Microscopy (FESEM) (FE-SEM Supra VP 55) and Atomic Force Microscopy (AFM) (Nanosurf easyScan 2). The X-ray Photoelectron Spectroscopy (XPS) with Al Ka X-ray gun was implemented to analyse the chemical bonding and valence band structure. The reference value of carbon 285 eV was considered in this analysis. Photoluminescence spectra were analysed (via PL Edinburgh Instruments) to measure the radiative recombination of the samples at excitation wavelength of 300 nm.

2.5. Theoretical methods

First principle DFT calculations were performed on QuantumWise-ATK [43] and results were visualized on VESTA and Virtual NanoLab Version 2017.1 [44]. Clinobisvanite BiVO₄ was used as such with Hall symmetry space group of I2/b [45]. The lattice parameters of the 24 atoms unit cell were optimized and a supercell (2 × 2 × 2) was then constructed for the fabrication of BiVO₄(001) slab. For the slab model calculations of surface energies and band edge positions, thickness of the slab was kept by four primitive unit cells of BiVO₄ (10 Å thick

having 96 atoms) to ensure that the centre of the slab can be regarded as the bulk phase. A vacuum space of about 10 Å was inserted between slabs to eliminate the fictitious interaction between the periodically repeating slabs. The (001) termination possesses low surface energy and represents the most probable surface termination [18]. Stability of these different slabs are confirmed from their positive surface formation energy and electrostatic potential; details of surface formation energy is given in Eq. (S1), Table S1 and Fig. S2 of the Supporting information. Both single layer and bulk g-C₃N₄ were considered for simulations: the structure of the single layer g-C₃N₄ is portrayed in Fig. 13, while that of bulk is presented in Fig. S11 and Table S2 of the Supporting information. Generalized Gradient Approximation (GGA) with the Perdew–Burke–Ernzerhof (PBE) exchange–correlation functional and Double Zeta Polarized (DZP) basis set were employed for the structural and energy optimization as a consequence of their superiority to hybrid pseudopotentials [46]. Moreover, linear combination of atomic orbitals (LCAO) method was applied to Bi, V, Ti, C, N, H, and O atoms [47]. A 7 × 7 × 3 Monkhorst-Pack k-grid with the energy cutoff of 1200 eV was deployed for the BiVO₄ unit cell while a 5 × 5 × 1 k-point mesh was utilized for its slabs. 7 × 7 × 7 Monkhorst-Pack k-grid with the energy cutoff of 900 eV was implemented for monolayer g-C₃N₄, and 5 × 5 × 1 k-point mesh with 1200 eV cutoff energy was utilized for g-C₃N₄/BiVO₄(001) heterostructure. The band structure calculations were performed with TB09LDA functional of meta-GGA that could accurately reproduce the experimental band gaps. Tran and Blaha assert that this accuracy is due to the use of local density ρ(r) (as in LDA), the gradient of the density ∇ρ(r) (as in GGA), and the kinetic-energy density τ(r) [48]. We have fitted the c-parameter of Tran and Blaha XC functional's equation to reproduce optimally the experimental band gaps [48]. Density of states (DOS), partial density of states (PDOS), band structure and effective masses of photogenerated electrons and holes were also calculated. The DFT occupied and unoccupied DOS were considered as the VB and CB edges, respectively and then separated by an energy equal to the known optical band gap [49].

3. Results and discussion

3.1. Structural analysis

XRD plots of g-C₃N₄ and TiO₂ along with their corresponding BiVO₄ heterojunctions are illustrated in Figs. 3 and 4, respectively. The peaks of TiO₂ and BiVO₄ suggest respectively a high crystalline phase of anatase and monoclinic sheet [10,50]. No extra peak for anatase TiO₂ was observed except for the two highest peaks ca. at (101) and (200) due to insufficient thickness of TiO₂. In case of g-C₃N₄ powder, two peaks ca. at (100) and (002) planes were found corresponding to interplanar separation of g-C₃N₄ sheets and interlayer stacking of the aromatic systems, respectively [30].

The g-C₃N₄/BiVO₄ thin film had sharper and clearer peaks compared with TiO₂/BiVO₄ thin film. This is confirmed by the appearance of (211) and (020) peaks and sharpening of (240) and (042) peaks (Figs. 3d and 4d). The increase in the intensity of (121), (040), (051), (042) and (161) peaks supports the fact that g-C₃N₄/BiVO₄ is better crystallized compared with TiO₂/BiVO₄. The Gaussian fit was performed on (121) peak and FWHM was found to be 0.346° and 0.263° for TiO₂/BiVO₄ and g-C₃N₄/BiVO₄, respectively. The crystallite size obtained from Scherrer formula was found to be 23.64 and 31.46 nm for TiO₂/BiVO₄ and g-C₃N₄/BiVO₄, respectively.

3.2. Morphology

The anodic electrodeposition of BiVO₄ involves co-precipitation of Bi³⁺ with V⁵⁺ that precipitates as amorphous Bi–V–O [51]. The initial morphology of host materials can highly affect the morphology of final crystalline heterojunction once the amorphous phase is annealed. This was also confirmed by Pihosh et al. [27] and Tong et al. [24] where the

anodic electrodeposition of amorphous Bi–V–O assumed the shape of WO_3 or TiO_2 nanostructures and established a core/shell structure by being covered around the nanorods.

A comparable phenomenon occurred in this research where the initial morphology of the substrate (planar $\text{g-C}_3\text{N}_4$ and TiO_2 , in this case) transformed the final morphology of the heterojunction thin film (Fig. 5a–c). This is lucidly depicted in Fig. 5d–i where the morphology of pristine BiVO_4 electrodeposited on bare FTO entirely differs from that of $\text{TiO}_2/\text{BiVO}_4$ and $\text{g-C}_3\text{N}_4/\text{BiVO}_4$. This change of morphology highly depends on the deposition technique since other methods such as spin coating/drop coating of BiVO_4 on planar/nanostructured WO_3 [29,52] or TiO_2 [53] substrate have resulted in no morphological change between pristine BiVO_4 and its heterojunction. Since final morphology of our heterojunction structure highly depends on the morphology of host substrate, the fabrication of $\text{g-C}_3\text{N}_4/\text{BiVO}_4$ heterojunction on other morphologies of $\text{g-C}_3\text{N}_4$ such as nanorods/nanoflowers appears to be a promising field for further investigation.

3.3. Light absorption

Formation of $\text{g-C}_3\text{N}_4/\text{BiVO}_4$ and $\text{TiO}_2/\text{BiVO}_4$ caused a significant increase in light absorption compared with BiVO_4 , illustrated in Fig. 6. Both $\text{g-C}_3\text{N}_4/\text{BiVO}_4$ and $\text{TiO}_2/\text{BiVO}_4$ demonstrated high absorbance below and above 500 nm. The higher absorbance of $\text{g-C}_3\text{N}_4/\text{BiVO}_4$ and $\text{TiO}_2/\text{BiVO}_4$, compared with BiVO_4 above 500 nm, does not contribute to photogenerated electrons, since BiVO_4 tends to transmit all that wavelength due to its band gap ($E_g \sim 2.4$ eV). Meanwhile, the lower wavelengths (500 nm) are effectively absorbed. Higher absorbance is noticeable for $\text{g-C}_3\text{N}_4/\text{BiVO}_4$ compared with $\text{TiO}_2/\text{BiVO}_4$ at the wavelengths shorter than 500 nm which can be one of the reasons of its superior performance compared with that of $\text{TiO}_2/\text{BiVO}_4$.

The higher light absorption of $\text{g-C}_3\text{N}_4/\text{BiVO}_4$ is due to the lower band gap of $\text{g-C}_3\text{N}_4$ ($E_g \sim 2.7$ eV) compared with TiO_2 ($E_g \sim 3.3$ eV) that tends to absorb larger portions of light. It is worth noting that larger grains of $\text{g-C}_3\text{N}_4/\text{BiVO}_4$ tend to increase its light trapping capability that, in turn, elevates its absorptivity [22,54–56]. This is also displayed in Fig. 2c where $\text{g-C}_3\text{N}_4/\text{BiVO}_4$ appears to be more opaque compared with $\text{TiO}_2/\text{BiVO}_4$.

3.4. XPS

Surface chemistry and valence band structure of the thin film heterojunctions were investigated by using XPS. The characteristic peaks of C1s bonding for $\text{g-C}_3\text{N}_4$ and $\text{g-C}_3\text{N}_4/\text{BiVO}_4$ are portrayed in Fig. 7a. The deconvolution peaks ca. at 285.0, 286.59, and 288.6 eV display the adventitious carbon sp^2 bonded (C–C) or (C=C) on the XPS instrument (reference value for carbon charging) [57,58], sp^3 hybridized C atom C–(N)₃ [57] and sp^2 C atoms bonded to N in (N–C=N) aromatic rings, respectively [59].

The N1s characteristic peaks of $\text{g-C}_3\text{N}_4$ and $\text{g-C}_3\text{N}_4/\text{BiVO}_4$ heterojunction are illustrated in Fig. 7b. The wide scan for $\text{g-C}_3\text{N}_4$ (Fig. S3) displays higher intensity of N1s peak compared with C1s, further

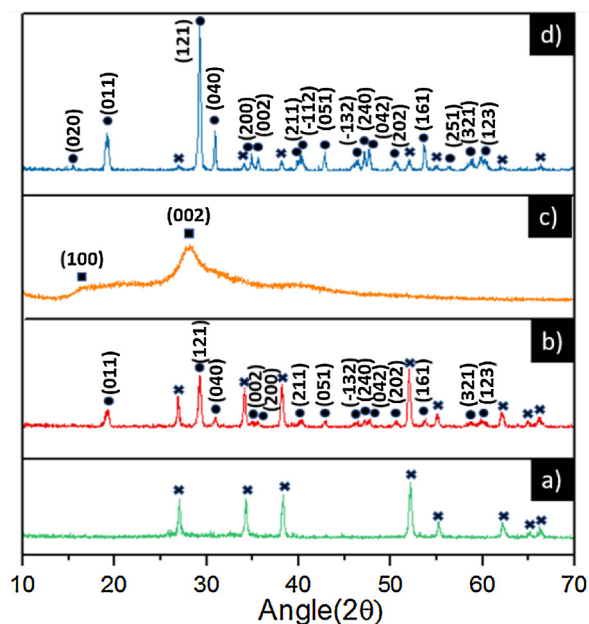


Fig. 3. XRD peaks for FTO (a), BiVO_4 (b), $\text{g-C}_3\text{N}_4$ (c) and $\text{g-C}_3\text{N}_4/\text{BiVO}_4$ (d).

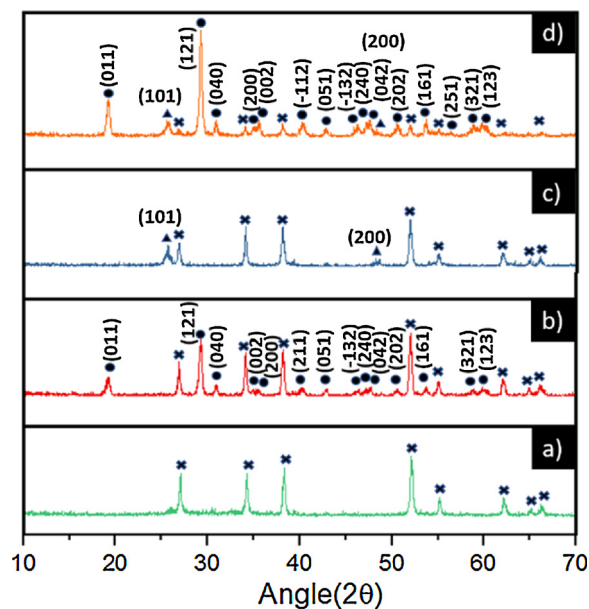


Fig. 4. XRD peaks for FTO (a), BiVO_4 (b), TiO_2 (c) and $\text{TiO}_2/\text{BiVO}_4$ (d).

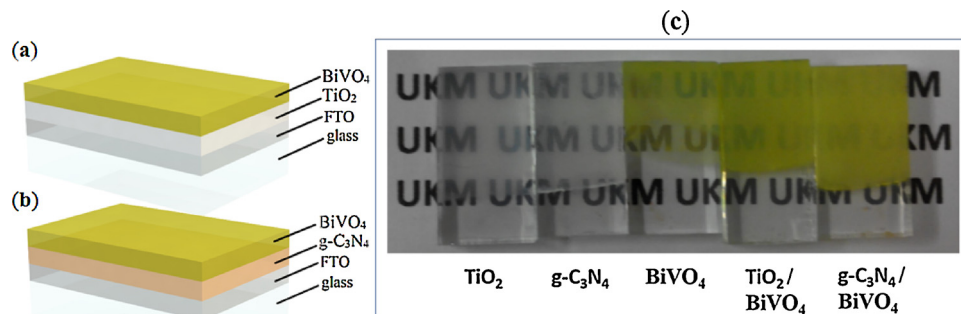


Fig. 2. 3D illustration of $\text{TiO}_2/\text{BiVO}_4$ (a) and $\text{g-C}_3\text{N}_4/\text{BiVO}_4$ (b) and actual fabricated thin films (c).

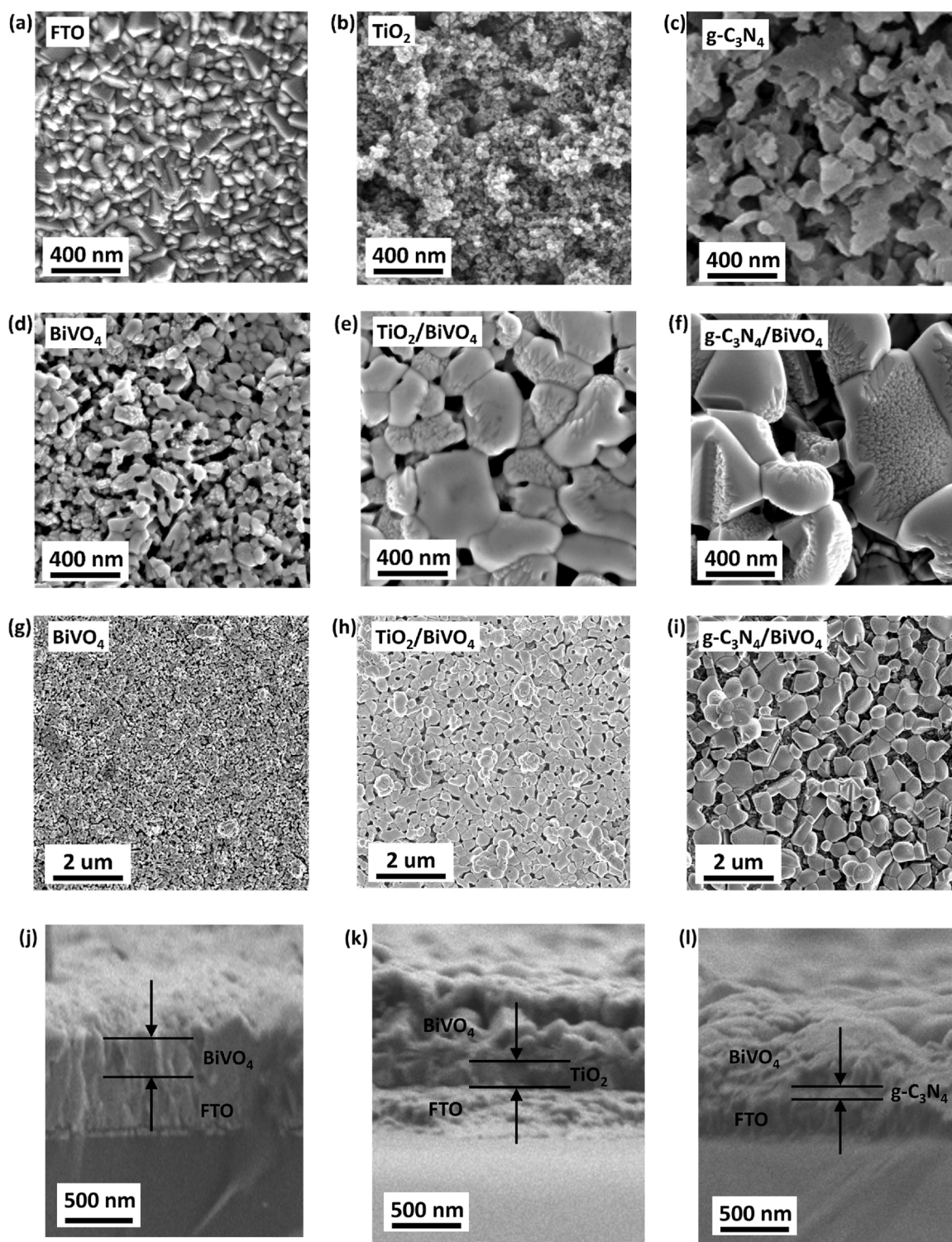


Fig. 5. FESEM images of pristine FTO (a), TiO_2 (b), $\text{g-C}_3\text{N}_4$ (c). FESEM surface images of BiVO_4 electrodeposited on FTO (d,g), on TiO_2 (e,h), on $\text{g-C}_3\text{N}_4$ (f,i). FESEM cross section images of BiVO_4 (j), $\text{TiO}_2/\text{BiVO}_4$ (k) and $\text{g-C}_3\text{N}_4/\text{BiVO}_4$ (l). These images affirm that the morphology of the host substrate can significantly affect the morphology of the electrodeposited BiVO_4 .

confirming the formation of $\text{g-C}_3\text{N}_4$. The sp^2 hybridized bonding of nitrogen with carbon ($\text{C}=\text{N}-\text{C}$) in the framework of the heptazine unit, tertiary nitrogen bonded to three carbon atoms $\text{N}-(\text{C})_3$, weak amino functional groups carrying hydrogen $\text{C}-\text{N}-\text{H}$ caused by incomplete condensation and π -excitations ($\pi \rightarrow \pi^*$ transition), respectively appeared ca. at 399.06, 400.36, 401.51, and 406.07 eV. The C1s and N1s peaks for $\text{g-C}_3\text{N}_4$ were quenched for $\text{g-C}_3\text{N}_4/\text{BiVO}_4$ heterojunction due

to wrapping of $\text{g-C}_3\text{N}_4$ by BiVO_4 (Fig. 7a–b). This peak, nonetheless, was expected for adventitious carbon on XPS instruments that existed for $\text{g-C}_3\text{N}_4/\text{BiVO}_4$ heterojunction. A similar effect was observed in another report by Wang et al. where C1s peak at 284.6 and N1s peaks were quenched due to $\text{g-C}_3\text{N}_4$ being wrapped by WO_3 [38]. A commensurable effect can be observed for $\text{TiO}_2/\text{BiVO}_4$ heterojunction in Fig. 7c where both $\text{Ti}2p_{3/2}$ and $\text{Ti}2p_{1/2}$ peaks are heavily quenched

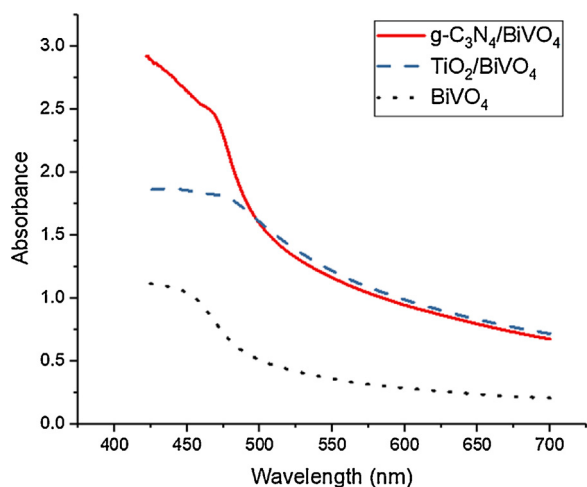


Fig. 6. Light absorption plots for BiVO₄, TiO₂/BiVO₄ and g-C₃N₄/BiVO₄.

by BiVO₄.

In Fig. 7d–e, the symmetric peaks of Bi4f 7/2, Bi4f 5/2, V2p 3/2 and V2p 1/2 bonds appear at 158.9, 164.23, 516.53, and 523.85 eV, respectively which underscore the presence of Bi³⁺ and V⁵⁺ state of BiVO₄. There is, nevertheless, a slight shift to higher energies for V2p 1/2 of TiO₂/BiVO₄ and a shift to lower energies for V2p 3/2 of g-C₃N₄/BiVO₄ compared with bare BiVO₄ (Fig. 7f–g). The shift to higher energies is congruous to that reported by Zalfani et al. for TiO₂@BiVO₄ photocatalyst where an up-shift for Bi4f and V2p displayed the oxidation of inherent V⁴⁺ to V⁵⁺ [58]. The shift, in the present research, to lower energies concurs with other researches where a similar down-shift of V2p to lower binding energy was reported for hydrogen treated BiVO₄, NaBH₄ reduced BiVO₄ and BiVO₄@g-C₃N₄ photocatalyst, affirming the reduction of inherent V⁵⁺ to V⁴⁺ due to the presence of hydrogen element [60–63].

The shift of V2p to higher energies occasions the excess formation of V⁵⁺ that reduces the shielding effect on the bismuth due to smaller electronic cloud around V⁵⁺ and increases the electronic density of Bi4f for TiO₂/BiVO₄ (Fig. 7d). Contrarily, the shift towards lower energies implies the formation of V⁴⁺, increasing the shielding effect on bismuth that reduces the electronic density around Bi4f for g-C₃N₄/BiVO₄ (Fig. 7d). The same effect was also investigated and explained by Zhang et al. for V⁴⁺ self-doped BiVO₄ where an increase in the electronic state was due to Bi4f [64].

The formation of V⁴⁺ state leads to the formation of oxygen vacancies that act as the centre of active catalytic sites and adsorption of superoxide O₂⁻ via atmospheric oxygen. The ratio of oxygen vacancy to lattice oxygen was found, using Gaussian fitting (Fig. 7h), and proved to be more for g-C₃N₄/BiVO₄ (1.33) compared with TiO₂/BiVO₄ (1.046). The higher ratio of adsorbed oxygen to lattice oxygen confirms more OH⁻ species can be attracted to the sites, further enhancing the catalytic performance.

In a nutshell, V⁴⁺ ions are made from the reduction of V⁵⁺ by hydrogen atoms, present in the interlayer of s-heptazine ring units of g-C₃N₄ that can generate oxygen vacancies which perform as active catalytic sites, with these catalytic sites adsorbing water molecules. Moreover, the carrier concentration is augmented due to the existence of self-doped V⁴⁺ further elaborated in later sections.

3.5. Band diagram

XPS, Mott-Schottky and UV–vis were performed to find the valence band maximum, Fermi level and conduction band minimum for the energy band diagram of bare semiconductors (Figs. S4–S7). The proposed heterojunctions are illustrated in Fig. 8, where TiO₂ and BiVO₄ form a Type (I) heterojunction while g-C₃N₄ and BiVO₄ comprise Type

(II) heterojunction. It is worth mentioning that the Fermi level shifts for two semiconductors when they interface one another, forming an overall band diagram (vide infra).

In the present research, type (I) heterojunction for TiO₂/BiVO₄ and type (II) heterojunction for g-C₃N₄/BiVO₄ can be further extended into a Z-scheme heterojunction under the application of a positive bias. The anodic photocurrent (to be further elaborated in the later sections of this paper) suggests oxidation reaction at BiVO₄ and reduction at the counter electrode. This implies that high energy electrons of TiO₂ and g-C₃N₄ directly reduce water at the counter electrode while the electrons at the conduction band energies of BiVO₄ are recombined with the holes at the valence band of TiO₂ and g-C₃N₄. Furthermore, the holes at the valence band of BiVO₄ surface are left to oxidize water. In both aforementioned heterojunctions, TiO₂ and g-C₃N₄ act as electron extraction layers as pathways to transfer electrons to the counter electrode as opposed to other structures where g-C₃N₄ acts as hole extraction layer [36,37].

3.6. PL spectra

The formation of heterojunction is proved from the decrease of PL radiative recombination at BiVO₄ and g-C₃N₄ (Fig. 9). The sharp peak in section (I), existent in all samples, suggests diffraction of the wavelength that occurs due to existence of FTO substrate and hence, it can be ignored. Although BiVO₄ photocatalyst presents one peak around ~520 nm [65], its thin-film photoelectrode behaves differently by having multiple peaks in sections II and III, presumably due to the scattering of light. However, the quench of radiative recombination, observed for two heterojunctions compared with bare BiVO₄, suggests successful formation of interface that facilitates charge transfer, hence, diminishing recombination. TiO₂ demonstrates the lowest PL intensity, attributable to recombination in singly ionized oxygen vacancy [66], with the g-C₃N₄ possessing its sharp characteristic fluorescence peak around 450 nm [67], being partially quenched after forming heterojunction structure (Fig. 9) [68,69].

3.7. Electrochemical properties

The Linear Sweep Voltammetry (LSV) was performed under back-illumination for dark and light to discover the photoelectrochemical response of the samples. The performance of g-C₃N₄/BiVO₄ and TiO₂/BiVO₄ thin films were optimized and the results are illustrated in Fig. 10a–b, demonstrating that the photocurrent of g-C₃N₄/BiVO₄ and TiO₂/BiVO₄ decreases when the thickness of g-C₃N₄ and TiO₂ increases. This occurs when some of the lights are blocked [70] by g-C₃N₄ and TiO₂ from reaching BiVO₄, generating less electron/hole pairs. Moreover, the increase in the thickness of g-C₃N₄ and TiO₂ presents high impedance in the path of electron/hole pairs [71] (to be elaborated under Fig. 12a–b), with this leading to the highest photocurrent of two thin films to be 0.42 and 0.22 mA for g-C₃N₄(1 L)/BiVO₄ and TiO₂(A)/BiVO₄, respectively.

The comparison of these two heterojunction photoanodes with that of pristine thin films of BiVO₄, TiO₂ and g-C₃N₄ is illustrated in Fig. 10c. The performance of unmodified BiVO₄ is enhanced by a factor of ~2 and ~4 times on TiO₂/BiVO₄ and g-C₃N₄/BiVO₄, respectively. The photocurrent of bare TiO₂ is negligible as a consequence of its large band gap which hinders the efficient absorption of sunlight. So is insignificant the photocurrent of bare g-C₃N₄ due to its high recombination (Fig. 9), rendering ineffective the transport of photogenerated electron-hole pairs [72]. Fig. 10d displays the chopped photocurrent response of TiO₂/BiVO₄ and g-C₃N₄/BiVO₄, indicating both samples' quick response to input light.

The stability of TiO₂/BiVO₄ and g-C₃N₄/BiVO₄ was tested under light for 35 min at 0.6 V vs. Ag/AgCl (Fig. 11). The sharp rise of photocurrent, immediately ensued by its sudden plunge, was observed for both samples due to excitation of electrons followed by the relaxation

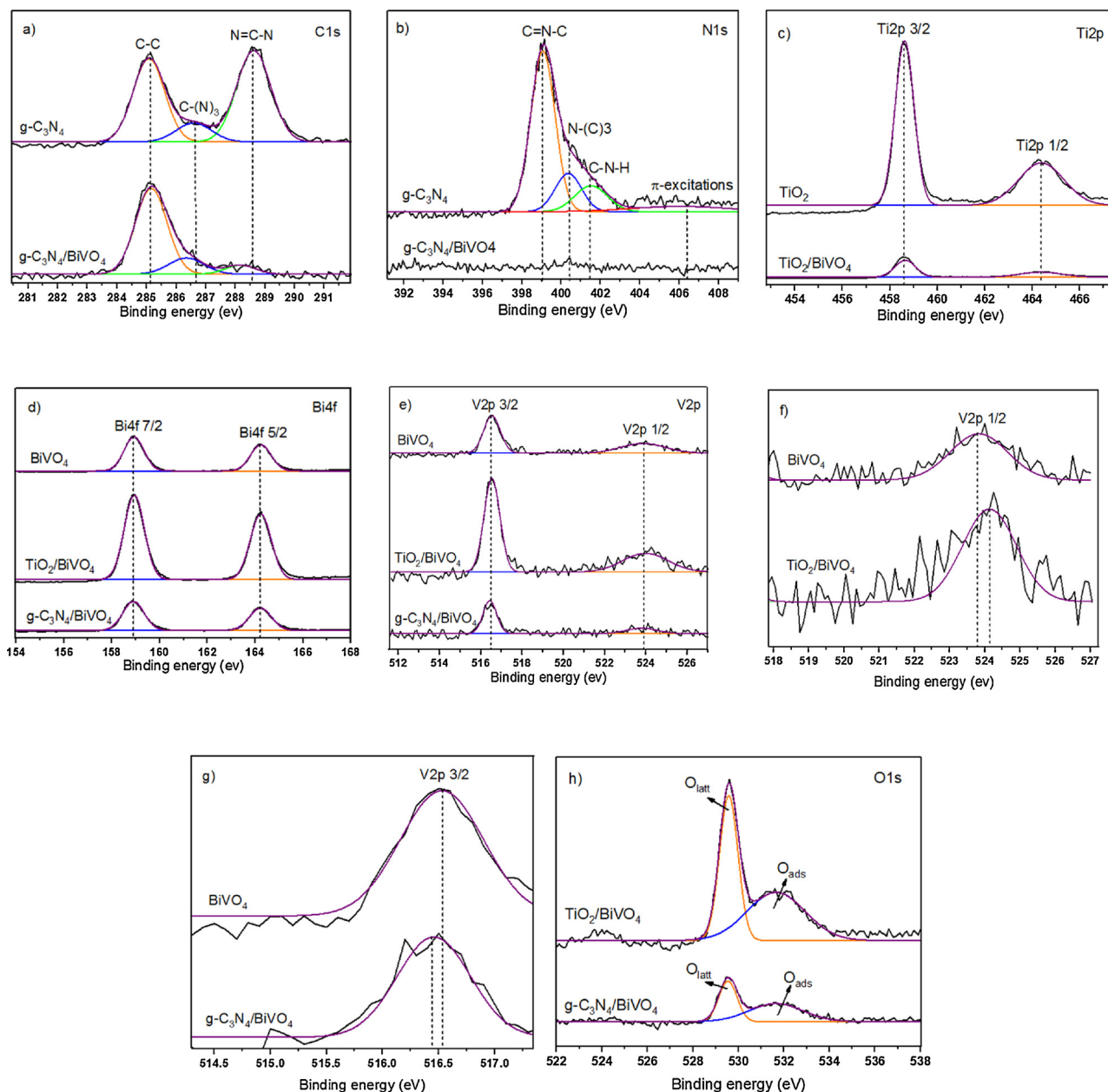


Fig. 7. XPS peaks of C1s and N1s for g-C₃N₄ and g-C₃N₄/ BiVO₄ (a, b), Ti2p peaks for TiO₂ and TiO₂/BiVO₄ (c), Bi4f and V2p peaks for BiVO₄, TiO₂/BiVO₄ and g-C₃N₄/ BiVO₄ (d, e), zoomed V2p 1/2 peaks of BiVO₄ and TiO₂/BiVO₄ (f), zoomed V2p 3/2 peaks of BiVO₄ and g-C₃N₄/ BiVO₄ (g) and O1s peaks for TiO₂/BiVO₄ and g-C₃N₄/ BiVO₄ (h).

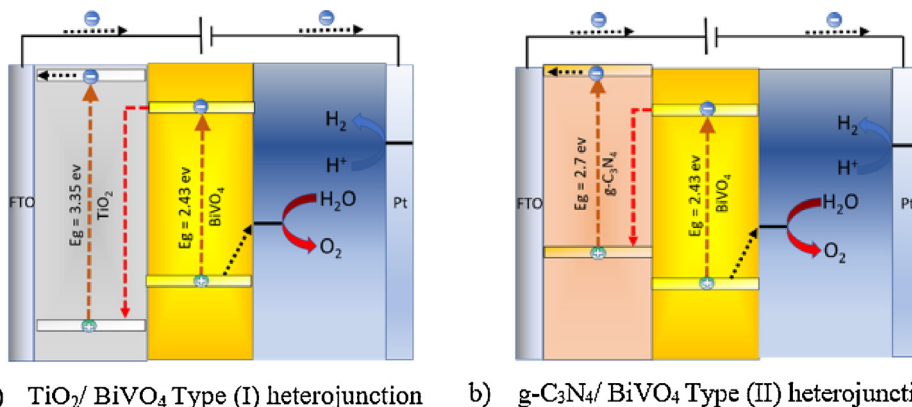


Fig. 8. The band diagram of (a) TiO₂/BiVO₄ type (I) heterojunction and (b) g-C₃N₄/BiVO₄ type (II) heterojunction.

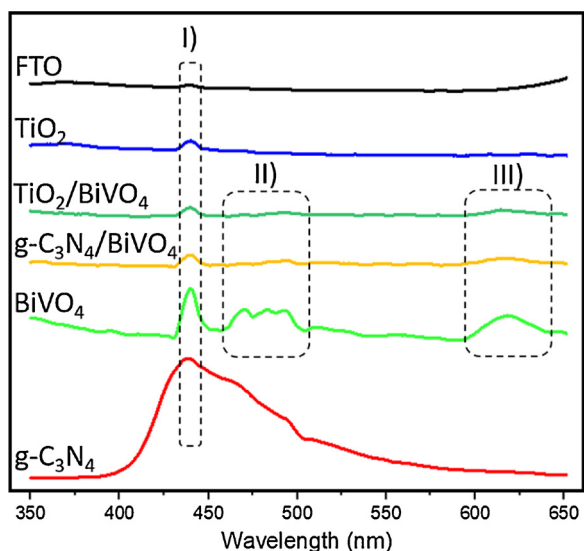


Fig. 9. Photoluminescence spectra of reference FTO (a), TiO₂ (b), TiO₂/BiVO₄ (c), g-C₃N₄/BiVO₄ (d), BiVO₄ (e), and g-C₃N₄ (f) thin films deposited on FTO.

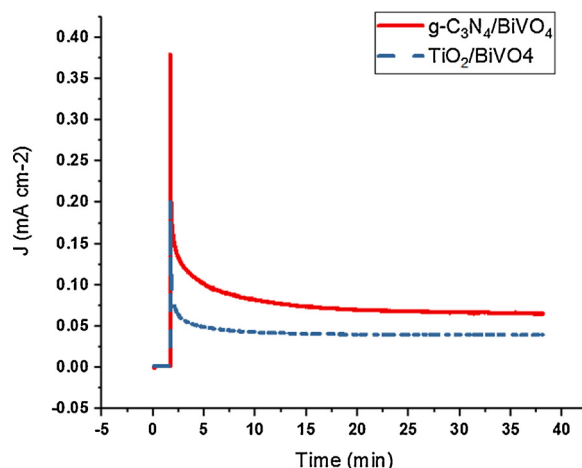


Fig. 11. Stability test of photoanodes under illumination for 35 min in 0.5 M Na₂SO₄ under 100 mW/cm² of light intensity at 0.6 V vs. Ag/AgCl.

toward the conduction band. Stable photocurrent was then achieved with small decay, attributable to the slow accumulation of holes reducing charge transfer kinetics, that can be further improved with the addition of OER catalyst [22]. TiO₂/BiVO₄ indicates a steady state

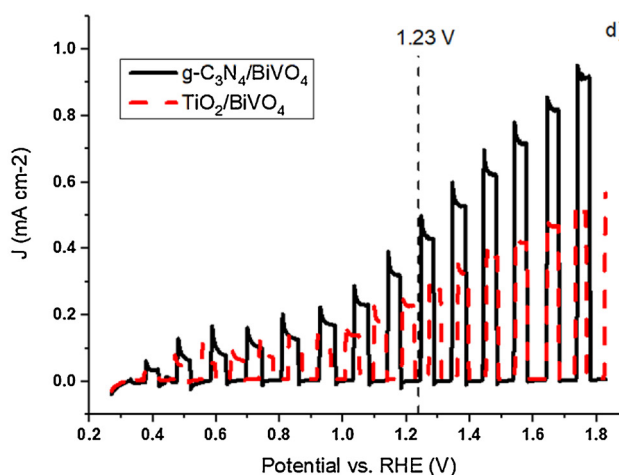
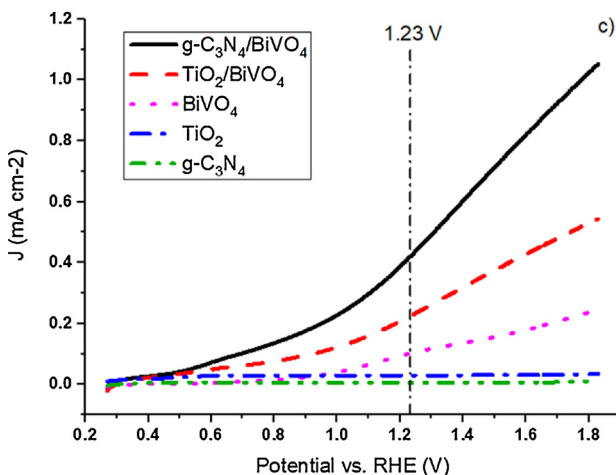
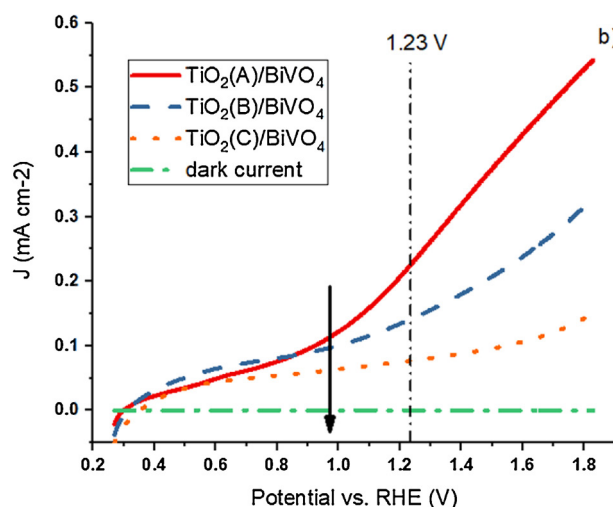
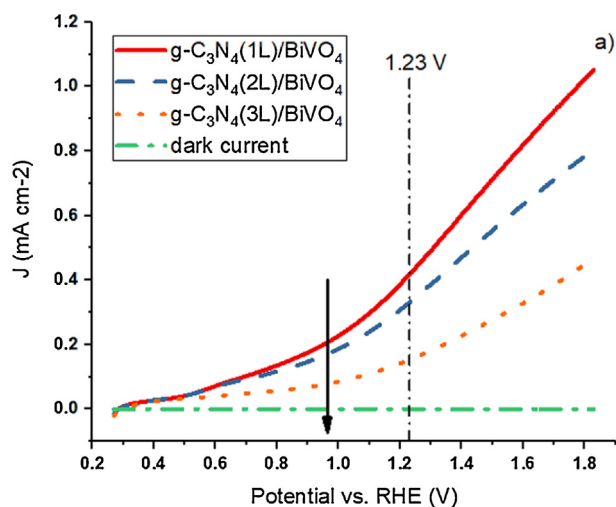


Fig. 10. LSV response of g-C₃N₄/BiVO₄ heterojunction (a), TiO₂/BiVO₄ heterojunction (b), bare and optimized heterojunction photoanodes (c) and g-C₃N₄/BiVO₄ and TiO₂/BiVO₄ heterojunction photoanodes under chopped illumination (d). All the tests were conducted in 0.5 M Na₂SO₄ under 100 mW/cm² of light intensity.

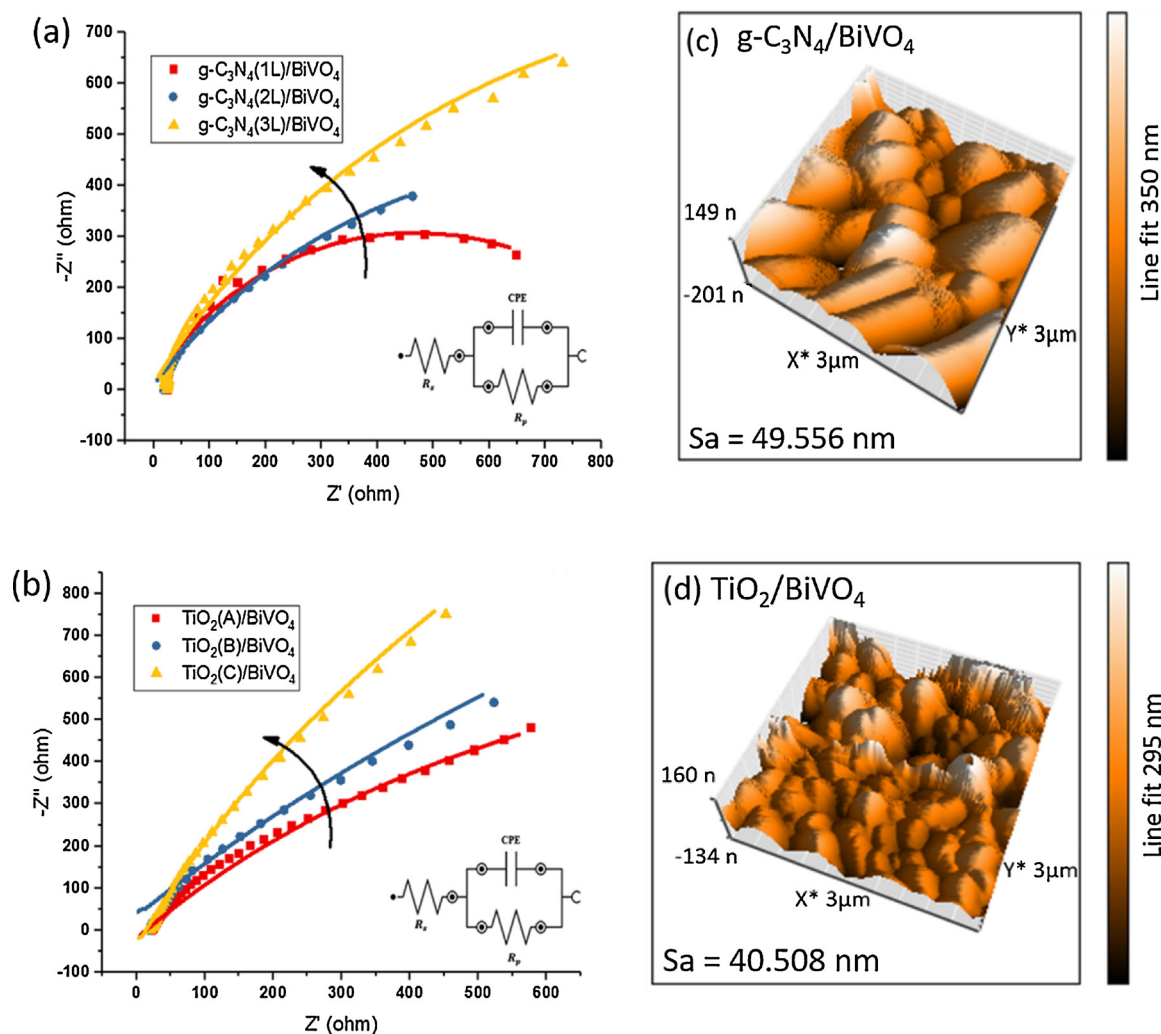


Fig. 12. EIS Nyquist plots for $g\text{-C}_3\text{N}_4/\text{BiVO}_4$ (a) and $\text{TiO}_2/\text{BiVO}_4$ (b). AFM result and its associated values for surface roughness (Sa) for $g\text{-C}_3\text{N}_4/\text{BiVO}_4$ (c) and $\text{TiO}_2/\text{BiVO}_4$ (d). The higher surface roughness of $g\text{-C}_3\text{N}_4/\text{BiVO}_4$ results in its higher double layer capacitance compared with $\text{TiO}_2/\text{BiVO}_4$.

photocurrent after 10 min while $g\text{-C}_3\text{N}_4/\text{BiVO}_4$ demonstrates a steady state photocurrent after 30 min. From 30 to 35 min both samples showed little degradation of about $1\ \mu\text{A}$ (from 65 to 64 μA) and (from 40 to 39 μA) for $g\text{-C}_3\text{N}_4/\text{BiVO}_4$ and $\text{TiO}_2/\text{BiVO}_4$, respectively. The results suggest that both photoanodes are highly stable in the aqueous electrolyte for long time operation.

The superior performance of $g\text{-C}_3\text{N}_4$ to TiO_2 was substantiated by Electrical Impedance Spectroscopy (EIS) test conducted under light from 100 kHz to 10 Hz, utilizing 10 mV sinusoidal voltage at DC bias of 1 V vs. RHE. As can be observed from Fig. 12a–b, the increase in Nyquist plot radius with the increase of $g\text{-C}_3\text{N}_4$ or TiO_2 thickness, highly accorded with the results of LSV (Fig. 10a–b) where less

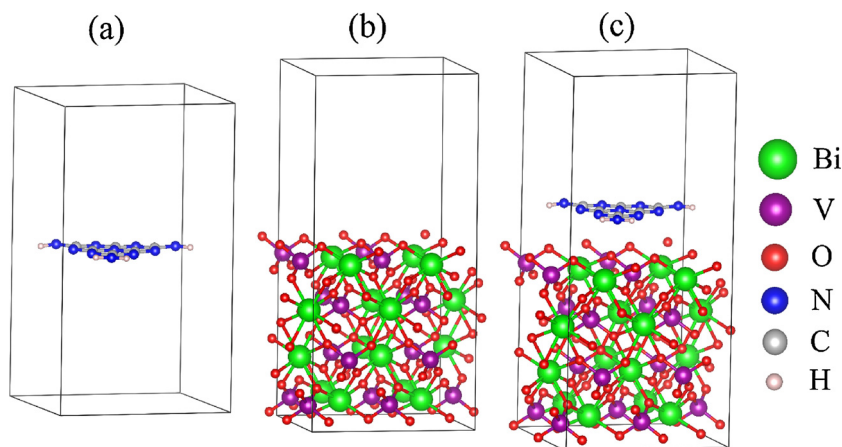


Fig. 13. Relaxed geometries of $g\text{-C}_3\text{N}_4$ (a), $\text{BiVO}_4(001)$ (b) and $g\text{-C}_3\text{N}_4/\text{BiVO}_4$ (c).

Table 1

EIS parameters conducted at 0.6 V vs. Ag/AgCl for g-C₃N₄(1 L)/BiVO₄ and TiO₂(1 L)/BiVO₄ photoanodes.

Sample	Rs (Ω)	Rp (Ω)	CPE (μF)
g-C ₃ N ₄ (1L)/BiVO ₄	22.81	973.7	1.01-E-05
TiO ₂ (A)/BiVO ₄	23.79	2428.2	6.55-E-06

photogenerated electrons were produced for thicker layers of TiO₂ and g-C₃N₄.

Electrochemical circuit fitting was performed with the employment of Randles equivalent circuit. The results are presented in Table 1. The higher values of double layer capacitance or Constant Phase Element (CPE) for g-C₃N₄/BiVO₄, compared with TiO₂/BiVO₄, were due to more active photocatalytic sites for water redox reaction. This is because high surface roughness was calculated from topological images obtained from Atomic Force Microscopy (AFM) of g-C₃N₄/BiVO₄ compared with TiO₂/BiVO₄, which act as trapping centres [73] (Fig. 12c–d).

The smaller values of Rp (charge transfer resistance) for g-C₃N₄/BiVO₄, compared with TiO₂/BiVO₄, are illustrative of less charge transfer resistance between photoelectrode and electrolyte, for more oxygen vacancy sites exist on g-C₃N₄/BiVO₄ in comparison with those of TiO₂/BiVO₄. Oxygen vacancy sites make additional chemisorption between water molecules and photoelectrode, thus reducing the charge transfer resistance. Besides, Mott-Schottky test (Fig. S8) demonstrated 3.18 times higher charge carrier density for g-C₃N₄/BiVO₄ compared with TiO₂/BiVO₄, confirming a more enhanced charge carrier mobility. Other factors contributing to superior carrier mobility are the low lattice mismatch between g-C₃N₄ and BiVO₄ as well as an additional non-covalent bonding between Bi–N, O–C, and O–N, further elaborated in Section 3.8. The higher light absorption for g-C₃N₄/BiVO₄ compared with that of TiO₂/BiVO₄ also contributes to the Rp, for a higher number of photogenerated electrons can participate in redox reactions.

Even though both g-C₃N₄/BiVO₄ and TiO₂/BiVO₄ formed Z-scheme structure under the application of a positive bias, g-C₃N₄ demonstrated a superior PEC performance compared with that of TiO₂ as electron extraction layer to enhance the performance of BiVO₄. This resulted from the more negative conduction band of g-C₃N₄ (–1.72 V vs. RHE) compared with TiO₂ (–1.2 V vs. RHE) that generates a higher potential energy for water reduction (Fig. S7). Compared with TiO₂/BiVO₄, higher light absorption at less than 500 nm for g-C₃N₄/BiVO₄ produces more photogenerated electrons/holes. Higher surface roughness and the existence of V⁴⁺, which induces oxygen vacancy, enhance the active catalytic sites and charge carrier mobility (see Fig. S9 in Supporting information). The doping of g-C₃N₄ to develop p-type semiconductor [74] and its incorporation with solid state mediators in p–n junction [75] are highly promising approaches that can be utilized to enhance the performance of g-C₃N₄/BiVO₄ photoanode.

3.8. Electronic properties of BiVO₄(001), g-C₃N₄, and g-C₃N₄/BiVO₄(001)

Drawing upon the experimental results already demonstrated in this paper, we affirm that g-C₃N₄/BiVO₄ heterojunction is superior to TiO₂/BiVO₄. To further corroborate our observations, periodic DFT calculations were performed for BiVO₄(001), g-C₃N₄, and g-C₃N₄/BiVO₄(001) heterostructure. Moreover, TiO₂/BiVO₄(001) heterojunction proved to possess a larger lattice mismatch (7.3%) compared with g-C₃N₄/BiVO₄ (0.02%) (see Fig. S10 of the Supporting information). The optimized structures and lattice parameters of monolayer g-C₃N₄, bulk g-C₃N₄, BiVO₄, BiVO₄(001), and g-C₃N₄/BiVO₄(001) are displayed in Fig. 13 and Table S2, respectively. As discussed previously [22,76], the BiVO₄(001) surface is stable and nonpolar which further confirms its positive surface formation energy of 1.95 J/m². As a consequence of this stability, BiVO₄(001) slab was selected to construct g-C₃N₄/

BiVO₄(001) heterostructure by placing a single layer of g-C₃N₄ on the top of BiVO₄(001) slab (Fig. 13c). The lattice mismatch in the heterojunction of g-C₃N₄/BiVO₄(001) proved considerably negligible (0.02%) due to similar surface areas of BiVO₄(001) and monolayer g-C₃N₄ (Table S2). Hereafter, the g-C₃N₄/BiVO₄(001) will be referred to as g-C₃N₄/BiVO₄. Relaxed crystal structures of BiVO₄ slab and its heterojunction as well as those of g-C₃N₄ bulk and monolayer are demonstrated in Fig. S11 of the Supporting information.

A 10 Å vacuum region was employed to minimize the interactions between the neighbouring systems of g-C₃N₄/BiVO₄ heterojunction. The g-C₃N₄ formed a non-covalent type interaction with the surface of BiVO₄ through Bi–N, O–C, and O–N with simulated distances of 3.10, 2.95, and 3.12 Å, respectively which reveals strong electrostatic interaction between them. The calculated adsorption energy of g-C₃N₄ nanosheet over the BiVO₄(001) was –0.68 eV which confirmed the thermodynamic stability of g-C₃N₄/BiVO₄ heterojunction. The adsorption or interface adhesion formation energy was calculated via Eq. (2).

$$\Delta E_{\text{ad}} = E_{\text{g-C}_3\text{N}_4/\text{BiVO}_4(001)} - (E_{\text{g-C}_3\text{N}_4} + E_{\text{BiVO}_4(001)}) \quad (2)$$

where $E_{\text{g-C}_3\text{N}_4/\text{BiVO}_4(001)}$, $E_{\text{g-C}_3\text{N}_4}$, and $E_{\text{BiVO}_4(001)}$ represent respectively the total energy of the relaxed g-C₃N₄/BiVO₄(001) heterojunction, monolayer g-C₃N₄, and BiVO₄(001) slab. The adsorption/interface binding energy between the g-C₃N₄ monolayer and the BiVO₄(001) of the heterostructure (–0.68 eV) predicts strong electrostatic interaction. To corroborate the experimental high photocatalytic activity of the g-C₃N₄/BiVO₄(001) heterostructure, the electronic properties such as band structure and DOS of g-C₃N₄/BiVO₄(001) heterostructure were calculated. The energy bands of single layer g-C₃N₄ and BiVO₄(001) surface were also calculated for comparison (Fig. 14). The simulated band gap of BiVO₄(001) was 2.46 eV, consistent with our experimentally observed band gap.

Monolayer g-C₃N₄ has an indirect band gap (2.70 eV) [30] where the valence band maximum (VBM) is located at Γ point and the conduction band minimum (CBM) is at C point (Fig. 14b). The g-C₃N₄/BiVO₄ heterostructure has an indirect gap (2.46 eV), and the VBM is located between B and Γ points, whereas the CBM is at Γ point (see Fig. 14c). Upon interaction of g-C₃N₄ with BiVO₄(001), flat bands are produced in the VB of the resulted heterojunction. These flat bands are responsible for the VB of heterojunction which consequently leads to holes trapping. The enhanced overall photocatalytic activity or high charge carrier mobility can be attributed to these flat bands (vide supra). Moreover, C and N atoms of monolayer g-C₃N₄ are responsible for these flat bands (vide infra). The effective masses of the photogenerated electrons (m_e^*) and holes (m_h^*) are estimated from the band structure along suitable directions of k-points by fitting parabolic approximation around the bottom of the CBM or the top of the VBM, respectively. The Eq. (3) is employed for the calculation of these photocarriers, where \hbar is the reduced Planck constant and E is the energy of an electron at wave vector k in the same band (VBM or CBM).

$$m^* = \hbar^2 (d^2 E/dk^2)^{-1} \quad (3)$$

Using meta-GGA, the simulated values of the effective masses of photogenerated electrons and holes of the BiVO₄ slab are 0.02 and 0.01 m_e , respectively (Table 2). These masses are comparatively lower than those in our previous report, utilizing LDA method [22,76]. Although pristine BiVO₄ has lighter effective masses of photocarriers, responsible for high carrier mobilities, its CBM (–4.57 eV) is situated at more negative potential (vs vacuum) than the reduction potential of water (–4.5 eV).

To probe the contribution of individual species (atoms), responsible for VBM and CBM, Partial Density of State (PDOS) of these three constituents were calculated, illustrated in Fig. 15a–c. The VBM and CBM of monolayer g-C₃N₄, BiVO₄(001), and g-C₃N₄/BiVO₄ heterojunction were simulated from the DOS calculations. Fig. 15a portrays how VBM of BiVO₄(001) is constructed by 2p orbitals of O atoms, situated at

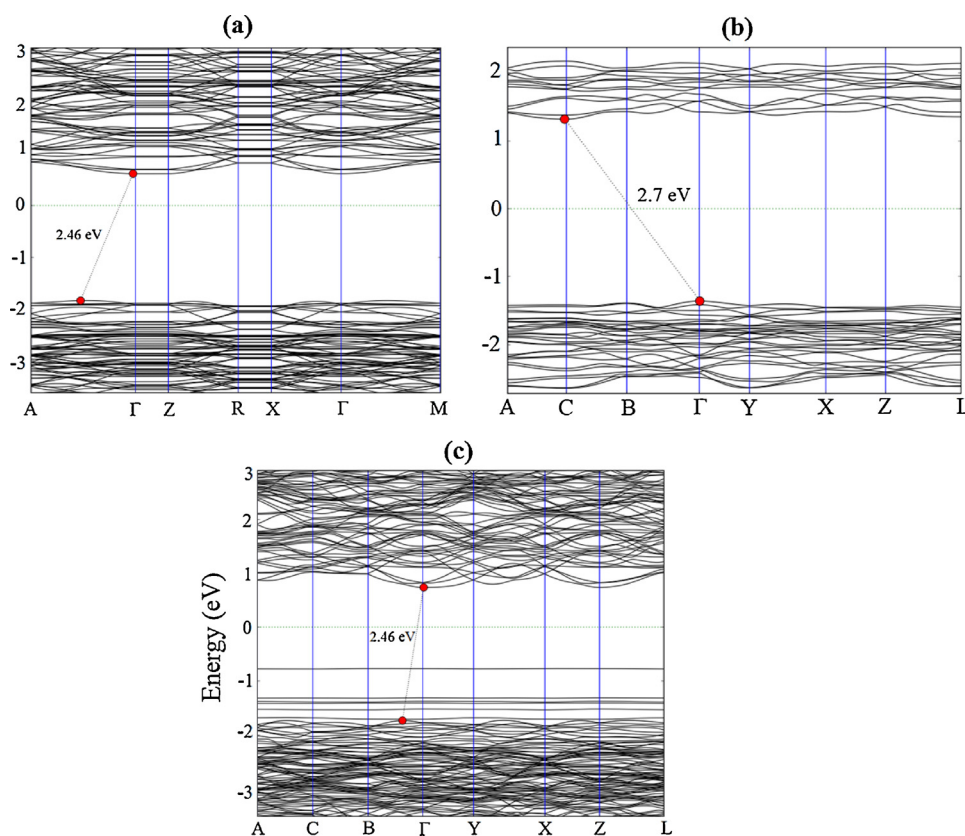


Fig. 14. Simulated band structures of BiVO₄(001) slab (a), g-C₃N₄ (b) and g-C₃N₄/BiVO₄ heterojunction (c); Fermi energy is set to zero.

Table 2

Work function, VBM, and CBM at vacuum level, band gap (in unit of eV), and effective masses of photogenerated electrons and holes; estimated from the calculated band structure along the suitable direction.

Species	Work function	m_e^*/m_0 (m_e)	m_h^*/m_0 (m_e)	VBM	CBM	Band Gap
BiVO ₄ (001)	5.18	0.02	0.01	-7.03	-4.57	2.46
g-C ₃ N ₄	4.38	0.12	0.44	-5.74	-3.07	2.70
g-C ₃ N ₄ /BiVO ₄	4.43	0.01	0.10	-6.16	-3.70	2.46

-7.03 eV (vs vacuum) while its CBM (-4.57 eV vs vacuum) is comprised of 5d orbitals of V atom. Furthermore, while VB of BiVO₄(001) is principally composed of O orbitals, its bottom section is comprised of equal contributions of V and Bi orbitals. CB of BiVO₄(001) is majorly composed of the anti-bonding orbitals of V atoms while its lower density section is made up of hybridized orbitals of O and Bi atoms. Both VB and CB of g-C₃N₄ are almost equally occupied by the N and C orbitals, where the VBM and CBM are situated at -5.74 and -3.07 eV (vs vacuum), respectively.

Figs. S12–S20 (Supporting information) presents the detailed contribution of s, p, and d orbitals in making VBs and CBs of these three different constituents. For the g-C₃N₄/BiVO₄ heterojunction, the VB (in the range of -5 to -6 eV) is chiefly occupied by N and C orbitals of g-C₃N₄ whereas the CB is dominated by the 5d anti-bonding orbitals of V of BiVO₄ (Fig. 15c). At vacuum level, both VBM and CBM of g-C₃N₄/BiVO₄ heterojunction are situated at -6.16 and -3.70 eV, respectively. Both experimental and theoretical results verify each other. Comparative analyses of VBM and CBM of the heterojunction with those of its individual constituents attest that these are respectively well below and above of the redox potential of water. Table 2 and Fig. 16 demonstrate VBM of BiVO₄(001) is higher than that of g-C₃N₄, whereas the CBM of g-C₃N₄ is lower than that of BiVO₄(001). In the resulted heterojunction, both Fermi energy and band edge positions are between

those of g-C₃N₄ and BiVO₄(001).

According to Fig. 16, VB and CB of heterojunction are shifted downward compared with g-C₃N₄, while these bands are shifted upward when compared with BiVO₄(001). Moreover, the changes in VB, CB, and Fermi energy result in band bending facilitating electron transfer [34], responsible for the enhanced photogenerated electrons. The photogenerated electrons from CB of g-C₃N₄ directly reduce water and produce H₂ while holes at VB of BiVO₄ directly oxidize water and generate O₂. Electrons from CB of BiVO₄ recombine with the holes from the VB of g-C₃N₄. The photocatalytic performance of heterojunction proved experimentally higher than that of individual g-C₃N₄ and BiVO₄. The enhanced performance was due to the combined band offset and built-in electric field that effectively transport the electrons and holes.

Fig. 16 demonstrates that CB edge position of heterojunction is more positive than that of H⁺/H₂ (vs vacuum), thereby efficiently reducing H⁺ to H₂. On the contrary, VB edge position of heterojunction proved more negative than that of g-C₃N₄ and positive in relation to BiVO₄. VB edge position of heterojunction is, in other words, at ideal position to perform oxygen evolution reaction (O₂/H₂O). Once a heterojunction is constructed, both Fermi level and the CB and VB of the resulted g-C₃N₄/BiVO₄ heterostructure are at diverse positions compared with those of their constituents. In brief, one can observe that g-C₃N₄/BiVO₄ heterojunction is a Type-II band alignment structure with lighter effective masses of electrons (0.01 m_e) and holes (0.10 m_e), responsible for high photocatalytic activities.

The inter-charge transfer at the g-C₃N₄/BiVO₄ heterojunction was calculated from the charge density difference (CDD) of the g-C₃N₄/BiVO₄ heterostructure, with the results presented in Fig. 17 where the green and yellow shaded areas represent charge accumulation and depletion, respectively. Fig. 17 also demonstrates that charge distribution principally occurs at the interface region of g-C₃N₄/BiVO₄ heterostructure, whereas almost no change was observed in the rest of BiVO₄(001), specifically in areas remote from the interface. This type of

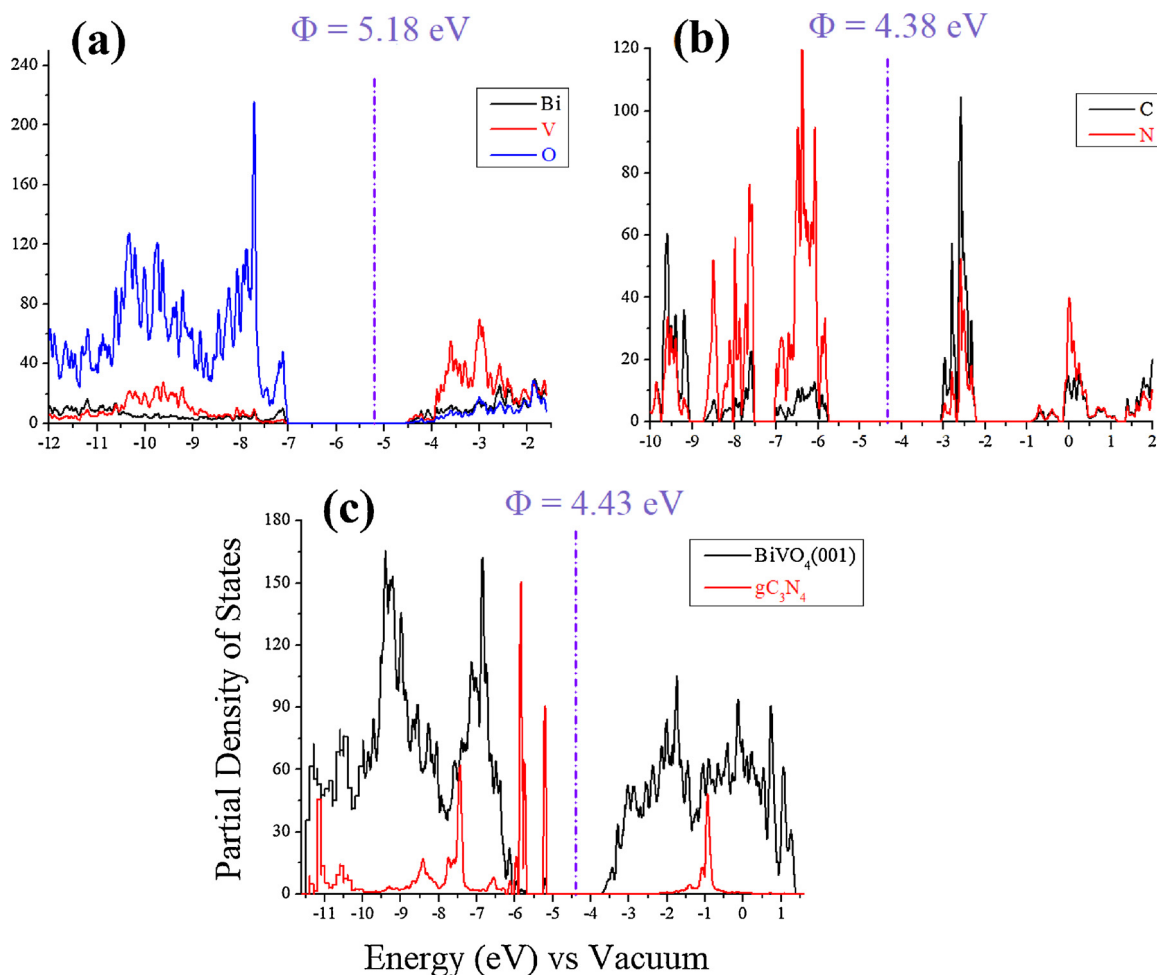


Fig. 15. PDOS plots of BiVO₄(001) (a), g-C₃N₄ (b) and g-C₃N₄/BiVO₄ (c) heterojunction. The vertical dashed lines represent the work function versus vacuum.

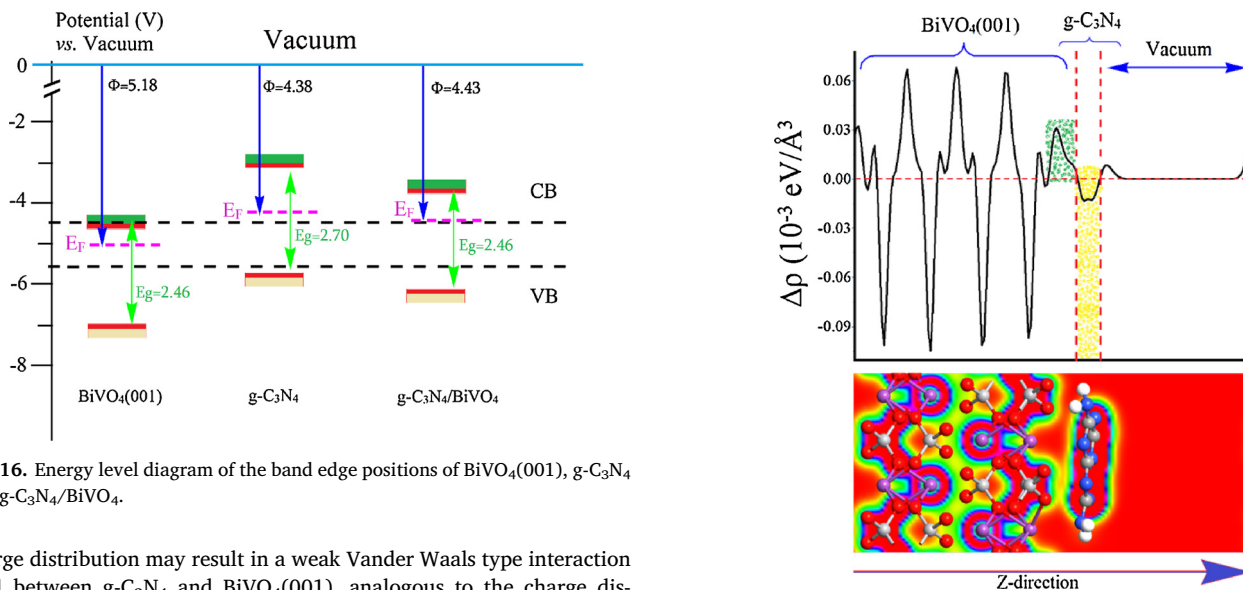


Fig. 16. Energy level diagram of the band edge positions of BiVO₄(001), g-C₃N₄ and g-C₃N₄/BiVO₄.

charge distribution may result in a weak Vander Waals type interaction [77] between g-C₃N₄ and BiVO₄(001), analogous to the charge distribution of a typical p–n junction [78]. Furthermore, a slice of the planar-averaged CDD along Z direction is depicted in Fig. 17 while that of pristine BiVO₄(001) is presented, for the sake of comparison, in Fig. S21 of the Supporting information. The charge redistribution at the interface of g-C₃N₄/BiVO₄ heterostructure attests that the electrons at CB of g-C₃N₄ directly reduce water while its holes recombine with the excited electrons of BiVO₄. In this process, holes at VB of BiVO₄ oxidize

Fig. 17. Average electron density difference ($\Delta\rho$) along Z-direction for g-C₃N₄/BiVO₄. The green and yellow shaded areas indicate electron accumulation and donation, respectively. (For interpretation of the references to colour in this figure legend, the reader is referred to the web version of this article.)

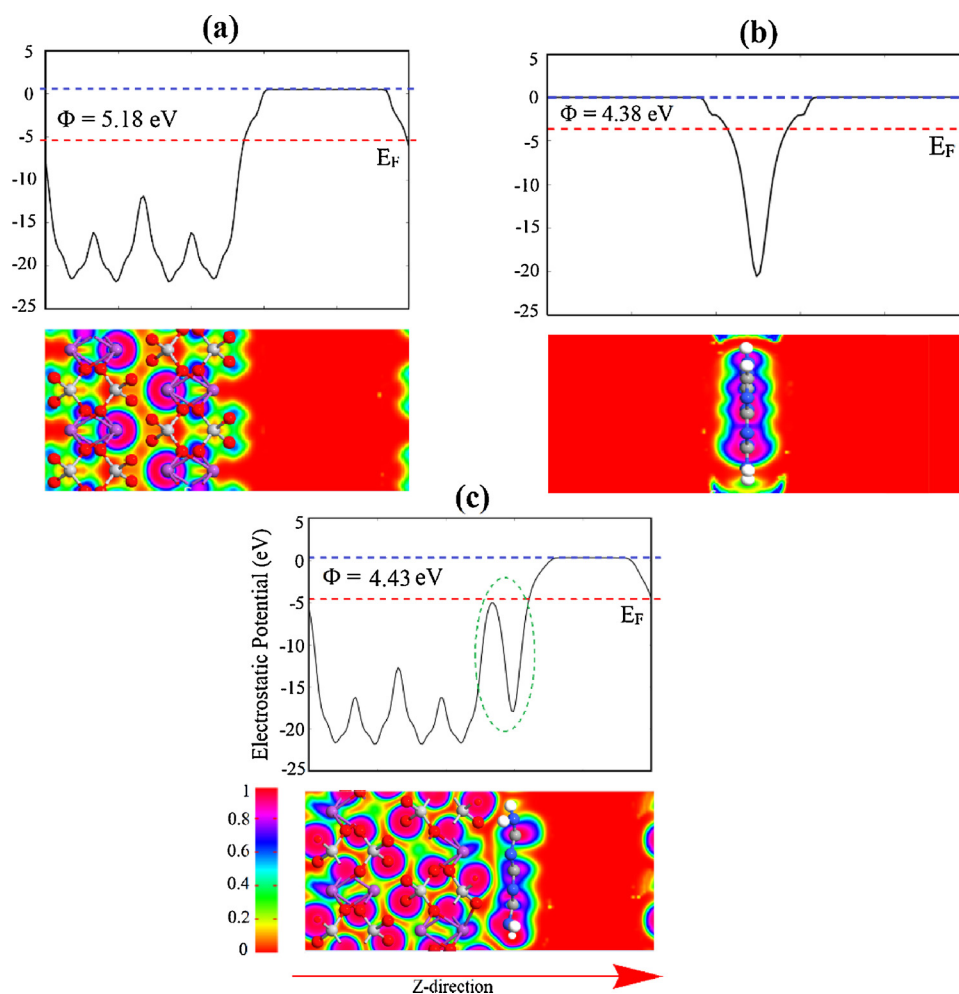


Fig. 18. Electrostatic potential maps of monolayer $g\text{-C}_3\text{N}_4$ (a), $\text{BiVO}_4(001)$ (b) and $g\text{-C}_3\text{N}_4/\text{BiVO}_4$ heterojunction (c). The red dashed lines represent Fermi energy level, blue denotes vacuum energy level and the green dashed circle highlights the interface of $g\text{-C}_3\text{N}_4/\text{BiVO}_4$ heterojunction. (For interpretation of the references to colour in this figure legend, the reader is referred to the web version of this article.)

water to germinate O_2 . The quantity of charge density difference is calculated (about 0.056 electrons) via Bader charge analysis of $g\text{-C}_3\text{N}_4/\text{BiVO}_4$ heterostructure. This charge accumulation and donation generates an electric field at the interface of $g\text{-C}_3\text{N}_4/\text{BiVO}_4$ heterostructure which further exerts the separation of electrons and holes (vide supra).

The band alignment of $\text{BiVO}_4(001)$, $g\text{-C}_3\text{N}_4$ and $g\text{-C}_3\text{N}_4/\text{BiVO}_4$ heterojunction were calculated from the difference of E_{vac} (energy of a stationary electron in the vacuum near by the surface) and Fermi energy level (E_{F}), using Eq. (4).

$$\Phi = E_{\text{vac}} - E_{\text{F}} \quad (4)$$

The calculated electrostatic potential maps of $\text{BiVO}_4(001)$, $g\text{-C}_3\text{N}_4$, and $g\text{-C}_3\text{N}_4/\text{BiVO}_4$ heterojunction along Z-direction are displayed in Fig. 18 and Table 2, with simulated work functions of $\text{BiVO}_4(001)$, $g\text{-C}_3\text{N}_4$, and $g\text{-C}_3\text{N}_4/\text{BiVO}_4$ heterojunction being 5.18, 4.38, and 4.43 eV, respectively. The difference in work function and band edge potentials (VB and CB) of $g\text{-C}_3\text{N}_4$ and $\text{BiVO}_4(001)$ demonstrate that the charge can be effectively transferred from $g\text{-C}_3\text{N}_4$ to $\text{BiVO}_4(001)$ at the interface of $g\text{-C}_3\text{N}_4/\text{BiVO}_4$ heterojunction. As indicated in Fig. 18 and Table 2, the work function of BiVO_4 surface (5.18 eV) is higher than that of monolayer $g\text{-C}_3\text{N}_4$ (4.38 eV), enforcing the charge to move from $g\text{-C}_3\text{N}_4$ to BiVO_4 until Fermi energy of these two constituents are aligned.

4. Conclusion

Z-scheme heterojunctions of $g\text{-C}_3\text{N}_4/\text{BiVO}_4$ and $\text{TiO}_2/\text{BiVO}_4$ were

successfully synthesized by electrodeposition of BiVO_4 on spin coated $g\text{-C}_3\text{N}_4$ and TiO_2 thin films, respectively. The obtained photocurrent response of $g\text{-C}_3\text{N}_4/\text{BiVO}_4$ proved nearly two times higher than that of $\text{TiO}_2/\text{BiVO}_4$, substantiating the superiority of $g\text{-C}_3\text{N}_4$ to TiO_2 . This superiority manifested itself in various properties such as light absorption, surface roughness, and charge carrier mobility. The presence of interplanar hydrogen elements in $g\text{-C}_3\text{N}_4$ induced the formation of V^{4+} , elevating its charge carrier mobility. Furthermore, V^{4+} produced oxygen vacancy that acts as the centre of catalytic sites and chemisorbed species, culminating in its higher photoelectrochemical properties. The experimental observations were counterchecked with Density Functional Theory (DFT) simulations. The simulated results attested that $g\text{-C}_3\text{N}_4$ and BiVO_4 formed a van der Waals type heterojunction, where an internal electric field facilitates the separation of electron/hole pair at the $g\text{-C}_3\text{N}_4/\text{BiVO}_4$ interface, restraining the carrier recombination. Comparative analyses of both experimental and theoretical studies affirm that the photogenerated electrons from CB of $g\text{-C}_3\text{N}_4$ directly reduce water while holes at VB of BiVO_4 directly oxidize water, with electrons from CB of BiVO_4 recombining with the holes from the VB of $g\text{-C}_3\text{N}_4$. The construction of Z-scheme based $g\text{-C}_3\text{N}_4$ PEC device engenders a promising field for further exploration and research.

Acknowledgments

The authors would like to acknowledge financial support from Universiti Kebangsaan Malaysia through internal grant GUP-2016-089

and also for providing facilities to perform this research. H.U. acknowledges the supercomputing facilities of ESI Beowulf Cluster, University of Exeter, UK.

Appendix A. Supplementary data

Supplementary material related to this article can be found, in the online version, at doi:<https://doi.org/10.1016/j.apcatb.2018.04.056>.

References

- [1] Y. Park, K.J. McDonald, K.-S. Choi, Progress in bismuth vanadate photoanodes for use in solar water oxidation, *Chem. Soc. Rev.* 42 (2013) 2321–2337.
- [2] M.D. Russell, P. Agrawal, A. Borgschulte, C.C. Hébert, D. Passerone, R. Erni, Direct evidence of surface reduction in monoclinic BiVO₄, *Chem. Mater.* 27 (2015) 3593–3600.
- [3] B.J. Morgan, G.W. Watson, A density functional theory + U study of oxygen vacancy formation at the (110), (100), (101), and (001) surfaces of rutile TiO₂, *J. Phys. Chem. C* 113 (2009) 7322–7328.
- [4] J. Pan, G. Liu, G.Q.M. Lu, H.M. Cheng, On the true photoreactivity order of {001}, {010}, and {101} facets of anatase TiO₂ crystals, *Angew. Chem. Int. Ed.* 50 (2011) 2133–2137.
- [5] M. Batzill, Fundamental aspects of surface engineering of transition metal oxide photocatalysts, *Energy Environ. Sci.* 4 (2011) 3275–3286.
- [6] H.S. Park, K.E. Kweon, H. Ye, E. Paek, G.S. Hwang, A.J. Bard, Factors in the metal doping of BiVO₄ for improved photoelectrocatalytic activity as studied by scanning electrochemical microscopy and first-principles density-functional calculation, *J. Phys. Chem. C* 115 (2011) 17870–17879.
- [7] K.R. Tolod, S. Hernández, N. Russo, Recent advances in the BiVO₄ photocatalyst for sun-driven water oxidation: top-performing photoanodes and scale-up challenges, *Catal. Today* 7 (2017) 13.
- [8] Y. Li, R. Wang, H. Li, X. Wei, J. Feng, K. Liu, Y. Dang, A. Zhou, Efficient and stable photoelectrochemical seawater splitting with TiO₂@g-C₃N₄ nanorod arrays decorated by Co-Pi, *J. Phys. Chem. C* 119 (2015) 20283–20292.
- [9] X. Shi, H. Jeong, S.J. Oh, M. Ma, K. Zhang, J. Kwon, I.T. Choi, I.Y. Choi, H.K. Kim, J.K. Kim, Unassisted photoelectrochemical water splitting exceeding 7% solar-to-hydrogen conversion efficiency using photon recycling, *Nat. Commun.* 7 (2016).
- [10] J.A. Seabold, K.-S. Choi, Efficient and stable photo-oxidation of water by a bismuth vanadate photoanode coupled with an iron oxyhydroxide oxygen evolution catalyst, *J. Am. Chem. Soc.* 134 (2012) 2186–2192.
- [11] J.H. Kim, S. Han, Y.H. Jo, Y. Bak, J.S. Lee, A precious metal-free solar water splitting cell with a bifunctional cobalt phosphide electrocatalyst and doubly promoted bismuth vanadate photoanode, *J. Mater. Chem. A* 6 (2018) 1266–1274.
- [12] Y. Park, D. Kang, K.-S. Choi, Marked enhancement in electron–hole separation achieved in the low bias region using electrochemically prepared Mo-doped BiVO₄ photoanodes, *Phys. Chem. Chem. Phys.* 16 (2014) 1238–1246.
- [13] F.F. Abdi, N. Firet, R. van de Krol, Efficient BiVO₄ thin film photoanodes modified with cobalt phosphate catalyst and W-doping, *ChemCatChem* 5 (2013) 490–496.
- [14] K.P.S. Parmar, H.J. Kang, A. Bist, P. Dua, J.S. Jang, J.S. Lee, Photocatalytic and photoelectrochemical water oxidation over metal-doped monoclinic BiVO₄ photoanodes, *ChemSusChem* 5 (2012) 1926–1934.
- [15] M. Zhou, J. Bao, Y. Xu, J. Zhang, J. Xie, M. Guan, C. Wang, L. Wen, Y. Lei, Y. Xie, Photoelectrodes based upon Mo: BiVO₄ inverse opals for photoelectrochemical water splitting, *ACS Nano* 8 (2014) 7088–7098.
- [16] S. Sun, W. Wang, D. Li, L. Zhang, D. Jiang, Solar light driven pure water splitting on quantum sized BiVO₄ without any cocatalyst, *ACS Catal.* 4 (2014) 3498–3503.
- [17] M. Xie, Z. Zhang, W. Han, X. Cheng, X. Li, E. Xie, Efficient hydrogen evolution under visible light irradiation over BiVO₄ quantum dot decorated screw-like SnO₂ nanostructures, *J. Mater. Chem. A* 5 (2017) 10338–10346.
- [18] G. Xi, J. Ye, Synthesis of bismuth vanadate nanoplates with exposed {001} facets and enhanced visible-light photocatalytic properties, *Chem. Commun.* 46 (2010) 1893–1895.
- [19] H. He, S.P. Berglund, A.J. Rettie, W.D. Chemelewski, P. Xiao, Y. Zhang, C.B. Mullins, Synthesis of BiVO₄ nanoflake array films for photoelectrochemical water oxidation, *J. Mater. Chem. A* 2 (2014) 9371–9379.
- [20] J. Li, J. Zhou, H. Hao, Z. Zhu, Silver-modified specific (040) facet of BiVO₄ with enhanced photoelectrochemical performance, *Mater. Lett.* 170 (2016) 163–166.
- [21] J. Li, J. Zhou, H. Hao, W. Li, G. Liu, Exposed specific (040) and (110) facets of BiVO₄ modified with Bi₂WO₆ nanoparticles for enhanced photocatalytic performance, *New J. Chem.* 41 (2017) 6922–6927.
- [22] S.N.F.M. Nasir, H. Ullah, M. Ebad, A.A. Tahir, J.S. Sagun, M.A. Mat Teridi, New insights into Se/BiVO₄ heterostructure for photoelectrochemical water splitting: a combined experimental and DFT study, *J. Phys. Chem. C* 121 (2017) 6218–6228.
- [23] X. Zhang, B. Zhang, K. Cao, J. Brilliet, J. Chen, M. Wang, Y. Shen, A perovskite solar cell-TiO₂@ BiVO₄ photoelectrochemical system for direct solar water splitting, *J. Mater. Chem. A* 3 (2015) 21630–21636.
- [24] R. Tong, X. Wang, X. Zhou, Q. Liu, H. Wang, X. Peng, X. Liu, Z. Zhang, H. Wang, P.D. Lund, Cobalt-phosphate modified TiO₂/BiVO₄ nanoarrays photoanode for efficient water splitting, *Int. J. Hydrogen Energy* 42 (2017) 5496–5504.
- [25] J. Resasco, H. Zhang, N. Kornienko, N. Becknell, H. Lee, J. Guo, A.L. Briseno, P. Yang, TiO₂/BiVO₄ nanowire heterostructure photoanodes based on type II band alignment, *ACS Cent. Sci.* 2 (2016) 80–88.
- [26] X. Shi, I.Y. Choi, K. Zhang, J. Kwon, D.Y. Kim, J.K. Lee, S.H. Oh, J.K. Kim, J.H. Park, Efficient photoelectrochemical hydrogen production from bismuth vanadate-decorated tungsten trioxide helix nanostructures, *Nat. Commun.* 5 (2014) 4775.
- [27] Y. Pihosh, I. Turkevych, K. Mawatari, J. Uemura, Y. Kazoe, S. Kosar, K. Makita, T. Sugaya, T. Matsui, D. Fujita, Photocatalytic generation of hydrogen by core-shell WO₃/BiVO₄ nanorods with ultimate water splitting efficiency, *Sci. Rep.* 5 (2015).
- [28] P.M. Rao, L. Cai, C. Liu, I.S. Cho, C.H. Lee, J.M. Weisse, P. Yang, X. Zheng, Simultaneously efficient light absorption and charge separation in WO₃/BiVO₄ core/shell nanowire photoanode for photoelectrochemical water oxidation, *Nano Lett.* 14 (2014) 1099–1105.
- [29] Q. Zeng, J. Li, L. Li, J. Bai, L. Xia, B. Zhou, Synthesis of WO₃/BiVO₄ photoanode using a reaction of bismuth nitrate with peroxovanadate on WO₃ film for efficient photoelectrocatalytic water splitting and organic pollutant degradation, *Appl. Catal. B: Environ.* 217 (2017) 21–29.
- [30] W.-J. Ong, L.-L. Tan, Y.H. Ng, S.-T. Yong, S.-P. Chai, Graphitic carbon nitride (g-C₃N₄)-based photocatalysts for artificial photosynthesis and environmental remediation: are we a step closer to achieving sustainability? *Chem. Rev.* 116 (2016) 7159–7329.
- [31] X. Wang, K. Maeda, A. Thomas, K. Takanabe, G. Xin, J.M. Carlsson, K. Domen, M. Antonietti, A metal-free polymeric photocatalyst for hydrogen production from water under visible light, *Nat. Mater.* 8 (2009) 76–80.
- [32] A. Naseri, M. Samadi, A. Pourjavadi, A.Z. Moshfegh, S. Ramakrishna, Graphitic carbon nitride (g-C₃N₄)-based photocatalysts for solar hydrogen generation: recent advances and future development directions, *J. Mater. Chem. A* 5 (2017) 23406–23433.
- [33] S. Cao, J. Low, J. Yu, M. Jaroniec, Polymeric photocatalysts based on graphitic carbon nitride, *Adv. Mater.* 27 (2015) 2150–2176.
- [34] J. Fu, J. Yu, C. Jiang, B. Cheng, g-C₃N₄ based heterostructured photocatalysts, *Adv. Energy Mater.* 8 (2017) 1701503.
- [35] H. Ullah, A.A. Tahir, S. Bibi, T.K. Mallick, S.Z. Karzhanov, Electronic properties of β-TaON and its surfaces for solar water splitting, *Appl. Catal. B: Environ.* 229 (2018) 24–31.
- [36] J. Alberio, E.M. Barea, J. Xu, I. Mora-Seró, H. Garcia, M. Shalom, Toward efficient carbon nitride photoelectrochemical cells: understanding charge transfer processes, *Adv. Mater. Interfaces* 4 (2017).
- [37] Š. Hajduk, S.P. Berglund, M. Podlogar, G. Dražić, F.F. Abdi, Z.C. Orel, M. Shalom, Conformal carbon nitride coating as an efficient hole extraction layer for ZnO nanowires-based photoelectrochemical cells, *Adv. Mater. Interfaces* 4 (2017).
- [38] C.-H. Wang, D.-D. Qin, D.-L. Shan, J. Gu, Y. Yan, J. Chen, Q.-H. Wang, C.-H. He, Y. Li, J.-J. Quan, Assembly of g-C₃N₄-based type II and Z-scheme heterojunction anodes with improved charge separation for photoelectrochemical water oxidation, *Phys. Chem. Chem. Phys.* 19 (2017) 4507–4515.
- [39] K.J. McDonald, K.-S. Choi, A new electrochemical synthesis route for a BiOI electrode and its conversion to a highly efficient porous BiVO₄ photoanode for solar water oxidation, *Energy Environ. Sci.* 5 (2012) 8553–8557.
- [40] D. Kang, Y. Park, J.C. Hill, K.-S. Choi, Preparation of Bi-based ternary oxide photoanodes BiVO₄, Bi₂WO₆, and Bi₂Mo₃O₁₂ using dendritic Bi metal electrodes, *J. Phys. Chem. Lett.* 5 (2014) 2994–2999.
- [41] C.K. Gupta, T. Mukherjee, *Hydrometallurgy in Extraction Processes*, CRC Press, 1990.
- [42] J.H. Kim, G. Magesh, H.J. Kang, M. Banu, J.H. Kim, J. Lee, J.S. Lee, Carbonate-coordinated cobalt co-catalyzed BiVO₄/WO₃ composite photoanode tailored for CO₂ reduction to fuels, *Nano Energy* 15 (2015) 153–163.
- [43] AtomistixToolKit, version 2017.1, QuantumWise A/S, (www.quantumwise.com).
- [44] VirtualNanoLab, version 2017.1, QuantumWise A/S, (www.quantumwise.com).
- [45] A. Sleight, H.-Y. Chen, A. Ferretti, D. Cox, Crystal growth and structure of BiVO₄, *Mater. Res. Bull.* 14 (1979) 1571–1581.
- [46] A.H. Larsen, M. Vanin, J.J. Mortensen, K.S. Thygesen, K.W. Jacobsen, Localized atomic basis set in the projector augmented wave method, *Phys. Rev. B* 80 (2009) 195112.
- [47] G. Kresse, D. Joubert, From ultrasoft pseudopotentials to the projector augmented-wave method, *Phys. Rev. B* 59 (1999) 1758.
- [48] F. Tran, P. Blaha, Accurate band gaps of semiconductors and insulators with a semilocal exchange-correlation potential, *Phys. Rev. Lett.* 102 (2009) 226401.
- [49] J. Endres, D.A. Egger, M. Kulbak, R.A. Kerner, L. Zhao, S.H. Silver, G. Hodes, B.P. Rand, D. Cahen, L. Kronik, Valence and conduction band densities of states of metal halide perovskites: a combined experimental–theoretical study, *J. Phys. Chem. Lett.* 7 (2016) 2722–2729.
- [50] E. Muniz, M. Goes, J. Silva, J.A. Varela, E. Joanni, R. Parra, P.R. Bueno, Synthesis and characterization of mesoporous TiO₂ nanostructured films prepared by a modified sol–gel method for application in dye solar cells, *Ceram. Int.* 37 (2011) 1017–1024.
- [51] D. Kang, T.W. Kim, S.R. Kubota, A.C. Cardiel, H.G. Cha, K.-S. Choi, Electrochemical synthesis of photoelectrodes and catalysts for use in solar water splitting, *Chem. Rev.* 115 (2015) 12839–12887.
- [52] J.H. Kim, Y.H. Jo, J.H. Kim, J.S. Lee, Ultrafast fabrication of highly active BiVO₄ photoanodes by hybrid microwave annealing for unbiased solar water splitting, *Nanoscale* 8 (2016) 17623–17631.
- [53] B.-Y. Cheng, J.-S. Yang, H.-W. Cho, J.-J. Wu, Fabrication of an efficient BiVO₄–TiO₂ heterojunction photoanode for photoelectrochemical water oxidation, *ACS Appl. Mater. Interfaces* 8 (2016) 20032–20039.
- [54] Y. Qiu, W. Liu, W. Chen, G. Zhou, P.-C. Hsu, R. Zhang, Z. Liang, S. Fan, Y. Zhang, Y. Cui, Efficient solar-driven water splitting by nanoscale BiVO₄ 4-perovskite tandem cells, *Sci. Adv.* 2 (2016) e1501764.
- [55] M. Ma, J.K. Kim, K. Zhang, X. Shi, S.J. Kim, J.H. Moon, J.H. Park, Double-deck inverse opal photoanodes: efficient light absorption and charge separation in

- heterojunction, *Chem. Mater.* 26 (2014) 5592–5597.
- [56] Y. Zhou, L. Zhang, L. Lin, B.R. Wygant, Y. Liu, Y. Zhu, Y. Zheng, C.B. Mullins, Y. Zhao, X.-H. Zhang, Highly efficient photoelectrochemical water splitting from hierarchical WO₃/BiVO₄ nanoporous sphere arrays, *Nano Lett.* 17 (2017) 8012–8017.
- [57] S. Le, T. Jiang, Q. Zhao, X. Liu, Y. Li, B. Fang, M. Gong, Cu-doped mesoporous graphitic carbon nitride for enhanced visible-light driven photocatalysis, *RSC Adv.* 6 (2016) 38811–38819.
- [58] M. Zalfani, B. van der Schueren, Z.-Y. Hu, J.C. Rooke, R. Bourguiga, M. Wu, Y. Li, G. Van Tendeloo, B.-L. Su, Novel 3DOM BiVO₄/TiO₂ nanocomposites for highly enhanced photocatalytic activity, *J. Mater. Chem. A* 3 (2015) 21244–21256.
- [59] J. Jiang, J. Yu, S. Cao, Au/PtO nanoparticle-modified gC₃N₄ for plasmon-enhanced photocatalytic hydrogen evolution under visible light, *J. Colloid Interface Sci.* 461 (2016) 56–63.
- [60] G. Wang, Y. Ling, X. Lu, F. Qian, Y. Tong, J.Z. Zhang, V. Lordi, C. Rocha Leao, Y. Li, Computational and photoelectrochemical study of hydrogenated bismuth vanadate, *J. Phys. Chem. C* 117 (2013) 10957–10964.
- [61] D.-D. Qin, T. Wang, Y.-M. Song, C.-L. Tao, Reduced monoclinic BiVO₄ for improved photoelectrochemical oxidation of water under visible light, *Dalton Trans.* 43 (2014) 7691–7694.
- [62] Z. Wang, J. Lv, J. Zhang, K. Dai, C. Liang, Facile synthesis of Z-scheme BiVO₄/porous graphite carbon nitride heterojunction for enhanced visible-light-driven photocatalyst, *Appl. Surf. Sci.* 430 (2017) 595–602.
- [63] J.H. Kim, Y. Jo, J.H. Kim, J.W. Jang, H.J. Kang, Y.H. Lee, D.S. Kim, Y. Jun, J.S. Lee, Wireless solar water splitting device with robust cobalt-catalyzed, dual-doped BiVO₄ photoanode and perovskite solar cell in tandem: a dual absorber artificial leaf, *ACS Nano* 9 (2015) 11820–11829.
- [64] Y. Zhang, Y. Guo, H. Duan, H. Li, C. Sun, H. Liu, Facile synthesis of V⁴⁺ self-doped, [010] oriented BiVO₄ nanorods with highly efficient visible light-induced photocatalytic activity, *Phys. Chem. Chem. Phys.* 16 (2014) 24519–24526.
- [65] F. Chen, Q. Yang, X. Li, G. Zeng, D. Wang, C. Niu, J. Zhao, H. An, T. Xie, Y. Deng, Hierarchical assembly of graphene-bridged Ag₃PO₄/Ag/BiVO₄ (040) Z-scheme photocatalyst: an efficient, sustainable and heterogeneous catalyst with enhanced visible-light photoactivity towards tetracycline degradation under visible light irradiation, *Appl. Catal. B: Environ.* 200 (2017) 330–342.
- [66] M. Ye, J. Gong, Y. Lai, C. Lin, Z. Lin, High-efficiency photoelectrocatalytic hydrogen generation enabled by palladium quantum dots-sensitized TiO₂ nanotube arrays, *J. Am. Chem. Soc.* 134 (2012) 15720–15723.
- [67] T. An, J. Tang, Y. Zhang, Y. Quan, X. Gong, A.M. Al-Enizi, A.A. Elzatory, L. Zhang, G. Zheng, Photoelectrochemical conversion from graphitic C₃N₄ quantum dot decorated semiconductor nanowires, *ACS Appl. Mater. Interfaces* 8 (2016) 12772–12779.
- [68] S. Le, T. Jiang, Y. Li, Q. Zhao, Y. Li, W. Fang, M. Gong, Highly efficient visible-light-driven mesoporous graphitic carbon nitride/ZnO nanocomposite photocatalysts, *Appl. Catal. B: Environ.* 200 (2017) 601–610.
- [69] S. Thaweesak, M. Lyu, P. Peerakiatkhajohn, T. Butburee, B. Luo, H. Chen, L. Wang, Two-dimensional g-C₃N₄/Ca₂Nb₂O₁₀ nanosheet composites for efficient visible light photocatalytic hydrogen evolution, *Appl. Catal. B: Environ.* 202 (2017) 184–190.
- [70] J. Su, P. Geng, X. Li, Q. Zhao, X. Quan, G. Chen, Novel phosphorus doped carbon nitride modified TiO₂ nanotube arrays with improved photoelectrochemical performance, *Nanoscale* 7 (2015) 16282–16289.
- [71] J. Liu, H. Wang, Z.P. Chen, H. Moehwald, S. Fiechter, R. van de Krol, L. Wen, L. Jiang, M. Antonietti, Microcontact-printing-assisted access of graphitic carbon nitride films with favorable textures toward photoelectrochemical application, *Adv. Mater.* 27 (2015) 712–718.
- [72] M. Yan, Y. Hua, F. Zhu, L. Sun, W. Gu, W. Shi, Constructing nitrogen doped graphene quantum dots-ZnNb₂O₆/g-C₃N₄ catalysts for hydrogen production under visible light, *Appl. Catal. B: Environ.* 206 (2017) 531–537.
- [73] M. Noh, F. Mohamad, M.F. Soh, M.A. Riza, J. Safaei, M. Nasir, N. Siti, M. Sopian, W. Norfaizatul, C.H. Teh, Effect of film thickness on photoelectrochemical performance of SnO₂ prepared via AACVD, *Phys. Status Solidi (B)* (2018) 1700570.
- [74] L. Jiang, X. Yuan, Y. Pan, J. Liang, G. Zeng, Z. Wu, H. Wang, Doping of graphitic carbon nitride for photocatalysis: a review, *Appl. Catal. B: Environ.* 217 (2017) 388–406.
- [75] Z. Wei, D. Benlin, Z. Fengxia, T. Xinyue, X. Jiming, Z. Lili, L. Shiyin, D.Y. Leung, C. Sun, A novel 3D plasmonic pn heterojunction photocatalyst: Ag nanoparticles on flower-like p-Ag₂S/n-BiVO₄ and its excellent photocatalytic reduction and oxidation activities, *Appl. Catal. B: Environ.* 229 (2018) 171–180.
- [76] H. Ullah, A.A. Tahir, T.K. Mallick, Structural and electronic properties of oxygen defective and Se-doped p-type BiVO₄ (001) thin film for the applications of photocatalysis, *Appl. Catal. B: Environ.* 224 (2018) 895–903.
- [77] J. Liu, Origin of high photocatalytic efficiency in monolayer g-C₃N₄/CdS heterostructure: a hybrid DFT study, *J. Phys. Chem. C* 119 (2015) 28417–28423.
- [78] M. Niu, D. Cheng, D. Cao, Understanding the mechanism of photocatalysis enhancements in the graphene-like semiconductor sheet/TiO₂ composites, *J. Phys. Chem. C* 118 (2014) 5954–5960.

[Article 4]

H. Ullah, A. A. Tahir, S. Bibi, T. K. Mallick, S. Z. Karazhanov, "Electronic properties of TaON and its surfaces for solar water splitting." *Appl. Catal., B: Environ.*, vol. 229, pp. 24-31, Aug. 2018.



Contents lists available at ScienceDirect

Applied Catalysis B: Environmental

journal homepage: www.elsevier.com/locate/apcatbElectronic properties of β -TaON and its surfaces for solar water splittingHabib Ullah^{a,*}, Asif A. Tahir^{a,*}, Salma Bibi^b, Tapas K. Mallick^a, Smagul Zh. Karazhanov^c^a Environment and Sustainability Institute (ESI), University of Exeter, Penryn Campus, Penryn, Cornwall TR10 9FE, UK^b National Centre of Excellence in Physical Chemistry, University of Peshawar, 25120 Peshawar, Pakistan^c Department for Solar Energy, Institute for Energy Technology, 2027 Kjeller, Norway

ARTICLE INFO

Keywords:

Photocarriers
 Periodic density functional theory
 Oxynitrides
 Water splitting
 Solar fuel

ABSTRACT

Recently, oxynitrides materials such as β -TaON has been using as a photoanode material in the field of photocatalysis and is found to be promising due to its suitable band gap and charge carrier mobility. Computational study of the crystalline β -TaON in the form of primitive unit cell, supercell and its N, Ta, and O terminated surfaces are carried out with the help of periodic density functional theory (DFT). Optical and electronic properties of all these different species are simulated, which predict TaON as the best candidate for photocatalytic water splitting contrast to their Ta₂O₅ and Ta₃N₅ counterparts. The calculated bandgap, valence band, and conduction band edge positions predict that β -TaON should be an efficient photoanodic material. The valence band is made up of N 2p orbitals with a minor contribution from O 2p, while the conduction band is made up of Ta 5d. Turning to thin films, the valence band maximum; VBM (−6.4 eV vs. vacuum) and the conduction band minimum; CBM (−3.3 eV vs. vacuum) of (010)-O terminated surface are respectively well below and above the redox potentials of water as required for photocatalysis. Charge carriers have smaller effective masses than in the (001)-N terminated film (VBM −5.8 and CBM −3.7 eV vs. vacuum). However, due to wide band gap (3.0 eV) of (010)-O terminated surface, it cannot absorb visible wavelengths. On the other hand, the (001)-N terminated TaON thin film has a smaller band gap in the visible region (2.1 eV) but the bands are not aligned to the redox potential of water. Possibly a mixed phase material would produce an efficient photoanode for solar water splitting, where one phase performs the oxidation and the other reduction.

1. Introduction

Solar fuel (H₂) is generated by photocatalytic water splitting when sunlight irradiates on a suitable semiconducting material [1–3]. Such catalytic materials should be robust, corrosion resistive and efficient light harvesters [4]. Since the discovery of photocatalytic water splitting by Honda and Fujishima [5], the use of many semiconducting materials and transition metal oxides in particular have been explored in the search for photon-energy conversion. Photocatalysts drive the dissociation of water by coupling this to the photo-excitation of electrons [6,7], and an ideal material must have a narrow band gap corresponding to the absorption of visible light and band edge positioned appropriately, so, that the valence band maximum (VBM) is more negative than the redox potential for oxidation of water (−5.7 eV vs. vacuum) and the conduction band minimum (CBM) more positive than the redox potential for reduction of water (−4.5 eV vs. vacuum). Some semiconductors have band edges positioned appropriately aligned with the redox potentials of water but they are either unstable or have large band gaps. Others have narrow band gaps but one of the band edges

(VBM or CBM) is aligned unsuitably (Scheme 1) [8].

Oxynitrides have recently attracted much attention [9–15] while transition metal oxide semiconductors are also suitable candidates as photocatalysts for storable fuels because of their low cost, nontoxicity, abundance, and high corrosion resistance [16–18]. They have low efficiencies due to their poor carrier conductivity and generally have large bandgaps [19]. To reduce the band gap, many methods have been tried, including defect formation and doping by cations and anion [20,21]. Incorporation of N is also a promising way as the N 2p states are energetically shallower than the deeper O 2p orbitals [22]. Generally, the CBM of a transition metal oxynitride is mainly formed from the empty metal orbitals while the VBM of oxynitrides are shifted to more negative energy by N 2p mixed states [23,24]. Thus the band gaps of oxynitrides can be narrower than those of the corresponding metal oxides [21,22]. Recently, Cui et al. and Respinis et al. have comprehensively investigated the electronic structures and photocatalytic activities of tantalum-based compounds such as Ta₂O₅, TaON, Ta₃N₅, and shown that the TaON exhibit visible-light photocatalytic activity since they have smaller band gaps compared to common oxides [25,26].

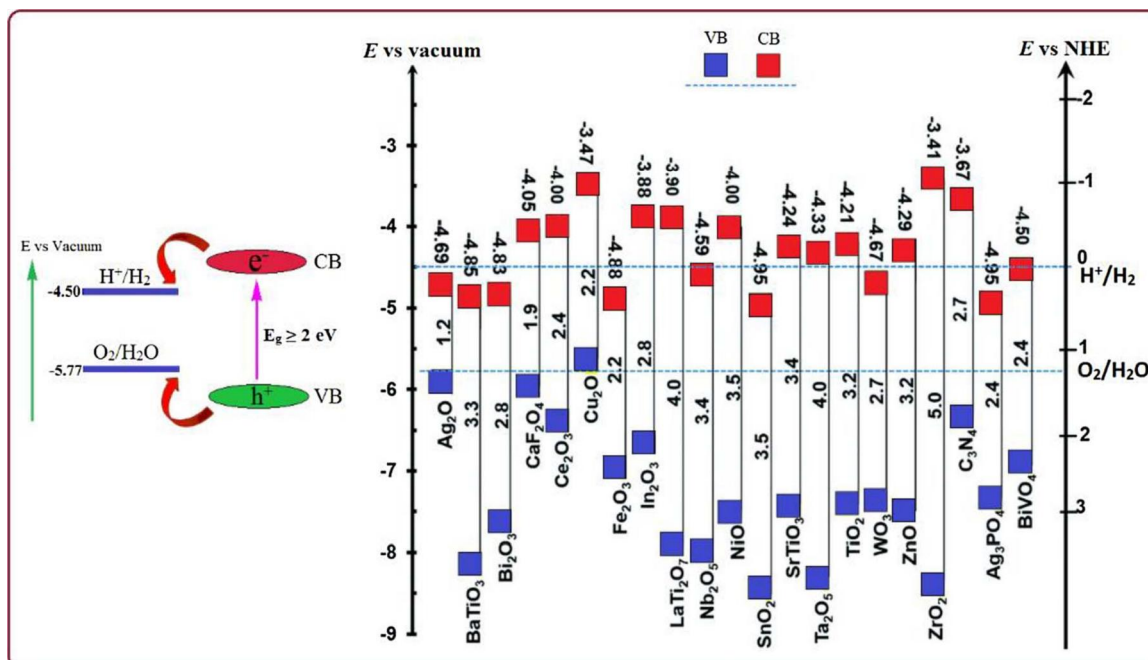
* Corresponding authors.

E-mail addresses: hu203@exeter.ac.uk (H. Ullah), A.Tahir@exeter.ac.uk (A.A. Tahir).<https://doi.org/10.1016/j.apcatb.2018.02.001>

Received 11 December 2017; Received in revised form 30 January 2018; Accepted 1 February 2018

Available online 05 February 2018

0926-3373/ © 2018 The Author(s). Published by Elsevier B.V. This is an open access article under the CC BY license (<http://creativecommons.org/licenses/by/4.0/>).



Scheme 1. VBM and CBM positions of selected semiconductors at pH 0 with respect to vacuum and normal hydrogen electrode (NHE) levels (in unit of eV): The redox potential of water is shown in blue solid and dotted lines.

Tantalum oxynitride (TaON) is one promising material as a photoanode for solar water splitting but works under external applied bias. Moreover, it has been reported that suitable energy of valence and conduction band edges of TaON make it an electrode material for both water oxidation and reduction, and a narrow band gap of ~ 2.4 eV allows absorption of visible light [16,27,28]. However, the photocatalytic activity of TaON is still limited, due to self-deactivation upon irradiation, conversion of TaON to Ta₂O₅, high exciton binding energy, and ultra-fast electron-hole recombination [27,29].

In this work, we employ first principle periodic density functional theory (DFT) simulations to examine the optical and electronic properties of β -TaON. TaON exists in three different polymorphs, a hexagonal α -TaON phase, monoclinic β -TaON, and a metastable γ -TaON phase [30,31]. The α -TaON polymorph, with 9-fold metal coordination, adopts the cotunnite structure [32]. Another TaON polymorph, γ -TaON, having a monoclinic crystal structure [30,33]. The archetypal oxynitride of tantalum, β -TaON has the baddeleyite structure in which the Ta coordination number is seven and an ordered O/N anionic sub lattice. β -TaON is thermodynamically the most stable (up to 800 °C) polymorph of TaON [34]. We consider bulk β -TaON and its six different slabs such as (001)-N, (010)-N, (001)-O, (010)-O, (001)-Ta, and (010)-Ta. Among all these slabs, the (010)-O and (001)-N terminated surfaces were found to be suitable ultra-thin films for solar water splitting applications. Finally, we examined water adsorption on these selected films because of their potential as water splitting photocatalyst.

2. Computational details

First principle DFT calculations were performed using Quantum Espresso [35] and QuantumWise-ATK [36] and the results are visualized using Virtual NanoLab Version 2017.1 [37]. β -TaON (hereafter denoted as TaON) has a monoclinic structure in the $P2_1/C$ space group [33]. The primitive unit cell contains 12 atoms and the initial crystal structure parameters in our calculations are taken from experimental data (Table S1) [38]. After optimizing the lattice parameters of the unit cell, a $(2 \times 2 \times 2)$ supercell was constructed. (010) and (001) slabs for each O, N, and Ta atoms were built by cleaving appropriately the 2×2 supercell of TaON. For the slab model calculations of surface energies

and band edge positions, the thickness of the slabs were four primitive unit cells of TaON (5 \AA thick, having 48 atoms), to ensure that the centre of the slab can be regarded as the bulk phase. Lattice parameters of all these stoichiometric slabs are given in Table S2 of the Supporting Information. A vacuum space of about 15 \AA was incorporated between slabs, to eliminate the fictitious interaction between periodically repeating slabs. Generalized gradient approximation (GGA) with the Perdew-Burke-Ernzerhof (PBE) exchange-correlation functional and double Zeta Polarized (DZP) basis set is used for the structural and energy optimization due to its superiority over hybrid pseudopotentials [39]. Moreover, linear combination of atomic orbitals (LCAO) method is used for Ta, N, H, and O atoms [40]. A $9 \times 9 \times 9$ Monkhorst-Pack k-grid and energy cutoff of 900 eV is used for the unit cell and supercell of TaON while a $9 \times 9 \times 1$ k-point mesh is used for the slabs. A complicated issue is the choice of appropriate basis and exchange-correlation function in DFT. Both the local density approximation (LDA) and GGA generally suffer from a large underestimation of bandgaps, while, meta-GGA can produce accurate values [41,42]. Hence meta-GGA is used for the band gap simulations in the Truhlar Blaha exchange functional and the correlation functional of Perdew-Zunger (LDA) in the form of TB09LDA [42]. Density of states (DOS), partial density of states (PDOS), band structure and effective masses of photogenerated electrons and holes are calculated. The DFT occupied and unoccupied DOS are considered as the VB and CB edges, respectively; separated by an energy equal to the known optical band gap [43]. The absorption spectra are calculated from the dielectric constant and plotted as a function of the wavelength, using TB09LDA [42].

3. Results and discussion

3.1. Selection of slabs and theoretical method

Geometries of unit cell, supercell, and slabs are optimized prior to their electronic and optical properties simulation. The crystal structure of unit cell is compared with the available crystallographic parameters of TaON (Fig. 1 and Table S1). PBE/GGA reproduces the experimental data accordingly as can be seen from Table S1 [38]. Moreover, we have also simulated the per atom cohesive formation energy of Ta, O, and N

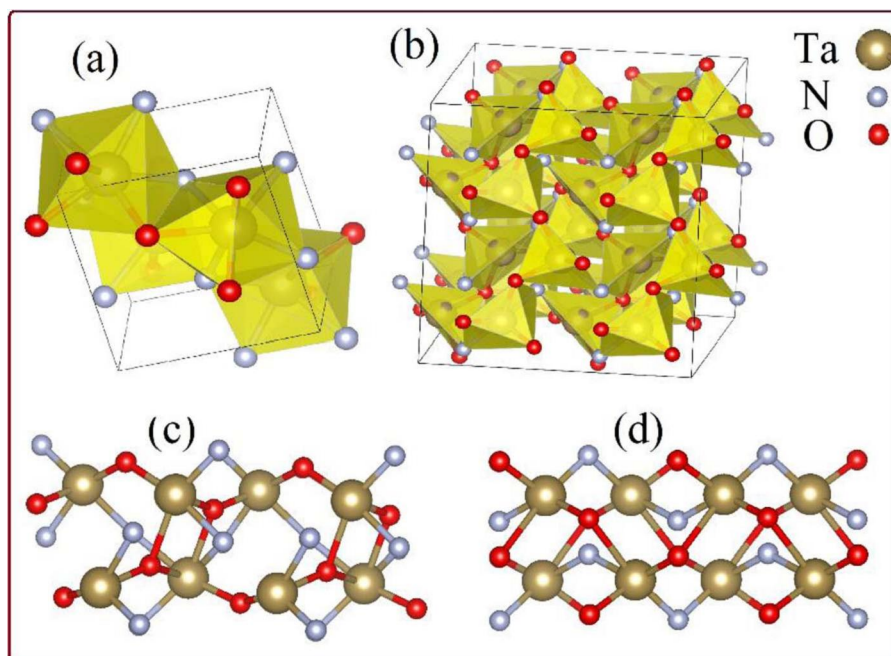


Fig. 1. Optimized Crystal structure of unit cell (a), supercell (b), N-terminated (c), and O-terminated (d) slab of TaON.

which has validated our computational method (see Table S3). The cohesive formation energy of Ta, at GGA/PBE using DZP basis set is 10 eV/atom and has nice correlation with the experimental reported one (8.10 eV/atom) [44]. The simulated cohesive formation energy of O and N are 3.7 and 3.1 eV/atom while their experimental values are 2.60 and 4.91 eV/atom, respectively [44].

The calculated band edge, band gap and formation energy of these six different slabs are listed in Table S4, where the (010)-O and (001)-N terminated surfaces have suitable VB, CB, band gap and formation energies, to be used for water splitting applications. Some of these slabs are either unstable or have inappropriately VB and CB positions, as can be seen from Table S4. So, we restrict our simulations to these two phases of TaON which are given in Fig. 1. These surfaces are constructed without any dipole; means the top and bottom layers were kept similar. The surface formation energy of these slabs was calculated using Eq. (1),

$$E_{\text{surf}} = \frac{1}{2A}(E_{\text{slab}} - NE_{\text{bulk}}) \quad (1)$$

where E_{slab} is the total energy of the slab, E_{bulk} is the energy per atom of the bulk, N denotes the number of atoms in the surface slab, and A is the cross-sectional area of the surface slab unit cell.

3.2. Electronic properties of TaON bulk

Using meta-GGA, the band structures and DOS/PDOS are calculated from the optimized crystal structures and shown in Fig. 2. The DOS of TaON bulk in the energy region between -10 and $+10$ eV is given in Fig. 3 where the Fermi energy (4.60 eV) is set to zero. The occupied Ta 5d band is lower in energy than to the N 2p and O 2p bands, resulting in an N 2p valence band and Ta 5d conduction band with a band gap of 2.44 eV.

Considering the PDOS of TaON, the top of valence band (VB) mainly consists of bonding N 2p states along with some contribution from O 2p states and a minor contribution from the bonding, Ta 5d states (Fig. 2). These orbitals of N 2p, O 2p, and Ta 5d states lead to a strong hybridization which respectively occupy the upper and lower part of the valence band, form the bonding states in this energy region. The middle of the VB contains Ta 5d hybridized with N and O 2p while the lowest energy edge of the VB has an increased contribution from O 2p mixed

with N 2p (Fig. 2). The CB of TaON bulk is mainly composed of the anti-bonding Ta 5d states along with a minor contribution from O and N 2p states. In this regard, the anti-bonding states in the conduction band of TaON is almost (totally) constituted by the electronic states of Ta atoms. Moreover, from the PDOS of TaON, it can be analyzed that there is no hybridization between the orbitals of these three different atoms in its conduction band region (Fig. 2a). The lower region of the CB is equally contributed by the 2p states of O and N which evidences their strong overlapping in form of hybridization.

To understand the individual fundamental electronic structure of the occupied and unoccupied states, within the VB and CB of TaON; they are given in Fig S1. From Fig S1 and Scheme S1, the contribution of N, O, and Ta both in the VB and CB can be clearly visualized.

Band structures of the primitive unit cell and supercell (bulk) of TaON are given in Fig S2 and Fig. 3, respectively. TaON has an indirect band gap (2.42 eV) which changes to direct (2.44 eV), considering the supercell ($2 \times 2 \times 2$) as can be seen from its band structure (Fig. 3). This band gap changes from the indirect to direct is because of the geometric change, as the computational settings are effectively different in these two calculations.

The theoretical band gap is also checked from the DOS plot as given in Fig. 2a. The direct band gap is due to the electronic excitation of an electron from the $\Gamma \rightarrow \Gamma$. More clearly, a direct band gap is characterized by having the band edges aligned in the similar k-space so, that an electron can transit from the valence to the conduction band, with the emission of a photon, without changing considerably the momentum. On the other hand, in the indirect band gap, the band edges are not aligned so, the electron does not transit directly to the conduction band where both photon and phonon are involved. At the Fermi energy of 4.60 eV, the vacuum phase VBM and CBM values are ca. -6.54 and -4.10 eV, respectively. Both the VBM and CBM are well below and above the redox potential of water (Scheme 1). Moreover, our computed band gap (2.44 eV) has nice correlation with that of the experimental (~ 2.40 eV) [28,45]. Furthermore, our simulated Fermi energy, VB and CB has also excellent correlation with the experimental work of Chun et al. [28], where the Fermi energy level is -4.41 eV, VB -6.45 eV and CB -4.10 eV (see Table 1). This nice correlation between the experimental and our theoretical data validate and confirm the method used.

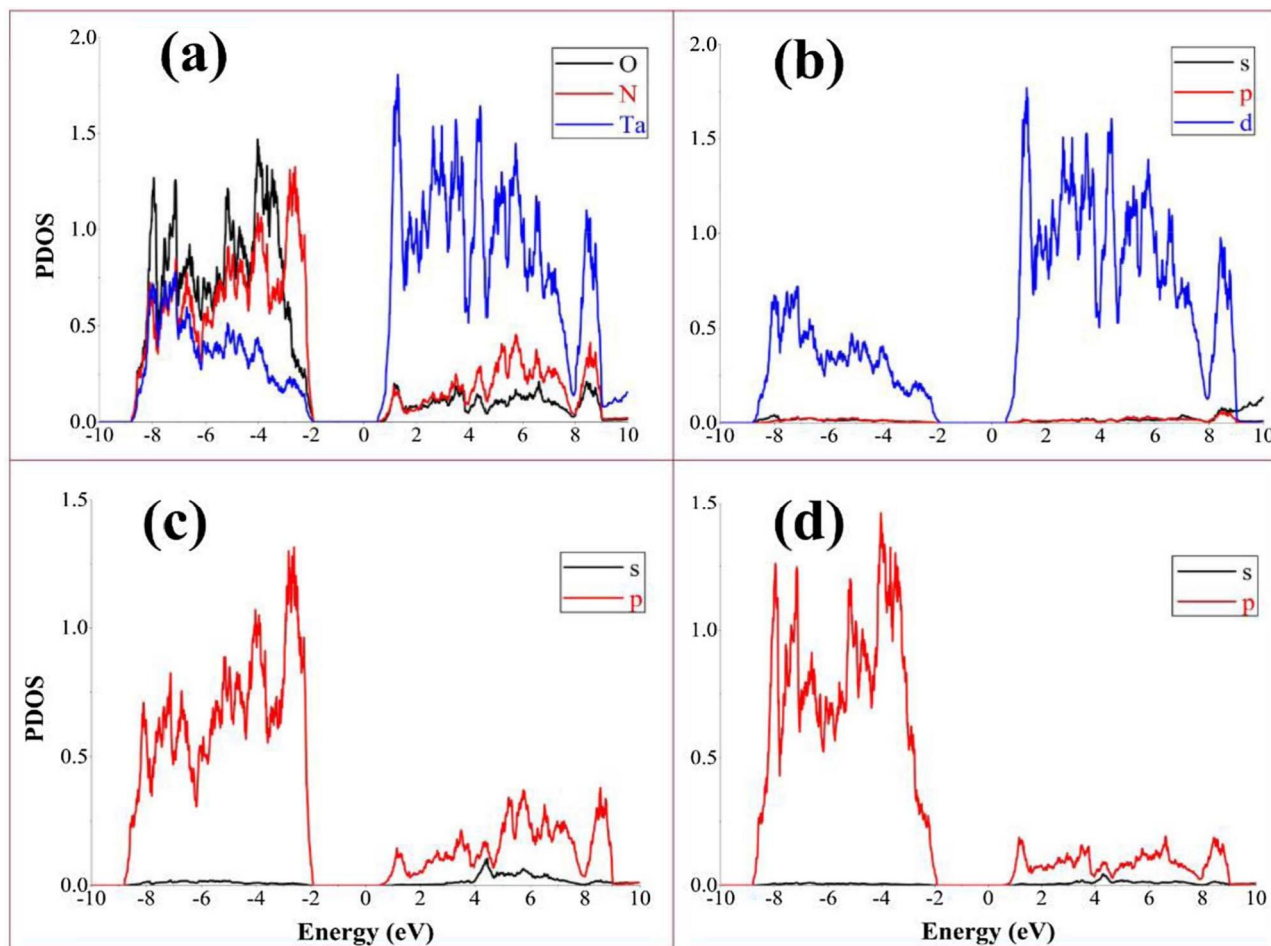


Fig. 2. PDOS of TaON bulk (a), Ta (b), N (c), and O PDOS (d); the Fermi Energy is set to zero.

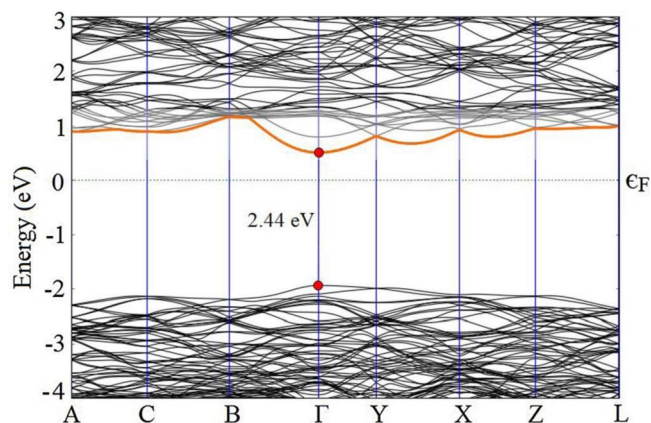


Fig. 3. Band Structure of the $2 \times 2 \times 2$ supercell of TaON; the Fermi Energy is set to zero.

3.3. Electronic and optical properties N terminated TaON(001) surface

The simulated PDOS of the N terminated TaON(001) surface is given in Fig. 4, where the VBM and CBM positions are located at -0.61 and $+1.50$ eV, respectively. The Fermi energy is set to zero which is 5.16 eV. The occupied band (-7.0 to -0.61 eV) which lie below the Fermi energy level is dominated by the $2p$ orbitals of N along with an equal contribution from $5d$ of Ta and $2p$ of O atoms (Fig. 4a). While its CBM is dominated by $5d$ of Ta with no contribution from either O or N orbitals. In case of water interacted systems; the VBM is constituted by N $2p$ and with an equal hybridized contribution of Ta $5d$ and O $2p$ orbitals. Again, the CBM is made of Ta atom but at a higher potential (2.46 eV compared to 1.50 eV) and with minor contribution of anti-bonding orbitals of O and N atoms (Fig. 4b). Hydrogen of water has slight contribution in the lower energy region of VBM as can be seen from Fig. 4b. At vacuum phase, the VBM and CBM of N terminated TaON(001) are situated ca. -5.77 and -3.66 eV, respectively (Table 1).

Table 1

Fermi Energy level, VBM, and CBM at vacuum level, Band Gap (in unit of eV), Effective Masses of Photogenerated Electrons and Holes; Estimated from the calculated Band Structure along the suitable direction.

Species	Surface atoms	Fermi level	m_e^*/m_0 (m_e)	m_h^*/m_0 (m_e)	VBM	CBM	Band gap
TaON	Bulk	-4.60	0.85	0.82	-6.54	-4.10	2.44
TaON(001)	N*	-5.16	0.81	3.99	-5.77	-3.66	2.11
TaON(001)@H ₂ O	~	-5.01	1.49	3.46	-5.64	-2.55	3.09
TaON(010)	O	-5.78	0.67	1.63	-6.36	-3.34	3.02
TaON(010)@H ₂ O	~	-4.83	0.72	1.64	-5.42	-2.24	3.18

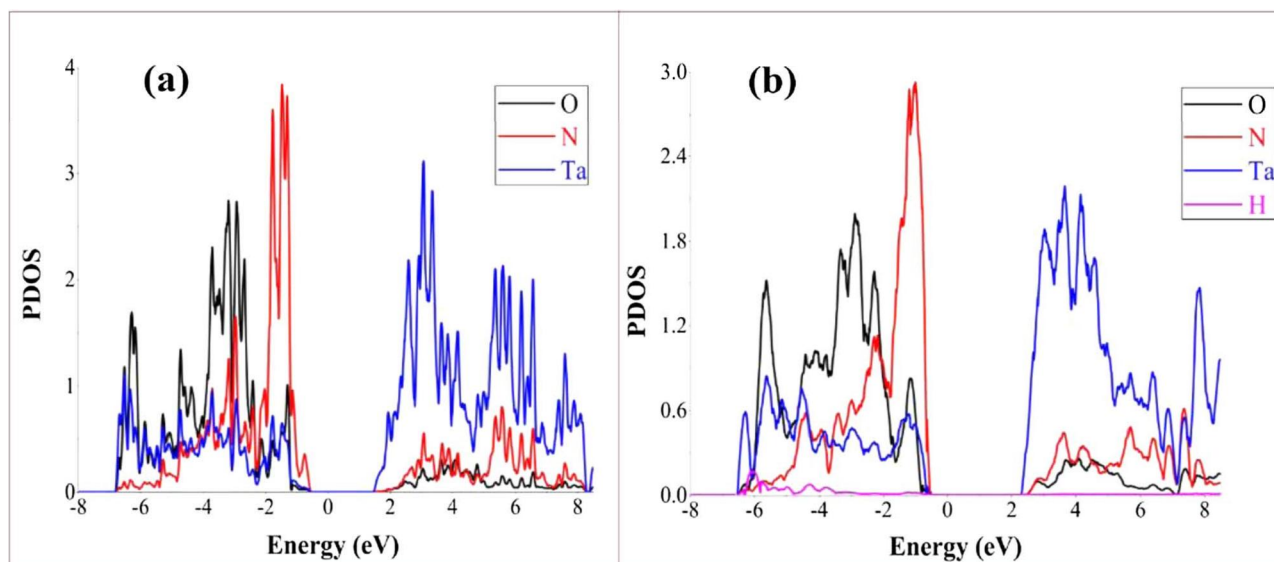


Fig. 4. PDOS of N-TaON(001), (a) and N-TaON(001)@H₂O, (b); the Fermi energy is set to zero.

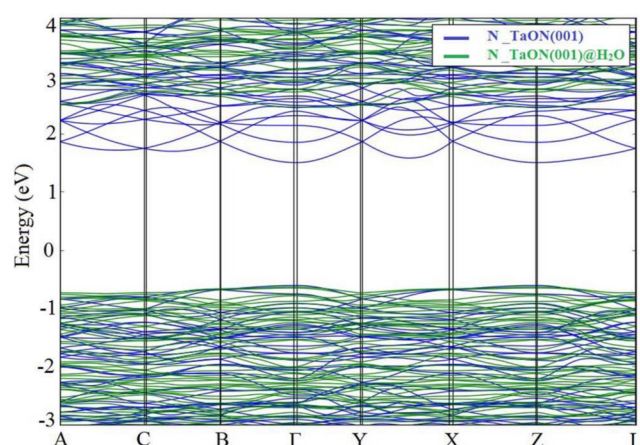


Fig. 5. Comparative band structures of N terminated TaON(001) and TaON(001)@H₂O; Fermi Energy is set to zero.

The simulated band structure of pristine N terminated TaON(001) is given in Fig. 5, having band gap of 2.11 eV. Upon adsorption of water molecule, its band gap elongates to 3.09 eV which is due to the reduction nature of H₂O. This band gap difference of 0.98 eV is because of the shifting of CBM towards more positive potential (2.46 eV) as can be seen from Figs. 4 and 5. The effective mass of photogenerated electrons and holes is an important parameter which determines the charge recombination rate. The quantum efficiency of a photocatalytic reaction is directly dependent on the relative transfer rate of photogenerated electrons to holes and whether these recombine or dissociate. When light irradiates on a photoactive material, it generates coulombically bound electron-hole pairs. The transfer rate of the photogenerated electrons and holes can be directly evaluated from their effective masses, using Eq. (2).

$$v = k/m^* \quad (2)$$

where m^* represent the effective mass of charge carrier, k is the wave vector and v is the transfer rate of photogenerated electrons and holes.

To investigate the photocatalytic activity of TaON, the effective mass of electrons (m_e^*) and holes (m_h^*) along the appropriate directions k-points are calculated by fitting parabolas on a 1 meV region for the bottom of the CBM or the top of the VBM, respectively and using Eq. (3):

$$m^* = \hbar^2 (d^2 E/dk^2)^{-1} \quad (3)$$

where \hbar is the reduced Planck constant, E is the energy of an electron at wave vector k in the same band (VBM or CBM). The estimated effective masses of electrons and holes for the different systems considered in this paper are listed in Table 1.

The adsorption of water molecule is non-dissociative where H of water interacts with the N and O of TaON(001) slab. The adsorption energy of these non-covalent bondings is about -118 kJ mol^{-1} (Table 2). The water adsorption energies were calculated by subtracting the energies of the optimized water molecule and adsorbent bare slab (E_{slab}) from the optimized water-slab complex (slab@water), using Eq. (4).

$$\Delta E_{\text{ad}} = E_{\text{slab@water}} - (E_{\text{water}} + E_{\text{slab}}) \quad (4)$$

As we know, these photogenerated electrons and holes thermally relax to the bottom of the conduction band and the top of the valence band, respectively so, that is why these regions are considered. The simulated values of the effective masses of photogenerated electrons and holes for the N-TaON(001) are 0.81 and $3.99 m_e$, respectively. On interaction with H₂O molecule the effective mass of electrons and holes change to 1.49 and $3.46 m_e$, respectively.

To further elaborate the interaction of water molecule on the N terminated TaON(001) surface, UV-vis absorption spectra are simulated which is given in Fig. 6. Pristine N-TaON(001) give rise to λ_{max} of 442 nm which became blue shifted (367 nm) when water is adsorbed. In summary, N-TaON(001) surface has good interaction ability towards H₂O besides its non-suitable VBM position (-5.77 eV vs vacuum). However, it can absorb the visible part of solar irradiation as can be seen from Fig. 6. The water adsorption over N-TaON(001) surface can also be visualized from its electron localization plot (Fig. 7).

3.4. Electronic and optical properties O terminated TaON(010) surface

The PDOS of O terminated TaON(010) is given in Fig. 8a, where the VBM and CBM are located at -0.58 and 2.44 eV , respectively (at Fermi

Table 2
Adsorption Energy of Water with the N and O terminated surfaces of TaON.

Species	Surface atoms	Adsorption Energy (kJ/mol)
TaON(001)@H ₂ O	N	-118
TaON(010)@H ₂ O	O	-148

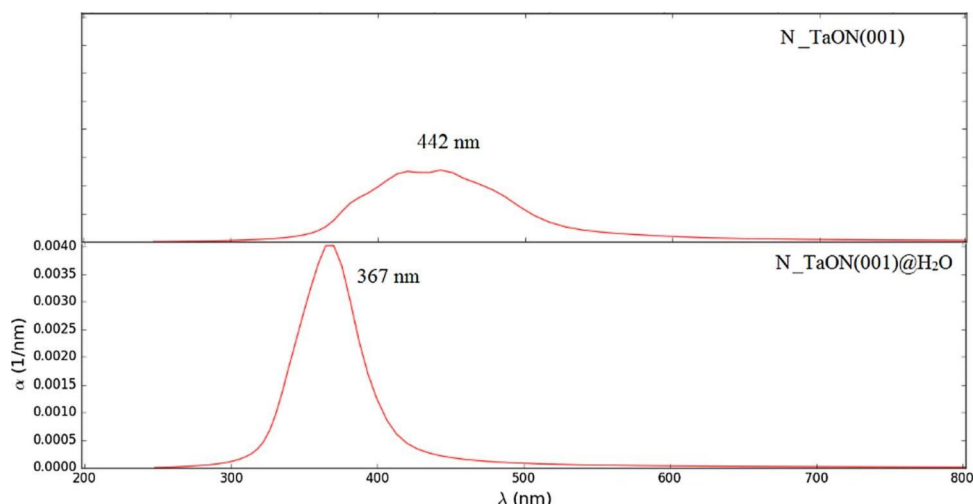


Fig. 6. UV-vis absorption spectra of N terminated TaON(001) and TaON(001)@H₂O.

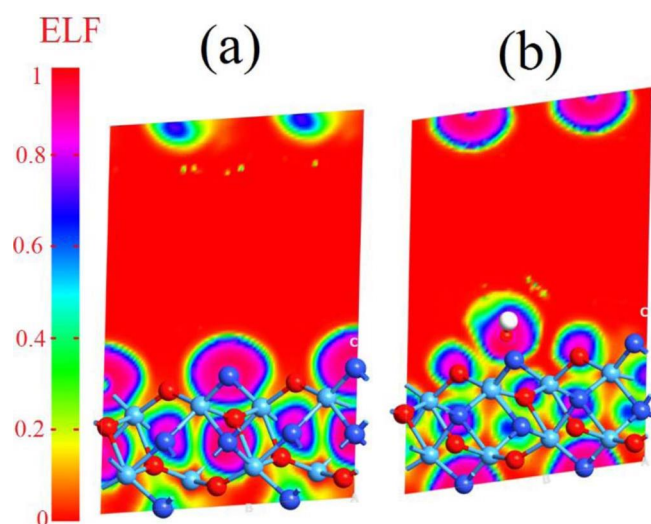


Fig. 7. Electron localization function map of (a) N-TaON(001) and (b) N-TaON(001)@H₂O.

energy of 5.78 eV). The PDOS of O-TaON(010) depicts that the VBM is located at -0.58 eV (-6.36 eV vs vacuum), having major contribution of N 2p along with minor participation of Ta 5d, and O 2p orbitals (Fig. 8a.) This behaviour is consistent with its respective bulk. The

electronic states of unoccupied band of O-TaON(010) are calculated in the range, $+2.44$ to $+10$ eV, where the CB edge is constituted by the anti-bonding orbitals of Ta 5d, along with almost no contribution of N 2p and O 2p orbitals. The whole CB of O-TaON(010) is uniformly made from the anti-bonding orbitals of Ta 5d and is situated (-3.34 eV vs vacuum) at well above the redox CBM level of water (Scheme 1). The bottom section of CB is equally contributed by the hybridized orbitals of 2p of N and O (Fig. 8a). On adsorption of water molecule, the CBM move towards more positive potential which results a wide band gap compared to parent slab (Fig. 8b).

The CBM of O-TaON(010) moved from 2.44 to 2.59 eV when water molecule is adsorbed on its surface, as can be clearly seen from their comparative band structures (Fig. 9). Analysis of Figs. 8 and 9 led us to conclude that the band gap of O-TaON(010) increases from 3.02 to 3.18 eV upon adsorption of H₂O. Furthermore, to check the photocatalytic efficiency of this surface, effective masses of photogenerated electrons and holes are estimated from its band structure. The effective masses of electrons and holes of parent O-TaON(010) are 0.67 and 1.63 m_0 , respectively which increase when water is adsorbed, as can be seen from Table 1.

As discussed earlier, O-TaON(010) surface has an ideal VBM and CBM positions along with small effective masses of electron and hole. However, due to its large band gap (3.01 eV) it cannot easily absorb the visible part of sun light as can be seen from its UV spectra (Fig. 10). A blue-shifting in λ_{max} is observed when H₂O is presents on the surface of O-TaON(010). Water molecule has shifted the λ_{max} of O-TaON(010)

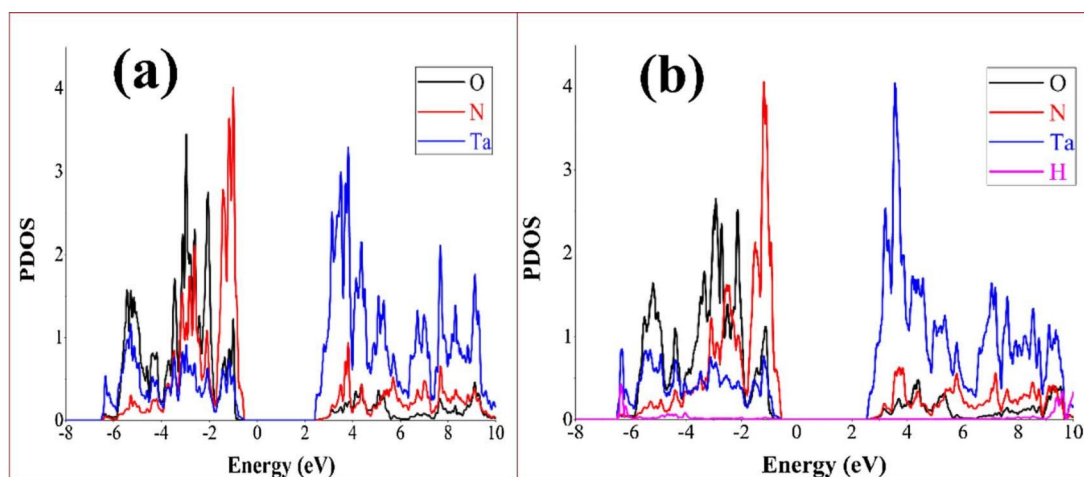


Fig. 8. PDOS of O-TaON(010), (a) and O-TaON(010)@H₂O, (b); Fermi energy is set to zero.

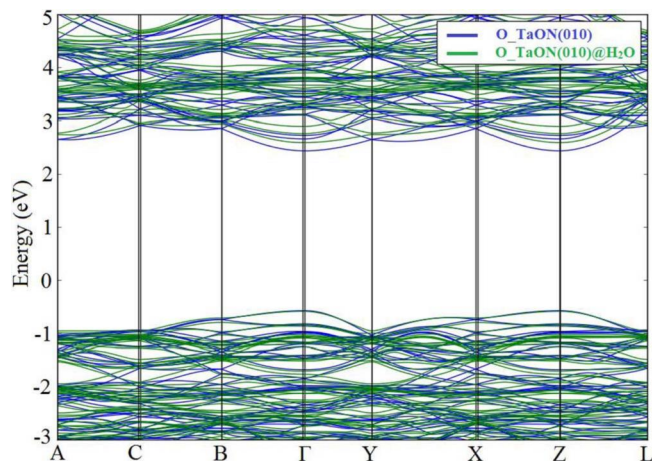


Fig. 9. Comparative band structure of O terminated TaON(010) and TaON(010)@H₂O; Fermi energy is set to zero.

from 368 to 332 nm which consequences its good adsorption capability. Moreover, this shifting in λ_{\max} (36 nm) strongly corroborates the previous characterizations such as effective masses of charge carriers and VBM and CBM positions.

An adsorption energy of -148 kJ mol^{-1} is observed between water molecule and O-TaON(010) surface. This non-dissociative high adsorption is because of H of water and O of slab along with contribution from the O of water and N of slab. Furthermore, this non-covalent interaction can also be seen from the electron localization function plots, given in Fig. 11.

4. Conclusion

Periodic density functional theory calculations for bulk and potential photoelectrode thin films of β -TaON are carried out considering N, Ta, and O terminations. We investigate their electronic and optical properties and photocarrier mobility. Firstly, the electronic properties of bulk β -TaON predict TaON is a better candidate for photocatalytic water splitting than either Ta₂O₅ or Ta₃N₅. The DOS and PDOS

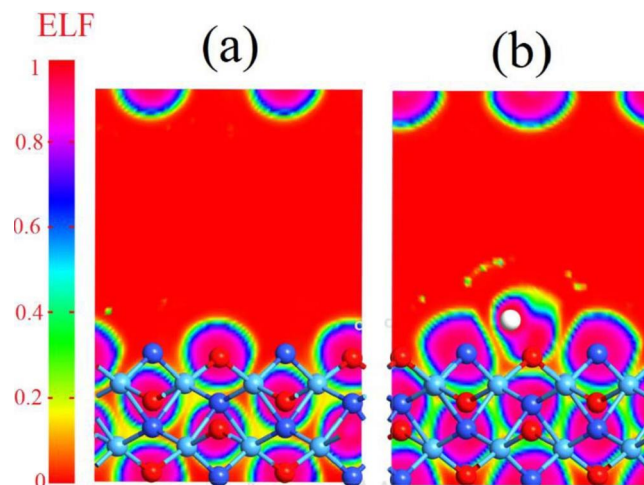


Fig. 11. Electron localization function map of O-TaON(010) and O-TaON(010)@H₂O.

simulation predict that valence band of all these studied systems is constituted by the 2p orbitals of N with a minor contribution of O 2p, while anti-bonding orbitals of 5d of Ta are responsible for the conduction band. We have simulated the effective masses of the photo-generated electrons and hole for the mentioned species. The large difference in the effective masses of electrons and hole are found which is a direct consequence of high charge dissociation instead of recombination. In summary, the oxygen and nitrogen terminated TaON along (010) and (001), respectively has good stability and sensitivity towards water molecule. Moreover, O terminated TaON has ideal band edge positions while N terminated has strong ability towards visible light absorption, so a mixed phase would result an efficient photoanode for water splitting. Furthermore, the development of effective dopants will be very crucial in improving the transport properties of the surface of TaON to further reduce the masses of photogenerated electrons and holes for high charge mobility rate.

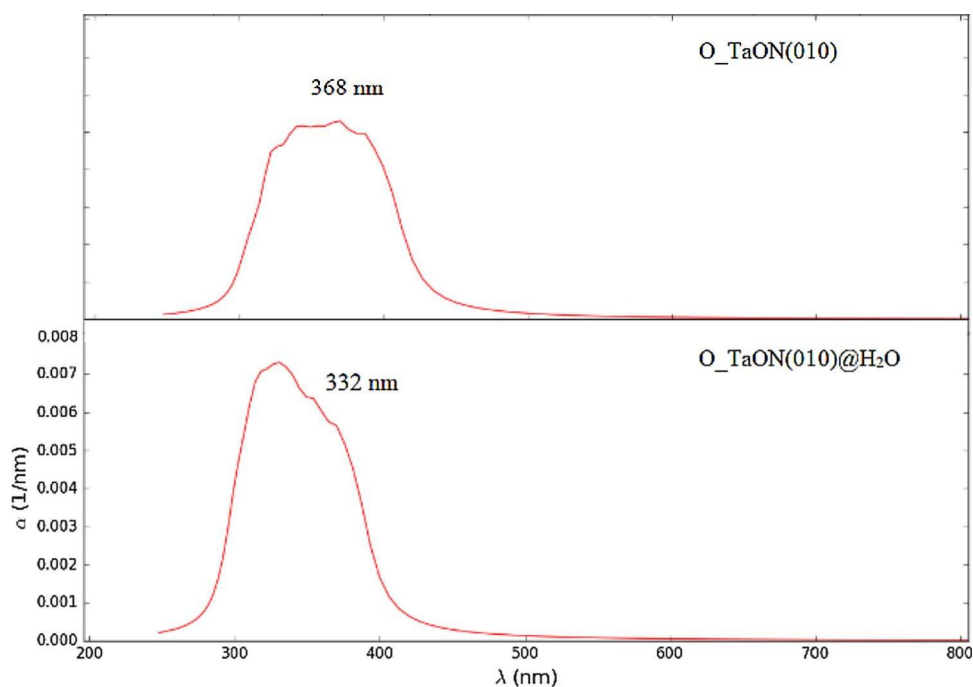


Fig. 10. UV-vis absorption spectra of O terminated TaON(010) and TaON(010)@H₂O.

Acknowledgments

We acknowledge the financial support of Engineering and Physical Science Research Council, UK (EPSRC) under the research grant Nos. EP/P510956/1, EP/P003435/1 and EP/R512801/1. S.K acknowledges the Notur Norwegian supercomputing facilities through project nn4608k and the HyMatSiRen project 272806 by the Research Council of Norway. We also acknowledge Prof. Neil Allan and Dr. Sergio C. Espindola for their help in completing this work.

Appendix A. Supplementary data

Table of crystallographic and simulated parameters, Schematic representation of VB and CB of TaON, band structure, and electron difference density plots of N₂ and O₂/TaON(010) along with water adsorbed systems are given in the supporting information.

Supplementary material related to this article can be found, in the online version, at doi:<https://doi.org/10.1016/j.apcatb.2018.02.001>.

References

- Y. Tachibana, L. Vayssieres, J.R. Durrant, Artificial photosynthesis for solar water-splitting, *Nat. Photon.* 6 (2012) 511–518.
- A.M. Hafez, A.F. Zedan, S.Y. AlQaradawi, N.M. Salem, N.K. Allam, Computational study on oxynitride perovskites for CO₂ photoreduction, *Energy Convers. Manage.* 122 (2016) 207–214.
- S.W. Boettcher, T.E. Mallouk, F.E. Osterloh, Themed issue on water splitting and photocatalysis, *J. Mater. Chem. A* 4 (2016) 2764–2765.
- S. Giménez, J. Bisquert, Photoelectrochemical Solar Fuel Production: From Basic Principles to Advanced Devices, Springer, 2016.
- A. Fujishima, K. Honda, Photolysis-decomposition of water at the surface of an irradiated semiconductor, *Nature* 238 (1972) 37–38.
- S. Sonoda, O. Kawasaki, J. Kato, M. Takenaga, photocatalyst material and photocatalyst device, (2016) US Patent 20,160,093,448.
- M. Fujihira, Introduction—solar to chemical energy conversion, *Solar to Chemical Energy Conversion*, Springer, 2016, pp. 1–3.
- J. Li, N. Wu, Semiconductor-based photocatalysts and photoelectrochemical cells for solar fuel generation: a review, *Catal. Sci. Technol.* 5 (2015) 1360–1384.
- R. Abe, M. Higashi, K. Domen, Facile fabrication of an efficient oxynitride TaON photoanode for overall water splitting into H₂ and O₂ under visible light irradiation, *J. Am. Chem. Soc.* 132 (2010) 11828–11829.
- C. Pan, T. Takata, M. Nakabayashi, T. Matsumoto, N. Shibata, Y. Ikuhara, K. Domen, A complex perovskite-type oxynitride: the first photocatalyst for water splitting operable at up to 600 nm, *Angew. Chem. Int. Ed.* 54 (2015) 2955–2959.
- J. Xu, C. Pan, T. Takata, K. Domen, Photocatalytic overall water splitting on the perovskite-type transition metal oxynitride CaTaO₂N under visible light irradiation, *Chem. Commun.* 51 (2015) 7191–7194.
- C. Pan, T. Takata, M. Nakabayashi, T. Matsumoto, N. Shibata, Y. Ikuhara, K. Domen, Innentitelbild: a complex perovskite-type oxynitride: the first photocatalyst for water splitting operable at up to 600 nm (*Angew. Chem.* 10/2015), *Angew. Chem.* 127 (2015) 2900.
- T. Takata, C. Pan, K. Domen, Recent progress in oxynitride photocatalysts for visible-light-driven water splitting, *Sci. Technol. Adv. Mater.* 16 (2015) 1468–6996.
- C. Pan, T. Takata, K. Domen, Overall water splitting on the transition-metal oxynitride photocatalyst LaMg_{1/3}Ta_{2/3}O₂N over a large portion of the visible-light spectrum, *Chem.-Eur. J.* 22 (2016) 1854–1862.
- S. Landsmann, A.E. Maegli, M. Trottmann, C. Battaglia, A. Weidenkaff, S. Pokrant, Design guidelines for high-performance particle-based photoanodes for water splitting: lanthanum titanium oxynitride as a model, *ChemSusChem* 8 (2015) 3451–3458.
- C. Zhen, R. Chen, L. Wang, G. Liu, H.-M. Cheng, Tantalum (oxy) nitride based photoanodes for solar-driven water oxidation, *J. Mater. Chem. A* 4 (2016) 2783–2800.
- S.S. Gujral, A.N. Simonov, M. Higashi, X.-Y. Fang, R. Abe, L. Spiccia, Highly dispersed cobalt oxide on TaON as efficient photoanodes for long-term solar water splitting, *ACS Catal.* 6 (2016) 3404–3417.
- Z. Zhao, Z. Wang, J. Bao, Nanomaterials for hydrogen generation from solar water splitting, *Nanomaterials for Sustainable Energy*, Springer, 2016, pp. 445–470.
- G. Hitoki, T. Takata, J.N. Kondo, M. Hara, H. Kobayashi, K. Domen, An oxynitride, TaON, as an efficient water oxidation photocatalyst under visible light irradiation ($\lambda \leq 500$ nm), *Chem. Commun.* (2002) 1698–1699.
- L. Lüdtkke, A. Schmidt, C. Göbel, A. Fischer, N. Becker, C. Reimann, T. Bredow, R. Dronskowski, M. Lerch, Synthesis and crystal structure of δ -TaON, a metastable polymorph of tantalum oxide nitride, *Inorg. Chem.* 53 (2014) 11691–11698.
- M. de Respini, M. Fravventura, F.F. Abdi, H. Schreuders, T.J. Savenije, W.A. Smith, B. Dam, R. van de Krol, Oxynitrogenography: controlled synthesis of single-phase tantalum oxynitride photoabsorbers, *Chem. Mater.* 27 (2015) 7091–7099.
- N.K. Allam, B.S. Shaheen, A.M. Hafez, Layered tantalum oxynitride nanorod array carpets for efficient photoelectrochemical conversion of solar energy: experimental and DFT insights, *ACS Appl. Mater. Interfaces* 6 (2014) 4609–4615.
- S. Balaz, S.H. Porter, P.M. Woodward, L.J. Brillson, Electronic structure of tantalum oxynitride perovskite photocatalysts, *Chem. Mater.* 25 (2013) 3337–3343.
- R. Sasaki, K. Maeda, Y. Kako, K. Domen, Preparation of calcium tantalum oxynitride from layered oxide precursors to improve photocatalytic activity for hydrogen evolution under visible light, *Appl. Catal. B: Environ.* 128 (2012) 72–76.
- Z.-H. Cui, H. Jiang, Theoretical investigation of Ta₂O₅, TaON, and Ta₃N₅: electronic band structures and absolute band edges, *J. Phys. Chem. C* 121 (2017) 3241–3251.
- M. de Respini, M. Fravventura, F.F. Abdi, H. Schreuders, T.J. Savenije, W.A. Smith, B. Dam, R. van de Krol, Oxynitrogenography: controlled synthesis of single-phase tantalum oxynitride photoabsorbers, *Chem. Mater.* 27 (2015) 7091–7099.
- P. Carvalho, J. Borges, M. Rodrigues, N. Barradas, E. Alves, J. Espinós, A. González-Elipe, L. Cunha, L. Marques, M. Vasilevskiy, Optical properties of zirconium oxynitride films: the effect of composition, electronic and crystalline structures, *Appl. Surf. Sci.* 358 (2015) 660–669.
- W.-J. Chun, A. Ishikawa, H. Fujisawa, T. Takata, J.N. Kondo, M. Hara, M. Kawai, Y. Matsumoto, K. Domen, Conduction and valence band positions of Ta₂O₅, TaON, and Ta₃N₅ by UPS and electrochemical methods, *J. Phys. Chem. B* 107 (2003) 1798–1803.
- C. Taviot-Guého, J. Cellier, A. Bousquet, E. Tomasella, Multiphase structure of tantalum oxynitride TaO_xN_y thin films deposited by reactive magnetron sputtering, *J. Phys. Chem. C* 119 (2015) 23559–23571.
- H. Wolff, T. Bredow, M. Lerch, H. Schilling, E. Irran, A. Stork, R. Dronskowski, A first-principles study of the electronic and structural properties of γ -TaON, *J. Phys. Chem. A* 111 (2007) 2745–2749.
- H. Schilling, A. Stork, E. Irran, H. Wolff, T. Bredow, R. Dronskowski, M. Lerch, γ -TaON: a metastable polymorph of tantalum oxynitride, *Angew. Chem. Int. Ed.* 46 (2007) 2931–2934.
- M.W. Lumey, R. Dronskowski, The electronic structure of tantalum oxynitride and the falsification of α -TaON, *Zeitschrift für anorganische und allgemeine Chemie* 629 (2003) 2173–2179.
- S. Yoon, A.E. Maegli, S.K. Matam, M. Trottmann, T. Hisatomi, C.M. Leroy, M. Grätzel, S. Pokrant, A. Weidenkaff, The influence of the ammonolysis temperature on the photocatalytic activity of β -TaON, *Int. J. Photoenergy* 2013 (2013).
- G. Brauer, J. Weidlein, Synthesis and properties of tantalum oxide nitride, TaON, *Angew. Chem. Int. Ed.* 4 (1965) 875.
- P. Giannozzi, S. Baroni, N. Bonini, M. Calandra, R. Car, C. Cavazzoni, D. Ceresoli, G.L. Chiarotti, M. Cococcioni, I. Dabo, QUANTUM ESPRESSO: a modular and open-source software project for quantum simulations of materials, *Phys. Condens. Matt.* 21 (2009) 395502.
- AtomistixToolKit, version 2017.1, QuantumWise A/S, (www.quantumwise.com).
- VirtualNanoLab, version 2017.1, QuantumWise A/S, (www.quantumwise.com).
- D. Armytage, B. Fender, Anion ordering in NaON: a powder neutron-diffraction investigation, *Acta Crystallogr. Sect. B: Crystallogr. Cryst. Chem.* 30 (1974) 809–812.
- A.H. Larsen, M. Vanin, J.J. Mortensen, K.S. Thygesen, K.W. Jacobsen, Localized atomic basis set in the projector augmented wave method, *Phys. Rev. B* 80 (2009) 195112.
- G. Kresse, D. Joubert, From ultrasoft pseudopotentials to the projector augmented-wave method, *Phys. Rev. B* 59 (1999) 1758.
- R. Peverati, D.G. Truhlar, Improving the accuracy of hybrid meta-GGA density functionals by range separation, *J. Phys. Chem. Lett.* 2 (2011) 2810–2817.
- J. Hafner, Materials simulations using VASP—a quantum perspective to materials science, *Comput. Phys. Commun.* 177 (2007) 6–13.
- J. Endres, D.A. Egger, M. Kulbak, R.A. Kerner, L. Zhao, S.H. Silver, G. Hodes, B.P. Rand, D. Cahen, L. Kronik, Valence and conduction band densities of states of metal halide perovskites: a combined experimental–theoretical study, *J. Phys. Chem. Lett.* 7 (2016) 2722–2729.
- C. Kittel, Introduction to Solid State Physics, Wiley, 2005.
- T.K. Ghosh, N.N. Nair, Nature of β -TaON surfaces at ambient conditions, *Surf. Sci.* 635 (2015) 19–26.

[Article 5]

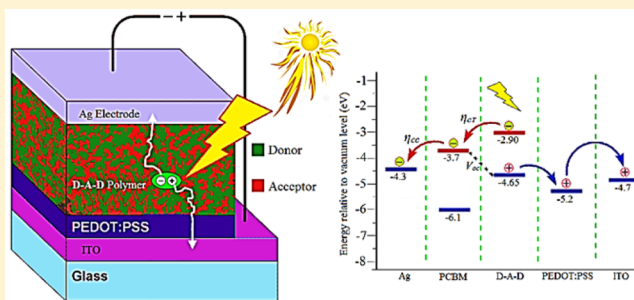
H. Ullah, S. Bibi, A. A. Tahir, T. K. Mallick, "Density functional theory study of selenium substituted low bandgap donor-acceptor-donor polymer." *J. Phys. Chem. C*. vol. 120, pp. 27200–27211, Nov. 2016.

Density Functional Theory Study of Selenium-Substituted Low-Bandgap Donor–Acceptor–Donor Polymer

Habib Ullah,^{*,†} Salma Bibi,[‡] Asif A. Tahir,^{*,†} and Tapas K. Mallick[†][†]Environment and Sustainability Institute (ESI), University of Exeter, Penryn Campus, Penryn, Cornwall TR10 9FE, United Kingdom[‡]National Centre of Excellence in Physical Chemistry, University of Peshawar, 25120 Peshawar, Pakistan

Supporting Information

ABSTRACT: Theoretical study of an optically transparent, near-infrared-absorbing low energy gap conjugated polymer, donor–acceptor–donor (D–A–D), 2,1,3-benzosele-nadiazole (A) as acceptor and 3,4-ethylenedioxy-selenophene (D) as donor fragments, with promising attributes for photovoltaic application is reported herein. The D and A moiety on the polymeric backbone has been found to be responsible for tuning the band gap, optical gap, open circuit (V_{OC}), and short-circuit current density (J_{SC}) in the polymers solar cells. D–A–D has a key role in charge separation and molecular architecture which ultimately influences the charge transport. Reduction in the band gap, high charge transformation, and enhanced visible light absorption in the D–A–D system is because of strong overlapping of molecular orbitals of D and A. The polaron and bipolaron effects are also investigated which has a direct relation with visible light photocurrent generation. In addition, the enhanced planarity and weak steric hindrance between adjacent units of D–A–D resulted in red-shifting of its onset of absorption. The simulated band gap of the D–A–D has excellent correlation with experimentally reported values for closely related systems, which validates the level of theory used. Finally, PSC properties of the designed D–A–D was modeled in the bulk heterojunction solar cell, which gives a theoretical V_{OC} of about 1.02 eV.



1. INTRODUCTION

Solar energy harvesting is one of the challenging tasks to current renewable energy scientists. Researchers are struggling to design a cheap, liable, elastic, and environmental friendly optoelectronic devices with high efficiency.^{1–4} Silicon-based materials are ideal in the current solar cells technology, but having a high cost and high operation temperature limits its portability and versatility.⁵ A step toward the development of low-cost, environmentally friendly, easily synthesizable, flexible, and efficient material for solar cells lead scientists to the use of conjugated organic polymers (COPs).^{4,6} COPs are emerging as promising materials due to their stability, low-cost processing, and ability to form tunable and robust structures. Four prominent generations of COPs are being explored by scientists, which has application in the field of solar to power energy conversion.^{7–11}

COPs have tunable band gap where one can precisely tune the desired band gap, HOMO, and LUMO energy levels during the synthesis, which directly affect the open circuit voltage (V_{OC}), charge transport (η_{CT}), and short-circuit current density (J_{SC}) in the polymer solar cell (PSC).⁴ Generally, a polymer with a band gap of more than 4 eV is considered to be an insulator while the underneath represents semiconducting nature.¹² Since the discovery of the conducting nature of polyacetylene (PA), researchers are working to minimize this

band gap.¹³ Many efforts are reported in this regard which are either copolymerization, composites, nanoparticles, or donor–acceptor copolymerization.¹⁴

The major issues with PSCs are their low efficiency in the photovoltaic devices which links to the incident photon to electron conversion. To date, the power conversion efficiency (PCE) of PSC has been enhanced up to 13.2%,^{15,16} means still large efforts are being required of making it acceptable all over the world. As explained elsewhere,⁴ the conduction mechanism of the PSC is also different from that of inorganic semiconductors. The other problem associated with the PSC is large exciton binding energy which requires the high energy of dissociation into electron and hole and thus results in less efficiency of the organic based PSC.¹⁷ Finally, COPs used in the PSC should have the ability to absorb the visible part of the solar spectrum (narrow band gap) and a well below HOMO energy level compared to the LUMO of phenyl-C₆₁-butyric acid methyl ester (PCBM), used in the bulk heterojunction.

COPs monomers such as 3,4-ethylenedioxythiophene (EDOT) and 3,4-ethylenedioxy-selenophene (EDOS) are working as a donor while 2,1,3-benzothiadiazole (BOD) and

Received: October 16, 2016

Revised: November 16, 2016

Published: November 18, 2016

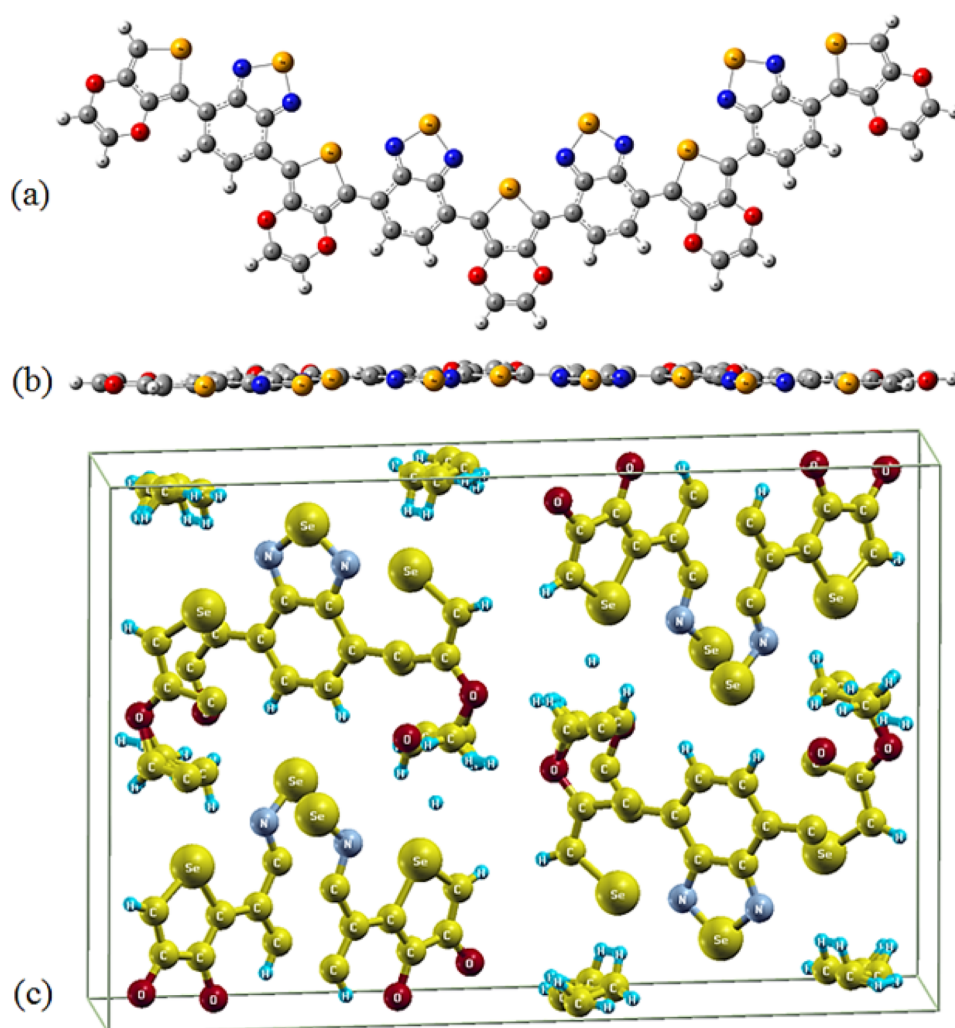


Figure 1. Optimized geometric structure of D-A-D (a) along with side view (b) and its crystal structure (c).

2,1,3-benzoselenadiazole (BSD) moieties act as an acceptor in the donor–acceptor combination (Scheme S1). The synthetic mechanism and electropolymerization of EDOS into poly 3,4-ethylenedioxysephenene (PEDOS) are given in Figure S1 and S2, respectively, while those of poly 3,4-ethylenedioxythiophene (PEDOT), poly 2,1,3-benzoselenadiazole (PBSD), and poly 2,1,3-benzothiadiazole (PBOD) can be found elsewhere.¹⁸

To overcome the challenges of PSC, a donor–acceptor approach has been used to efficiently tune the HOMO–LUMO levels and optical band gap.^{19–23} As we know, the processes are not so simple and require a lot of effort to get insight into the underlying phenomenon.¹⁷ The combination of the donor (electron donating species) and acceptor moieties (electron withdrawing) in a copolymer can tune the optical gap and efficiently harness the solar energy influx which is consequently responsible for the increase of J_{SC} . This would not simply solve our problem but band gap engineering of a polymer can lead to increase in the V_{OC} , followed by efficient exciton dissociation in the PSC.²⁴

The purpose of this work is to design and suggest such a polymer that can be used in the bulk heterojunction (organic solar cell), having enhanced V_{OC} , J_{SC} , and fill factor (FF).²⁵ In this work, we used a different conjugated organic monomer having a donor and acceptor nature which can give rise to a low band gap polymer with desired bandwidth positions. More

interestingly, these exciting materials are rarely investigated for solar to power energy conversion and have not been simulated to design an efficient PSCs. Finally, this theoretical investigation will minimize the synthetic effort for the future experimentalists.

2. COMPUTATIONAL METHODOLOGY

Both molecular and periodic boundary condition's (PBC) simulations of the donor, acceptor, and their combinations have been carried out on Gaussian 09²⁶ and Quantum Espresso,²⁷ respectively, while visualizations are achieved on *Gabedit*,²⁸ QuantumWise,²⁹ and GaussView.³⁰ Electronic structure properties of n BSD, n EDOS, and their co-oligomeric combination in the form of n EDOS-BSD (where $n = 1, 2, 3, \dots, \text{infinity}$) are carried out with the help of density functional theory (DFT) at the hybrid functional of the B3LYP/6-31G** level of theory. The oligomeric chain length of 9BSD (A), 9EDOS (D), and 9EDOS-BSD (D-A-D) represent their polymeric nature very well; therefore, calculations are restricted to nine repeating units. The D-A-D crystal with an orthorhombic structure in the *Pbcn* (60) space group with 204 atoms, having lattice constants $a = 4.4551 \text{ \AA}$, $b = 15.982 \text{ \AA}$, and $c = 23.91 \text{ \AA}$, are used for the PBC simulations. PBC/DFT simulations at generalized gradient approximation (GGA) with a Perdew–Burke–Ernzerhof (PBE) exchange–correlation functional with a double

zeta polarized basis set is performed for the structural and energy optimization due to its superiority over other pseudopotentials. Monkhorst–Pack k-grid of $9 \times 9 \times 9$ and energy cutoff of 400 eV is used in these simulations. The B3LYP hybrid pseudopotential is employed for the optical properties simulations of **D-A-D**. From computational and accuracy points of view, TD-DFT is optimistic between semiempirical and wave function approaches.^{31–33} TD-DFT calculations can incorporate environmental effects and quickly give best quantitative fit to UV–vis spectra (excitation energy) of these species, especially using hybrid functionals (B3LYP).^{33–35} In the case of approximate DFT, negative orbital energies (HOMO and LUMO) do not give accurate ionization potentials (IP) and electron affinities (EA), but the deviation is about 1 eV. Since the error is method dependent and consistent for all oligomers, orbital energies can be still used to examine trends consistently.^{36–48}

Furthermore, to verify our computational method, oligomeric properties of these species are extrapolated to the polymer using second order polynomial fit eqs (Table S1–S3). Bendikov et al. have extensively studied this group of polymers both experimentally and theoretically and confirmed the superiority of the B3LYP/6-31G** level of theory over other methods.^{16,49–52} Our simulated results also have a nice correlation with the experimental data as can be seen from Table S4, so that is why the current level of theory is employed for the rest of the simulations.^{18,52}

Key parameters of the photovoltaic system such as reorganization energy (λ), polaron, bipolaron, UV–vis spectra, and exciton binding energy (E_b) are also simulated with said level of theory. The stability, perturbation in electroactivity, and conductivity upon mixing of donor and acceptor species are estimated from the energy of HOMO, LUMO, and band gap. The electrons and holes carrying nature are simulated from the reorganization energy and also from the contours of HOMO and LUMO, respectively. UV–vis, UV–vis-near IR spectra, and an optical gap of the **D-A-D** are simulated, using the TD-B3LYP/6-31G** level of theory.

3. RESULTS AND DISCUSSION

3.1. Optimized Geometries. Planarity in molecular geometry and the corresponding π -electrons conjugation over the backbone play an important role in the visible light absorption of a chemical substance. Optimized molecular and crystal structure of **D-A-D** are given in Figure 1. An ideal 180° dihedral angle (Table 1) of the **D-A-D** shows that the

Table 1. Dihedral Angles between the Neighboring Rings of **D**, **A**, and **D-A-D**

no.	Φ_1	Φ_2	Φ_3	Φ_4	Φ_5	Φ_6	Φ_7	Φ_8
D	179	180	179	179	179	179	180	179
A	146	148	147	149	147	149	147	148
D-A-D	180	180	180	180	180	180	180	180

combination of donor and acceptor moieties has planarized the geometry of the resulting polymer via establishing a delocalized π -electronic cloud density over the backbone. This intrachain dihedral angle (180°) of the **D-A-D** is responsible for its low cost and straightforward synthetic approach. This statement is also inconsistent with the recently reported work.^{16,49–52}

The dihedral angles in the intramolecular rings of **D** are also near to planarity; however, in the case of **A** this is about 146° .

The deviation in **A** from 180° is due to the internal steric hindrance of N atoms of the adjacent rings of benzo selenadiazole, causing them to be out of the plane as well. This out of the plane behavior of the benzo selenadiazole rings in the polymeric body may be responsible for the high resistance in delocalization of the electron cloud density (Figure 2).

3.2. Electronic Prosperities. Charge transformation and the localized and delocalized nature of the electronic cloud density of these three different oligomers are estimated from their frontier molecular orbitals, as the electronic cloud density over the HOMO predict holes and LUMO determines the possibility of the electron. The greater the delocalization of the charge density, the higher the electron/hole mobility will be, and vice versa. HOMO and LUMO of **D**, **A**, and **D-A-D** are comparatively given in Figure 3 while their orbital correlation diagram is shown in Figure 4. Molecular orbitals energy of small oligomers of these species, from monomers up to infinite chain length, are simulated and listed in Table S1–3 of the Supporting Information.

Comparative analysis of the data of Table 2 and a visual look of the contours of HOMO and LUMO (Figure 3) predict that excited state properties in **D-A-D** are optimum compared to their individuals' **D** and **A** species. The data shown in Table 2 are specifically for the nine repeating units; however, the rest of the oligomeric species is given in the Supporting Information. Variation in characteristic properties is very common in short oligomers, but beyond the seven or eight repeating units, they remain almost constant. The purpose of other repeating units is to provide a range of entities which may be useful as a guideline for other experimentalists, as short oligomers are more electroactive but tricky to synthesize.

Our simulated HOMO, LUMO, and band gap values has excellent correlation with the recently reported data.¹⁸ Excited state properties of the different oligomers of **D-A-D**, estimated from the frontier molecular orbitals, give a clue of the free availability of π -electrons over its conjugated body (Figures 3 and S1). These molecular orbital overlapping in the **D-A-D** (delocalized π -electrons) provides an easy pathway for the motion of free electrons which make it an excellent transparent material in the visible region of solar light (vide infra).

The electrical band gap (estimated from the HOMO–LUMO difference) of the isolated **D** (2.42 eV) and **A** (2.22 eV) provide the evidence of their absorption in the green region of the visible spectrum. Prominent near-IR absorption (red regions of the visible spectrum) by the **D-A-D** can be correlated with its band gap of 1.75 eV. Simulated band gaps of the **D**, **A**, and **D-A-D** are comparatively shown in Figure 4. The band gap reduction in all the resulted co-oligomers of **D-A-D** (Figure S3–6) highlights the importance of two opposing species in a single junction. The band structure of **D-A-D** is also obtained from the PBC simulations and has a good correlation with the molecular one, as given in Figure 5. The purpose of the PBC simulated band gap of **D-A-D** is to clarify and confirm our level of theory used.

3.3. Reorganization Energy. Reorganization energy (λ) is directly associated with the geometrical distortion of a chemical substance when it changes from neutral to cationic state. This energy is responsible for an electron to be excited from its ground state potential, charge carrier, and related geometrical distortion which may be either polaron or bipolaron. Moreover, hole mobility in an organic semiconductor can be understood in terms of its reorganization energy; the lower the

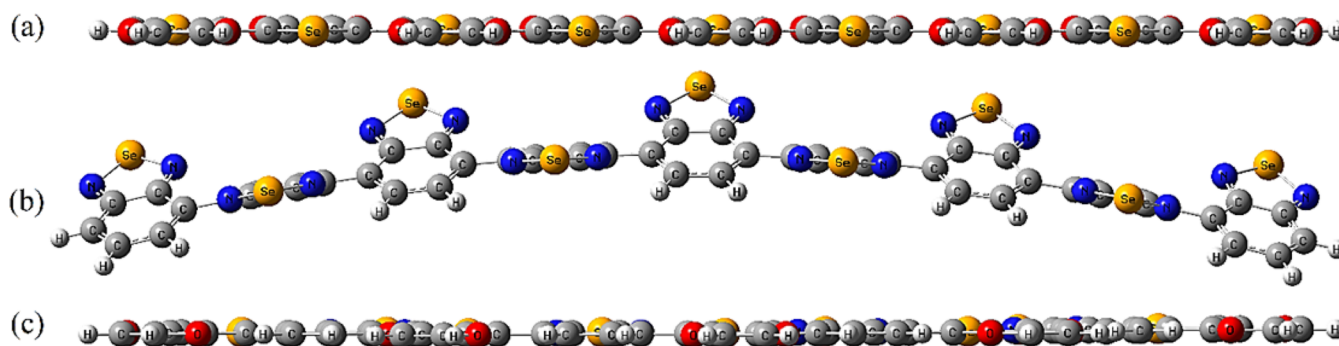


Figure 2. Optimized geometric structures of D (a), A (b), and D-A-D (c).

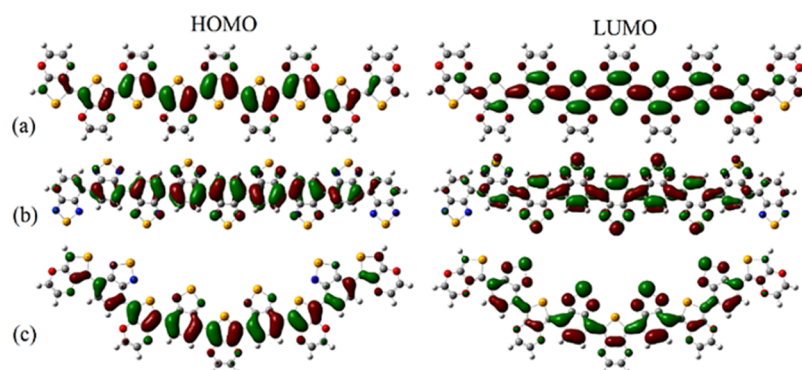


Figure 3. Contours of the HOMO and LUMO of D (a), A (b), and D-A-D (c).

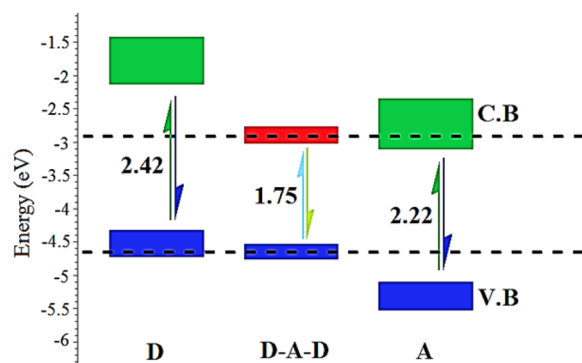


Figure 4. Orbital correlation diagram for D, D-A-D, and A.

Table 2. HOMO, LUMO, Band Gap, Optical Gap, Exciton Binding, and Reorganization Energy in eV of the Studied Species at the B3LYP/6-31G** Level of Theory

no.	HOMO	LUMO	band gap	optical gap	E_b	λ
D	-4.44	-2.02	2.42	2.04	0.38	0.22
A	-5.22	-2.99	2.22	1.85	0.37	0.16
D-A-D	-4.65	-2.90	1.75	1.46	0.29	0.20

reorganization energy, the faster will be hole transformation and vice versa. The internal reorganization energies of an oligomer decrease with chain length elongation which is due to the greater positive charge (π -electrons) delocalization over the oligomeric backbone. The internal reorganization energy of A, D, and D-A-D are simulated, using the adiabatic potential energy surface method with eq 1 (Table 2).

$$\lambda = \lambda_1 + \lambda_2 = (E_0^* - E) + (E_+^* - E_+) \quad (1)$$

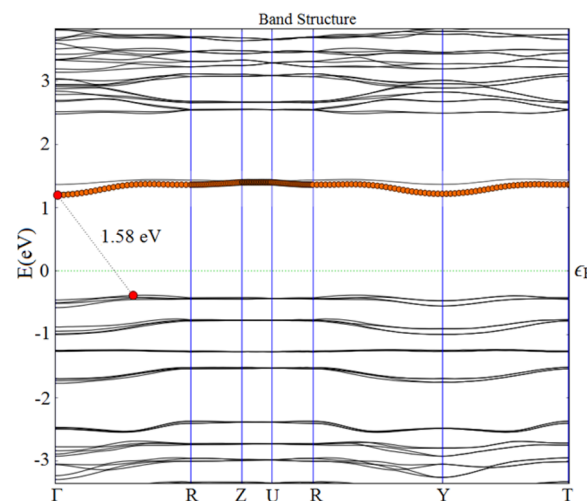


Figure 5. Band structure of D-A-D.

The E_0 and E_+ are the energies of neutral and cationic species in their lowest energy geometries and E_0^* and E_+^* represent the energy of a neutral molecule at the geometry of charged molecule and charged molecule at the geometry of the neutral molecule.

The reorganization energy of D is 0.22 eV which is a little higher than that of A (0.16 eV) while that of D-A-D has a λ of 0.20 eV. Comparative analysis of the reorganization energies of these three different species (Table 2) led us to conclude that geometrical distortion in A is quite easy, but on the other hand its exciton binding (0.37 eV) is higher because of its electron accepting nature. So, D-A-D has an optimum reorganization energy compared to the isolated D, and A but a much lower E_b (0.29 eV) which ultimately easily separate the electron-hole

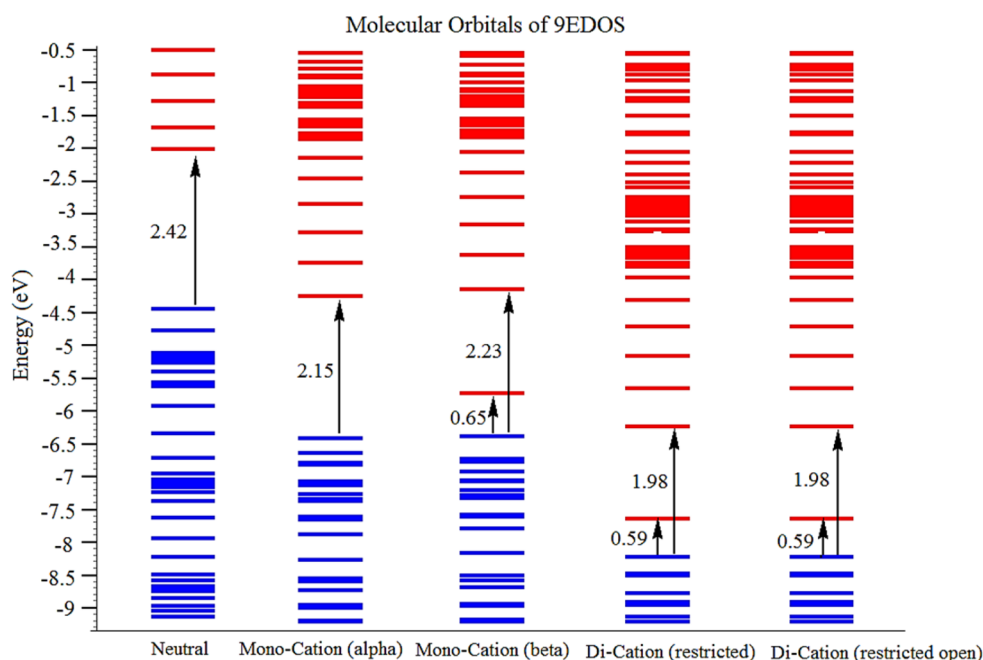


Figure 6. Energy level diagram of the neutral, mono, and dicationic state of D.

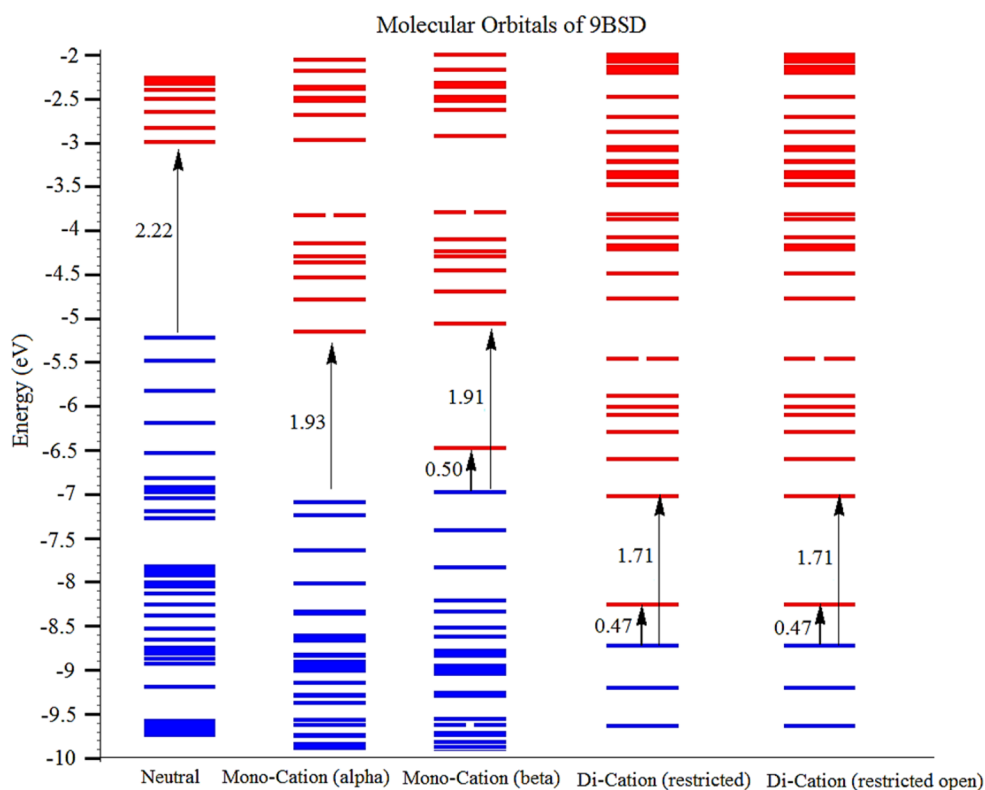


Figure 7. Energy level diagram of the neutral, mono, and dicationic state of A.

pair upon visible light irradiation. Moreover, we also compared our simulated λ to the already reported hole transporting organic semiconducting materials.^{53,54} These hole transporting materials such as *N,N'*-diphenyl-*N,N'*-bis(3-methylphenyl)-(1,1'-biphenyl)-4,4'-diamine has 0.33 eV,⁵⁵ ((*N,N'*-bis(2,4-dimethylphenyl)-*N*-(4'-((2,4-dimethylphenyl) (phenyl)amino)-[1,1'-biphenyl]-4-yl)-*N'*-phenyl-[1,1'-biphenyl]-4,4'-diamine has 0.23 eV, 4-(4-phenyl-4- α -naphthylbutadienyl)-*N,N'*-di(4-tolyl)-phenylamine has 0.24⁵³ and silole-based organic

semiconductors has 0.50 eV⁵⁴ internal reorganization energy. So, it is verified that **D-A-D** has a better hole transferability due to lower reorganization energy which may be correlated to its fully planar geometrical structure with an ideal dihedral of 180°.

3.4. Polaron, Bipolaron, and Exciton Binding Energy.

It is generally believed that PSCs require well-controlled movement of charges for efficient photon conversion.⁵⁶ In conjugated polymers, usually polaronic and bipolaronic states

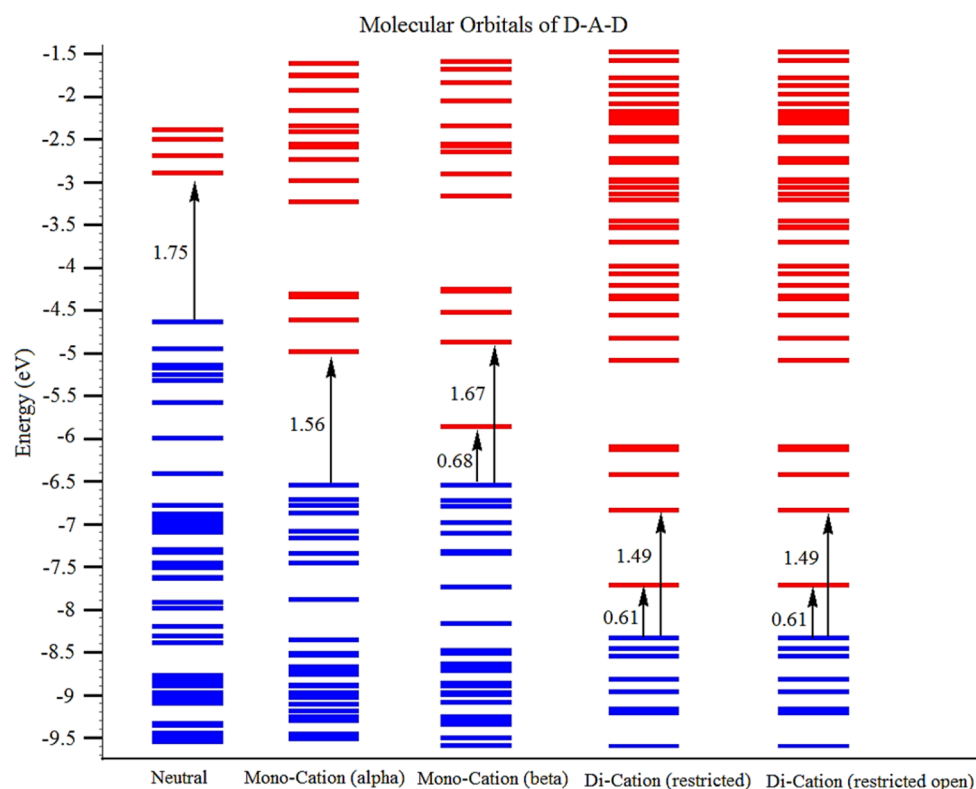


Figure 8. Energy level diagram of the neutral, mono, and dicationic state of D-A-D.

appear within the parent band gap⁵⁷ upon doping with appropriate doping agents. These are the key tools for charge storage and charge transportation in COPs. Charge and the associated distortion along the backbone of COP create either polaron or bipolaron. Single charge and the associated distortion are termed as polaron (delocalized state), denoted as E_p while a pair of charges and their distortion in the polymeric body is regarded as bipolaron. Bipolarons states are comparatively stable, localized and less electroactive to that of polarons. Donation of charge by a particular conjugated system is followed by intramolecular relaxation which can be precisely called as polaronic effect. Polaron-binding energy can be easily obtained from the reorganization energy (λ) using an expression such as $E_p = (1/2 \lambda)$. On the other hand, exciton binding energy or an electron–hole binding energy is the amount of that barrier (Coulombic energy) with which the lowest unoccupied orbital accepts an extra electron and left behind the occupied orbital as degenerate. We have simulated the exciton binding energy (E_b) from the energy difference of neutral exciton and the two free charge carriers, using an expression such as $E_b = E_{\text{Band gap}} - E_{\text{Optical gap}}$.

Molecular orbital energy diagram of the neutral, cationic, and dicationic states of D is depicted in Figure 6, where orbital transition along with energy is clearly shown. Band gap and exciton binding energy of D in its neutral state are 2.42 and 0.38 eV, respectively. Monocationic state in the unrestricted formalism and in the absence of counterion is considered to efficiently explore the polaronic effect. Removal of an electron from the oligomeric backbone of D induces an extra band within its parental band gap, regarded as interband. Monocationic state not only reduces the band gap (2.23 or 2.15 eV) of parent D by lowering the HOMO and LUMO energy levels but also increases the delocalization over the polymeric backbone (Figure S7). The delocalization over the

oligomeric body of monocationic state can be seen from the nondegenerate molecular orbitals, termed as Alpha and Beta (Figure 6) or polaron. However, restricted and unrestricted formalisms of the Kohn–Sham orbitals have a similar effect on the molecular orbital distribution of dicationic state in D. Dicationic state of D, creates a bipolaronic state as can be seen from its degenerate frontier molecular orbitals (Figure 6). This degenerate state in the highly cationic state is not only responsible for reducing the band gap but promotes stability compared to that of the polaronic state.

A similar trend in the molecular orbital distribution of A is observed upon making its cationic and dicationic states, as shown in Figure 7. Band gap of the acceptor species in the neutral state is found to be 2.22 eV while the Coulombic force which holds the electron–hole pair is 0.37 eV. The frontier molecular orbital cloud densities of the neutral, cationic, and dicationic states are given in Figure S8 of the Supporting Information.

The combination of the D and A moieties in the oligomeric form such as D-A-D has much stretched down the HOMO and LUMO energy levels which result in a band gap of 1.75 eV. Analysis of the contours of HOMO and LUMO (Figure S9) of D-A-D reflect an evidence of strong overlapping of the D and A orbitals. Keeping in mind the exciton binding energies of D and A, this donor–acceptor combination has considerably lowered the E_b (0.29 eV). So, this lower exciton binding energy and narrow band gap are clear indications for the charge separation (electron–hole pair) at the donor–acceptor interface (here acceptor is the PCBM in the PSC device) and high short-circuit current density, respectively (vide infra).

The simulated narrow band gap (1.75 eV) of the D-A-D has a good correlation with the experiment, which strongly validates the level of theory we used.¹⁸ To further validate the electronic properties of the designed polymer, cationic and

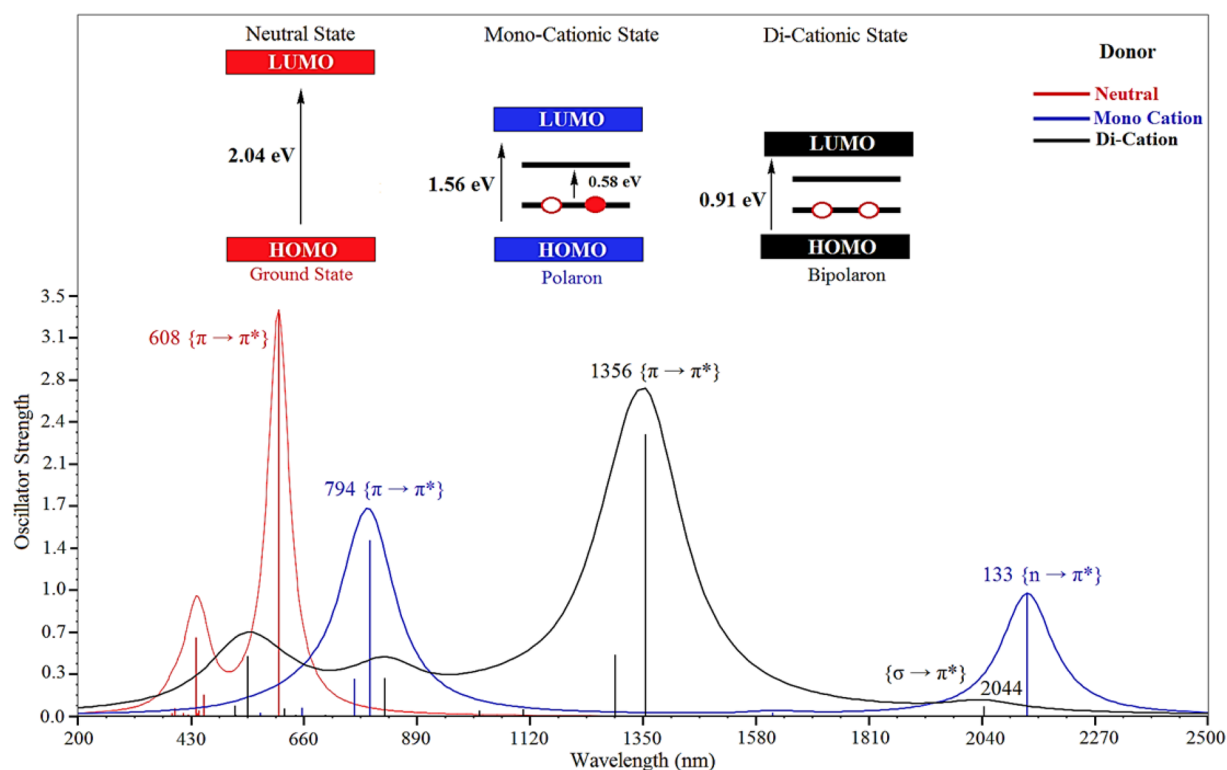


Figure 9. UV-vis spectra along with optical band gaps of neutral, mono, and dicationic states of D at B3LYP/6-31G**.

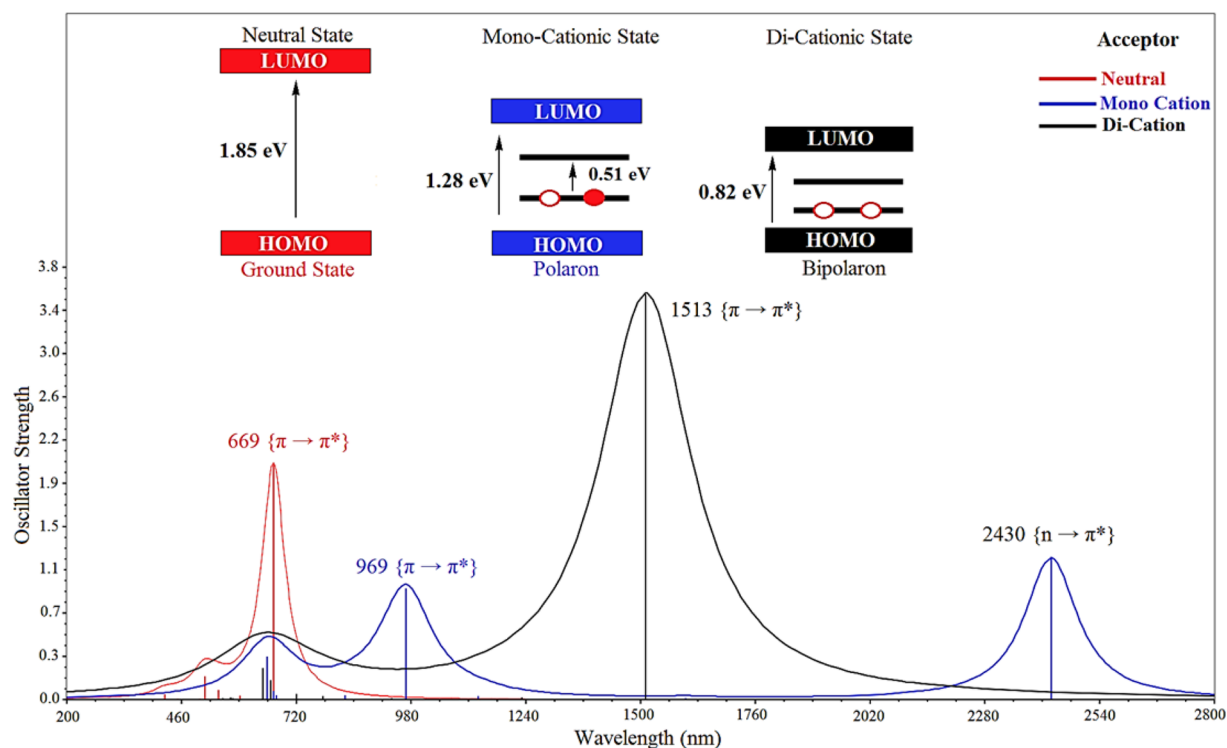


Figure 10. UV-vis spectra along with optical band gaps of the neutral, mono, and dicationic states of A at B3LYP/6-31G**.

dicationic states are considered, upon removal of one and two electrons in the absence of counterions, respectively. Oxidation causes a reduction in the band gap from 1.75 to 1.56 eV (considering the Alpha orbitals) and 1.75 to 1.67 eV on considering the Beta orbital distributions. As explained earlier, a cation along with associated distortion produces a non-

degenerate state: polaron (Figure 8). Further oxidation of the D-A-D species (extraction of a pair of electrons) in the absence of counterions results in a bipolaronic state over the π -conjugated backbone which further reduces the orbitals band gap to 1.49 eV. The bipolaronic state creates an extra band, called interband transition, which arises from the $\sigma \rightarrow \pi^*$

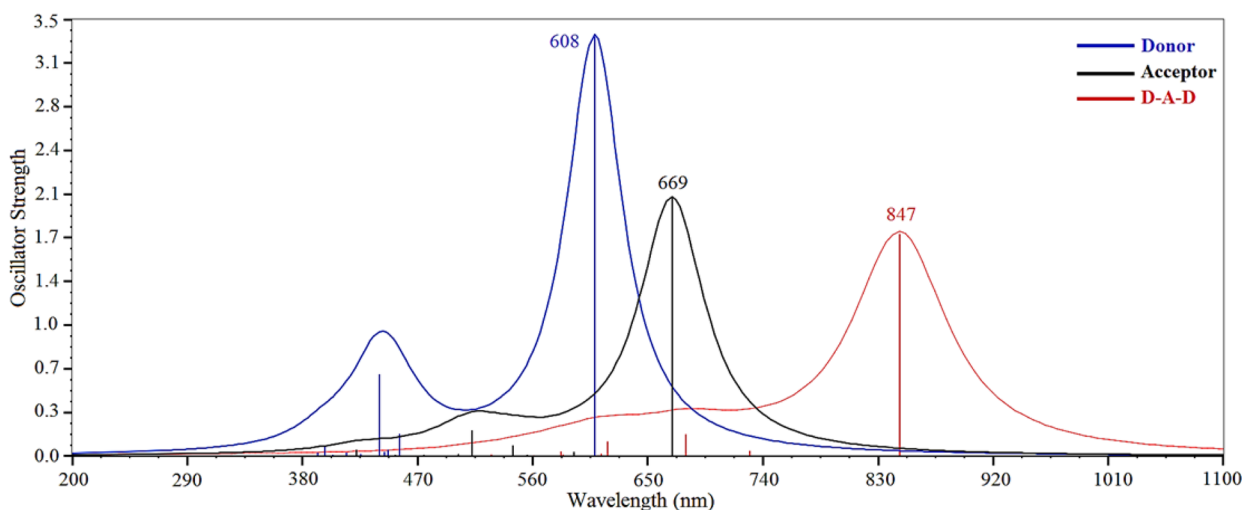


Figure 11. UV-vis spectra of A, D, and D-A-D at B3LYP/6-31G**.

orbital transition and has an energy of 0.61 eV. As explained earlier, the stability of bipolaron over the polaron is due to these degenerate molecular orbitals. Moreover, restricted and unrestricted formalism has a similar effect in the dicationic states.

3.5. UV-vis and UV-vis-Near-IR Absorption Spectral Analysis. UV-vis and UV-vis-near-IR absorption spectra of the D, A, and D-A-D along with their corresponding mono and dicationic states are simulated at TD-DFT. Generally, light absorption by conjugated polymers causes single and strong absorption in the visible region where an electron transferred from HOMO to LUMO. Moreover, this absorption band peak red-shifts with chain length elongation of the conjugated body.^{58,59} Absorption spectra of all these three species along with their defective states are categorized into separate sections.

Mostly COPs are positively charged when experimentally synthesized, so that is why the cationic and dicationic states are considered to efficiently explore the solar light absorption abilities. The UV-vis spectra of the neutral state of D (Figure 9) show two distinct peaks at ca. 608 and 440 nm and arises from $\pi \rightarrow \pi^*$ and HOMO-1 to LUMO-1 transition, respectively. The effect of cationic and dicationic is investigated in the absence of counterion, where the monocation induces polaron and deficiency of two electrons create a bipolaron state.

Removal of an electron from the oligomeric backbone of D creates an extra absorption peak in the near-IR region at ca. 2133 nm. Compared to the parent D, a red-shifting of about 186 nm in the λ_{\max} is achieved in its cationic state. The lower energy absorption peak at a longer wavelength (2133 nm) is because of the delocalized polaronic state which is simply due to $\sigma \rightarrow \pi^*$ transition or interband transition. This longer wavelength absorption, near the IR region, is responsible for the delocalized electronic cloud density over the oligomeric chain length (vide supra). From the UV-vis-near-IR spectra, we can see that monocationic state may be much efficient for the solar spectrum absorption but unstable compared to the ground state.

Creation of a dicationic state in D significantly red-shifts the λ_{\max} from 608 to 1356 nm and gives rise to a weak $\sigma \rightarrow \pi^*$ transition (2044 nm) within the parent optical band gap. The lower excitation energy of the $\pi \rightarrow \pi^*$ in the bipolaronic state is a direct consequence of its stability and localized nature compared to that of the polaronic state. The reduced optical

band gap of the dicationic state has a wide range absorption of near-IR radiation besides visible spectrum of light. So, both of these polaron and bipolaron states can be easily induced in the polymeric body to enhance the visible light absorption in the PSC device, upon covalent and noncovalent doping. In summary, a well-doped state of the D can also give desirable efficiency if used in the BHJ of the PSC (vide supra).

UV-vis spectra of A give rise to a strong absorption band peak which is peaked at 669 nm and is termed as the first allowed $\pi \rightarrow \pi^*$ transition, capable of red light absorption of the solar spectrum, shown in Figure 10. In the polaronic state (monocationic), a significant amount of red-shifting in absorption is simulated in the λ_{\max} (669 to 969 nm) and generate an interband transition. This interband peak arises from the transition of the partially occupied (n) molecular orbital to the vacant conduction (π^*) band state. This forbidden absorption band peak is situated at 2430 nm and consequences a high delocalized π -electronic cloud density over the oligomeric body. The $n \rightarrow \pi^*$ transition in the higher wavelength region is because of the absence of counterion, which creates high electroactivity and instability. This polaronic trend in A is almost similar to that of D but substantially pronounced. Removal of two electrons from the oligomeric chain length of A establishes a stable and very prominent bipolaronic state compared to D. The first allowed $\pi \rightarrow \pi^*$ transition in A spans in the range of 1513 nm, which is capable of absorbing both the visible and Near-IR radiations of the solar spectrum. Furthermore, this localized dicationic state along with associated distortion provide an easy pathway for the electron/hole transformation along the π -conjugated backbone (vide supra). The bipolaronic state has wide range absorption of the solar spectrum as can be seen from the broad and high-intensity band peak at ca. 1513 nm.

Comparative UV-vis spectra of D, A, and D-A-D are given in Figure 11, where the maximum absorption band peaks are peaked at 608, 669, and 847 nm, respectively. These bands can also be regarded as the first allowed maximum electronic excitation (the one with higher oscillator strength) in the visible region and are due to $\pi \rightarrow \pi^*$ transitions (Table 3). The absorption band peak at ca. 847 nm in D-A-D is strong evidence of its efficient absorption in the visible region and is responsible for charge transferring ability as well. Moreover, this simulated λ_{\max} has a strong correlation with the already

Table 3. First three vertical allowed transitions along with f and MO transition

species	excited energy (eV)	λ (nm)	f	electronic transition
D	1	608	3.35	HOMO \rightarrow LUMO
	2	456	0.17	HOMO $_{-3}\rightarrow$ LUMO
	3	440	0.65	HOMO $_{-1}\rightarrow$ LUMO $_1$
A	1	669	2.06	HOMO \rightarrow LUMO
	2	544	0.08	HOMO \rightarrow LUMO $_2$
D-A-D	3	512	0.20	HOMO $_{-1}\rightarrow$ LUMO $_1$
	1	847	1.78	HOMO \rightarrow LUMO
	2	680	0.17	HOMO $_{-1}\rightarrow$ LUMO
	3	618	0.12	HOMO $_{-1}\rightarrow$ LUMO $_1$

experimental observed UV-vis spectra (843 nm)¹⁸ which also supports and confirmed the level of theory used (See Figure S10 of the Supporting Information). Furthermore, it can be concluded that this wide range of the visible light absorption in the D-A-D is responsible for higher efficiency, compared to that of their individual counterparts. From Figure 11, it is evident that how the donor and acceptor moieties in the form of D-A-D increase the visible light absorption in a particular polymer.

As discussed above, a reduction in the optical band gap of the resulted polymer along with wide UV-vis absorption is achieved through a mutual overlapping of the molecular orbitals of donor and acceptor. The UV-vis spectra of D-A-D has three distinct absorptions; two small peaks in the visible and a broad one near the IR region, which is an indication of its efficient light-harvesting ability. Furthermore, we also predicted the polaron and bipolaron states in the extended conjugation of D-A-D, which is given in Figure 12.

Once again, a similar trend is observed in the case of D-A-D, upon creation of polaronic and bipolaronic states. Optical band

gap of the parent D-A-D is 1.46 eV, which reduces to 1.10 eV in the monocationic state. The optical band gap of the bipolaronic state is about 1.12 eV which is due to the $\pi \rightarrow \pi^*$ transition. Unlike the D and A, UV-vis-near-IR spectra of the dicationic state are ideal and transparent in the whole region of the solar spectrum. Additionally, two extra low energy band peaks, located at 1501 and 2277 nm, strengthen the absorption ability of D-A-D in the bipolaronic state. These near-IR absorptions arise from the electronic transition of $\sigma \rightarrow \pi^*$ orbitals.

3.6. Theoretical Performance of Polymer Solar Cells.

To get the high efficiency of bulk heterojunction (BHJ) polymer solar cell, scientists are struggling to achieve higher (i) short-circuit current density (J_{SC}), (ii) open circuit voltage (V_{OC}), (iii) and a high fill factor (FF). The efficiency of a PSC can be obtained using eq 2:⁴

$$\eta = \frac{V_{OC}J_{SC}FF}{P_{in}} \times 100 \quad (2)$$

where η is efficiency and P_{in} is the power density of incident light.

The J_{SC} has an inverse relation with the band gap value in PSC; the lower the band gap, much higher the short-circuit current density will be, and vice versa. So, narrow band gap polymer can harvest a sufficient amount of sunlight and lead to enhanced J_{SC} . Furthermore, J_{SC} is also dependent on the LUMO energy levels of the hole transporting material (here D-A-D) and acceptor (PCBM) in the PSC device. If the difference is more than 0.3 eV (eq 3), then the device will result in high J_{SC} and this energy difference can also be correlated with charge transport (η_{eT}) within PSC. The smaller-scale phase separation creates a larger area of interfaces where charge separation can take place. A large energy difference between the

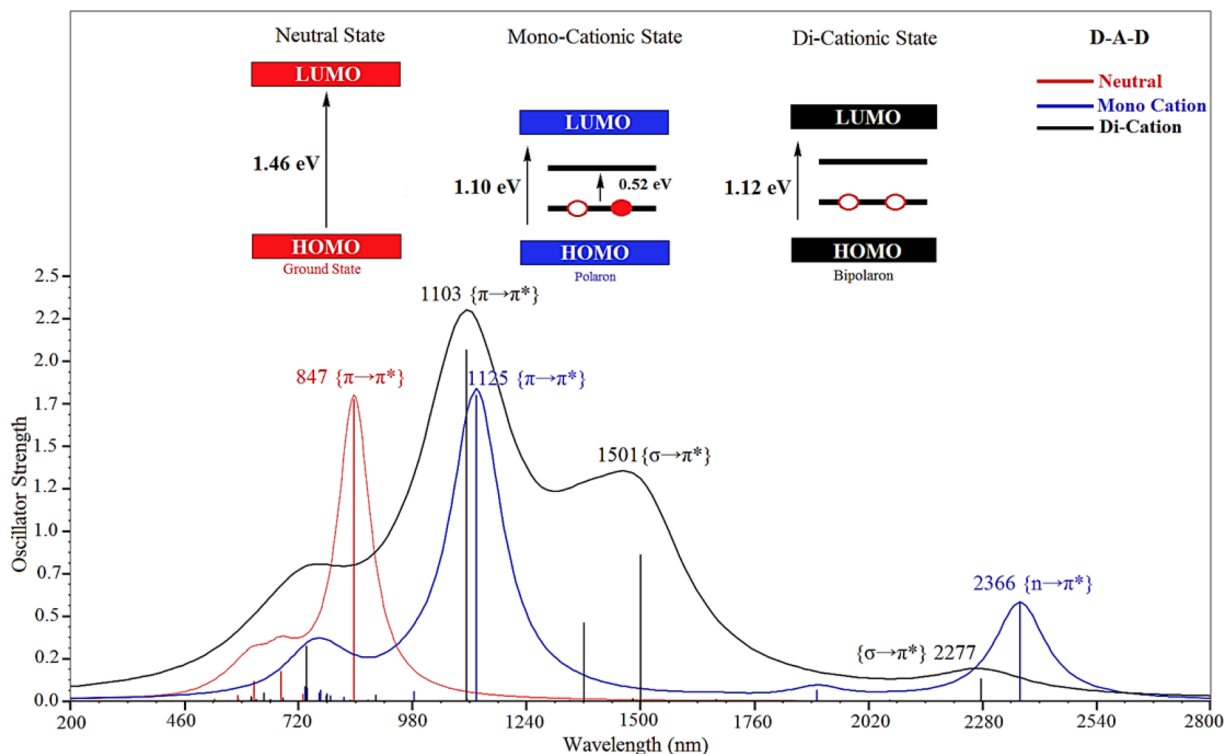


Figure 12. UV-vis spectra along with optical band gaps of neutral, mono, and dicationic states of D-A-D at B3LYP/6-31G**.

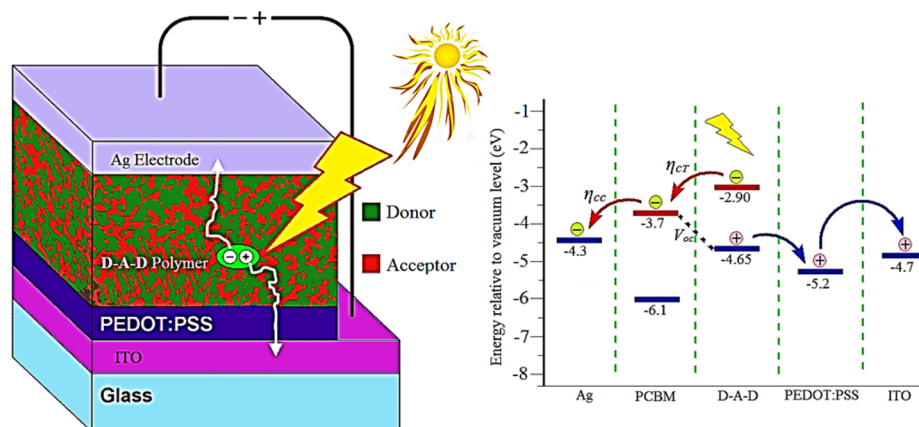


Figure 13. Supposed device structure of the inverted organic solar cell along with energy band diagram of D-A-D and other species.

LUMO of D-A-D (donor) and the LUMO of PCBM (acceptor) is required for ultrafast photoinduced electron transfer.⁶⁰ The next important parameter of the PSC is the V_{OC} , which can be tuned/enhanced by lowering the HOMO level of the polymer in the BHJ. Theoretically, the V_{OC} of PSCs can be estimated from the orbital difference of D-A-D (HOMO) and PCBM (LUMO), using eq 3:⁴

$$V_{OC} = e^{-1}(|E_{HOMO}^{Donor}| - |E_{LUMO}^{Acceptor}| - 0.3 \text{ eV}) \quad (3)$$

where e^{-} is the elementary charge, E is the energy level, and 0.3 eV is an empirical value for efficient charge separation (minimum difference of the LUMOs of donor and acceptor). The final crucial parameter in getting the high efficiency of PSC is the FF, which is simply a ratio between the maximum obtainable power and the product of V_{OC} and J_{SC} . FF is strongly dependent on the film morphology, interface recombination, miscibility of polymer and PCBM and high charge carrier mobility in the PSC. So, from a molecular point of view, a planner polymer with high delocalized π -electrons, molecular chain packing, and good crystallinity are prime factors for high FF.

Theoretical performance of our investigated D-A-D is finally modeled for the solar cell application in a BHJ structure which is schematically given in Figure 13. The photovoltaic properties of D-A-D are modeled in a device structure of ITO|PEDOT:PSS/D-A-D:PCBM|Ag (where ITO, indium tin oxide; PEDOT:PSS, poly(styrenesulfonate)-doped poly(ethylene-dioxythiophene); PCBM, and other fullerenes derivatives). Theoretical open circuit voltage (V_{OC}) and the corresponding LUMO–LUMO difference of D-A-D and PCBM derivatives are correlated with J_{SC} and charge transport energy (η_{CT}), respectively. All other parameters of the device are taken from experimental work such as illumination of AM 1.5G, and weight ratios of D-A-D and PCBM (fullerene derivatives) were 1:1.⁶¹

The photovoltaic properties of D-A-D in the PSC device such as V_{OC} and charge transport are simulated which are listed in Table 4. Different HOMO and LUMO energy levels of the fullerenes derivatives are reported (Table 4); however, a few of them are considered with our investigated D-A-D polymer. From Table 4, it can be analyzed that the V_{OC} of the PSC has a direct relation with the LUMO energy level of PCBM; a higher LUMO level results in large V_{OC} . A PC₆₁BM⁶² with LUMO energy level of -3.63 eV, produces V_{OC} of 1.02 eV with our designed D-A-D; however, this voltage drops down to 0.65 eV

Table 4. HOMO, LUMO of fullerene derivatives and open circuit voltage (V_{OC}) and LUMO^{Donor}–LUMO^{Acceptor} energy difference (L-L) of D-A-D^a

no.	species	HOMO	LUMO	V_{OC}	L-L
1	PC ₆₁ BM ⁶²	-6.10	-3.63	1.02	0.73
2	PC ₆₁ BM ⁶³	-6.10	-3.70	0.95	0.80
3	IC ₆₀ BA ⁶⁴	-5.80	-3.70	0.95	0.80
4	IC ₆₀ BA ⁶⁵	-5.85	-3.74	0.91	0.84
5	IC ₆₀ MA ⁶⁵	-5.91	-3.86	0.79	0.90
6	PC ₆₀ BM ⁶⁶	-5.93	-3.91	0.74	1.01
7	PC ₇₀ BM ⁶⁷	-5.87	-3.91	0.74	1.01
8	PC ₇₀ BM ⁶⁸	-6.0	-4.0	0.65	1.10
9	PC ₇₁ BM ⁶⁴	-6.0	-4.0	0.65	1.10
10	PC ₆₁ BM ⁶⁹	-6.2	-4.10	0.55	1.20

^aAll values are in eV.

when PC₇₁BM⁶⁴ is used (LUMO, -4.0 eV). Comparative analysis of the data of Table 4 led us to predict that an average open circuit voltage of roundabout 0.90 eV can be achieved, using D-A-D as donor material in the BHJ solar cell devices. Compared to individual D and A conformers, the resulted constituent has planner geometry, so a high FF is expected, and the narrow optical band gap (1.46 eV) and electrical band gap (1.75 eV) are responsible for high J_{SC} (vide supra).

4. CONCLUSION

Solar to power energy conversion via photovoltaic process is a clean and renewable energy technology which holds a sustainable development. We have used density functional theory (DFT) and time-dependent (TD-DFT) at hybrid functional to assess the nature and electronic properties of a near-infrared-absorbing, low energy gap conjugated polymer: D-A-D. The D-A-D is consisting of 2,1,3-benzosele-nadiazole (A) as acceptor and 3,4-ethylenedioxy-selenophene (D) as donor fragments. The D and A moieties in the polymeric backbone have been found to be responsible for reducing the band gap, open circuit (V_{OC}) and increasing short-circuit current density (J_{SC}) in polymers solar cells (PSC). Our theoretical studies revealed that charge transportation efficiency (η_{CT}), V_{OC} , and J_{SC} and, in turn, device performance, are influenced by electronic energy level alignment at interfaces. A lower HOMO energy level (-4.65 eV) of designed D-A-D is responsible for increasing the ambient stability during device operation and results in high V_{OC} of 1.02 eV. Furthermore, it is found that donor–acceptor combination has a key role in

charge separation, weak steric hindrance, and molecular architecture (planarity of the polymeric backbone) which directly influences the charge transport compared to that of counterpart homopolymers (either **D** or **A**). Reduction in the band gap, high charge transformation, and enhanced visible light absorption in **D-A-D** system is because of strong overlapping of the frontier molecular orbitals of the **D** and **A**. A highly energetic, unstable and delocalized polaronic state exists when the polymer was oxidized (cationic state), while further oxidation (dicationic state) generates a comparatively stable and localized state, bipolaron. Finally, these polaron and bipolaron are found to have a direct relation with visible light absorbed photocurrent generation.

■ ASSOCIATED CONTENT

Supporting Information

The Supporting Information is available free of charge on the ACS Publications website at DOI: 10.1021/acs.jpcc.6b10441.

Tables for the values of the valence band, conduction band, and band gaps of **D**, **A**, and **D-A-D** from monomer up to infinite chain length. Figures of the band development upon chain length elongation, molecular orbital contours, and absorption spectra of **D**, **A**, and **D-A-D**. (PDF)

■ AUTHOR INFORMATION

Corresponding Authors

*E-mail: habib_chemist@yahoo.com; hu203@exeter.ac.uk.

*E-mail: A.Tahir@exeter.ac.uk.

ORCID

Habib Ullah: 0000-0001-9290-0265

Notes

The authors declare no competing financial interest.

■ ACKNOWLEDGMENTS

We gratefully thank Professor Ulrike Salzner for helpful discussions, the University of Exeter, ESI Beowulf Cluster, NOTUR Supercomputing facilities within the project nn4608k, and the UK Solar Fuel Network (SFN).

■ REFERENCES

- (1) Wolf, J.; Babics, M.; Wang, K.; Saleem, Q.; Liang, R. Z.; Hansen, M. R.; Beaujuge, P. M. Benzo[1,2-b:4,5-b']Dithiophene-Pyrido[3,4-b]Pyrazine Small-Molecule Donors for Bulk Heterojunction Solar Cells. *Chem. Mater.* **2016**, *28*, 2058–2066.
- (2) Wang, M.; Cai, D.; Yin, Z.; Chen, S. C.; Du, C. F.; Zheng, Q. Asymmetric-Indenothiophene-Based Copolymers for Bulk Heterojunction Solar Cells with 9.14% Efficiency. *Adv. Mater.* **2016**, *28*, 3359–3365.
- (3) Scharber, M.; Sariciftci, N. Efficiency of Bulk-Heterojunction Organic Solar Cells. *Prog. Polym. Sci.* **2013**, *38*, 1929–1940.
- (4) Li, G.; Zhu, R.; Yang, Y. Polymer Solar Cells. *Nat. Photonics* **2012**, *6*, 153–161.
- (5) Green, M. A.; Emery, K.; Hishikawa, Y.; Warta, W.; Dunlop, E. D. Solar Cell Efficiency Tables (Version 45). *Prog. Photovoltaics* **2015**, *23*, 1–9.
- (6) Scharber, M. C.; Mühlbacher, D.; Koppe, M.; Denk, P.; Waldauf, C.; Heeger, A. J.; Brabec, C. J. Design Rules for Donors in Bulk-Heterojunction Solar Cells—Towards 10% Energy-Conversion Efficiency. *Adv. Mater.* **2006**, *18*, 789–794.
- (7) Heeger, A. J. Semiconducting and Metallic Polymers: The Fourth Generation of Polymeric Materials (Nobel Lecture). *Angew. Chem., Int. Ed.* **2001**, *40*, 2591–2611.

(8) Heeger, A. J. Semiconducting and Metallic Polymers: The Fourth Generation of Polymeric Materials. *J. Phys. Chem. B* **2001**, *105*, 8475–8491.

(9) Facchetti, A. π -Conjugated Polymers for Organic Electronics and Photovoltaic Cell Applications. *Chem. Mater.* **2011**, *23*, 733–758.

(10) Ullah, H.; Tahir, A. A.; Mallick, T. K. Polypyrrole/TiO₂ Composites for the Application of Photocatalysis. *Sens. Actuators, B* **2016**, DOI: 10.1016/j.snb.2016.10.019.

(11) Ullah, H. Inter-Molecular Interaction in Polypyrrole/TiO₂: A DFT Study. *J. Alloys Compd.* **2017**, *692*, 140–148.

(12) Salzner, U. Quantitatively Correct UV-Vis Spectrum of Ferrocene with TD-B3LYP. *J. Chem. Theory Comput.* **2013**, *9*, 4064–4073.

(13) Mikhnenko, O. V.; Azimi, H.; Scharber, M.; Morana, M.; Blom, P. W.; Loi, M. A. Exciton Diffusion Length in Narrow Bandgap Polymers. *Energy Environ. Sci.* **2012**, *5*, 6960–6965.

(14) Müllen, K.; Pisula, W. Donor–Acceptor Polymers. *J. Am. Chem. Soc.* **2015**, *137*, 9503–9505.

(15) Scharber, M. C. On the Efficiency Limit of Conjugated Polymer: Fullerene-Based Bulk Heterojunction Solar Cells. *Adv. Mater.* **2016**, *28*, 1994–2001.

(16) Tan, H.; Furlan, A.; Li, W.; Arapov, K.; Santbergen, R.; Wienk, M. M.; Zeman, M.; Smets, A. H.; Janssen, R. A. Highly Efficient Hybrid Polymer and Amorphous Silicon Multijunction Solar Cells with Effective Optical Management. *Adv. Mater.* **2016**, *28*, 2170–2177.

(17) Brédas, J.-L.; Norton, J. E.; Cornil, J.; Coropceanu, V. Molecular Understanding of Organic Solar Cells: The Challenges. *Acc. Chem. Res.* **2009**, *42*, 1691–1699.

(18) Poverenov, E.; Zamoshchik, N.; Patra, A.; Ridelman, Y.; Bendikov, M. Unusual Doping of Donor–Acceptor-Type Conjugated Polymers Using Lewis Acids. *J. Am. Chem. Soc.* **2014**, *136*, 5138–5149.

(19) Wang, D. H.; Kim, D. Y.; Choi, K. W.; Seo, J. H.; Im, S. H.; Park, J. H.; Park, O. O.; Heeger, A. J. Enhancement of Donor–Acceptor Polymer Bulk Heterojunction Solar Cell Power Conversion Efficiencies by Addition of Au Nanoparticles. *Angew. Chem.* **2011**, *123*, 5633–5637.

(20) Alam, M. M.; Jenekhe, S. A. Efficient Solar Cells from Layered Nanostructures of Donor and Acceptor Conjugated Polymers. *Chem. Mater.* **2004**, *16*, 4647–4656.

(21) Kim, K.; Liu, J.; Namboothiry, M. A.; Carroll, D. L. Roles of Donor and Acceptor Nanodomains in 6% Efficient Thermally Annealed Polymer Photovoltaics. *Appl. Phys. Lett.* **2007**, *90*, 163511.

(22) Yu, G.; Gao, J.; Hummelen, J. C.; Wudl, F.; Heeger, A. J. Polymer Photovoltaic Cells: Enhanced Efficiencies Via a Network of Internal Donor–Acceptor Heterojunctions. *Science* **1995**, *270*, 1789.

(23) Benten, H.; Mori, D.; Ohkita, H.; Ito, S. Recent Research Progress of Polymer Donor/Polymer Acceptor Blend Solar Cells. *J. Mater. Chem. A* **2016**, *4*, 5340–5365.

(24) Ogawa, Y.; White, M. S.; Sun, L.; Scharber, M. C.; Sariciftci, N. S.; Yoshida, T. Substrate-Oriented Nanorod Scaffolds in Polymer–Fullerene Bulk Heterojunction Solar Cells. *ChemPhysChem* **2014**, *15*, 1070–1075.

(25) Kim, S.-O.; Kim, Y.-S.; Yun, H.-J.; Kang, I.; Yoon, Y.; Shin, N.; Son, H. J.; Kim, H.; Ko, M. J.; Kim, B. N-Octyl-2, 7-Dithia-5-Azacyclopenta [a] Pentalene-4, 6-Dione-Based Low Band Gap Polymers for Efficient Solar Cells. *Macromolecules* **2013**, *46*, 3861–3869.

(26) Frisch, M. J.; et al. *Gaussian 09*, revision D.0.1; Gaussian, Inc.: Wallingford, CT, 2013.

(27) Giannozzi, P.; Baroni, S.; Bonini, N.; Calandra, M.; Car, R.; Cavazzoni, C.; Ceresoli, D.; Chiarotti, G. L.; Cococcioni, M.; Dabo, I. Quantum Espresso: A Modular and Open-Source Software Project for Quantum Simulations of Materials. *J. Phys.: Condens. Matter* **2009**, *21*, 395502.

(28) Allouche, A. R. Gabedit: A Graphical user Interface for Computational Chemistry Softwares. *J. Comput. Chem.* **2011**, *32*, 174–182.

(29) Virtual NanoLab Version 2016.2, QuantumWise A/S (www.quantumwise.com).

- (30) Dennington, R. D.; Keith, T. A.; Millam, J. M. *Gaussview 5.0.8*; Gaussian Inc.: Wallingford, CT, 2008.
- (31) Jacquemin, D.; Wathélet, V.; Perpète, E. A.; Adamo, C. Extensive TD-DFT Benchmark: Singlet-Excited States of Organic Molecules. *J. Chem. Theory Comput.* **2009**, *5*, 2420–2435.
- (32) Cramariuc, O.; Hukka, T. I.; Rantala, T. T.; Lemmetyinen, H. TD-DFT Description of Photoabsorption and Electron Transfer in a Covalently Bonded Porphyrin-Fullerene Dyad. *J. Phys. Chem. A* **2006**, *110*, 12470–12476.
- (33) Sun, H.; Autschbach, J. Electronic Energy Gaps for Π -Conjugated Oligomers and Polymers Calculated with Density Functional Theory. *J. Chem. Theory Comput.* **2014**, *10*, 1035–1047.
- (34) Jacquemin, D.; Perpète, E. A.; Scuseria, G. E.; Ciofini, I.; Adamo, C. TD-DFT Performance for the Visible Absorption Spectra of Organic Dyes: Conventional Versus Long-Range Hybrids. *J. Chem. Theory Comput.* **2008**, *4*, 123–135.
- (35) Berardo, E.; Hu, H.-S.; Shevlin, S. A.; Woodley, S. M.; Kowalski, K.; Zwijnenburg, M. A. Modeling Excited States in TiO_2 Nanoparticles: On the Accuracy of a TD-DFT Based Description. *J. Chem. Theory Comput.* **2014**, *10*, 1189–1199.
- (36) Zade, S. S.; Zamoshchik, N.; Bendikov, M. From Short Conjugated Oligomers to Conjugated Polymers. Lessons from Studies on Long Conjugated Oligomers. *Acc. Chem. Res.* **2011**, *44*, 14–24.
- (37) Baer, R.; Livshits, E.; Salzner, U. Tuned Range-Separated Hybrids in Density Functional Theory. *Annu. Rev. Phys. Chem.* **2010**, *61*, 85–109.
- (38) Becke, A. D. Density-Functional Exchange-Energy Approximation with Correct Asymptotic Behavior. *Phys. Rev. A: At, Mol., Opt. Phys.* **1988**, *38*, 3098.
- (39) Casanovas, J.; Alemán, C. Comparative Theoretical Study of Heterocyclic Conducting Oligomers: Neutral and Oxidized Forms. *J. Phys. Chem. C* **2007**, *111*, 4823–4830.
- (40) Lukeš, V.; Rápta, P.; Idzik, K. R.; Beckert, R.; Dunsch, L. Charged States of 1, 3, 5-Triazine Molecules as Models for Star-Shaped Molecular Architecture: A DFT and Spectroelectrochemical Study. *J. Phys. Chem. B* **2011**, *115*, 3344–3353.
- (41) Mishra, A. K.; Tandon, P. A Comparative Ab Initio and DFT Study of Polyaniline Leucoemeraldine Base and its Oligomers. *J. Phys. Chem. B* **2009**, *113*, 14629–14639.
- (42) Petrova, J. N.; Romanova, J. R.; Madjarova, G. K.; Ivanova, A. N.; Tadjer, A. V. Fully Doped Oligomers of Emeraldine Salt: Polaronic Versus Bipolaronic Configuration. *J. Phys. Chem. B* **2011**, *115*, 3765–3776.
- (43) Salzner, U. Quantitatively Correct UV-Vis Spectrum of Ferrocene with TDB3LYP. *J. Chem. Theory Comput.* **2013**, *9*, 4064–4073.
- (44) Ullah, H.; Ayub, K.; Ullah, Z.; Hanif, M.; Nawaz, R.; Shah, A. A.; Bilal, S. Theoretical Insight of Polypyrrole Ammonia Gas Sensor. *Synth. Met.* **2013**, *172*, 14–20.
- (45) Ullah, H.; Shah, A. A.; Bilal, S.; Ayub, K. DFT Study of Polyaniline NH_3 , CO_2 and CO Gas Sensors: Comparison with Recent Experimental Data. *J. Phys. Chem. C* **2013**, *117*, 23701–23711.
- (46) Ullah, H.; Shah, A. A.; Ayub, K.; Bilal, S. Density Functional Theory Study of Poly (*O*-Phenylenediamine) Oligomers. *J. Phys. Chem. C* **2013**, *117*, 4069–4078.
- (47) Zamoshchik, N.; Salzner, U.; Bendikov, M. Nature of Charge Carriers in Long Doped Oligothiophenes: The Effect of Counterions. *J. Phys. Chem. C* **2008**, *112*, 8408–8418.
- (48) Bibi, S.; Ullah, H.; Ahmad, S. M.; Shah, A. A.; Bilal, S.; Tahir, A. A.; Ayub, K. Molecular and Electronic Structure Elucidation of Polypyrrole Gas Sensors. *J. Phys. Chem. C* **2015**, *119*, 15994–16003.
- (49) Patra, A.; Agrawal, V.; Bhargav, R.; Bhardwaj, D.; Chand, S.; Sheynin, Y.; Bendikov, M. Metal Free Conducting Pedos, Pedot, and Their Analogues Via an Unusual Bromine-Catalyzed Polymerization. *Macromolecules* **2015**, *48*, 8760–8764.
- (50) Patra, A.; Bendikov, M.; Chand, S. Poly (3, 4-Ethylenedioxy-selenophene) and its Derivatives: Novel Organic Electronic Materials. *Acc. Chem. Res.* **2014**, *47*, 1465–1474.
- (51) Li, M.; Sheynin, Y.; Patra, A.; Bendikov, M. Tuning the Electrochromic Properties of Poly (Alkyl-3, 4-Ethylenedioxy-selenophenes) Having High Contrast Ratio and Coloration Efficiency. *Chem. Mater.* **2009**, *21*, 2482–2488.
- (52) Patra, A.; Wijsboom, Y. H.; Zade, S. S.; Li, M.; Sheynin, Y.; Leitens, G.; Bendikov, M. Poly (3, 4-Ethylenedioxy-selenophene). *J. Am. Chem. Soc.* **2008**, *130*, 6734–6736.
- (53) Alberga, D.; Mangiatordi, G. F.; Labat, F.; Ciofini, I.; Nicolotti, O.; Lattanzi, G.; Adamo, C. Theoretical Investigation of Hole Transporter Materials for Energy Devices. *J. Phys. Chem. C* **2015**, *119*, 23890–23898.
- (54) Risko, C.; Kushto, G.; Kafafi, Z.; Brédas, J.-L. Electronic Properties of Silole-Based Organic Semiconductors. *J. Chem. Phys.* **2004**, *121*, 18.
- (55) Duan, Y. A.; Geng, Y.; Li, H. B.; Jin, J. L.; Wu, Y.; Su, Z. M. Theoretical Characterization and Design of Small Molecule Donor Material Containing Naphthodithiophene Central Unit for Efficient Organic Solar Cells. *J. Comput. Chem.* **2013**, *34*, 1611–1619.
- (56) Coropceanu, V.; Cornil, J.; da Silva Filho, D. A.; Olivier, Y.; Silbey, R.; Brédas, J.-L. Charge Transport in Organic Semiconductors. *Chem. Rev.* **2007**, *107*, 926–952.
- (57) Okawa, Y.; Akai-Kasaya, M.; Kuwahara, Y.; Mandal, S. K.; Aono, M. Controlled Chain Polymerisation and Chemical Soldering for Single-Molecule Electronics. *Nanoscale* **2012**, *4*, 3013–3028.
- (58) Okur, S.; Salzner, U. Theoretical Modeling of the Doping Process in Polypyrrole by Calculating UV/Vis Absorption Spectra of Neutral and Charged Oligomers. *J. Phys. Chem. A* **2008**, *112*, 11842–11853.
- (59) Ullah, H.; Shah, A.-u.-H. A.; Bilal, S.; Ayub, K. Doping and Dedoping Processes of Polypyrrole: DFT Study with Hybrid Functionals. *J. Phys. Chem. C* **2014**, *118*, 17819–17830.
- (60) Park, S. H.; Roy, A.; Beaupre, S.; Cho, S.; Coates, N.; Moon, J. S.; Moses, D.; Leclerc, M.; Lee, K.; Heeger, A. J. Bulk Heterojunction Solar Cells with Internal Quantum Efficiency Approaching 100%. *Nat. Photonics* **2009**, *3*, 297–302.
- (61) Wang, M.; Hu, X.; Liu, P.; Li, W.; Gong, X.; Huang, F.; Cao, Y. Donor–Acceptor Conjugated Polymer Based on Naphtho [1, 2-C: 5, 6-c] Bis [1, 2, 5] Thiadiazole for High-Performance Polymer Solar Cells. *J. Am. Chem. Soc.* **2011**, *133*, 9638–9641.
- (62) Ayachi, S.; Mabrouk, A.; Alimi, K.; Bouachrine, M. *Photophysical Properties of Two New Donor-Acceptor Conjugated Copolymers and Their Model Compounds: Applications in Polymer Light Emitting Diodes (Pleds) and Polymer Photovoltaic Cells (Ppcs)*; INTECH Open Access Publisher, 2012.
- (63) Li, L.; Huang, Y.; Peng, J.; Cao, Y.; Peng, X. Enhanced Performance of Solution-Processed Solar Cells Based on Porphyrin Small Molecules with a Diketopyrrolopyrrole Acceptor Unit and a Pyridine Additive. *J. Mater. Chem. A* **2013**, *1*, 2144–2150.
- (64) Dou, L.; You, J.; Yang, J.; Chen, C.-C.; He, Y.; Murase, S.; Moriarty, T.; Emery, K.; Li, G.; Yang, Y. Tandem Polymer Solar Cells Featuring a Spectrally Matched Low-Bandgap Polymer. *Nat. Photonics* **2012**, *6*, 180–185.
- (65) He, Y.; Chen, H.-Y.; Hou, J.; Li, Y. Indene–C60 Bisadduct: A New Acceptor for High-Performance Polymer Solar Cells. *J. Am. Chem. Soc.* **2010**, *132*, 1377–1382.
- (66) Hou, J.; Guo, X. *Organic Solar Cells*; Springer: Berlin, 2013; pp 17–42.
- (67) Wang, F.; Zhang, B.; Li, Q.; Shi, Z.; Yu, L.; Liu, H.; Wang, Y.; Dai, S.; Tan, Z. a.; Li, Y. Management of the Light Distribution within the Photoactive Layer for High Performance Conventional and Inverted Polymer Solar Cells. *J. Mater. Chem. A* **2016**, *4*, 1915.
- (68) Yang, Y. M.; Chen, W.; Dou, L.; Chang, W.-H.; Duan, H.-S.; Bob, B.; Li, G.; Yang, Y. High-Performance Multiple-Donor Bulk Heterojunction Solar Cells. *Nat. Photonics* **2015**, *9*, 190–198.
- (69) Cheun, H.; Kim, J.; Zhou, Y.; Fang, Y.; Dindar, A.; Shim, J.; Fuentes-Hernandez, C.; Sandhage, K. H.; Kippelen, B. Inverted Polymer Solar Cells with Amorphous Indium Zinc Oxide as the Electron-Collecting Electrode. *Opt. Express* **2010**, *18*, A506–A512.

[Article 6]

H. Ullah, S. Bibi, A. A. Tahir, T. K. Mallick, "Donor-acceptor polymer for the design of all-solid-state dye-sensitized solar cells." *J. Alloys Compd.*, vol. 696, pp. 914-922, Mar. 2017.



Donor-acceptor polymer for the design of *All-Solid-State* dye-sensitized solar cells



Habib Ullah ^{a,*}, Salma Bibi ^{b,c}, Asif A. Tahir ^{a,**}, Tapas K. Mallick ^a

^a *Environment and Sustainability Institute (ESI), University of Exeter, Penryn Campus, Penryn, Cornwall, TR10 9FE, United Kingdom*

^b *National Centre of Excellence in Physical Chemistry, University of Peshawar, 25120, Peshawar, Pakistan*

^c *Women University Swabi, Guloo Dehri, Swabi, Khyber Pakhtunkhwa, 23430, Pakistan*

ARTICLE INFO

Article history:

Received 24 October 2016

Received in revised form

30 November 2016

Accepted 5 December 2016

Available online 8 December 2016

Keywords:

DSSC

Reorganization energy

Donor-acceptor polymer

Polaron

Bi-polaron

Open-circuit voltage

DFT

ABSTRACT

Density functional theory study has been carried out to design a new *All-Solid-State* dye-sensitized solar cell (SDSC), by applying a donor-acceptor conjugated polymer instead of liquid electrolyte. The typical redox mediator (I^1-/I^3-) is replaced with a narrow band gap, hole transporting material (HTM). The electronic and optical properties predict that donor and acceptor moieties in the polymeric body have increased the visible light absorption and charge transporting ability, compared to their parent polymers. A unique “upstairs” like band energy diagram is created by packing N3 between HTM and TiO_2 . Upon light irradiation on the proposed configuration, electrons will move from the dye to TiO_2 and from HTM to dye (to regenerate dye), simultaneously. Our theoretical simulations prove that the proposed configuration will be highly efficient as the HOMO level of HTM is 1.19 eV above the HOMO of sanitizer (dye); providing an efficient pathway for charge transfer. High short-circuit current density and power conversion efficiency is promised from the strong overlapping of molecular orbitals of HTM and sensitizer. A low reorganization energy of 0.21 eV and exciton binding energy of 0.55 eV, confirm the high efficiency of HTM. Finally, a theoretical open-circuit voltage of 1.49 eV would results high quantum yield while, the chemical stability of HTM towards oxidation can be estimated from its high ionization potential value (4.57 eV).

© 2016 Elsevier B.V. All rights reserved.

1. Introduction

When Sun strikes the earth for an hour, if that energy is properly harvest then it can fulfill whole the world energy demand for a year, but unfortunately, we are not able to harvest it properly [1,2]. Solar energy technology in the market is mostly Silicon-based photovoltaic cells, which is a promising renewable energy technique for [3]. Silicon-based solar cells are ideal, but having a high cost and high operation temperature limits its portability and versatility, so, it is an urgent need to replace Si with a better and efficient material for photovoltaic applications [4–6]. Thin film solar technology based on CdTe, *p*-GaAs/*n*-GaAs, and ZnO/CdS/CuInSe₂ etc., exhibiting ~20% efficiency, however, this is more expensive and having elements which are not earth abundance and toxic for

environment [7].

Dye-sensitized solar cell (DSSC) is considered as the best way forward to fulfill our energy requirements due to its low-cost, easy fabrication and environmentally friendly [8]. A basic DSSC consist of molecular dye, adsorbed on a mesoporous wide band gap semiconductor oxide (frequently TiO_2), a redox couple (I^1-/I^3-) usually liquid electrolyte and a *p*-type hole collector/counter electrode [9,10]. The dye molecule (photosensitizer) absorb light and injects its excited electrons into the conduction band of TiO_2 and become oxidized. The redox electrolyte act as an intermediate to transfer hole from dye to counter electrode for regeneration of dye [11–13]. Although, highly efficient DSSCs have been reported but they are facing long-term performance and durability problems which are stem to liquid electrolytes; the I^1-/I^3- redox couple, leads to serious problems such as electrode corrosion and electrolyte leakage [14–16]. The crucial solution would be the purely solid-state cells, given the expected issues of any liquid electrolyte, such as leakage, heavyweight and complex chemistry.

Chung et al. [17] has designed an SDSC model with all inorganic material using TiO_2 , Dye, and $CsSnI_3$, where an efficient e^-/h^+

* Corresponding author.

** Corresponding author.

E-mail addresses: hu203@exeter.ac.uk (H. Ullah), A.Tahir@exeter.ac.uk (A.A. Tahir).

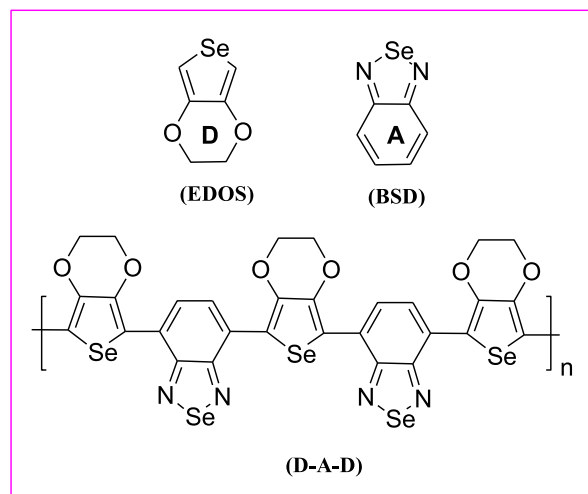
transferring occurred due to the development of a better band diagram of the mixing constituents [17]. The efficiency of this combination is found to have exceeded over the performance of a liquid electrolyte Grätzel cell [17]. The valance band (VB) edge positions of all these three interacting materials had sufficient gaps and are best suitable for h^+ transferring, however, conduction band (CB) edge levels; where the e^- of the excited dye can go to either side (CsSnI₃ or TiO₂), has not proper energy gap difference (upstairs). Moreover, CsSnI₃ is used as hole collector to regenerate dye but contains less abundant earth metals and also has processing issue similar to the thin film solar cell, making it expensive to fabricate.

Solid state hole transporting material (HTM)-based DSSC, termed as all solid-state DSSC (SDSC), has overcome the liquid electrolyte problems [17], but facing the challenge of modest conversion efficiency [18,19]. Some HTM has a weak interaction with the dye which leads to the interruption of the hole-conducting path between HTM and dye molecule. So, designing of an efficient, flexible and cost-effective HTM is needed for the high-performance SDSC.

Conjugated organic polymers (COPs) are promising emerging materials and are considered to be superior over other materials (inorganic semiconductors) due to their possibility of processing to form useful, tunable, robust structures, having material diversity, mechanical flexibility, light weight, low-temperature processing, roll to roll printing (just like a newspaper printing) and large-area capability [20–23]. Photovoltaic is one of the efficient applications of COPs, especially in the form of donor-acceptor co-polymer, possess low band gaps are much suitable for solar energy harnessing technique [24]. These narrow band gap materials have better absorption capability within the active region of solar spectrum especially in the near-infrared region which consequently increases the generation of photocurrent.

Using our previous experience of COPs, here for the first time we are proposing an efficient all-solid-state organic-inorganic hybrid DSSC, preliminary based on their band edge positions (Fig. 1), where COP is used as HTM [25–27]. A series of different COPs, such as 3,4-ethylenedioxythiophene (EDOT), 3,4-ethylenedioxysephenone (EDOS), 2,1,3-benzothiadiazole (BOD), 2,1,3-benzoselenadiazole (BSD), and their combination in the form of donor-acceptor moieties are used (Scheme 1) [28,29], has been simulated to replace electrolyte in the conventional DSSC.

To design an ideal configuration for the SDSC, which would be cheap, easy to handle, environmental friendly and responsible for high efficiency, a perfect upstairs energy level diagram of the



Scheme 1. Chemical structure of the monomers EDOS, BSD, and its Copolymer (EDOS + BSD) [27].

interacting materials is required where the band edge positions of TiO₂, Dye and HTM should have difference of at least of 0.50 eV (Fig. 1). The HTM used in this work is a donor-acceptor co-polymer; a combination of EDOS and BSD moieties.

2. Methods

Quantum mechanical study of the molecular (TiO₂)₂₈ cluster, N3, EDOS, BSD, EDOS + BSD (HTM) and their non-bonded interacting systems are carried out with the help of density functional theory (DFT). GAUSSIAN 09 [30] is used for the DFT calculations [31] while the results are visualized through Gabedit [32], GaussSum [33], and GaussView [34]. DFT and time-dependent DFT (TD-DFT) calculations are used for the electronic properties simulations of the mentioned materials, to predict an efficient model for SDSC. Different oligomeric chain lengths of EDOS, BSD and HTM from monomers up to nine repeating are considered and extended to polymers, using second order polynomial fit equation [31]. Prior to property simulations of the interacting systems such as N3-HTM, N3-TiO₂, and HTM-N3-TiO₂; the DFT method was confirmed through correlation of the HTM simulated HOMO, LUMO and band gaps with experimental data (see Table S1) [28,35]. Hybrid functional such as B3LYP has been successfully applied for this type of polymers and has been found to be superior over other functionals [35–38]. In the case of inter-molecular study of the proposed model, N3 was sandwiched between TiO₂ and HTM and then optimized at B3LYP functional with LanL2DZ basis set. The interaction energy of these three components is simulated with the help of inter-molecular energy simulation as explained elsewhere [25–27,39,40]. The quantitative and qualitative behavior of charge transferring phenomena of the entitled complexes are simulated at natural bonding orbital (NBO) analysis. The prediction of stability, electroactivity, conductivity and donor/acceptor nature are estimated from ionization energy (IP), electron affinity (EA), and band gap analysis. UV–vis spectra and Δ SCF energy gap (optical gap) were simulated in a solvent medium such as chlorobenzene, using a conductor like polarized continuum model (CPCM) at TD-B3LYP/LanL2DZ level which unveils our results regarding the optical and electrical properties.

3. Results and discussion

The 84 atoms cluster of titanium dioxide [(TiO₂)₂₈] is used as a

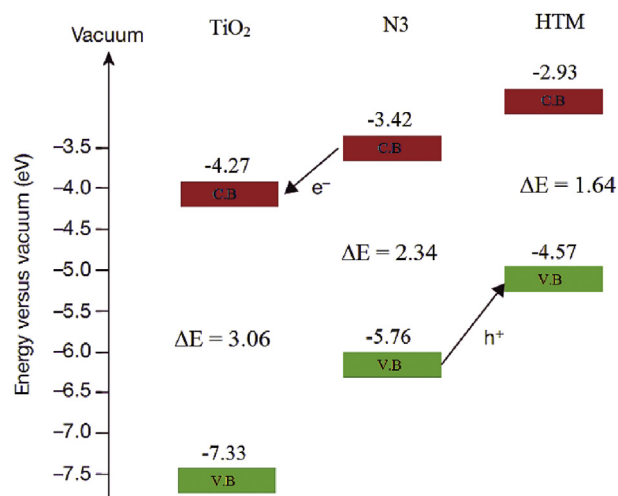


Fig. 1. Energy level diagram of simulated TiO₂, N3, and HTM for high efficient DSSC.

representative of the [101] surface of anatase [41–45]. The choice of a molecular cluster of $\text{Ti}_{28}\text{O}_{56}$ contrast to periodic calculations is that the excited states within TD-DFT are not generally implemented and in any case standard continuum solvation models are not applicable due to the impossibility of defining an infinite solvation cavity [41–43]. The major part of this paper is devoted to the hole transporting material (HTM), its applicability in SDSC and the corresponding efficiency. However, HTM interaction with dye, $\text{N}_3\text{-TiO}_2$, and $\text{HTM-N}_3\text{-TiO}_2$ systems are also highlighted. Charge transferring phenomena, electron-hole exchange and band edge positions of these systems are simulated and discussed in their respective parts.

3.1. Geometrical and electronic properties of HTM

The light absorption capability of a chemical substance can be predicted from its dihedral angles, UV–vis absorption spectra, conjugation of π -electrons, and planarity. As discussed elsewhere [46,47], oligomers up to seven or eight repeating units represent the characteristics of their infinite polymer so that is why the chain length is restricted to nine repeating units. Our current simulations on the nine repeating units of HTM also shows a similar trend and corroborates its polymeric properties. The optimized geometric structure of HTM is given in Fig. 2, where an ideal dihedral angle of 180° (Table S2) is because of donor and acceptor moieties; which has planarized the geometry of the resulting polymer through establishing a delocalized π -electronic cloud density over its polymeric backbone.

The electrons and holes carrying properties of a species can be precisely estimated from the contours of its molecular orbitals; where the electronic cloud density of the localized HOMO represent holes and the LUMO determines the facility with which the electron moves under the external electric biased. Both the HOMO and LUMO of HTM are fully covered by electronic cloud density (Fig. S1), a clear indication of the free availability of π -electrons in the HTM (Fig. 3). Moreover, this molecular orbital overlapping (delocalized π -electrons in HTM) of the C, H, O, N, and Se atoms provides an easy pathway for the movement of free electrons which make it as a donor species (hole donor) in the bulk hetero-junction solar cell.

3.2. Reorganization energy (λ) of HTM

The energy of geometrical distortion of a chemical species between the neutral and cationic state can be termed as

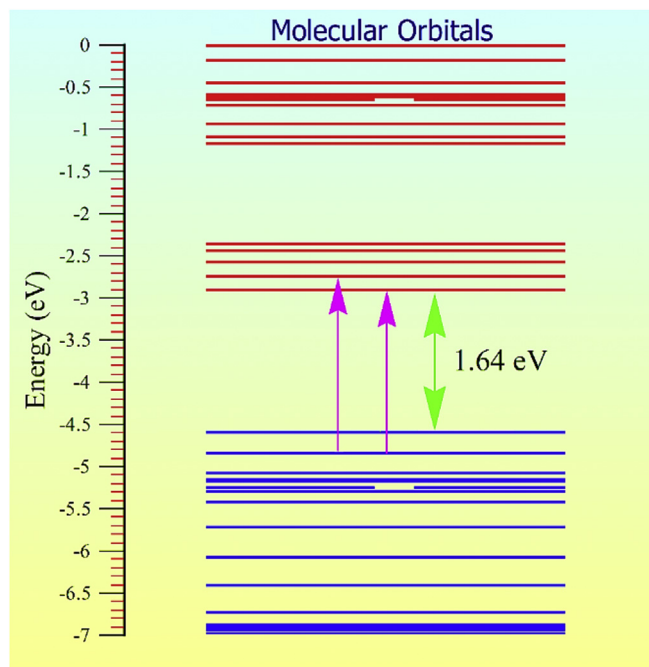


Fig. 3. Energy level diagram of HTM.

reorganization energy (λ). Hole mobility in an organic semiconductor can be understood in terms of its reorganization energy; lower the reorganization energy the faster will be the hole transfer and vice versa. The internal reorganization energy (λ) of HTM is 0.21 eV, which is simulated by the adiabatic potential energy surface method, using equation (1).

$$\lambda = \lambda_1 + \lambda_2 = (E_0^* - E) + (E_+^* - E_+) \quad (1)$$

where E_0 and E_+ , represent energies of neutral and charged species in their lowest energy geometries, while E_0^* and E_+^* represent the energy of a neutral molecule at the geometry of charged molecule and charged molecule at the geometry of the neutral molecule.

Comparative analysis of the reorganization energy of HTM with the already reported hole transporting materials such as N,N' -diphenyl- N,N' -bis(3-methylphenyl)-(1,1'-biphenyl)-4,4'-diamine (0.33 eV) [48], N,N' -bis(2,4-dimethyl-phenyl)- N -(4'-((2,4-

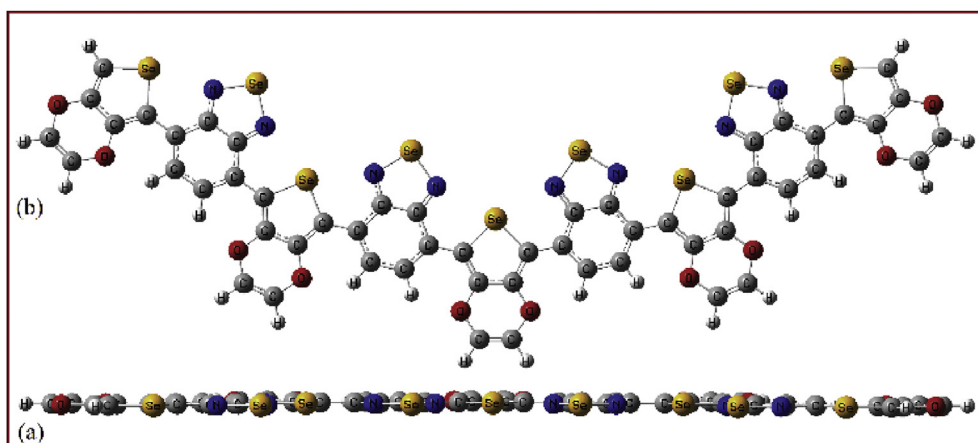


Fig. 2. Optimized Geometric Structure of HTM along with side view.

dimethylphenyl) (phenyl)amino-[1,1'-bi-phenyl]-4-yl)-N'-phenyl-[1,1'-biphenyl]-4,4'-diamine (0.23), 4-(4-phenyl-4- α -naphthylbutadienyl)-N,N-di(4-tolyl)-phenylamine (0.24) [49] and silole-based organic semiconductors (0.50 eV) [50] shows that our proposed HTM has better hole transfer ability due to lower reorganization energy. This low reorganization energy of HTM can also be correlated to its fully planar geometrical structure, where an ideal dihedral of 180° is present.

3.3. Polaron and exciton binding energy of HTM

The combination of charge and the associated lattice distortion in a chemical substance can be appropriately termed as Polaron, denoted as E_p . Distortion in the polymeric back establishes when a π -conjugated polymer donates electronic charge density, this intra-molecular relaxation can also be referred to as a polaronic effect. The polaron-binding energy that relates to the reorganization energy; transfer of a charge from one molecule to other can be calculated from this formula $E_p = (1/2) \lambda$, where λ is the reorganization energy. A 0.105 eV polaron-binding energy is simulated for the proposed HTM, which evidences its ease of electron donation. In terms of molecular orbitals analysis, an electron–hole binding energy is that energy when an electron adds in the LUMO and only one (instead of two) electron in the HOMO.

The electron–hole exciton binding energy (E_b) is actually the energy difference between the neutral exciton and the two free charge carriers. This can be simulated as $E_b = E_{\text{band gap}} - E_{\text{optical gap}}$, or the difference between the electrical gap and optical gap of a particular HTM. For the simulations of these gaps, TD-DFT method at LanL2DZ level and CPCM solvent model is used. The energy required to fully separate the electron–hole pair against the Coulomb attraction is known as exciton binding energy. In Fig. 4, the E_b , optical and band gap are schematically illustrated [51]. A lower E_b is responsible for the charge separation (prevent electron/hole recombination) and high charge carrier mobility in a particular solar cell. The intra-molecular charge transfer (E_b) in HTM has a binding energy of 0.55 eV. The E_b of the investigated HTM is also compared with the already reported hole transfer materials which concluded its lower binding energy. So, an easier dissociation of free charge carriers can be promised in our HTM. Furthermore, binding energy can also be used for the determination of short-circuit current density in a solar cell; lower exciton binding energy of a particular HTM is responsible for its higher short-circuit current density and vice versa.

3.4. Partial charge difference analysis

Partial charge difference on the conjugated backbone of HTM is simulated by using eq. (2). NBO charge on a particular atom in the neutral as well as in the cationic state is considered for the charge transferring phenomena in HTM. Partial charge difference analysis of HTM predicts that H and Se atoms are responsible for the charge donation.

$$\Delta Q_X = \sum Q_{X_i}^+ - \sum Q_{X_i}^0 \quad (2)$$

where ΔQ is a charge on particular X atom, either in cationic (X^+) or neutral state (X^0).

The partial charge difference of the atoms involved in HTM backbone is given in Table 1, which demonstrates that the ΔQ_H value is slightly larger than ΔQ_{Se} to about 0.05 e^- . Comparative analysis of the data of Table 1 led us to conclude that Se and H atoms are mainly involved for the charge transfer in HTM, however, H atom plays a significant role compared to Se atom. The partial

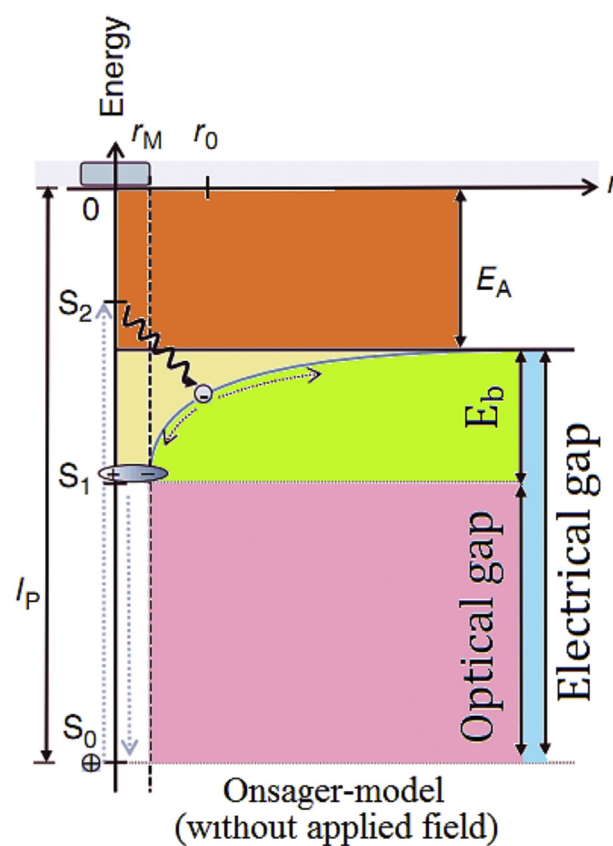


Fig. 4. Schematic representation of exciton binding energy, band, and optical gap.

Table 1
Partial charge difference analysis of HTM.

Species	Cation	Neutral	Difference
Se	7.084	6.844	0.24
N	-5.552	-5.578	0.026
O	-5.520	-5.574	0.054
C	0.126	0.126	0
H	4.868	4.572	0.296

charge difference of ΔQ_H is 0.296 e^- while that of ΔQ_{Se} is 0.24 e^- . Partial charge difference values for N, O, and C are 0.026, 0.054 and 0 e^- , respectively. In summary, partial charge difference between the neutral and the corresponding cation state directly reflects the geometric structures, whether planar, zig-zag or curl.

3.5. UV–vis absorption spectra of HTM

The first allowed maximum electronic excitation energy of HTM (λ_{max}) at ca. 925 nm has strong evidence to be an efficient charge transporting material, as it can easily absorb in the visible region. Furthermore, it is expected that higher efficiency is associated with high absorption ability of solar radiation, especially in the visible part. The effect of the alternating donor and acceptor moieties in the polymeric backbone is found in the form of visible light absorption as can be seen from Fig. 5. Furthermore, the vertical excitation energy of the isolated donor, acceptor and HTM increases with chain length elongation (Figs. S2–S4). Oligomeric chain length elongation produces a single but strong feature in the visible region and confirms that this excitation (the one with low energy) is dominated by a single absorption during which an electron is

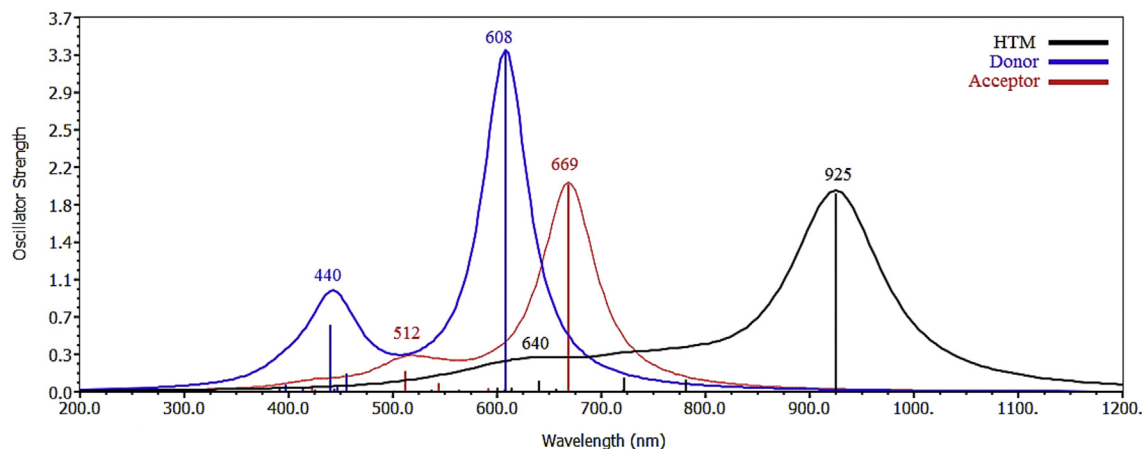


Fig. 5. UV-vis spectra of BSD, EDOS, and HTM at CAM-B3LYP/LanL2DZ.

transferred from π to π^* orbital. Analysis of the data of Tables S3–S5 proves that chain length elongation shifts the strong absorption to lower energy with high intensity and high oscillator strength. Moreover, it is observed that the contribution of HOMO-LUMO transition decreases and new absorption from HOMO-1 \rightarrow LUMO+1, HOMO-2-LUMO, and HOMO-LUMO+2 excitations start to contribute (Tables S2–S4). The strong transition (the one with high oscillator strength) of HTM in the visible region corresponds to the transitions from HOMO to LUMO (Table 2).

The UV-vis spectra of HTM has three absorption band peaks; two in the visible and one near to the IR region of the spectrum, which is an indication of its efficient light-harvesting ability. Charge-transfer character occurs at the lower energy part of UV-vis absorption and a low-lying wide conduction band (Fig. 3) [52].

3.6. HTM and N3 interacting system

Inter-molecular charge transferring and dye regeneration is simulated from the interaction study of HTM and Dye. The interaction between N3 and HTM is purely non-dissociative but quite strong due to the establishment of non-covalent bonding. The carboxylic anchoring groups of N3 establishes non-covalent bonding with the N and Se of HTM (Fig. 6) which is a clear evidence of their strong interaction. Two of the oxygen atoms of N3 make an inter-molecular bond with the Se of HTM, each having non-bonding distances of 3.13 Å. Other atoms involved in this electrostatic type of interaction are H atoms which lead to hydrogen bonding i.e., H of N3 with Se at ca. 3.54 Å and two H atoms of N3 with N of HTM each having distance of 2.74 Å (Fig. 6). The inter-molecular electrostatic energy of this interaction is -8.72 kcal/mol, which further confirms the evidence of charge transferring between HTM and N3. It is well-known from the literature that a good amount of this type of dye work as donor- π -electrons –acceptor where a large orbital density of the LUMO should cover the carboxylic anchoring groups and a small electronic cloud density cover their HOMO [11–16,53]. This similar type of phenomenon is observed in the molecular orbitals of N3 (Fig. S5)

which is consistent with the already reported work [11–16,53]. The higher electronic cloud density at LUMO compared to that of HOMO shows that the charge injection is favored from HTM to dye and prevents charge recombination in the dye molecule. The energies of HOMO, LUMO, band gap and an optical gap of these three species, before and after interaction are listed in Table 2.

Frontier molecular orbitals of HTM-N3 are shown in Fig. 7, where the π -electron donation from HTM towards dye can be seen. The position of HOMO level of HTM which is considerably above (0.61 eV) the HOMO of dye (N3); obviously evidences the hole injection from N3 to HTM. Furthermore, the HOMO and LUMO of HTM in the HTM-N3 system indicates how the transformation of π -electrons towards N3 is achieved. Frontier molecular orbital analysis led us to conclude that a nice overlap in the orbitals coupling of HTM and N3 occurs, which can lead to the high efficiency of the corresponding solar cell.

As discussed earlier, the electrons and holes carrying species can be more precisely determined from the contours of their HOMO and LUMO, respectively. Lower the HOMO energy level (more negative) of the HTM the higher will be its open-circuit voltage in the corresponding solar cells, and a high adiabatic IP ensures its high stability in terms of resistance towards ionization. The high IP (4.57 eV) of HTM which is 1.19 eV above the HOMO of dye is responsible for the hole exchange as well as high chemical stability toward oxidation. The adiabatic IP and EA are obtained from the negative of the DFT orbital (HOMO and LUMO) energy; using Koopman's theorem. The electrical gap (band gap) is estimated from the difference of IP and EA while the optical gap is simulated from the Δ SCF TD-DFT calculation, where first allowed electronic excitation with higher oscillator strength is considered (Table 2). In a typical DSSC, dye provides an electron to a wide bandgap material (TiO_2) and then regenerates itself from the liquid electrolyte. In our proposed SDSC configuration the regeneration of dye has been achieved from HTM, due to its low reorganization energy (*vide supra*). So, when the charge moves to N3, relaxation energies is needed to remove this charge from HTM to regenerate the dye which is about 0.21 eV (eq. (1)).

According to NBO charge analysis, HTM and N3 share about

Table 2

Excitation Energy, HOMO, LUMO, Band gap, optical gap, Exciton Binding Energy (E_b) and reorganization energy in eV of HTM (in solvent), N3, and TiO_2 .

Species	HOMO	LUMO	Band gap	Optical gap	λ (eV)	Orbital transition	E_b (eV)
HTM	-4.57	-2.93	1.64	1.34	0.21	H \rightarrow L	0.55
TiO_2	-7.33	-4.27	3.06	2.62		H \rightarrow L	
N3	-5.76	-3.42	2.34	2.27		H ₋₂ \rightarrow L	

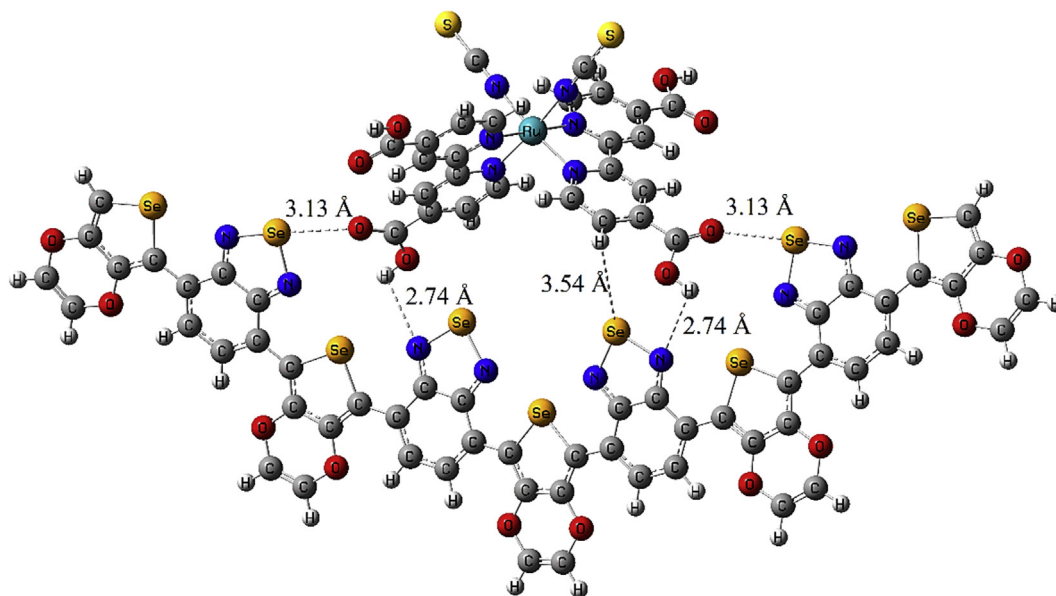


Fig. 6. Optimized geometry of HTM-N3 complex.

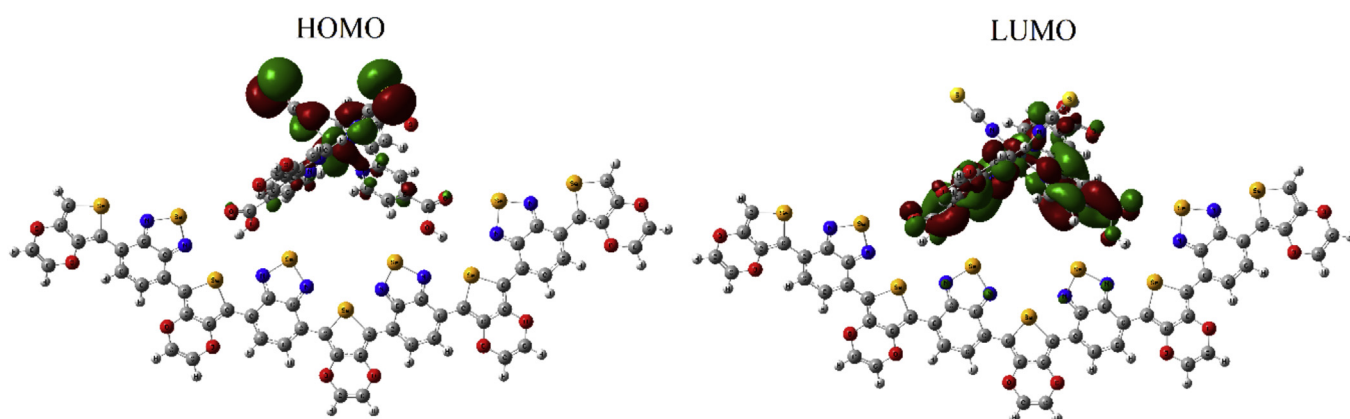


Fig. 7. Contours of the HOMO and LUMO of HTM-N3 system.

0.184 e^- of electronic cloud density (Fig. S6a), moreover, the individual charge (NBO) on each atom of this complex is shown in Fig. S6b.

3.7. N3 and TiO_2 interacting system

In order to understand the electron transferring phenomena in the proposed solar cell, we further investigated the MOs analysis of N3- TiO_2 system; as shown in Fig. 8. Contours of the HOMO and LUMO of N3- TiO_2 system indicate that dye has delocalized π -electrons which are ready for donation. So, a clear and sophisticated picture of electron transformation is observed from N3 to mesoporous titanium dioxide. The estimated open circuit voltage of this solar cell is 1.49 eV which is simulated from the difference of the quasi-Fermi levels of the TiO_2 and the HOMO energy level of N3 (Table 2).

3.8. HTM, N3, and TiO_2 interacting system

Finally, the three components are simultaneously interacted via non-covalent bonding interaction to find/confirm the net electron-

hole transformation. The HTM-N3- TiO_2 complex is optimized with LanL2DZ pseudopotential, using hybrid functional of DFT such as B3LYP (Fig. 9). On the electrostatic energy surface, both dissociative and non-dissociative strong interactions are found among these three components as can be seen from Fig. 9. The interaction of N3 with TiO_2 is dissociative where oxygen atoms of the carboxylic groups make covalent bonds with the Ti atom of TiO_2 . However, the HTM and N3 interaction is non-dissociative but quite strong, due to the establishment of Hydrogen bonding (Se-H), see Fig. 9. Furthermore, the HOMO and LUMO of this three components system are also simulated to find the contours of the electronic cloud density (Fig. 10). Results of the HOMO and LUMO are also inconsistent with the previous results, where an ideal and classical phenomenon is justified. Based on these simulations, we can say that when light shines on the proposed configuration, the delocalized π -electrons of N3 would become activated and move to TiO_2 and ultimately would regenerate itself by sharing an electron from the HOMO of HTM.

An easy pathway for the movement of electrons in the said complex is made possible due to the alliance of the energy levels (HOMO and LUMO) of TiO_2 , N3, and HTM; having an upstairs ladder

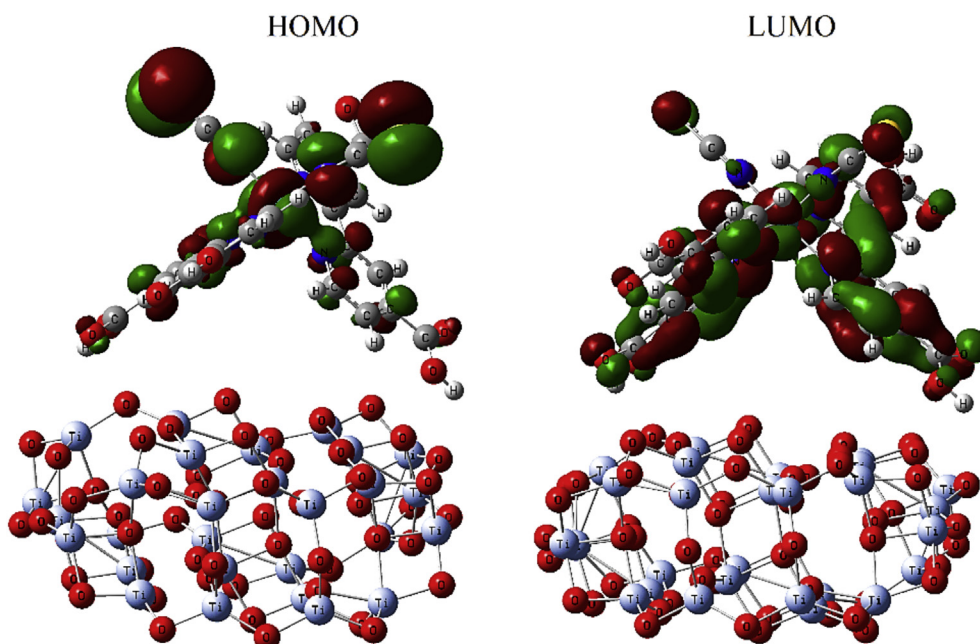


Fig. 8. HOMO and LUMO contours of the N3-TiO₂ system.

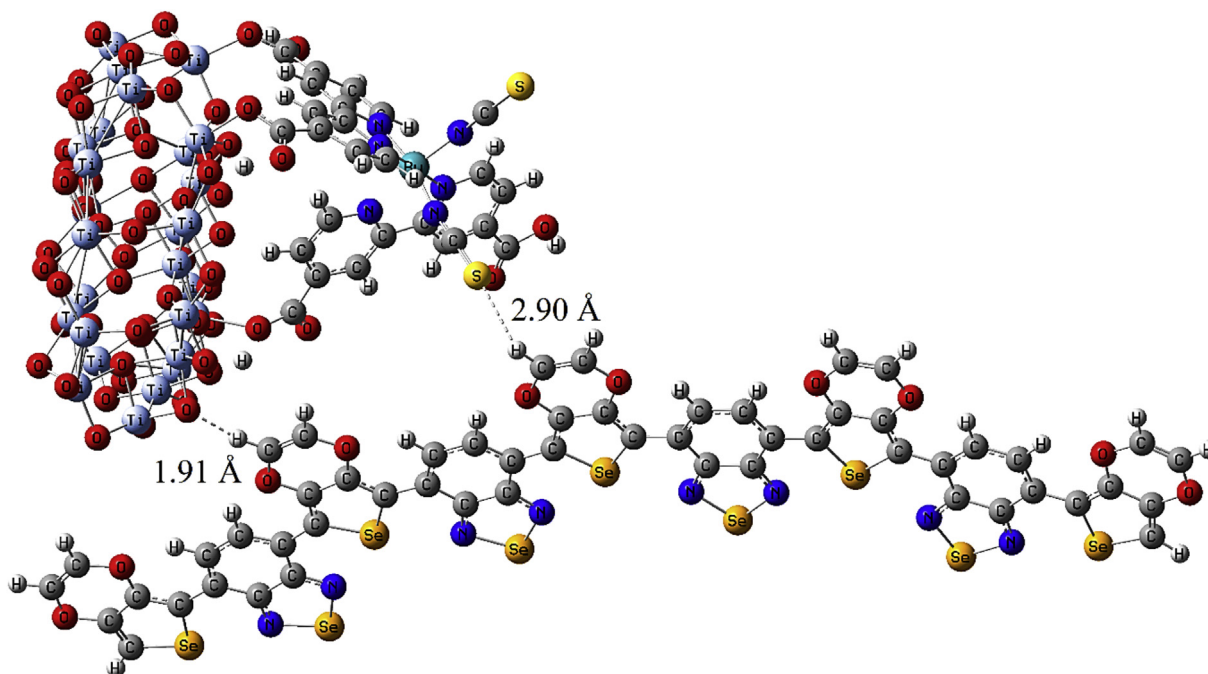


Fig. 9. Optimized Geometric Structure of the HTM-N3-TiO₂ system.

like band diagram (Fig. 1). Analysis of the data of Table 2 and Fig. 10, led us to conclude that it is not unusual for the electron to shift from the LUMO of HTM to N3 or from N3 to TiO₂ under the applied biased. As the LUMO energy level of HTM is about 0.49 eV above the LUMO edge position of N3 while that of dye and TiO₂ has 0.85 eV of difference in their LUMOs energy levels.

In summary, if the proposed configuration of SDSC is exposed to light; the excited electrons of both of the dye and HTM become delocalize and move from the dye to nanoporous TiO₂ and consequently the oxidized dye would be regenerated from the HTM via exchanging of the electron.

4. Conclusion

It is believed that all-solid-state DSSC (SDSC) is cost effective and a stable solar cell compared to the classically reported one. We have carried out structural, electronic, optical, and charge-transport properties of a donor-acceptor-donor polymer; a Hole transporting material (HTM), N3 and TiO₂ for the design of an efficient SDSC. We proposed an ideal setup for an SDSC, where the HTM, N3, and TiO₂ are chosen, based on their upstairs like energy levels (band edge positions); having a difference of at least 0.50 eV. Our theoretical simulations prove that if we shine a light on the

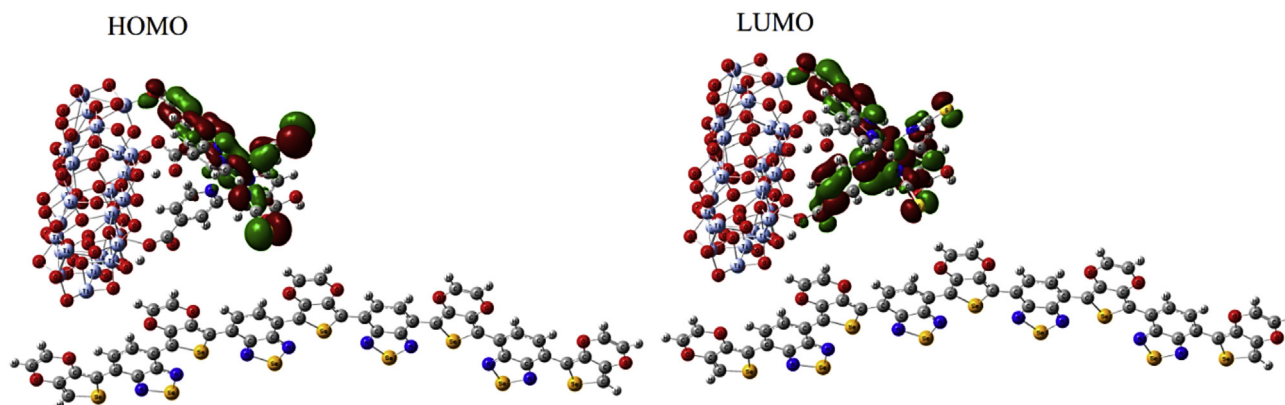


Fig. 10. HOMO and LUMO contours of the HTM-N3-TiO₂ system.

proposed setup, the electron would move from the dye to TiO₂ and from HTM to dye, to be regenerate. HOMO level of our investigated HTM lies about 1.19 eV above the sanitizer, provides an easy pathway for hole injection. Strong overlapped molecular orbitals of HTM with that of sensitizer and their lower reorganization energy (0.21 eV) which led to 0.55 eV exciton binding energy, responsible for high short-circuit current density and high power conversion efficiency. The theoretical open-circuit voltage of about 1.49 eV is responsible for high quantum yield. Moreover, the HTM is chemically stable to oxidation due to 4.57 eV of IP and has excellent transparency in the visible region of sunlight (λ_{max} of 925 nm).

Acknowledgments

We gratefully thank Professor Ulrike Salzner for helpful discussions, the University of Exeter, ESI Beowulf Cluster, NOTUR supercomputing facilities within the project nn4608k and the UK Solar Fuel Network (SFN).

Appendix A. Supplementary data

Supplementary data related to this article can be found at <http://dx.doi.org/10.1016/j.jallcom.2016.12.076>.

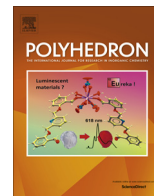
References

- [1] J.D. Servaites, B.M. Savoie, J.B. Brink, T.J. Marks, M.A. Ratner, Modeling geminate pair dissociation in organic solar cells: high power conversion efficiencies achieved with moderate optical bandgaps, *Energy & Environ. Sci.* 5 (2012) 8343–8350.
- [2] J. Twidell, T. Weir, *Renewable Energy Resources*, Routledge, 2015.
- [3] A. Colli, Failure mode and effect analysis for photovoltaic systems, *Renew. Sustain. Energy Rev.* 50 (2015) 804–809.
- [4] C. Liu, J. Tang, H.M. Chen, B. Liu, P. Yang, A fully integrated nanosystem of semiconductor nanowires for direct solar water splitting, *Nano Lett.* 13 (2013) 2989–2992.
- [5] T. Sekiguchi, S. Kambe, S. Yamada, T. Ooashi, *Dye-sensitized Solar Cell*, 2015. Google Patents.
- [6] K. Iwashina, A. Iwase, Y.H. Ng, R. Amal, A. Kudo, Z-Schematic water splitting into H₂ and O₂ using metal sulfide as a hydrogen-evolving photocatalyst and reduced graphene oxide as a solid-state electron mediator, *J. Am. Chem. Soc.* 137 (2015) 604–607.
- [7] M.A. Mughal, R. Engelken, R. Sharma, Progress in indium (III) sulfide (In₂S₃) buffer layer deposition techniques for CIS, CIGS, and CdTe-based thin film solar cells, *Sol. Energy* 120 (2015) 131–146.
- [8] M. Grätzel, Dye-sensitized solar cells, *J. Photochem. Photobiol. C Photochem. Rev.* 4 (2003) 145–153.
- [9] M. Grätzel, Dye-sensitized solar cells, *J. Photochem. Photobiol. C Photochem. Rev.* 4 (2003) 145–153.
- [10] V.K. Narra, H. Ullah, V.K. Singh, L. Giribabu, S. Senthilarasu, S.Z. Karazhanov, A.A. Tahir, T.K. Mallick, H.M. Upadhyaya, D- π -A system based on zinc porphyrin dyes for dye-sensitized solar cells: combined experimental and DFT–TDDFT study, *Polyhedron* 100 (2015) 313–320.
- [11] S.-H. Liu, H. Fu, Y.-M. Cheng, K.-L. Wu, S.-T. Ho, Y. Chi, P.-T. Chou, Theoretical study of N749 dyes anchoring on the (TiO₂)₂₈ surface in DSSCs and their electronic absorption properties, *J. Phys. Chem. C* 116 (2012) 16338–16345.
- [12] R. Ullah, H. Ullah, S. Bilal, K. Ali, Oligomeric synthesis and density functional theory of leucoemeraldine base form of polyaniline, *J. Mol. Struct.* 1127 (2017) 734–741.
- [13] D. Moia, U.B. Cappel, T. Leijtens, X. Li, A.M. Telford, H.J. Snaith, B.C. O'Regan, J. Nelson, P.R. Barnes, The role of hole transport between dyes in solid-state dye-sensitized solar cells, *J. Phys. Chem. C* 119 (2015) 18975–18985.
- [14] X.-L. He, G.-J. Yang, C.-J. Li, M. Liu, S.-Q. Fan, Failure mechanism for flexible dye-sensitized solar cells under repeated outward bending: cracking and spalling off of nano-porous titanium dioxide film, *J. Power Sources* 280 (2015) 182–189.
- [15] M.G. Lobello, S. Fantacci, F. De Angelis, Computational spectroscopy characterization of the species involved in dye oxidation and regeneration processes in dye-sensitized solar cells, *J. Phys. Chem. C* 115 (2011) 18863–18872.
- [16] S. Fantacci, F. De Angelis, M.K. Nazeeruddin, M. Grätzel, Electronic and optical properties of the spiro-MeOTAD hole conductor in its neutral and oxidized forms: a DFT/TDDFT investigation, *J. Phys. Chem. C* 115 (2011) 23126–23133.
- [17] I. Chung, B. Lee, J. He, R.P. Chang, M.G. Kanatzidis, All-solid-state dye-sensitized solar cells with high efficiency, *Nature* 485 (2012) 486–489.
- [18] U. Bach, D. Lupo, P. Comte, J. Moser, F. Weissörtel, J. Salbeck, H. Spreitzer, M. Grätzel, Solid-state dye-sensitized mesoporous TiO₂ solar cells with high photon-to-electron conversion efficiencies, *Nature* 395 (1998) 583–585.
- [19] A. Fujishima, X.-T. Zhang, Solid-state dye-sensitized solar cells, *Proc. Jpn. Acad. Ser. B* 81 (2005) 33–42.
- [20] F.C. Krebs, Polymer solar cell modules prepared using roll-to-roll methods: knife-over-edge coating, slot-die coating and screen printing, *Sol. Energy Mater. Sol. Cells* 93 (2009) 465–475.
- [21] G. Gustafsson, Y. Cao, G. Treacy, F. Klavetter, N. Colaneri, A. Heeger, Flexible light-emitting diodes made from soluble conducting polymers, *Nature* 357 (1992) 477–479.
- [22] C.J. Brabec, N.S. Sariciftci, J.C. Hummelen, Plastic solar cells, *Adv. Funct. Mater.* 11 (2001) 15–26.
- [23] M. Kamran, H. Ullah, A.A. Shah, S. Bilal, A.A. Tahir, K. Ayub, Combined experimental and theoretical study of poly (aniline-co-pyrrole) oligomer, *Polymer* 72 (2015) 30–39.
- [24] H. Van Mellekom, J. Vekemans, E. Meijer, Band-gap engineering of donor–acceptor-substituted π -conjugated polymers, *Chem. Eur. J.* 4 (1998) 1235–1243.
- [25] S. Bibi, H. Ullah, S.M. Ahmad, A.-u.-H. Ali Shah, S. Bilal, A.A. Tahir, K. Ayub, Molecular and electronic structure elucidation of polypyrrole gas sensors, *J. Phys. Chem. C* 119 (2015) 15994–16003.
- [26] H. Ullah, A.-u.-H.A. Shah, S. Bilal, K. Ayub, Doping and dedoping processes of polypyrrole: DFT study with hybrid functionals, *J. Phys. Chem. C* 118 (2014) 17819–17830.
- [27] H. Ullah, K. Ayub, Z. Ullah, M. Hanif, R. Nawaz, S. Bilal, Theoretical insight of polypyrrole ammonia gas sensor, *Synth. Met.* 172 (2013) 14–20.
- [28] E. Poverenov, N. Zamoshchik, A. Patra, Y. Ridelman, M. Bendikov, Unusual doping of donor–acceptor-type conjugated polymers using lewis acids, *J. Am. Chem. Soc.* 136 (2014) 5138–5149.
- [29] H. Ullah, S. Bibi, A.A. Tahir, T.K. Mallick, Density functional theory study of selenium-substituted low-bandgap donor–acceptor–donor polymer, *J. Phys. Chem. C* 120 (48) (2016) 27200–27211.
- [30] M.J.T.G.W.S. Frisch, H.B. Schlegel, G.E. Scuseria, M.A. Robb, J.R. Cheeseman, G. Scalmani, V. Barone, B. Mennucci, G.A. Petersson, et al., *Gaussian 09*, Rev. D. 0.1, Gaussian, Inc., Wallingford, CT, 2013.
- [31] H. Ullah, A.-u.-H.A. Shah, K. Ayub, S. Bilal, Density functional theory study of poly (o-Phenylenediamine) oligomers, *J. Phys. Chem. C* 117 (2013) 4069–4078.
- [32] A.R. Allouche, Gabedit, 2011. <http://gabedit.sourceforge.net>.

- [33] N. O'Boyle, A. Tenderholt, K. Langner, J. Comp. Chem. 29 (2008) 839. Direct Link: Abstract Full Article (HTML) PDF (158K) References Web of Science® Times Cited 59.
- [34] R. Dennington, T. Keith, J.G. Millam, Version 5.0, 9 Semichem Inc., Shawnee Mission KS, 2013.
- [35] A. Patra, Y.H. Wijssboom, S.S. Zade, M. Li, Y. Sheynin, G. Leitus, M. Bendikov, Poly (3, 4-ethylenedioxy-selenophene), J. Am. Chem. Soc. 130 (2008) 6734–6736.
- [36] A. Patra, V. Agrawal, R. Bhargav, D. Bhardwaj, S. Chand, Y. Sheynin, M. Bendikov, Metal free conducting PEDOS, PEDOT, and their analogues via an unusual bromine-catalyzed polymerization, Macromolecules 48 (2015) 8760–8764.
- [37] A. Patra, M. Bendikov, S. Chand, Poly (3, 4-ethylenedioxy-selenophene) and its derivatives: novel organic electronic materials, Acc. Chem. Res. 47 (2014) 1465–1474.
- [38] M. Li, Y. Sheynin, A. Patra, M. Bendikov, Tuning the electrochromic properties of poly (alkyl-3, 4-ethylenedioxy-selenophenes) having high contrast ratio and coloration efficiency, Chem. Mater. 21 (2009) 2482–2488.
- [39] H. Ullah, A.-u.-H.A. Shah, S. Bilal, K. Ayub, DFT study of polyaniline NH₃, CO₂, and CO gas sensors: comparison with recent experimental data, J. Phys. Chem. C 117 (2013) 23701–23711.
- [40] Z. Ullah, A. Rauf, M. Yaseen, W. Hassan, M. Tariq, K. Ayub, A.A. Tahir, H. Ullah, Density functional theory and phytochemical study of 8-hydroxyisodiospyrin, J. Mol. Struct. 1095 (2015) 69–78.
- [41] F. Nunzi, S. Agrawal, A. Selloni, F. De Angelis, Structural and electronic properties of photoexcited TiO₂ nanoparticles from first principles, J. Chem. Theory Comput. 11 (2015) 635–645.
- [42] M. Pastore, F. De Angelis, First-principles modeling of a dye-sensitized TiO₂/IrO₂ photoanode for water oxidation, J. Am. Chem. Soc. 137 (2015) 5798–5809.
- [43] E. Ronca, G. Marotta, M. Pastore, F. De Angelis, Effect of sensitizer structure and TiO₂ protonation on charge generation in dye-sensitized solar cells, J. Phys. Chem. C 118 (2014) 16927–16940.
- [44] H. Ullah, Inter-molecular interaction in Polypyrrole/TiO₂: a DFT study, J. Alloys Compd. 692 (2017) 140–148.
- [45] H. Ullah, A.A. Tahir, T.K. Mallick, Polypyrrole/TiO₂ composites for the application of photocatalysis, Sens. Actuators B (2016), <http://dx.doi.org/10.1016/j.snb.2016.10.019>.
- [46] S.S. Zade, N. Zamoshchik, M. Bendikov, From short conjugated oligomers to conjugated polymers. Lessons from studies on long conjugated oligomers, Acc. Chem. Res. 44 (2010) 14–24.
- [47] H. Sun, J. Autschbach, Electronic energy gaps for π -conjugated oligomers and polymers calculated with density functional theory, J. Chem. Theory Comput. 10 (2014) 1035–1047.
- [48] Y.A. Duan, Y. Geng, H.B. Li, J.L. Jin, Y. Wu, Z.M. Su, Theoretical characterization and design of small molecule donor material containing naphthodithiophene central unit for efficient organic solar cells, J. Comput. Chem. 34 (2013) 1611–1619.
- [49] D. Alberga, G.F. Mangiatordi, F. Labat, I. Ciofini, O. Nicolotti, G. Lattanzi, C. Adamo, Theoretical investigation of hole transporter materials for energy devices, J. Phys. Chem. C 119 (2015) 23890–23898.
- [50] C. Risko, G. Kushto, Z. Kafafi, J.-L. Brédas, Electronic properties of silole-based organic semiconductors, J. Chem. Phys. 121 (2004) 18.
- [51] A. Köhler, H. Bässler, Electronic Processes in Organic Semiconductors: an Introduction, John Wiley & Sons, 2015.
- [52] U. Salzner, Electronic structure of conducting organic polymers: insights from time-dependent density functional theory, Wiley Interdiscip. Rev. Comput. Mol. Sci. 4 (2014) 601–622.
- [53] E.L. Spitler, S.P. McClintock, M.M. Haley, Dynamic proton-induced emission switching in donor-functionalized dehydrobenzopyrid [15] annulenes, J. Org. Chem. 72 (2007) 6692–6699.

[Article 7]

V. K. Narra, H. Ullah, V. K. Singh, L. Giribabu, S. Senthilarasu, S. Z. Karazhanov, A. A. Tahir, T. K. Mallick, H. M. Upadhyaya, "D-π-a system based on zinc porphyrin dyes for dye-sensitized solar cells: Combined experimental and dft-tddft study." *Polyhedron*. vol. 100, pp. 313-320, Nov. 2015.



D- π -A system based on zinc porphyrin dyes for dye-sensitized solar cells: Combined experimental and DFT-TDDFT study



Vamsi K. Narra^a, Habib Ullah^b, Varun K. Singh^a, Lingamallu Giribabu^{a,*}, S. Senthilarasu^{b,*}, S.Zh. Karazhanov^c, Asif A. Tahir^b, Tapas K. Mallick^b, Hari M. Upadhyaya^d

^a Inorganic and Physical Chemistry Division, Indian Institute of Chemical Technology, Hyderabad 500 007, India

^b Environment and Sustainability Institute (ESI), University of Exeter, Penryn Campus, TR10 9FE, UK

^c Department for Solar Energy, Institute for Energy Technology, 2027 Kjeller, Norway

^d Wolfson Centre for Materials Processing, Institute of Materials and Manufacturing, Department of Mechanical, Aerospace and Civil Engineering, Brunel University, Uxbridge, UB8 3PH London, UK

ARTICLE INFO

Article history:

Received 4 July 2015

Accepted 26 August 2015

Available online 1 September 2015

Keywords:

Porphyrin

Furan

Redox electrolyte

Solar cells

DFT

ABSTRACT

A series of four new porphyrin-furan dyads were designed and synthesized by having anchoring group either at *meso*-phenyl or pyrrole- β position of a zinc porphyrin based on donor- π -acceptor (D- π -A) approach. The porphyrin macrocycle acts as donor, furan hetero cycle acts as π -spacer and either cyanoacetic acid or malonic acid group acts as acceptor. These dyads were fully characterized by UV-Visible, ¹H NMR, MALDI-MS and fluorescence spectroscopies and cyclic voltammetry. Both of the observed and TD-DFT simulated UV-Vis spectra has strong correlation which validate and confirm the synthesized dyads and theoretical method for this type of compounds. Both *soret* and *Q*-bands are red shifted in the case of pyrrole- β substituted dyads. The redox potentials of all four dyads are not altered in comparison with their individual constituents. The dyads were tested in dye sensitized solar cells and found pyrrole- β substituted zinc porphyrins are showing better performance in comparison with the corresponding *meso*-phenyl dyads. Optical band gap, Natural bonding, and Molecular bonding orbital (HOMO-LUMO) analysis are in favour of pyrrole- β substituted zinc porphyrins contrast to *meso*-phenyl dyads.

© 2015 Elsevier Ltd. All rights reserved.

1. Introduction

Porphyrins and their derivatives have been intensively studied for many years because of their importance in the photochemistry and photo-biology processes [1–3]. Under the influence of the large planar π -conjugated structure, porphyrin derivatives exhibit good thermal stability, strong two-photon absorption [4], efficient electron transfer [5–7], and interesting photo-electrochemical properties [8]. Therefore, porphyrins have been frequently employed in various fields such as biomimetic natural photosynthesis [9–11], chemical and biological sensors [12], organic light-emitting diodes [13], field effect transistors [14], non-linear optical properties [15] and dye-sensitized solar cells (DSSCs) [16,17].

DSSCs have emerged as an innovative solar energy conversion technology which provides a pathway for the development of low-cost, renewable and environmentally acceptable energy production [18–20]. However, the technology is not yet

commercialized due to several technical problems. The sensitizer is one of the key components in achieving high conversion efficiency and durability of the devices. The widely used sensitizers are Ru(II) polypyridyl complexes with a certified conversion efficiency of 11.4% [18,21,22]. In spite of this, the main drawbacks of these sensitizers are the lack of absorption in the red region of the visible spectrum and also relatively low molar extinction coefficient above 600 nm. In this regard, porphyrins and their derivatives are found to be alternative sensitizers to Ru(II) polypyridyl complexes based on their absorption and thermal properties.

Some metalloporphyrins have been tested for the photosensitization of wideband-gap semiconductors, the most common being either free-base or its zinc derivative of the *meso*-benzoic acid substituted porphyrins [23–25]. However, the efficiency of *meso*-substituted porphyrins remained around 3% for a long time till 2007. In order to further improve the efficiency and durability of porphyrin based DSSC devices, one has to tune photophysical properties of porphyrin macrocycle by introducing substituents either at *meso*-phenyl or at pyrrole- β position/s. Officer and co-workers have reported a combination of conjugated ethenyl

* Corresponding authors.

E-mail address: S.Sundaram@exeter.ac.uk (S. Senthilarasu).

or diethenyl linker at the pyrrole- β position and a carboxylate binding group to give the device efficiencies up to 7.1% [26]. Grätzel and co-workers have redesigned and reported a porphyrin sensitizer (YD2-o-C8) based on D- π -A concept [27]. The new porphyrin with co-sensitization of an organic dye (Y123) using cobalt redox electrolyte attained a power conversion efficiency of 12.3%. Recently, same group has further re-designed the porphyrin macrocycle by introducing benzenethiadiazole group with an efficiency of 13% [28], which is superior to those developed based on Ru(II) polypyridyl complexes and becomes a new milestone in this area. The high efficiency of porphyrins sensitizers is probably due to the bathochromic shift of absorption and minimization of charge recombination. The bathochromic shift of absorption spectra of porphyrins were also done by introduction of hetero aromatic molecules like thiophene and furan either at *meso*-phenyl or at pyrrole- β position [29,30]. However, introducing the similar hetero aromatic groups either at *meso*-phenyl or at pyrrole- β position of porphyrin macrocycle and compare their photovoltaic performance was not reported in the literature to the best of our knowledge.

In the present work, we have synthesized a series of four new porphyrin based sensitizers having a furan hetero aromatic ring between the porphyrin macrocycle and anchoring group either at *meso*-phenyl or at pyrrole- β position of porphyrin. The porphyrin macrocycle acts as donor, furan hetero cycle acts as π -spacer and either cyanoacetic acid or malonic acid group acts as acceptor. They are 5,10,15,20-tris(4-methylphenyl)zinc(II)porphyrinato-furan-2-(2-cyano-2-yl-acrylic acid) [β -Zn-CAA], 5,10,15,20-tris(4-methylphenyl)zinc(II)porphyrinato-furan-2-(2-yl-methylene malonic acid) [β -Zn-MA], 5-(5-(4-Phenyl)-10,15,20-tris(4-methylphenyl) zinc (II) porphyrinato)-furan-(2-cyano-2-yl-acrylic acid) [*meso*-Zn-CAA] and 5-(5-(4-Phenyl)-10,15,20-tris(4-methylphenyl) zinc (II) porphyrinato)-furan-(2-yl-methylene malonic acid) [*meso*-Zn-MA]. The structure of the photosensitizers is shown in Schemes 1 and 2. All four compounds were characterized by UV-Visible, ^1H NMR, MALDI-MS, and fluorescence spectroscopies as well as cyclic voltammetry and their device efficiency was evaluated by using I^-/I_3^- redox couple. Theoretical study of the compounds has also been performed by the first-principles calculations.

2. Experimental

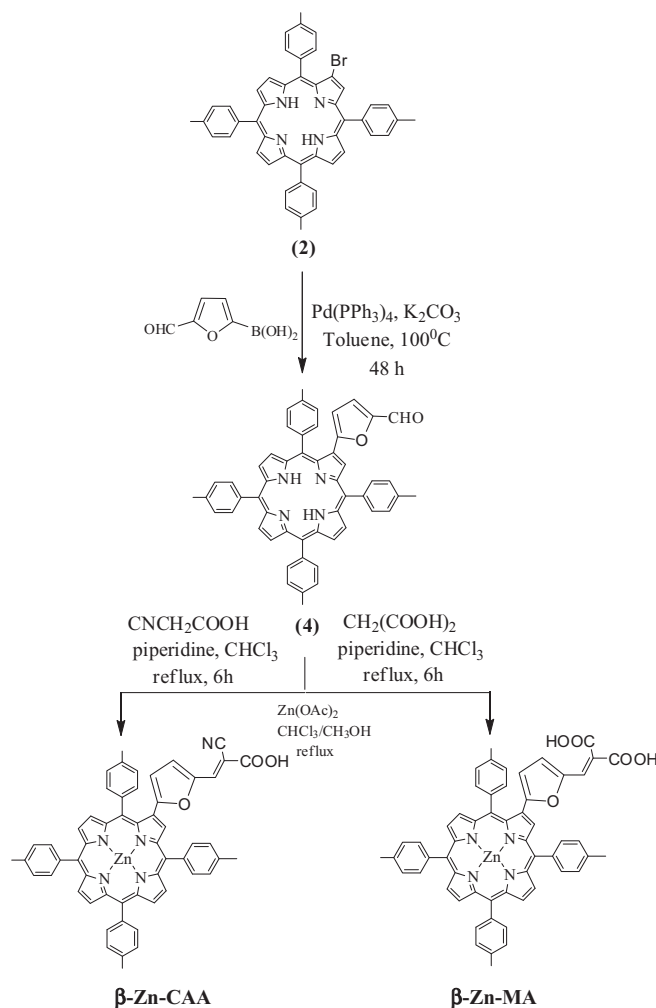
2.1. Materials

Analytical reagent grade solvents and reagents were used for synthesis, and distilled laboratory grade solvents were used for chromatography. Milli-Q water was used for synthetic and purification purpose. Dry toluene, chloroform and dichloromethane were prepared by argon-degassed solvent through activated alumina columns. N_2 (oxygen-free) was passed through a KOH drying column to remove moisture.

ACME silica gel (100–200 mesh) was used for column chromatography and thin-layer chromatography was performed on Merck-precoated silica gel 60-F₂₅₄ plates. Either gravity or flash chromatography was used for compound purification. Where a dual solvent system was used, gradient elution was employed, and the major band was collected. All porphyrin reactions were carried out under nitrogen or argon atmosphere using dry degassed solvents, and the apparatus was shielded from ambient light.

2.2. Synthesis

The compounds 5,10,15,20-tetratolyl porphyrin (H_2TTP), 5,10,15,20-tetratolyl porphyrinato zinc(II) (ZnTTP), 2-bromo-5,10,15,20-tetratolyl porphyrin (**1**), and 5-(4-bromophenyl)-



Scheme 1. Synthetic Scheme of β -Zn-CAA and β -Zn-MA.

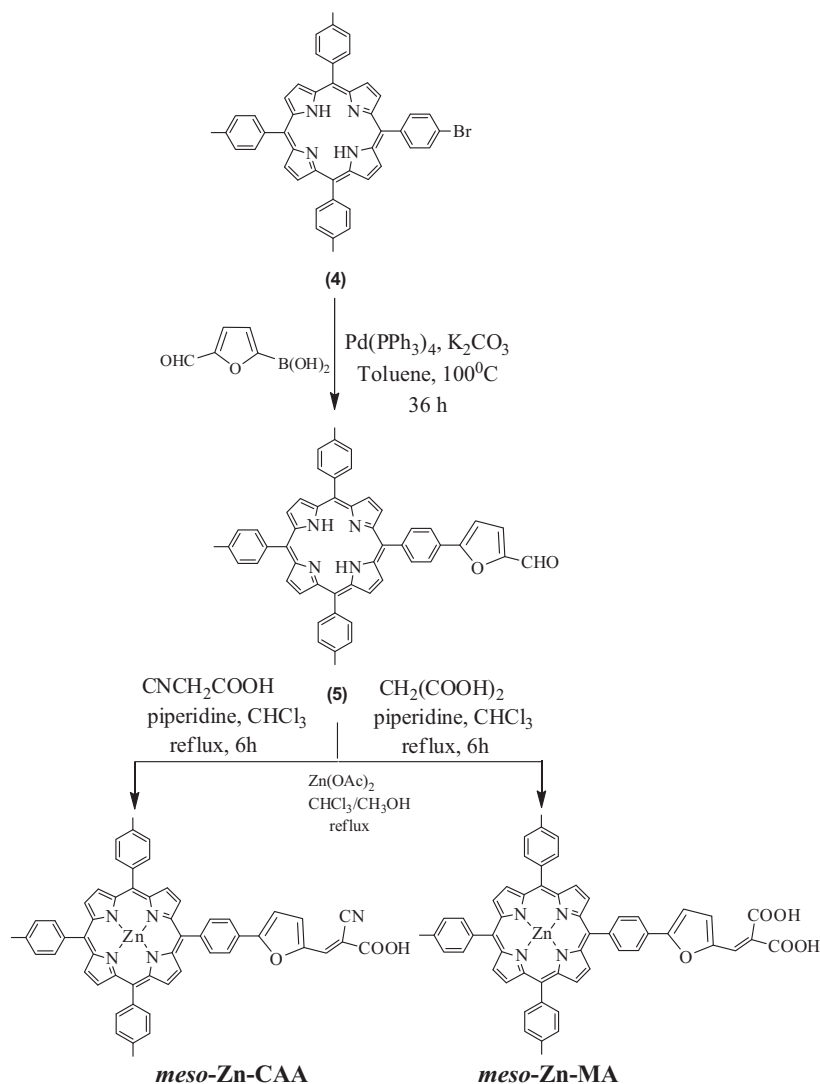
10,15,20-tritoyl porphyrin (**2**) were synthesized according to the reported procedures in the literature [31].

2.2.1. Synthesis of 2-(5-formylfuran)-5,10,15,20-tetra(tolyl) porphyrin (**3**)

1 (35 mg, 0.047 mmol), 5-formyl furan-2-boronic acid (26.32 mg, 0.188 mmol), K_2CO_3 (52.61 mg, 0.380 mmol), Palladium tetrakis (triphenyl phosphine), (5.42 mg, 0.0047 mmol) in a dried single neck round bottom flask, evacuated with nitrogen and then refilled. To this 20 ml of toluene was added and the resulting reaction mixture was heated to 90–100 °C for 48 h. The solvent was removed under vacuum and obtained solid was washed three times with CHCl_3 , filtered, dried over anhydrous Na_2SO_4 and solvent removed under vacuum. The brown colour crude material obtained was subjected to silica gel column chromatography and eluted with CHCl_3 . The second brown colour band was the desired compound in 62% yield. *Anal.* Calc. for $\text{C}_{52}\text{H}_{38}\text{N}_4\text{O}_2$ (764.91): C, 83.22; H, 5.27; N, 7.32. Found: C, 83.21; H, 5.25; N, 7.30%. ^1H NMR: 9.49 (s, 1 H), 8.96–8.78 (m, 7 H), 8.11 (d, 8 H), 7.56–7.54 (m, 8 H), 7.10 (d, 1 H, $J = 3.77$ Hz), 6.40 (d, 1H, $J = 3.77$ Hz), 2.70 (s, 12 H), –2.61 (s, 2 H). ESI MS ($\text{C}_{53}\text{H}_{40}\text{N}_4\text{O}_2$) m/z : 765 (M+1), 766 (M+2).

2.2.2. Synthesis of β -Zn-CAA

3 (200 mg, 0.24 mmol) and cyanoacetic acid (107.53 mg, 1.265 mmol) was dissolved in 100 ml of CHCl_3 . To this piperidine



Scheme 2. Synthetic Scheme of *meso*-Zn-CAA and *meso*-Zn-MA.

(0.956 ml, 9.18 mmol) was added drop-wise and the reaction mixture was heated to reflux for 5 h. After cooling to room temperature, the reaction mixture was washed with water and 0.1 M HCl. The organic layer was dried over anhydrous Na₂SO₄. The solvent was removed under vacuum and the residue was subjected to silica gel column chromatography and eluted with methanol/dichloromethane (95:5% v/v) mixture as eluent. The solvent front running brown colour band was collected. The obtained free-base compound was then subjected to Zinc metallation using Zn(OAc)₂ and CHCl₃/Methanol to get the corresponding zinc derivative in 75% yield. *Anal. Calc.* for C₅₆H₃₉N₅O₃Zn (895.33): C, 75.12; H, 4.39; N, 7.82. Found: C, 75.15; H, 4.40; N, 7.80%. ESI MS (C₅₆H₃₉N₅O₃Zn) m/z: 894 (M⁺), 917 (M+Na⁺). ¹H NMR: 8.99 (s, 1 H), 8.87–8.75 (m, 7 H), 8.10–7.90 (m, 8 H), 7.97 (d, 2 H), 7.68–7.60 (m, 8 H), 2.69 (s, 12 H). FT IR (KBr, λ_{max}/cm⁻¹): 2210 (–CN). UV–Vis(λ_{abs}, nm) in THF: 425 (5.03), 554 (4.06), 607 (3.90).

2.2.3. Synthesis of β-Zn-MA

This compound was synthesized by an analogous manner to that described above for the synthesis of β-Zn-CAA, but only the difference is that by replacing cyanoacetic acid with malonic acid. *Anal. Calc.* for C₅₆H₃₉N₅O₃Zn (914.33): C, 73.56; H, 4.41; N, 6.13.

Found: C, 73.55; H, 4.40; N, 7.10%. ESI MS (C₅₆H₄₀N₄O₅Zn) m/z: 912 (M–2), 849 (M⁺–Zn). FT IR (KBr, ν_{max}/cm⁻¹): 1615 (C=O). UV–Vis (λ_{abs}, nm) in THF: 429 (5.11), 564 (4.33), 607 (4.21).

2.2.4. 5-(5-(4-Phenyl)-10,15,20-tris(4-methylphenyl)porphyrin)-furan-2-carbaldehyde (4)

This compound was synthesized by an analogous manner to that described above for the synthesis of **3**, but by replacing **1** with **2**. *Anal. Calc.* for C₅₂H₃₈N₄O₂ (750.88): C, 83.18; H, 5.10; N, 7.46. Found: C, 83.20; H, 5.12; N, 7.50%. ESI MS (C₅₂H₃₈N₄O₂) m/z: 756 (M⁺). ¹H NMR: 9.8 (s, 1H), 8.84–8.78 (m, 8H), 8.31 (d, 2H), 8.10–8.08 (m, 8H), 7.90 (d, 1H), 7.81 (d, 1H, J = 8.12 Hz), 7.55 (d, 6H), 2.72 (s, 9H), –2.76 (s, 2H).

2.2.5. Synthesis of Meso-Zn-CAA

This compound was synthesized by an analogous manner to that described above for the synthesis of β-Zn-CAA, but by replacing **3** with **4**. *Anal. Calc.* for C₅₅H₃₇N₅O₃Zn (881.30): C, 74.96; H, 4.23; N, 7.95. Found: C, 74.92; H, 4.20; N, 7.90%. ESI MS (C₅₅H₃₇N₅O₃Zn) m/z: 883 (M+3), 903 (M+Na⁺). ¹H NMR: 8.88–8.54 (m, 8H), 8.30–8.17 (m, 3H), 8.1–7.8 (m, 8H), 7.64–7.33 (m, 8H), 2.72 (s, 9H). UV–Vis (λ_{abs}, nm) in THF: 423 (5.12), 558 (4.40), 597 (3.89).

2.2.6. Synthesis of Meso-Zn-MA

This compound was synthesized by an analogous manner to that described above for the synthesis of β -Zn-MA, but by replacing cyanoacetic acid with malonic acid. *Anal. Calc.* for $C_{55}H_{38}N_4O_5Zn$ (900.30): C, 73.37; H, 4.25; N, 6.22. *Found:* C, 73.40; H, 4.22; N, 6.20%. *ESI MS* ($C_{55}H_{38}N_4O_5Zn$) *m/z*: 901 (M+1), 903 (M+2), 923 (M+Na⁺). *UV-Vis* (λ_{abs} , nm) in THF: 424 (5.13), 556 (4.18), 598 (4.02).

2.3. Characterization methods

The UV-Visible spectra were recorded with a Shimadzu model UV-3600 spectrophotometer for 1×10^{-6} M (porphyrin Soret band) and 5×10^{-5} M (porphyrin Q bands) solutions in THF solvent. Steady state fluorescence spectra were recorded using a Spex model Fluorolog-3 spectrofluorometer for solutions having optical density at the wavelength of excitation (λ_{ex}) ≈ 0.11 . The fluorescence quantum yields (ϕ) were estimated by integrating the fluorescence bands 5,10,15,20-tetratolyl porphyrinato zinc(II) ([ZnTPP]) ($\phi = 0.036$ in CH_2Cl_2) as the standards [32]. Time-resolved fluorescence measurements have been carried out using HORIBA jobin yvon spectrofluorometer. Briefly, the samples were excited at 370 nm and the emission was monitored at 700 nm, in all unsymmetrical phthalocyanines. The count rates employed were typically 10^3 – 10^4 s⁻¹. Deconvolution of the data was carried out by the method of iterative reconvolution of the instrument response function and the assumed decay function using DAS-6 software. The goodness of the fit of the experimental data to the assumed decay function was judged by the standard statistical tests (i.e., random distribution of weighted residuals, the autocorrelation function and the values of reduced χ^2).

2.4. Dye-sensitized solar cell fabrication

The DSSCs were made using a procedure similar to the one reported previously [33,34]. The TiO₂ electrode of 9 μ m of transparent layer (TiO₂ paste DSL 18NR-T, Dyesol) and 6 μ m of scatter layer (TiO₂ paste DSL 18NR-AO, Dyesol) was screen printed onto FTO substrate (TEC15, Pilkington, UK). Prior to the deposition of TiO₂, FTO substrates were treated with 40 mM TiCl₄ at 70 °C for 30 min by chemical bath deposition. The deposited films were annealed in air at 325 °C for 5 min, at 375 °C for 5 min, and at 450 °C for 15 min, and finally, at 500 °C for 15 min before having another TiCl₄ treatment (40 mM at 70 °C for 30 min). The electrodes were annealed at 450 °C for 30 min in air. The electrodes were then sensitized with a 0.2 mM solution dye molecules in THF solvent for 20 h. Platinised counter electrodes were made with transparent platinum paste (Plastisol T/SP, Solaronix SA) on FTO substrates, and heated at 450 °C for 15 min. The counter and working electrodes were then sealed together using a hot melt polymer film (Surlyn, Solaronix, SA) gas ket, before a solution of 0.05 M I₂, 0.1 M LiI, 0.6 M 1-butyl-3-methylimidazolium iodide and 0.5 M tertbutylpyridine in a 85:15 volume ratio of acetonitrile and valeronitrile was introduced into the cell through a pre-drilled hole in the counter electrode. The device was then sealed with the hot melt polymer and glass cover.

2.5. Theory

In the design of this series of porphyrin sensitizers, the introduction of furan group is expected to be extended π -conjugation, which broadens and red-shifts absorption spectra. The studies were performed using the density functional theory (DFT) [35,36] approach implemented in GAUSSIAN 09 [37], while the results were visualized through Gabedit [38] and GaussView [39]. We have considered the dye molecules as shown in Schemes 1 and 2. DFT and

time depended DFT (TD-DFT) calculations at B3LYP/6-31G* level of theory were used for the electronic structure properties of the mentioned materials; further detail of this method can be found in our previous work [40–43]. Theoretical study of the porphyrin macrocycle which acts as donor, furan hetero cycle as π -spacer and either cyanoacetic acid or malonic acid group acts as acceptor are investigated with electronic properties such as frontier molecular orbitals (HOMO–LUMO), and UV-Vis spectral analysis. Charge analysis are simulated at natural bonding orbital (NBO) and Mulliken charge analyses. THF was used a solvent medium, using polarized continuum model (PCM) for the UV-Vis spectra and Δ SCF energy gap (optical gap) at TD-DFT-B3LYP/6-31G* level of theory.

3. Results and discussion

3.1. Design and synthesis

The broadening of the absorption of the sensitizer can improve the conversion efficiency. It can be achieved by introducing extended π -conjugation in the molecular structure of the sensitizer. The Q-band absorption bands of porphyrins are broadened by introduction of hetero aromatic molecules like thiophene [29,30]. Here, we have achieved the broadening of absorption porphyrin macrocycle with furan hetero aromatic molecule. The new sensitizers based on porphyrin-furan conjugates have been synthesized as per the Schemes 1 and 2. The purification of all the compounds were done by silica gel column chromatography and followed by recrystallization. All these sensitizers were characterized by CHN analysis, UV-Visible, ¹H NMR, Mass and fluorescence spectroscopies (both steady-state & life-time) as well as cyclic voltammetry. The elemental analyses data presented in experimental sections were found to be satisfactory. Each of the Mass spectrum consists of molecular ion peak ascribe to the presence of corresponding porphyrin sensitizer (see Section 2).

3.2. Optical and electrochemical properties

The electronic absorption spectra of these porphyrin based sensitizers were recorded in THF solution. Fig. 1 shows the absorption spectra of β -Zn-CAA and meso-Zn-CAA, while their TD-DFT simulated UV-Vis spectra are given in Fig. 2. Both of the theoretical and experimental wavelengths of maximum absorbance (λ_{max}) and molar extinction coefficient (ϵ) values of these porphyrin-furan conjugates as obtained from UV-Vis studies, are summarized in Tables 1 and 2, respectively. The absorption spectra of these

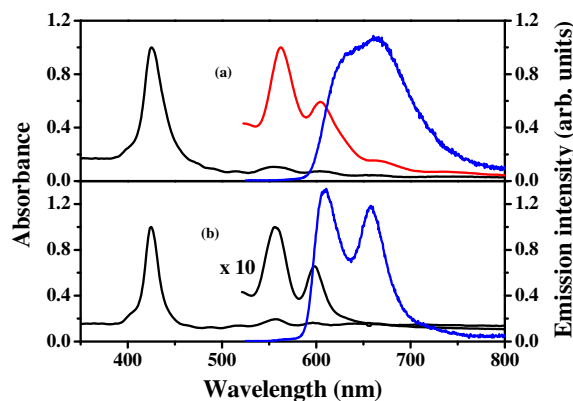


Fig. 1. (a) UV-Visible absorption spectra of (–) & emission spectrum of (–) β -Zn-CAA. (b) UV-Visible absorption spectra of (–) & emission spectrum of (–) meso-Zn-CAA in THF solvent.

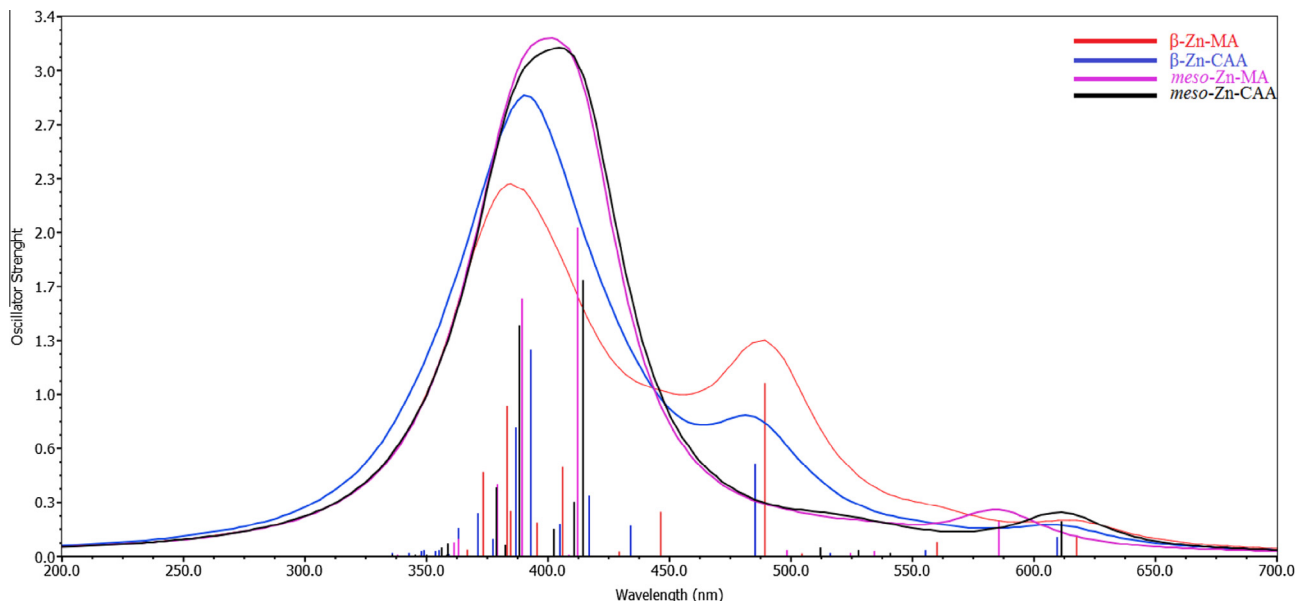


Fig. 2. TD-DFT simulated UV-Vis spectra of Zn Porphyrin-Furan dyes.

porphyrin-furan conjugates in THF solution shows an intense Soret band between 420–430 nm and two less intense Q-bands between 500 to 625 nm due to π - π^* absorption of the conjugated macrocycle. Observed and simulated UV-Vis spectra has strong correlation among their absorption band peaks as can be seen from Figs. 1 and 2 and Table 1 and 2. Both Soret and Q-bands are red-shifted (5–10 nm in case of pyrrole- β substituted and 3–5 nm in case of meso-phenyl substituted porphyrins) in comparison with its parent porphyrin *i.e.*, ZnTTP. The shift in absorption bands are probably due to the electron with-drawing nature of furan substituent. A similar red shift was also observed in other pyrrole- β and meso- substituted porphyrins [29,30,44,45].

Fig. 1 also shows the emission spectra of β -Zn-CAA and meso-Zn-CAA in THF solvent at room temperature and the corresponding emission maxima & quantum yield data are presented in Table 1. The emission maxima (Table 1) are independent of the excitation wavelength between 400 and 600 nm, and spectra shown characteristic vibronic bands between 610 and 675 nm similar to those reported other zinc porphyrins. The emission maxima of all four porphyrin-furan conjugates are red-shifted in comparison with its constituent ZnTTP. The quantum yields are slightly reduced in comparison with ZnTTP probably due to the substituent effect of furan group on porphyrin macrocycle. The excitation spectrum obtained by exciting emission maximum at 660 nm exhibit an intense Soret and Q-bands that corresponds to the ground state absorption spectra, indicating the presence of single emitting species in each case. Based on absorption and emission, the singlet excited state [$E_{0,0}$] energy of β -Zn-CAA, β -Zn-Ma, meso-Zn-CAA and

Table 2

TD-DFT calculated electronic excitations (λ_{max}) and optical gap of Zn porphyrin-furan dyes.

Species	Maximum excitation	Oscillator strength	Electronic transition	Optical Gap (eV)
β -Zn-MA	617	0.13	$\pi \rightarrow \pi^*$	2.00
β -Zn-CAA	609	0.11	$\pi \rightarrow \pi^*$	2.03
meso-Zn-MA	585	0.22	$\pi \rightarrow \pi^*$	2.11
meso-Zn-CAA	611	0.22	$\pi \rightarrow \pi^*$	2.02

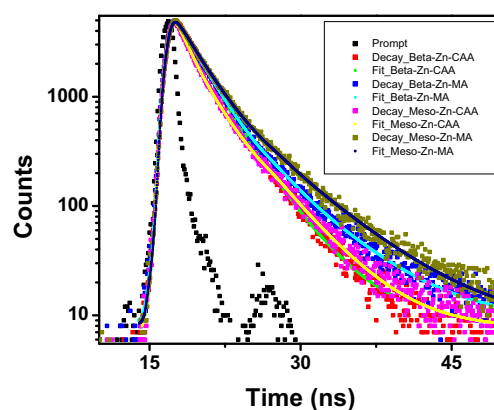


Fig. 3. Fluorescence decay of all four porphyrin-furan conjugates.

Table 1

Absorption, steady state and time resolved emission data.^a

Sample	λ_{max} , nm, log $\epsilon/M^{-1} cm^{-1b}$	λ_{em} , (nm) ^c	τ_1 (ns)	τ_2 (ns)
Beta-Zn-CAA	425 (5.03), 554 (4.06), 607 (3.90)	664 (0.032)	1.04 (62)	1.84 (38)
Beta-Zn-MA	429 (5.11), 564 (4.33), 607 (4.21)	660 (0.026)	1.08 (69)	2.67 (31)
Meso-Zn-CAA	423 (5.12), 558 (4.40), 597 (3.89)	659 (0.027)	1.97 (52)	6.73 (48)
Meso-Zn-MA	424 (5.13), 556 (4.18), 598 (4.02)	657 (0.030)	1.02 (57)	2.80 (43)

^a Solvent THF.

^b Error limits: λ_{max} , ± 1 nm, log ϵ , $\pm 10\%$.

^c Error limits: λ_{em} = ± 1 nm.

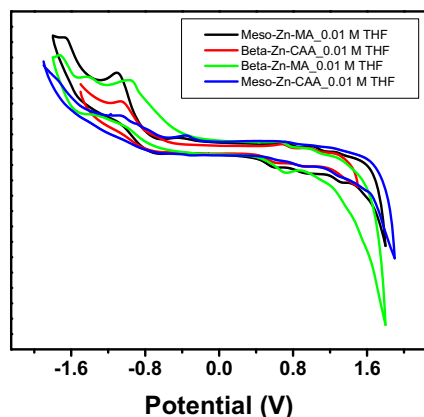


Fig. 4. Cyclic and Differential Pulse Voltammogrammes in THF and 0.1 M TBAP.

β -Zn-CAA and *meso*-Zn-MA are found to be 2.05, 2.05, 2.06, and 2.07 eV, respectively. We also simulated this singlet excited state (optical band gap) energy at Δ SCF method, which has excellent matching as can be seen from Table 2. The simulated optical band gap of β -Zn-MA is 2.0 eV, β -Zn-CAA has 2.03 eV, *meso*-Zn-MA has 2.11 eV and *meso*-Zn-CAA has 2.02 eV optical band gap.

No emission spectra are observed for the porphyrin-furan conjugates adsorbed onto 6 μ m thick TiO₂ layer as a consequence of electron injection from excited singlet state of porphyrin into

the conduction band of TiO₂. Fig. 3 illustrates fluorescence decay curves of all four investigated compounds in THF solvent. The singlet excited life-time of all four porphyrin-furan conjugates were measured in THF solvent and found 1.04, 1.08, 1.97 & 1.02 ns for β -Zn-CAA, β -Zn-Ma, *meso*-Zn-CAA and *meso*-Zn-MA, respectively. In all these cases the excited state life-time quenched when adsorbed onto 2 μ m thick TiO₂ layer.

With a view to evaluate the HOMO–LUMO levels of porphyrin-furan conjugates, we performed the electrochemistry by using cyclic and differential pulse voltammetric techniques in THF solvent. Fig. 4 shows the cyclic voltammogramme of β -Zn-CAA and the corresponding data are presented in Table 3. Analysis of Fig. 4 and Table 3 it is evident that each porphyrin-furan conjugate undergoes two oxidations and two reductions under the experimental conditions employed in this study. Wave analysis suggested that while the first two oxidation and first two reduction processes represent reversible ($i_{pc}/i_{pa} = 0.9–1.0$) and diffusion controlled ($i_{pc}/\nu^{1/2} = \text{constant}$ in the scan rate (ν) range 50–500 mV/s) one-electron transfer ($\Delta E_p = 60–70$ mV; $\Delta E_p = 65 \pm 3$ mV for Fc⁺/Fc couple) reactions, left over electrode processes are either quasi-reversible ($i_{pc}/i_{pa} = 0.6–0.8$ and $\Delta E_p = 80–150$ mV) or irreversible under similar experimental conditions. Analysis of the data given in Table 1 reveals that the redox potentials of these porphyrin-furan conjugates are not altered when compared to its reference compound. Each porphyrin-furan conjugate undergoes oxidation at 0.73, 0.69, 0.64, and 0.63 V vs. SCE generating π -cation for β -Zn-CAA, β -Zn-Ma, *meso*-Zn-CAA and *meso*-Zn-MA, respectively.

Table 3
Electrochemical data.

Sample	$E_{1/2\text{Oxd}}$ (V) ^a	$E_{1/2\text{Red}}$ (V) ^a	E_{0-0} (eV) ^b	E_{oxd}^* (V) ^c	$\Delta G_{\text{inj.}}$ (V)	$\Delta G_{\text{reg.}}$ (V)
Beta-Zn-CAA	0.73	−1.58	2.05	−1.32	−0.82	0.23
Beta-Zn-MA	0.69	−1.56	2.05	−1.36	−0.86	0.19
Meso-Zn-CAA	0.64	−1.59	2.06	−1.42	−0.99	0.07
Meso-Zn-MA	0.63	−1.58	2.07	−1.44	−0.94	0.13

E_{0-0} = HOMO–LUMO gap calculated from the intersection of the absorption and fluorescence spectra.

$\Delta G_{\text{inj.}}$ = driving force for electron injection from the LUMO of the dye to the conduction band of TiO₂.

$\Delta G_{\text{reg.}}$ = driving force for regeneration of the oxidized dye from the redox electrolyte.

^a Error limits, $E_{1/2}$, ± 0.03 V, 0.1 M TBAP.

^b Error limits: ± 0.05 eV. $E_{\text{oxd}}^* = E_{1/2} - E_{0-0}$.

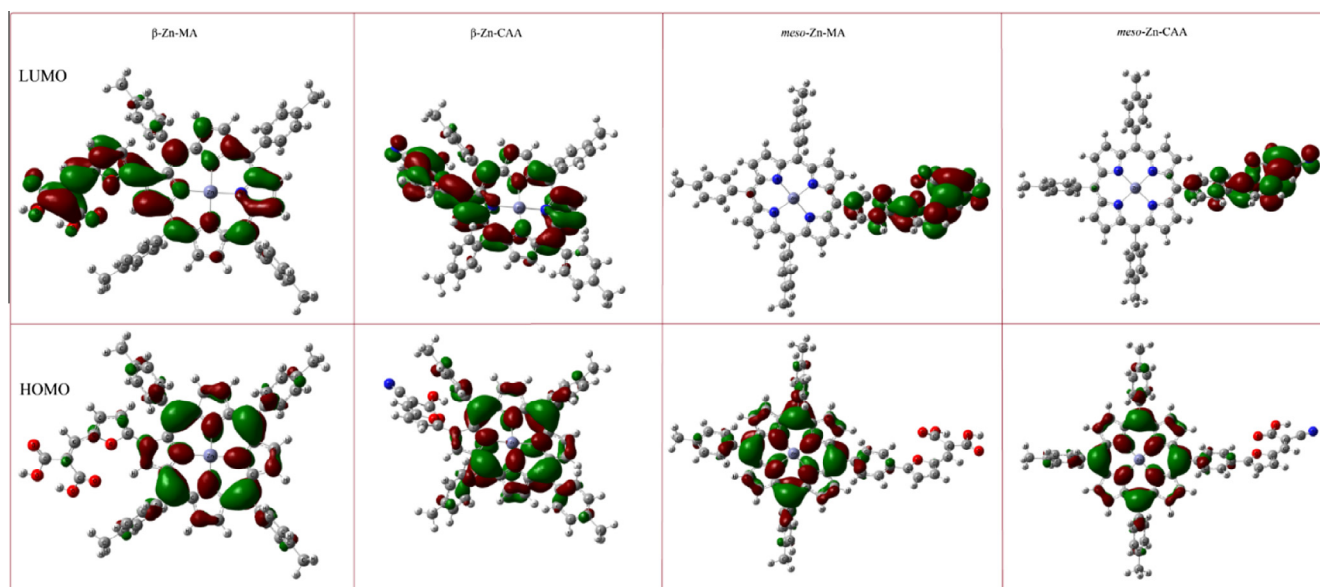


Fig. 5. Contours of HOMO and LUMO of Zn porphyrin-furan dyes.

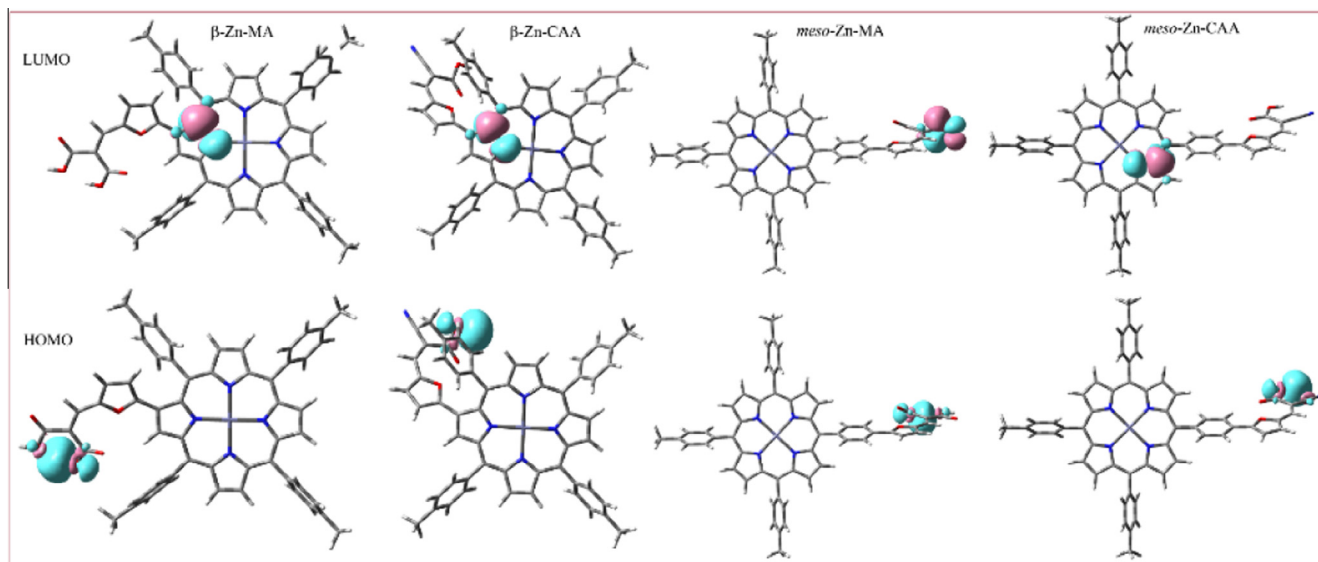


Fig. 6. Contours of occupied and unoccupied NBO of Zn porphyrin-furan dyes.

With respect to dye-sensitization of wide-band-gap semiconductors, e.g. TiO_2 , the oxidation potentials of porphyrin sensitizers and the E_{0-0} transition energy, the energy levels of the singlet excited states (excited state oxidation potential) of β -Zn-CAA, β -Zn-MA, *meso*-Zn-CAA and *meso*-Zn-MA -1.32 , -1.36 , -1.42 , and -1.44 , respectively. Whereas the energy level of the conduction band edge of TiO_2 is ca. -0.74 V vs. SCE [46]. This makes electron injection from the excited state of porphyrin sensitizer into the conduction band of TiO_2 thermodynamically feasible. Furthermore, the HOMO level of the porphyrins is lower than the energy level of the redox couple I^-/I_3^- (0.2 V vs. SCE) in the electrolyte, enabling the dye regeneration by electron transfer from iodide ions in the electrolyte.

The theoretical predicted frontier molecular and natural bonding orbital's (NBO) contours of these dyes are shown in Figs. 5 and 6. Topmost HOMO is strongly contributed by the N $2p$ states whereas the lowest LUMO is strongly contributed by C $2p$ -like states slightly hybridized with O $2p$ and C $2p$ states. Most contribution to the highest HOMO and lowest LUMO states are coming from p electrons whereas contribution from s -electrons

is modest. Since the p - p electrons transitions are not allowed, very strong absorption of sunlight by the molecule is not expected. Fig. 6 displays electron localization function for the dyes. Analysis shows that the electrons are distributed around the ring, so the dye molecules can be oxidized. The electrons are localized around H, N, O, and C atoms and are located in the covalent C-C, C-O, C-Zn, C-H bonds. Although good light absorption properties of the dyes are important for high efficiency solar cells, electrical properties of the molecules, charge transfer between the molecule and TiO_2 as well as the interface are the other important factors. That might explain the reason of getting the low efficiency of the cells.

Highest electronic cloud density on the HOMO at anchoring sites of these dyes clearly predict that charge injection is favoured while the lowest one on the LUMO shows that charge recombination is prevented. From the NBO contours of all these dyes (Fig. 6), it is evident that except the *meso*-Zn-MA, the rest of them have good electron donating ability.

3.3. Photovoltaic properties

Fig. 7 shows the performance of the DSSCs of different sensitizers on the basis of their steady-state current-voltage characteristics. Table 4 summarizes the key cell parameters for DSSCs as a function of different porphyrin sensitizers. DSSC parameters are significantly influenced by the porphyrin sensitizers. The maximum conversion efficiency has been achieved for the cells sensitized with β -CAA. It shows slightly improved J_{sc} (0.813 ± 0.15 mA cm^{-2}) and V_{oc} (467 ± 10 mV) than its *meso*-CAA which shows J_{sc} (0.569 ± 15 mA cm^{-2}) and V_{oc} (462 ± 10 mV) effects in the frontier orbitals. This might be due

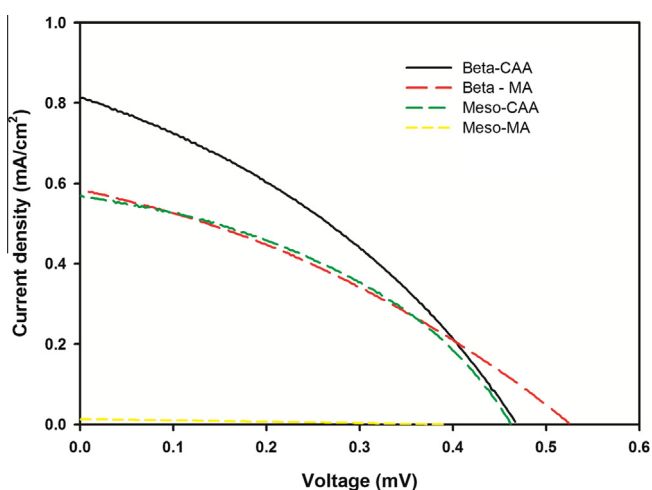


Fig. 7. J–V characteristics of DSSCs constructed with different porphyrin sensitizers under 1 sun illumination.

Table 4
Test cell data.^a

Sensitizer	V_{oc} (mV)	J_{sc} (mA/cm^2)	ff(%)	η (%)
Beta-CAA	467 ± 10	0.813 ± 0.15	35.24 ± 0.10	0.1330 ± 0.01
Beta-MA	525 ± 10	0.584 ± 0.15	33.49 ± 0.10	0.1020 ± 0.01
Meso-CAA	462 ± 10	0.569 ± 0.15	40.42 ± 0.10	0.1060 ± 0.01
Meso-MA	391 ± 10	0.013 ± 0.15	27.38 ± 0.10	0.0013 ± 0.01

^a Photoelectrode: TiO_2 ($9 + 6$ μm and 0.74 cm^2); electrolyte: 0.6 M 1-butyl-3-methylimidazoliumiodide, 0.05 M I_2 , 0.5 M tertbutylpyridine and 0.1 M guanidine thiocyanate in a 85:15 volume ratio of acetonitrile and valeronitrile.

to the presence of π -electron cloud at β -pyrrole position than at *meso* phenyl position. More over the sensitizers having cyanoacetic acid anchoring group showing better performance than the corresponding sensitizers having dicarboxylic acid anchoring group probably due to the presence of electron withdrawing $-\text{CN}$ group. However, the overall conversion efficiency is less than the controlled cells made with standard N719 sensitizer ($J_{sc} 18.1 \pm 0.15 \text{ mA cm}^{-2}$ and $V_{oc} 622 \pm 10 \text{ mV}$) [47].

The reason for the low efficiency compared to the previously reported thiophene spacer porphyrins might be related to poor electrical conductivity of furan derivatives [30,48], offset between HOMO/LUMO of the porphyrins and valence/conduction bands of TiO_2 , as well as quality of interface between them. However, one has to investigate in detail about the charge injection of present sensitizers and compare with thiophene derivatives. The detailed charge injections studies are currently under progress.

4. Conclusions

In conclusion, we have designed, synthesized and theoretically counterchecked for the first time porphyrin–furan conjugates, in which anchoring group either at *meso*-phenyl or at pyrrole- β position of a zinc porphyrin based on donor- π -acceptor approach. The newly synthesized dyes are characterized by UV–Visible, ^1H NMR, MALDI-MS and fluorescence spectroscopies and cyclic voltammetry. Theoretical data simulated with DFT and TD-DFT at B3LYP/6-31G* level theory has nice correlation with our experiment. It is found that this level of theory can be used for the new dyes to predict and improve their efficiency. Both optical and electrochemical properties of pyrrole- β substituted dyads are altered whereas its *meso*-phenyl substituted dyads are not altered, when compared to its reference zinc porphyrin. The dyads were tested in dye sensitized solar cells using I^-/I_3^- redox couple. The pyrrole- β substituted porphyrins are showing better efficiency than its *meso*-phenyl substituted dyads. Overall the efficiency of these sensitizers are found to very low. Optical band gap, Natural bonding, and Molecular bonding orbital (HOMO–LUMO) analysis are also in favour of pyrrole- β substituted zinc porphyrins contrast to *meso*-phenyl dyads.

Acknowledgements

The authors are thankful to DST(India)-EPSRC(UK) ('APEX') programme and the EPSRC Supergen programme for financial support of this work.

References

- [1] L. Giribabu, K. Sudhakar, J. Photochem. Photobiol., A 296 (2015) 11.
- [2] F. D'Souza, O. Ito, Chem. Soc. Rev. 41 (2012) 86.
- [3] D. Gust, T.A. Moore, A.L. Moore, Acc. Chem. Res. 42 (2009) 1890.
- [4] M.-M. Yu, J. Li, W.-J. Sun, M. Jiang, F.-X. Zhang, J. Mater. Sci. 49 (2014) 5519.
- [5] M.E. El-Khouly, D.K. Ju, K.-Y. Kay, F. D'Souza, S. Fukuzumi, Chem. Eur. J. 16 (2010) 6193.
- [6] G. Pagona, G.E. Zervaki, A.S. Sandanayaka, O. Ito, G. Charalambidis, T. Hasobe, A.G. Coutsolelos, N. Tagmatarchis, J. Phys. Chem. C 116 (2012) 9439.
- [7] C.M. Davis, K. Ohkubo, A.D. Lammer, D.S. Kim, Y. Kawashima, J.L. Sessler, S. Fukuzumi, Chem. Commun. 51 (2015) 9789.
- [8] T. Ripolles-Sanchis, B.-C. Guo, H.-P. Wu, T.-Y. Pan, H.-W. Lee, S.R. Raga, F. Fabregat-Santiago, J. Bisquert, C.-Y. Yeh, E.W.-G. Diau, Chem. Commun. 48 (2012) 4368.
- [9] B. Basheer, D. Mathew, B.K. George, C.P. Reghunadhan Nair, Solar Energy 108 (2014) 479.
- [10] J. Kandhadi, R.K. Kanaparthi, L. Giribabu, J. Porphyrins Phthalocyanines 16 (2012) 282.
- [11] L. Giribabu, P.S. Reeta, R.K. Kanaparthi, M. Srikanth, Y. Soujanya, J. Phys. Chem. A 117 (2013) 2944.
- [12] F.-C. Gong, D.-X. Wu, Z. Cao, X.-C. He, Biosens. Bioelectron. 22 (2006) 423.
- [13] V.A. Montes, C. Pérez-Bolívar, N. Agarwal, J. Shinar, P. Anzenbacher, J. Am. Chem. Soc. 128 (2006) 12436.
- [14] M.-L. Seol, S.-J. Choi, C.-H. Kim, D.-I. Moon, Y.-K. Choi, ACS Nano 6 (2012) 183.
- [15] S.V. Rao, N.K.M. Naga Srinivas, D.N. Rao, L. Giribabu, B.G. Maiya, R. Philip, G.R. Kumar, Opt. Commun. 192 (2001) 123.
- [16] L. Giribabu, R.K. Kanaparthi, V. Velkannan, Chem. Rec. 12 (2012) 306.
- [17] R.K. Kanaparthi, J. Kandhadi, L. Giribabu, Tetrahedron 68 (2012) 8383.
- [18] H.M. Upadhyaya, S. Senthilarasu, M.-H. Hsu, D.K. Kumar, Sol. Energy Mater. Sol. Cells 119 (2013) 291.
- [19] M. Urbani, M. Grätzel, M.K. Nazeeruddin, T.S. Torres, Chem. Rev. 114 (2014) 12330.
- [20] T. Higashino, H. Imahori, Dalton Trans. 44 (2015) 448.
- [21] B. O'Regan, M. Grätzel, Nature 353 (1991) 737.
- [22] M.K. Nazeeruddin, A. Kay, I. Rodicio, R. Humphry-Baker, E. Mueller, P. Liska, N. Vlachopoulos, M. Graetzel, J. Am. Chem. Soc. 115 (1993) 6382.
- [23] L. Han, A. Yslah, H. Chen, C. Malapaka, B. Chiranjeevi, S. Zhang, X. Yang, M. Yanagida, Energy Environ. Sci. 5 (2012) 6057.
- [24] W.M. Campbell, A.K. Burrell, D.L. Officer, K.W. Jolley, Coord. Chem. Rev. 248 (2004) 1363.
- [25] J. Jasieniak, M. Johnston, E.R. Waclawik, J. Phys. Chem. B 108 (2004) 12962.
- [26] W.M. Campbell, K.W. Jolley, P. Wagner, K. Wagner, P.J. Walsh, K.C. Gordon, L. Schmidt-Mende, M.K. Nazeeruddin, Q. Wang, M. Grätzel, D.L. Officer, J. Phys. Chem. C 111 (2007) 11760.
- [27] A. Yella, H.-W. Lee, H.N. Tsao, C. Yi, A.K. Chandiran, M.K. Nazeeruddin, E.W.-G. Diau, C.-Y. Yeh, S.M. Zakeeruddin, M. Grätzel, Science 334 (2011) 629.
- [28] S. Mathew, A. Yella, P. Gao, R. Humphry-Baker, F.E. Curchod, Basile, N. Ashari-Astani, I. Tavernelli, U. Rothlisberger, K. Nazeeruddin, M. Grätzel, Nat. Chem. 6 (2014) 242.
- [29] Y. Liu, N. Xiang, X. Feng, P. Shen, W. Zhou, C. Weng, B. Zhao, S. Tan, Chem. Commun. (2009) 2499.
- [30] V.A. Nuay, D.-H. Kim, S.-H. Lee, J.-J. Ko, Bull. Korean Chem. Soc. 30 (2009) 2871.
- [31] J.-H. Fuhrhop, K.M. Smith, Laboratory Methods in Porphyrin and Metalloporphyrin Research, Elsevier Science & Technology, 1975.
- [32] D.J. Quimby, F.R. Longo, J. Am. Chem. Soc. 97 (1975) 5111.
- [33] L. Giribabu, V.K. Singh, C.V. Kumar, Y. Soujanya, P.Y. Reddy, M.L. Kantam, Sol. Energy 85 (2011) 1204.
- [34] J.W. Bowers, H.M. Upadhyaya, S. Calnan, R. Hashimoto, T. Nakada, A.N. Tiwari, Prog. Photovoltaics 17 (2009) 265.
- [35] H. Ullah, A.-U.-H. A. Shah, K. Ayub, S. Bilal, J. Phys. Chem. C 117 (2013) 4069.
- [36] H. Ullah, A.A. Shah, S. Bilal, K. Ayub, J. Phys. Chem. C 117 (2013) 23701.
- [37] M.J. Frisch, G.W. Trucks, H.B. Schlegel, G.E. Scuseria, M.A. Robb, J.R. Cheeseman, G. Scalmani, V. Barone, B. Mennucci, G.A. Petersson, et al., Gaussian 09, Rev. D. 0.1, Gaussian Inc, Wallingford, CT, 2013.
- [38] Allouche, A.R. Gabedit, <http://gabedit.sourceforge.net>, 2011.
- [39] R. Dennington, T. Keith, J.G. Millam, Semichem Inc., Shawnee Mission KS, 2008.
- [40] H. Ullah, A.-U.-H. A. Shah, S. Bilal, K. Ayub, J. Phys. Chem. C 118 (2014) 17819.
- [41] H. Ullah, K. Ayub, Z. Ullah, M. Hanif, R. Nawaz, S. Bilal, Synth. Met. 172 (2013) 14.
- [42] S. Bibi, H. Ullah, S.M. Ahmad, A.-U.-H. Ali Shah, S. Bilal, A.A. Tahir, K. Ayub, J. Phys. Chem. C 119 (2015) 15994.
- [43] M. Kamran, H. Ullah, A.S. Anwar-ul-Haq, S. Bilal, A.A. Tahir, K. Ayub, Polymer 72 (2015) 30.
- [44] L. Giribabu, C.V. Kumar, P.Y. Reddy, J. Porphyrins Phthalocyanines 10 (2006) 1007.
- [45] P. Silviya Reeta, J. Kandhadi, G. Lingamallu, Tetrahedron Lett. 51 (2010) 2865.
- [46] A. Hagfeldt, M. Graetzel, Chem. Rev. 95 (1995) 49.
- [47] P.S. Reeta, L. Giribabu, S. Senthilarasu, M.-H. Hsu, D.K. Kumar, H.M. Upadhyaya, N. Robertson, T. Hewat, RSC Adv. 4 (2014) 14165.
- [48] S.J. Lind, K.C. Gordon, S. Gambhir, D.L. Officer, Phys. Chem. Chem. Phys. 11 (2009) 5598.

[Article 8]

H. Ullah, A. A. Tahir, T. K. Mallick, "Polypyrrole/TiO₂ composites for the application of photocatalysis." *Sens. Actuators, B: Chem.*, vol. 241, pp. 1161-1169, Mar. 2017.



Polypyrrole/TiO₂ composites for the application of photocatalysis



Habib Ullah*, Asif Ali Tahir*, Tapas K. Mallick

Environment and Sustainability Institute (ESI), University of Exeter, Penryn Campus, Penryn, Cornwall TR10 9FE, UK

ARTICLE INFO

Article history:

Received 17 March 2016
Received in revised form 4 October 2016
Accepted 5 October 2016
Available online 6 October 2016

Keywords:

Band gap engineering
DFT
Molecular interaction
Photocatalysis
Redox potential

ABSTRACT

Density functional theory (DFT) study of polypyrrole-TiO₂ composites has been carried out to explore their optical, electronic and charge transfer properties for the development of an efficient photocatalyst. Titanium dioxide (Ti₁₆O₃₂) was interacted with a range of pyrrole (Py) oligomers to predict the optimum composition of nPy-TiO₂ composite with suitable band structure for efficient photocatalytic properties. The study has revealed that Py-Ti₁₆O₃₂ composites have narrow band gap and better visible light absorption capability compared to individual constituents. The simulated results of band structure (band gap, and band edge positions), molecular orbitals, and UV–vis spectra of the optimized nPy-Ti₁₆O₃₂ systems strongly support the existence of strong interactions between Py and TiO₂ in the composite. A red-shifting in λ_{\max} , narrowing band gap, and strong intermolecular interaction energy (–41 to –72 kcal/mol) of nPy-Ti₁₆O₃₂ composites confirm the existence of strong covalent type interactions. Electron–hole transferring phenomena are simulated with natural bonding orbital analysis where Py oligomers found as donor and Ti₁₆O₃₂ as an acceptor in nPy-Ti₁₆O₃₂ composites.

© 2016 Elsevier B.V. All rights reserved.

1. Introduction

Nanostructured TiO₂ is one of the most investigated photoactive materials due to its excellent electronic structure and high stability to photocorrosion under redox conditions [1–3]. TiO₂ has drawn much attention due to its potential applications in solar energy conversion (such as photocatalytic water splitting and dye-sensitized solar cell), environmental cleaning (photocatalytic degradation of pollutants, self-cleaning, and water purification), and bio-sensing [4–7]. The solar energy conversion and photocatalytic efficiency of TiO₂ is limited due to its wide band gap (3.20 eV), as it can only absorb UV region of the solar spectrum [8]. Along with wide band gap, TiO₂ also suffer from high charge recombination rate (photogenerated electron–hole pair) which hindered the photocatalytic activity [9]. Strategies such as noble metal deposition as co-catalyst, metal or non-metal doping and photosensitization have been adopted to tailor band gap and enhance the charge transport properties to improve the photocatalytic performance of TiO₂ [10,11].

Conjugated organic polymer (COPs) [12–14] having spatially extended π -bonding system become potential energy materials due to their unique electrical and optical properties, such as high

photon absorption coefficients under visible light irradiation, high electron mobility, excellent stability, material diversity, mechanical flexibility, light weight, low-temperature processing, roll to roll printing and large-area capability [15]. They have been successfully applied in organic electronic devices and solar cells [16]. Conducting polymers are mostly *p*-type semiconductors which work as an electron donor in the *p*-*n* junction solar cell. Polyaniline (PANI), polypyrrole (PPy), polythiophene (PT), polyacetylene (PA), polythiophene (PT), polyparaphenylene (PPP), polyparaphenylen-ene (PPV), poly(3,4-ethylenedioxythiophene) (PEDOT), poly(*o*-phenylenediamine) (POPD) are prominent examples of COPs which are being explored in this area [12–14,17]. Recently, it has been found that composite of metal oxide and COP into intimate contact on both physical and electronic levels have significantly improved solar energy conversion and photocatalytic performance compared to metal oxide or COP individually [18]. Moreover, an increasing interest is found on the fabrication of COP-TiO₂ nanocomposites for photocatalytic degradation of environmental pollutants as well as water splitting to generate hydrogen [19,20].

Although, experimental study of PPy-TiO₂ as a photocatalyst is reported but facing lower photocatalytic efficiency which is due to lack of theoretical investigation [21–24]. The fully explored theoretical insight of optical, electronic structure, surface interactions, electroactivity and charge transfer mechanism between PPy and TiO₂ is essential to tailor and improve photocatalytic activity of PPy-TiO₂ nanocomposite. Our recent investigation on PPy and pyrrole oligomers (nPy, where *n* is a number of repeating units) has proved

* Corresponding authors.

E-mail addresses: Hu203@exeter.ac.uk (H. Ullah), A.Tahir@exeter.ac.uk (A.A. Tahir).

that nPy has excellent tunable, optical and electroactive properties [25–27]. In this work, we have detailed theoretical investigation of charge transfer mechanism between nPy and TiO₂ (molecular cluster; Ti₁₆O₃₂) in a connected junction such as nPy-TiO₂ nanocomposite. The present article is focused on the investigation of important photocatalytic parameters such as (i) interaction of Ti₁₆O₃₂ with PPy oligomers to find out electron–hole transformation, (ii) band structure alteration, (iii) mechanism of charge (electron/hole) transport (vi) optimisation of oligomeric length of Py for efficient performance and (v) structure-property relationship. The study is aimed to provide a better understanding of the electronic structure of nPy-Ti₁₆O₃₂ nanocomposite and will open new direction to synthesize an efficient nPy-TiO₂ nanocomposite photocatalyst with the optimized composition for visible light photocatalysis. Moreover, this work will also inspire computational scientists to explore structural property relationship of other COP-metal oxide nanocomposites.

2. Methodology

Interaction of molecular cluster of Ti₁₆O₃₂ with nPy oligomers (n=3, 5, and 9) are performed with the help of density functional theory (DFT). All DFT calculations [28,29] were carried out on GAUSSIAN 09 [30] and the results were visualized through Gabedit [31], GaussSum [32], and GaussView [33]. DFT and time-dependent DFT (TD-DFT) calculations were performed at B3LYP with LanL2DZ basis set for the determination of electronic structure properties of nPy-Ti₁₆O₃₂, as an efficient photocatalyst. Oligomers up to eight repeating units can accurately represent its polymeric characteristics so, oligomeric size is restricted to nine repeating units [28,29]. A molecular cluster of Ti₁₆O₃₂ is added to the oligomeric backbone of nPy and then optimized. Geometries of nPy-Ti₁₆O₃₂ (n = 3 to 9) systems were optimized at B3LYP/LanL2DZ level and confirmed from frequency calculations. The non-bonding and bonding interaction energies in nPy-Ti₁₆O₃₂ are simulated with help of interaction energy (ΔE_{int}) and geometrical counterpoise correction (gCP). The gCP is able to treat both inter- and intra-molecular BSSE on the same footing at low computational cost. The B3LYP-gCP-D3 [34] interaction energy is simulated from the Grimme Web service [35]. The ΔE_{int} and gCP-D3 are calculated from equations 1 and 2, respectively.

$$\Delta E_{int} = E_{Ti16O32} + E_{nPy} - E_{nPy-Ti16O32} \quad (1)$$

$$\Delta E_{gCP-D3} = E_{(nPy-Ti16O32)gCP-D3} - E_{(nPy)gCP-D3} - E_{(Ti16O32)gCP-D3} \quad (2)$$

UV–vis spectra are simulated at hybrid TD-DFT with pseudopotential of LanL2DZ. Natural bonding orbitals (NBO) analysis performed for the charge simulations. All these calculations were performed in the gas phase.

Table 1

Electronic properties of isolated TiO₂, Ti₁₆O₃₂, and Ti₂₈O₅₆ Anatase clusters.

Species	Band gap (eV)	HOMO (eV)	LUMO (eV)	Optical gap (nm)
Ti ₁₆ O ₃₂	3.06	−7.33	−4.33	333
Ti ₂₈ O ₅₆	2.61	−7.39	−4.78	471
Isolated TiO ₂	1.86	−5.28	−3.42	647

3. Results and discussion

3.1. Choice of TiO₂ cluster

To understand physical significance of nPy-TiO₂ at the molecular level, it is important to select an appropriate TiO₂ cluster as a representative of its bulk. The interactions between nPy and TiO₂ surface can be described in two different ways; the cluster model and periodic surface models [36]. For the surface representation of TiO₂, we have used cluster models, consisting of 48 and 84 atoms which are applicable to the molecular quantum chemistry [36]. Electronic properties such as HOMO, LUMO, band gap, and optical gap of isolated TiO₂, Ti₁₆O₃₂, and Ti₂₈O₅₆ clusters are simulated which are comparatively listed in Table 1. On the basis of band gap simulation and computational point of view, it is evident that Ti₁₆O₃₂ (band gap 3.06 eV) is a better representative of bulk anatase (Fig. 1). The current study is focused on Ti₁₆O₃₂ and their interaction with different Py oligomers.

3.2. Optimized geometries

Geometrical relaxation of nPy, Ti₁₆O₃₂, and nPy-Ti₁₆O₃₂ bound species are carried out at DFT- B3LYP/LanL2DZ level. Optimized geometric structure of 48 atoms (Ti₁₆O₃₂) is given in Fig. 1, while their comparative geometrical parameters are listed in Table 2. Analysis of the data (Table 2) proves that there is no significant difference between geometrical parameters of bulk (crystal/condensed phase) and molecular cluster (gas phase), confirming that Ti₁₆O₃₂ is the best representative of bulk TiO₂.

The optimized geometric structures of 7Py-Ti₁₆O₃₂ and 9Py-Ti₁₆O₃₂ along with their inter-molecular bond distances are shown in Figs. 2 and 3, respectively, while 3Py-Ti₁₆O₃₂ and 5Py-Ti₁₆O₃₂ are given in S1 and S2 of the Supplementary information. During the optimization, Ti₁₆O₃₂ circulated and finally attached at the middle of nPy oligomer by establishing strong non-covalent bonds with H and C atoms of Py. The interaction of Ti₁₆O₃₂ with nPy oligomers, results distortion in nPy geometries (Figs. 2 and 3), which is a direct consequence of their strong orbital overlapping. Six different types of inter-molecular interactions are observed in the case of the 7Py-Ti₁₆O₃₂ system; where Ti and O of Ti₁₆O₃₂ have made the strong electrostatic type of bonding with the C and H atoms of 7Py; ranging at ca. 1.90 to 2.80 Å. In all these composites, Ti atom of Ti₁₆O₃₂

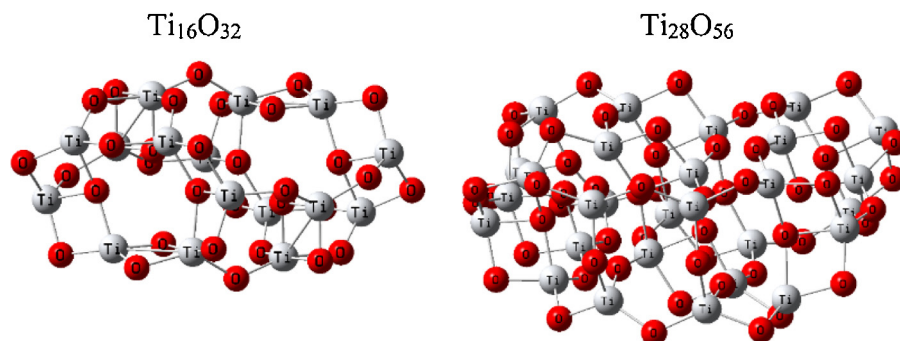
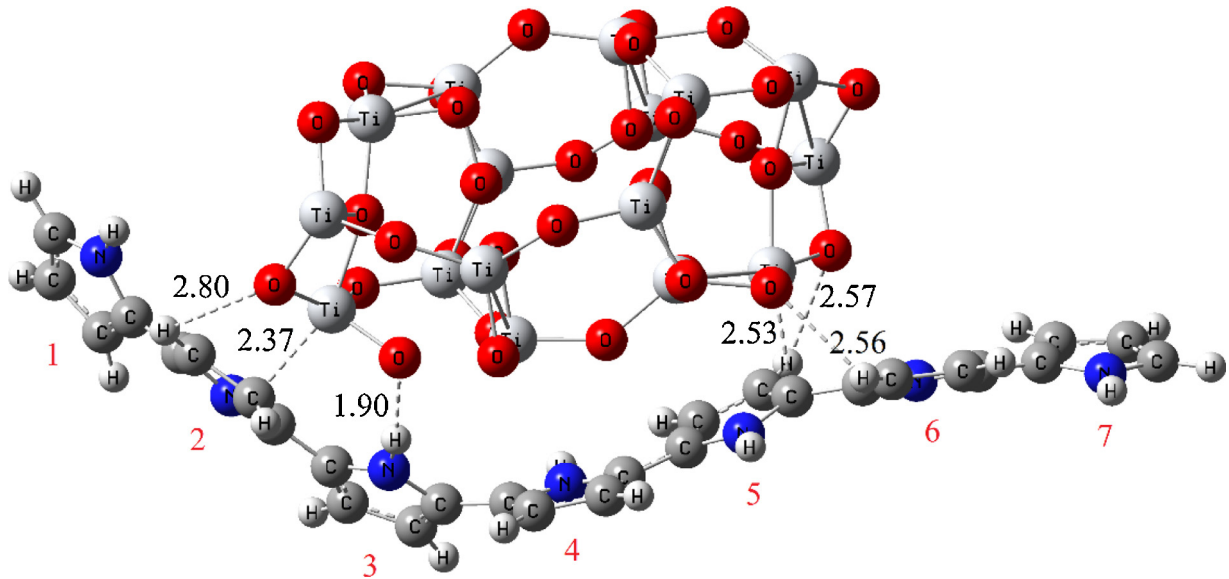
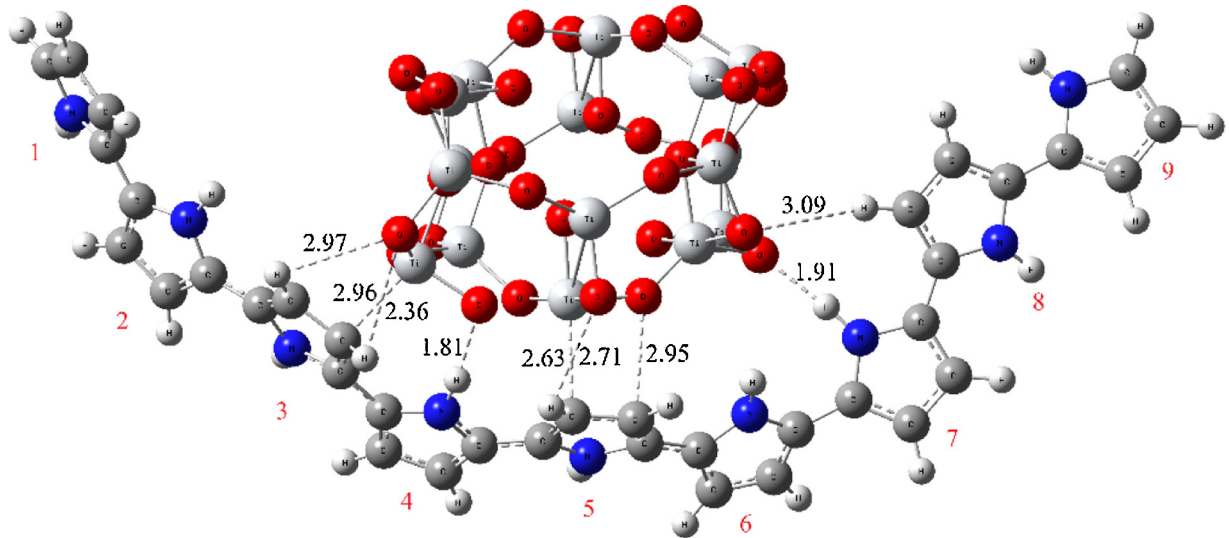


Fig. 1. Optimized Geometric Structure of Ti₁₆O₃₂ and Ti₂₈O₅₆ clusters.

Table 2B3LYP/LanL2DZ ground states bond angles and distances in the Vacuum for Molecular TiO_2 , cluster of $\text{Ti}_{16}\text{O}_{32}$, and in the Bulk for structural Rutile and Anatase.

Parameters	This study	TiO_2 Vacuum	TiO_2 Vacuum ¹	Rutile bulk properties ¹	Anatase bulk properties ¹
dTi–O	1.71/92 Å	1.63 Å	1.67 Å	1.96 Å	1.83 Å
dTi–Ti	2.78 Å	–	–	3.61 Å	3.03 Å
dO–O	2.46 Å	–	–	2.57 Å	2.29 Å
O–Ti–O	82.96°	110.7°	110.6°	81.6°	74.1°
Ti–O–Ti	102.82°	–	–	130.8°	105.9°

**Fig. 2.** Optimized Geometric Structure of 7Py- $\text{Ti}_{16}\text{O}_{32}$.**Fig. 3.** Optimized Geometric Structure of 9Py- $\text{Ti}_{16}\text{O}_{32}$.

makes an inter-molecular electrostatic bond with C of nPy and a Hydrogen bond between the O of $\text{Ti}_{16}\text{O}_{32}$ and H atoms of nPy.

The O–H inter-molecular bonds in the studied systems are strong bonds and can be regarded as covalent bonding. On the other hand, simulated Ti–C bond distances in the range of 2.30–2.70 Å confirm the formation of a strong electrostatic interaction. Jeffery et al. have reported that 2.2–2.5 Å of hydrogen bonding will be “strong, mostly covalent”, 2.5–3.2 Å as “moderate, mostly electrostatic” while 3.2–4.0 Å as “weak, mostly electrostatic” along with following bond energies, –40 to –14, –15 to –4, and <–4 kcal/mol, respectively [37]. Comparative analysis of

simulated inter-molecular bonding (including Fig. S1 and S2) led us to conclude that $\text{Ti}_{16}\text{O}_{32}$ make a strong composite with Py oligomers.

3.3. Interaction energy in nPy- $\text{Ti}_{16}\text{O}_{32}$ composites

$\text{Ti}_{16}\text{O}_{32}$ and PPy oligomers have a good interaction which is mostly covalent and electrostatic, simulated from interaction energy (ΔE_{int}) and geometrical counterpoise corrected ($\Delta E_{\text{gCP-D3}}$) methods (Table 3). The $\Delta E_{\text{gCP-D3}}$ method is employed to minimize the geometrical and dispersion factors. The result of this

Table 3
Inter-molecular interaction energy (ΔE_{int}), geometrical counterpoise corrected energy ($\Delta E_{\text{gCP-D3}}$), in kcal/mol, and NBO charges analysis of nPy-Ti₁₆O₃₂.

Species	ΔE_{int}	$\Delta E_{\text{gCP-D3}}$	Q_{NBO}
3Py-Ti ₁₆ O ₃₂	-42.54	-54.09	0.409
5Py-Ti ₁₆ O ₃₂	-34.22	-47.50	0.469
7Py-Ti ₁₆ O ₃₂	-41.10	-72.47	0.709
9Py-Ti ₁₆ O ₃₂	-41.47	-68.21	0.599

inter-molecular interaction energy proved that a very strong interaction is present in nPy and Ti₁₆O₃₂ species. In the 3Py-Ti₁₆O₃₂ composite, the ΔE_{int} is -42.54 kcal/mol while this interaction energy is simulated to be -54.09 kcal/mol with $\Delta E_{\text{gCP-D3}}$ method which is 11.55 kcal/mol higher than the ΔE_{int} method.

A comparatively weak inter-molecular forces are present in 5Py-Ti₁₆O₃₂ for which these energies are; -34.22 kcal/mol based on ΔE_{int} and -47.50 kcal/mol based on $\Delta E_{\text{gCP-D3}}$. This decrement in inter-molecular interaction energy is due to its geometrical shape compared to the 3Py-Ti₁₆O₃₂ composite. With chain length elongation, a slight difference in ΔE_{int} is observed as can be seen from data in Table 3. In the case of 7Py-Ti₁₆O₃₂, this inter-molecular non-bonding energy is about -41.10 kcal/mol, based on ΔE_{int} while -72.47 kcal/mol based on $\Delta E_{\text{gCP-D3}}$. This highest interaction energy ($\Delta E_{\text{gCP-D3}}$) in 7Py-Ti₁₆O₃₂ can be attributed to the suitable oligomeric length of PPy. Moreover, strong interaction of 7Py-Ti₁₆O₃₂ can be correlated to the fully relaxed geometric structure, which allows 7Py to wrap around Ti₁₆O₃₂ cluster much effectively compared to other compositions of nPy-Ti₁₆O₃₂ (Fig. 2). A similar but less pronounced trend is observed in 9Py-Ti₁₆O₃₂ composite, where the ΔE_{int} and $\Delta E_{\text{gCP-D3}}$ are -41.47 and -68.21 kcal/mol, respectively. Comparative analysis of the interaction energy of 7Py-Ti₁₆O₃₂ and 9Py-Ti₁₆O₃₂ indicate that 7Py make stronger nanocomposite. In summary, the amount of this interaction energy also evidences the existence of strong types of bonds between these two species which led to the confirmation of stable composite.

3.4. Natural bonding orbital analysis

Inter-molecular charge transfer between nPy and Ti₁₆O₃₂ are simulated with natural bonding orbital (Q_{NBO}) charge analysis at B3LYP with pseudopotential of LanL2DZ. As discussed elsewhere, these charge analyses are basis set dependent but with the same level of theory [such as B3LYP/6-31G (d), UB3LYP/6-31G (d), UB3LYP/6-311++G (d, p) or B3LYP/LanL2DZ] etc., for different structures the results would provide meaningful trends [38,39].

In connection with previous sections, Ti₁₆O₃₂ interacts with nPy oligomers through strong hydrogen (mostly covalent) and electrostatic (Ti-C). The analysis of NBO simulation indicates that Ti-C bond is the main charge transferring paths in all nPy-Ti₁₆O₃₂ composites. The net charge transfer in all nPy-Ti₁₆O₃₂ composites is listed in Table 3 while individual ring charges are listed in Table 4 along with Ti₁₆O₃₂ attached-Py rings. Analysis of data in Table 4 confirms the electron accepting nature of Ti₁₆O₃₂ in the composite as it withdraws electronic cloud density from Py oligomers to about 0.40 to 0.70 e⁻ which results in a cationic state in nPy oligomers, responsible for better electrical conductivity [40–42].

Table 4
NBO charge Analysis in unit of electron of nPy-Ti₁₆O₃₂ rings.

Species	Ring 1	Ring 2	Ring 3	Ring 4	Ring 5	Ring 6	Ring 7	Ring 8	Ring 9
3Py-Ti ₁₆ O ₃₂	0.228	0.11	0.071						
5Py-Ti ₁₆ O ₃₂	0.087	0.102	0.204	0.034	0.042				
7Py-Ti ₁₆ O ₃₂	0.065	0.16	0.103	0.108	0.121	0.105	0.047		
9Py-Ti ₁₆ O ₃₂	0.039	0.043	0.158	0.126	0.156	0.041	0.021	0.011	0.004

Table 5
Molecular Orbital Energy, Band Gap (in eV) and Dipole moment (Debye) of nPy and nPy-Ti₁₆O₃₂ composites.

Species	HOMO	LUMO	Dipole moment	Band Gap
Ti ₁₆ O ₃₂	-7.33	-4.27	0.0007	3.06
3Py	-4.71	-0.44	1.56	4.27
3Py-Ti ₁₆ O ₃₂	-5.67	-2.12	13.63	2.55
5Py	-4.45	-0.76	1.08	3.69
5Py-Ti ₁₆ O ₃₂	-5.04	-3.53	10.89	1.51
7Py	-4.34	-0.91	0.58	3.43
7Py-Ti ₁₆ O ₃₂	-5.24	-3.37	9.97	1.87
9Py	-4.28	-0.98	0.07	3.30
9Py-Ti ₁₆ O ₃₂	-4.42	-3.68	8.75	0.74

Finally, a unique charge distribution can be seen in the Py rings of 7Py-Ti₁₆O₃₂ system which suggest that 7Py-Ti₁₆O₃₂ is an optimum composition with greater charge transferring ability.

3.5. Electronic properties simulation

The electronic properties such as IP, EA, HOMO, LUMO, ESP, DOS and band gap of isolated as well as nPy-Ti₁₆O₃₂ composites was estimated at B3LYP/LanL2DZ level. The ΔSCF and negative of HOMO orbital energies are almost similar, especially for long chain systems. The IP energy is estimated from the negative of HOMO while the EA is obtained from negative of LUMO, using Koopman's theorem. Higher the EA and IP values of a chemical substance, greater will be its electroactivity and stability. The HOMO and LUMO energies (band edge positions) of isolated Ti₁₆O₃₂ are listed in Table 5 while frontier molecular orbitals are shown in Fig. 4.

Our simulated band gap value for Ti₁₆O₃₂ is 3.06 eV at B3LYP/LanL2DZ level, which is close to that of the observed data (3.20 eV) [40]. The difference is because of molecular cluster simulation as reported by Troisi et al. [41]; different simulation packages, cluster size, and level of theories give rise to different band gaps. Usually, the band gap decrease with increase in the size of the cluster and it is expected that this will also converge to the bulk value like that of the total energy [41]. Best reactive sites of both of the Ti₁₆O₃₂ and nPy oligomers are estimated from molecular electrostatic potential (MEP) as shown in Fig. 4 and 5. Based on these MEP plots, Ti₁₆O₃₂ and nPy oligomers interacted at a suitable distance.

3.6. Ionization potential

Interaction of Ti₁₆O₃₂ with nPy increases the IP of nPy oligomers indicating the increased stability of the resulted composite as can be seen from the delocalized contours (Fig. 5). Higher the IP more will be the stability of a chemical substance. In case of 3Py-Ti₁₆O₃₂ composite, the increase in IP is about 0.96 eV which consequently narrow its band gap from 4.27 to 2.12 eV (as discussed in band gap section below). A similar trend is observed in rest of the nPy oligomers in nPy-Ti₁₆O₃₂ composites, except 9Py-Ti₁₆O₃₂ composite, where negligible change (IP value) has been observed which can be attributed to lower interaction ability of their molecular orbitals. The increase in IP value of nPy-Ti₁₆O₃₂ composites is clearly depicted in Fig. 6.

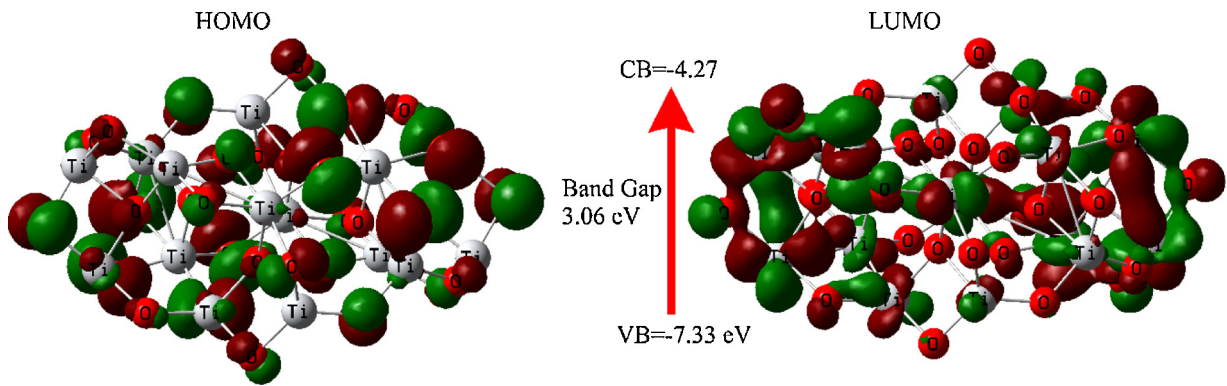


Fig. 4. Contours of the HOMO and LUMO of $\text{Ti}_{16}\text{O}_{32}$.

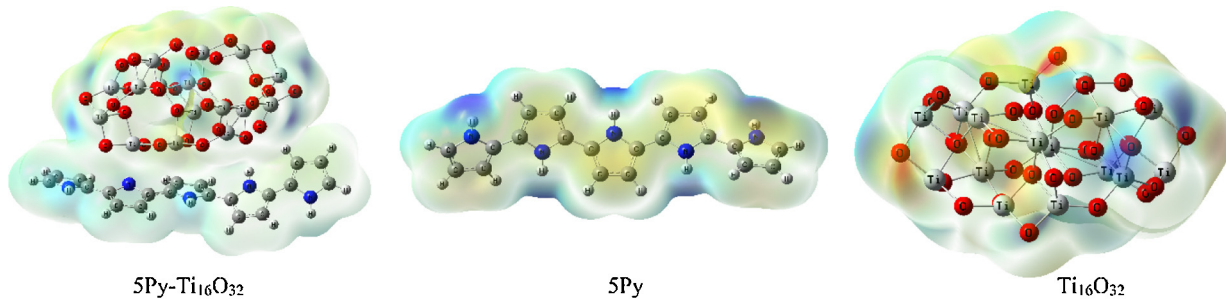


Fig. 5. Molecular Electrostatic Potential plots of $\text{Ti}_{16}\text{O}_{32}$, 5Py and 5Py- $\text{Ti}_{16}\text{O}_{32}$.

3.6.1. Electron affinity

EA is estimated from the negative of LUMO, which found to be increasing in nPy oligomers upon interacting with $\text{Ti}_{16}\text{O}_{32}$. A substantial shift in LUMO to narrow the band gap is observed in nPy- $\text{Ti}_{16}\text{O}_{32}$ bounded species compared to individual $\text{Ti}_{16}\text{O}_{32}$ and nPy as shown in Fig. 7. $\text{Ti}_{16}\text{O}_{32}$ shifts the EA of 3Py from 0.44 to 2.12 eV, 2.77 eV in 5Py- $\text{Ti}_{16}\text{O}_{32}$, 2.46 eV in 7Py- $\text{Ti}_{16}\text{O}_{32}$ and 2.70 eV in 9Py- $\text{Ti}_{16}\text{O}_{32}$ composite. As discussed in the optimized geometric analysis, $\text{Ti}_{16}\text{O}_{32}$ has an excellent interaction with nPy oligomers which is also in agreement with the EA analysis. The overall increase in EA value proves that the nPy- $\text{Ti}_{16}\text{O}_{32}$ composites are cationic in nature where polaron and bipolaron states may exist.

3.6.2. Band gap and molecular orbitals energy

Both optical and electrical band gaps are simulated at ΔSCF (excitation energy with higher oscillator strength) and B3LYP (difference of HOMO-LUMO orbitals), listed in Tables 5 and 6. Analysis of the data (Table 5) clarifies that the band gap of nPy oligomers become narrow upon interaction with $\text{Ti}_{16}\text{O}_{32}$, which is an evidence of their excellent electroactive property in the resulted composite.

Frontier molecular orbitals and dipole moments of these interacting species before and after interaction are calculated at B3LYP/LanL2DZ level. The contours of HOMO and LUMO along with band gap of nPy and nPy- $\text{Ti}_{16}\text{O}_{32}$ composites are given in Figs. 8 and 9, respectively. It can be easily predicted from the data that molecular orbitals of $\text{Ti}_{16}\text{O}_{32}$ strongly interact with the

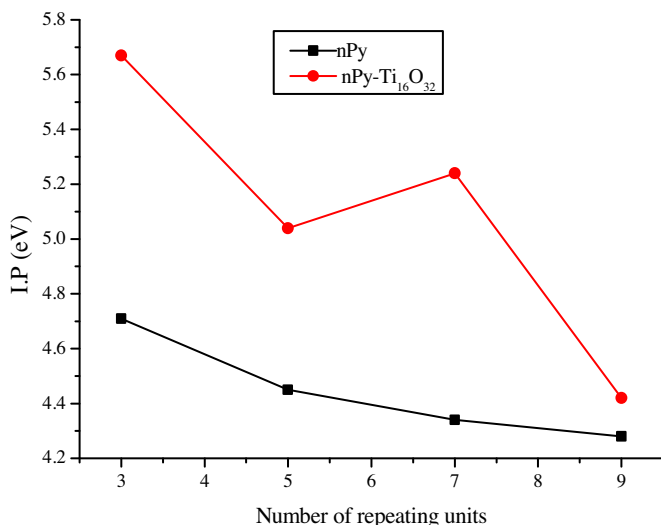


Fig. 6. Change in IP of nPy and nPy- $\text{Ti}_{16}\text{O}_{32}$ composites.

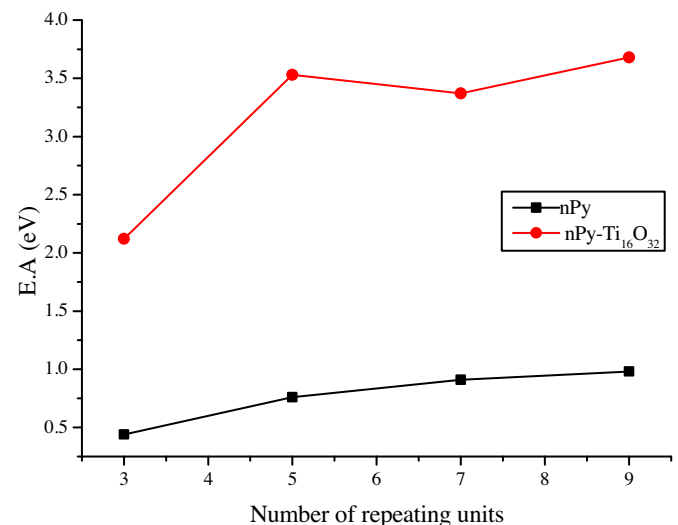


Fig. 7. Change in E.A. of nPy and nPy- $\text{Ti}_{16}\text{O}_{32}$ composites.

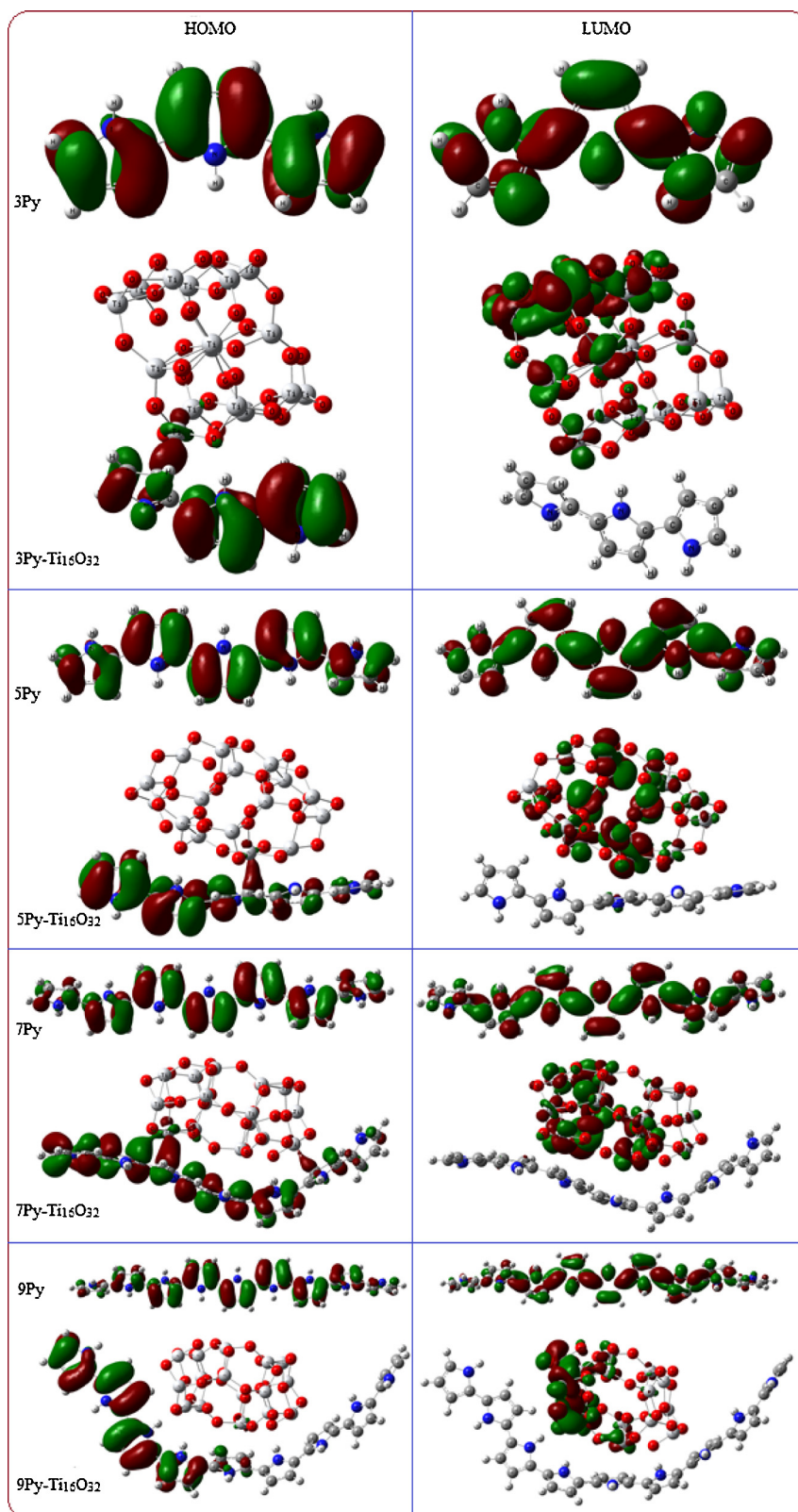


Fig. 8. Frontier molecular orbitals of $\text{Ti}_{16}\text{O}_{32}$, nPy and nPy- $\text{Ti}_{16}\text{O}_{32}$ bounded complexes.

HOMO/LUMO of nPy through establishing strong covalent types of bonding (Table 5). The strong covalent type of bonding indicate the stability of nPy- $\text{Ti}_{16}\text{O}_{32}$ composites which have an intermediate band gap and highest dipole moment.

The LUMO energy of $\text{Ti}_{16}\text{O}_{32}$ has considerably reduced from -0.44 to -2.12 eV while the band gap of Py reduced from 4.27 to 2.55 eV in all nPy- $\text{Ti}_{16}\text{O}_{32}$ composites as shown in Figs. 8 and 9. Dipole moment of 3Py- $\text{Ti}_{16}\text{O}_{32}$ (13.63 Debye) clearly demonstrates a substantial increment in its electroactivity.

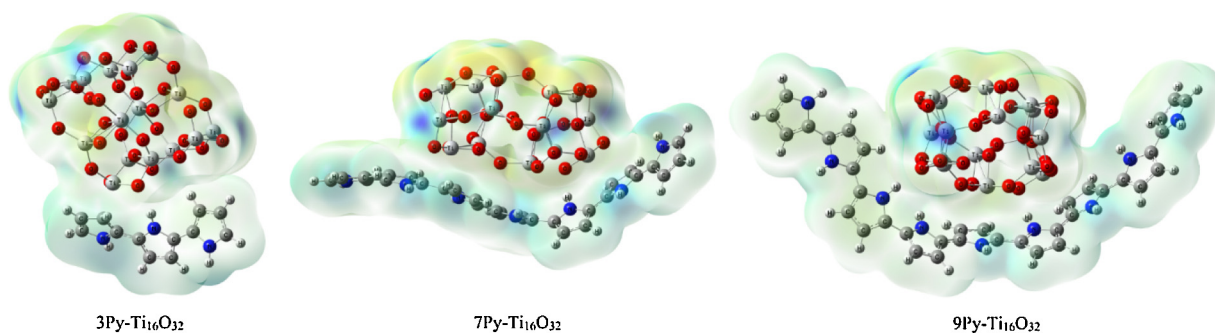


Fig. 9. Molecular electrostatic potential plot of 3, 7 and 9Py-Ti₁₆O₃₂ composites.

Moreover, narrowing band gap, have also a direct relationship with chain length elongation of Py as obvious from Fig. 10. Ti₁₆O₃₂ reduces the HOMO of 5Py from -4.45 to -5.04 eV (actually increase in negative charge), LUMO from -0.76 to -3.53 eV and band gap from 3.69 to 1.51 eV. Similar, but more pronounced reduction in these values can be seen in 7Py-Ti₁₆O₃₂, 0.90 eV in HOMO, 2.46 eV in LUMO, and a reduction of 1.56 eV in its band gap. Electronic cloud densities of the contours of HOMO and LUMO of 9Py-Ti₁₆O₃₂ compared to that of 9Py are enhanced to about 0.14 eV and 2.70 eV, respectively. While their dipole moment and band gap change from 0.07 to 8.75 Debye and 3.30 to 0.74 eV, respectively. The molecular electrostatic potential plot of 3, 7 and 9Py-Ti₁₆O₃₂ are shown in Fig. 9, which clearly visualize their electroactive nature.

Furthermore, the density of states plots for four these composites are correlatively shown in Fig. 10, which highlight a substantial variation in their band edges shifting compared to their individual constituents.

The homogeneous MEP plot (Fig. 9) of these composites confirm the excellent interaction between nPy and Ti₁₆O₃₂ cluster by mutually sharing of their electronic cloud densities. One can easily observe how the HOMO and LUMO of Ti₁₆O₃₂ (red spectra) and nPy (black spectra) interacted and resulted stable and ideal (align band edges with redox potential of water) nPy-Ti₁₆O₃₂ (blue spectra) composites. This theoretical investigation will guide and minimize the synthetic effort in term of interaction and mixing ratios. So, from experimental point view, we don't need to synthesize an

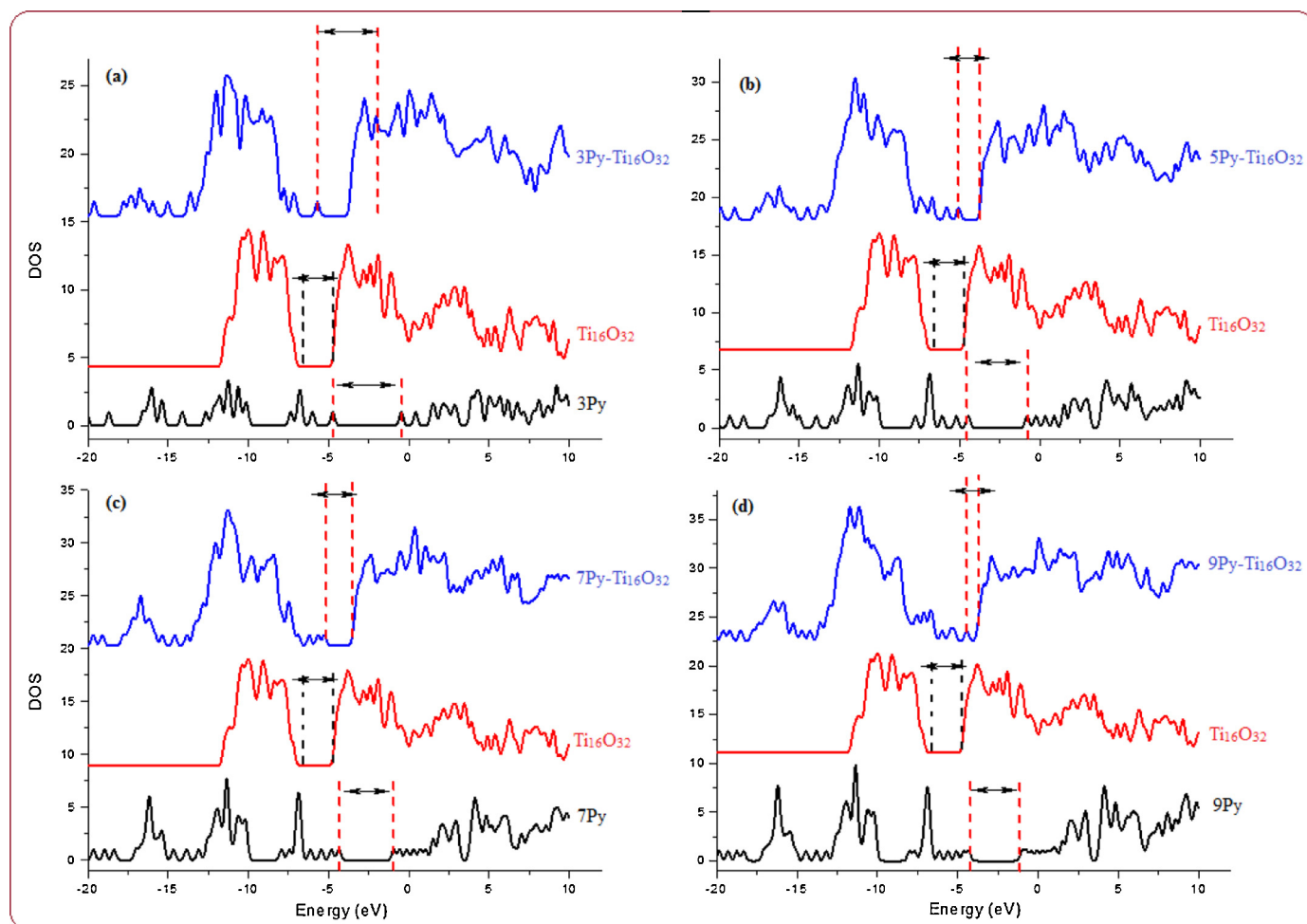


Fig. 10. Density of states plots of Ti₁₆O₃₂, nPy and nPy-Ti₁₆O₃₂ bounded complexes.

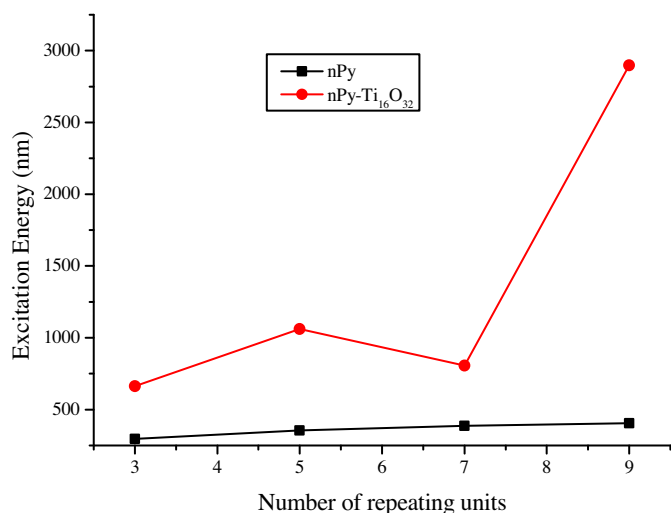


Fig. 11. First allowed electronic excitation energy of nPy and nPy-Ti₁₆O₃₂ composites.

infinite chain length of PPy, the routine oligomer (up to 6 or 8 repeating units) will be a best fit for the commercially available TiO₂ (anatase). Furthermore, the study also provides insight into improving the band structure, charge transport and determination of physical and chemical bonding between nPy and TiO₂ species.

3.7. UV-vis study

UV-vis spectra of nPy, Ti₁₆O₃₂, and nPy-Ti₁₆O₃₂ are simulated in the gas phase at TD-DFT/UB3LYP/LanL2DZ level. The first allowed electronic excitation energies are correlated with the experimentally observed λ_{\max} , which are listed in Fig. 11 and Table 6. Three prominent band peaks are found in the UV-vis spectra of nPy oligomers where the high wavelengths one is referred as λ_{\max} ; the transition of an electron from valence to conduction band. Interaction of Ti₁₆O₃₂ with nPy oligomers (Fig. 11 and Table 6) cause a red-shifting in the λ_{\max} of nPy. This red-shifting in λ_{\max} of all nPy oligomers illustrates the *n*-type doping nature of Ti₁₆O₃₂.

In the case of 3Py, the excitation energy of $\pi \rightarrow \pi^*$ transition increased from 296 to 663 nm in the resulted composite (3Py-Ti₁₆O₃₂), which evidences the establishment of strong bonding. As shown in Table 6, Ti₁₆O₃₂ increases the first allowed electronic excitation energy of 5Py to about 707 nm, 420 nm in 7Py, and 2493 nm in 9Py. This substantial increase can be attributed to improved conductivity/delocalization of the composites compared to isolated nPy oligomers (*vide infra*).

The individual Ti₁₆O₃₂ and nPy oligomers are unable to absorb in the visible range, however, nPy-Ti₁₆O₃₂ composites have excellent absorption capability in the visible region (Table 6) due to

Table 6

Calculated excitation energies, oscillator strengths, and molecular orbitals (MOs) of the first allowed singlet transition involved in the excitation for nPy and nPy-Ti₁₆O₃₂ composites.

Species	Energy (eV)	Wavelength (nm)	Oscillator Strength	MOs	Coefficient
Ti ₁₆ O ₃₂	3.71	333	0.01	S ₀ → S ₁	0.46
3Py	4.18	296	0.87	S ₀ → S ₁	0.70
3Py-Ti ₁₆ O ₃₂	1.86	663	0.005	S ₀ → S ₁	0.37
5Py	3.49	354	1.50	S ₀ → S ₁	0.70
5Py-Ti ₁₆ O ₃₂	1.16	1061	0.008	S ₀ → S ₁	0.50
7Py	3.19	387	2.08	S ₀ → S ₁	0.70
7Py-Ti ₁₆ O ₃₂	1.53	807	0.02	S ₀ → S ₁	0.68
9Py	3.05	405	2.67	S ₀ → S ₁	0.69
9Py-Ti ₁₆ O ₃₂	0.42	2898	0.0002	S ₀ → S ₁	0.70

a substantial decrease in the band gap. The red-shifting from the ultraviolet to visible elucidates/evidences the excellent photo-voltaic and photocatalytic activity of nPy-Ti₁₆O₃₂ composites over their individual constituents. Analysis of the simulation results led us to conclude that all nPy-Ti₁₆O₃₂ composites have a wide range of visible light absorption capability. Among the long chain oligomeric systems, the first allowed excitation energy of ($\pi \rightarrow \pi^*$ transition) of 9Py-Ti₁₆O₃₂ is more prominent compared to other compositions (Fig. 11) indicating that eight or nine repeating unit of PPy would be an excellent oligomeric chain length to develop an efficient visible light active photocatalyst (composite). This argument is also in good agreement with the other parameters discussed above.

4. Conclusions

Density functional theory study (DFT) of pyrrole-Ti₁₆O₃₂ bounded systems are carried out to find their interaction to tailor the best composite for the photodegradation of environmental pollutants and solar water splitting. Inter-molecular interaction energy in nPy-Ti₁₆O₃₂ composites is simulated in the range of -41 to -72 kcal/mol which confirmed the existence of strong covalent and electrostatic type bonding. This energy is simulated with the help of single point energy and $\Delta E_{\text{GCP-D3}}$ methods. So, after confirming the composite formation, band gap narrowing and better visible light absorption capability is observed compared to their individual nPy and Ti₁₆O₃₂ constituents. Electronic properties such as HOMO and LUMO of nPy, Ti₁₆O₃₂ and nPy-Ti₁₆O₃₂ composites estimated using B3LYP/LanL2DZ level, indicate excellent visible light absorption and charge transport efficiency of nPy-Ti₁₆O₃₂. Other electronic properties such as ESP, DOS, band gap, and UV-vis spectra also support the formation of efficient photoactive nPy-Ti₁₆O₃₂ composites. Moreover, UV-vis spectra of these composites predict the visible light absorption compared to nPy and Ti₁₆O₃₂. Electron-hole transferring define Py oligomers as a donor and Ti₁₆O₃₂ cluster as an acceptor in the resulted composites. Finally, the oligomeric length of eight/nine in the composite is found to be an optimum for the designing of an efficient photocatalyst. This theoretical investigation will minimize the synthetic effort such as mixing ratios of TiO₂ and PPy oligomers. Although, other components present in the cell might affect the nPy-TiO₂ interactions, but this basic theoretical study guides us about its possibility to be used as a photocatalyst. The study will also guide experimental scientists to improve the band structure, optical, physical and chemical properties of COP-TiO₂ and other metal oxide composites.

Acknowledgment

H.U acknowledges the partial financial support of the UK Solar Fuel Network (SFN).

Appendix A. Supplementary data

Supplementary data associated with this article can be found, in the online version, at <http://dx.doi.org/10.1016/j.snb.2016.10.019>.

References

- [1] S. Cherian, C.C. Wamser, Adsorption and photoactivity of tetra (4-carboxyphenyl) porphyrin (TCPP) on nanoparticulate TiO₂, *J. Phys. Chem. B* 104 (2000) 3624–3629.
- [2] Y.-G. Kim, J. Walker, L.A. Samuelson, J. Kumar, Efficient light harvesting polymers for nanocrystalline TiO₂ photovoltaic cells, *Nano Lett.* 3 (2003) 523–525.
- [3] I. Robel, V. Subramanian, M. Kuno, P.V. Kamat, Quantum dot solar cells Harvesting light energy with CdSe nanocrystals molecularly linked to mesoscopic TiO₂ films, *J. Am. Chem. Soc.* 128 (2006) 2385–2393.

- [4] Y.-Y. Song, F. Schmidt-Stein, S. Bauer, P. Schmuki, Amphiphilic TiO₂ nanotube arrays: an actively controllable drug delivery system, *J. Am. Chem. Soc.* 131 (2009) 4230–4232.
- [5] K. Woan, G. Pyrgiotakis, W. Sigmund, Photocatalytic carbon-nanotube-TiO₂ composites, *Adv. Mater.* 21 (2009) 2233–2239.
- [6] V. Chabot, D. Higgins, A. Yu, X. Xiao, Z. Chen, J. Zhang, A review of graphene and graphene oxide sponge: material synthesis and applications to energy and the environment Energy, *Environ. Sci.* 7 (2014) 1564–1596.
- [7] D. Wen, S. Guo, J. Zhai, L. Deng, W. Ren, S. Dong, Pt nanoparticles supported on TiO₂ colloidal spheres with nanoporous surface: preparation and use as an enhancing material for biosensing applications, *J. Phys. Chem. C* 113 (2009) 13023–13028.
- [8] S. Banerjee, S.C. Pillai, P. Falaras, K.E. O'shea, J.A. Byrne, D.D. Dionysiou, New insights into the mechanism of visible light photocatalysis, *J. Phys. Chem. Lett.* 5 (2014) 2543–2554.
- [9] N. Serpone, Is the band gap of pristine TiO₂ narrowed by anion- and cation-doping of titanium dioxide in second-generation photocatalysts? *J. Phys. Chem. B* 110 (2006) 24287–24293.
- [10] X. Chen, S. Shen, L. Guo, S.S. Mao, Semiconductor-based photocatalytic hydrogen generation, *Chem. Rev.* 110 (2010) 6503–6570.
- [11] H.-i. Kim, J. Kim, W. Kim, W. Choi, Enhanced photocatalytic and photoelectrochemical activity in the ternary hybrid of CdS/TiO₂/WO₃ through the cascaded electron transfer, *J. Phys. Chem. C* 115 (2011) 9797–9805.
- [12] G. Li, V. Shrotriya, J. Huang, Y. Yao, T. Moriarty, K. Emery, Y. Yang, High-efficiency solution processable polymer photovoltaic cells by self-organization of polymer blends, *Nat. Mater.* 4 (2005) 864–868.
- [13] R. Friend, R. Gymer, A. Holmes, J. Burroughes, R. Marks, C. Taliani, D. Bradley, D. Dos Santos, J. Bredas, M. Lögdlund, Electroluminescence in conjugated polymers, *Nature* 397 (1999) 121–128.
- [14] G. Li, R. Zhu, Y. Yang, Polymer solar cells, *Nat. Photonics* 6 (2012) 153–161.
- [15] F.C. Krebs, Polymer solar cell modules prepared using roll-to-roll methods: knife-over-edge coating: slot-die coating and screen printing, *Sol. Energy Mater. Sol. Cells* 93 (2009) 465–475.
- [16] C.J. Brabec, N.S. Sariciftci, J.C. Hummelen, Plastic solar cells, *Adv. Funct. Mater.* 11 (2001) 15–26.
- [17] J. Janata, M. Josowicz, Conducting polymers in electronic chemical sensors, *Nat. Mater.* 2 (2003) 19–24.
- [18] C. Janaky, N.R. de Tacconi, W. Chanmanee, K. Rajeshwar, Bringing conjugated polymers and oxide nanoarchitectures into intimate contact: light-induced electrodeposition of polypyrrole and polyaniline on nanoporous WO₃ or TiO₂ nanotube array, *J. Phys. Chem. C* 116 (2012) 19145–19155.
- [19] R.J. Nussbaumer, W.R. Caseri, P. Smith, T.ervoort, Polymer-TiO₂ nanocomposites: a route towards visually transparent broadband UV filters and high refractive index materials, *Macromol. Mater. Eng.* 288 (2003) 44–49.
- [20] W. Feng, E. Sun, A. Fujii, H. Wu, K. Niihara, K. Yoshino, Synthesis and characterization of photoconducting polyaniline-TiO₂ nanocomposite bull, *Chem. Soc. Jpn.* 73 (2000) 2627–2633.
- [21] X.C. Li, J.S. Sun, G.H. He, G.L. Jiang, Y. Tan, B. Xue, Macroporous polypyrrole-TiO₂ composites with improved photoactivity and electrochemical sensitivity, *J. Colloid Interface Sci.* 411 (2013) 34–40.
- [22] J.B. Zhu, X. Zhao, M.L. Xiao, L. Liang, C.P. Liu, J.H. Liao, W. Xing, The construction of nitrogen-doped graphitized carbon-TiO₂ composite to improve the electrocatalyst for methanol oxidation, *Carbon* 72 (2014) 114–124.
- [23] J.J. Li, J.T. Feng, W. Yan, Excellent adsorption and desorption characteristics of polypyrrole/TiO₂ composite for Methylene Blue, *Appl. Surf. Sci.* 279 (2013) 400–408.
- [24] F. Deng, L.J. Min, X.B. Luo, S.L. Wu, S.L. Luo, Visible-light photocatalytic degradation performances and thermal stability due to the synergetic effect of TiO₂ with conductive copolymers of polyaniline and polypyrrole, *Nanoscale* 5 (2013) 8703–8710.
- [25] H. Ullah, K. Ayub, Z. Ullah, M. Hanif, R. Nawaz, A.A. Shah, S. Bilal, Theoretical insight of polypyrrole ammonia gas sensor, *Synth. Met.* 172 (2013) 14–20.
- [26] H. Ullah, A.A. Shah, S. Bilal, K. Ayub, Doping and dedoping processes of polypyrrole: DFT study with hybrid functionals, *J. Phys. Chem. C* 118 (2014) 17819–17830.
- [27] S. Bibi, H. Ullah, S.M. Ahmad, A.-u.-H. A. Shah, S. Bilal, A.A. Tahir, K. Ayub, Molecular and electronic structure elucidation of polypyrrole gas sensors, *J. Phys. Chem. C* (2015).
- [28] H. Ullah, A.A. Shah, K. Ayub, S. Bilal, Density functional theory study of poly(o-Phenylenediamine) oligomers, *J. Phys. Chem. C* 117 (2013) 4069–4078.
- [29] H. Ullah, A.A. Shah, S. Bilal, K. Ayub, DFT study of polyaniline NH₃ CO₂, and CO gas sensors: comparison with recent experimental data, *J. Phys. Chem. C* 117 (2013) 23701–23711.
- [30] M.J.T. Frisch, G.W. Schlegel, H.B. Scuseria, G.E. Robb, M.A. Cheeseman, J.R. Scalmani, G. Barone, V. Mennucci, B. Petersson, G.A. Gaussian 09, Revision C. 01; Gaussian, Inc.: Wallingford, CT, 2009, Gaussian 09.
- [31] A. R. Allouche, Gabedit, <http://gabedit.sourceforge.net> (2011).
- [32] N.M. O'boyle, A.L. Tenderholt, K.M. Langner, Cclib: a library for package-independent computational chemistry algorithms, *J. Comp Chem* 29 (2008) 839–845.
- [33] R. Dennington, T. Keith, and J. G. Millam, Version 5.0. 8 Semicem Inc., Shawnee Mission KS (2008).
- [34] J.G. Brandenburg, M. Alessio, B. Civalleri, M.F. Peintinger, T. Bredow, S. Grimme, Geometrical correction for the inter- and intramolecular basis set superposition error in periodic density functional theory calculations, *J. Phys. Chem. A* 117 (2013) 9282–9292.
- [35] H. Kruse, L. Goerigk, S. Grimme, Why the standard B3LYP/6-31G* model chemistry should not be used in DFT calculations of molecular thermochemistry: understanding and correcting the problem, *J. Org. Chem.* 77 (2012) 10824–10834.
- [36] A.M. Asaduzzaman, G. Schreckenbach, Computational studies of the interactions of I⁻ and I₃⁻ with TiO₂ clusters: implications for dye-sensitized solar cells, *Theor. Chem. Acc.* 129 (2011) 199–208.
- [37] G.A. Jeffrey, An Introduction to Hydrogen Bonding, vol 12, Oxford university press, New York, 1997.
- [38] C. Fonseca Guerra, J.W. Handgraaf, E.J. Baerends, F.M. Bickelhaupt, Voronoi deformation density (VDD) charges: assessment of the Mulliken Bader, Hirshfeld, Weinhold, and VDD methods for charge analysis, *J. Comput. Chem.* 25 (2004) 189–210.
- [39] F. Martin, H. Zipse, Charge distribution in the water molecule—a comparison of methods, *J. Comput. Chem.* 26 (2005) 97–105.
- [40] D.O. Scanlon, C.W. Dunnill, J. Buckeridge, S.A. Shevlin, A.J. Logsdail, S.M. Woodley, C.R.A. Catlow, M.J. Powell, R.G. Palgrave, I.P. Parkin, Band alignment of rutile and anatase TiO₂, *Nat Mater* 12 (2013) 798–801.
- [41] N. Martinsinovich, D.R. Jones, A. Troisi, Electronic structure of TiO₂ surfaces and effect of molecular adsorbates using different DFT implementations, *J. Phys. Chem. C* 114 (2010) 22659–22670.

Biographies



Habib Ullah received M.Sc degree in Physical Chemistry from Hazara University, Mansehra in 2010 and M.Phil from the Institute of Chemical Sciences, University of Peshawar, Pakistan in 2014. Currently, he is doing Ph.D under the supervision of Dr. Asif and Prof. Tapas, in Renewable Energy, at College of Engineering, Mathematics and Physical Science (CEMPS), University of Exeter, UK. His research involves, Design of novel Materials i.e., conjugated organic polymers (graphene), inorganic metal oxides, perovskites and their composites, for sensors, solar cells, rechargeable batteries, light-emitting diodes, and corrosion inhibition applications.



Asif A. Tahir graduated from the Department of Inorganic Chemistry at Quaid-i-Azam University, Pakistan, in 2009. He worked as a research associate at Loughborough University for three years and then moved to the University of Liverpool before joining the College of Engineering, Mathematics and Physical Sciences (CEMPS) at the University of Exeter as a Lecturer in Renewable Energy. He specializes in the fabrication of nanomaterials using state-of-the-art techniques for solar energy conversion and photocatalysis. His research focus includes the design, synthesis, and characterization of new materials using soft chemistry approaches and the optimization of nanomaterials for high performance.



Tapas K. Mallick received the Ph.D. degree from the University of Ulster, Coleraine, UK, in 2003. From 2007 to 2012, he was a Lecturer with Heriot-Watt University, UK. He is currently a Professor with the Renewable Energy and Chair in Clean Technologies with the Environment and Sustainability Institute, University of Exeter, Penryn, UK. His research interests include renewable energies, concentrating photovoltaics, building integrated photovoltaics, integration of renewables, modelling and biomimicking of solar energy

[Article 9]

S. Bibi, H. Ullah, S. M. Ahmad, A.-u.-H. Ali Shah, S. Bilal, A. A. Tahir, K. Ayub,
"Molecular and electronic structure elucidation of polypyrrole gas sensors." *J.*
Phys. Chem. C. vol. 119, pp. 15994-16003, Jun. 2015.

Molecular and Electronic Structure Elucidation of Polypyrrole Gas Sensors

Salma Bibi,[†] Habib Ullah,[‡] Shah Masood Ahmad,[§] Anwar-ul-Haq Ali Shah,[§] Salma Bilal,^{*,†} Asif Ali Tahir,[‡] and Khurshid Ayub^{||}

[†]National Centre of Excellence in Physical Chemistry, University of Peshawar, 25120 Peshawar, Pakistan

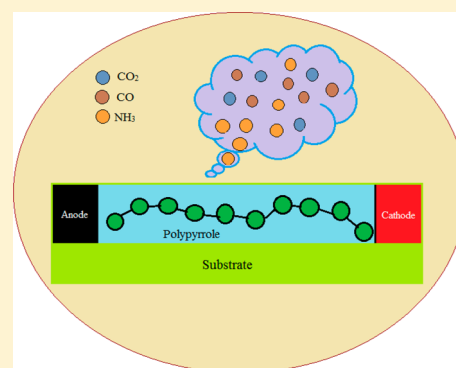
[‡]Environment and Sustainability Institute (ESI), University of Exeter, Penryn Campus, Penryn, Cornwall TR10 9FE, U.K.

[§]Institute of Chemical Sciences, University of Peshawar, 25120 Peshawar, Pakistan

^{||}Department of Chemistry, COMSATS Institute of Information Technology, University Road, Tobe Camp, 22060 Abbottabad, Pakistan

S Supporting Information

ABSTRACT: Sensitivity and selectivity of polypyrrole (PPy) toward NH₃, CO₂, and CO have been studied at density functional theory (DFT). PPy oligomers are used both in the doped (PPy⁺) and neutral (PPy) form for their sensing abilities to realize the best state for gas sensing. DFT calculations are performed at the hybrid functional, B3LYP/6-31G(d), level of theory. Detection/interaction of CO is investigated from carbon [CO(1)] and oxygen termini of CO [CO(2)]. Interaction energies and charge transfer are simulated which reveal the sensing ability of PPy toward these gases. Furthermore, these results are supported by frontier molecular orbital energies and band gap calculations. PPy, in both the doped and neutral state, is more sensitive to NH₃ compared to CO₂ and CO. More interestingly, NH₃ causes doping of PPy and dedoping of PPy⁺, providing evidence that PPy/PPy⁺ is an excellent sensor for NH₃ gas. UV-vis and UV-vis-near-IR spectra of nPy, nPy⁺, and nPy/nPy⁺-X complexes demonstrate strong interaction of PPy/PPy⁺ with these atmospheric gases. The better response of PPy/PPy⁺ toward NH₃ is also consistent with the experimental observations.



1. INTRODUCTION

Conjugated organic polymers (synthetic metals) are conducting due to the presence of delocalized π electrons along the polymer backbone.^{1,2} The conjugated organic polymers (COPs) have several advantages over other semiconducting materials due to ease of synthesis and processing and their cheap, tunable, and robust nature. Polyaniline (PANI), polyacetylene (PA), polythiophene (PT), polypyrrole (PPy), polyparaphenylene (PPP), polyparaphenylenevinylene (PPV), and poly(*o*-phenylenediamine) (POPD) are some prominent members of COPs.³ Most COPs have nonlinear response to the electronic excitation, but doping and dedoping (injection of an electron and a hole) of the conjugated chain lead to a self-localized excited state (imprinted).⁴ Therefore, COPs are potential candidates for energy storage,⁵ electrocatalysis,⁶ smart windows,⁷ membrane gas separation,⁸ organic sensors,⁹ electrochromic displays,¹⁰ microwave screening,¹¹ corrosion protection,¹² etc.

Recently, the interest of the scientific community has increased in the application of COPs in high performance solid state gas sensor devices.^{13–16} Gas sensors are very important in environmental monitoring, home safety, and chemical controlling (both in the industries and laboratories). The most frequently reported sensors are metal oxide

semiconductors,¹⁷ quartz crystal microbalance,¹⁸ surface acoustic wave,¹⁹ field effect transistor,²⁰ and conducting polymers (CPs).^{16,21–23} The metal oxide semiconductor (inorganic material) gas sensors work on the principle of change in conductivity upon interaction with gas molecules, but they suffer from low selectivity (specific target gases). Moreover, high operation temperature leads to increased power consumption which reduces sensor life and limits the portability. In order to overcome these issues, research is directed to explore sensors which are stable, selective, and highly sensitive and have a quick response mechanism.

COPs have found a worthy place as room-temperature gas sensors. Several reports have shown that COPs are sensitive to a wide range of gases,^{24–29} vapors,³⁰ metals,^{31,32} and volatile organic solvents.^{33,34} COP-based sensors are also superior to other sensors because of their chemical diversity, stability, selectivity, high sensitivity, and quick response mechanism.³⁵

COPs consist of very large molecules of repeating units which may be homo, hetero, or blend, with a range of molecular weights (polydisperse); therefore, predicting their

Received: April 3, 2015

Revised: June 8, 2015

Published: June 15, 2015

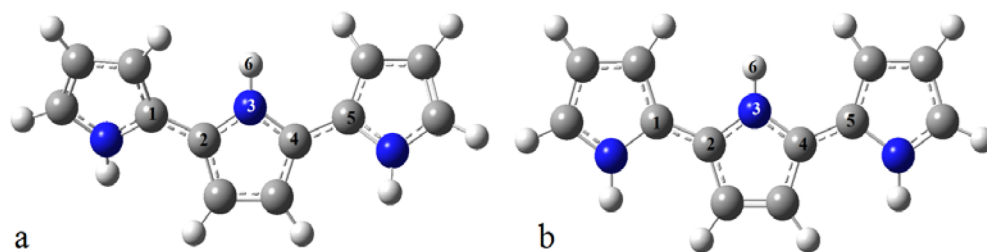


Figure 1. Reference optimized geometric structure of 3Py (a) and 3Py⁺ (b) using B3LYP/6-31G(d) and UB3LYP/6-31G(d) levels of theory, respectively.

electronic properties is quite challenging (especially theoretically). Generally, two distinct approaches are applied to calculate the properties of polymers: (a) periodic boundary condition (PBC) simulations and (b) extrapolation of oligomeric properties to infinite chain lengths, using the polynomial fit equation. Similar to metal-based sensors, COPs also change their conducting behavior/doping level upon interaction with different organic^{36,37} and inorganic analytes.^{24,38} The change in conductivity is one of the best tools to understand the gas sensing of COPs both theoretically and experimentally.^{15,39–41}

Among the studied COPs, PPy is a very promising candidate for gas sensing applications due to its ease of synthesis, high redox properties, tunable nature,⁴² stability in either the neutral or doped form, and good electrical conductivity. Changes in electrical conductivity of PPy can easily be observed, upon interaction with various volatile organic and inorganic analytes. Several reports are presented in this regard, where change in conductivity of PPy is measured upon exposure to different gases such as O₂, NO₂, CO, CO₂, and NH₃. Blance et al.⁴³ reported NH₃ gas sensing properties of PPy upon exposure to a mixture of O₂, NO₂, and NH₃. On the other hand, Lui et al.⁴⁴ fabricated a CO gas sensor by growing a PPy film through electropolymerization. A gas sensor for CO₂ based on PPy film is also reported²⁶ showing the interactive ability of PPy but not counter checked by theory. Among other fascinating properties, the ability of PPy to form covalent bonding with inorganic substances like diamond makes it a valuable material for molecularly imprinted sensors.⁴⁵

In this paper, the sensing mechanism of both cationic and neutral forms of different oligomers of PPy are investigated with the help of electronic structure theory simulations. Intermolecular interaction and charge transferring phenomena between the interacting systems are carried out. Calculations for excited state properties such as UV–vis, UV–vis–near IR, density of state (DOS), HOMO, LUMO, and band gap are performed to explore whether, and how, the analytes shift electronic configuration of the parent oligomers and polymer.

2. COMPUTATIONAL METHODOLOGY

All calculations are performed using GAUSSIAN 09,⁴⁶ and the results are analyzed/visualized with GaussView⁴⁷ and Gabedit programs.⁴⁸ Density functional theory (DFT) is quite accurate for the study of COPs and has been widely accepted.^{42,49–51} Therefore, molecular and electronic structure elucidation of PPy as a gas sensor, both doped and neutral forms, is achieved with DFT methods. Individual geometries of *n*Py and their complexes (*n*Py–X) were optimized at the 6-31G(d) level of theory, using a hybrid functional: B3LYP [Becke 3-Parameter (Exchange), Lee, Yang and Parr].⁵² Charged species, *n*Py⁺ (Figure 1), and their complexes (*n*Py⁺–X) (Figure 2) were

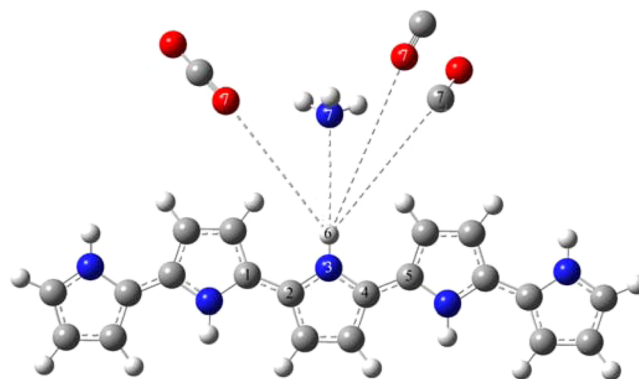


Figure 2. Reference optimized geometric structure of 5Py⁺–X (X = NH₃, CO₂, and CO).

optimized using an unrestricted formalism such as UB3LYP⁵³ at the 6-31G(d) level of theory, where *n* = 3, 5, 7, and 9. Optimized geometries are obtained from gradient minimization of energy without any symmetry constraint.^{54,55} Intermolecular interaction (total and counterpoise corrected interaction energies), charge analysis (Mulliken and natural bonding orbital), molecular orbital analysis (HOMO and LUMO), and UV–vis/UV–vis–near-IR spectral analysis are simulated at the above-mentioned level of theory. Although Mulliken and natural bonding orbital (NBO) analysis are basis set dependent, the trend obtained can be used to explain the sensing phenomenon. Band gap is estimated from the difference of HOMO and LUMO energies, and it gives an idea about the change in conductivity of polymer upon interaction with different substances. Oligomeric properties are extrapolated to polymer, using a second degree polynomial fit equation.⁵⁶

3. RESULTS AND DISCUSSION

I. Interaction Energy Analysis. For quantitative estimation of the strength of interaction between *n*Py (both doped and neutral) and analytes (NH₃, CO₂, CO), the interaction energy is simulated using DFT methods. The greater this interaction energy, the greater the response will be of the *n*Py/*n*Py⁺ toward analytes. The calculated interaction energies are also counterpoise corrected. The counterpoise corrected energy method removes the error arising from the use of finite basis sets. Adsorbent species (PPy/PPy⁺ in this case) interact with analytes and become stable due to these interaction energies. The complexes are stable because of either a hydrogen bond or weak dipole-induced-dipole or ion–dipole interaction with adsorbate (NH₃, CO₂, CO). Simple and BSSE interaction energies of PPy/PPy⁺ with these different analytes are listed in Table 1 and Table 2.

Table 1. ΔE_{int} , $\Delta E_{\text{int,CP}}$, Q_{NBO} , and Q_{Mulliken} of $n\text{Py}-X$ ($X = \text{NH}_3, \text{CO}_2, \text{ and CO}$) ($n = 3, 5, 7, \text{ and } 9$) Using the B3LYP/6-31G(d) Level of Theory

species	ΔE_{int}	$\Delta E_{\text{int,CP}}$	Q_{NBO}	Q_{Mulliken}
3Py-NH ₃	-9.98	-7.66	-0.046	-0.043
5Py-NH ₃	-10.23	-7.91	-0.045	-0.044
7Py-NH ₃	-10.44	-7.89	-0.048	-0.046
9Py-NH ₃	-10.53	-8.09	-0.050	-0.048
$\infty\text{Py}-\text{NH}_3$	-11.04	-8.31		
3Py-CO ₂	-3.07	-1.44	-0.005	-0.011
5Py-CO ₂	-3.01	-1.39	-0.007	-0.012
7Py-CO ₂	-3.39	-1.88	-0.006	-0.010
9Py-CO ₂	-3.33	-1.76	-0.005	-0.011
$\infty\text{Py}-\text{CO}_2$	-4.16	-2.71		
3Py-CO(1)	-2.76	-1.32	-0.013	-0.027
5Py-CO(1)	-3.39	-1.45	-0.017	-0.034
7Py-CO(1)	-3.38	-1.43	-0.017	-0.036
9Py-CO(1)	-3.39	-1.45	-0.017	-0.035
$\infty\text{Py}-\text{CO}(1)$	-2.89	-1.35		
3Py-CO(2)	-1.63	-1.11	-0.008	-0.022
5Py-CO(2)	-2.13	-1.23	-0.008	-0.022
7Py-CO(2)	-2.13	-1.23	-0.008	-0.022
9Py-CO(2)	-2.13	-1.23	-0.008	-0.022
$\infty\text{Py}-\text{CO}(2)$	-1.74	-1.14		

Table 2. ΔE_{int} , $\Delta E_{\text{int,CP}}$, Q_{NBO} , and Q_{Mulliken} of $n\text{Py}^+-X$ ($X = \text{NH}_3, \text{CO}_2, \text{ and CO}$) ($n = 3, 5, 7, \text{ and } 9$) Using the UB3LYP/6-31G(d) Level of Theory

species	ΔE_{int}	$\Delta E_{\text{int,CP}}$	Q_{NBO}	Q_{Mulliken}
3Py ⁺ -NH ₃	-16.69	-15.62	-0.071	-0.080
5Py ⁺ -NH ₃	-14.68	-13.74	-0.061	-0.070
7Py ⁺ -NH ₃	-13.74	-12.80	-0.060	-0.068
9Py ⁺ -NH ₃	-13.05	-12.11	-0.057	-0.065
$\infty\text{Py}^+-\text{NH}_3$	-10.74	-9.69		
3Py ⁺ -CO ₂	-5.08	-4.58	-0.018	-0.045
5Py ⁺ -CO ₂	-4.27	-4.10	-0.015	-0.038
7Py ⁺ -CO ₂	-3.95	-3.45	-0.013	-0.037
9Py ⁺ -CO ₂	-3.64	-3.50	-0.013	-0.035
$\infty\text{Py}^+-\text{CO}_2$	-2.78	-2.41		
3Py ⁺ -CO(1)	-4.46	-3.22	-0.030	-0.056
5Py ⁺ -CO(1)	-4.02	-3.01	-0.026	-0.050
7Py ⁺ -CO(1)	-3.70	-2.61	-0.024	-0.047
9Py ⁺ -CO(1)	-3.51	-2.31	-0.023	-0.045
$\infty\text{Py}^+-\text{CO}(1)$	-2.63	-0.80		
3Py ⁺ -CO(2)	-3.20	-1.76	-0.015	-0.039
5Py ⁺ -CO(2)	-2.70	-1.50	-0.012	-0.033
7Py ⁺ -CO(2)	-2.51	-1.19	-0.011	-0.033
9Py ⁺ -CO(2)	-2.32	-1.02	-0.010	-0.030
$\infty\text{Py}^+-\text{CO}(2)$	-1.81	-0.07		

$n\text{Py}/n\text{Py}^+-\text{NH}_3$. Interaction energy of $n\text{Py}$ with NH_3 (3Py-NH₃ complex) is about $-9.98 \text{ kcal mol}^{-1}$, whereas the counterpoise corrected energy is $-7.66 \text{ kcal mol}^{-1}$. For $n\text{Py}$, the binding energy increases as the oligomer size increases. The binding energy increases to $-10.23 \text{ kcal mol}^{-1}$ (BSSE, $-7.91 \text{ kcal mol}^{-1}$) in 5Py-NH₃, $-10.44 \text{ kcal mol}^{-1}$ (BSSE, $-7.89 \text{ kcal mol}^{-1}$) in 7Py-NH₃, and $-10.53 \text{ kcal mol}^{-1}$ (BSSE, $-8.09 \text{ kcal mol}^{-1}$) in the 9Py-NH₃ complex. The binding energy of the infinite polymer (PPy) with NH_3 is obtained through the second degree polynomial fit equation. This energy is $11.04 \text{ kcal mol}^{-1}$ based on simple energy calculation and $-8.31 \text{ kcal mol}^{-1}$ based on BSSE simulation (see Table 1). The interaction

energy (between PPy and NH_3) is indicative of a hydrogen type of bond, typically between 5 and 12 kcal mol^{-1} . Intermolecular nonbonding distance analysis also supports the establishment of a strong hydrogen bonding between PPy and NH_3 .

Doped PPy (PPy⁺) oligomers exhibit remarkable interaction with NH_3 , and ion dipole electrostatic forces are believed to operate instead of H-bonding. The doped (PPy⁺) ion interacts through ion-dipole interactions with NH_3 . 3Py⁺ interacts with NH_3 with $-16.69 \text{ kcal mol}^{-1}$ of energy ($15.62 \text{ kcal mol}^{-1}$ based on BSSE). With chain length elongation this binding energy decreases, which is contrary to the effect of the neutral polymer (see Table 1 and Table 2). It decreases to $-14.68 \text{ kcal mol}^{-1}$ in the case of 5Py⁺-NH₃ (BSSE corrected $-13.74 \text{ kcal mol}^{-1}$), $-13.74 \text{ kcal mol}^{-1}$ (BSSE, $-12.80 \text{ kcal mol}^{-1}$) in 7Py⁺-NH₃, and $-13.05 \text{ kcal mol}^{-1}$ (BSSE, $-12.11 \text{ kcal mol}^{-1}$) in the 9Py⁺-NH₃ complex. The extrapolated binding energy for infinite chain length of PPy⁺ is $-10.74 \text{ kcal mol}^{-1}$ based on ΔE_{int} and the counterpoise corrected energy is $-9.69 \text{ kcal mol}^{-1}$ (Table 2).

$n\text{Py}/n\text{Py}^+-\text{CO}_2$. Interaction energies for complexation of CO_2 with $n\text{Py}/n\text{Py}^+$ are relatively less compared to ammonia bound complexes. $n\text{Py}$ oligomers interact with CO_2 from the O site, through a weak type of van der Waals interaction (Table 1). Noncovalent interaction energy in the 3Py-CO₂ complex is $-3.07 \text{ kcal mol}^{-1}$ (counterpoise corrected energy is $-1.44 \text{ kcal mol}^{-1}$). Contrary to NH_3 bound complexes, a rather irregular trend is observed in the binding energies of $n\text{Py}-\text{CO}_2$ complexes with oligomeric length increment. For example, the binding energy first slightly decreases up to $-3.01 \text{ kcal mol}^{-1}$ (BSSE, $-1.39 \text{ kcal mol}^{-1}$) in 5Py-CO₂ and then increases to $-3.39 \text{ kcal mol}^{-1}$ (BSSE, $-1.88 \text{ kcal mol}^{-1}$) in 7Py-CO₂. Again it decreases to about $-3.33 \text{ kcal mol}^{-1}$ ($-1.76 \text{ kcal mol}^{-1}$ based on BSSE) in the case of the 9Py-CO₂ complex. The extrapolated interaction energy for $\infty\text{Py}-\text{CO}_2$ turns out to be $-4.16 \text{ kcal mol}^{-1}$ (counterpoise corrected is $-2.71 \text{ kcal mol}^{-1}$). $n\text{Py}^+-\text{CO}_2$ complexes show slightly greater interaction compared to $n\text{Py}-\text{CO}_2$ complexes. This may be due to the cationic nature of PPy oligomers ($n\text{Py}^+$). But here again, as the chain length increases, the interaction energy decreases. This decrease in interaction energy can be attributed to a drop in delocalization due to the bulkiness of polymer which retards the interaction with CO_2 in larger units.

$n\text{Py}/n\text{Py}^+-\text{CO}$. Binding energies for the complexes of CO with $n\text{Py}$ and $n\text{Py}^+$ are studied from both ends of CO. Binding energies for both positions are given in Table 1 and Table 2 for neutral and doped forms of PPy, respectively. The interaction energies are high when CO interacts with $n\text{Py}$ through the carbon terminus. The 3Py-CO(1) complex is stabilized by $-2.76 \text{ kcal mol}^{-1}$ compared to 3Py and CO (counterpoise corrected energy is $-1.32 \text{ kcal mol}^{-1}$). The interaction energy increases with an increase in the chain length of the oligomer. The calculated binding energy between infinite polymer ($n\text{Py}$) and CO(1) is $-2.89 \text{ kcal mol}^{-1}$ (counterpoise corrected $-1.35 \text{ kcal mol}^{-1}$). The van der Waals type of bond in the 3Py-CO(2) complex has $-1.63 \text{ kcal mol}^{-1}$ of stabilization energy. The counterpoise corrected energy for this complex is $-1.11 \text{ kcal mol}^{-1}$. A slight increase is found in the case of 5Py-CO(2) and then constant values for the rest of complexes. Finally, the extrapolated oligomer bounded complex energies are simulated which is about $1.74 \text{ kcal mol}^{-1}$ and $1.14 \text{ kcal mol}^{-1}$ (based on counterpoise corrected energy). The binding energies for infinite doped polymer with CO are 2.63 and $1.81 \text{ kcal mol}^{-1}$

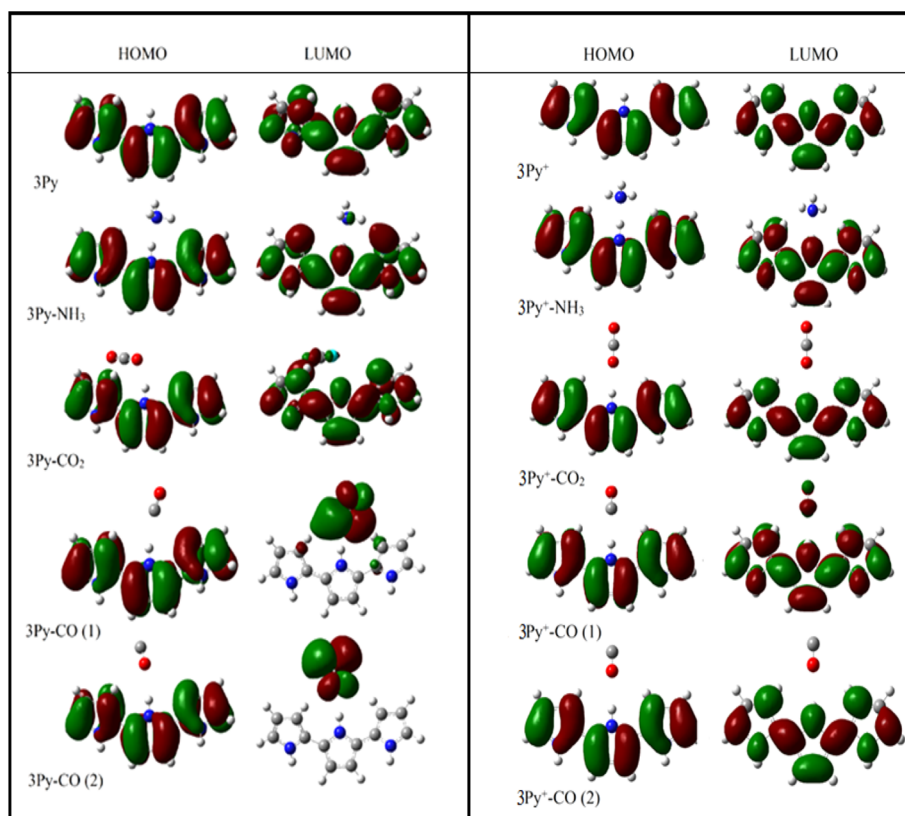


Figure 3. Frontier molecular orbitals of 3Py/3Py⁺ and 3Py/3Py⁺-X (X = NH₃, CO₂, CO(1), and CO(2)), using B3LYP/6-31G(d) and UB3LYP/6-31G(d) levels of theory.

for *n*Py-CO(1) and *n*Py-CO(2), respectively. These results indicate that *n*PPy⁺ has more response with CO(1).

Furthermore, comparative analysis of the above results illustrates that PPy oligomers in either the doped or neutral state are sensitive and selective toward NH₃. The interaction energy analysis also supports the experimental evidence of high sensitivity of PPy toward NH₃ gas.

II. Charge Analysis. Interaction between two or more species is often associated with charge transfer. Charge transfer alters the electronic and structural properties of these interacting species. The sensing capability and, therefore, selectivity of PPy oligomers (doped and neutral forms) toward NH₃, CO₂, and CO are investigated through amount of charge transfer between the oligomer and analyte. The extent of charge transfer between *n*Py/*n*Py⁺ and analytes [NH₃, CO₂, CO(1), and CO(2)] is simulated at the 6-31G(d) level of theory. The amount of charge transfer is simulated from Mulliken and NBO charge analyses, which are given in Table 1 for *n*Py-X and Table 2 for *n*Py⁺-X complexes.

*n*Py/*n*Py⁺-NH₃. In the 3Py-NH₃ complex, ammonia transfers about 0.043 e⁻ charge to 3Py, based on Mulliken and 0.046 e⁻ based on NBO charge analysis. This phenomenon can also be regarded as an *n*-doping process of 3Py. This extra charge does not remain confined on the bridging NH group of the Py; rather, it is distributed along the entire complex through delocalization which alters the electronic structure of the 3Py. The charge transfer is rather stronger in higher repeating units such as the 5Py-NH₃ complex. The 5Py gains -0.044 e⁻ from ammonia (based on Mulliken) and -0.045 e⁻ based on NBO charge analysis. Similarly, 7Py accepts -0.046 e⁻ in units of electrons (based on Mulliken) and -0.048 e⁻ (based on NBO)

from NH₃. In the case of the 9Py-NH₃ complex, the polymeric backbone gets -0.048 e⁻ (based on Mulliken) and -0.050 e⁻ (based on NBO).

Charge transfer from analytes to *n*Py⁺ oligomers is more intensive due to the electrophilic nature of the latter. For instance, 3Py⁺ gets 0.071 e⁻ charge based on NBO and 0.080 e⁻ based on Mulliken charge analysis. This charge transfer, from ammonia to doped oligomer, causes dedoping of 3Py⁺. In large repeating units this charge transfer is relatively low (Table 2). This could be probably because of the delocalization of charge in large oligomers. Transfer of electronic cloud density from NH₃ to either *n*Py or *n*Py⁺ provides a platform for the sensing ability of this polymer.

*n*Py/*n*Py⁺-CO₂. Neutral PPy oligomers interact with CO₂ and accept electronic charge from CO₂ (Table 1). CO₂ donates about 0.005 e⁻ charge to 3Py, based on NBO and 0.011 e⁻ based on Mulliken charge analysis. With the chain length elongation of the neutral *n*Py, the amount of charge transferred increases, i.e., 0.007 e⁻ (based on NBO) and 0.012 e⁻ based on Mulliken in 5Py-CO₂, 0.006 e⁻ (0.010 e⁻ based on Mulliken) in 7Py-CO₂, and 0.008 e⁻ (*Q*_{Mulliken}) and 0.022 e⁻ (*Q*_{NBO}) in the 9Py-CO₂ complex (see Table 1). The doped form of PPy oligomers has more potential to interact with CO₂, and hence this donation is more compared to the neutral species. For example, 3Py⁺ gets 0.018 e⁻ charge based on NBO and 0.045 e⁻ based on Mulliken charge analysis (Tables 1 and 2). A quite similar effect is observed in higher repeating units, but the doped ones are more responsive toward these analytes. However, the interaction is reduced with chain length elongation, which may be due to the increase in conjugation and delocalization (*vide supra*).

$n\text{Py}/n\text{Py}^+-\text{CO}$. Interestingly, the interaction of $n\text{Py}$ oligomers with CO is slightly greater than that of CO_2 , regarding charge transferring. PPy receives about 0.008 e^- charge (Q_{NBO}) and 0.022 e^- (Q_{Mulliken}) from CO in the case of $3\text{Py}-\text{CO}(1)$ (see Table 1). On the other hand, 3Py gets 0.013 e^- charge (Q_{NBO}) and 0.027 e^- (Q_{Mulliken}) in the $3\text{Py}-\text{CO}(2)$ complex. This charge transferring increases up to 0.008 e^- (Q_{NBO}) and 0.022 e^- (Q_{Mulliken}) in $9\text{Py}-\text{CO}(1)$. However, the $9\text{Py}-\text{CO}(2)$ complex is stronger than that of $9\text{Py}-\text{CO}(1)$, where charge transfer is about 0.017 e^- (Q_{NBO}) and 0.035 e^- (Q_{Mulliken}). It can be observed that CO(1) (at C terminus) shows strong interaction with $n\text{Py}$ oligomers, compared to CO(2) (at Oxygen terminus). Both NBO and Mulliken charge analyses are also consistent with the interaction energy simulations. A similar, but more distinct, effect can be seen in $n\text{Py}^+-\text{CO}(1)$ and $n\text{Py}^+-\text{CO}(2)$ complexes (see Table 2).

The trend obtained from the charge analysis shows that this polymer is more sensitive and selective toward NH_3 , among CO_2 , CO, and NH_3 . Although the results obtained from the charge analysis support the interaction energy analysis, the amount of charge transfer cannot provide useful information about the sensitivity and selectivity of the polymer solely. Here the charge transfer is too low to give a conclusive result about the sensing ability of the polymer. This may be due to the fact that Mulliken and NBO charge analyses are highly method dependent.

III. Frontier Molecular Orbital and Band Gap Analysis.

Interaction between two species (chemically or physically) is considered because of the interaction of molecular orbitals, occupied and unoccupied. When two species come close to each other, their molecular orbitals start interacting with each other and develop electrostatic/van der Waals type of interactions between them. Sensing properties of a substance are also greatly dependent on the interaction of molecular orbitals of oligomer with analyte. Molecular orbitals of sensing material, particularly HOMO and LUMO, get perturbed after interaction with analyte. This perturbation greatly affects other properties of the sensing substance (polymer in our case) such as IP, EA, and band gap. These theoretical electronic properties are translated in experimental redox potential and conductivity.

Contours of the HOMO and LUMO of isolated $n\text{Py}/n\text{Py}^+$ and analyte bounded complexes are given in Figure 3 and Figures S3–S5 (Supporting Information). Frontier molecular orbital energies and corresponding band gaps are listed in Tables S6 and S7 (Supporting Information).

$n\text{Py}/n\text{Py}^+-\text{NH}_3$. NH_3 donates electronic cloud density to $n\text{Py}$ and causes doping of the polymer. This transfer of electronic cloud density decreases the energy of HOMO of $n\text{Py}$ (Tables S6 and S7, Supporting Information). A decrease of about 0.3 eV is observed in the energy of HOMO of 3Py after interacting with NH_3 . Similarly, a decrease of about 0.23 eV is simulated in the case of 5Py , 0.18 eV in 7Py , and 0.16 eV in 9Py on sensing NH_3 . A change in the LUMO energy also indicates transfer of charge from NH_3 to the $n\text{Py}$ (Table S6, Supporting Information). Alteration in orbital energies also alters the corresponding band gap of the $n\text{Py}$ oligomers. A slight shortening of band gap from 4.39 to 4.36 eV is observed in $3\text{Py}-\text{NH}_3$, 3.79 to 3.74 eV in $5\text{Py}-\text{NH}_3$, 3.53 to 3.51 eV in $7\text{Py}-\text{NH}_3$, and 3.41 to 3.39 eV in $9\text{Py}-\text{NH}_3$ complexes. A decrease in the band gap value also strengthens the evidence of doping in $n\text{Py}$ upon interaction with NH_3 .

NH_3 donates electronic cloud density and causes dedoping of $n\text{Py}^+$ oligomers. This transferring of electronic density from

NH_3 decreases the HOMO energy of $n\text{Py}^+$, indicating its sensing ability. A 0.31 eV decrease in HOMO energy can be observed in $3\text{Py}^+-\text{NH}_3$, 0.19 eV in $5\text{Py}^+-\text{NH}_3$, 0.13 eV in $7\text{Py}^+-\text{NH}_3$, and 0.10 eV in $9\text{Py}^+-\text{NH}_3$ complexes, compared to isolated 3Py^+ . HOMO and LUMO energies decrease correspondingly which leads to the enlargement of band gap, showing dedoping of the polymer (Table S6, Supporting Information). The band gap increases from 3.85 to 3.95 eV in $3\text{Py}^+-\text{NH}_3$, 3.23 to 3.31 eV in $5\text{Py}^+-\text{NH}_3$, 3.00 to 3.07 eV in $7\text{Py}^+-\text{NH}_3$, and 2.92 to 2.97 eV in $9\text{Py}^+-\text{NH}_3$ complexes. The extrapolated values up to infinite repeating units for HOMO, LUMO, and band gap are also simulated (see Tables S6 and S7, Supporting Information).

$n\text{Py}/n\text{Py}^+-\text{CO}_2$. CO_2 causes perturbation in the HOMO energy of $n\text{Py}$ oligomers but to a lesser extent (about 0.01 – 0.02 eV for all oligomers) as compared to NH_3 . For example, HOMO energy decreases from -4.43 to -4.42 eV in $3\text{Py}-\text{CO}_2$, -4.17 to -4.16 eV in $5\text{Py}-\text{CO}_2$, -4.06 to -4.05 in $7\text{Py}-\text{CO}_2$, and -4.02 to -4.00 eV in $9\text{Py}-\text{CO}_2$ complexes. A decrease in the energies of LUMO is relatively high which leads to a decrease in band gap (Table S6, Supporting Information). A decrease in band gap is less pronounced which is due to the inertness of $n\text{Py}$ oligomers with CO_2 (Table S6, Supporting Information).

Interaction of CO_2 with $n\text{Py}^+$ also changes the HOMO and LUMO energies. The band gap of $n\text{Py}^+$ increases after interaction with CO_2 which can be regarded as dedoping of $n\text{Py}^+$ oligomers, due to charge transfer. The band gap increases from 3.85 to 3.87 eV in $3\text{Py}^+-\text{CO}_2$, 3.23 to 3.25 eV in $5\text{Py}^+-\text{CO}_2$, 3.00 to 3.02 eV in $7\text{Py}^+-\text{CO}_2$, and 2.92 to 2.93 eV in $9\text{Py}^+-\text{CO}_2$ complexes. It can also be observed that CO_2 has less effective interaction on a large oligomer. Very miniscule changes are observed in the HOMO, LUMO, and band gap, compared to shorter repeating units. These inferences from band gap analyses are also consistent with interaction energy analysis (*vide supra*); therefore, a weak type of sensing is deduced between $n\text{Py}^+$ and CO_2 , compared to the $n\text{Py}^+$ and NH_3 system.

$n\text{Py}/n\text{Py}^+-\text{CO}$. The effect of two sites of CO on $n\text{Py}/n\text{Py}^+$ is also analyzed for HOMO, LUMO, and band gaps. Molecular orbitals of CO(1) interact with 3Py and decrease its energy from -4.43 to -4.39 eV , i.e., transfer some amount of charge to 3Py . However, the effect on the LUMO energy is opposite as it increases from -0.04 to -1.02 eV . Changes in HOMO and LUMO energies consequently affect the band gap. Similar increases in the energies of HOMOs of other oligomers are also observed.

Transfer of electronic cloud density from CO(2) to $n\text{Py}$ oligomers is almost negligible, compared to CO(1) and NH_3 (Table S6, Supporting Information). The smaller the change in HOMO energy, the lesser the sensing response toward CO(2). Interaction of CO with $n\text{Py}^+$ also follows the same trend as for $n\text{Py}$; however, the overall interaction is very small (see Table S7, Supporting Information). Comparative analyses of HOMO, LUMO, and band gap combined with energetic parameters illustrate that the carbon terminus of CO is the favorable binding site.

IV. UV–vis/UV–vis–Near-IR Spectroscopic Analysis.

UV–vis and UV–vis–near-IR spectra of both of the isolated $n\text{Py}/n\text{Py}^+$ and analyte-bound coplexes are simulated at TD-B3LYP/6-31G(d) and TD-UB3LYP/6-31G(d) level of theories, respectively. Three distinct peaks can be observed in $n\text{Py}$ and $n\text{Py}-\text{X}$, and these results are consistent with earlier

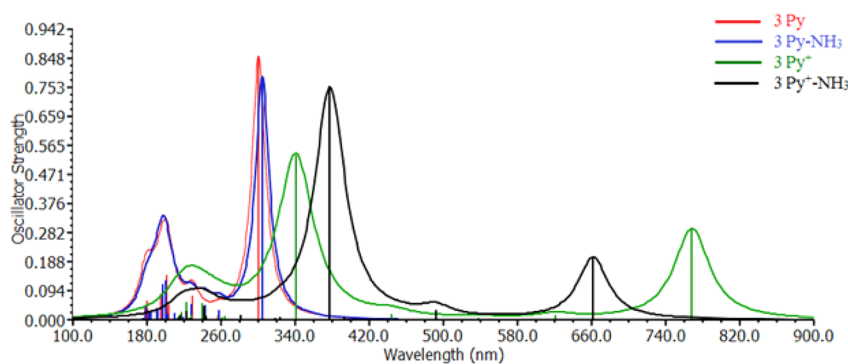


Figure 4. UV-vis/UV-vis-near-IR of 3Py (red), 3Py-NH₃ (blue), 3Py⁺ (green), and 3Py⁺-NH₃ (black).

Table 3. Calculated Excitation Energies, Oscillator Strengths, and Molecular Orbitals (MOs) of the First Allowed Singlet Transition Involved in the Excitation for *n*Py and *n*Py-X (X = NH₃, CO₂, and CO) (*n* = 3, 5, 7, and 9) Using the TD-B3LYP/6-31G(d) Level of Theory

species	wavelength (nm)	energy (eV)	oscillator strength	coefficient	MOs
3Py	301.22	4.1161	0.8513	0.70651	52→53
3Py-NH ₃	305.10	4.0637	0.7845	0.70428	57→58
3Py-CO ₂	304.13	4.0767	0.7697	0.70257	63→64
3Py-CO(1)	446.27	2.7782	0.0066	0.70655	59→60
3Py-CO(2)					
5Py	312.68	3.9652	1.4910	0.70588	86→87
5Py-NH ₃	365.99	3.3876	1.4401	0.70563	91→92
5Py-CO ₂	363.02	3.4153	1.4385	0.70556	97→98
5Py-CO(1)	501.22	2.4736	0.0017	0.55787	93→94
5Py-CO(2)	481.79	2.5734	0.0007	0.70633	93→94
7Py	395.65	3.1337	2.0941	0.70091	120→121
7Py-NH ₃	398.00	3.1152	2.0563	0.70079	125→126
7Py-CO ₂	398.48	3.1114	2.0363	0.70085	131→132
7Py-CO(1)	509.97	2.4312	0.0087	0.59400	127→128
7Py-CO(2)	492.08	2.5196	0.0007	0.70434	127→128
9Py	414.45	2.9915	2.6992	0.69125	154→155
9Py-NH ₃	416.99	2.9733	2.6131	0.69079	159→160
9Py-CO ₂	418.94	2.9595	2.6270	0.69176	165→166
9Py-CO(1)	517.31	2.3967	0.0042	0.55014	161→162
9Py-CO(2)	496.96	2.4949	0.0006	0.70112	161→162

theoretical and experimental work. The experimental UV-vis spectrum of PPy has three prominent absorption band peaks. In short oligomers, the third peak is not very prominent but can be observed beyond five repeating units. UV-vis spectra of *n*Py/*n*Py⁺ and *n*Py/*n*Py⁺-X complexes (containing more than three repeating units of Py) are given in the Supporting Information of Figures S6–S17, while 3Py/Py⁺ and their complexes are given in the subsequent sections. A peak in the near-IR region can be observed in the doped form of *n*Py (*n*Py⁺) and their analyte bound complexes, besides the three main peaks.

*n*Py/*n*Py⁺-NH₃. *n*Py shows three distinct band peaks which get shifted to longer wavelength upon interaction with NH₃ (Figure 4 and Figures S6–S8, Supporting Information). The red shift illustrates the doping process of PPy by NH₃. NH₃ donates electronic cloud density to PPy and decreases its band gap. 3Py shows three peak bands at about 301, 229, and 201 nm, but with chain length elongation, these band peaks appear in the visible region. The major band peak of 3Py with low energy (301 nm) is red-shifted to 305 nm on interaction with NH₃ (Table 3). In 5Py, this peak appears at 361 nm and red shifts to 366 nm on interaction with NH₃. In longer oligomers,

the red shifts are from 395 to 398 nm in 7Py and from 414 to 418 nm in the case of 9Py.

The UV-vis spectrum of *n*Py⁺ shifts to the low energy (compared to *n*Py) band peak in the near-IR region which clearly shows the doping phenomenon of *n*Py. NH₃ decreases the doping intensity of *n*Py⁺ by transferring electronic charge density; therefore, it causes a blue shift in the low energy band peak. The band peak appearing at ca. 769 nm shows blue shifting to 662 nm in 3Py⁺-NH₃. The similar band peak is blue-shifted from 1034 to 1014 nm in 5Py⁺-NH₃ (Table 4), from 1440 to 1395 nm in 7Py⁺-NH₃, and from 1907 to 1830 nm in 9Py⁺-NH₃. This blue shifting of low energy band peaks is also consistent with interaction energy and molecular orbital analysis.

*n*Py/*n*Py⁺-CO₂. CO₂ also shows a similar but less pronounced effect, compared to NH₃, on interaction with *n*Py/*n*Py⁺ (Figure 5 and Figures S9–S11, Supporting Information). The prominent absorption band peak of 3Py at 301 nm is slightly red-shifted to 304 nm, upon interaction with CO₂. Similarly, the peak at 361 nm in 5Py-CO₂ shifts to 363 nm. The shifts of absorption bands in larger oligomers upon complexation with CO₂ are 396–398 nm in 7Py-CO₂ and

Table 4. Calculated Excitation Energies, Oscillator Strengths, and Molecular Orbitals (MOs) of the First Allowed Singlet Transition Involved in the Excitation for $n\text{Py}^+$ and $n\text{Py}^+-\text{X}$ ($\text{X} = \text{NH}_3, \text{CO}_2, \text{and CO}$) ($n = 3, 5, 7, \text{and } 9$) Using the TD-B3LYP/6-31G(d) Level of Theory

species	wavelength	energy (eV)	oscillator strength	coefficient	MOs
3Py^+	768.91	1.6125	0.2959	0.97876	51→52
$3\text{Py}^+-\text{NH}_3$	662.09	1.8726	0.2004	0.92789	56→57
$3\text{Py}^+-\text{CO}_2$	664.58	1.8656	0.1940	0.92105	62→63
$3\text{Py}^+-\text{CO}(1)$	666.90	1.8591	0.1950	0.92280	58→59
$3\text{Py}^+-\text{CO}(2)$	664.97	1.8645	0.1934	0.92030	58→59
5Py^+	1034.23	1.1988	0.5353	0.97559	85→86
$5\text{Py}^+-\text{NH}_3$	1014.36	1.2223	0.5381	0.97817	90→91
$5\text{Py}^+-\text{CO}_2$	1025.88	1.2086	0.5321	0.97560	96→97
$5\text{Py}^+-\text{CO}(1)$	1033.94	1.1991	0.5340	0.97747	92→93
$5\text{Py}^+-\text{CO}(2)$	1029.12	1.2048	0.5335	0.97595	92→93
7Py^+	1439.77	0.8611	0.8754	1.01455	119→120
$7\text{Py}^+-\text{NH}_3$	1395.23	0.8886	0.8715	1.01065	124→125
$7\text{Py}^+-\text{CO}_2$	1418.77	0.8739	0.8734	1.01204	130→131
$7\text{Py}^+-\text{CO}(1)$	1435.88	0.8635	0.8686	1.01430	126→127
$7\text{Py}^+-\text{CO}(2)$	1426.43	0.8692	0.8732	1.01281	126→127
9Py^+	1907.08	0.6501	1.1050	1.05743	153→154
$9\text{Py}^+-\text{NH}_3$	1829.73	0.6776	1.1167	1.04297	158→159
$9\text{Py}^+-\text{CO}_2$	1871.04	0.6626	1.1186	1.04990	164→165
$9\text{Py}^+-\text{CO}(1)$	1898.76	0.6530	1.1027	1.05472	160→161
$9\text{Py}^+-\text{CO}(2)$	1884.23	0.6580	1.1156	1.05231	160→161

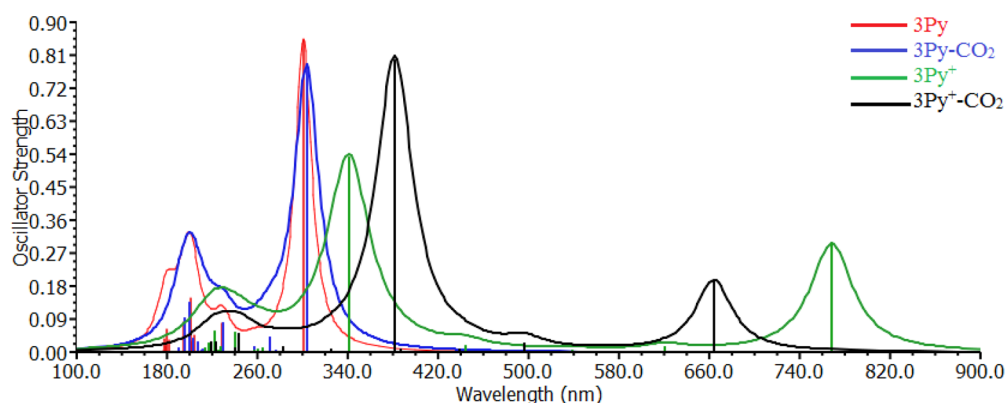


Figure 5. UV-vis/UV-vis-near-IR of 3Py (red), $3\text{Py}-\text{CO}_2$ (blue), 3Py^+ (green), and $3\text{Py}^+-\text{CO}_2$ (black).

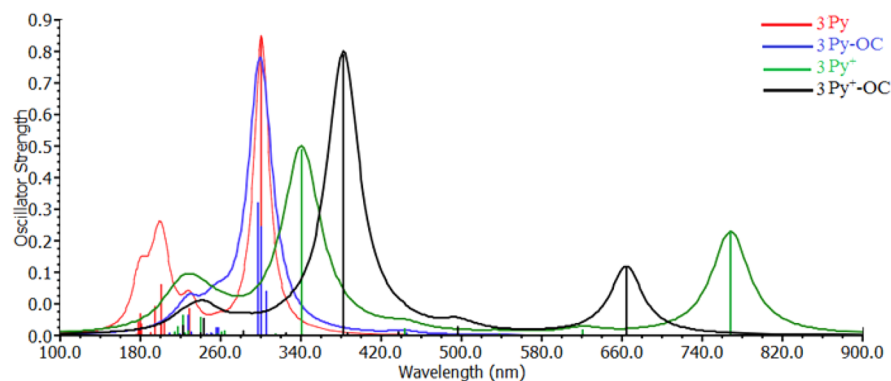


Figure 6. UV-vis/UV-vis-near-IR of 3Py (red), $3\text{Py}-\text{OC}$ (blue), 3Py^+ (green), and $3\text{Py}^+-\text{OC}$ (black).

414–418 nm in $9\text{Py}-\text{CO}_2$. The red shifting explains the doping effect in PPy due to CO_2 . The lower energy peak appearing in the near-IR region in doped form of PPy gets shifted to higher energy upon interaction with CO_2 . The band peak at 769 nm shifts to 664 nm in $3\text{Py}^+-\text{CO}_2$, at 1034 shifts to 1026 nm in $5\text{Py}^+-\text{CO}_2$, at 1440–1419 nm in $7\text{Py}^+-\text{CO}_2$, and at 1907–

1871 nm in $9\text{Py}^+-\text{CO}_2$. These results are consistent with the above-discussed parameters. The peak shifting is less pronounced as compared to NH_3 , depicting more sensitivity of PPy/ 3Py^+ toward NH_3 .

$n\text{Py}/n\text{Py}^+-\text{CO}$. The UV-vis and UV-vis-near-IR spectra of the isolated $n\text{Py}$, $n\text{Py}^+$, and their CO complexes [$\text{CO}(1)$ and

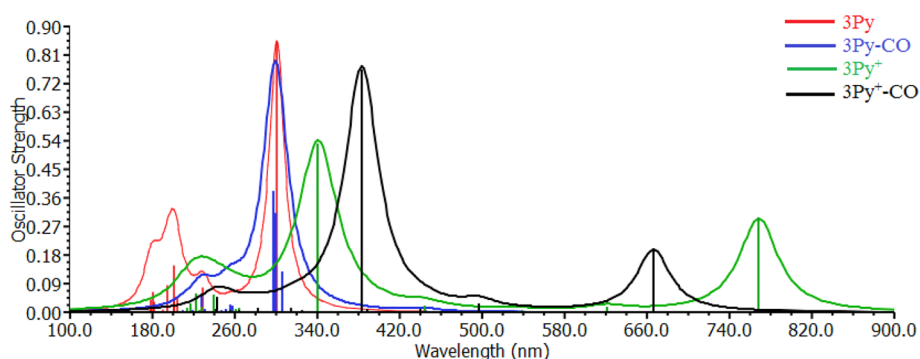


Figure 7. UV-vis/UV-vis-near-IR of 3Py (red), 3Py-CO (blue), 3Py⁺ (green), and 3Py⁺-CO (black).

CO(2)] are given Figures 6 and 7 and Figures S12–17 (Supporting Information). Trends in the shift of the absorption are different than revealed by analyses of other properties. The peak observed in 3Py at ca. 301 shifts to 298 nm in 3Py-CO(1) and to 302 nm in the 3Py-CO(2) complex. The absorption peak appearing at ca. 361 nm in 5Py moves to 363 nm in 5Py-CO(1) and to 366 nm in the 5Py-CO(2) complex. Similarly, absorption peaks appearing in 7Py and 9Py also shift after interaction with CO.

V. CONCLUSIONS

DFT study of $n\text{Py}/n\text{Py}^+$ (where $n = 3, 5, 7, 9$) and their complexes with NH_3 , CO_2 , and CO are carried out to analyze the sensitivity and selectivity of PPy, in both neutral and doped form. The intermolecular interaction energies are calculated and counter poise corrected. The bond energies are in the range of -9.98 to -10.53 kcal mol⁻¹ in the case of $n\text{Py}-\text{NH}_3$ complexes (hydrogen bonding) and -16.65 to -13.05 kcal mol⁻¹ in the case of $n\text{Py}^+-\text{NH}_3$ complexes (ion-dipole interaction). The intermolecular interaction is found to be weak electrostatic/weak van der Waals type bonding in CO_2 , CO(1), and CO(2) bound complexes. Interaction energies of CO(2) bound complexes show the inertness of CO(2) toward PPy. The results of sensing of analytes by PPy are in excellent correlation with the experimental results. CO interaction to $n\text{Py}/\text{Py}^+$ from the carbon side is more prominent compared to the interaction with the oxygen atom. Comparative results of interaction energy of neutral and doped forms of PPy reveal greater response for the doped form toward different analytes. It is also indicated from interaction energy that PPy shows more response to CO_2 than CO. The NBO and Mulliken charge analyses support the results obtained from interaction energy analysis, although the amount of charge transfer is too low. Frontier molecular orbital energies of $n\text{Py}-\text{X}$ and $n\text{Py}^+-\text{X}$, before and after sensing, confirm that NH_3 perturbed the orbital energy of PPy to a greater extent than the perturbation caused by CO_2 , CO(2), and CO(1). Therefore, orbital studies also add to the conclusion that PPy is very selective to NH_3 . In neutral forms, red shifting in UV-vis spectra is observed upon interacting with NH_3 , CO_2 , CO(1), and CO(2), which confirm the doping process. These analytes cause blue shifting in UV-vis and UV-vis-near IR spectra of $n\text{Py}^+$, which confirm the dedoping chemistry PPy^+ . NH_3 has high peak shifting ability in PPy/ PPy^+ compared to that of CO_2 , CO(1), and CO(2). In conclusion, PPy (both the $n\text{Py}$ and $n\text{Py}^+$) has greater response/selectivity with NH_3 , in the presence of CO_2 and CO gases.

■ ASSOCIATED CONTENT

📄 Supporting Information

Figures of IR spectra, tables of selected IR band peaks along with approximate assignments, HOMO and LOMO orbitals, UV-vis near-IR spectra. The Supporting Information is available free of charge on the ACS Publications website at DOI: 10.1021/acs.jpcc.5b03242.

■ AUTHOR INFORMATION

Corresponding Author

*E-mail: dresalmabilal@gmail.com.

Notes

The authors declare no competing financial interest.

■ ACKNOWLEDGMENTS

The authors are very much thankful to the Higher Education Commission (HEC) Islamabad for financial support for purchase of Lab equipments and computational facilities under research grant # 20-3111/ NRP/ R&D/HEC/13.

■ REFERENCES

- Bredas, J. L.; Street, G. B. Polarons, Bipolarons, and Solitons in Conducting Polymers. *Acc. Chem. Res.* **1985**, *18*, 309–315.
- Swager, T. M. The Molecular Wire Approach to Sensory Signal Amplification. *Acc. Chem. Res.* **1998**, *31*, 201–207.
- Janata, J.; Josowicz, M. Conducting Polymers in Electronic Chemical Sensors. *Nat. Mater.* **2003**, *2*, 19–24.
- Wang, X.; Zhi, L.; Müllen, K. Transparent, Conductive Graphene Electrodes for Dye-Sensitized Solar Cells. *Nano Lett.* **2008**, *8*, 323–327.
- Pan, L.; Qiu, H.; Dou, C.; Li, Y.; Pu, L.; Xu, J.; Shi, Y. Conducting Polymer Nanostructures: Template Synthesis and Applications in Energy Storage. *Int. J. Mol. Sci.* **2010**, *11*, 2636–2657.
- Kulesza, P. J.; Matczak, M.; Wolkiewicz, A.; Grzybowski, B.; Galkowski, M.; Malik, M. A.; Wieckowski, A. Electrocatalytic Properties of Conducting Polymer Based Composite Film Containing Dispersed Platinum Microparticles Towards Oxidation of Methanol. *Electrochim. Acta* **1999**, *44*, 2131–2137.
- Baetens, R.; Jelle, B. P.; Gustavsen, A. Properties, Requirements and Possibilities of Smart Windows for Dynamic Daylight and Solar Energy Control in Buildings: A State-of-the-Art Review. *Solar Energy Mater. Solar Cells* **2010**, *94*, 87–105.
- Anderson, M.; Mattes, B.; Reiss, H.; Kaner, R. Gas Separation Membranes: A Novel Application for Conducting Polymers. *Synth. Met.* **1991**, *41*, 1151–1154.
- Ramanavičius, A.; Ramanavičienė, A.; Malinauskas, A. Electrochemical Sensors Based on Conducting Polymer—Polypyrrole. *Electrochim. Acta* **2006**, *51*, 6025–6037.

- (10) Pages, H.; Topart, P.; Lemordant, D. Wide Band Electrochromic Displays Based on Thin Conducting Polymer Films. *Electrochim. Acta* **2001**, *46*, 2137–2143.
- (11) Xia, Y.; Ouyang, J. Salt-Induced Charge Screening and Significant Conductivity Enhancement of Conducting Poly (3, 4-Ethylenedioxythiophene): Poly (Styrenesulfonate). *Macromolecules* **2009**, *42*, 4141–4147.
- (12) Rammelt, U.; Nguyen, P.; Plieth, W. Corrosion Protection by Ultrathin Films of Conducting Polymers. *Electrochim. Acta* **2003**, *48*, 1257–1262.
- (13) Bartlett, P. N.; Archer, P.; Ling-Chung, S. K. Conducting Polymer Gas Sensors Part I: Fabrication and Characterization. *Sens. Actuators* **1989**, *19*, 125–140.
- (14) Bidan, G. Electroconducting Conjugated Polymers: New Sensitive Matrices to Build up Chemical or Electrochemical Sensors. A Review. *Sens. Actuators, B* **1992**, *6*, 45–56.
- (15) Janata, J.; Josowicz, M. Conducting Polymers in Electronic Chemical Sensors. *Nat. Mater.* **2003**, *2*, 19–24.
- (16) Bai, H.; Shi, G. Gas Sensors Based on Conducting Polymers. *Sensors* **2007**, *7*, 267–307.
- (17) Korotcenkov, G. Metal Oxides for Solid-State Gas Sensors: What Determines Our Choice? *Mater. Sci. Eng., B* **2007**, *139*, 1–23.
- (18) Bao, L.; Deng, L.; Nie, L.; Yao, S.; Wei, W. Determination of Microorganisms with a Quartz Crystal Microbalance Sensor. *Anal. Chim. Acta* **1996**, *319*, 97–101.
- (19) Grate, J. W. Acoustic Wave Microsensor Arrays for Vapor Sensing. *Chem. Rev.* **2000**, *100*, 2627–2648.
- (20) Natori, K. Ballistic Metal-Oxide-Semiconductor Field Effect Transistor. *J. Appl. Phys.* **1994**, *76*, 4879–4890.
- (21) Yagüe, J. L.; Borrós, S. Plasma Process. Polym. *5/2012. Plasma Process. Polym.* **2012**, *9*, n/a–n/a.
- (22) Albert, K. J.; Lewis, N. S.; Schauer, C. L.; Sotzing, G. A.; Stitzel, S. E.; Vaid, T. P.; Walt, D. R. Cross-Reactive Chem. Sens. Arrays. *Chem. Rev.* **2000**, *100*, 2595–2626.
- (23) Penza, M.; Cassano, G.; Aversa, P.; Antolini, F.; Cusano, A.; Cutolo, A.; Giordano, M.; Nicolais, L. Alcohol Detection Using Carbon Nanotubes Acoustic and Optical Sensors. *Appl. Phys. Lett.* **2004**, *85*, 2379.
- (24) Virji, S.; Huang, J.; Kaner, R. B.; Weiller, B. H. Polyaniline Nanofiber Gas Sensors: Examination of Response Mechanisms. *Nano Lett.* **2004**, *4*, 491–496.
- (25) Wanna, Y.; Srisukhumbowornchai, N.; Tuantranont, A.; Wisitorsaot, A.; Thavarungkul, N.; Singjai, P. The Effect of Carbon Nanotube Dispersion on CO Gas Sensing Characteristics of Polyaniline Gas Sensor. *J. Nanosci. Nanotechnol.* **2006**, *6*, 3893–3896.
- (26) Waghuley, S.; Yenorkar, S.; Yawale, S.; Yawale, S. Application of Chemically Synthesized Conducting Polymer-Polypyrrole as a Carbon Dioxide Gas Sensor. *Sens. Actuators, B* **2008**, *128*, 366–373.
- (27) Nicolas-Debarnot, D.; Poncin-Epaillard, F. Polyaniline as a New Sensitive Layer for Gas Sensors. *Anal. Chim. Acta* **2003**, *475*, 1–15.
- (28) Yan, X.; Han, Z.; Yang, Y.; Tay, B. NO₂ Gas Sensing with Polyaniline Nanofibers Synthesized by a Facile Aqueous/Organic Interfacial Polymerization. *Sens. Actuators, B* **2007**, *123*, 107–113.
- (29) Jun, H.-K.; Hoh, Y.-S.; Lee, B.-S.; Lee, S.-T.; Lim, J.-O.; Lee, D.-D.; Huh, J.-S. Electrical Properties of Polypyrrole Gas Sensors Fabricated under Various Pretreatment Conditions. *Sens. Actuators, B* **2003**, *96*, 576–581.
- (30) Jiang, L.; Jun, H.-K.; Hoh, Y.-S.; Lim, J.-O.; Lee, D.-D.; Huh, J.-S. Sensing Characteristics of Polypyrrole–Poly (Vinyl Alcohol) Methanol Sensors Prepared by in Situ Vapor State Polymerization. *Sens. Actuators, B* **2005**, *105*, 132–137.
- (31) Punning, A.; Kruusmaa, M.; Aabloo, A. A Self-Sensing Ion Conducting Polymer Metal Composite (IPMC) Actuator. *Sens. Actuators, A* **2007**, *136*, 656–664.
- (32) Zhu, S. S.; Carroll, P. J.; Swager, T. M. Conducting Polymetalloporphyrins: A Supramolecular Approach to Transition Metal Ion Sensors. *J. Am. Chem. Soc.* **1996**, *118*, 8713–8714.
- (33) Kukla, A.; Pavluchenko, A.; Shirshov, Y. M.; Konoshchuk, N.; Posudievsky, O. Y. Application of Sensor Arrays Based on Thin Films of Conducting Polymers for Chemical Recognition of Volatile Organic Solvents. *Sens. Actuators, B* **2009**, *135*, 541–551.
- (34) Pirsai, S.; Alizadeh, N. Design and Fabrication of Gas Sensor Based on Nanostructure Conductive Polypyrrole for Determination of Volatile Organic Solvents. *Sens. Actuators, B* **2010**, *147*, 461–466.
- (35) Rahman, M. M.; Ahammad, A.; Jin, J. H.; Ahn, S. J.; Lee, J. J. A Comprehensive Review of Glucose Biosensors Based on Nanostructured Metal-Oxides. *Sensors* **2010**, *10*, 4855–4886.
- (36) Athawale, A. A.; Kulkarni, M. V. Polyaniline and Its Substituted Derivatives as Sensor for Aliphatic Alcohols. *Sens. Actuators, B* **2000**, *67*, 173–177.
- (37) Ayad, M. M.; El-Hefnawey, G.; Torad, N. L. A Sensor of Alcohol Vapours Based on Thin Polyaniline Base Film and Quartz Crystal Microbalance. *J. Hazard. Mater.* **2009**, *168*, 85–88.
- (38) Selampinar, F.; Toppare, L.; Akbulut, U.; Yaşın, T.; Süzer, Ş. A Conducting Composite of Polypyrrole II. As a Gas Sensor. *Synth. Met.* **1995**, *68*, 109–116.
- (39) Bartlett, P. N.; Ling-Chung, S. K. Conducting Polymer Gas Sensors Part III: Results for Four Different Polymers and Five Different Vapours. *Sens. Actuators* **1989**, *20*, 287–292.
- (40) Liu, S.-S.; Bian, L.-J.; Luan, F.; Sun, M.-T.; Liu, X.-X. Theoretical Study on Polyaniline Gas Sensors: Examinations of Response Mechanism for Alcohol. *Synth. Met.* **2012**, *162*, 862–867.
- (41) Ullah, H.; Shah, A. A.; Bilal, S.; Ayub, K. DFT Study of Polyaniline NH₃, CO₂, and CO Gas Sensors: Comparison with Recent Experimental Data. *J. Phys. Chem. C* **2013**, *117*, 23701–23711.
- (42) Ullah, H.; Shah, A.-u.-H. A.; Bilal, S.; Ayub, K. Doping and Dedoping Processes of Polypyrrole: DFT Study with Hybrid Functionals. *J. Phys. Chem. C* **2014**, *118*, 17819–17830.
- (43) Blanc, J.; Derouiche, N.; El Hadri, A.; Germain, J.; Maleysson, C.; Robert, H. Study of the Action of Gases on a Polypyrrole Film. *Sens. Actuators, B* **1990**, *1*, 130–133.
- (44) Liu, D.; Aguilar-Hernandez, J.; Potje-Kamloth, K.; Liess, H. A New Carbon Monoxide Sensor Using a Polypyrrole Film Grown on an Interdigital-Capacitor Substrate. *Sens. Actuators, B* **1997**, *41*, 203–206.
- (45) Ratautaite, V.; Janssens, S. D.; Haenen, K.; Nesládek, M.; Ramanaviciene, A.; Baleviciute, I.; Ramanavicius, A. Molecularly Imprinted Polypyrrole Based Impedimetric Sensor for Theophylline Determination. *Electrochim. Acta* **2014**, *130*, 361–367.
- (46) Frisch, M. J. T. G. W.; Schlegel, H. B.; Scuseria, G. E.; Robb, M. A.; Cheeseman, J. R.; Scalmani, G.; Barone, V.; Mennucci, B.; Petersson, G. A.; et al. *Gaussian 09*, Rev. D. 0.1; Gaussian, Inc.: Wallingford, CT, 2013.
- (47) Dennington, R. D.; Keith, T. A.; Millam, J. M. *Gaussview 5.0*, 8. Gaussian Inc.: Wallingford, CT, 2008.
- (48) Allouche, A. R. Gabedit—a Graphical User Interface for Computational Chemistry Softwares. *J. Comput. Chem.* **2011**, *32*, 174–182.
- (49) Ullah, H.; Ayub, K.; Ullah, Z.; Hanif, M.; Nawaz, R.; Shah, A. A.; Bilal, S. Theoretical Insight of Polypyrrole Ammonia Gas Sensor. *Synth. Met.* **2013**, *172*, 14–20.
- (50) Ullah, H.; Shah, A. A.; Bilal, S.; Ayub, K. Dft Study of Polyaniline NH₃, CO₂, and CO Gas Sensors: Comparison with Recent Experimental Data. *J. Phys. Chem. C* **2013**, *117*, 23701–23711.
- (51) Ullah, H.; Shah, A. A.; Ayub, K.; Bilal, S. Density Functional Theory Study of Poly (O-Phenylenediamine) Oligomers. *J. Phys. Chem. C* **2013**, *117*, 4069–4078.
- (52) Becke, A. D. Density-Functional Exchange-Energy Approximation with Correct Asymptotic Behavior. *Phys. Rev. A* **1988**, *38*, 3098.
- (53) Alemán, C.; Ferreira, C. A.; Torras, J.; Meneguzzi, A.; Canales, M.; Rodrigues, M. A.; Casanovas, J. On the Molecular Properties of Polyaniline: A Comprehensive Theoretical Study. *Polymer* **2008**, *49*, 5169–5176.
- (54) Yanai, T.; Tew, D. P.; Handy, N. C. A New Hybrid Exchange–Correlation Functional Using the Coulomb-Attenuating Method (CAM-B3LYP). *Chem. Phys. Lett.* **2004**, *393*, 51–57.

(55) Blomquist, J.; Andersson, M. P.; Uvdal, P. Inducing H/D Exchange in Ultrathin Ice Films by Proton Deficiency. *Phys. Rev. Lett.* **2011**, *107*, 216101.

(56) Zade, S. S.; Bendikov, M. From Oligomers to Polymer: Convergence in the HOMO-LUMO Gaps of Conjugated Oligomers. *Org. Lett.* **2006**, *8*, 5243–5246.

[Article 10]

A. Ali Tahir, H. Ullah, P. Sudhagar, M. Asri Mat Teridi, A. Devadoss, S. Sundaram, "The application of graphene and its derivatives to energy conversion, storage, and environmental and biosensing devices." *The Chemical Record*. vol. 16, pp. 1591-1634, Jun. 2016.

The Application of Graphene and Its Derivatives to Energy Conversion, Storage, and Environmental and Biosensing Devices

Asif Ali Tahir,^[a] Habib Ullah,^[a] Pitchaimuthu Sudhagar,^[b] Mohd Asri Mat Teridi,^[c] Anitha Devadoss,^[d] and Senthilarasu Sundaram^{*,[a]}

ABSTRACT: Graphene (GR) and its derivatives are promising materials on the horizon of nanotechnology and material science and have attracted a tremendous amount of research interest in recent years. The unique atom-thick 2D structure with sp^2 hybridization and large specific surface area, high thermal conductivity, superior electron mobility, and chemical stability have made GR and its derivatives extremely attractive components for composite materials for solar energy conversion, energy storage, environmental purification, and biosensor applications. This review gives a brief introduction of GR's unique structure, band structure engineering, physical and chemical properties, and recent energy-related progress of GR-based materials in the fields of energy conversion (e.g., photocatalysis, photoelectrochemical water splitting, CO_2 reduction, dye-sensitized and organic solar cells, and photosensitizers in photovoltaic devices) and energy storage (batteries, fuel cells, and supercapacitors). The vast coverage of advancements in environmental applications of GR-based materials for photocatalytic degradation of organic pollutants, gas sensing, and removal of heavy-metal ions is presented. Additionally, the use of graphene composites in the biosensing field is discussed. We conclude the review with remarks on the challenges, prospects, and further development of GR-based materials in the exciting fields of energy, environment, and bioscience.

Keywords: energy conversion, energy storage, graphene, photocatalysis, sensors

1. Introduction

The main challenges for scientific and technological research into solar energy conversion, energy storage, and environment are the stability, durability, and performance of low-cost func-

tional materials. The discoveries of sp^2 -hybridized carbon nanomaterials such as buckminsterfullerene,^[1,2] carbon nanotubes,^[3] and graphene (GR)^[4] have revolutionized the research directions in the fields of physics, material science, chemistry,

^[a]A. Ali Tahir, H. Ullah, S. Sundaram
Environment and Sustainability Institute (ESI)
University of Exeter
Penryn Campus
Penryn
Cornwall TR10 9FE (UK)
E-mail: a.tahir@exeter.ac.uk
E-mail: hu203@exeter.ac.uk
E-mail: s.sundaram@exeter.ac.uk

^[b]P. Sudhagar
School of Chemistry and Chemical Engineering
Queen's University Belfast
David Keir Building
Belfast BT9 5AG (UK)
E-mail: S.Pitchaimuthu@qub.ac.uk

^[c]M. Asri Mat Teridi
Solar Energy Research Institute
National University of Malaysia
43600 Bangi
Selangor
(Malaysia)
E-mail: asri@ukm.edu.my

^[d]A. Devadoss
College of Engineering
Swansea University
Singleton Park
Swansea SA2 8PP (UK)
E-mail: anitha.devadoss@swansea.ac.uk

and life sciences.^[5] These carbon nanomaterials will continue to play a vital role in overcoming the major technological and practical challenges of material science. Among the carbon nanomaterials, GR is the most exciting material due to its monolayer structure composed of a network of six-membered rings.^[6] Considering its planar state, GR can be rolled into zero-dimensional spherical fullerenes, one-dimensional carbon nanotubes, or two-dimensional honeycomb structures, or stacked

into three-dimensional graphite.^[7] GR can be used as a basic building block for all carbon nanomaterials and in composites with other materials. GR has unique and stimulating properties, such as high theoretical surface area ($2630 \text{ m}^2 \text{ g}^{-1}$),^[8] high room-temperature charge carrier mobility ($\sim 100000 \text{ cm}^2 \text{ V}^{-1} \text{ s}^{-1}$),^[9] the highest electrical conductivity (10^6 S cm^{-1}), high thermal conductivity (~ 2000 to $5000 \text{ W m}^{-1} \text{ K}^{-1}$),^[10] and the capacity to support large electrical current density (10^8 A

Asif A. Tahir graduated from the Department of Inorganic Chemistry at Quaid-i-Azam University, Pakistan, in 2009. He worked as a research associate at Loughborough University for three years and then moved to the University of Liverpool before joining the College of Engineering, Mathematics and Physical Sciences (CEMPS) at the University of Exeter as a Lecturer in Renewable Energy. He specializes in the fabrication of nanomaterials using state-of-the-art techniques for solar energy conversion and photocatalysis. His research focus includes the design, synthesis, and characterization of new materials using soft chemistry approaches and the optimization of nanomaterials for high performance.



Habib Ullah obtained his M.Phil. in Physical Chemistry from the Institute of Chemical Sciences, University of Peshawar, Pakistan, in 2014. Currently, he is doing his Ph.D. in Renewable Energy at CEMPS, University of Exeter, under the supervision of Dr. Asif A. Tahir. His research involves the design of novel materials, i.e., conjugated organic polymers (graphene), inorganic metal oxides, and their composites, for sensors, solar cells, rechargeable batteries, light-emitting diodes, and corrosion inhibition applications.



Pitchaimuthu Sudhagar is currently working as a Research Fellow at the School of Chemistry and Chemical Engineering, Queen's University Belfast, UK. He was the recipient of a JSPS Post-Doctoral Fellow Award under the guidance of Prof. Akira Fujima at the Photocatalysis International Research Center, Tokyo University of Science, Japan, during 2013–2015. He received his Ph.D. degree (Physics) from Bharathiar University, India, and later moved to the Center for Next Generation Dye-Sensitized Solar Cells of Hanyang University, South Korea (2009–2013). He has published about 67 articles in peer-reviewed international journals and three book chapters. His research interest is to pioneer the creation of nanostructured electro-



des, semiconductor photoabsorbers, and electrocatalysts for high-efficiency solar cells and solar fuel cells.

Mohd Asri Mat Teridi received his Ph.D. on cathodic sensitization solar cells in 2012 from Loughborough University. He joined the Solar Energy Research Institute, National University of Malaysia, as a Junior Research Fellow/Lecturer in 2007. After he received his Ph.D., he was appointed as Research Fellow/Senior Lecturer at the same university in 2013. His recent research activity has focused on nanostructured metal oxides for solar water splitting, perovskite solar cells, polymer solar cells, and dye-sensitized solar cells.



Anitha Devadoss received her Ph.D. from Dublin City University in 2011 under the supervision of Prof. Robert J. Forster and Prof. Tia E. Keyes. She worked as a Brain-Korea-21 postdoctoral fellow at Hanyang University, South Korea, and later as a researcher at Tokyo University of Science, Japan. Currently, she works at Swansea University, UK, and her research focuses on developing various biosensors (electrochemical, ECL, and photoelectrochemical) and signal amplification strategies for highly sensitive and selective bioanalysis. She has published over 25 research articles.



Senthilarasu Sundaram graduated from Bharathiar University, Coimbatore, India, in 2006. Currently, he works at the University of Exeter, UK, and his research focuses on the development of nanostructured solar cells, especially dye-sensitized solar cells and perovskite thin-film solar cells through low-cost fabrication techniques. He is concentrating specifically on scale-up engineering challenges in novel solar cells, system-level integration, and spectral dependence analysis.



cm^{-2}).^[11] Thus, GR is a unique material for capacitors,^[12] batteries,^[13] and sensors.^[14] On the other hand, its high surface area, excellent transparency, light absorption, and charge transport properties have triggered huge interest from different research fields concerned with energy conversion and environmental pollution remediation, which are gaining traction in modern society.^[7,15] Along with energy conversion, storage, and photocatalysis of environmental pollution, GR also has a wide range of other applications in the fields of nanoelectronics, optoelectronics, chemical and biochemical sensing, polymer composites, intercalation materials, and drug delivery.^[16]

Certainly, the discovery of GR in 2004 has opened up enormous scientific opportunities. Recently, technologies for preparing GR, its derivatives, and GR-based nanomaterials/nanocomposites have grown rapidly because of more sophisticated fabrication methods. The versatile methods developed for the synthesis of GR and its derivatives include chemical vapor deposition (CVD) on metal surfaces; epitaxial growth on single-crystal SiC; micromechanical cleavage of graphite crystals; and “top-down” exfoliation of graphite by means of oxidation, intercalation, and/or sonication.^[17] The chemical oxidation of graphite to GR oxide (GO) and its subsequent reduction to reduced GR oxide (rGO) was considered as an effective method for preparing GR nanosheets because of its scalability, high yield, and low cost.^[18] The rGO possesses reactive groups, such as epoxide, hydroxyl, carbonyl, and carboxylic groups, allowing the development of functionalized GR-based materials.^[18] There is increased popularity in the use of GR, GO, and rGO in energy conversion (photoelectrochemical (PEC) water splitting, photocatalytic water splitting, and photovoltaic devices), energy storage (capacitors and batteries), and environmental applications (photocatalytic degradation of pollutants, gas sensors and heavy-metal removal). Therefore, it is necessary to compile a comprehensive review of the energy and environmental applications of GR and its derivatives.

The progress made in GR-based materials for energy and environmental applications has been discussed in several review articles with a focus on either specific materials or general preparation methods and functionalization.^[1,7,13,19] Recently, Zhang et al. have compiled a few excellent reviews highlighting the importance of GR as a template for composite photocatalyst synthesis and an excellent candidate for artificial photosynthesis.^[7,20] They also critically reviewed the entrepreneurial aspects of the commercialization of GR-based technologies.^[7] This article aims to give a relatively systematic update on the development and current research status of GR-based materials from the perspective of energy conversion, energy storage, and environmental purification. After a brief introduction of the structure and properties of GR, GO, and rGO, we will discuss the electron acceptor and transport properties of GR and its derivatives. Each section provides key challenges

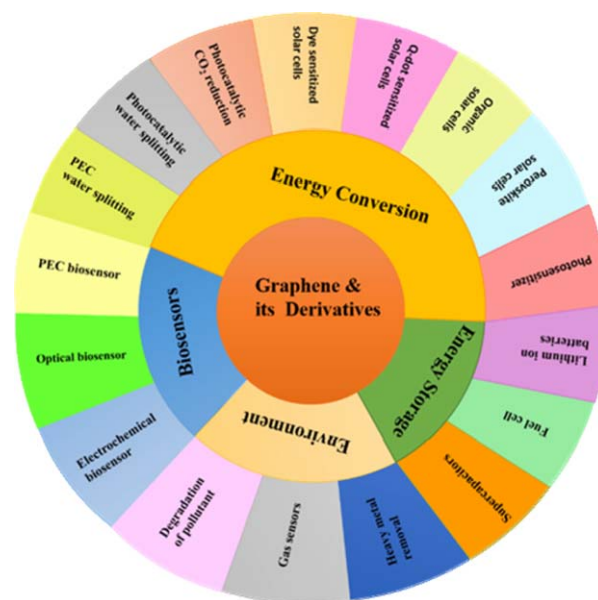


Fig. 1. Overview of GR-based materials in energy conversion, energy storage, environmental, and sensing applications.

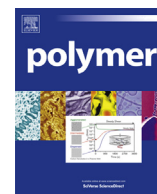
and requirements to enhance the performance of GR-based materials in photocatalysis and energy storage. Afterwards, we explore and summarize the recent progress of GR usage and its derivatives for PEC and photocatalytic water splitting and photocatalytic conversion for fuels, photovoltaics, and applications in supercapacitors, batteries, degradation of pollutants, heavy-metal removal, and so forth. The main applications of GR and its derivatives are summarized in Figure 1. In addition, key challenges encountered with GR-based materials, for their effective use in energy conversion, storage, and environmental applications, are discussed in the final section. This update promotes a more efficient and rational review of the structural and electronic properties of GR and a more efficient design of GR-based materials for solar energy conversion, energy storage, biosensors, and environmental applications.

1.1. Structure and Properties of Graphene

Carbon, which is a past, present, and future backbone of chemistry, regained popularity in the last decade and won the Nobel Prize for Physics in 2010.^[21] The different types of carbon produced at different stages and in different forms such as C^{12} , coal, and gasoline have been used in electrode technologies, lubricants, carbon-fiber-reinforced plastics, pencil lead, and nanotechnology. GR is a carbon-containing compound that has a two-dimensional stable geometrical structure containing delocalized π -conjugated systems. Generally, GR exists in different isotropic forms, three of which are depicted in Figure 2. The versatile applications of GR stem from its unique structure and highly anisotropic properties. Its characteristic

[Article 11]

M. Kamran, H. Ullah, A. S. Anwar-ul-Haq, S. Bilal, A. A. Tahir, K. Ayub,
"Combined experimental and theoretical study of poly (aniline-co-pyrrole)
oligomer." *Polymer*. vol. 72, pp. 30-39, Aug. 2015.



Combined experimental and theoretical study of poly(aniline-co-pyrrole) oligomer



Muhammad Kamran^a, Habib Ullah^{b,*}, Anwar-ul-Haq A. Shah^a, Salma Bilal^c,
Asif A. Tahir^b, Khurshid Ayub^d

^a Institute of Chemical Sciences, University of Peshawar, 25120 Peshawar, Pakistan

^b Environment and Sustainability Institute (ESI), University of Exeter, Penryn Campus, Penryn, Cornwall TR10 9FE, UK

^c National Centre of Excellence in Physical Chemistry, University of Peshawar, 25120 Peshawar, Pakistan

^d Department of Chemistry, COMSATS Institute of Information Technology, University Road, Tobe Camp, 22060 Abbottabad, Pakistan

ARTICLE INFO

Article history:

Received 24 March 2015

Received in revised form

5 June 2015

Accepted 2 July 2015

Available online 10 July 2015

Keywords:

DFT

Poly(Ani-co-Py)

PPy

PANI

Band gap

IR

UV–vis

IP

EA

HOMO–LUMO

ABSTRACT

Quantum mechanical calculations are performed to establish the structure of an oligomer of aniline and pyrrole [Poly(Ani-co-Py)], through comparison of experimental and theoretically calculated properties, including conductivity. The copolymer was synthesized through chemical oxidative polymerization and then confirmed from the experimental IR, UV–vis, mass spectra, elemental, XRD, TGA, and SEM analysis. Quantum mechanical calculations are performed at Density Functional Theory (DFT) and Time dependent DFT (TD-DFT) methods for the electronic and spectroscopic properties of the oligomer. A very nice correlation is found between the theory and experiment which consequences the structure of Poly(Ani-co-Py). Poly(Ani-co-Py) is not explored like other conducting polymers; however, by tuning this molecular structure, the electro-active nature of this material can be enhanced adequately.

© 2015 Elsevier Ltd. All rights reserved.

1. Introduction

Advanced functional macromolecules such as conjugated organic polymers (COPs) [1–3] are promising due to their wide range of technological applications in the area of rechargeable batteries [4], optoelectronic devices [5], light emitting diodes [6], photovoltaic, sensors [7], biosensors [6,8], electrochromic display material, electromagnetic shielding [9], artificial muscles, and solar cell. Among COPs; poly(*o*-phenylenediamine) (POPD) [9], poly(3,4-ethylenedioxythiophene) (PEDOT), polyparaphenylene (PPP), polyparaphenylenevinylene (PPV), polythiophene (PT), polypyrrole (PPy) [10], and polyaniline (PANI) have been studied both theoretically [11,12] and experimentally for efficient synthesis, characterization and applications [13–15]. Physical, electronic and

mechanical properties of the conducting polymers can be enhanced by doping, de-doping [12], nanotube additives, and copolymerization [16–18]. Poly(Ani-co-Py) double-walled nanotube arrays for electrochemical energy storage (high-performance supercapacitor) have been fabricated by Z. –L. Wang et al. [18]. Composites formation is another efficient way to tune the properties of COPs. Compared to pure COP, composites of COP with other materials such as metals are gaining attentions due to unique properties and applications. Blinova et al. [19,20], synthesized PANI-silver nanocomposites and reported higher conductivity of the nanocomposites as compared to pure PANI.

On the other hand, copolymerization is an efficient way to get some new unique properties which are non-existent for homo polymer [21–24]. Solanki et al. [24] has efficiently electro-polymerized Poly(Ani-co-Py)-immobilized cholesterol oxidase (ChOx) film (Poly(Ani-co-Py)/ChOx), and used as biosensor (bio-electrode) with sensitivity of 93.3 mA/mM. A remarkable increase of sensitivity in Poly(Ani-co-Py)/ChOx is observed compared to

* Corresponding author.

E-mail address: hu203@exeter.ac.uk (H. Ullah).

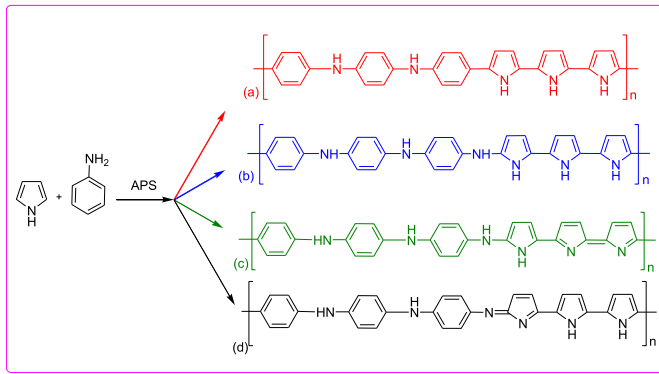


Fig. 1. Four proposed structures of Poly(Ani-co-Py).

their homo polymer-immobilized ChOx, i.e. PANI/ChOx (69.0 mA/mM) and PPy/ChOx (32.2 mA/mM). S. E. Mavundla et al. [25] has chemically synthesized Poly(Ani-co-Py) using ammonium persulfate (APS) and ferric chloride as oxidants. They reported the physicochemical and morphological properties of Poly(Ani-co-Py), with amorphous, disordered structure, and lower conductivity compared to their homo polymers of PANI and PPy. These authors had assigned the lower conductivity of Poly(Ani-co-Py) due to ineffective complex formation between PANI and PPy, induced by the use of APS as the oxidant. These authors has described the structural properties with different characterizations but did not mention the proper structure of Poly(Ani-co-Py). Poly(Ani-co-Py) is an interesting blend, consisting of 5 and 6 membered rings however, little attention has been paid toward its exact structure [21–24].

A few other reports on the copolymerization of PPy and PANI with certain limitations are also available (*vide supra*) [21–24,26], but its structure is not properly discussed. D. K. Moon et al. [22] has copolymerized pyrrole (Py) and aniline (Ani) and concluded that conductivity of the resulted species declined contrary to their individual homo polymers [27]. They had used different comonomers ratios of Py and Ani (1:9 ... 9:1) and found that the properties of co-polymer shifted to PPy at 9:1, 8:2, 7:3, and 6:4 ratio. Whereas, shift were observed towards PANI at 1:9, 2:8, 3:7,

4:6, 5:5 M ratios. Overall, their work was just a confirmation of the copolymerization, not the structure determination. Stejskal et al. [20] and Lim et al. [27] reported a copolymer of Poly(Ani-co-Py), and found a nonlinear trend in the conductivities of Poly(Ani-co-Py) samples, which were synthesized using HCl as dopants. They attributed the decrease in conductivity of the copolymer, with increase in Py, to the shortening effect of PANI chain through the copolymerization or heterodiads formation of Ani with Py rather than to forming Ani blocks. M. J. Antony et al. [28] did not observe any nonlinear behavior in their synthesized random copolymer therefore, rejected the heterodiad formation (Lim and Stejskal work) [20,21,27]. They described the unusual nonlinear conductivity behaviors in the copolymers materials to variation in the morphology, and difference in the three-dimensional solid-state ordering. Y. Zhu et al. [29] has successfully synthesized hollow Poly(Ani-co-Py)-Fe₃O₄ nanospheres via the oxidative polymerization of Ani and Py in the presence of a magnetic fluid. Their copolymer had interesting electromagnetic and super para-magnetic properties. Moreover, increase in conductivity were found with Fe₃O₄ contents. Among all these reports K. Moon et al. has proposed the molecular structure of Poly(Ani-co-Py) as shown in Fig. 1a. However, they were unsuccessful to support their structure from spectroscopic and other related analytical techniques. Taking into account these considerations (ambiguities), we set to synthesize a copolymer from Ani and Py in the presence of APS. The objectives of the current work is to: (I) confirm the copolymerization (II) determine decrease or increase in conductivity on copolymerization (III) validate the structure of the copolymer (if formed) through experimental and theoretical studies. DFT methods at B3LYP/6-31G (d) level of theory [30,31] is employed which gives fruitful results especially in the field of COPs [9,12,26,32–35].

2. Methodology

2.1. Experimental

Poly(Ani-co-Py) was synthesized from double distilled Ani and Py of analytical grade (Aldrich Sigma) by a well-known common oxidative polymerization method [36] at ambient temperature. We also attempted inverse emulsion (chemical) [27,37] and

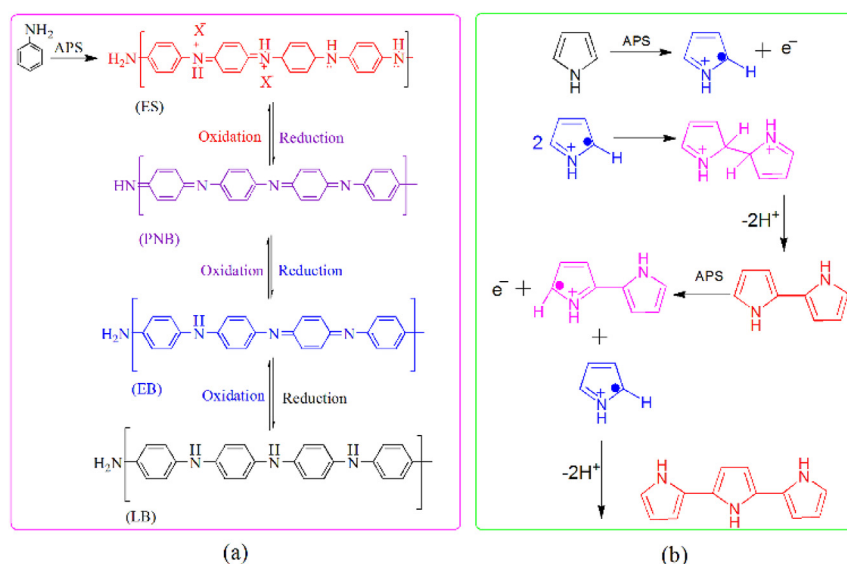


Fig. 2. Polymerization mechanism of ANI (a) and Py (b).

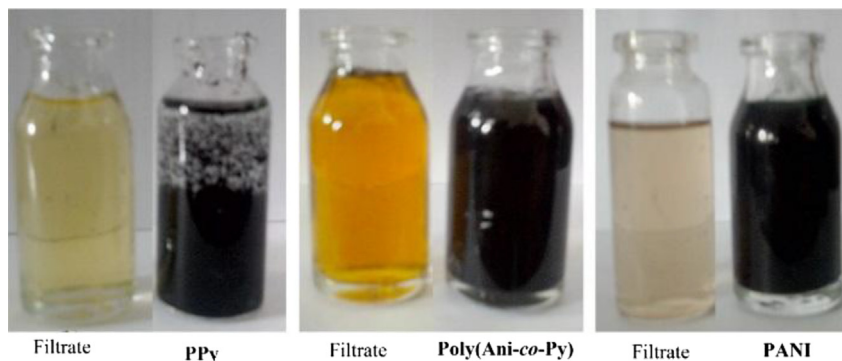


Fig. 3. Solubility of PPy, PANI, and Poly(Ani-co-Py) in NMP along with their corresponding filtrate.

electrochemical polymerization techniques but, found that chemical oxidative polymerization is much superior [38,39]. APS (analytical grade) and HCl(aq) (37% pure) were used as oxidizing agent and supporting electrolyte, respectively. In a typical procedure, 10 mL (0.1 M) of Ani(aq) and 10 mL (0.1 M) of Py(aq) solutions were mixed with stirring. After 20 min, 10 mL of HCl (0.1 M) solution (catalyst) were added and then after another hour, 10 mL of APS (0.1 M) were added. The reaction mixture was left to stir for 24 h. The mixture was filtered and washed with distilled water and then with acetone. The bluish-black precipitate was dried in an oven at 60 °C for two hours. In another optimization, the ratios of Ani, Py and HCl were kept constant however; different concentration of APS such as 0.5, 1, 1.5 and 2 M were employed. A Shimadzu UV–vis 1700 spectrophotometer was used to record the UV–vis spectra. The sample was dissolved in NMP and the spectra were recorded in spectral region ranging from 200 to 800 nm. Elemental analysis was performed in Pakistan Council of Scientific and Industrial Research (PCSIR) Laboratory Peshawar, Pakistan, using Elementar CHNS-O elemental analyzer Germany. IR spectra were measured as KBr pellets, using Perkin Elmer spectrophotometer series 400 IR, in the region from 400 to 4000 cm^{-1} with a resolution of 4 cm^{-1} . The spectra were collected in ATR mode with 10 numbers of scans for all samples. The experimental band gap of the powder sample of Poly(Ani-co-Py) was measured in the range of 200–1000 nm, using Perkin Elmer spectrophotometer Lambda-1050.

2.2. Computational methods

All DFT calculations were carried out on GAUSSIAN 09 [33] and the results were visualized through Gabedit [40] and GaussView [41]. DFT and time depended DFT (TD-DFT) calculations were performed to determine the approximate structure of Poly(Ani-co-Py) and its conductivity. We have shown in our previous reports that oligomers up to five or six repeating units can accurately represent the polymeric characteristics [9–12]. Geometries of type **a**, **b**, **c** and **d** (Fig. 1) of Poly(Ani-co-Py) were considered for calculations. Optimizations of these oligomers were confirmed from frequency calculation. Some of the calculated properties such as ionization potential (I.P), electron affinity (E.A), HOMO, LUMO, and band gap of all these three types (see Fig. 1) of Poly(Ani-co-Py) were simulated. IR spectra were simulated and scaled with a common scaling factor of 0.9613. The UV–vis spectra and natural bond orbitals (NBO), Mulliken charge analyses were simulated at TD-DFT-B3LYP/6-31G (d) and DFT-B3LYP/6-31G (d) level of theories, respectively. All calculations were performed in the gas phase, except UV–vis spectra which is

simulated in CHCl_3 medium, using polarized continuum model (PCM).

3. Results and discussion

3.1. Synthesis of PANI and PPy

There are three different fundamental oxidation states of PANI; Leucoemeraldine (LB), Emeraldine Base (EB), and Pernigraniline Base (PNB). The EB form of PANI can be converted into a conducting state upon protonation, emeraldine salt (ES). Synthesis of all these states by chemical oxidative polymerization method is shown in Fig. 2a. Neutral PANIs have the general formula $[(-\text{B}-\text{NH}-\text{B}-\text{NH}-)\text{y}(-\text{B}-\text{N}=\text{Q}=\text{N}-)\text{1-y}]_x$, where B and Q represent benzenoid and quinoid units, respectively. In this formula, y is the oxidation number and can be varied from 1, 0.5 and 0; from reduced to the fully oxidized one. PANI was synthesized with a common oxidative polymerization technique, although various reports are available on its chemical synthesis [36,42–45]. Similarly, PPy typical polymerization mechanism is depicted in Fig. 2b. These both homopolymers are synthesized, compared with the well-known reported work for the validation of our experimental procedure. We found an excellent correlation among our and reported work [36,42–45].

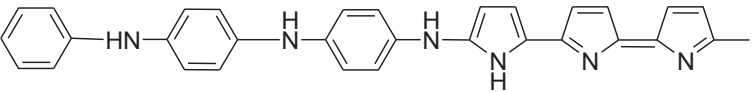
3.2. Synthesis of Poly(Ani-co-Py)

Before the synthesis of copolymer, we synthesized homopolymers; PANI and PPy according to the literature methods [36,42–45]. The characteristics of the homo polymers were correlated with the reported work which validated our protocol. Experimental results and discussion in the subsequent discussions is limited to the copolymer. The synthesized Poly(Ani-co-Py) color is compared with their homo polymers analogs. Synthesized PANI is soluble in N-methyl-2-pyrrolidone (NMP), and blue in color (EB form). On the other hand, PPy is partially soluble in NMP (see Fig. 3) but completely soluble in m-cresol and dark black in color. Copolymer, Poly(Ani-co-Py) is completely soluble in NMP and has black color with light orange (in the web version) filtrate (see Fig. 3), where these three polymers are given along with their corresponding filtrates.

Table 1
Elemental analysis of Poly(Ani-co-Py).

Sample	Oxi/Mon	% Yield	% C	% H	% N	C/N ratio
Poly(Ani-co-Py)	1	74.2	66.75	5.25	23.87	2.79

Table 2
Proposed structure of Poly(Ani-co-Py) based on mass spectral result.

Peak position	Proposed structure
468.3	

3.3. Elemental analysis

Elemental analysis of Poly(Ani-co-Py) is listed in Table 1, percentages of C, H and N are 66.75, 5.25 and 23.87, respectively. A comparison of the theoretical and observed values demonstrates that hydrogen and oxygen are in more percentage than expectation, which may be attributed to moisture or incomplete combustion. The C/N ratio of the sample is close to 3. Given the close resemblance of structures **a-d** and the associated uncertainties in the experimental results, it is pointed out that the elemental analysis would not play a significant role in the identification of structure (Table 2).

3.4. Mass spectral analyses

The mass spectrum provides vital information in assigning the structure of a compound. The structures **a-d** (shown in Fig. 1) can be distinguished from the fragmentation pattern. The HR-ESI-MS spectrum of poly(Ani-co-Py) is shown in Fig. 4. The spectra indicate that the peak at highest m/z for Poly(Ani-co-Py) product is

467.3, which is one unit lower than the theoretically calculated molecular mass (m/z 468 for type **c** and **d**) of a 3:3 oligomer of aniline and pyrrole (3:3: ANI:Py). For a 3:3 oligomer, the molecular mass should be an even number (Nitrogen rule). Therefore, the peak at ca. $m/z = 467.3$ is assigned to the M-1 fragment of 3:3 oligomer of ANI and Py (molecular formula $C_{30}H_{24}N_6$). A prominent peak at M-1 in the mass spectrum is common for the molecules containing acidic protons. The structures **a** and **b** have two hydrogens more than the structure **c** and **d**, and therefore, expected to have the highest m/z at 470. The lack of peak at m/z 470 probably eliminates the possibility of structures **a** and **b**. The structures **c** and **d** are the oxidized forms of **b** (dehydrogenation). Therefore, mass fragmentation pattern has been evaluated to determine the position of oxidation in order to differentiate between **c** and **d**. The mass spectrum of Poly(Ani-co-Py) consisted of several peaks, as shown in Fig. 4. The mass fragmentation patterns of type **c** and **d** are shown in Fig. 5. Structures **c** and **d** are expected to differ in the fragmentation of pyrrole part of the oligomer. Type **c** is expected to have a peak at m/z 440 whereas the type **d** is expected to have a peak at m/z 439. Analysis of the spectra indicate

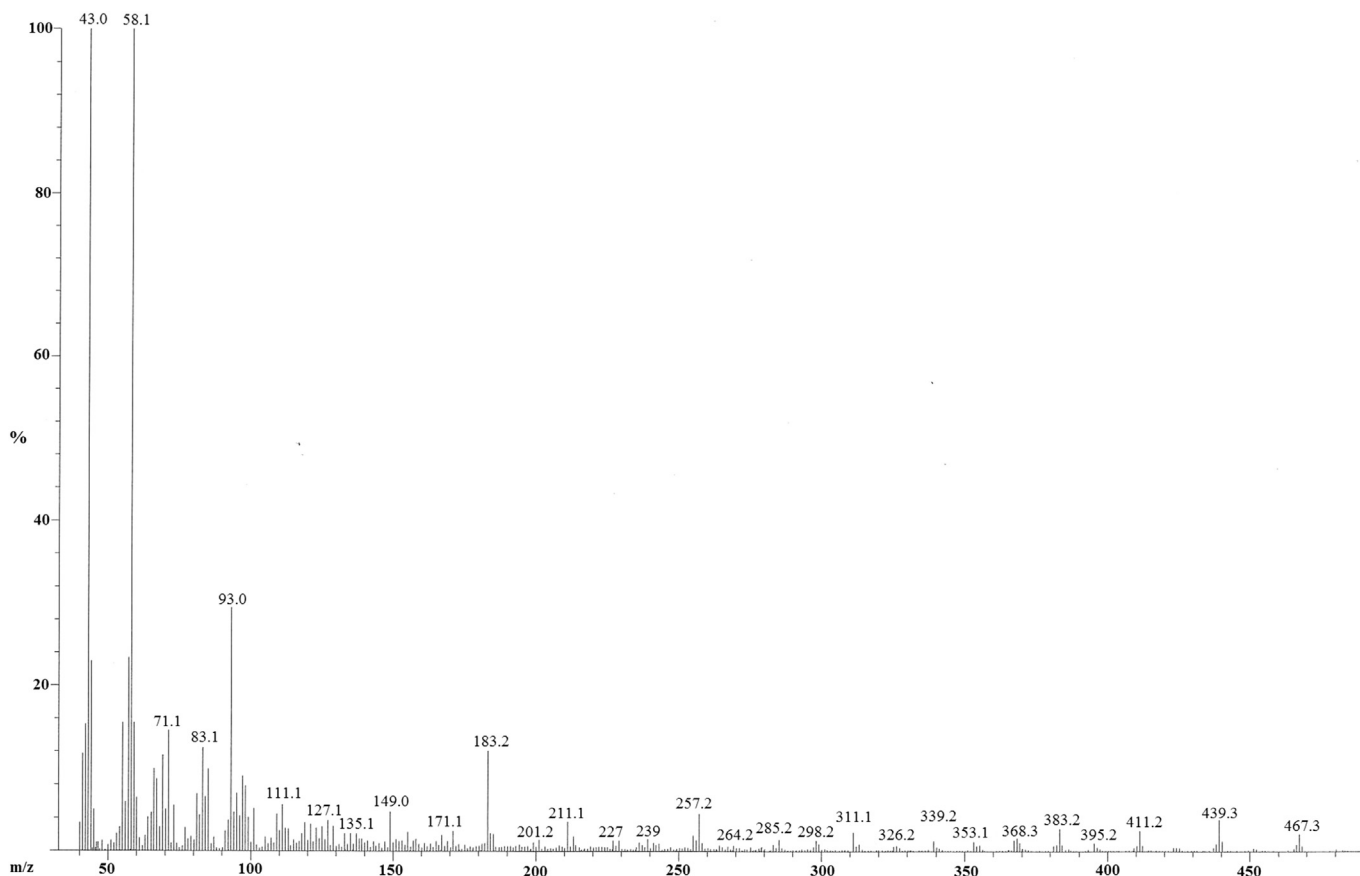


Fig. 4. Mass spectrum of Poly(Ani-co-Py).

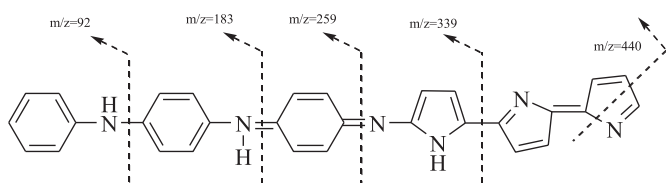


Fig. 5. Mass fragmentation of Poly(Ani-co-Py) from M–1 ion peak at m/z 467.3.

that the peaks are present at m/z 439 and 440 therefore, no conclusive remarks can be made from the analysis of these peaks. However, type **c** is expected to have a peak at m/z 339 compared to 337 or 338 (depending on the position of hydrogen loss for M–1 ion) for type **d**. Indeed, a peak at m/z 339 is observed in the spectrogram whereas no peaks were observed at m/z 337 and 338. The peak at m/z 339 is very helpful in deciding the position of oxidation. For any other position of oxidation, a peak at m/z 339 is not logical. The connectivity of three aniline rings can be rationalized by peaks at m/z 92 (Ph-NH), 183 (Ph-NH-Ph-NH) and 259 (Ph-NH-Ph-NH-Ph-). We believe that the M–1 peak was observed due to loss of proton from the NH next to pyrrole fragment because the fragment (Ph-NH-Ph-NH-Ph-NH) could not be located. So, this spectrogram and elemental analysis suggest that the sample has an oligomeric structure, consisting of 3ANI and

3Py rings. The mass spectral analysis suggests that the structure is probably **c**.

3.5. Optimized geometric structure

Geometries optimization of structures “**a**”, “**b**”, “**c**” and “**d**” of Poly(Ani-co-Py) were carried out at DFT method with B3LYP/6-31G (d) level of theory. The optimized geometric structures of types **a**, **b**, **c** and **d** of Poly(Ani-co-Py) are shown in Fig. 6. Since the mass spectrum analysis suggest that the structure of the oligomer is more likely “**c**”. The optimized geometry of type **c** is not planar but bent at one end. We discussed earlier that a planer structure of polymers provides an easy pathway for the movement of delocalized π -electron along its backbone. The oligomer in type “**c**” is not completely planar; therefore, delocalization of the π -electrons over the polymer backbone would be reduced. It would be expected to have less conductivity compared to homo polymers of aniline or pyrrole. These observations are consistent with the reported literature; Poly(Ani-co-Py) bears low conductivity contrast to their individual homo polymers [19,20,28]. We have also analyzed the geometries of type **d**. The optimized geometry of **d** is also bent. Both structures **c** and **d** are less bent compared to structure **b**. The structure **b** is bent much from planarity and it leads to very low conductivity (*vide infra*). Moreover, the structure **b** is also not

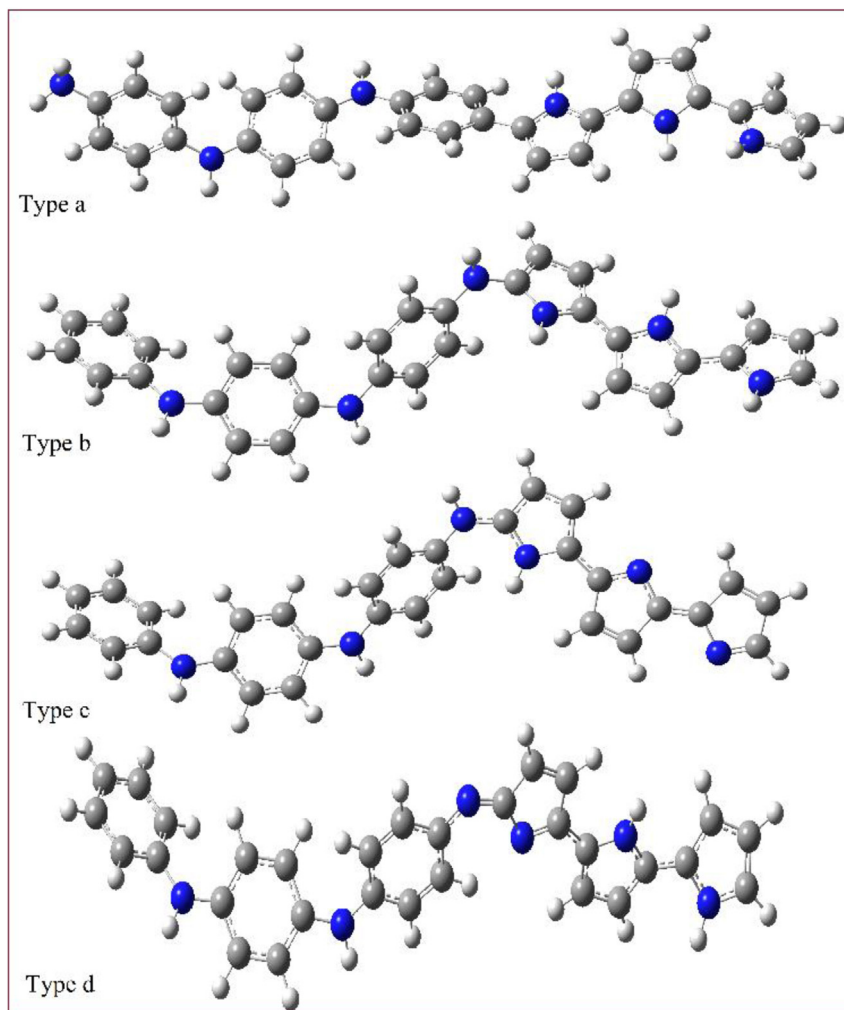


Fig. 6. Optimized geometric structures of type **a–d**.

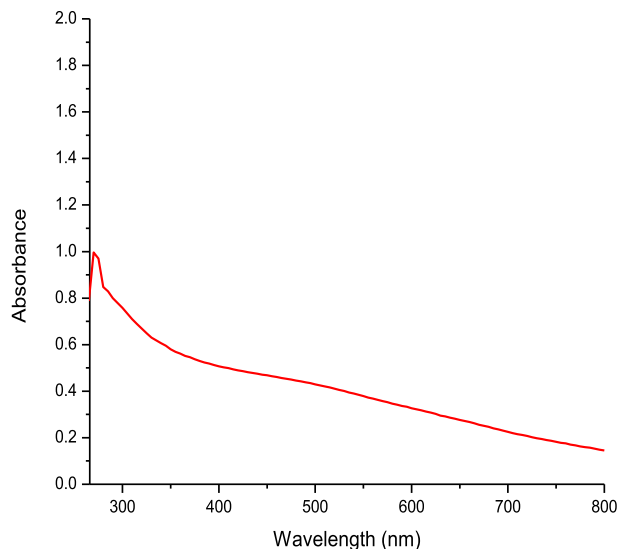


Fig. 7. UV–vis spectrum of Poly(Ani-co-Py).

supported by mass spectral analysis while type **a** has linear geometric structure.

3.6. UV–vis spectral characteristics

The experimental UV–vis spectrum of Poly(Ani-co-Py) is shown in Fig. 7, whereas the simulated ones (type **a**, **b**, **c** and **d**) are depicted in Fig. 8. The experimental UV–vis spectrum of Poly(Ani-co-Py) show uniform absorption throughout the whole visible region and gives a broad peak in the UV region ca. 520 nm. Our experimental UV–vis spectrum are also in close agreement with recently reported work [21–24]. This single maximum absorption band peak is due to the transition of valance electron to the conduction band. This absorption band peak is correlated with the λ_{\max} of type **a**, **b**, **c** and **d** which are listed in Table 3.

The TD-DFT simulated UV–vis spectrum of type **c** shows two peaks ca at of 574 (λ_{\max}) and 337 nm. The simulated UV–vis spectrum of type **d** also shows two absorption transitions at 631 and 321 nm. The maximum absorption peak (631 nm) is due to $\pi \rightarrow \pi^*$. Although the experimental UV–vis spectrum show a single broad peak in the region of 500–600 nm (specifically at 520 nm) but the diffuse nature of the peaks shows close resemblance to type **c**, where peak of low oscillator strength (574 nm, λ_{\max}) is simulated. It may be argued that two peaks may be present but their low molar

Table 3
Experimental and simulated UV–vis absorption bands of 6Poly(Ani-co-Py).

Simulated UV–vis of PPy	Absorption		Assignment
	Calculated	Experimental	
Type a	387 nm (2.10)		$S_0 \rightarrow S_1$
Type b	342 nm (1.40)		$S_0 \rightarrow S_1$
Type c	574 nm (0.56)	520 nm	$S_0 \rightarrow S_1$
Type d	631 nm (1.46)		$S_0 \rightarrow S_1$

absorptivity might have resulted in the overall appearance of a single peak. The types **a** and **b** give maximum excitation energies at 387 and 3342 nm, respectively. Excitations energies of the type **a**, **b**, **c** and **d** of Poly(Ani-co-Py) along with their oscillator strengths and transitions states are shown in Table 3.

The observed 520 nm (λ_{\max}) of the UV–vis spectrum can be easily correlated with the first allowed optical electronic excitation of type **c**, ca. at 574 nm, containing disturbed conjugation with spiral symmetry (*vide infra*). The experimental UV–vis spectra has nice correlation with that of type **c**, besides of having 50 nm difference. On the basis of this similar assignments and band peak position, we can easily conclude that the structure of the synthesized sample is just like type **c** (6Poly(Ani-co-Py), not **a**, **b** and **d**). Besides time dependent simulation, molecular orbital simulation and their different excitation transitions correlate nicely between the experiment and theory (especially in our case, see “Electronic Properties” section below).

3.7. Electronic properties

Electronic properties such as HOMO, LUMO, IP, EA, and band gap of type **a**, **b**, **c** and **d** of Poly(Ani-co-Py) are simulated at B3LYP/6-31G (d) level of theory. Negative of HOMO and LUMO are taken as IP and EA, respectively using Koopman’s theorem. Contours of HOMO and LUMO are depicted in Fig. 9. The experimental band gap (indirect band gap) was measured from the synthesized powder of Poly(Ani-co-Py), which is 2.40 eV and is given in Fig. 10. The experimental band gap is also correlated to the calculated band gaps of type **a**, **b**, **c** and **d** of Poly(Ani-co-Py), (see Table 4).

Electronic properties are simulated to account for the conductivity of Poly(Ani-co-Py), compared to homo polymers. The conductivity issue is extensively explained in the introduction, where J. Stejskal et al. reported a low conducting nature of the resulted copolymer [Poly(Ani-co-Py)]. The simulated band gaps are correlated with the experimental band gap, obtained from the powder sample of Poly(Ani-co-Py). The estimated band gaps of type **a**, **b**, **c**

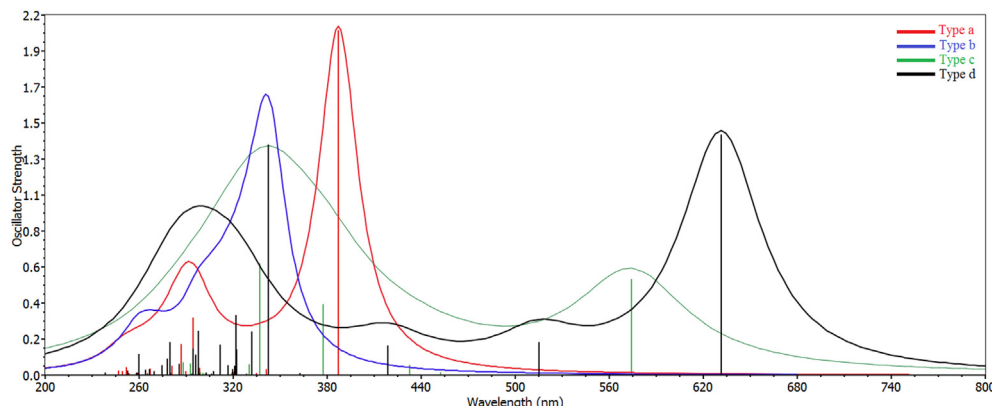


Fig. 8. Simulated UV–Vis spectra of type a-d of 6Poly(Ani-co-Py).

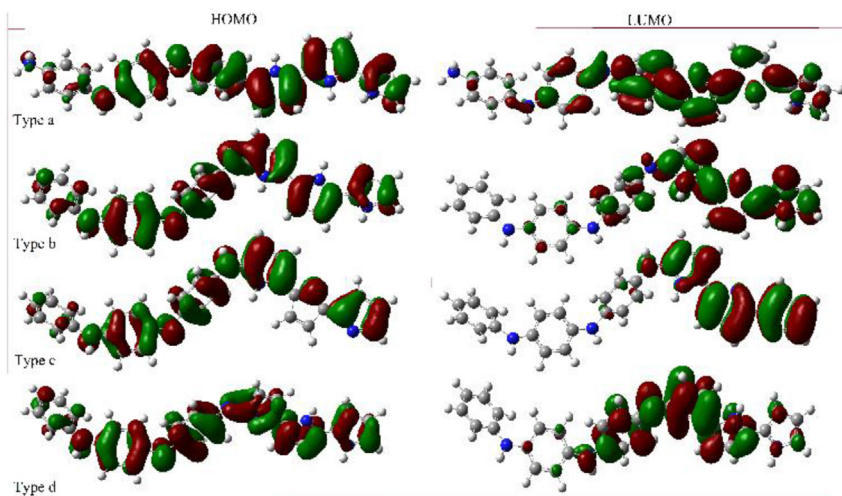


Fig. 9. HOMO and LUMO of type a-d of 6Poly(Ani-co-Py).

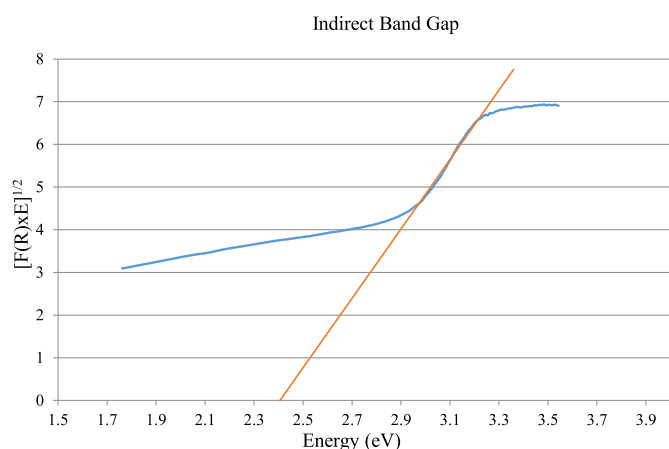


Fig. 10. Experimental Band gap of Poly(Ani-co-Py).

and **d** are listed in Table 4 which has 3.67, 4.10, 2.09 and 2.30 eV band gap, respectively. The band gap for type **c** can be correlated to the observed band gap of 2.40 eV. Although, this value is close to the simulated type **d**, but the UV–vis spectral analysis cannot be ignored as well (*vide supra*). The I.P and E.A of type **c** are 4.63 and 2.54 eV, which give rise to band gap of 2.09 eV. We have also evaluated the electronic nature of type **a** and **b**, but these structures are not supported by mass spectral analysis. Type **b** is less conducting than type **c** and **d**. Type **a** provides a relatively easy way for the delocalization of π -electron, whereas in **b**, this electronic cloud density is concentrated at one side.

3.8. Vibrational spectral characteristics of Poly(Ani-co-Py)

Simulated IR spectra of type **a**, **b**, **c** and **d** of Poly(Ani-co-Py) are given in Fig. 11, whereas a comparison of the observed and

Table 4
IP, EA, and band gap (both theoretical and experimental) in eV of type **a–d**.

Type	IP	EA	Band gap	Exp band gap
a	4.11	0.44	3.67	
b	4.30	0.20	4.10	
c	4.63	2.54	2.09	2.40
d	4.53	2.23	2.30	

simulated type **c** is shown in Fig. 12. The experimental IR spectrum of Poly(Ani-co-Py) reveals peaks ca. at 3296, 3052, 2934, 2364–2327, 1491, 1247, 1180, 1091, 981, 840, and 755 cm^{-1} . On the other hand, the simulated IR spectra of type **a**, **b**, **c** and **d** consist of 19 prominent band peaks. The experimental and calculated scaled

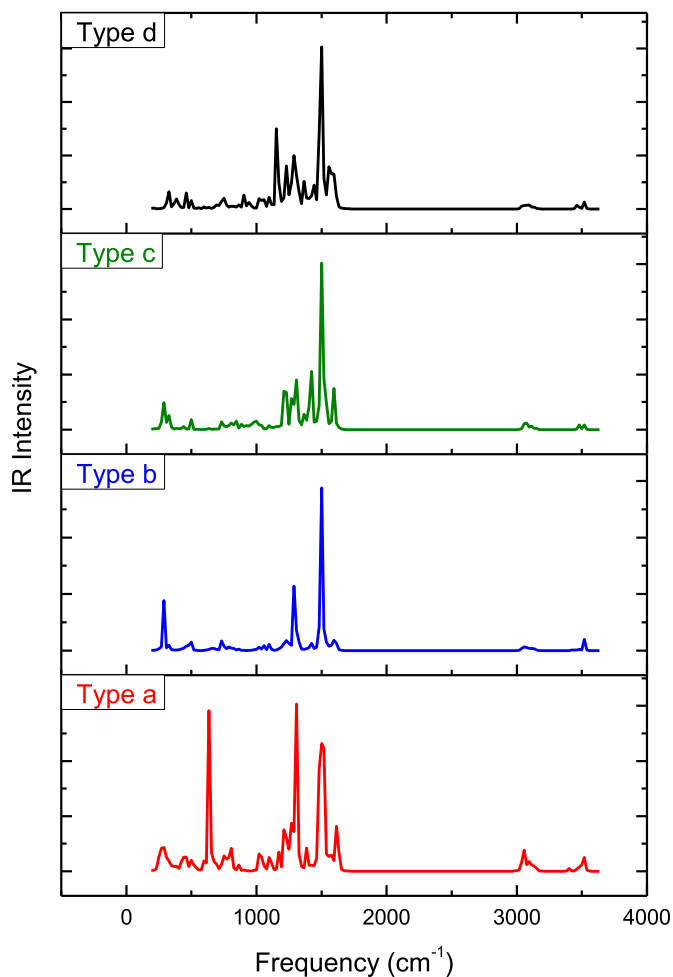


Fig. 11. Simulated IR spectra of type **a–d**.

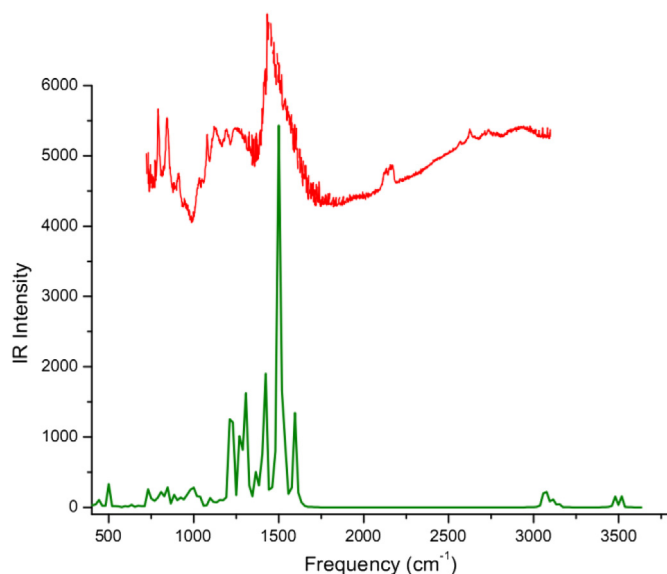


Fig. 12. Experimental (red) and theoretical (green) IR spectra (type c) of Poly(Ani-co-Py). (For interpretation of the references to colour in this figure legend, the reader is referred to the web version of this article.)

IR peaks (type **a**, **b**, **c** and **d**) of Poly(Ani-co-Py), along with their approximate assignments are listed in Table 5. The simulated and observed NH stretching has little difference, as the theoretical data is for an isolated oligomer in the vacuum state while the experimental is that of condensed phase. Two NH bands are simulated for the type **a**, **b**, **c** and **d** whereas only one broad peak is observed experimentally which probably encompasses both peaks. The band peak due to N–H stretching of Py ring is simulated at ca. 3512 (type **a**), 3516 (type **b**), 3517 cm^{-1} (type **c**) and 3521 cm^{-1} (type **d**) in 6Poly(Ani-co-Py). The observed peak at ca. 3296 cm^{-1} is also because of N–H stretching of the aromatic amines. This peak (3296 cm^{-1}) has 176, 134, 189 and 168 cm^{-1} differences to that of the type **a**, **b**, **c** and **d**, respectively. The peaks at ca. 2934–2852 cm^{-1} in the experimental IR spectrum have C–H stretching vibrations of the aromatic ANI rings. The functional group region of the infrared spectrum is not very helpful in differentiating among different

types (**a–d**), more particularly between type **c** and **d**, mainly because of the presence of the similar functional groups. The fingerprint region is more helpful in assigning the structure of the oligomer. The most prominent and broad band peak in the observed spectrum of Poly(Ani-co-Py) is at ca. 1491 cm^{-1} which may be attributed to C=C and C–N stretching of both the Py and ANI rings. Band peak at ca. 1247 cm^{-1} of the experimental IR spectrum is a combination of C=C, C–N stretching and C–H wagging. This band peak has good correlation with the calculated 1293 cm^{-1} of type “**c**” compared to 1313 cm^{-1} for type “**d**” (see Table 5). The observed band peak at 1180 cm^{-1} has theoretical counterpart peak in type “**c**” at ca. at 1218 cm^{-1} , and it shows better correlation with the experiment. The observed peak at 1180 cm^{-1} is assigned to C–N stretching and N–H, C–H wagging. Although the peak for type **d** appears at 1177 cm^{-1} but it is lower than the experimental peaks. The simulated values are, on the average, higher than the experimental values. Another observed peak at ca. 1090 cm^{-1} is assigned to the in-plane bending vibration of C–H and N–H bond. The next prominent experimental band peak in the fingerprint region is situated at 840 cm^{-1} on the basis of similar assignment (C–H and NH out of plane bending) it has good correlation with the calculated 846 cm^{-1} for type “**c**” than 908 cm^{-1} for type **d** (see Table 5). The last observable peak of the chemically synthesized Poly(Ani-co-Py) is at 754 cm^{-1} which is attributed to out of plane of C–H and N–H bond of the Py rings. This band peak is also in close agreement with the simulated ones for type **c** (756 cm^{-1}) than type **d** (752 cm^{-1}). Moreover, not only the peaks in the simulated spectrum of type **c** show better correlation with the experimental IR spectrum, but also the shape of the peaks in the fingerprint region correlate nicely (particularly the peaks around 1200 cm^{-1}). Comparative discussion of the data of Table 5 gives more inclination towards type **c** compared to type **d**. This is consistent with the above characterization.

3.9. X-ray diffraction analysis

The X-ray diffraction pattern of the PANI, PPy, and Poly(Ani-co-Py) are given in Fig. 13a–c, while a comparative (smoothed) XRD plot of all these species given in Fig. 13d. It is widely explored in the literature that both PANI and PPy has amorphous nature [46,47]. PANI gives a broad peak at 2θ of 25.30 which corresponds

Table 5
Experimental and calculated frequencies (in cm^{-1}) of Type **a**, **b**, **c** and **d**.

S. no	Exp I.R	Calculated frequency				Approximate assignment
		Type a	Type b	Type c	Type d	
1		3512	3516	3517	3521	v N–H (Py ring)
2	3296	3472	3430	3485	3464	v N–H (Bridging NH)
3	3052	3121	3083	3115	3125	v C–H (Py ring) (Asym)
4	2934	3050	3045	3084	3086	v C–H (Ani ring) (Asym)
5				3060		v C=C; Wag C–H, H–N
6		1605	1600	1594	1565	v C=C; Wag C–H, H–N
7	1491	1508	1498	1506	1502	v C=C, C–N; Wag C–H, H–N
8		1305	1417	1409	1447	v C–N, C=C; Wag C–H
9	1247	1291	1286	1293	1313	v C=C, C–N; Wag C–H
10		1224	1236		1283	v C–N; Wag N–H, C–H
11	1180	1213	1201	1218	1177	v C–N; Wag N–H, C–H
12		1173		1032	1153	Cis C–H (Ani rings)
13	1090	1098	1094	1004	1098	Cis C–H, N–H (Py rings)
14	981	1044	992		1032	v C–N; Wag C–H, N–H (Py ring)
15	840	795	801	846	908	γ C–H, N–H; for type c Def (ring)
16	754	741	739	756	752	γ C–H, N–H (Py rings)
17		634			560	γ N–H (NH ₂)
18		598	500	497	500	Def (ring); γ C–H (Ani ring)
19		487			460	γ N–H (Py ring)

Note: v: stretching; Wag: Wagging; cis: scissoring; β : bending; Def: deformation mod; γ : Out of plane bending.

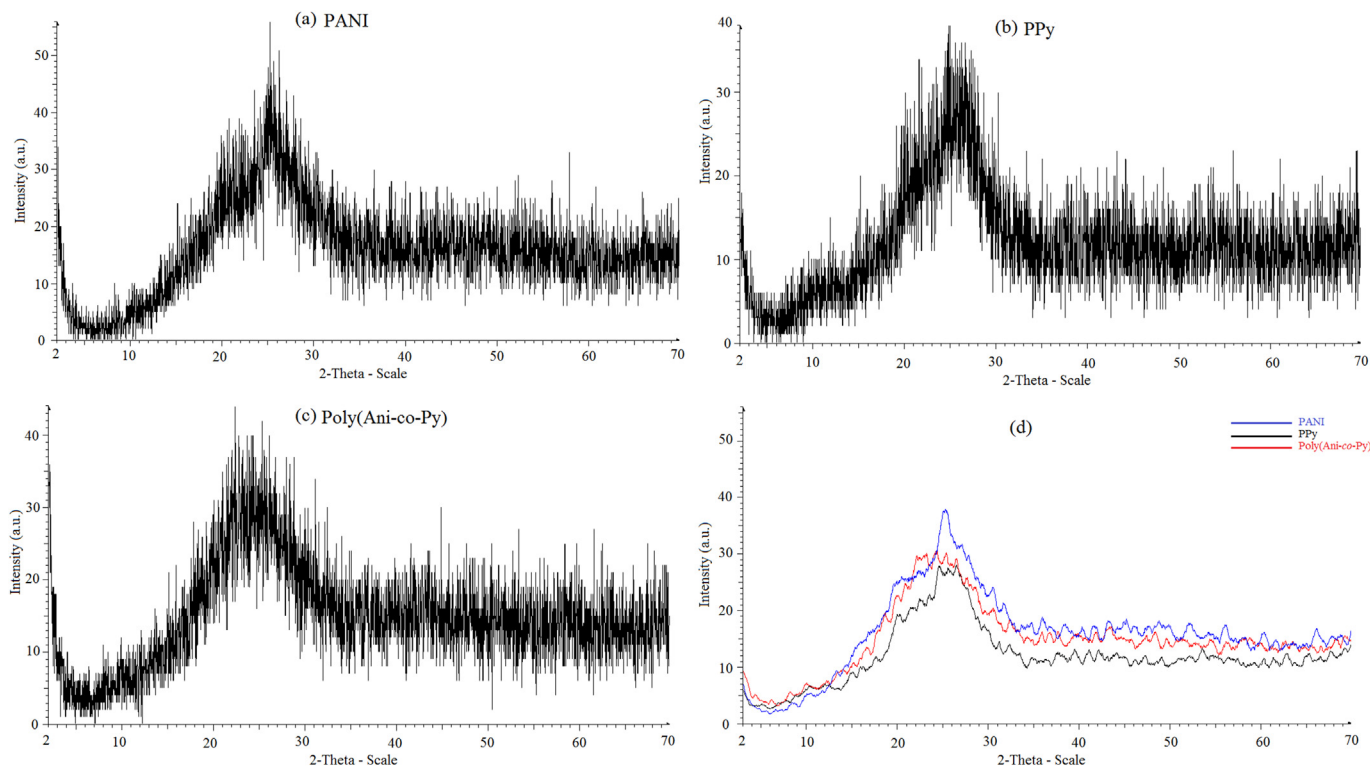


Fig. 13. XRD graph of PANI, PPy and Poly(Ani-co-Py).

to (110) plane of PANI as can be clearly seen from Fig. 13a. Furthermore, this broad peak indicates the amorphous nature of PANI with little amount of crystallinity [47]. On the other hand XRD spectra of PPy powders (Fig. 13b) confirm its complete amorphous nature, without any sharp peak and broad peak ca at $2\theta = 25^\circ$ [46]. The broad peaks are characteristic of amorphous PPy and are due to the scattering from PPy chains at the inter-planar spacing.

XRD spectra of Poly(Ani-co-Py) has also a broad peak (see Fig. 13c) which is located at $2\theta = 25^\circ$. Poly(Ani-co-Py) has much broader peak compared to their counterpart PANI and PPy oligomers. So, comparative analysis of the XRD spectra led us to conclude that Poly(Ani-co-Py) has high amorphous nature (lower crystallinity) which would be responsible for lower conducting nature as well.

3.10. Thermogravimetric analysis

The thermal stability of Poly(Ani-co-Py) was studied through thermogravimetric analysis (shown in Fig. 14) where 8 mg sample was used. The maximum weight loss was observed from 500 to 650 °C in which 42.5% of sample were lost. For convenience, the weight loss of the sample is divided into three steps, weight loss occurs from 0 to 100 °C, this weight loss is about 8.75% which is due to the loss of water of hydration. This number is consisted with % value of the elemental analysis. In the second step, weight loss occurs from 100 to 200 °C corresponding to the presence of trace amount of oligomers (both of ANI and Py) and may be some doped ion of the supporting electrolyte. From 200 to 300 °C, 10% weight of the sample is lost whereas it is about 12.5% at a temperature range of 300–400 °C. The weight loss further increases from 400 to 500 °C which is 26.25% of the total sample. In the third step which start from 500 up to 650 °C, where continuous loss of mass occurred and stopped at 650 °C, at which the copolymer is

completely dissociated. The TGA analysis led us to conclude that our copolymer has good stability up to 650 °C.

3.11. Morphological study

The scanning electron micrograph (SEM) of Poly(Ani-co-Py) at two different megapixels (2000 and 10,000) is depicted in Fig. 15. Our SEM results of Poly(Ani-co-Py) are in line with the recently reported work of J. Stejskal, P. Xu, J. Wilson, and co-workers [21–24,46]. The different particle size can be distinguished into three categories, very big, average, and small as shown in Table S1

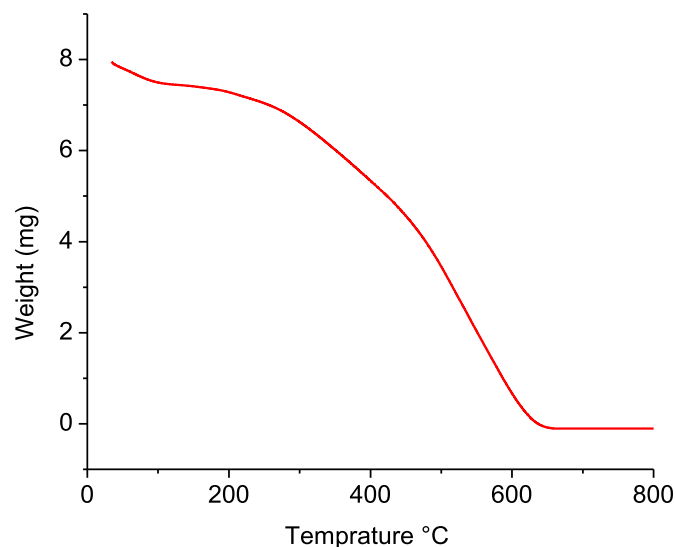


Fig. 14. TGA graph of Poly(Ani-co-Py).

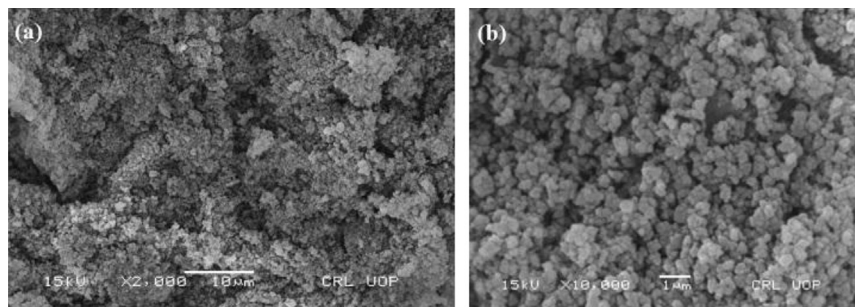


Fig. 15. SEM of Poly(Ani-co-Py) at 2000 (a) and 10,000 (b) magnification.

and Figure S1. The particle size was measured with nano-measure software. The 0.5 μm particles (first category), average size of all particles are of 0.27 μm , and small ones are about 0.05 μm . SEM analysis confirm the copolymer formation of Poly(Ani-co-Py) with granular morphology/flake structures, completely different form that of its counterpart PANI (fibrillar morphology) [24] and PPy (convoluted tubules, dendrites, or fibrillar) [48]. The results of SEM image also favor the formation of Poly(Ani-co-Py) with closely packing.

4. Conclusions

We have determined the structure of an oligomer (copolymer) of aniline and pyrrole [Poly(Ani-co-Py)], through a combination of theoretical and experimental techniques. Molecular formula of Poly(Ani-co-Py) is determined by elemental analysis and mass spectrometry. The molecular mass 468 corresponds to a copolymer, containing three aniline and three pyrrole units. The sequence of monomeric units in the oligomer is determined by mass spectral analysis and then confirmed by a comparison of theoretical and experimental spectroscopic properties. IR spectra reveal reasonable conclusive information about type c of 6Poly(Ani-co-Py). UV–vis spectral analysis strongly supports the type “c” as the approximate structure of the resulted oligomer. Moreover, the spiral nature of the 6Poly(Ani-co-Py) (type “c”) can be account for its low conductivity. Estimated energy of the contours of HOMO and LUMO of type “c” is also supportive to low conducting nature of Poly(Ani-co-Py).

Appendix A. Supplementary information

Supplementary information related to this article can be found at <http://dx.doi.org/10.1016/j.polymer.2015.07.003>.

References

- [1] U. Salzner, *Curr. Org. Chem.* 8 (2004) 569–590.
- [2] J. Burroughes, D. Bradley, A. Brown, R. Marks, K. Mackay, R. Friend, P. Burns, A. Holmes, *Nature* 347 (1990) 539–541.
- [3] J.L. Bredas, G.B. Street, *Acc. Chem. Res.* 18 (1985) 309–315.
- [4] H.S. Nalwa, *Silicon-based Material and Devices, Two-volume Set: Materials and Processing, Properties and Devices, vol. 1*, Academic Press, 2001.
- [5] S. Loser, C.J. Bruns, H. Miyauchi, R.P. Ortiz, A. Facchetti, S.I. Stupp, T.J. Marks, *J. Am. Chem. Soc.* 133 (2011) 8142–8145.
- [6] L. Pan, G. Yu, D. Zhai, H.R. Lee, W. Zhao, N. Liu, H. Wang, B.C.-K. Tee, Y. Shi, Y. Cui, *Proc. Nat. Acad. Sci.* 109 (2012) 9287–9292.
- [7] L. Pan, A. Chortos, G. Yu, Y. Wang, S. Isaacson, R. Allen, Y. Shi, R. Dauskardt, Z. Bao, *Nat. Commun.* 5 (2014).
- [8] L. Li, Y. Wang, L. Pan, Y. Shi, W. Cheng, Y. Shi, G. Yu, *Nano Lett.* 15 (2015) 1146–1151.
- [9] H. Ullah, A.-u.-H.A. Shah, K. Ayub, S. Bilal, *J. Phys. Chem. C* 117 (2013) 4069–4078.
- [10] H. Ullah, K. Ayub, Z. Ullah, M. Hanif, R. Nawaz, S. Bilal, *Synth. Met.* 172 (2013) 14–20.
- [11] H. Ullah, A.-u.-H.A. Shah, S. Bilal, K. Ayub, *J. Phys. Chem. C* 117 (2013) 23701–23711.
- [12] H. Ullah, A.-u.-H.A. Shah, S. Bilal, K. Ayub, *J. Phys. Chem. C* 118 (2014) 17819–17830.
- [13] J. Libert, J. Brédas, A. Epstein, *Phys. Rev. B* 51 (1995) 5711.
- [14] T.A. Skotheim, J. Reynolds, *Handbook of Conducting Polymers, 2 Volume Set*, CRC press, 2007.
- [15] C.K. Chiang, C. Fincher Jr., Y. Park, A. Heeger, H. Shirakawa, E. Louis, S. Gau, A.G. MacDiarmid, *Phys. Rev. Lett.* 39 (1977) 1098.
- [16] G. Gustafsson, Y. Cao, G. Treacy, F. Klavetter, N. Colaneri, A. Heeger, *Nature* 357 (1992) 477–479.
- [17] Y. Cao, P. Smith, A.J. Heeger, *Synth. Met.* 48 (1992) 91–97.
- [18] Z.-L. Wang, X.-J. He, S.-H. Ye, Y.-X. Tong, G.-R. Li, *ACS Appl. Mater Interfaces* 6 (2013) 642–647.
- [19] N.V. Blinova, J. Stejskal, M. Trchová, I. Sapurina, G. Ćirić-Marjanović, *Polymer* 50 (2009) 50–56.
- [20] J. Stejskal, M. Trchová, I.A. Ananieva, J. Janča, J. Prokeš, S. Fedorova, I. Sapurina, *Synth. Met.* 146 (2004) 29–36.
- [21] M. Omastová, K. Mosnáčková, M. Trchová, E.N. Konyushenko, J. Stejskal, P. Fedorko, J. Prokeš, *Synth. Met.* 160 (2010) 701–707.
- [22] D.K. Moon, J.-Y. Yun, K. Osakada, T. Kambara, T. Yamamoto, *Mol. Cryst. Liq. Cryst.* 464 (2007), 177/[759]–185/[767].
- [23] P. Xu, X. Han, C. Wang, B. Zhang, H.-L. Wang, *Synth. Met.* 159 (2009) 430–434.
- [24] P.R. Solanki, S. Singh, N. Prabhakar, M. Pandey, B. Malhotra, *J. Appl. Polym. Sci.* 105 (2007) 3211–3219.
- [25] S.E. Mavundla, G.F. Malgas, D.E. Motaung, E.I. Iwuoha, *J. Mater. Sci.* 45 (2010) 3325–3330.
- [26] S. Okur, U. Salzner, *J. Phys. Chem. A* 112 (2008) 11842–11853.
- [27] V. Lim, E. Kang, K. Neoh, Z. Ma, K. Tan, *Appl. Surf. Sci.* 181 (2001) 317–326.
- [28] M.J. Antony, M. Jayakannan, *J. Phys. Chem. B* 115 (2011) 6427–6436.
- [29] Y.-F. Zhu, L. Zhang, T. Natsuki, Y.-Q. Fu, Q.-Q. Ni, *Synth. Met.* 162 (2012) 337–343.
- [30] J.E. Del Bene, W.B. Person, K. Szczepaniak, *J. Phys. Chem.* 99 (1995) 10705–10707.
- [31] L. Yang, J.-K. Feng, A.-M. Ren, J.-Z. Sun, *Polymer* 47 (2006) 1397–1404.
- [32] J. Bredas, R. Chance, R. Silbey, *Phys. Rev. B* 26 (1982) 5843.
- [33] M. Frisch, G. Trucks, H. Schlegel, G. Scuseria, M. Robb, J. Cheeseman, G. Scalmani, V. Barone, B. Mennucci, and G. Petersson, Inc., Wallingford, CT (2009).
- [34] U. Salzner, *J. Phys. Chem. A* 112 (2008) 5458–5466.
- [35] U. Salzner, *J. Chem. Theory Comput.* 3 (2007) 1143–1157.
- [36] P.S. Rao, S. Subrahmanya, D. Sathyanarayana, *Synth. Met.* 128 (2002) 311–316.
- [37] K.K. Kanazawa, A. Diaz, R.H. Geiss, W.D. Gill, J.F. Kwak, J.A. Logan, J.F. Rabolt, G.B. Street, *J. Chem. Soc. Chem. Commun.* (1979) 854–855.
- [38] V. Seshadri, L. Wu, G.A. Sotzing, *Langmuir* 19 (2003) 9479–9485.
- [39] A. Watanabe, K. Mori, A. Iwabuchi, Y. Iwasaki, Y. Nakamura, O. Ito, *Macromolecules* 22 (1989) 3521–3525.
- [40] A.R. Allouche, *J. Comput. Chem.* 32 (2011) 174–182.
- [41] R. Dennington, Inc.: Shawnee Mission, KS (2008).
- [42] A. Pron, F. Genoud, C. Menardo, M. Nechtschein, *Synth. Met.* 24 (1988) 193–201.
- [43] I. Sapurina, J. Stejskal, *Polym. Int.* 57 (2008) 1295–1325.
- [44] N. Gospodinova, P. Mokreva, L. Terlemezyan, *Polymer* 34 (1993) 2438–2439.
- [45] A.G. MacDiarmid, A.J. Epstein, *Faraday Discuss. Chem. Soc.* 88 (1989) 317–332.
- [46] J. Wilson, S. Radhakrishnan, C. Sumathi, V. Dharuman, *Sens. Actuators B* 171 (2012) 216–222.
- [47] Q.-F. Lü, Z.-W. He, J.-Y. Zhang, Q. Lin, *J. Anal. Appl. Pyrolysis* 93 (2012) 147–152.
- [48] S.N. Atchison, R.R. Burford, T.A. Darragh, T. Tongtam, *Polym. Inter* 26 (1991) 261–266.

[Article 12]

H. Ullah, "Inter-molecular interaction in polypyrrole/TiO₂: A dft study." *J. Alloys Compd.*, vol. 692, pp. 140-148, Jan. 2017.



Inter-molecular interaction in Polypyrrole/TiO₂: A DFT study



Habib Ullah

Environment and Sustainability Institute (ESI), University of Exeter, Penryn Campus, Penryn, Cornwall TR10 9FE, UK

ARTICLE INFO

Article history:

Received 3 June 2016

Accepted 17 August 2016

Available online 4 September 2016

Keywords:

Band gap engineering
Non-covalent interaction
Photocatalysis
Redox potential

ABSTRACT

Density functional theory study of Polypyrrole/TiO₂ have been carried out at molecular level, to find its internal nature for the tuning of photocatalytic efficiency. Molecular isolated TiO₂ interacts with various pyrrole oligomers for the investigation of inter-molecular interaction. A narrowing in band gap and better visible light absorption are achieved compared to their individual constituents, based on electronic properties simulations. Electrostatic potential, the density of states, IP, EA, UV–vis spectra and band gap are also supportive to the composite formation. Inter-molecular interaction energy (–28 to –45 kcal mol^{–1}), counterpoised corrected (BSSE), and $\Delta E_{\text{gCP-D3}}$ methods are employed which confirm the existence of a strong covalent type of bonding between Py and TiO₂ in nPy-TiO₂ composites. Finally, Mulliken and natural bonding orbital analysis have pointed out that Py oligomers are *p*-type and donated electron cloud density to TiO₂ in all of the nPy-TiO₂ composites.

© 2016 Elsevier B.V. All rights reserved.

1. Introduction

Conducting polymer (CPs) have been using in the fields of organic electronic devices and solar cells because of having unique electrical and optical properties, such as high photon absorption coefficients under visible light irradiation, high electron mobility, excellent stability, material diversity, mechanical flexibility, light weight, low-temperature processing, roll to roll printing and large-area capability [1]. The conducting nature of these materials is because of having delocalized π -electrons (presence of alternating double and single bonds) which provide an easy pathway for electron mobility. CPs such as polyaniline (PANI), polypyrrole (PPy), polythiophene (PT), polyacetylene (PA), polythiophene (PT), poly-paraphenylene (PPP), polyparaphenylenevinylene (PPV), poly(3,4-ethylenedioxythiophene) (PEDOT), poly(*o*-phenylenediamine) (POPD) are widely explored both by theoreticians and experimentalists [2–5]. CPs are mostly *p*-type semiconducting materials, working as an electron donor species upon doping/mixing with other *n*-type metal oxides, especially in a *p*-*n* junction. Conducting polymers have been using in the polymer solar cell and photocatalysis but facing a severe problem of low efficiency. This deficiency can be either improved by doping and de-doping process or making their composite with metal oxides such as TiO₂, Fe₂O₃, ZnO, etc [6–8].

Among metal oxides, titanium dioxide has been attracted many

researchers since the last decade. It is used as an efficient light harvesting material and has enormously wide range of applications in solar energy conversion and photocatalysis due to its electronic structure and high stability to photocorrosion under redox conditions [9–11]. Moreover, TiO₂ has drawn much attention because of its potential applications, in CO₂ reduction, water purification, photocatalytic water splitting, dye-sensitized solar cell, and bio-sensing [12–15]. However, TiO₂ has lower visible light conversion efficiency which is due to its wide band gap (3.20 eV), absorb only in the UV region [16]. Another limitation of TiO₂ is high charge recombination rate of the photogenerated electron-hole pair which is responsible for its low photocatalytic activity [17].

Although PPy-TiO₂ composites have been reported as experimental photocatalysts, they have low efficiency, and so need to be explored through extensive theoretical modeling. The theoretical study may consist of optical, electronic structure, surface interactions, electroactivity and charge transfer mechanism between PPy and TiO₂ [18–21]. Salzner et al. and our group have reported that PPy and pyrrole oligomers are excellent tunable electroactive materials [22–26]. In this work, the charge transferring between molecular nPy and TiO₂ are carried out which will give the idea of the electron-hole transferring phenomenon in the resulted nPy-TiO₂ system. The current work can be divided into four different sections, (i) optimized geometries (ii) Inter-molecular interaction energy (iii) charge analysis (iv) and electronic properties simulations.

E-mail address: hu203@exeter.ac.uk.

2. Methodology

Density functional theory (DFT) calculations at hybrid functional such as B3LYP with 6-31G* level of theory are performed for the molecular isolated TiO₂, nPy oligomers (n = 1, 2, 3 ... 8) and nPy-TiO₂ systems [27,28]. These simulations were carried out on GAUSSIAN 09 [29] and the results were visualized through Gabedit [30] and GaussView [31]. DFT and time-dependent DFT (TD-DFT) calculations were performed to determine the electronic structure properties of nPy-TiO₂, as an efficient photocatalyst. As we discussed elsewhere, oligomers beyond six repeating units can precisely represent its polymeric characteristics so, that is why the current oligomeric size is restricted to eight repeating units [27,28]. Molecular isolated TiO₂ interacts near the oligomeric backbone of nPy. Geometries of 1Py-TiO₂, 2Py-TiO₂ ... up to 8Py-TiO₂ were optimized at the said level of theory and confirmed from frequency calculations. The non-bonding and bonding interaction energy in nPy-TiO₂ systems are simulated with interaction energy, basis set superposition error (BSSE), and geometrical counterpoise correction (gCP). The B3LYP-gCP-D3/6-31G* energy corrections are made from the Grimme's Webservice (<http://www.tc.thch.uni-bonn.de/>) [32,33]. The equations used for ΔE_{int} , ΔE_{BSSE} and gCP-D3 are given below.

$$\Delta E_{int} = E_{nPy} + E_{TiO_2} - E_{nPy-TiO_2} \quad (1)$$

$$\Delta E_{intCP} = \Delta E_{int} - E_{BSSE} \quad (2)$$

$$\Delta E_{gCP-D3} = E_{(nPy-TiO_2)gCP-D3} - E_{(TiO_2)gCP-D3} - E_{(nPy)gCP-D3} \quad (3)$$

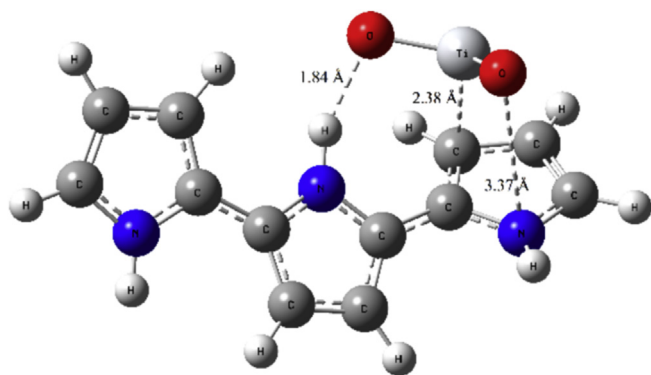


Fig. 1. Optimized geometric structures of 3Py-TiO₂ system.

The time-dependent DFT at B3LYP/6-31G* level of theory is used for the UV–vis spectra while the charge on these composites was estimated from the natural bond orbitals (NBO) and Mulliken charge analysis. All these calculations were performed in the gas phase.

3. Results and discussion

3.1. Optimized geometries

Optimized molecular TiO₂ interacted near the backbone of nPy; i.e., optimized geometries of 3Py bounded TiO₂ systems is given in Fig. 1, however, rest of the nPy-TiO₂ geometries are given in the Supporting Information (Figs. S1–S8). Isolated molecular TiO₂ interacted with 3Py by forming Hydrogen and electrostatic types of bonding; the former is due to O of TiO₂ and H of 3Py while the latter is between Ti and C atom of TiO₂ and 3Py, respectively. These intermolecular distances such as 1.84 and 2.38 Å, revealed the strong type of bonding and may be regarded as covalent. Jeffery et al. have investigated that inter-molecular bond distance in the range of 2.2–2.5 Å will be hydrogen bonding “strong, mostly covalent”, 2.5–3.2 Å will be “moderate, mostly electrostatic”, and 3.2–4.0 Å as “weak, electrostatic” [34]. Moreover, the energies for these bonds should be round about –40 to –14 kcal/mol, –15 to –4 kcal/mol, and <–4 kcal/mol, respectively [34]. Ti of the TiO₂ establishes a covalent type of bonding (2.38 Å) with the C of 3Py and this is the main charge transferring bond in PPy-TiO₂ composite [35]. This strong interaction and short bond distances strongly suggest that there may be chemisorption in the experimental PPy-TiO₂ composite.

Stable geometrical structures of nPy, TiO₂, and nPy-TiO₂ bounded species are optimized at the DFT-B3LYP/6-31G* level of theory. A reference optimized structure of 1Py-TiO₂, from three different sides' is shown in Fig. 2. During the optimization, TiO₂ circulated in the middle of Py ring through establishing strong non-covalent bonds with its N and C atoms. Ti of TiO₂ make a strong electrostatic type of bonding with the C1 and C4 of 1 Py at ca. 2.74 Å, this bond is about 2.57 Å with the C2 and C3 atoms. A 2.87 Å, non-bonding distance is simulated between the Ti and N atoms, which is comparatively long than that of the Ti–C bonding.

Optimized molecular isolated TiO₂ is interacted near the backbone of nPy to find the chain length elongation effect of the polymer (see Figs. S1–S8). In case of a 6Py-TiO₂ system, TiO₂ is fully interacted with 6Py on the ground state potential energy surface as can be seen in Fig. 3, where Oxygen atoms of TiO₂ form hydrogen bonding with 6Py with a non-bonding distance of 1.92 Å. Ti of TiO₂ forms an electrostatic type of two non-covalent bonds with C atoms

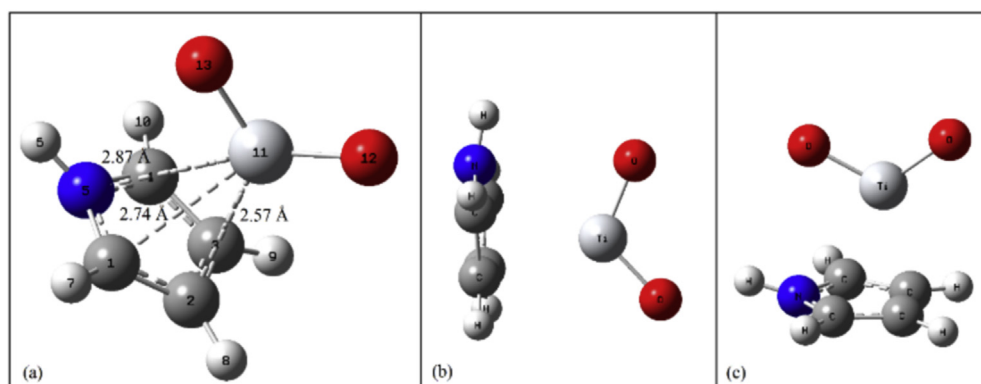


Fig. 2. Optimized geometric structure of 1Py-TiO₂.

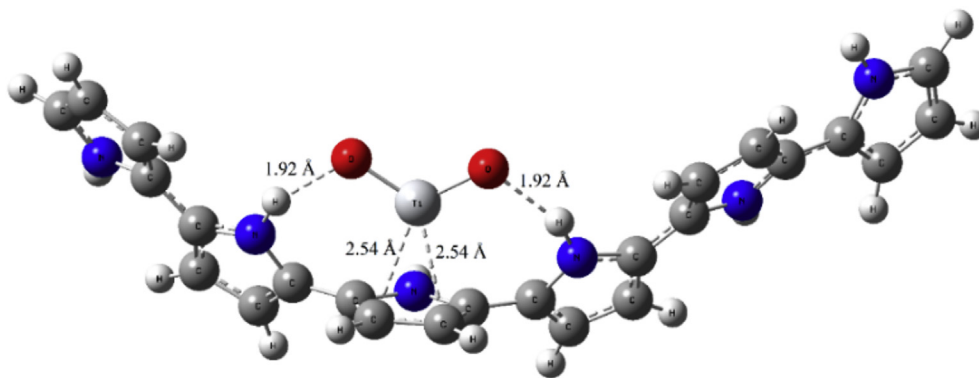


Fig. 3. Optimized geometric structures of 6Py-TiO₂.

of Py rings, each with a distance of 2.54 Å.

It has also been pointed out that isolated molecular TiO₂ interacts with other nPy oligomers via two types of essential bonding; a strong hydrogen bonding (mostly covalent), O–H (where O of TiO₂ attach to N-bonded H) and electrostatic, Ti–C (between the Ti of TiO₂ and C of Py) [34].

Comparative analysis of the optimized geometric structures of all nPy-TiO₂ systems predict that only these two types of bonding exist in PPy-TiO₂ composites (Figs. S1–S8) but with variant strength. In 2Py-TiO₂ composite, the O–H bond length is 1.86 Å which further decreases with chain length elongation of Py, 1.84 Å in 3Py-TiO₂, 1.83 Å in 4Py-TiO₂, and 1.81 Å in 5Py-TiO₂. A similar trend is found in the case of Ti–C bonding, 2.54 Å in 1Py-TiO₂ which decreases to 2.39 Å in 2Py-TiO₂ and 2.38 Å in case of 3Py-TiO₂ after which elongates to 2.63 Å in 4Py-TiO₂ and again decreases in the rest of the oligomers. Weak hydrogen bonding is found in the 5Py-TiO₂ composite as can be estimated from its electrostatic inter-molecular bonding distance of 2.57 Å. A very strong inter-molecular interaction can be seen in the 6Py-TiO₂ system, where two strong hydrogens and an electrostatic bonding established, each having 1.92 and 2.54 Å distances, respectively. On further chain length elongation of Py, the interaction becomes weakened as can be seen in 7Py and 8Py-TiO₂ composites. In the 7Py-TiO₂ system, one hydrogen and two electrostatic type bondings are found, having a distance of 1.81, 2.54, and 2.57 Å, respectively. On the other hand, two types of inter-molecular bonding exist in 8Py-TiO₂ composite, O–H with a bond distance of 1.85 Å and Ti–C bond with 2.38 Å, however, the net interaction is found to be dropped compared to other composites. Analysis of Figs. S2–S8 clearly depicts that TiO₂ has distorted the parent geometrical structures of all nPy oligomers, however, prominent extent is found in 6Py-TiO₂ composite (see Fig. 3). In summary, inter-molecular bond distance analysis led us to conclude that nPy and TiO₂ strongly interact each other through creating covalent and electrostatic types of bonding.

3.2. Interaction energy of nPy-TiO₂ systems

Interaction energy between molecular TiO₂ and nPy are calculated with interaction energy (ΔE_{int}), counterpoise corrected energy ($\Delta E_{\text{int,CP}}$) and with geometrical counterpoise corrected methods ($\Delta E_{\text{gCP-D3}}$) which are listed in Table 1. We employed the $\Delta E_{\text{gCP-D3}}$ method to minimize the geometrical and dispersion factors. A minor difference is found in all of these three methods but on the average concludes the existence of a very strong interaction energy between the nPy and TiO₂.

In the 1Py-TiO₂ system, the ΔE_{int} is -35.14 kcal/mol which is 4.70 kcal/mol lower than the $\Delta E_{\text{gCP-D3}}$ method while upon removal

Table 1

Inter-molecular interaction energy (ΔE_{int}), counterpoise corrected energy ($\Delta E_{\text{gCP-D3}}$), counterpoise correction ($\Delta E_{\text{int,CP}}$), $\Delta E_{\text{gCP-D3}}$ in kcal/mol), NBO and Mulliken charges analysis of nPy-TiO₂.

Species	ΔE_{int}	$\Delta E_{\text{gCP-D3}}$	$\Delta E_{\text{int,CP}}$	Q _{NBO}	Q _{MULLIKEN}
Py-TiO ₂	-35.14	-39.84	-28.92	0.15	0.25
2Py-TiO ₂	-40.53	-43.17	-43.17	0.10	0.20
3Py-TiO ₂	-40.41	-44.42	-32.75	0.10	0.20
4Py-TiO ₂	-42.98	-44.69	-34.82	0.13	0.23
5Py-TiO ₂	-43.42	-45.26	-35.14	0.13	0.23
6Py-TiO ₂	-45.11	-44.05	-35.83	0.11	0.20
7Py-TiO ₂	-43.73	-42.67	-35.39	0.13	0.24
8Py-TiO ₂	-40.47	-41.35	-32.75	0.11	0.21

of basis set superposition error (BSSE), this interaction energy is -28.92 kcal/mol. A comparatively strong inter-molecular forces are observed in 2Py-TiO₂, where these energies are; -40.53 kcal/mol based on ΔE_{int} , -43.17 kcal/mol based on $\Delta E_{\text{gCP-D3}}$ and -43.17 kcal/mol based on $\Delta E_{\text{int,CP}}$ methods. These interaction energies have similar values in 3Py-TiO₂ systems, excluding the $\Delta E_{\text{int,CP}}$ which is 11 kcal/mol lowered. In larger repeating units of PPy bounded TiO₂ systems, the counterpoise energy increases up to 7Py-TiO₂. The $\Delta E_{\text{int,CP}}$ of 4Py-TiO₂ system is -34.82 kcal/mol while this binding energy is about -44.69 and 42.98 kcal/mol based on $\Delta E_{\text{gCP-D3}}$ and ΔE_{int} methods, respectively. In case of 5Py-TiO₂, this inter-molecular non-bonding energy is about 0.5 kcal/mol stronger, compared to that of 4Py-TiO₂ composite; -43.42 kcal/mol based on ΔE_{int} , -45.26 kcal/mol based on $\Delta E_{\text{gCP-D3}}$, and -35.14 kcal/mol based on $\Delta E_{\text{int,CP}}$. These inter-molecular interaction energies are much stronger in case of 6Py-TiO₂, where the ΔE_{int} is -45.11 kcal/mol, $\Delta E_{\text{gCP-D3}}$ is -44.05 kcal/mol and $\Delta E_{\text{int,CP}}$ -35.83 kcal/mol. The overall effect of these three interaction energies in 6Py-TiO₂ system has relatively stronger compared to that of other systems which may be attributed to the suitable oligomeric size of PPy.

The 7Py-TiO₂ system has 2 kcal/mol lower binding energy compared to 6Py-TiO₂, based on both of ΔE_{int} and $\Delta E_{\text{gCP-D3}}$ methods while a 0.44 kcal/mol decreased is found in the counterpoise corrected energy. So, it is concluded that due to the bulkiness of PPy rings, it may be difficult for TiO₂ molecule to interact sufficiently for the exchange of electron cloud density. A further decline of about 2 kcal/mol is simulated in 8Py-TiO₂ compared to the 7Py-TiO₂ system. This analysis also evidences that a specific ratio/composition of TiO₂ and Py is necessary for an efficient composite (photo-catalyst). These strong covalent and electrostatic types of bonding predict that molecular TiO₂ and PPy oligomers have a good interaction which results in composite formation instead of weak type interactions.

3.3. Mulliken and NBO charge analysis

The nature of charge transfer estimation between nPy and TiO₂ are simulated with the help of Mulliken (Q_{MULLIKEN}) and natural bonding orbital (Q_{NBO}) analysis. As we know that these charge analyses are basis set dependent; however, using a similar level of theory for various systems [such as B3LYP/6-31G*, UB3LYP/6-31G* or UB3LYP/6-311++G (d, p)] etc., then the results would be meaningful [36,37].

As discussed earlier, molecular TiO₂ interacts with nPy with two types of bonding, strong hydrogen (covalent bond) and electrostatic bonding (Ti–C). The net charge transfer in all nPy–TiO₂ composites is listed in Table 1. Moreover, the individual ring charges in nPy–TiO₂ systems are listed in Table 2. Examination of this data (Tables 1 and 2) confirms the electron accepting nature of TiO₂ in these composites, simulated on both of the Q_{MULLIKEN} and Q_{NBO} charge analysis. TiO₂ withdraws electronic cloud density of about 0.20–0.25 e[−] from nPy oligomers based on Q_{MULLIKEN} and 0.10 to 0.15 e[−] based on Q_{NBO} analysis. TiO₂ created net cationic states in all of the nPy oligomers in the resulted composites, which would be responsible for better electrical conductivity. As evident from the work of Veloso, Ajayan, and Desiraju et al., that higher charge transferring is present in the covalently bounded atoms and molecules rather than electrostatically [38–40]. So, here the O–H and Ti–C bonds are the main charge transferring pathway in all of the nPy–TiO₂ composites. As far as the optimized oligomeric size of nPy is concerned, again a unique charge distribution can be seen in the 6Py–TiO₂ as shown in Table 2, proved to be a better composite with greater charge transferring ability.

3.4. Electronic properties simulation

Electronic properties such as IP, EA, UV–vis spectra, HOMO, LUMO, ESP, DOS and band gap of nPy, TiO₂, and nPy–TiO₂ composites are calculated at the mentioned level of theory. As discussed elsewhere, IP is obtained from the negative of HOMO while the EA from negative of LUMO using Koopmans theorem [41]. The electron-accepting power of a chemical substance has a direct relation with EA and on the other hand, greater the IP high will be the electron donating ability.

Our simulated band gap value for the isolated molecular TiO₂ (Table 3) can be correlated with the experimental data (band gap 3.48 eV). Moreover, the band gap of isolated TiO₂ is also calculated at ΔSCF which is 3.24 eV (see UV–vis section). We selected molecular TiO₂, having a band gap of 3.24 eV to precisely represent the real anatase, as band gap is considered to be a key parameter especially in the field of photocatalysis and photovoltaics. In the case of 1.68 eV band gap (molecular anatase), it has overestimated the experimental results. That is why throughout the text we used isolated TiO₂; a representation of the observed TiO₂ and to minimize the computational cost.

Table 2
NBO charge Analysis in unit of electron of nPy–TiO₂ rings.

	Ring 1	Ring 2	Ring 3	Ring 4	Ring 5	Ring 6	Ring 7	Ring 8
Py–TiO ₂	0.151							
2Py–TiO ₂	0.07	0.02						
3Py–TiO ₂	0.041	0.039	0.021					
4Py–TiO ₂	0.043	0.025	−0.024	0.09				
5Py–TiO ₂	0.009	0.033	0.023	−0.021	0.09			
6Py–TiO ₂	0.011	0.030	0.017	−0.006	0.016	0.042		
7Py–TiO ₂	0.008	−0.003	0.034	0.021	−0.028	0.058	0.045	
8Py–TiO ₂	0.004	−0.006	0.036	0.039	−0.040	0.044	0.011	0.021

The bold texts show net NBO charge of the nth Py ring, upon TiO₂ interaction.

Table 3
HOMO, LUMO, Band Gap (in eV) and Dipole moment (Debye) of nPy and nPy–TiO₂ composites.

Species	HOMO	LUMO	Dipole moment	Band gap
TiO ₂	−6.48	−3.00	6.62	3.48
Py	−5.48	1.38	1.90	6.86
Py–TiO ₂	−5.48	−1.50	9.52	3.98
2Py	−4.75	0.35	0.97	5.10
2Py–TiO ₂	−5.49	−1.85	6.17	3.64
3Py	−4.43	−0.03	1.41	4.40
3Py–TiO ₂	−4.62	−1.83	6.29	2.79
4Py	−4.26	−0.25	1.49	4.01
4Py–TiO ₂	−4.82	−1.59	8.72	3.23
5Py	−4.16	−0.38	0.89	3.78
5Py–TiO ₂	−4.43	−1.63	9.06	2.80
6Py	−4.11	−0.46	1.78	3.65
6Py–TiO ₂	−4.54	−2.01	5.85	2.53
7Py	−4.06	−0.53	0.33	3.53
7Py–TiO ₂	−4.23	−1.66	7.98	2.57
8Py	−4.03	−0.57	1.82	3.46
8Py–TiO ₂	−4.09	−1.72	9.03	2.37

Table 4
Calculated excitation energies, oscillator strengths, and molecular orbitals (MOs) of the first allowed singlet transition involved in the excitation for nPy and nPy–TiO₂ composites.

Species	Energy (eV)	Wavelength (nm)	Osc. strength	MOs	Coefficient
TiO ₂	3.24	382	0.001	H → L	0.70
Py	6.75	183	0.14	H → L	0.69
Py–TiO ₂	2.75	450	0.001	H → L	0.66
2Py	4.87	254	0.55	H → L	0.70
2Py–TiO ₂	3.04	406	0.009	H → L	0.57
3Py	4.11	301	0.85	H → L	0.70
3Py–TiO ₂	2.26	547	0.006	H → L	0.70
4Py	3.68	336	1.18	H → L	0.70
4Py–TiO ₂	2.72	454	0.11	H → L	0.70
5Py	3.43	361	1.49	H → L	0.70
5Py–TiO ₂	2.36	523	0.09	H → L	0.70
6Py	3.26	380	1.78	H → L	0.70
6Py–TiO ₂	2.04	606	0.06	H → L	0.69
7Py	3.13	395	2.09	H → L	0.70
7Py–TiO ₂	2.21	559	0.13	H → L	0.70
8Py	3.05	443	2.39	H → L	0.69
8Py–TiO ₂	1.96	631	0.01	H → L	0.69

Prior to interaction study simulations, best reactive sites of both of the TiO₂ and nPy oligomers are estimated from molecular electrostatic potential (MEP) (Fig. 4) and then reacted. The different colors in these Figures are used as a symbol for the different value of electrostatic potential; where red and blue colors show electron rich and electron deficient (high positivity) regions of the molecule and the green color shows the region of zero potential. The MEP also provides a visual method for understanding the relative polarity of these species. Analysis of the MEP surfaces clearly indicate that the most electronegative part of TiO₂ is the area around O

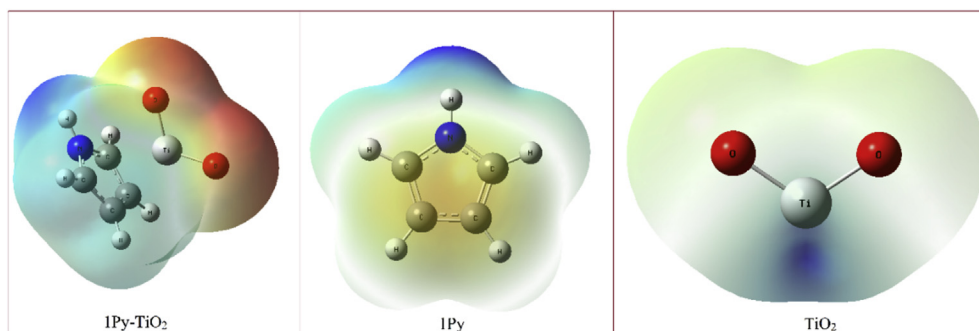


Fig. 4. MEP plots of isolated TiO_2 , 1Py and 1Py- TiO_2 .

atoms which is the most electron rich regions (red) and Ti is the most electropositive with electron deficient regions (blue). In case of 1Py, the area around the N is electropositive (blue) while C atoms have resulted in an electronegative region (red).

3.4.1. Ionization potential

An appreciable amount of increase is estimated in the IP values of nPy oligomers upon making their composites with TiO_2 which is also a direct consequence of its stability (Fig. 5). No change in IP is observed in the case of 1Py and 8Py- TiO_2 composites which may be due to their lower interaction ability between the molecular orbitals. In case of 2Py- TiO_2 , IP increases about 0.74 eV which consequently decreases its band gap from 5.10 to 3.64 eV (as discussed in band gap section). Same is the case of rest of the pPy TiO_2 -bounded oligomers, 0.19 eV in 3Py- TiO_2 , 0.56 eV in 4Py- TiO_2 , 0.27 eV in 5Py- TiO_2 , 0.43 eV in 6Py- TiO_2 and 0.17 eV increment are found in 7Py- TiO_2 composite. This increase in IP value of nPy- TiO_2 composites is clearly depicted in Fig. 5.

3.4.2. Electron affinities

EA of nPy oligomers increases even shift from negative to a positive value, on interacting with TiO_2 . TiO_2 shifts the EA of 1Py from -1.38 – 1.50 eV, an increase of 2 eV in 2Py- TiO_2 , 1.80 eV in 3Py- TiO_2 and then a similar increment of about 1.30 eV are estimated in the rest of repeating units, excluding 6Py- TiO_2 composite (Fig. 6). As discussed in the optimized geometric analysis, TiO_2 has an excellent interaction with the 6Py which is also in agreement with the EA analysis; increased its EA to about 1.55 eV. So, it can be easily concluded that the resulted composites are cationic in nature where the polaron and bipolaron states may also exist.

3.4.3. Band gap and molecular orbitals simulations

We simulated the band gap at ΔSCF ; excitation energy of higher oscillator strength, and from B3LYP, where the difference of LUMO-HOMO orbitals is accounted. Energies of the HOMO, LUMO orbitals and band gap of these species are listed in Tables 3 and 4. The TD-B3LYP (ΔSCF) values are slightly lower compared to the ones obtained at B3LYP as can be seen from Table 4. From the comparison of band gap analysis of Table 3, it is concluded that it decreases in nPy oligomers upon interaction with TiO_2 , which also evidences their excellent electroactivity in the resulted composites.

Frontier molecular orbitals and dipole moments of these interacting species; before and after interaction are calculated at the B3LYP/6-31G* level of theory. Change in the valence band (HOMO), conduction band position (LUMO), dipole moment, and the band gap of TiO_2 and nPy oligomers and their composites can be seen from Table 4. Moreover, contours of HOMO and LUMO along with band gap of nPy and nPy- TiO_2 systems are given in Figs. 7 and 8, respectively. Comparative analysis of the data of Table 3 led us to conclude that molecular orbitals of TiO_2 strongly interact with the frontier orbitals of nPy and led to strong covalent bonding in the resulted composites; having an intermediate band gap, highest dipole moment and stable nature (*vide supra*).

The interaction of TiO_2 has considerably reduced the LUMO energy level (from 1.38 to -1.50 eV) and band gap (from 6.86 to 3.98 eV) of 1Py in the 1Py- TiO_2 composite. Dipole moment of 1Py- TiO_2 (9.52 Debye) clearly demonstrates a substantial increment in the electroactivity of this composite. As discussed earlier, narrowing the band gap of Py has a direct relationship with chain length elongation (more conjugation) as can be seen from Fig. 7. TiO_2 decreases the HOMO of 2Py from -4.75 to -5.49 eV, shift LUMO from 0.35 to -1.85 eV and reduces band gap from 5.10 to 3.64 eV.

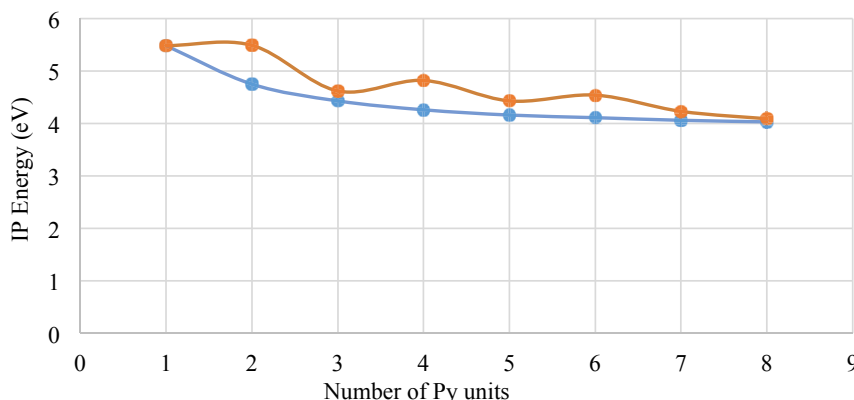


Fig. 5. Variation in IP of nPy (blue) and nPy- TiO_2 (orange). (For interpretation of the references to colour in this figure legend, the reader is referred to the web version of this article.)

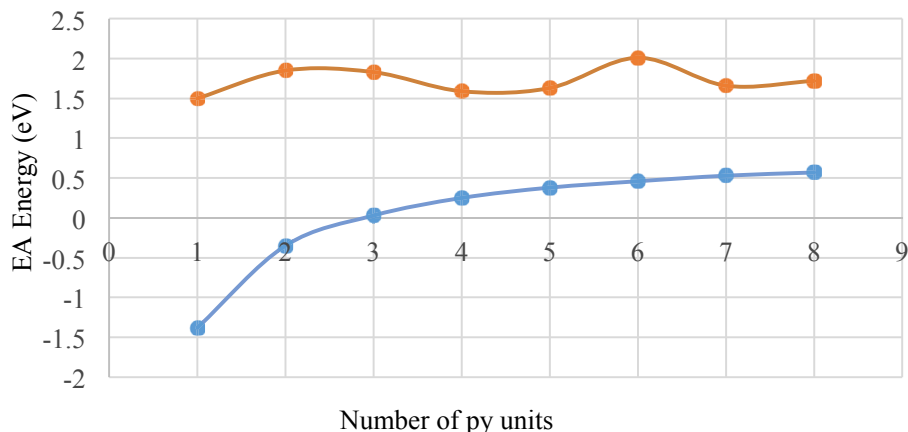


Fig. 6. Variation in EA of nPy (blue) and nPy-TiO₂ (orange). (For interpretation of the references to colour in this figure legend, the reader is referred to the web version of this article.)

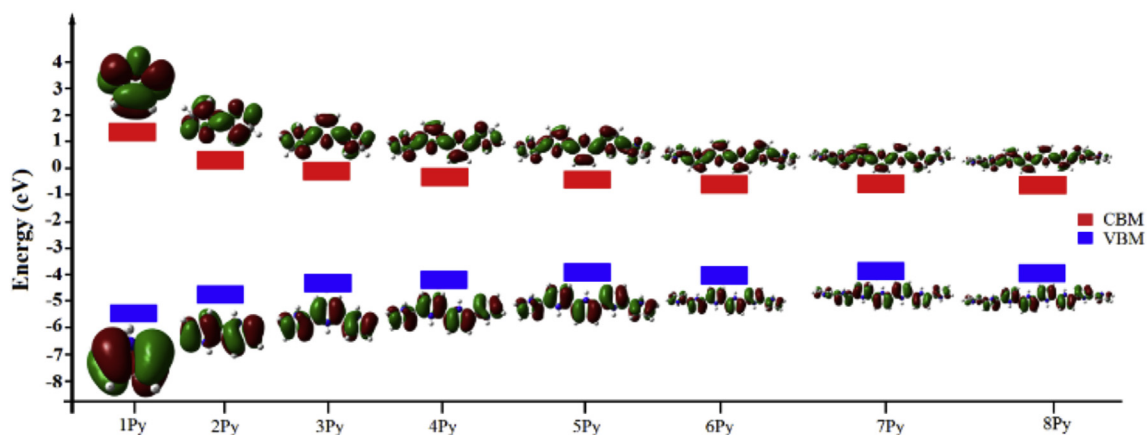


Fig. 7. Developments of band structure of PPY from energy levels of oligomers. (The monomer is used as a repeat unit.)

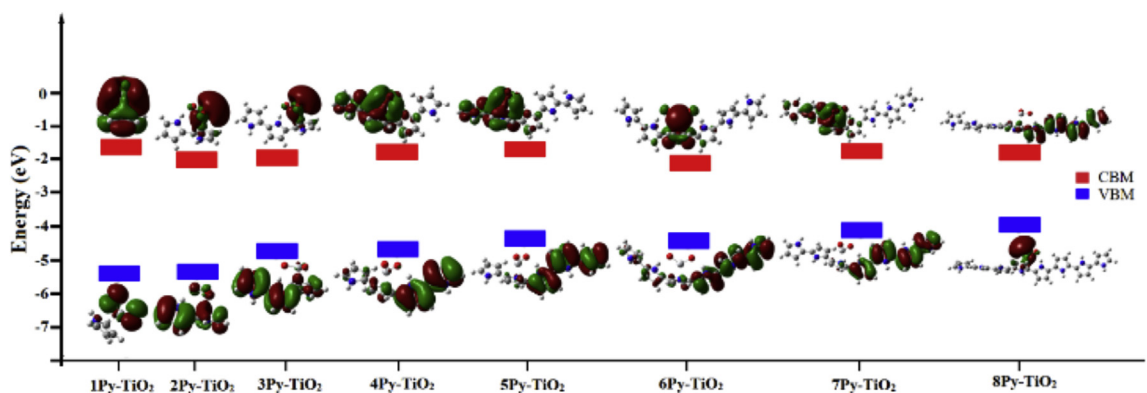


Fig. 8. Developments of band structure of nPy-TiO₂ from energy levels of oligomers. (The monomer is used as a repeat unit.)

Similar, but little more pronounced reduction in these energies are estimated in 3Py-TiO₂, 0.19 eV in HOMO, 1.80 eV in LUMO, and 1.61 eV in the band gap.

Electronic cloud densities over the HOMO and LUMO of 4Py-TiO₂ are found to have enhanced compared to that of isolated 4Py, a roundabout to 0.56 eV and 1.34 eV, respectively. The dipole moment and band gap change from 1.49 to 8.72 Debye and 4.01 to 3.23 eV, respectively. In case of the 5Py-TiO₂ composite, HOMO of

5Py decreases from -4.16 to -4.43 eV, LUMO from -0.46 to -2.01 eV, dipole moment changes from 0.89 to 9.06 eV, and band gap reduced to 2.80 eV (from 3.78 eV). Prominent perturbation in these properties can be seen in case of 6Py-TiO₂, where HOMO (-4.54 eV) and LUMO (-2.01 eV) orbitals became closer with a difference of 2.53 eV (band gap), which is 1.12 eV narrower than that of 6Py. Beyond six repeating units of Py, a large shift in the orbitals positions is found as can be seen in 7 and 8Py-TiO₂ systems.

The high dipole moment of the 7Py-TiO₂ system can be assigned to its zigzag geometry, and wider band gap (2.57 eV) compared to that of 6Py-TiO₂. Orbital (HOMO and LUMO) energies of 8Py increase to 0.06 and 1.15 eV upon interaction with molecular TiO₂. However, this change is negligible which may be regarded due to the bulk structure of 8Py-TiO₂, having 9.03 Debye dipole moment and 2.37 eV band gap.

This section has highlighted that optimum molecular oligomeric size for the efficient nPy-TiO₂ composite should be six repeating units. A molecular electrostatic potential plot of 6Py-TiO₂ is given in Fig. 9, where the orbitals intermixing can be easily seen. Moreover, DOS and energy level diagram of this composite are separately shown in Figs. 10 and 11, respectively.

The homogeneous MEP plot of 6Py-TiO₂ led us to conclude that how these two molecular constituents have made excellent interaction by sharing their electronic cloud densities. For the clarity reason, molecular orbitals interaction of this composite along with their interacting species is also depicted in Fig. 11. In Fig. 11, orbitals contours are shown in the form of the density of states, TiO₂ (red contours), 6Py (yellow contours) and the green color contours are for 6Py-TiO₂ system.

Energy level diagram of this interacting system is simulated in the form of band structure position, where the band gap of TiO₂, 6Py and 6Py-TiO₂ are clearly shown. Furthermore, this study will also open an idea for modifying the band structure position of this type of composites, by improving their physical and chemical bonding between the reacting species.

3.4.4. UV-vis study

UV-vis spectra of nPy, TiO₂, and nPy-TiO₂ systems are simulated at TD-DFT which is shown in Figs. S9 and 10 of the Supplementary Information, while their first allowed electronic excitation energies are given and listed in Fig. 12 and Table 4, respectively. It is reported in a number of papers that nPy give rise to three prominent absorption band peaks in the UV-vis spectra [23,26,42]. The λ_{\max} , having high wavelength and low absorption energy is referred to the transition of an electron from valence to conduction band. Interaction of TiO₂ with nPy oligomers (shown in Fig. 12 and Table 4) resulted red-shifting in the λ_{\max} of nPy-TiO₂. This red-shifting in λ_{\max} of all nPy oligomers with TiO₂ illustrates its *n*-type doping nature. In small oligomers, the λ_{\max} of nPy became doubled as can be seen from Table 4, which is a direct consequence of improved conductivity/delocalization in the composites over their isolated nPy oligomers (*vide infra*).

In the case of 1Py, the excitation energy for the $\pi \rightarrow \pi^*$ transition is 183 nm which increased to 450 nm in the 1Py-TiO₂, evidences the establishment of strong bonding. As shown in Table 4 and Fig. 12,

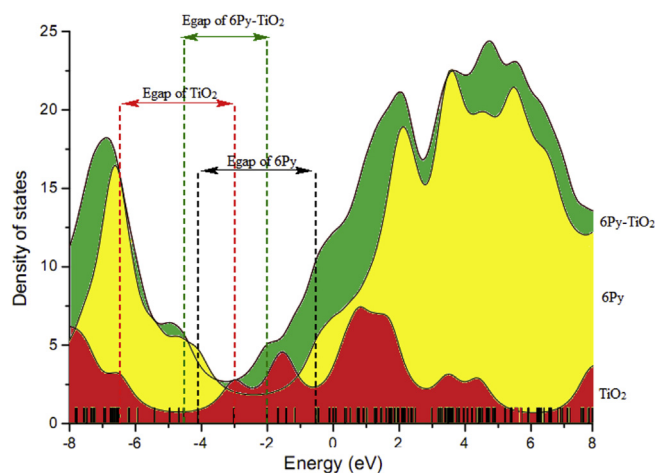


Fig. 10. Density of states (DOS) of TiO₂, 6Py, and 6Py-TiO₂.

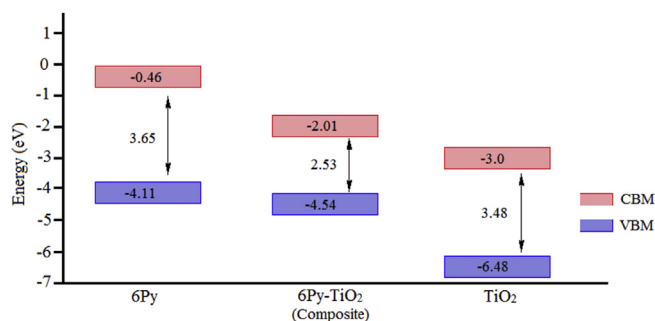


Fig. 11. Comparative energy level diagram of 6Py, TiO₂ and 6Py-TiO₂ composite.

TiO₂ increases the first allowed electronic excitation energy of 2Py to about 152 nm, 246 nm in 3Py, 118 nm in 4Py, 162 nm in 5Py, 226 nm in 6Py, 164 nm in 7Py, and 188 nm in 8Py. TiO₂ and nPy oligomers can absorb only in the UV region as evident from their λ_{\max} values, however, their composites have excellent absorption capability in the visible region (Table 4). The red-shifting from the ultraviolet to visible predicts the excellent photocatalytic activity of nPy-TiO₂ composites over their individual constituents. Among the long oligomeric systems, the first allowed excitation energy of ($\pi \rightarrow \pi^*$ transition) of 6Py-TiO₂ is more prominent compared to their other TiO₂ bounded oligomers (Fig. 12). So, as far as the optimum chain length of molecular PPy is concerned, six repeating unit would be an excellent oligomer, compared to other repeating units.

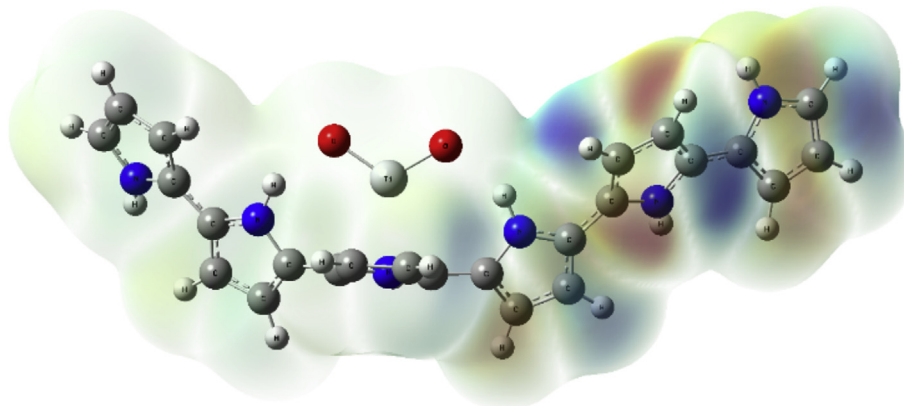


Fig. 9. Molecular electrostatic potential of 6Py-TiO₂ composite.

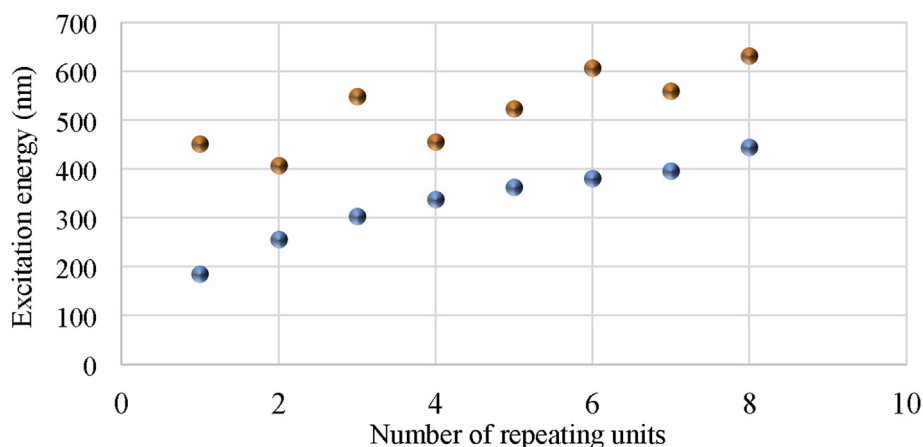


Fig. 12. First allowed electronic excitation energy of nPy (blue) and nPy-TiO₂ (pink) composites. (For interpretation of the references to colour in this figure legend, the reader is referred to the web version of this article.)

So, UV–vis spectroscopic study is also in good agreement with the rest of the characterizations, discussed above.

4. Conclusions

Density functional theory study of molecular pyrrole-TiO₂ bounded systems are carried out to find its nature of interaction for tailoring best composite, used in the photocatalysis of environmental pollutants and solar water splitting to produce solar fuel. The chemical nature of interaction in nPy-TiO₂ composites is simulated with the help of inter-molecular interaction energy analysis, NBO and Mulliken charge simulations, optimized geometric parameters, and electronic properties calculations. The simulated inter-molecular interaction energy, in the range of -28 to -45 kcal mol⁻¹ confirmed the existence of strong covalent bonding. This energy is simulated with the help of simple energy, BSSE, and $\Delta E_{\text{GCP-D3}}$ methods. So, after confirming the composite formation, narrowing in band gap and better visible light absorption capability is observed, compared to their individual nPy and TiO₂ constituents. Electronic properties such as HOMO and LUMO of nPy, TiO₂, and nPy-TiO₂ systems are estimated with B3LYP/6-31G* level of theory, predicts the excellent efficiency of the resulted species. Other electronic properties such as ESP, DOS, band gap, and UV–vis spectra are found to have in support of the efficient nPy-TiO₂ composites. A red-shifting in λ_{max} and narrow band gap are found when nPy and TiO₂ interact. Electron-hole transferring phenomena are simulated with Mulliken and natural bonding orbital analysis, which define pyrrole oligomers as donor and TiO₂ an acceptor. Finally, the molecular 6Py-TiO₂ system is estimated to be the best candidate for better photocatalytic activities. This isolated molecular gas phase simulations will minimize our synthetic efforts such as mixing ratios of TiO₂ and PPy. The study will also guide experimental scientists in modifying the band structure, optical, physical and chemical properties for the improved performance of nPy-TiO₂ and other related composites.

Appendix A. Supplementary data

Supplementary data related to this article can be found at <http://dx.doi.org/10.1016/j.jallcom.2016.08.169>.

References

- [1] F.C. Krebs, Polymer solar cell modules prepared using roll-to-roll methods: knife-over-edge coating, slot-die coating and screen printing, *Sol. Energy Mater. Sol. Cells* 93 (2009) 465–475.
- [2] R. Friend, R. Gymer, A. Holmes, J. Burroughes, R. Marks, C. Taliani, D. Bradley, D. Dos Santos, J. Bredas, M. Lögdlund, Electroluminescence in conjugated Polymers, *Nature* 397 (1999) 121–128.
- [3] J. Janata, M. Josowicz, Conducting polymers in electronic chemical sensors, *Nat. Mater.* 2 (2003) 19–24.
- [4] G. Li, V. Shrotriya, J. Huang, Y. Yao, T. Moriarty, K. Emery, Y. Yang, High-efficiency solution processable polymer photovoltaic cells by self-organization of polymer blends, *Nat. Mater.* 4 (2005) 864–868.
- [5] G. Li, R. Zhu, Y. Yang, Polymer solar cells, *Nat. Photonics* 6 (2012) 153–161.
- [6] R. Haggenueller, H. Gommans, A. Rinzler, J.E. Fischer, K. Winey, Aligned single-wall carbon nanotubes in composites by melt processing methods, *Chem. Phys. Lett.* 330 (2000) 219–225.
- [7] Z. Jin, K. Pramoda, G. Xu, S.H. Goh, Dynamic mechanical behavior of melt-processed multi-walled carbon nanotube/poly (methyl methacrylate) composites, *Chem. Phys. Lett.* 337 (2001) 43–47.
- [8] M. Fahlman, D. Beljonne, M. Lögdlund, R. Friend, A. Holmes, J.-L. Brédas, W. Salaneck, Experimental and theoretical studies of the electronic structure of Na-doped poly (para-phenylenevinylene), *Chem. Phys. Lett.* 214 (1993) 327–332.
- [9] S. Cherian, C.C. Wamser, Adsorption and photoactivity of tetra (4-carboxyphenyl) porphyrin (TCPP) on nanoparticulate TiO₂, *J. Phys. Chem. B* 104 (2000) 3624–3629.
- [10] Y.-G. Kim, J. Walker, L.A. Samuelson, J. Kumar, Efficient light harvesting polymers for nanocrystalline TiO₂ photovoltaic cells, *Nano Lett.* 3 (2003) 523–525.
- [11] I. Robel, V. Subramanian, M. Kuno, P.V. Kamat, Quantum dot solar cells. Harvesting light energy with CdSe nanocrystals molecularly linked to mesoscopic TiO₂ films, *J. Am. Chem. Soc.* 128 (2006) 2385–2393.
- [12] Y.-Y. Song, F. Schmidt-Stein, S. Bauer, P. Schmuki, Amphiphilic TiO₂ nanotube arrays: an actively controllable drug delivery system, *J. Am. Chem. Soc.* 131 (2009) 4230–4232.
- [13] K. Woan, G. Pyrgiotakis, W. Sigmund, Photocatalytic carbon-nanotube–TiO₂ composites, *Adv. Mater.* 21 (2009) 2233–2239.
- [14] V. Chabot, D. Higgins, A. Yu, X. Xiao, Z. Chen, J. Zhang, A review of graphene and graphene oxide sponge: material synthesis and applications to energy and the environment, *Energy & Environ. Sci.* 7 (2014) 1564–1596.
- [15] D. Wen, S. Guo, J. Zhai, L. Deng, W. Ren, S. Dong, Pt nanoparticles supported on TiO₂ colloidal spheres with nanoporous surface: preparation and use as an enhancing material for biosensing applications, *J. Phys. Chem. C* 113 (2009) 13023–13028.
- [16] S. Banerjee, S.C. Pillai, P. Falaras, K.E. O’Shea, J.A. Byrne, D.D. Dionysiou, New insights into the mechanism of visible light photocatalysis, *J. Phys. Chem. Lett.* 5 (2014) 2543–2554.
- [17] N. Serpone, Is the band gap of pristine TiO₂ narrowed by anion- and cation-doping of titanium dioxide in second-generation photocatalysts? *J. Phys. Chem. B* 110 (2006) 24287–24293.
- [18] X.C. Li, J.S. Sun, G.H. He, G.L. Jiang, Y. Tan, B. Xue, Macroporous polypyrrole-TiO₂ composites with improved photoactivity and electrochemical sensitivity, *J. Colloid Interface Sci.* 411 (2013) 34–40.
- [19] J.B. Zhu, X. Zhao, M.L. Xiao, L. Liang, C.P. Liu, J.H. Liao, W. Xing, The construction of nitrogen-doped graphitized carbon-TiO₂ composite to improve the electrocatalyst for methanol oxidation, *Carbon* 72 (2014) 114–124.
- [20] J.J. Li, J.T. Feng, W. Yan, Excellent adsorption and desorption characteristics of polypyrrole/TiO₂ composite for Methylene Blue, *Appl. Surf. Sci.* 279 (2013) 400–408.
- [21] F. Deng, L.J. Min, X.B. Luo, S.L. Wu, S.L. Luo, Visible-light photocatalytic degradation performances and thermal stability due to the synergetic effect of TiO₂ with conductive copolymers of polyaniline and polypyrrole, *Nanoscale* 5 (2013) 8703–8710.

- [22] H. Ullah, K. Ayub, Z. Ullah, M. Hanif, R. Nawaz, A.-u.-H.A. Shah, S. Bilal, Theoretical insight of polypyrrole ammonia gas sensor, *Synth. Met.* 172 (2013) 14–20.
- [23] H. Ullah, A.-u.-H.A. Shah, S. Bilal, K. Ayub, Doping and dedoping processes of polypyrrole: DFT study with hybrid functionals, *J. Phys. Chem. C* 118 (2014) 17819–17830.
- [24] S. Bibi, H. Ullah, S.M. Ahmad, A.-u.-H. Ali Shah, S. Bilal, A.A. Tahir, K. Ayub, Molecular and electronic structure elucidation of polypyrrole gas sensors, *J. Phys. Chem. C* 119 (2015) 15994–16003.
- [25] U. Salzner, J. Lagowski, P. Pickup, R. Poirier, Comparison of geometries and electronic structures of polyacetylene, polyborole, polycyclopentadiene, polypyrrole, polyfuran, polysilole, polyphosphole, polythiophene, polyselenophene and polytellurophene, *Synth. Met.* 96 (1998) 177–189.
- [26] S. Okur, U. Salzner, Theoretical modeling of the doping process in polypyrrole by calculating UV/vis absorption spectra of neutral and charged oligomers, *J. Phys. Chem. A* 113 (2009) 9050.
- [27] H. Ullah, A.-u.-H.A. Shah, K. Ayub, S. Bilal, Density functional theory study of poly (*o*-Phenylenediamine) oligomers, *J. Phys. Chem. C* 117 (2013) 4069–4078.
- [28] H. Ullah, A.A. Shah, S. Bilal, K. Ayub, DFT study of polyaniline NH₃, CO₂, and CO gas sensors: comparison with recent experimental data, *J. Phys. Chem. C* 117 (2013) 23701–23711.
- [29] M.J.T. Frisch, G.W. Schlegel, H.B. Scuseria, G.E. Robb, M.A. Cheeseman, J.R. Scalmani, G. Barone, V. Mennucci, B. Petersson, G. A.; Gaussian 09, Revision C. 01, Gaussian, Inc., Wallingford, CT, 2009. Gaussian 09.
- [30] A.R. Allouche, Gabedit, 2011. <http://gabedit.sourceforge.net>.
- [31] R. Dennington, T. Keith, and J. G. Millam, Version 5.0. 8 Semichem Inc., Shawnee Mission KS (2008).
- [32] J.G. Brandenburg, M. Alessio, B. Civalleri, M.F. Peintinger, T. Bredow, S. Grimme, Geometrical correction for the inter-and intramolecular basis set superposition error in periodic density functional theory calculations, *J. Phys. Chem. A* 117 (2013) 9282–9292.
- [33] H. Kruse, L. Goerigk, S. Grimme, Why the standard B3LYP/6-31G* model chemistry should not be used in DFT calculations of molecular thermochemistry: understanding and correcting the problem, *J. Org. Chem.* 77 (2012) 10824–10834.
- [34] G.A. Jeffrey, *An Introduction to Hydrogen Bonding*, vol. 12, Oxford University Press, New York, 1997.
- [35] N.M. Dimitrijevic, S. Tepavcevic, Y. Liu, T. Rajh, S.C. Silver, D.M. Tiede, Nanostructured TiO₂/polypyrrole for visible light photocatalysis, *J. Phys. Chem. C* 117 (2013) 15540–15544.
- [36] F. Martin, H. Zipse, Charge distribution in the water molecule—A comparison of methods, *J. Comput. Chem.* 26 (2005) 97–105.
- [37] C. Fonseca Guerra, J.W. Handgraaf, E.J. Baerends, F.M. Bickelhaupt, Voronoi deformation density (VDD) charges: assessment of the Mulliken, Bader, Hirshfeld, Weinhold, and VDD methods for charge analysis, *J. Comput. Chem.* 25 (2004) 189–210.
- [38] M.V. Veloso, A. Souza Filho, J. Mendes Filho, S.B. Fagan, R. Mota, *Ab initio* study of covalently functionalized carbon nanotubes, *Chem. Phys. Lett.* 430 (2006) 71–74.
- [39] P.M. Ajayan, J.M. Tour, Materials science: nanotube composites, *Nature* 447 (2007) 1066–1068.
- [40] G. R. Desiraju and T. Steiner, *Weak Hydrogen Bond* 2001: Oxford University Press New York.
- [41] T. Koopmans, Über die Zuordnung von Wellenfunktionen und Eigenwerten zu den einzelnen Elektronen eines Atoms, *Physica* 1 (1934) 104–113.
- [42] S. Okur, U. Salzner, Theoretical modeling of the doping process in polypyrrole by calculating UV/vis absorption spectra of neutral and charged oligomers, *J. Phys. Chem. A* 112 (2008) 11842–11853.

[Article 13]

B. Y. Alfaifi, H. Ullah, S. Alfaifi, A. A. Tahir, T. K. Mallick,
"Photoelectrochemical solar water splitting: From basic principles to advanced
devices." *Veruscript Funct. Nanomater.*, vol. 2, pp. 1-26, Feb. 2018.

Photoelectrochemical solar water splitting: From basic principles to advanced devices

Review

Article history:

Received: 20 September 2017

Accepted: 29 October 2017

Published: 12 February 2018



*Correspondence:

BYA: ba283@exeter.ac.uk

Peer review:

Double blind

Copyright:

© 2018 Alfaifi et al. © This is an open access article distributed under the Creative Commons Attribution License ([CC-BY 4.0](https://creativecommons.org/licenses/by/4.0/)), which permits unrestricted use, distribution, and reproduction in any medium, provided the original work is properly cited and its authors credited.

Keywords:

photoelectrode; metal oxide; water splitting

Citation:

Alfaifi B. Y., Ullah H., Alfaifi S., Tahir A. A., and Mallick T. K. Photoelectrochemical solar water splitting: From basic principles to advanced devices. *Veruscript Functional Nanomaterials*. 2018; 2: #BDJOC3. <https://doi.org/10.22261/FNAN.BDJOC3>

Bandar Y. Alfaifi^{1,*}, Habib Ullah¹, Sulaiman Alfaifi², Asif A. Tahir¹, Tapas K. Mallick¹

¹*Environment and Sustainability Institute (ESI), University of Exeter, Penryn Campus, Penryn, Cornwall, TR10 9FE, United Kingdom*

²*Department of Chemistry, King Abdulaziz University, Jeddah 21589, Saudi Arabia*

Abstract

Photoelectrochemical water splitting (PEC) offers a promising path for sustainable generation of hydrogen fuel. However, improving solar fuel water splitting efficiency facing tremendous challenges, due to the energy loss related to fast recombination of the photogenerated charge carriers, electrode degradation, as well as limited light harvesting. This review focuses on the brief introduction of basic fundamental of PEC water splitting and the concept of various types of water splitting approaches. Numerous engineering strategies for the investigating of the higher efficiency of the PEC, including charge separation, light harvesting, and co-catalysts doping, have been discussed. Moreover, recent remarkable progress and developments for PEC water splitting with some promising materials are discussed. Recent advanced applications of PEC are also reviewed. Finally, the review concludes with a summary and future outlook of this hot field.

Introduction

The traditional sources of energy such as coal, oil and natural gas have supplied the world with energy that drives society for long decades. But the energy consumption around the world is incredibly increased and is estimated to be double by 2050 [1]. Since the fossil fuel resources are limited and concentrated in certain region around the world, while global demand is increasing; subsequently, a secure supply is increasingly challenging to assure [2]. Furthermore, pollution created from fossil fuel plants has significant impact on our health. Moreover, the emissions of greenhouse gas and Carbon dioxide have negative impact on our planet.

Renewable energy resources such as wind, biomass and solar fuel have been investigated for years to help in the replacement of fossil fuels. Extensive research and development are required to produce such a technology that can compete the fossil fuel and commercially available everywhere. However,



the most developed renewable energy sources are based on electricity generation, producing transportable and storable fuel, which remains a challenge.

Among these energy resources, solar energy is considered a primary carrier that may hold potential promise for a sustainable and clean energy future [3]. Solar energy focused on direct conversion of sunlight into chemical fuels in the form of hydrogen gas (H₂) [4]. The advantages and attractiveness of solar water splitting, include sufficient water resources, small reaction potential required (1.23 eV), and zero CO₂ emission [5].

In this review, we are aiming to briefly introduce the basic principles of PEC. An overview of the common used materials that have been investigated for photoelectrochemical water splitting will be presented. In addition, the current state of the technology is discussed. Finally, the review concluded with a summary and future viewpoint in this hot topic of research.

Basic principles of photocatalytic water splitting

Generating Hydrogen fuel directly from sunlight, comes from natural phenomena called natural photosynthesis (NP), exist in plants [6,7], where sunlight is used to convert water and carbon dioxide into oxygen and carbohydrates. The potential technology that converts water into H₂ and O₂ using sunlight for generation of solar fuel is called artificial photosynthesis (AP), which aims to mimic NP using man-made materials [7,8].

The water splitting reactions (see reactions 1–3) is an uphill reaction with a net Gibbs free energy of 238 kJ/mol or 1.23 eV, as shown in Equation (1),



The basic mechanism of photocatalysis water splitting in general is based on the generation of photo-excited charge carriers. Generally, photocatalytic water splitting reaction on semiconductor particles involves three main steps: (1) absorption of light irradiation with energies exceeding the semiconductor bandgap, generate electrons (e⁻) and holes (h⁺) pairs inside the semiconductor particles; (2) the generated electrons and holes are separated followed by migration of these charges to the interface of the semiconductor particles; (iii) surface chemical reactions between these carriers with various compounds (*e.g.*, H₂O); electrons and holes to produce H₂ and O₂, respectively as it shown in Figure 1 [9,10]. Recombination of electrons and holes may also occurs on a very fast timescale without participating in any chemical reactions [5,9,11,12].

General approaches for water splitting

Production of Hydrogen, using water splitting technique mainly fall into three categories; photocatalyst system (PC), photoelectrochemical system (PEC), and photovoltaic-photoelectrochemical system (PV-PEC) [13,14]. In photocatalytic system (PC), which is considered as the simplest, cheapest, and for potential scalable method for water splitting. Photocatalyst which form as powders are dispersed in water for water splitting under light irradiation (Figure 2). Photocatalysts possess the advantage that the water splitting can occur in the homogeneous phase without the need of transparent electrodes and without the need of directional illumination [10]. Whereas, PC have many disadvantages that limit its use for water splitting. (1) Separation of the generated hydrogen and oxygen immediately when formed are required, which will consume additional energy, causing low efficiency of water splitting process. (2) The illumination of PC systems without fast removal of the catalysts will eventually cause a photostationary state, where all forward and backward reactions have identical rates, and no more water splitting can take place. (3) Implementing PC system at high scale still challenging. Due to these limitation, PC system will not be covered in this review.

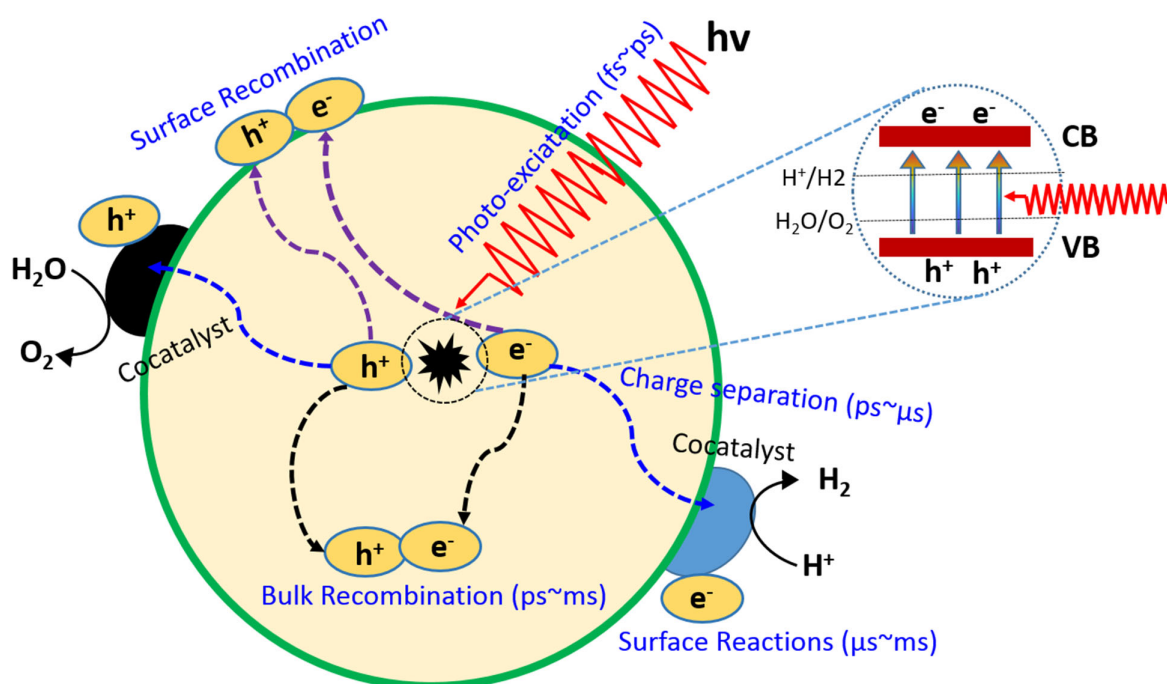


Figure 1. Fundamental principle of photocatalytic water splitting on semiconductor.

Adapted with permission from ref [8]. Copyright 2011 Materials Research Society.

Photoelectrochemical water splitting has been reported for the first time early 1968 by illumination a conductive electrode made from TiO_2 in aqueous solution [15]. The interaction of incident light with TiO_2 , generate electron hole pairs, where the holes oxidize water at the TiO_2 surface to generate oxygen, and the electrons travel to the Pt counter electrode to reduce water to produce hydrogen (Figure 3a)[11–14]. In PEC technique, the photocatalysts initially prepared on conductive substrates as electrodes and additional small bias applied for water splitting.

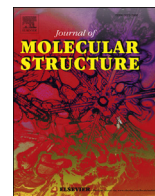
To make this cell, one or both electrodes should be a photoactive semiconductor, where the charge separation forms at the semiconductor/liquid interface (Figure 3b and 3c). When the cell is exposed to sun-light, photogenerated carriers are separated by the space-charge field and the minority charges (holes for an n -type photoanode and electrons for a p -type photocathode) travel to the semiconductor electrode-liquid interface for reaction [17]. Compared to photocatalyst system (PC), PEC have advantage that there is no need for gas separation in PEC systems because the generation of H_2 and O_2 is spatially separated at different electrode sides [17,18]. PEC will be described in this review with focus on different semiconductor materials used to fabricate both photoanode and photocathode.

Photocathode for hydrogen evolution

Water splitting photocathodes are generally p -type semiconductors and must generate the required cathodic current to reduce water to hydrogen and need to have high stability in aqueous environments. The optimal photocathode material, need to have the conduction band edge potential to be more negative than the hydrogen redox potential. Many earlier studies on electrochemical photocathodes mainly focused on p -type silicon and III–V semiconductor such as InP and GaP. Recently, p -type semiconductor including oxides and sulphide have received lots of attention. In this section, the review is focused on various photocathodes materials, which include monometallic and bimetallic oxides, chalcopyrites, silicon, and III–V semiconductors.

[Article 14]

R. Ullah, H. Ullah, S. Bilal, K. Ali, "Oligomeric synthesis and density functional theory of leucoemeraldine base form of polyaniline." *J. Mol. Struc.*, vol. 1127, pp. 734-741, Jan. 2017.



Oligomeric synthesis and density functional theory of leucoemeraldine base form of polyaniline



Rizwan Ullah ^a, Habib Ullah ^{a, b}, Anwar-ul-Haq Ali Shah ^{a, *}, Salma Bilal ^c, Khurshid Ali ^a

^a Institute of Chemical Sciences, University of Peshawar, 25120 Peshawar, Pakistan

^b Environment and Sustainability Institute (ESI), University of Exeter, Penryn Campus, Penryn, Cornwall TR10 9FE, UK

^c National Centre of Excellence in Physical Chemistry, University of Peshawar, 25120 Peshawar, Pakistan

ARTICLE INFO

Article history:

Received 13 May 2016

Received in revised form

1 July 2016

Accepted 6 August 2016

Available online 8 August 2016

Keywords:

PANI LB

CuCl₂

B3LYP/6-31G (d)

IR spectroscopy

HOMO-LUMO

ABSTRACT

Oligomeric synthesis of phenyl-end-capped oligoaniline (4PANI LB) has been carried out through a weak oxidizing agent, CuCl₂, using chemical oxidative polymerization protocol. The sample was characterized by mass spectrometry, UV–vis, IR, and CHN elemental analysis. The experimental results are counter-checked with the aid of Quantum mechanical calculations such as density functional theory (DFT). DFT at B3LYP/6-31 G (d) level of theory was used for the geometric and electronic properties simulations which also confirm the existence of 4PANI LB. Excellent correlation is observed between the experiment and theory, particularly in the UV–vis spectra which conclude the formation of tetramer (fully reduced form) 4PANI LB (C₂₄H_{20.06}N_{4.07}). Electronic properties such as Ionization Potential (I.P), Electron Affinities (E.A), the coefficient of highest occupied molecular orbital (HOMO), the coefficient of lowest unoccupied molecular orbital (LUMO) of 4PANI LB were evaluated at the above-mentioned level of theory.

© 2016 Elsevier B.V. All rights reserved.

1. Introduction

Conducting polymers (CPs) have recently received considerable attention due to their wide range of applications in solar cells, lightweight batteries, sensors, actuators, corrosion protection, light emitting diodes, surgical instruments, and mercury removal from waste water etc [1–3]. CPs such as polypyrrole (PPy), polythiophene (PT), polyaniline (PANI), polyacetylene (PA) and redox polymers such as poly(*o*-phenylenediamine) (POPD) and Poly (*o*-aminophenol) [4] have extensively been explored both experimentally and theoretically after the discovery of PA by Shirakawa et al. in 1975 [5]. Among CPs, PANI is of great interest mainly due to its ease of synthesis, easy doping de-doping ability, environmentally friendly and of low-cost monomer [6]. PANI exists in four different fundamental oxidation states; leucoemeraldine base (PANI LB), emeraldine base (PANI EB), pernigraniline base (PANI PNB), and the conducting emeraldine salt form (PANI ES). The interconversion of all these states of PANI is shown in Scheme 1 [7]. Neutral PANIs have the general formula $[(-B-NH-B-NH-)]_y(-B-N=Q=N-)_x$, where B and Q represent benzenoid and quinoid units, respectively. In this formula, y is the oxidation number and

can be varied from 1, 0.5, and 0 while moving from completely reduced (PANI LB) to semi-oxidized (PANI EB) and fully oxidized (PANI PNB) respectively.

Conventional methods such as oxidative polymerization, usually give high yields for the bulk synthesis of PANI and its oligomers, where aniline (ANI) monomer are oxidized into PANI in few hours under strong acidic medium/solution [8]. A number of synthetic techniques are reported regarding the oligomeric state of PANI for a wide range of applications [9,10].

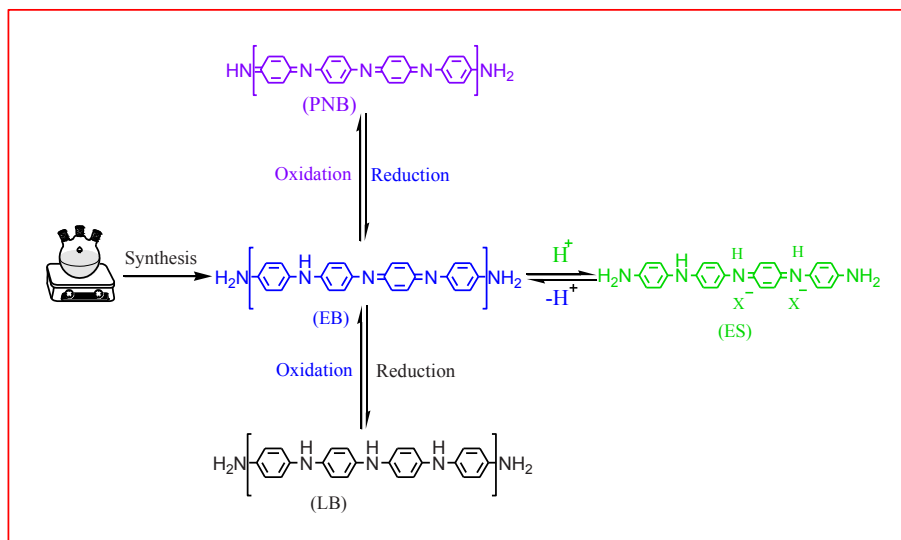
The oxidized oligomeric states (highly reactive oligomers) of phenyl-capped di-aniline and tetra-aniline are also reported through simple chemical polymerization method, further, their polaronic and bipolaronic nature were confirmed by EPR, IR and XPS [11]. In this connection a similar study from Zotti and co-workers is also reported, where a linear relation between 1/n (n = 1, 2, 4) and optical band gap of phenyl-N-capped aniline oligomers is found [12].

An interesting report in the synthetic roots of aniline oligomers was proposed by Wei and co-workers [13] who synthesized aniline oligomers from three amine segments up to eight units, without using any external oxidizing agent. Aniline trimers (high oxidation state) cause oxidation of ANI monomers.

Synthesis of ANI oligomers in the presence of a catalyst and the acidic reaction medium is also one of the prominent methods of chemical synthesis [14] including oxidative and inverse emulsion

* Corresponding author.

E-mail address: anwarulhaqalishah@upesh.edu.pk (A.-u.-H.A. Shah).



Scheme 1. Synthesis of PANI and its different oxidation states.

polymerization. Oxidative polymerization of ANI oligomers is extensively investigated [15] using ammonium persulfate (APS) as an oxidizing agent in the presence of hydrochloric acid. Different oxidizing agents and supporting electrolytes (medium) are reported for the chemical oxidative polymerization [10,16] such as KIO_3 , FeCl_3 (oxidizing agent) and HCl , CHCl_3 (reaction medium). Chemical synthetic protocol generally involves: (a) rapid mixing [17] in which reaction kinetics are modified in such a way to use all reactants during the initial stage of synthesis; (b) dilute polymerization [18] where the formation of agglomerates is hindered by reducing the concentration of both the oxidant and monomer; (c) interfacial polymerization [19] where the reactants are separated into immiscible aqueous and organic phases, and the polymerization reaction proceeds between the interfaces of two phases; and (d) avoiding mechanical agitation [20] where the reaction is carried out at high temperature, responsible for the growth process and hinders the formation of granular morphology. Besides synthesis, the crystalline arrangement of both PANI and its different oligomers are determined through simply subjecting a mixture of *p*-amino diphenylamine (ANI dimer) and ANI, followed by fractionation [21].

The conductivity of conducting polymer system is related to molecular size. The electronic cloud is delocalized in the long conjugated system resulting high conductivity; however, increasing the molecular size beyond a certain level may cause distortion of the molecular chain symmetry which adversely leads to the decrease in conductivity. High level of conductivity is obtained with a tetramer of PANI [6,22–25]. Most of the applications of PANI are reported for the tetramer system such as PANI (4LEB) was as cathode material [26]. Similarly, partial oxidation of 4 PANI LB leads to the formation of EB-PANI which on 50% doping show the highest conductivity and has many industrial applications. The molecular size, level of doping, oxidation level and percentage of crystallinity play a significant role to achieve high conductivity which is easily possible with tetramer PANI system [25,27–29].

The relatively weak photo-induced absorption capacity of 4PANILB (EB, LEB, and PNB) makes it an appropriate medium for erasable optical information and in non-linear optics [26,30–32].

Udeh et al. [33] have presented various synthetic routes and strategies for the synthesis and modification of tetra (aniline)s oligomers in their review article. A theoretical investigation has been shown to support the experimental data regarding the synthesis of tetra (aniline)s, tri and di-block structures. The usefulness

of aniline oligomers and their possible applications in various technological fields have been highlighted.

PANI can be converted from almost insulating leucoemeraldine form (LB) to highly conducting emeraldine salt form (ES) which enables it to be used in digital memory devices [26]. Applications of short and medium size ANI oligomers for the protection of steel corrosion were recently reported by Grgur and co-workers [10,16]. The oligomers were electrochemically coated on mild steel electrode for the study corrosion protection mechanism. They found a slight change in the structure of ANI oligomers during this process of corrosion. The use of *para*-toluenesulfonic acid (*p*-TSA) as a soft template and dopant for the synthesis of ANI oligomers have been reported in the literature [34]. APS was used as an oxidizing agent via *in situ* self-assembly method. They reported the effect of *p*-TSA and ANI molar ratio on the thermal stability and magnetization values of the oligomers. Ding et al. [26] have used, FeCl_3 , cerium sulfate, and high concentration of CuCl_2 to control the diameter of PANI nanofibers. Ozkazanc et al. [35] have used ammonium persulfate as an oxidizing agent in addition to CuCl_2 as a dopant. PANI has been synthesized/polymerized in different states extensively in the presence of strong oxidizing agents at favorable condition by various groups as we discussed (*vide supra*) [36–40]. However very less is known about the synthesis of PANI oligomers using weak oxidizing agents.

In this paper we report on the oligomerization of phenyl-ended capped oligoaniline (4PANILB) from ANI under a nitrogen atmosphere, using CuCl_2 , as a weak oxidizing agent in the presence of *p*-TSA. The study of these small oligomers is important because these oligomers have different characteristics properties especially from that of infinite chains. Sometimes the bulkiness of a polymer decreases its valuable traits such as conductivity, crystallinity, stability and solubility [41–43] etc. A cost effective chemical method for the synthesis of different oligomers is presented. The experimental data is validated and correlated the data with theoretical findings.

2. Experimental

2.1. Materials

ANI monomer (Analytical grade) was purchased (Sigma-Aldrich) and distilled twice at reduced pressure prior to use. *p*-TSA

(Synthesis grade from Scharlau) and anhydrous copper chloride (97% from Sigma-Aldrich) were used as received.

2.2. Procedure

A solution of 0.2 M p-TSA and 0.2 M ANI was prepared in de-ionized water at a pH 4.80. 10 mL of this solution was cooled in a refrigerator for 15–20 min and then 10 mL of pre-cooled (5–10 °C) 0.01 M copper chloride solution was added dropwise (2–3 min) to the ANI and p-TSA solution. The reaction was carried out under a nitrogen atmosphere at room temperature (15–20 °C) by constant stirring for 24 h. The final pH of the reaction mixture was 3.7. The crude precipitate was centrifuged followed by washing with de-ionized water and acetone, to remove un-reacted materials. The product obtained was dried for 24 h at room temperature in a vacuum oven and labeled as PANI LB. The oxidant: monomer ratios; 0.05, 0.25, 0.50, 0.75, 1 and 1.25 were evaluated for the yield of oligomers. The same procedure at high oxidant: monomer ratio (15) leads to the production of polymeric emeraldine base form of PANI as discussed in the literature [44].

2.3. Characterization

IR spectra were obtained, using Perkin Elmer spectrophotometer series 400 IR, in the region from 4000 to 400 cm^{-1} with a resolution of 4 cm^{-1} . The spectra were collected in ATR mode with 10 numbers of scans for all samples. A Shimadzu UV–Vis 1700 spectrophotometer was used to record the UV–Vis spectra. The spectra were recorded in the spectral region ranging from 200 to 800 nm. Elemental analysis was performed in Pakistan Council of Scientific and Industrial Research (PCSIR) Laboratory Peshawar, Pakistan by using Elementar CHNS-0 elemental analyzer Germany.

3. Computational methodology

All DFT calculations were performed at Becke three-parameter (exchange), Lee, Yang, and Parr (LYP) both local and nonlocal (correlation; DFT) (B3LYP) [45] with 6-31G (d) [46–54] basis set, using *Gaussian 09* [55]. Results were visualized by using *GaussView* [56] and *Gabedit* [57]. The geometries of all PANI LB from monomer up to six repeating units labeled as, 1PANI LB, 2PANI LB, 3PANI LB, 4PANI LB, 5PANI LB, and 6PANI LB were optimized. Optimization was obtained by gradient minimization at the above-mentioned level of theory without any symmetry constraints. This was further confirmed when the stationary point was located [55,56]. DFT is one of the suitable approaches to study short, medium, and long π -conjugated system without spin contamination [7,58–61]. Therefore, DFT at B3LYP/6-31G (d) level was employed for our target species. The ionization potential (IP), electron affinity (EA), highest occupied molecular orbital (HOMO), lowest unoccupied molecular orbital (LUMO), and band gap calculations were performed on these optimized structures. Frequencies were scaled with a common scaling factor 0.9613 [62], to better correlate with the experimental one. The assignments of frequencies were manually performed, using *GaussView*. The band gap ($\pi \rightarrow \pi^*$) was estimated from the difference of HOMO and LUMO orbital energies. As we discussed earlier, the negative of HOMO is estimated as IP [63,64] whereas the negative of LUMO is estimated as EA [45,65]. The UV–vis spectra of PANI LB from monomer up to 6 repeating

units were simulated at TD-DFT using B3LYP/6-31G (d) level of theory.

4. Results and discussion

4.1. Elemental analysis

Elemental analysis of PANI LB sample is listed in Table 1 in which the percentage of C, H and N were found to be 76.87, 5.64 and 15.20, corresponds to PANI LB. Comparative analysis of Table 1, manifests that hydrogen is in more percentage than expectation, which may be due to trace amount of moisture [66]. Moreover, the percentage of carbon is also less than expected due to the incomplete combustion. However, the C/N ratios are close to the expected value 6.0 for PANI LB, the $\text{C}_{24}\text{H}_{20.06}\text{N}_{4.07}(\text{H}_2\text{O})_{0.5}$ (empirical formula) of our sample (*vide infra*), represented as 4PANI LB.

4.2. Mass spectral analysis

Elemental analysis delivers information about the empirical formula; therefore, to determine the molecular formula, the mass spectral analysis was performed. The high-resolution electron spray ionization mass spectra (HR-ESI-MS) of PANI LB are shown in Fig. S1. The spectrogram indicates that the molecular mass of the resulting PANI product is 364 which is in agreement with the theoretically calculated value of the molecular mass of PANI LB with four repeating units (*vide supra*). This data is in close agreement with the earlier reported work by Dolan et al. [15] for the tetramer of aniline. The highest peak at ca. $m/z = 364.1$ is assigned to the four benzenoid units of PANI LB (here called 4PANI LB) having molecular formula $\text{C}_{24}\text{H}_{20}\text{N}_4$. The mass spectra of 4PANI LB can be divided into seven major peaks, which are further analyzed to accord for the structure of fragment (Table 2). The peak at 288.1 is assigned to $\text{C}_{18}\text{H}_{16}\text{N}_4$, obtained by the loss of phenyl ring from $\text{C}_{24}\text{H}_{20}\text{N}_4$ [15] and 276.1 is for the $\text{C}_{18}\text{H}_{16}\text{N}_3$ group. The peak at ca. 260.1 is for the $\text{C}_{18}\text{H}_{16}\text{N}_2$, obtained by the loss of an NH_2 from 276.1. The peak at 185 is for the dimer with a formula of $\text{C}_{12}\text{H}_{12}\text{N}_2$ and the last peak at ca. 93.1 is attributed to the unreacted aniline radical cation (see Table 2). Since the reaction was carried out by using a weak oxidizing agent (CuCl_2), therefore, the formation of 4PANI LB is attributed to the low oxidation potential of CuCl_2 .

4.3. pH measurement of the sample

The percent yield of the product and pH of the solution as a function of oxidant/monomer ratio is shown in Table 3. With the increase of oxidant to monomer ratio, pH of the reaction mixture decreases (see Table 3). While, on the other hand, percent yield (product obtained) increases with the increase of oxidant/monomer ratio, which is due to the increase in oxidation of CuCl_2 with the increase in its molar concentration [67].

4.4. Geometric structure

The DFT optimized geometries of nPANI LB ($n = 1, 2 \dots 6$) end capped with NH_2 are given in Fig. 1 (one end of all oligomers are capped with NH_2). Our main focus is on the 4PANI LB where neighboring rings in the optimized geometry are slightly bent away from planarity. The calculated bond distances of C–C, C–N, C–H,

Table 1
Elemental analysis of 4PANI LB.

Sample	Oxi/Mon	%Yield	% C	% H	% N	Composition	C/N ratio
PANI LB	1	23	76.87	5.64	15.20	$\text{C}_{24}\text{H}_{20.06}\text{N}_{4.07}(\text{H}_2\text{O})_{0.5}$	5.89

Table 2
Proposed structures for the main series of oligomers with reference to Fig S1.

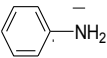
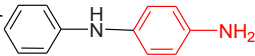
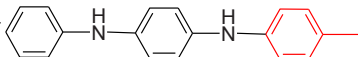
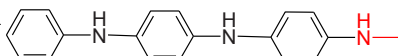
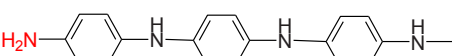
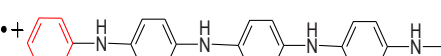
Peak position	Proposed structure
93	
185	• + 
260	• + 
276	• + 
288	
364.1	• + 

Table 3
Oxidant to monomer ratio and mass yield along with initial and final pH.

Oxi/Mon	Initial pH	Final pH	% Yield
0.05	4.72	4.58	9.18
0.25	4.85	4.60	15.03
0.50	4.83	4.47	18.36
0.75	4.70	4.37	19.12
1.0	4.75	4.23	20.02
1.25	4.71	4.10	20.26

and N–H are about 1.39, 1.40, 1.08, and 1.01 Å, respectively. The bridging bond angles between phenyl rings are found to be 128.63°, which is very close to the experiment and the earlier simulations [52,53] while inner ring angle was about 121.20°. Lim et al. have shown that conformation of PANI obtained at B3LYP is more stable than the other level of theories such as RHF/6-31G and is probably due to the inclusion of electron correlation in the B3LYP [23]. Based on the structural analysis discussed above, it may be proposed that the most stable B3LYP conformations were mainly achieved through the inclusion of electron correlation in the geometry optimization. All of the optimized geometric structures of nPANI LB ($n = 1, 2 \dots 6$) were twisted.

4.5. IR spectroscopy

The percent yield provided in Table 3 corresponds to the 4PANI LB. The yield is less than 20% which is what we can expect from the use of a weak oxidizing agent (CuCl_2). The FTIR spectrum of the initial products (Fig. 2) show intense peaks in the range of 3361–3445 cm^{-1} which are assigned to the NH stretching mode of nucleated aniline [68–70], thus the majority of the product is supposed to be un-reacted nucleated aniline along with 4PANI LB.

The comparison of spectra of 4PANI LB and 4PANI EB have been done to determine the difference between these two forms. The synthesized sample (4PANI LB) was further investigated by IR spectroscopy; comparative IR spectra of pure 4PANI EB and 4PANI LB samples are shown in Fig. 3. The EB (tetramer) form of PANI has usually intense peaks at ca. 1575–1600 and 1490–1500 cm^{-1} (which are responsible for the quinoid and benzenoid units, respectively [71]). In our case (4PANI LB) the peak for a quinoid unit at 1585 cm^{-1} vanishes, which is very prominent in (PANI EB) of PANI. However, the peak for a benzenoid unit at 1493 cm^{-1} in (PANI EB) is shifted towards 1469 cm^{-1} in 4PANI LB confirming the

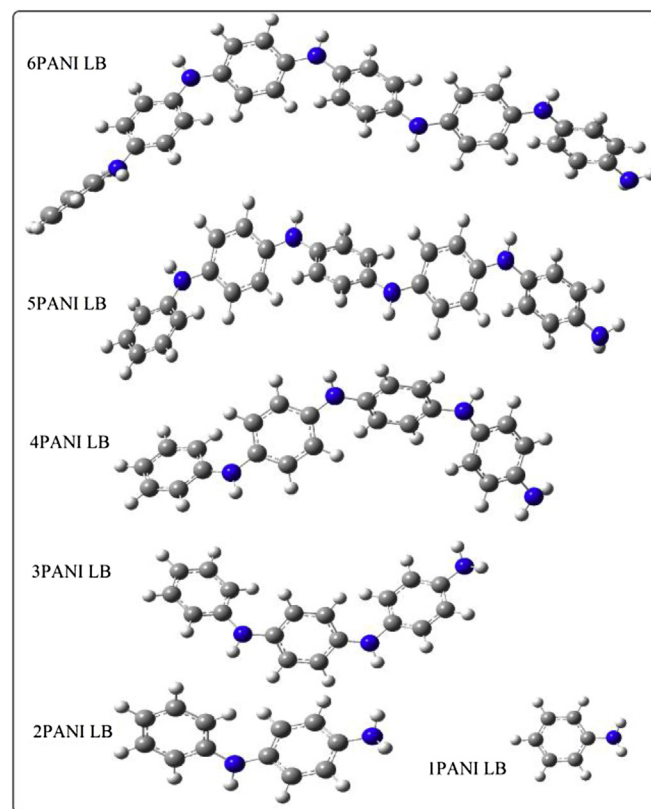


Fig. 1. Optimized Geometric Structure of nPANI LB (where $n = 1, 2, \dots, 6$).

leucoemeraldine. The band peak at ca. 1209 cm^{-1} is because of C–N stretching of the 4PANI LB [2], and the C–H out of plane bending give rise to 866 cm^{-1} band peak [72]. Another intense peak in 4PANI LB at 1290 cm^{-1} , indicating the presence of a secondary amine [1]. Comparative analyses of both spectra lead us to conclude that the synthesized product is the fully reduced form of PANI LB, which is also in agreement with the mass spectral and elemental analysis (*vide supra*).

Furthermore, vibrational spectroscopy is elaborated with the aid of simulated IR spectra of 4PANI LB, at DFT with B3LYP/6-31G (d) level of theory. Comparative simulated and observed IR spectra of 4PANI LB are presented in Fig. 4, whereas detailed simulated IR spectra of PANI LB from monomer up to six repeating units are depicted in Fig. 5. For convenience, IR spectral discussion is divided into 12 major band peaks (shown in Table 3 along with their approximate assignments). The calculated IR spectrum of 4PANI LB has two prominent band peaks in the functional group region at ca. 3476 and 3056 cm^{-1} , for N–H and C–H stretching, respectively. The calculated 3476 cm^{-1} band peak has a large difference (120 cm^{-1}) from its counterpart 3356 cm^{-1} of the observed one. This large difference (3476 cm^{-1}) can be attributed to the missing solvent effects [73–80] in our calculations of an isolated molecule of 4PANI LB, and the underestimation of anharmonic effects for the strongly anharmonic NH vibration [81,82].

This has already been discussed in the literature by us and others [73–80]. On the other hand, calculated 3056 cm^{-1} shows nice correlation with the experimental 3052 cm^{-1} . The calculated peak at 1600 cm^{-1} can be assigned to C=C and C–H wagging, and correlates with the experimental 1593 cm^{-1} peak. The calculated 1505 cm^{-1} band peak is the most prominent peak of the fingerprint region which is 36 cm^{-1} greater in frequency compared, to the experimental 1469 cm^{-1} . This band peak has intense C=C, C–N

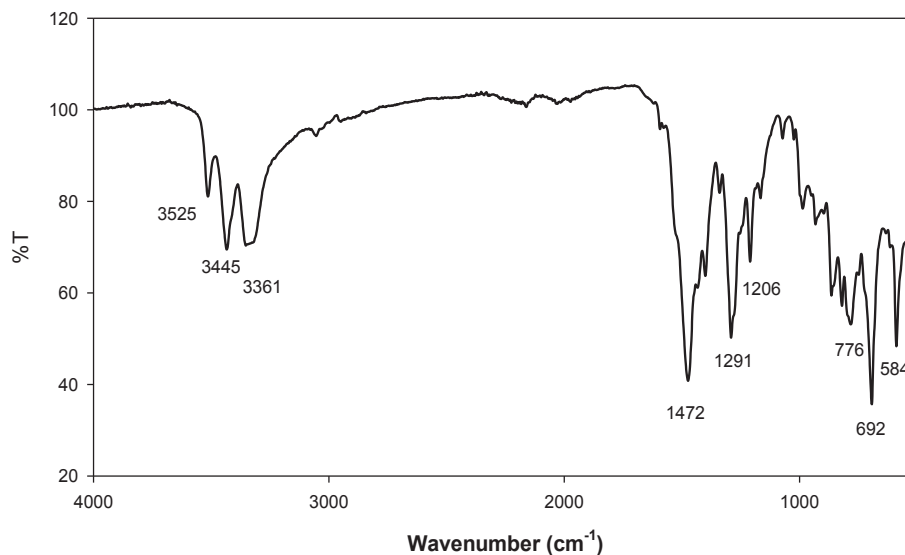


Fig. 2. FTIR spectrum of the initial product before washing.

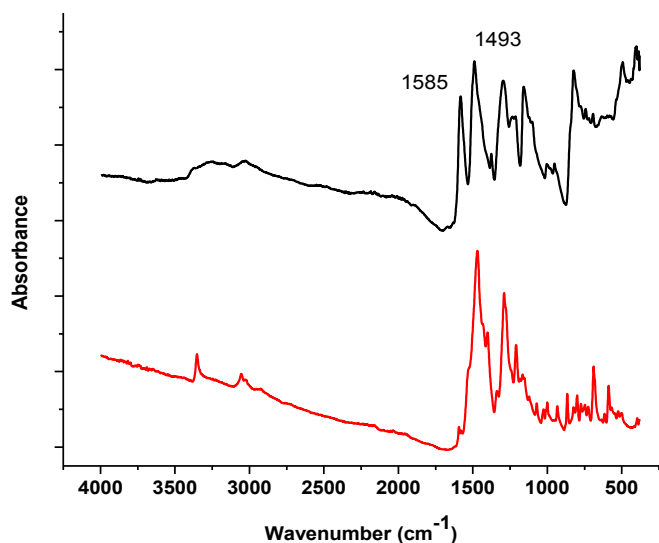


Fig. 3. Experimental IR spectra of PANI EB (black) and CuCl_2 doped (red) of 4PANI LB.

stretching and C–H, N–H wagging component. The calculated 1291, 1230, 1168 and 855 cm^{-1} band peaks show nice correlation with the experimental 1290, 1209, 1166, and 866 cm^{-1} , respectively. The last two prominent band peaks in the calculated IR spectra, 807 and 694 cm^{-1} correspond to out of plane bending and are very close to the observed bands at 804 and 689 cm^{-1} . Analysis of data in Table 4 points that both theory and experiment correlate each other quite well, with minor differences.

4.6. UV–vis spectroscopy

UV–vis spectra of PANI LB, PANI EB are analyzed to further confirm that the oligomer synthesized is PANI LB (Fig. S2). PANI EB shows two strong absorption bands at 320–340 and 600–660 nm, corresponding to the benzenoid and quinoid units of PANI, respectively [83]. UV–vis spectra of pure EB have two peaks at 629 and 324 nm, which strongly validate the reported literature. In the case of our synthesized sample i.e., labeled as PANI LB, the quinoid

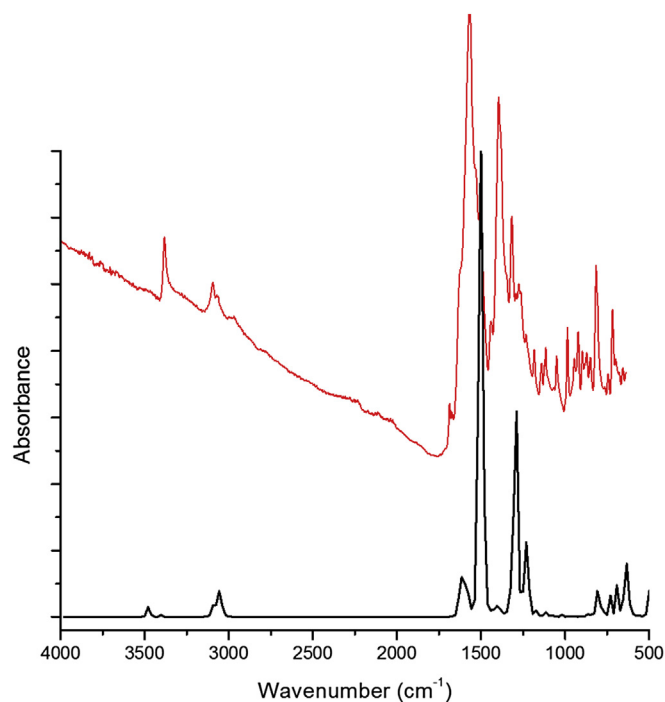


Fig. 4. Experimental (red) and simulated (black) IR spectra of 4PANI LB.

unit was absent in its UV–vis spectrum, confirming the fully reduced, PANI LB. The information provided by the UV–vis analysis also corroborates the IR spectra and other characterizations (*vide supra*).

UV–vis spectrum of PANI LB has a prominent absorption peak at ca. 336 nm. It is very difficult to determine the oligomeric size of the PANI LB from the UV–vis spectral results. However, we carried out TD-DFT calculations at various level of theories such as B3LYP/6-31G, B3LYP/6-31G (d), B3LYP/6-31G (d,p), B3LYP/6-31 + G (d,p), both in the gas phase and chloroform media, for monomer up to six repeating units (see S3–S8 of the Supporting Information). We correlated all these spectra with the observed one and finally concluded that UV–vis spectra (Fig. S9) of four repeating units

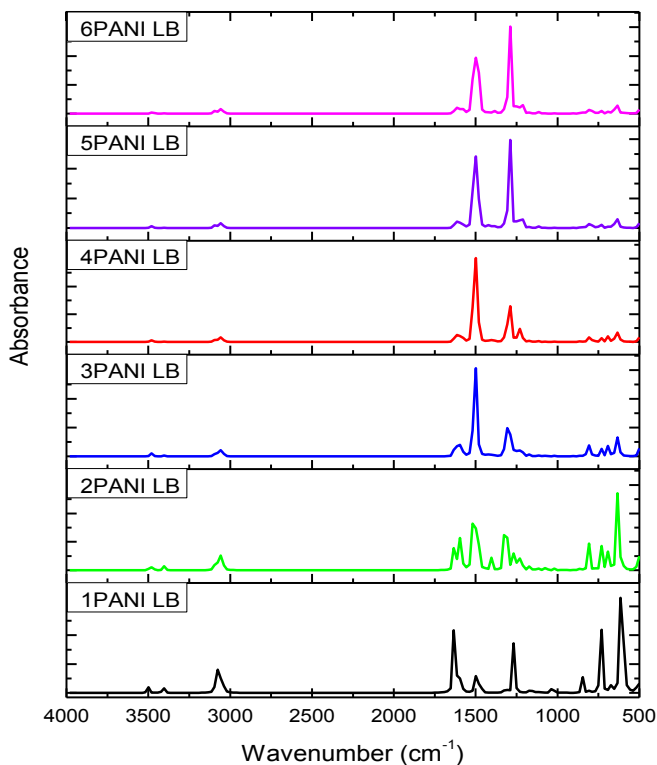


Fig. 5. Simulated scaled IR spectra of nPANI LB (where $n = 1, 2, \dots, 6$).

Table 4
Experimental and calculated frequencies (in cm^{-1}) of 4PANI LB.

S.no	Experimental IR	Simulated IR	Approximate assignment
1	3356	3476	ν N–H
2	3052	3056	ν C–H
3	1593	1600	ν C=C; Wag C–H
4	1469	1504	ν C=C, C–N; Wag C–H, N–H
5	1290	1291	ν C=C, C–N; Wag C–H
6	1209	1230	ν C=C, C–N; Wag C–H, N–H
7	1166	1168	Cis C–H
8	866	855	γ C–H; Ring breathing
9	804	807/730	γ C–H
10	689	694	γ C–H
11	588	640	γ N–H
12	496	497	γ C–H, N–H

Note: ν stretching; Wag: Wagging; cis: scissoring; γ : Out of plane bending.

(4PAN LB) at TD-B3LYP/6-31G (d), correlates with the experimental spectrum. Three different optical absorptions band peaks of 4PANI LB, both in the CHCl_3 solvent and gas phase are summarized in Table 5 along with their oscillator strength, electronic excitation, and experimental peaks as well. There are no allowed absorptions in the visible range for both the observed and calculated spectra. The first peak in the simulated UV–vis with high oscillator strengths occurs at 338 nm in the vacuum and 346 nm in the CHCl_3 . This maximum absorption peak (λ_{max}) is 2 nm (gas phase) and 10 nm (solution phase) greater in wavelength from that of the experimental λ_{max} (336 nm). As shown in Table 5, the absorption is due to the $\pi \rightarrow \pi^*$ transition ($S_0 \rightarrow S_1$), excitation electron from 97 to 98 molecular orbital (*vide infra*).

Chloroform solvent effect is predicted by the polarized continuum model (PCM) [84]. In chloroform, the excitation energy of all the three peaks decreases compared to gas phase however, oscillator strength increases. This indicates that π -conjugation increases in solvent compared to the gas phase. The second absorption in the

Table 5
First three vertical allowed electronic excitations in 4PANI LB.

Peak	Excitation energy (nm)		Oscillator strength		Electronic transition	
	CHCl_3	Vacuum	CHCl_3	Vacuum	CHCl_3	Vacuum
1	336	346	0.90	0.75	H \rightarrow L	H \rightarrow L
2	279	293	0.20	0.11	H \rightarrow L ₅	H ₋₁ \rightarrow L ₂
3	273	256	0.19	0.17	L ₋₁ \rightarrow L ₅	H ₋₁ \rightarrow L ₅

experimental UV–Vis is at 279 nm and shows a strong correlation with both gas (280 nm) and solution phase (293 nm) theoretical bands.

This absorption is due to the electronic excitation from HOMO-1 to LUMO+3 in gas spectra, while in solvent medium this excitation is from HOMO to LUMO+5. Another, high energy absorption appeared only in the theoretical spectra ca. 254 nm (gas phase) and 256 nm (CHCl_3) can be assigned to the observed 273 nm. This absorption is because of the electronic transition of molecular orbital, HOMO-1 to LUMO+5. The 2nd and 3rd absorption peaks are not cleared in the experimental UV–vis spectra; this is also evident from the ΔSCF calculations, huge gap difference between the ground and excited orbitals (see Table 5 and Fig. S10).

4.7. Ionization potential, electron affinities, and band gap analysis

The electronic properties of nPANI LB oligomers are calculated at B3LYP/6-31 G (d) level of theory. The negative orbital energies of DFT do not give well accurate IP and EA at B3LYP/6-31 G (d) level of theory, but the deviation is less than 1 eV. Since the error is systematic, orbital energies can be used to investigate trends reliably. Furthermore, pure DFT methods underestimate excitation energies, underestimate band gaps, overestimate conjugation, overestimate defect sizes and this error gets larger with increasing chain length. B3LYP is quite accurate for our system (medium sized system) [85,86], implementation of hybrid functional (B3LYP), which accounts for the effects of self-interaction, is used to achieve better correlation.

The IP and EA were obtained from the negative of the DFT orbital (HOMO and LUMO) energy using Koopman's theorem with typical exchange-correlation functional. The IP and EA of both of PANI LB from monomer up to infinite repeating units are listed in Table 6. Polymer IP and EA are obtained by extrapolation of oligomers data, using second order polynomial fit equation. The data of Table 6 reveal that all of the IPs from monomers up to infinite repeating units is positive, whereas some of the EA values are in negative. The negative EA means that this oligomeric state is unbound. This trend exists in the monomer, diphenylamine, and triphenylamine as depicted in Table 6. IP decreases and EA increases (Table 6) with the increasing of repeating units, this change is due to increasing of π -electron conjugation (delocalization) along the oligomeric backbone of nPANI LB. The high π -electron density with chain length elongation leads to smaller band gap as shown in Fig. 6, and a consequence of numbers of delocalized π -molecular bonding orbitals. The band gap is obtained from the difference of the orbital energies (valence and conduction band). Our estimated band gap of PANI LB is 3.57 eV which has good correlation with earlier reports of both calculated (4.01 eV) and experimental work (3.8–4.0 eV) [52,53,87]. This also concludes the hybrid DFT methods are more accurate than pure DFT methods. Generally, in conducting copolymer, the extent of conjugation increases with chain length elongation of oligomers. But on the other hand, the planarity of the polymer decreases due to steric contribution. Similarly, an increase in the number of atoms decreases the electron density of HOMO and LUMO thereby preventing delocalization over the entire frame.

Table 6
IP, EA, and Band Gap of nPANI LB, where n is the number of repeating units.

n	IP (eV)	EA (eV)	Band gap (eV)
1	5.39	−0.25	5.64
2	4.64	−0.05	4.69
3	4.34	−0.008	4.34
4	4.21	0.06	4.15
5	4.13	0.10	4.03
6	4.09	0.13	3.96
∞	3.80	0.21	3.57

The conductivity depends on planarity of the system and band gap and polymers having smaller band gap and planer geometry are considered to show good conductivities.

A band gap of an extended periodic system is defined as the difference between the lowest energy in the conduction band and the highest energy in the valence band. Band gaps are parameters of considerable importance for the determination of possible applications of conducting polymers. In this study, we investigated finite size systems such as monomer and oligomers of PANI of different sizes. The term band gap is used here also to represent a property of a finite system that converges to infinite band structure when the size of the oligomer increases. The word “gap” also indicates a difference between electronic energy levels. These can either be observable energy gaps or some type of calculated molecular orbital energy gap such as the difference between HOMO and LUMO.

The HOMO, LUMO contours and molecular electrostatic potential (MEP) plots of nPANI LB (n = 1, 2 ... 6) are estimated by using B3LYP/6-31G (d) level of theory are given in Fig S11 and S12 of the supplementary material. The HOMO and LUMO of monomer, diphenylamine and triphenylamine are found to extend on all carbons, hydrogens, and nitrogens and involve delocalization over the entire molecular framework. Where in larger oligomers (n = 4, 5, 6) electron density in the HOMO and LUMO is not spread over the entire skeleton, which indicates decreases of delocalization. The HOMO and LUMO energies of PANI LB, from monomer up to infinite repeating units, are shown in Fig. 6.

The details of extrapolating oligomer data plot up to polymer are given in the Supporting information (see S13–S18). With increasing conjugation, the energy of HOMO increases, whereas the energy of LUMO decreases, and this causes a decrease in the band gap (*vide supra*). The HOMO–LUMO energy differences of 4PANI LB is 4.15 eV, and this corresponds to $\pi \rightarrow \pi^*$ transition energies which are also close to the λ_{\max} (3.67 eV or 338 nm) of the Δ SCF results. Lim et al. reported 4.0 eV $\pi \rightarrow \pi^*$ transition of leucoemeraldine base

and 2.0 eV Peirls gap transition of pernigraniline base on the basis of DFT calculations to investigate the geometric and electronic structures of various neutral aniline oligomers.

5. Conclusion

An oxidative oligomerization of aniline (ANI) for the synthesis of phenyl-end-capped oligoaniline is achieved through CuCl_2 as an oxidant with the aid of density functional theory (DFT) calculations. Chemical oxidative polymerization of ANI was carried out at room temperature under nitrogen atmosphere for 24 h. The prepared sample was characterized by mass spectrometry, UV–vis, IR, and CHN elemental analysis. Both spectroscopic and elemental analyses indicate the formation of tetramer (fully reduced form of PANI) up to four repeating units, 4PANI LB ($\text{C}_{24}\text{H}_{20.06}\text{N}_{4.07}$). DFT at hybrid functional was used for the geometric and electronic properties simulations of 4PANI LB, to confirm its oligomeric structure. Good correlation between the experiment and theory is observed in the UV–vis spectra and with minor exceptions in case of vibrational frequencies. All calculated vibrational bands of 4PANI LB were scaled with a common scaling factor of 0.963. Spectroscopic data (IR, UV–vis spectral analyses) for 4PANI LB is also compared with that of 4PANI EB which confirms the presence of 4PANI LB.

Acknowledgements

The authors highly acknowledge Higher Education Commission Islamabad for financial support under research grant # 20-3111/NRPU/R&D/HEC/13.

Appendix A. Supplementary data

Supplementary data related to this article can be found at <http://dx.doi.org/10.1016/j.molstruc.2016.08.009>.

References

- [1] S. Sathiyarayanan, V. Karpakam, K. Kamaraj, S. Muthukrishnan, G. Venkatachari, Surf. Coat. Technol. 204 (2010) 1426–1431.
- [2] Y. Zhang, Q. Li, L. Sun, R. Tang, J. Zhai, J. Hazard. Mater. 175 (2010) 404–409.
- [3] K. Naoi, H. Sakai, S. Ogano, T. Osaka, J. Power Sour. 20 (1987) 237–242.
- [4] H. Ullah, A.A. Shah, K. Ayub, S. Bilal, J. Phys. Chem. C 117 (2013) 4069–4078.
- [5] H. Shirakawa, E.J. Louis, A.G. MacDiarmid, C.K. Chiang, A.J. Heeger, J. Chem. Soc. Chem. Commun. (1977) 578–580.
- [6] A.J. Heeger, Angew. Chem. Inter. Ed. 40 (2001) 2591–2611.
- [7] H. Ullah, A.A. Shah, S. Bilal, K. Ayub, J. Phys. Chem. C 117 (2013) 23701–23711.
- [8] E.T. Kang, K.G. Neoh, K.L. Tan, Prog. Polym. Sci. 23 (1998) 277–324.
- [9] M.T. Greiner, M. Festin, P. Kruse, J. Phys. Chem. C 112 (2008) 18991–19004.
- [10] M.R. Gizdavic-Nikolaidis, J. Bennett, Z. Zujovic, S. Swift, G.A. Bowmaker, Synth. Met. 162 (2012) 1114–1119.
- [11] D. Rodrigue, M. Domingue, J. Riga, J. Verbist, Synth. Met. 57 (1993) 4802–4806.
- [12] G. D’Aprano, M. Leclerc, G. Zotti, Synth. Met. 82 (1996) 59–61.
- [13] Y. Wei, C. Yang, G. Wei, G. Feng, Synth. Met. 84 (1997) 289–291.
- [14] E. Rebourt, J. Joule, A. Monkman, Synth. Met. 84 (1997) 65–66.
- [15] A.R. Dolan, T.D. Wood, Synth. Met. 143 (2004) 243–250.
- [16] B.N. Grgur, Synth. Met. 187 (2014) 57–60.
- [17] K. Gupta, P.C. Jana, A.K. Meikap, Synth. Met. 160 (2010) 1566–1573.
- [18] K. Gupta, G. Chakraborty, P.C. Jana, A.K. Meikap, Solid State Commun. 151 (2011) 573–578.
- [19] Y. Li, B. Ying, L. Hong, M. Yang, Synth. Met. 160 (2010) 455–461.
- [20] J. Li, X. Tang, H. Li, Y. Yan, Q. Zhang, Synth. Met. 160 (2010) 1153–1158.
- [21] F. Lux, E. Samuelsen, E. Kang, Synth. Met. 69 (1995) 167–169.
- [22] V. Jousseume, M. Morsli, A. Bonnet, S. Lefrant, J. Appl. Polym. Sci. 67 (1998) 1209–1214.
- [23] A. Malinauskas, R. Holze, J. Appl. Polym. Sci. 73 (1999) 287–294.
- [24] L. Liang, J. Liu, J.C.F. Windisch, G.J. Exarhos, Y. Lin, Angew. Chem. Inter. Ed. 41 (2002) 3665–3668.
- [25] A.G. MacDiarmid, Synth. Met. 84 (1997) 27–34.
- [26] H. Ding, M. Wan, Y. Wei, Adv. Mater. 19 (2007) 465–469.
- [27] S. Bhadra, S. Chattopadhyay, N.K. Singha, D. Khastgir, J. Appl. Polym. Sci. 108 (2008) 57–64.
- [28] Z. Wei, M. Wan, Adv. Mater. 14 (2002) 1314–1317.

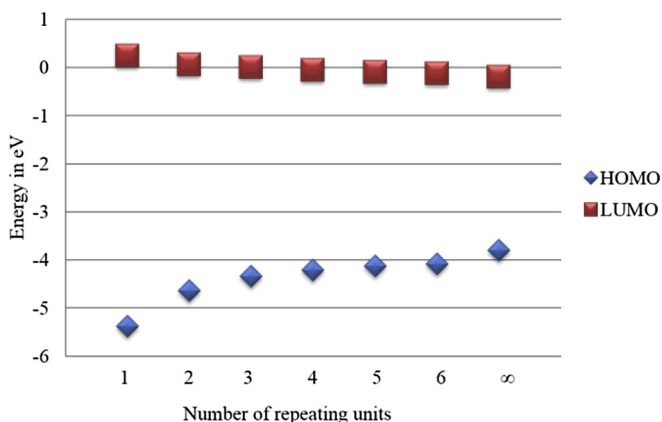
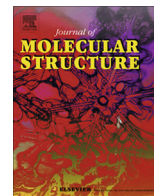


Fig. 6. Development of band structure of PANI LB from energy levels of oligomers. (The monomer is used as a repeat unit).

- [29] L. Zhang, M. Wan, *Adv. Funct. Mater.* 13 (2003) 815–820.
- [30] K.A. Coplin, J.M. Leng, R.P. McCall, A.J. Epstein, S.K. Manohar, Y. Sun, A.G. MacDiarmid, *Synth. Met.* 55 (1993) 7–14.
- [31] Y. Xia, P. Yang, Y. Sun, Y. Wu, B. Mayers, B. Gates, Y. Yin, F. Kim, H. Yan, *Adv. Mater.* 15 (2003) 353–389.
- [32] N.R. Chiou, A.J. Epstein, *Adv. Mater.* 17 (2005) 1679–1683.
- [33] C.U. Udeh, N. Fey, C.F.J. Faul, *J. Mater. Chem.* 21 (2011) 18137–18153.
- [34] K. Basavaiah, A. Rao, *J. Chem.* 9 (2012) 1175–1180.
- [35] E. Ozkazanc, S. Zor, H. Ozkazanc, *Polym. Comp.* 31 (2010) 1862–1868.
- [36] A. Pron, F. Genoud, C. Menardo, M. Nechtschein, *Synth. Met.* 24 (1988) 193–201.
- [37] E. Marie, R. Rothe, M. Antonietti, K. Landfester, *Macromolecules* 36 (2003) 3967–3973.
- [38] Y. Cao, A. Andreatta, A.J. Heeger, P. Smith, *Polymer* 30 (1989) 2305–2311.
- [39] P.S. Rao, S. Subrahmanya, D. Sathyanarayana, *Synth. Met.* 128 (2002) 311–316.
- [40] X. Zhang, W.J. Goux, S.K. Manohar, *J. Am. Chem. Soc.* 126 (2004) 4502–4503.
- [41] J.D. Yuen, J. Fan, J. Seifert, B. Lim, R. Hufschmid, A.J. Heeger, F. Wudl, *J. Am. Chem. Soc.* 133 (2011) 20799–20807.
- [42] J. Prokes, J. Stejskal, *Polym. Degrad. Stab.* 86 (2004) 187–195.
- [43] J. Guay, P. Kasai, A. Diaz, R. Wu, J.M. Tour, L.H. Dao, *Chem. Mater.* 4 (1992) 1097–1105.
- [44] R. Ullah, G.A. Bowmaker, C. Laslau, G.I.N. Waterhouse, Z.D. Zujovic, K. Ali, A.A. Shah, J. Travas-Sejdic, *Synth. Met.* 198 (2014) 203–211.
- [45] A.D. Becke, *Phys. Rev. A* 38 (1988) 3098.
- [46] C. Sutton, T. Korzdorfer, M.T. Gray, M. Brunsfeld, R.M. Parrish, C.D. Sherrill, J.S. Sears, J.L. Bredas, *J. Chem. Phys.* (2014) 140.
- [47] C. Sutton, T. Korzdorfer, V. Coropceanu, J.L. Bredas, *J. Phys. Chem. C* 118 (2014) 3925.
- [48] C. Alemán, C.A. Ferreira, J. Torras, A. Meneguzzi, M. Canales, M.A.S. Rodrigues, J. Casanovas, *Polymer* 49 (2008) 5169–5176.
- [49] J. Casanovas, C. Alemán, *J. Phys. Chem. C* 111 (2007) 4823–4830.
- [50] R. Colle, A. Curioni, *J. Am. Chem. Soc.* 120 (1998) 4832–4839.
- [51] W. Förner, *J. Mol. Struct. (THEOCHEM)* 682 (2004) 115–136.
- [52] S. Lim, K. Tan, E. Kang, W. Chin, *J. Chem. Phys.* 112 (2000) 10648.
- [53] A.K. Mishra, P. Tandon, *J. Phys. Chem. B* 113 (2009) 14629–14639.
- [54] A.K. Mishra, P. Tandon, *J. Phys. Chem. B* 113 (2009) 9702–9707.
- [55] M. Frisch, H.B. Schlegel, G.E. Scuseria, M.A. Robb, J.R. Cheeseman, G. Scalmani, V. Barone, B. Mennucci, G.A. Petersson, et al., *Gaussian 09, Rev. D. 0.1*, Gaussian, Inc., Wallingford, CT, 2013.
- [56] R. Dennington, T. Keith, J.G. Millam, *Semichem Inc., Shawnee Mission KS*, 2008.
- [57] A.R. Allouche, *Gabedit*, 2011. <http://gabedit.sourceforge.net>.
- [58] H. Ullah, K. Ayub, Z. Ullah, M. Hanif, R. Nawaz, A.A. Shah, S. Bilal, *Synth. Met.* 172 (2013) 14–20.
- [59] H. Ullah, A.A. Shah, S. Bilal, K. Ayub, *J. Phys. Chem. C* 118 (2014) 17819–17830.
- [60] S. Bibi, H. Ullah, S.M. Ahmad, A.-u.-H. Ali Shah, S. Bilal, A.A. Tahir, K. Ayub, *J. Phys. Chem. C* 119 (2015) 15994–16003.
- [61] M. Kamran, H. Ullah, A.A. Anwar-ul-Haq, S. Bilal, A.A. Tahir, K. Ayub, *Polymer* 72 (2015) 30–39.
- [62] J. Foresman, E. Frish, *Gaussian Inc., Pittsburg, USA*, 1996.
- [63] J.B. Foresman, Æ. Frisch, and I. Gaussian, 1996.
- [64] U. Salzner, P. Pickup, R. Poirier, J. Lagowski, *J. Phys. Chem. A* 102 (1998) 2572–2578.
- [65] U. Salzner, *J. Phys. Chem. A* 112 (2008) 5458–5466.
- [66] X.-R. Zeng, T.-M. Ko, *Polymer* 39 (1998) 1187–1195.
- [67] M. Lundström, J. Aromaa, O. Forsén, *Hydrometallurgy* 95 (2009) 285–289.
- [68] O. Abdulrazzaq, S.E. Bourdo, V. Saini, F. Watanabe, B. Barnes, A. Ghosh, A.S. Biris, *RSC Adv.* 5 (2015) 33–40.
- [69] S. Pramanik, G. Das, N. Karak, *RSC Adv.* 3 (2013) 4574–4581.
- [70] N.-A. Rangel-Vazquez, C. Sánchez-López, F.R. Felix, *Polímeros* 24 (2014) 453–463.
- [71] L. Zhang, H. Peng, P.A. Kilmartin, C. Soeller, R. Tilley, J. Travas-Sejdic, *Macromol. Rapid Comm.* 29 (2008) 598–603.
- [72] L. Zhang, M. Wan, Y. Wei, *Macromol. Rapid Commun.* 27 (2006) 366–371.
- [73] N. Van Hieu, N.Q. Dung, P.D. Tam, T. Trung, N.D. Chien, *Sens. Actuat B Chem.* 140 (2009) 500–507.
- [74] C. De Melo, B. Neto, E. De Lima, L. De Lira, J. De Souza, *Sens. Actuat B Chem.* 109 (2005) 348–354.
- [75] J. Yadong, W. Tao, W. Zhiming, L. Dan, C. Xiangdong, X. Dan, *Sens. Actuat B Chem.* 66 (2000) 280–282.
- [76] S.J. Vigmond, V. Ghaemmaghami, M. Thompson, *Can. J. Chem.* 73 (1995) 1711–1718.
- [77] J.L. Yagüe, S. Borrós, *Plasma Pro. Polym.* 9 (2012) 485–490.
- [78] N. Bhat, A. Gadre, V. Bambole, *J. Appl. Polym. Sci.* 88 (2003) 22–29.
- [79] S. Waghuley, S. Yenorkar, S. Yawale, S. Yawale, *Sens. Actuat B Chem.* 128 (2008) 366–373.
- [80] A. Joshi, S. Gangal, S. Gupta, *Sens. Actuat B Chem.* 156 (2011) 938–942.
- [81] C. Cappelli, S. Monti, G. Scalmani, V. Barone, *J. Chem. Theo. Comput.* 6 (2010) 1660–1669.
- [82] T. Fornaro, M. Biczysko, J. Bloino, V. Barone, *Phys. Chem. Chem. Phys.* 18 (2016) 8479–8490.
- [83] J. Laska, J. Widlarz, *Polymer* 46 (2005) 1485–1495.
- [84] V. Barone, M. Cossi, *J. Phys. Chem. A* 102 (1998) 1995–2001.
- [85] U. Salzner, *J. Phys. Chem. A* 114 (2010) 10997–11007.
- [86] N. Zamoschik, U. Salzner, M. Bendikov, *J. Phys. Chem. C* 112 (2008) 8408–8418.
- [87] R. McCall, J. Ginder, J. Leng, H. Ye, S. Manohar, J. Masters, G. Asturias, A. MacDiarmid, A. Epstein, *Phys. Rev. B* 41 (1990) 5202.

[Article 15]

Z. Ullah, A. Rauf, M. Yaseen, W. Hassan, M. Tariq, K. Ayub, A. A. Tahir, H. Ullah, "Density functional theory and phytochemical study of 8-hydroxyisodiospyrin." *J. Mol. Struc.*, vol. 1095, pp. 69-78, 2015.



Density functional theory and phytochemical study of 8-hydroxyisodiospyrin



Zakir Ullah^a, Ata-ur-Rahman^{a,*}, Fazl-i-Sattar^a, Abdur Rauf^a, Muhammad Yaseen^a, Waseem Hassan^a, Muhammad Tariq^b, Khurshid Ayub^{c,*}, Asif Ali Tahir^d, Habib Ullah^{a,d,*}

^a Institute of Chemical Sciences, University of Peshawar, 25120 Peshawar, Pakistan

^b National Centre of Excellence in Physical Chemistry, University of Peshawar, 25120 Peshawar, Pakistan

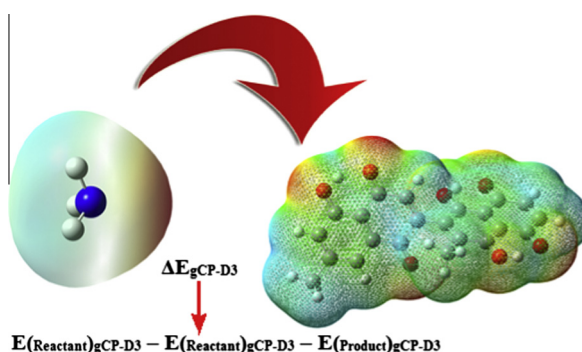
^c Department of Chemistry, COMSATS, Tobe Camp, 22060 Abbottabad, Pakistan

^d Environment and Sustainability Institute (ESI), University of Exeter, Penryn Campus, Penryn, Cornwall TR10 9FE, UK

HIGHLIGHTS

- Theoretical and phytochemical study of 8-hydroxyisodiospyrin.
- Spectroscopic and electronic structure simulations.
- Non-covalent interaction of gases with HDO.
- Inter-molecular study via DFT calculations.

GRAPHICAL ABSTRACT



ARTICLE INFO

Article history:

Received 11 March 2015
 Received in revised form 16 April 2015
 Accepted 21 April 2015
 Available online 28 April 2015

Keywords:

DFT
 Hydroxyisodiospyrin
 B3LYP-gCP-D3/6-31G*
 BSSE
 UV–vis
 HOMO–LUMO gap

ABSTRACT

Comprehensive theoretical and experimental studies of a natural product, 8-hydroxyisodiospyrin (HDO) have been carried out. Based on the correlation of experimental and theoretical data, an appropriate computational model was developed for obtaining the electronic, spectroscopic, and thermodynamic parameters of HDO. First of all, the exact structure of HDO is confirmed from the nice correlation of theory and experiment, prior to determination of its electroactive nature. Hybrid density functional theory (DFT) is employed for all theoretical simulations. The experimental and predicted IR and UV–vis spectra [B3LYP/6-31+G(d,p) level of theory] have excellent correlation. Inter-molecular non-covalent interaction of HDO with different gases such as NH₃, CO₂, CO, H₂O is investigated through geometrical counterpoise (gCP) i.e., B3LYP-gCP-D3/6-31G* method. Furthermore, the inter-molecular interaction is also supported by geometrical parameters, electronic properties, thermodynamic parameters and charge analysis. All these characterizations have corroborated each other and confirmed the electroactive nature (non-covalent interaction ability) of HDO for the studied gases. Electronic properties such as Ionization Potential (IP), Electron Affinities (EA), electrostatic potential (ESP), density of states (DOS), HOMO, LUMO, and band gap of HDO have been estimated for the first time theoretically.

© 2015 Elsevier B.V. All rights reserved.

* Corresponding authors at: Institute of Chemical Sciences, University of Peshawar, 25120 Peshawar, Pakistan; Environment and Sustainability Institute (ESI), University of Exeter, Penryn Campus, Penryn, Cornwall TR10 9FE, UK (H. Ullah).

E-mail address: hu203@exeter.ac.uk (H. Ullah).

Introduction

Medicinal plants are the consistent source for the treatment of many health problems in our modern as well as ancient Egypt, Assyrian, China and Indus valley human societies [1–5]. Plants extract derived-medicines have been usually used for primary health care, across the world from pre-historically [6,7]. In the research laboratory round the world, it is desired to discover and devise new drugs from natural sources, which are often more useful, cheaper and easily available. For curing of common diseases, developing countries have restricted approach to medical services, therefore, therapeutics sources are the medicinal plants [8].

The genus *Diospyros* (Ebenaceae) consists of woody shrubs and trees distributed in the tropical and subtropical regions of the world. Around 500 species are known worldwide of which 24 species are native to India and Pakistan [9,10]. *Diospyros lotus* (DL) is a deciduous tree, growing in China and Asia. DL has been cultivated for its edible fruits. The fruits of DL is used as a sedative, astringent, nutritive, antiseptic, antidiabetic, antitumor, astringent, laxative, nutritive and as a febrifuge and for the treatment of constipation. DL fruits are used for the treatment of diarrhea, dry coughs and hypertension [9,10].

Phytochemical studies have been previously carried out on many *Diospyros* species, and have revealed the widespread presence of naphthoquinones and naphthalene derivatives, dimeric naphthoquinones and lupane triterpenes. Chemical investigation of the fruits of DL led to identification of some fatty acids, sugars, phenolic compounds and non-volatile acids [11,12]. 8-Hydroxyisodiospyrin (HDO) and Diospyrin (DO) are bisnaphthoquinone which have been isolated by our group from DL [13]. DO was obtained as a polar orange–red crystalline compound [12] while HDO has violet amorphous nature (see extraction and isolation section). HDO also displayed good activity against *Plasmodium falciparum* (strain K1 and NF54, stages IEF). In cytotoxicity studies toward rat skeletal myoblasts, L-6 cells showed that HDO (see Fig. 1) was responsive to all parasitic protozoa. HDO also possesses *in vitro* activity against *T. cruzi* [14].

In spite of the above medicinal related investigations, HDO still need extensive technological exploration which will open new ways for the future scientists [15]. Lots of useful experimental studies on HDO reveal its high potential and reactivity toward biological species [13,14]. In this work, we have explained, how computational chemistry methods can successfully be applied to a phytochemically isolated organic molecule (HDO) [16]; determination/confirmation of its exact chemical structure. Moreover, we have predicted its technological application (interaction ability toward different gases such as NH₃, CO₂, CO, and moisture) with the help of electronic structure properties simulations. This study also emphasize on non-covalent interactions, which play an important role to understand structures and energetic of organic molecules [17–19].

For the study of non-covalent interactions [20], Grimme and Co-workers have suggested that B3LYP-gCP-D3/6-31G* [21] is a well

accurate “Model Chemistry” for the non-covalent/Van der Waals type interactions study [22–27].

Materials and methods

Plant material

Roots of *D. lotus* were collected from Toormang Razagram, Dir, KPK, Pakistan, in May 2009. The sample was authenticated by Taxonomist, and Botanist at Department of Botany, University of Peshawar, Pakistan. A voucher specimen (Bot. 20036 (PUP)) has been deposited at the Herbarium, Department of Botany, University of Peshawar, Pakistan.

Extraction and isolation

Shade-dried roots of *D. lotus* (14 kg) were crushed to powder and kept at room temperature in MeOH for six days with continuous stirring by simple percolation. After this period, the extracts were combined and concentrated by evaporating solvents using rotary vacuum evaporator under reduced pressure at temperature below 55 °C to obtain a dark red residue (202 g). It was suspended in water and successively partitioned with hexane, CHCl₃, EtOAc and *n*-BuOH using standard protocol. The chloroform fraction (30 g) was subjected to column chromatography on silica gel [Merck Silica gel 60 (0.063–0.200 mm), 5 × 60 cm]. The column was eluted with hexane–ethyl acetate (100:0 → 0:100) as solvent system. A total of 105 fractions, RF-1 to RF-105 were obtained based on TLC profiles. Elution of the chromatogram with hexane–EtOAc (100:0 → 7:93) gave a violet amorphous solid, HDO with m.p. 275–276 °C (1.4 g). The structure of HDO was partially confirmed by comparing the physical and chemical data with reported one [28].

Characterization

IR spectra were measured on KBr pellets, using Perkin Elmer spectrophotometer series 400 IR, in the region from 400 to 4000 cm⁻¹ with a resolution of 4 cm⁻¹. The spectra were collected in ATR mode with 10 numbers of scans for all samples. A Shimadzu UV–vis 1700 spectrophotometer was used to record the UV–vis spectra. The sample was dissolved in chloroform and the spectra were recorded in spectral region ranging from 200 to 800 nm.

Computational methodology

Quantum mechanical calculations with DFT method at Becke three parameter (exchange), Lee, Yang, and Parr both local and nonlocal (correlation; DFT) [29–31] at B3LYP/6-31G* level of theory are employed [16,32–34]. DFT is chosen due to its more accurate prediction, as explained in our previous work [35]. Vibrational I.R spectra were simulated at the above mentioned level of theory using optimized geometric parameters. Excited state properties such as Ionization Potential (IP), Electron Affinities (EA), electrostatic potential (ESP), density of states (DOS), co-efficient of highest occupied molecular orbital (HOMO), co-efficient of lowest unoccupied molecular orbital (LUMO) and band gap are also simulated at the above mentioned level of theory. Using Koopmans' theorem the negative HOMO energy corresponds to the first IP while the negative of LUMO energy corresponds to the EA [36]. TD-B3LYP/6-31+G(d,p) level of theory is used for the UV–vis spectra, both for the gas phase and in chloroform media. Band gap is estimated as the difference of LUMO and HOMO. The non-bonding (non-covalent) interaction of HDO with the mentioned gases are simulated at geometrical counterpoise correction (gCP) which is able to treat

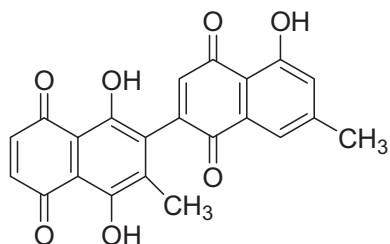


Fig. 1. Molecular structure of HDO.

both inter- and intra-molecular basis set superposition error (BSSE) on the same footing at low computational cost [37]. The B3LYP-gCP-D3/6-31G* [38] energy corrections are also made from the Grimme's Webservice (<http://www.tch.uni-bonn.de/>) [21]. Equations for the ΔE_{int} and ΔE_{BSSE} calculations are clearly explained in our previous report [37]. All calculations were performed in gas phase except UV-vis (which is simulated both in gas and solvent phase) using GAUSSIAN 09 [39]. The visualization of results is achieved with Gabedit and Gauss View [40].

Results and discussion

Geometry optimization of HDO

The molecular optimized geometric structure of HDO along with numbering of atoms is shown in Fig. 2. Some of the prominent optimized geometric parameters at B3LYP/6-31G* and B3LYP/6-31G(d,p) level of theories are listed in Table 1, while their coordinates are listed in S1. Due to the amorphous nature of HDO, we could not get its crystallographic structure (experimental) however, for comparison reason; simulated optimized geometrical parameters at the two different levels of theories are correlated (see Table 1). All C–C bonds distance are in the range of 1.47 and 1.41 Å, using these both level of theories.

Analyses of the listed data in Table 1 clearly indicate that the C–H bond distances of HDO have similar lengths at both levels of theories. The oxygen–hydrogen (O42–H43) bond distance is about 0.99 Å. The calculated C–O bond distance (C242–O39) is 1.24 Å. Intra-molecular hydrogen bonding also present in HDO at three different positions. These hydrogen bonds are present at H37··O42, H35··O38, and H43··O39 positions, and have distances of 1.72, 1.66 and 1.68 Å, respectively. The bond angles of C342–C242–C1 and O3942–C242–C1 are 117.75° and 119.96°, respectively. The dihedral angles among C642–C142–C242–C3 and H4342–O4242–C842–C3 atoms are –0.7 to 0.05. Comparative geometric analysis lead us to conclude that both B3LYP/6-31G* and B3LYP/6-31G(d,p) level of theories have almost similar results.

Infra-red spectral characteristics

According to the non-linear vibrational mode formula (3N-6), HDO consists of 43 atoms (H₁₄,O₇,C₂₂) and expected to have 123 normal modes of vibrations under C1 symmetry. Among all these

Table 1
Optimized Geometric Parameters of HDO.

Geometrical parameters	B3LYP/6-31G*	B3LYP/6-31G(d,p)
<i>Bond length (Å)</i>		
C1–C2	1.47	1.47
C2–O39	1.24	1.24
O42–H43	0.99	0.99
C14–H17	1.08	1.08
C19–C18	1.41	1.41
<i>Bond angle (°)</i>		
C3–C2–C1	117.75	117.71
O39–C2–C1	119.73	119.96
H17–C14–C13	121.60	121.57
C14–C13–C11	122.49	122.42
H37–O36–C21	108.62	108.85
H31–C30–C22	110.92	110.86
<i>Dihedral angle (°)</i>		
C6–C1–C2–C3	–0.07	–0.05
H7–C1–C6–C5	–179.95	–179.94
O39–C2–C1–C6	179.90	179.92
H43–O–C8–C3	0.05	0.03
H27–C25–C12–C11	–20.13	–22.61

Table 2
Experimental and calculated IR frequencies (in cm⁻¹) of HDO.

S.No	Experimental	Scaled	Unscaled	Approximate assignment
1	3667	3652	3800	v O–H
2	3072	3055	3178	v O–H
3	2922	3022	3144	v O–H
4	1642	1679	1747	v C=C, C=O
5	1599	1611	1676	v C=O, C=C; Wag O–H
6	1571	1589	1654	v C=C, C–C; Wag C–H
7	1455	1451	1510	Cis C–H
8	1409	1405	1462	v C=C, C–O; Cis C–H
9	1368	1398	1455	v C–O; Cis C–H; Wag O–H
10	1332	1350	1405	v C=C; Wag C–H, O–H
11	1284	1263	1314	v C–C; Wag C–H, O–H
12	1205	1219	1269	Wag C–H, O–H
13	1143	1151	1198	Wag C–H
14	1110	1059	1102	Wag C–H
15	856	855	890	β O–H, C–H
16	461	441	459	Rings breathing

Note: v: for stretching, β: out of plan bending, Wag: for wagging.

123 normal modes of vibrations, 16 prominent IR band peaks are given in Table 2 along with their approximate assignments. The observed and simulated scaled IR spectra of HDO are given in

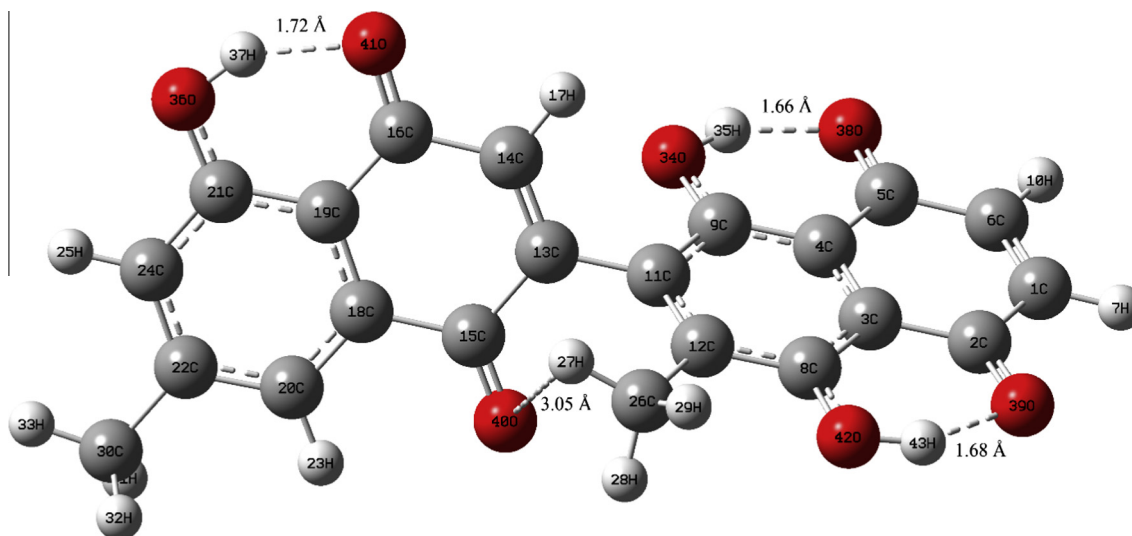


Fig. 2. Optimized Geometric Structure of HDO.

Fig. 3, whereas some of the major band peaks, both simulated (scaled and unscaled) and observed are collectively listed in Table 2.

The experimental IR spectrum of compound HDO shows characteristic absorption bands for ketone, OH, and $-\text{CH}$ functional groups. The simulated IR spectrum at B3LYP/6-31G* level of theory was scaled with a factor of 0.9613 to correlate with the experiment. The O–H stretching band appeared in the functional group region at ca. 3667 cm^{-1} which has good agreement with the computed band appeared at 3652 cm^{-1} . Other two prominent band peaks (simulated) of the functional group region are 3055 and 3022 cm^{-1} , and have O–H stretching. These simulated bands can be correlated with the experimental 3072 and 2922 cm^{-1} , which has 17 and 100 cm^{-1} differences, the large difference (100 cm^{-1}) is because of the theoretically isolated molecule whereas experiment is for the condense phase.

The finger print region has 11 major vibrations; the simulated peak at 1679 cm^{-1} is assigned to C=C and C=O stretching, and has strong correlation with the experimental peak at ca. 1642 cm^{-1} . Calculated band peaks at 1611 also has contribution from C=O and C=C stretching. The simulated bands at 589 , and 1451 cm^{-1} assigned to the O–H, and C–H wagging, respectively. The experimental band peaks for these vibrations are ca. 1571 , and 1454 cm^{-1} and has 18 , and 3 cm^{-1} difference from that of theoretical. The last two peak of the observed IR spectra peaked at 856

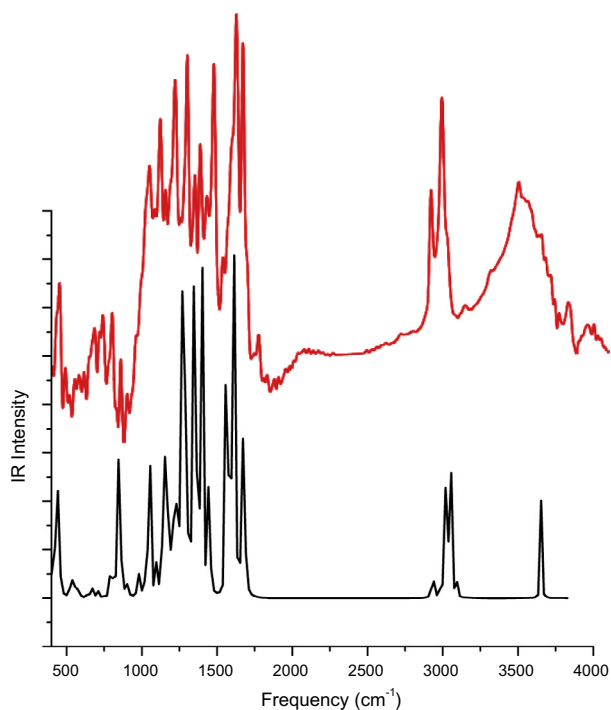


Fig. 3. Experimental (red) and simulated (black) IR Spectra of HDO. (For interpretation of the references to color in this figure legend, the reader is referred to the web version of this article.)

Table 3
Experimental and TD-B3LYP/6-31+G(d,p) calculated electronic excitations of HDO.

Peak	Experimental	Excitation energy (nm)		Oscillator strength		Electronic transition	
		Vacuum	CHCl ₃	Vacuum	CHCl ₃	Vacuum	CHCl ₃
1	553	556	562	0.04	0.06	S ₀ → S ₁	S ₀ → S ₁
2	483	495	501	0.15	0.19	S ₀ → S ₃	S ₀ → S ₃
3	414	433	434	0.04	0.04	S ₋₁ → S ₃	S ₋₁ → S ₃
4	292	281	283	0.05	0.04	S ₋₉ → S ₁	S ₋₉ → S ₁

and 461 cm^{-1} can be correlated with the simulated vibrations ca. 855 and 441 cm^{-1} on the basis of their similar assignments, as listed in Table 2. Comparative analysis of the calculated and experimental IR bands led us to conclude that both theory and experiment validate each other.

Experimental and theoretical UV–vis spectra of HDO

In order to understand the electronic transitions (UV–vis spectra) in HDO, TD-DFT calculations at B3LYP/6-31+G(d,p) level of theory are performed. The calculations are performed both in vacuum as well as in chloroform solvent (using polarized continuum model, PCM), to ensure the maximum correlation of experiment and theory. The experimental absorption wavelengths and simulated electronic excitation values, such as absorption wavelength (λ_{max}), excitation energies (E), oscillator strengths (f) and major contributions of the transitions along with their assignments (electronic transitions) are given in Table 3. The experimental UV–visible spectra of HDO have four absorption bands at ca. 292 , 414 , 483 , and 553 nm , as depicted in Fig. 4. The strong absorption band peak (λ_{max}) observed at 553 nm is because of the $\pi \rightarrow \pi^*$ transition and has correlation with the simulated 556 nm (gas phase) and 562 nm (CHCl₃). Solvent causes red shifting of wavelength, and it has been discussed in our earlier reports [33]. Moreover, the remaining observed absorbance band peaks such as 483 , 414 , and 292 nm have also good correlation with their counterpart calculated ones.

The experimental absorption band peak at ca. 483 nm can be correlated with the theoretical 495 nm (gas phase) and 501 nm (CHCl₃). This experimental absorbance band peak has 8 and 18 nm differences to that of simulated gas phase and solvent media, respectively. This peak is because of the electronic transition from the molecular orbital of HOMO–1 to LUMO+2 and can also be regarded as $n \rightarrow \pi^*$ transitions. The $n \rightarrow \pi^*$ transitions are expected to occur relatively at lower wavelength. Another, absorption in the observed UV–vis spectra is at ca. 414 nm which is because of S₋₂ → S₊₂ transition, and can be matched with the calculated 433 nm (gas phase) and 434 nm (CH₃Cl).

The last forbidden electronic excitation of HDO in the experimental UV–vis spectra is 292 nm , which again has very nice correlation with their calculated 281 nm (gas phase) and 283 nm (CHCl₃). This absorbance is because of the electronic excitation from HOMO–9 to LUMO. Analysis of the data of Table 3, Figs. 4 and 5 led us to conclude that theoretical results at TD-B3LYP/6-31+G(d,p) level of theory correlate nicely with the experiment.

Interaction study of HDO

Reactive site simulation

Non-bonding interacting ability of HDO is investigated with four different gaseous molecules such as ammonia (NH₃), carbon dioxide (CO₂), carbon monoxide (CO) and moisture (H₂O). Optimized geometric coordinates of HDO-X are listed in S2–S5 of the Supplementary materials. These gases are the main focus of the study because they are usually available in a common laboratory, industry or other related areas, and the current study. Some of

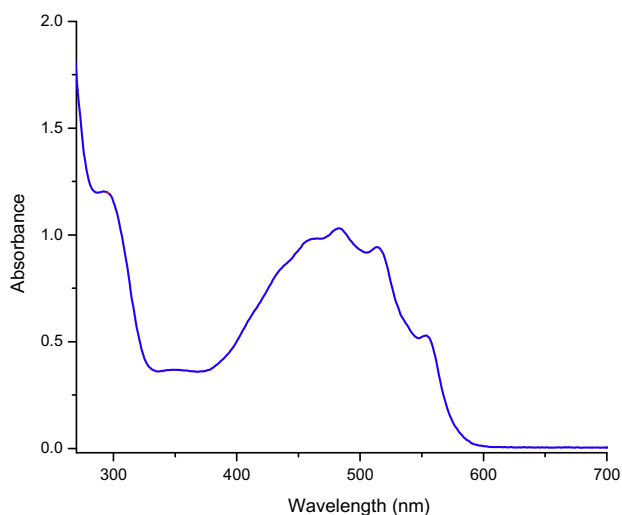


Fig. 4. Experimental UV-vis Spectrum of HDO.

these gases in ppm or ppb level concentration in the atmosphere are dangerous for human health. In order to explore the best possible interaction of HDO with these gases, first of all the most suitable (reactive) sites are investigated by electrostatic potential (ESP), Mulliken, and NBO charge analysis, see Figs. 6 and 7. The different colors in Figs. S6 and S7 are used as a symbol for the

different value of electrostatic potential; red and blue colors show electron rich and electron deficient (high positivity) regions of the molecule whereas the green color shows the region of zero potential. The ESP also provides a visual method for understanding the relative polarity of the molecules (Figs. S6 and S7). Analyses of the ESP surfaces clearly indicate that the nucleophile (most electronegative) part of HDO is the area around O₄₁ and O₃₆ (ref to Fig. 2), which is the most electron rich regions (red). Moreover, other electron rich areas near O₄₀, O₄₂, O₃₉, O₃₈ and O₃₄ cannot be ignored but they are less nucleophilic compared to O₄₁ as can be seen from Fig. S6. The second most electronegative atom is O₄₀ followed by O₃₈, and O₃₄. The weakest nucleophilic region is around O₃₉ and O₄₂ atoms.

Prior to simulation of non-covalent interaction of HDO with different gases, they are interacted at suitable reactive sites as predicted from MEP (Fig. S6). We also tried all the four regions of HDO without keeping in mind its MEP plot, and found that only the H₃₇ is the best region for attacking of these gases. For details, see S8–S10 of the Supplementary material where HDO and these gases are interacted at different positions. From MEP (Fig. S6) of H₂O and NH₃, it is clear that O and N of water and ammonia are nucleophilic, respectively, and the H of HDO are to the electrophilic. In case of CO₂, both O are nucleophile while C is more nucleophilic than O in CO.

In order to ensure the electron rich and deficient areas (as predicted by ESP) of HDO, Mulliken and NBO charges analysis are also carried out (see Figs. S11–S12). Mulliken and NBO charge analysis reveal that the O₃₆ and O₄₁ are in the most negative states

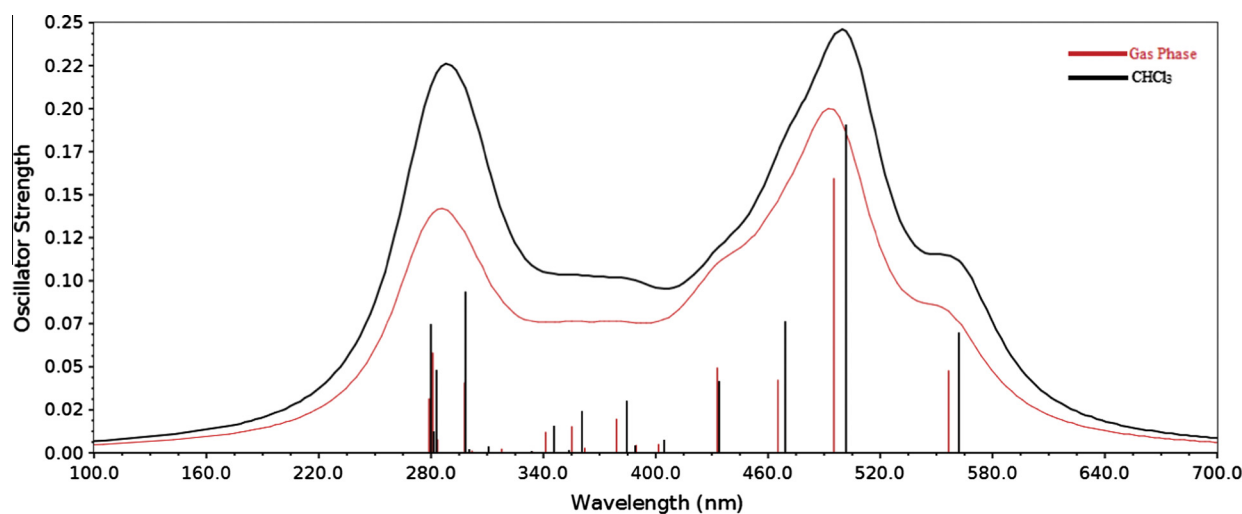


Fig. 5. Simulated UV-vis spectra of HDO gas phase (black) and solvent media (red). (For interpretation of the references to color in this figure legend, the reader is referred to the web version of this article.)

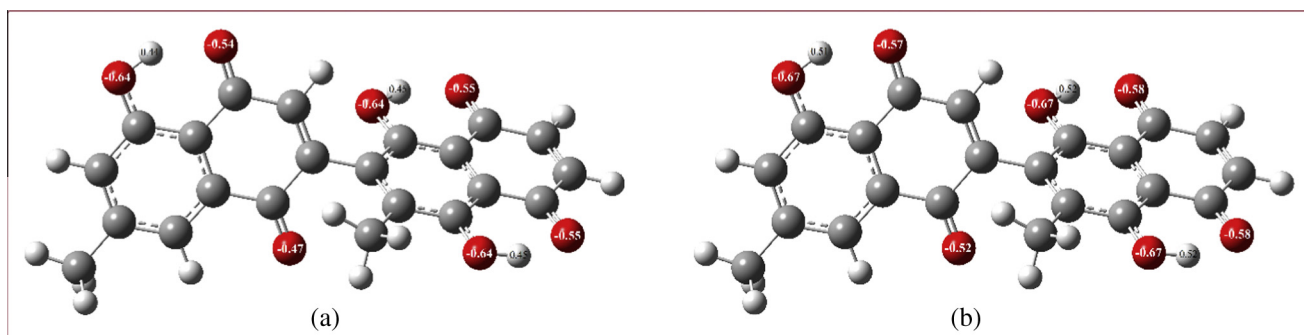


Fig. 6. Mulliken (a) and NBO (b) Charges on HDO.

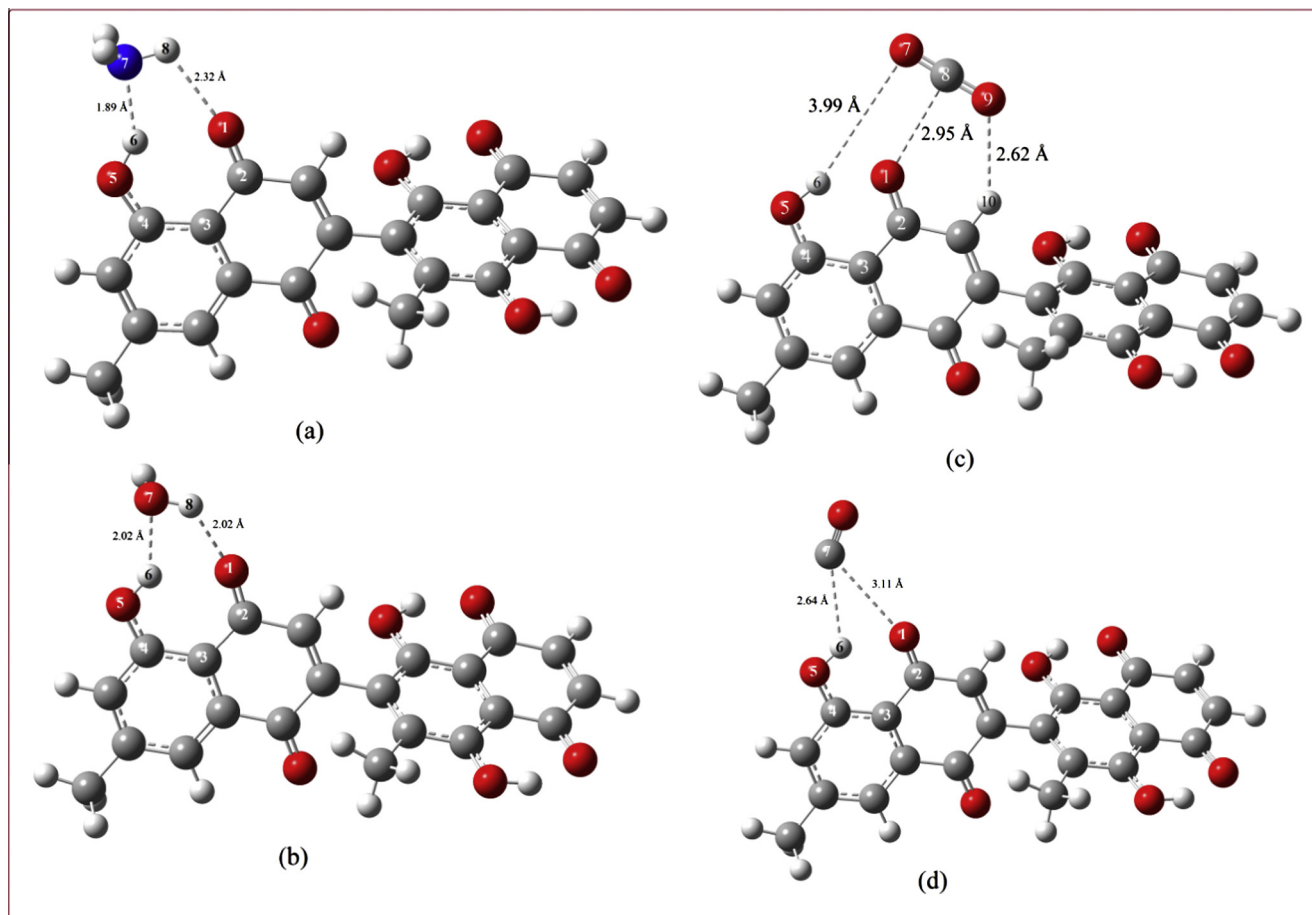


Fig. 7. Optimized Geometric Structures of HDO-X (X = NH₃, CO₂, H₂O, CO, and CO).

(Fig. 6a and b). O36 and O41 have about 0.64 and 0.54 e⁻ unit of charges based on Mulliken charge analysis, while these atoms have 0.67 and 0.57 e⁻ unit of charges based NBO. The oxygen O34 has 0.67 (based on NBO) and 0.64 e⁻ unit of charge based on Mulliken charge analysis. Area near O36 and O41 are the best nucleophilic region compared to O34, O38, O42, and O39. Although, the rest of oxygen atoms such as O34, O38, O42, and O39 have also significant amount of negative charge compared to O36 and O41 but their effect is little. These charge analysis also corroborate the ESP investigation, and confirmed that this is the attacking area for the electrophile.

Intermolecular interaction of HDO with gases

Non-covalent interaction between HDO and NH₃, CO₂, H₂O, CO, and CO are simulated at two different methods, simple interaction energy (ΔE_{int}) and geometrical counterpoise correction energy ($\Delta E_{\text{gCP-D3}}$). The optimized geometries of all these HDO-X complexes are given in Fig. 7, whereas some of important inter- and intra-molecular optimized geometrical parameters such as

$d_{X1...Y8}$, $d_{X6...Y7}$ (Å), $\angle O_1C_2C_3$, $\angle C_4O_5H_6$, (°) and $\Delta E_{\text{gCP-D3}}$, ΔE_{int} , Q_{NBO} and Q_{Mulliken} are listed in Table 4.

HDO-NH₃ complex

The optimized geometric structure of NH₃-HDO complex is depicted in Fig. 7a, wherein the N₇ (for general representation the symbol Y₇ is used) of ammonia forms a hydrogen type bonds to the H₆ of HDO. This non-bonding distance is about 1.89 Å. Nitrogen of ammonia acts as a nucleophile (*vide supra*), and attacks on the H6 of HDO and changes its electronic structure properties through charge transfer, (donate electron) of about 0.05 and 0.04 e⁻ based on of Q_{NBO} and Q_{Mulliken} , respectively. This trend is very nicely estimated from the MEP of HDO-NH₃ complex, see Fig. S7. Ammonia also establishes another hydrogen bond with HDO via H8 and O1 with a distance of 2.32 Å. This charge transfer alter the band gap, λ_{max} (*vide infra*), and optimized geometric structure of HDO especially, near the analytes (NH₃), which are in fact the sensitivity measurements parameters.

Table 4
Optimized geometric parameters, $\Delta E_{\text{gCP-D3}}$, ΔE_{int} , Q_{NBO} and Q_{Mulliken} of HDO-X (X = NH₃, CO₂, H₂O, CO, and CO): atomic labels are with reference to Fig. 7.

Species	$d_{X1...Y8}$	$d_{X6...Y7}$	$\angle O_1C_2C_3$	$\angle C_4O_5H_6$	$\Delta E_{\text{gCP-D3}}$	ΔE_{int}	Q_{NBO}	Q_{Mulliken}
HDO			122.43	106.85			0	0
HDO-NH ₃	2.32	1.89	123.45	118.37	-4.70	-4.76	-0.05	-0.04
HDO-H ₂ O	2.02	2.02	123.08	114.10	-4.45	-5.77	-0.02	-0.03
HDO-CO ₂	2.95	3.99	121.95	107.39	-2.66	-2.60	-0.003	-0.002
HDO-CO	3.11	2.64	122.56	108.18	-1.88	-1.31	-0.005	-0.007

The interaction energy (HDO-NH₃) is about $-4.76 \text{ kcal mol}^{-1}$ based on ΔE_{int} . The $\Delta E_{\text{gCP-D3}}$ which is accurate one because of the inclusion of Van-der Waal and dispersion forces gives similar estimates of interaction energy i.e., $-4.70 \text{ kcal mol}^{-1}$. Interaction of ammonia with HDO, increases its $\angle \text{O}_1\text{C}_2\text{C}_3$ and $\angle \text{C}_4\text{O}_5\text{H}_6$ angles from 122.43° to 123.45° and 106.85° to 118.37° , respectively.

HDO-H₂O complex

Interaction of moisture with HDO is established due to the transferring of electrons from analyte (H₂O) to HDO, which distorts the HDO geometry especially near the adjoining rings as can be seen from Table 4 and Fig. S7. H₂O donate about 0.02 charge of e⁻ based on Q_{NBO} and 0.03 e⁻ based on Q_{Mulliken} to HDO molecule, and forms intermolecular hydrogen type of bonds at position O1...H8 and H6...O7. These intermolecular non-covalent bond distances are about 2.02 Å. The gCP-D3 energy for this complex is $-4.45 \text{ kcal mol}^{-1}$ whereas the simple interaction energy is $-5.77 \text{ kcal mol}^{-1}$.

HDO-CO₂ complex

HDO has little affinity toward CO₂ gas, as revealed from intermolecular distances, charge transfer, and interaction energy

calculations. A relatively weak interaction is found to be present in the HDO-CO₂ complex, with Van der Waal type of bond. These non-bonding distances are 3.99 for H₆...O₇, 2.95 for O₁...C₈ and 2.62 Å for the H₁₀...O₉ (see Fig 7c) which are comparatively larger than those of NH₃, and H₂O complexes. The molecular electrostatic simple interaction energy of HDO-CO₂ complex is $-2.60 \text{ kcal mol}^{-1}$ and with a $\Delta E_{\text{gCP-D3}}$ energy is $-2.66 \text{ kcal mol}^{-1}$. These binding energies are lower than the binding energies for the HDO-NH₃, and HDO-H₂O complexes. The overall low interaction is because of the zero dipole movement of CO₂. The charge transferring is also very low; CO₂ donate negligible amount of charge (about -0.003 e^-) based on NBO and -0.002 e^- charge based on Mulliken charge analysis.

HDO-CO complex

Carbon monoxide has very little interaction with the HDO molecule as can be seen from the geometric parameters, charge exchange and amount of interaction energy (Table 4). Very slight changes are observed in the intra-molecular bond distances upon interaction of CO with HDO. The intermolecular non-bonding distances are found to be 3.11 and 2.64 Å (see Fig7), which are even greater than that of HDO-CO₂ complex. The amount of charge

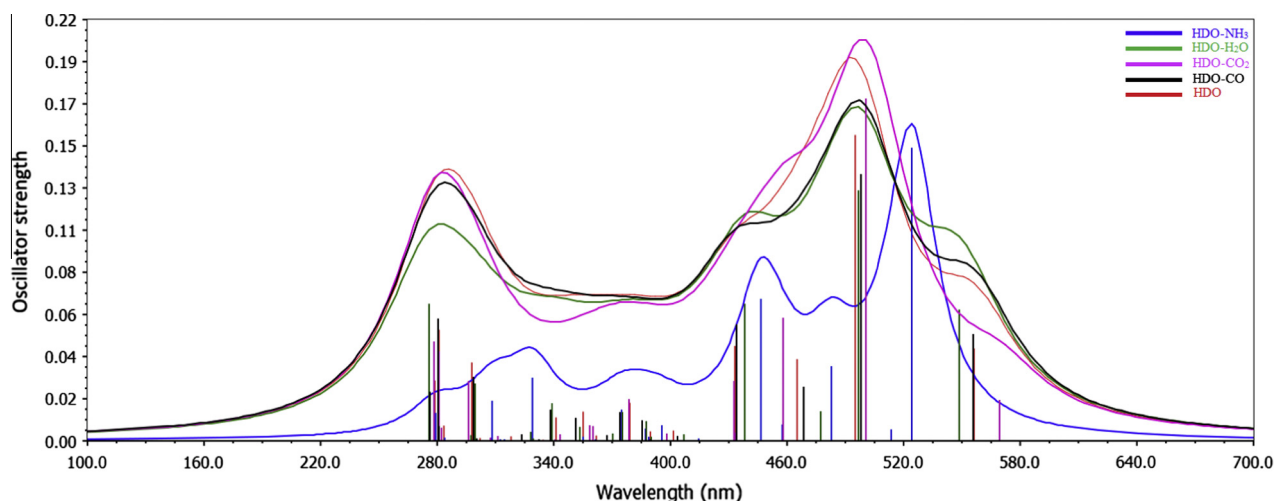


Fig. 8. Combined UV-vis spectra of HDO and HDO-X (where X = NH₃, H₂O, CO₂, and CO).

Table 5
TD-B3LYP/6-31+G(d,p) calculated electronic excitations of HDO and HDO-X.

Species	Peak	Excitation Energy (nm)	Oscillator Strength	Electronic Transition
HDO	1	556	0.04	S ₀ → S ₁
HDO-NH ₃		524	0.15	S ₀ → S ₁
HDO-H ₂ O		548	0.06	S ₀ → S ₁
HDO-CO ₂		569	0.02	S ₀ → S ₁
HDO-CO		556	0.05	S ₀ → S ₁
HDO	2	501	0.15	S ₀ → S ₂
HDO-NH ₃		482	0.03	S ₀ → S ₂
HDO-H ₂ O		496	0.13	S ₀ → S ₂
HDO-CO ₂		500	0.17	S ₀ → S ₂
HDO-CO		498	0.13	S ₀ → S ₂
HDO	3	434	0.04	S ₋₁ → S ₂
HDO-NH ₃		446	0.07	S ₋₁ → S ₂
HDO-H ₂ O		438	0.07	S ₋₁ → S ₂
HDO-CO ₂		433	0.03	S ₋₁ → S ₂
HDO-CO		433	0.06	S ₋₁ → S ₂
HDO	4	283	0.05	S ₋₉ → S ₁
HDO-NH ₃		308	0.02	S ₋₉ → S ₁
HDO-H ₂ O		276	0.07	S ₋₁₀ → S ₁
HDO-CO ₂		278	0.05	S ₋₉ → S ₁
HDO-CO		280	0.06	S ₋₉ → S ₁

Table 6
IP, EA and band gap (eV) of HDO and HDO-X.

Species	IP	EA	Band gap
HDO	6.14	3.49	2.65
HDO-NH ₃	6.00	3.34	2.66
HDO-H ₂ O	6.13	3.48	2.65
HDO-CO ₂	6.51	3.84	2.66
HDO-CO	6.13	3.48	2.65

transfer from CO to HDO is $-0.005 e^-$ (based on NBO) and $-0.007 e^-$ (based on Q_{Mulliken}). Very low ΔE_{int} is present in this complex, which is $-1.31 \text{ kcal mol}^{-1}$. The geometrical counterpoise correction energy is also low for this non-covalent bond ($-1.88 \text{ kcal mol}^{-1}$), which may be because of the stable nature of CO.

UV-vis spectroscopic analysis of HDO-X

Comparative UV-vis spectra of HDO and HDO-X are given in Fig 8, whereas the prominent vertical excitation band peaks along with their oscillator strength, orbital transition both of the experimental and simulated ones are listed in Table 5. Parent molecule (HDO) has four major absorptions in its UV-vis spectra (*vide supra*). Interestingly, NH₃ blue-shifts the first two high wavelength absorptions peaks of HDO, while red-shifts are observed for the higher energy absorption, i.e., shifting from 434 to 446 and 283 to 308 nm. NH₃ shifts HOMO-LUMO excitation energy of HDO to about 32 nm (556 nm in HDO compared to 524 nm in HDO-NH₃ complex), the $S_0 \rightarrow S_2$ excitation energy from 501 to 482 nm, $S_{-1} \rightarrow S_2$ from 434 to 446 nm, and shifts the forbidden excitation energy band peak ($S_{-9} \rightarrow S_1$) from 283 to 308 nm. Besides the

above mentioned peaks, HDO-NH₃ complex shows one extra absorption at ca. 329 nm which is because of $S_{-5} \rightarrow S_2$ transitions. Overall, a strong interaction can be concluded from the UV-vis spectra of HDO-NH₃ complex (*vide supra*).

On the other hand moisture has also considerable interaction with HDO, as can be seen from Fig 8 and Table 5. H₂O blue-shifts the first two and last absorptions band peaks of HDO (from 556 to 548 nm, 501 nm to 496 nm, 283 to 276 nm) and red-shifts the remaining third one; 434 to 438 nm. These shifting are small, but the system is purely vacuum phase therefore, these minute changes cannot be ignored.

Analysis of the UV-vis spectra of HDO-CO₂ reveals that a weak inter-molecular interaction is present between the CO₂ and HDO compared to that of HDO-NH₃ and HDO-H₂O complexes. The absorption band peaks of HDO-CO₂ are similar to that of HDO-H₂O complex; red shifting in the low energy excitations and blue-shifting in the high energy absorptions (Table 5). UV-vis spectra of HDO-CO₂ complex have extra absorption peak at 458 nm with an oscillator strength of 0.06 ($S_{-1} \rightarrow S_1$).

Effect of CO on HDO is negligible as can be seen from the UV-vis spectra HDO-CO complex. CO interacts with HDO from C side only however, the absorption spectrum is similar to that of parent HDO. All four distinct absorption peaks are observed at the same wavelength, oscillator strength and even transitions (Table 5). This result is also in consistence with the geometric, charge analysis and intermolecular interaction energy simulations which confirmed the lower intermolecular interaction of HDO-CO.

Electronic properties of HDO and HDO-X

The electronic properties simulations such as IP, EA, HOMO, LUMO, band gap, and density of states (DOS) of HDO and HDO-X

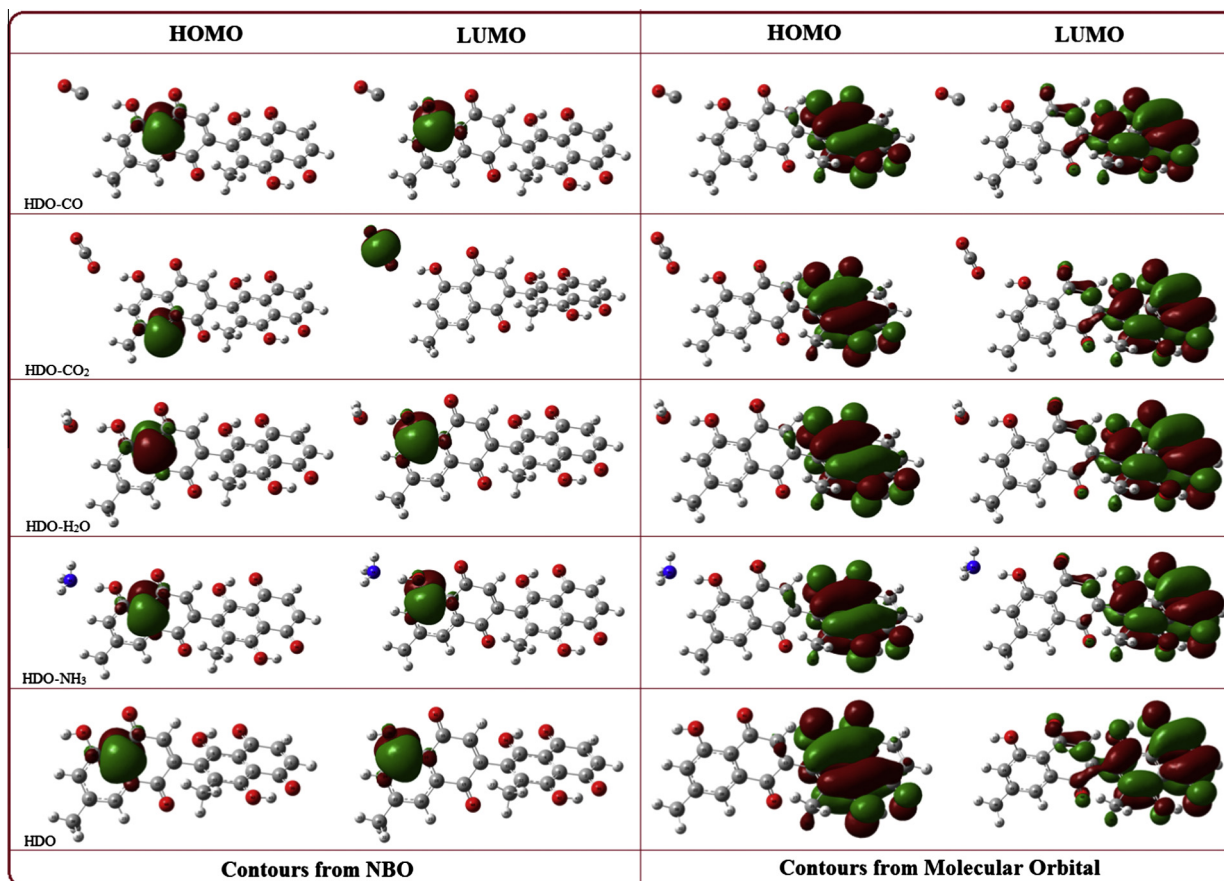


Fig. 9. Molecular orbitals of HDO and HDO-X.

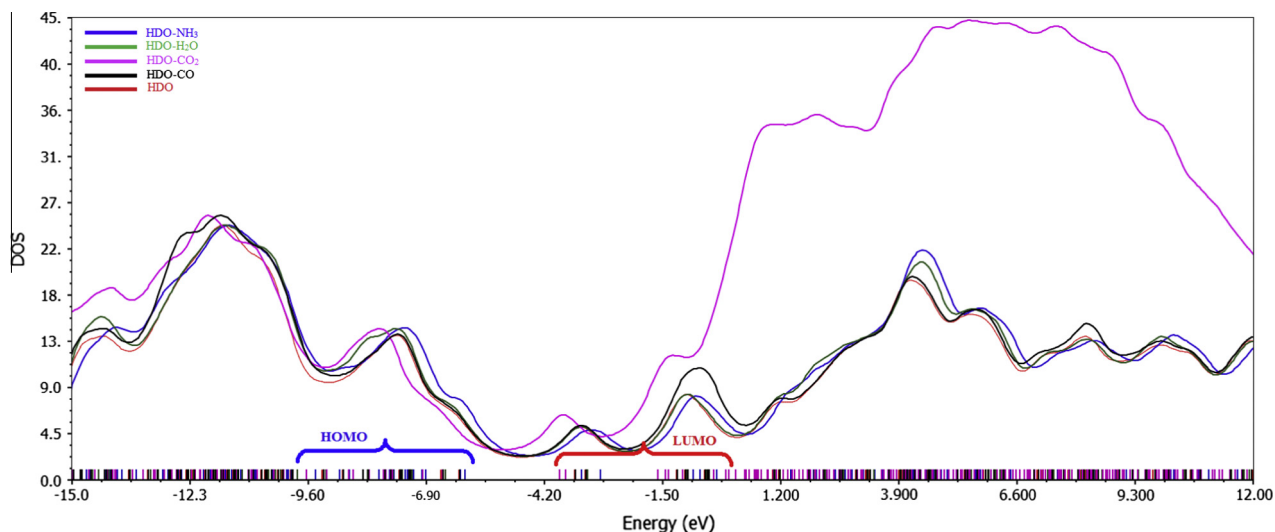


Fig. 10. Combined DOS plot of HDO and HDO-X (where X = NH₃, H₂O, CO₂, and CO).

are carried out at the mentioned level of theory (B3LYP/6-31G*). These properties are simulated for the confirmation of non-covalent interaction and determination of activity, reactivity and interaction ability of HDO (Table 6). The contours of NBO, HOMO, LUMO and DOS plots of HDO and HDO-X are depicted in Figs. 9 and 10. The role of frontier molecular orbitals in the electronic, optical properties and in chemical reactions is of great importance. The changes in these molecular orbitals reveal a chemical reaction, bond formation, old bond breaking, etc.

Moreover, the HOMO energy characterizes the capacity of electron donation while the LUMO energy describes the ability of electron acceptance. On the other hand, an ESP indicates the reactive site (*vide supra*), and HOMO–LUMO gap estimates the molecular chemical stability of a molecule. The IP and EA of parent HDO is 6.14 and 3.49 eV, respectively. Upon interaction with NH₃, lowering in IP, EA, and band gap is observed as can be seen from Table 6 and Fig. 10. This lowering in IP and EA indicate that the HDO-NH₃ complex is comparatively inert (stable) as that of parent HDO, with little electron donating and withdrawing ability. NH₃ decreases the IP of HDO from 6.14 to 6.00 eV and EA from 3.49 to 3.34 eV, while a minute increase in the band gap from 2.65 to 2.66 eV. The difference between the total DOS plots of HDO and HDO-NH₃ clearly shows the *n*-type doping of HDO (Fig. 10). Furthermore, these results also conclude that a strong non-covalent is established in this complex. Moisture has comparatively little effect on the electronic properties of HDO. Both IP and EA of HDO-H₂O complex decreases about 0.01 eV but without any change in the band gap. This behavior can also be seen from the DOS plot as depicted in Fig. 10. Non-bonding interaction of CO₂ and CO with HDO has also similar effect as that of H₂O.

Conclusion

We have carried out a comprehensive phytochemical and Density Functional Theory (DFT) study of a natural product 8-hydroxyisodiospyrin (HDO). After isolation, different experimental characterizations of the sample are performed to elucidate its chemical structure. The structure of HDO is then supported by the comparison of theoretically simulated data (DFT simulations at B3LYP/6-31G* level of theory) with the experimental values. The experimental and predicted IR and UV–vis spectra [B3LYP/6-31+G(d,p)] have excellent correlation with minor exception, which can be attributed to the condensed phase nature of HDO in the

experiment. It is also found that B3LYP/6-31G* level of theory is a proper protocol for this class of compounds. The electroactive nature of HDO is also studied quantum mechanically at B3LYP/6-31G*, and B3LYP-gCP-D3/6-31G* methods. From the comparison of these two methods, we concluded that inter-molecular interaction of HDO with gasses such as NH₃, H₂O, CO₂, and CO can be accurately and easily determined at B3LYP-gCP-D3/6-31G* method. Inter-molecular interaction of HDO with gasses is also investigated through geometrical parameters, electronic, thermodynamic, and charge analysis. Electronic properties includes Ionization Potential (IP), Electron Affinities (EA), density of states (DOS), co-efficient of highest occupied molecular orbital (HOMO), co-efficient of lowest unoccupied molecular orbital (LUMO), and band gap simulations.

Appendix A. Supplementary material

Supplementary data associated with this article can be found, in the online version, at <http://dx.doi.org/10.1016/j.molstruc.2015.04.027>.

References

- [1] J. Burns, T. Yokota, H. Ashihara, M.E. Lean, A. Crozier, *J. Agric. Food Chem.* 50 (2002) 3337–3340.
- [2] S.M.K. Rates, *Toxicol.* 39 (2001) 603–613.
- [3] A.B. Rao, E.S. Rubin, *Environ. Sci. Technol.* 36 (2002) 4467–4475.
- [4] J. Bruneton, *Pharmacognosy, Phytochemistry, Medicinal Plants*, Lavoisier publishing, 1995.
- [5] N.R. Farnsworth, D. Soejarto, *Conserv. Med. Plants* (1991) 25–51.
- [6] R.A. Halberstein, *Ann. Epidemiol.* 15 (2005) 686–699.
- [7] Y. Velioglu, G. Mazza, L. Gao, B. Oomah, *J. Agri. Food Chem.* 46 (1998) 4113–4117.
- [8] G.M. Rishton, *Am. J. Cardiol.* 101 (2008) S43–S49.
- [9] M. Arfan, A. Rauf, M.N. Tahir, M. Ali, G. Uddin, *Acta Crystallogr. Sect. E: Struct. Rep. Online* 67 (2011). o711.
- [10] G. Uddin, W. Ullah, B.S. Siddiqui, S.Q. Shah, *Nat. Prod. Res.* 27 (2013) 215–220.
- [11] A. Loizzo, S. Loizzo, A. Capasso, *Open Biochem. J.* 3 (2009) 18.
- [12] Fazl-i-Satta, Z. Ullah, A. Rauf, M. Tariq, A.A. Tahir, K. Ayub, H. Ullah, *Spectrochim. Acta Part A: Mol. Biomol. Spectrom.* 141 (2015) 71–79.
- [13] G. Uddin, A. Rauf, B. Siddiqui, A. Khan, B. Marasini, *Chemotherapy* 2 (2013) 2.
- [14] M.A. Dev, N. Rajarajeshwari, S. Ganapaty, B. Parixi, R. Brun, *J. Nat. Remedies* 12 (2012) 129–134.
- [15] G. Ji, S.K. Shukla, P. Dwivedi, S. Sundaram, R. Prakash, *Ind. Eng. Chem. Res.* 50 (2011) 11954–11959.
- [16] H. Ullah, A. Rauf, Z. Ullah, M. Anwar, A.-U.-H.A. Shah, G. Uddin, K. Ayub, *Spectrochim. Acta Part A: Mol. Biomol. Spectrom.* 118 (2014) 210–214.
- [17] K. Müller-Dethlefs, P. Hobza, *Chem. Rev.* 100 (2000) 143–168.
- [18] S. Grimme, J. Antony, T. Schwabe, C. Mück-Lichtenfeld, *Org. Biomol. Chem.* 5 (2007) 741–758.

- [19] S. Ehrlich, J. Moellmann, S. Grimme, *Acc. Chem. Res.* 46 (2012) 916–926.
- [20] S. Grimme, J. Antony, S. Ehrlich, H. Krieg, *J. Chem. Phys.* 132 (2010) 154104.
- [21] H. Kruse, L. Goerigk, S. Grimme, *J. Org. Chem.* 77 (2012) 10824–10834.
- [22] M. Piacenza, S. Grimme, *Chem. Phys. Chem.* 6 (2005) 1554–1558.
- [23] C. Diedrich, A. Lüchow, S. Grimme, *J. Chem. Phys.* 123 (2005) 184106.
- [24] S. Grimme, C. Mück-Lichtenfeld, J. Antony, *J. Phys. Chem. C* 111 (2007) 11199–11207.
- [25] M. Korth, A. Lüchow, S. Grimme, *J. Phys. Chem. A* 112 (2008) 2104–2109.
- [26] S. Grimme, *Angew. Chem. Int. Ed.* 47 (2008) 3430–3434.
- [27] J. Antony, B. Brüske, S. Grimme, *Phys. Chem. Chem. Phys.* 11 (2009) 8440–8447.
- [28] R.W. Baker, L. Song, M.V. Sargent, *Aust. J. Chem.* 51 (1998) 255–266.
- [29] C. Lee, W. Yang, R.G. Parr, *Phys. Rev. B* 37 (1988) 785.
- [30] C. Lee, C. Sosa, *J. Chem. Phys.* 100 (1994) 9018–9024.
- [31] W. Kohn, A.D. Becke, R.G. Parr, *J. Phys. Chem.* 100 (1996) 12974–12980.
- [32] U. Salzner, P. Pickup, R. Poirier, J. Lagowski, *J. Phys. Chem. A* 102 (1998) 2572–2578.
- [33] H. Ullah, A.A. Shah, S. Bilal, K. Ayub, *J. Phys. Chem. C* 117 (2013) 23701–23711.
- [34] H. Ullah, A.A. Shah, K. Ayub, S. Bilal, *J. Phys. Chem. C* 117 (2013) 4069–4078.
- [35] H. Ullah, A.A. Shah, S. Bilal, K. Ayub, *J. Phys. Chem. C* 118 (2014) 17819–17830.
- [36] U. Salzner, *Curr. Org. Chem.* 8 (2004) 569–590.
- [37] H. Ullah, K. Ayub, Z. Ullah, M. Hanif, R. Nawaz, A.A. Shah, S. Bilal, *Synth. Met.* 172 (2013) 14–20.
- [38] J.G. Brandenburg, M. Alessio, B. Civalleri, M.F. Peintinger, T. Bredow, S. Grimme, *J. Phys. Chem. A* 117 (2013) 9282–9292.
- [39] M. Frisch, G. Trucks, H.B. Schlegel, G. Scuseria, M. Robb, J. Cheeseman, G. Scalmani, V. Barone, B. Mennucci, G. Petersson, Inc., Wallingford, CT 200, 2009.
- [40] A.R. Allouche, *J. Comput. Chem.* 32 (2011) 174–182.

[Article 16]

Z. Ullah, A. Rauf, M. Tariq, A. A. Tahir, K. Ayub, H. Ullah, "Phytochemical, spectroscopic and density functional theory study of diospyrin, and non-bonding interactions of diospyrin with atmospheric gases." *Spectrochim. Acta, Part A*. vol. 141, pp. 71-79, Apr. 2015.



Contents lists available at ScienceDirect

Spectrochimica Acta Part A: Molecular and Biomolecular Spectroscopy

journal homepage: www.elsevier.com/locate/saa

Phytochemical, spectroscopic and density functional theory study of Diospyrin, and non-bonding interactions of Diospyrin with atmospheric gases



Fazl-i-Sattar^a, Zakir Ullah^a, Ata-ur-Rahman^{a,*}, Abdur Rauf^a, Muhammad Tariq^b, Asif Ali Tahir^c, Khurshid Ayub^{d,e}, Habib Ullah^{a,c,*}

^a Institute of Chemical Sciences, University of Peshawar, 25120 Peshawar, Pakistan

^b National Centre of Excellence in Physical Chemistry, University of Peshawar, 25120 Peshawar, Pakistan

^c Environment and Sustainability Institute (ESI), University of Exeter, Penryn Campus, Penryn, Cornwall TR10 9FE, UK

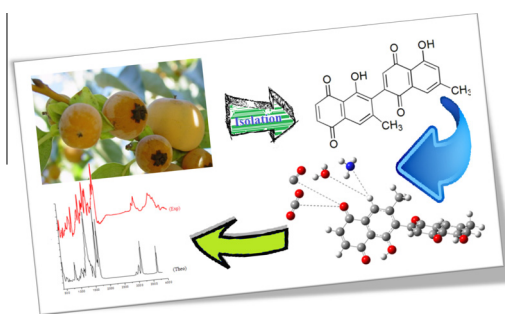
^d Department of Chemistry, COMSATS Institute of Information Technology, University Road, Tobe Camp, 22060 Abbottabad, Pakistan

^e Department of Chemistry, College of Science, King Faisal University, Al-Hafouf 31982, Saudi Arabia

HIGHLIGHTS

- DFT and phytochemical study of *Diospyrin*.
- Non-covalent interaction atmospheric gases with *Diospyrin*.
- NH₃, H₂O, CO₂ and CO gases.
- IR, UV-vis, HOMO, and LUMO.

GRAPHICAL ABSTRACT



ARTICLE INFO

Article history:

Received 11 November 2014

Received in revised form 8 January 2015

Accepted 14 January 2015

Available online 21 January 2015

Keywords:

Density functional theory
 Diospyrin
 B3LYP/6-31G (d,p)
 BSSE
 UV-vis
 HOMO-LUMO gap

ABSTRACT

Density functional theory (DFT) and phytochemical study of a natural product, *Diospyrin* (DO) have been carried out. A suitable level of theory was developed, based on correlating the experimental and theoretical data. Hybrid DFT method at B3LYP/6-31G (d,p) level of theory is employed for obtaining the electronic, spectroscopic, inter-molecular interaction and thermodynamic properties of DO. The exact structure of DO is confirmed from the nice validation of the theory and experiment. Non-covalent interactions of DO with different atmospheric gases such as NH₃, CO₂, CO, and H₂O were studied to find out its electroactive nature. The experimental and predicted geometrical parameters, IR and UV-vis spectra (B3LYP/6-31+G (d,p) level of theory) show excellent correlation. Inter-molecular non-bonding interaction of DO with atmospheric gases is investigated through geometrical parameters, electronic properties, charge analysis, and thermodynamic parameters. Electronic properties include, ionization potential (I.P.), electron affinities (E.A.), electrostatic potential (ESP), density of states (DOS), HOMO, LUMO, and band gap. All these characterizations have corroborated each other and confirmed the presence of non-covalent nature in DO with the mentioned gases.

© 2015 Elsevier B.V. All rights reserved.

* Corresponding authors at: Institute of Chemical Sciences, University of Peshawar, 25120 Peshawar, Pakistan, Environment and Sustainability Institute (ESI), University of Exeter, Penryn Campus, Penryn, Cornwall TR10 9FE, UK (H. Ullah).

E-mail address: atasafi@upesh.edu.pk (H. Ullah).

Introduction

Medicinal plants are the factory of producing thousands of secondary metabolites in most selective and precise way. These plants

were/are used directly or indirectly by 80% of the world population for their basic health needs. Current estimates suggest that in many developing countries, a large proportion of population relies heavily on the traditional practitioner and medicinal plants to meet their primary health care needs. Although, modern medicine are available in these countries but they prefer traditional medicines. Natural product isolated from marine and terrestrial plant, play a significance role in the drug discovery. The relationship between human, plants and drugs derived from plants, describe the history of mankind. Plants contain potential compounds for the treatment of diseases which are not easily curable. Pakistan has rich countless floras, especially the Khyber Pakhtunkhwa (KPK) province [1,2]. The country has more than 6000 species of wild plants, out of them about 400–600 are considered to be medicinally important. During the past decades, traditional systems of medicine have become a topic of global importance [3]. Herbal medicines have maintained their popularity both for historic and cultural reasons. Currently, many people in the developed countries have begun to turn on alternative or complementary therapies, including medicinal herbs [4].

In this regards, the genus *Diospyros* (Ebenaceae) is medicinally quite important, and consists of woody shrubs and trees which are distributed in the tropical and subtropical regions of the world. Around 500 species are known worldwide of which, 24 species are native to Asia [5]. *Diospyros lotus* (DL) is a deciduous tree, growing in China and Asia. DL has been cultivated for its edible fruits. The fruits of DL is used as a sedative, astringent, nutritive, antiseptic, antidiabetic, antitumor, astringent, laxative, nutritive and for the treatment of constipation [6]. DL fruits are also used for the treatment of diarrhea, dry coughs and hypertension.

We also investigated the phytochemical studies on many of *Diospyros* species, and have shown widespread presence of naphthoquinones, naphthalene derivatives, dimeric naphthoquinones and lupane triterpenes. Chemical investigation of the fruits of DL led to identification of some fatty acids, sugars phenolic compounds and non-volatile acids [7]. Diospyrin (DO) is bisnaphthoquinone, which has been isolated from fruits of DL, and exhibited significant lipoxigenase inhibitory activity [8]. DO has been reported from DL which poses significant inhibitory effect on the growth of *Leishmania donovani* promastigotes. DO inhibit the catalytic activity of DNA topoisomerase I of the parasite and its chemical structure is given in Fig. 1. DO induces topoisomerase I mediated DNA cleavage in vitro bioassay. Thus DO is a precise inhibitor of the parasitic topoisomerase I. [9].

We have reported number of biological activities of DO which are attributed to high potential and reactivity. In addition to biological activities (earlier investigations), the present work is going to describe a comparative experimental and density functional theory (DFT) study of DO to confirm its exact structure by correlation of experimental and theoretical spectroscopic data. Finally, its non-covalent interaction abilities towards atmospheric gases are also investigated. Non-covalent interaction is a hot research topic of organic chemistry (aromatic compounds) which has number of applications in the field of sensors, drug design, protein folding,

etc. This non-bonding interaction study of DO with atmospheric gases such as NH_3 , CO_2 , CO , and moisture are studied. For the first time, sensor potential of a natural product toward the atmospheric gases is studied.

Materials and methods

Plant material

Roots of DL were collected from Toormang Razagram, Dir, KPK, Pakistan, in May 2009. The sample was authenticated by a Taxonomist in the Botany Department, University of Peshawar, Pakistan. A voucher specimen (Bot. 20036 (PUP)) has been deposited at the Herbarium, department of Botany, University of Peshawar, Pakistan.

Extraction and isolation

Shade-dried roots of DL (14 kg) were powdered, and kept at room temperature in MeOH for 6 days (four times each) with continuous stirring through simple percolation. After this period, the extracts was combined and concentrated by evaporating the solvents under controlled temperature (55 °C) using a rotary vacuum evaporator at a reduced pressure to deliver a dark red residue (202 g). Furthermore, it was suspended in water and successively partitioned with hexane, CHCl_3 , EtOAc and *n*-BuOH according to a standard protocol. The chloroform fraction (30 g) was subjected to column chromatography on silica gel (Merck Silica gel 60 (0.063–0.200 mm), 5 × 60 cm). The column was eluted with hexane–ethyl acetate (100:0 → 0:100) as a solvent system. A total of 105 fractions, RF-1 to RF-105 were obtained based on TLC profiles. Elution of the chromatogram with hexane–EtOAc (100:0 → 10:100) gave a reddish color, oil of fatty acid residues and red crystals of various sizes and shape. The crystals were separated from the solution by washing with *n*-hexane. To obtain pure and larger crystals, these crystals were re-grown from a mixture of hexane–chloroform. DO was obtained as a polar orange–red crystalline compound (1.4 g) at m.p. 252–255 °C. The ^1H and ^{13}C NMR data were found to be identical to the data reported previously for DO [10], so that is why we did not include here.

Computational methodology

DFT calculations at B3LYP/6-31G (d,p) level of theory were performed for DO and DO–X (X = NH_3 , CO_2 , CO , and H_2O) [11]. DFT method has been chosen because of our previous experience and accuracy associated [12–16]. Vibrational spectra (IR) are simulated on the optimized geometries at the same level of theory [17,18]. Frequency simulation has also confirmed that the molecule is completely optimized (no imaginary frequency). Excited state properties such as ionization potential (I.P.), electron affinities (E.A.), co-efficient of highest occupied molecular orbital (HOMO), co-efficient of lowest unoccupied molecular orbital (LUMO) and band gap are simulated at the above mentioned level of theory [B3LYP/6-31G (d,p)]. Interaction energy (ΔE_{int}), counterpoise corrected energy ($\Delta E_{\text{int,CP}}$) such as basis set superposition error (BSSE), and geometrical counterpoise corrected energy ($\Delta E_{\text{gCP-D3}}$) [13,19,20] simulations are performed for the determination of non-covalent interaction. UV–vis spectra are simulated at time depended (TD), TD-B3LYP/6-31+G (d,p) level of theory, using both gas phase and chloroform media. Band gap are simulated as the difference of LUMO and HOMO orbital energies. All calculations were performed on GAUSSIAN 09 [21] suite of program in the gas phase, except UV–vis (chloroform media). The visualizations of results are achieved with GaussView and Gabedit [22].

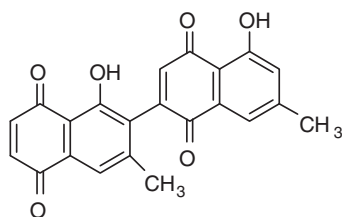


Fig. 1. Molecular structure of Diospyrin.

Results and discussion

Optimized geometry

The optimized molecular structure of DO is shown in Fig. 2. The prominent optimized structural parameters (bond length, bond angle and dihedral angle) calculated at DFT-B3LYP/6-31G (d,p) level of theory are listed in Table 1. DO is an orange color semi-crystalline substance. Major prominent observed bond lengths (only) [23] are correlated with the simulated ones and are listed in Table 1.

The bond distances for the calculated C–H and O–H are 1.08 and 0.9 Å, respectively and no correlation can be made due to the non-availability of experimental data. The observed bond length of C–O is in the range of 1.21–1.47 Å, and has nice correlation with their counterpart simulated ones (1.22–1.48 Å). The C–C bonds are found to be in the range of 1.32–1.50 Å in the experiment and can be correlated to the predicted 1.24–1.50 Å. There are also existing hydrogen bonds between the H42...O41 and H36...O38, which are 1.69 and 1.66 Å, respectively. The bond angle among H–C–H is 108° while the C–C–C at ca. 122.2–117.0°, and C–C–O angle is 118.6–122.5°. The last distinguished bond angle of DO is C–C–H, which is found to be in the range of 115.6–122.3°. About six different major dihedral angles can be observed in DO which are listed in Table 1.

Infra-red spectral characteristics

According to non-linear molecular vibrational mode formula ($3N - 6$), DO consist of 42 atoms with molecular formula of $C_{22}H_{14}O_6$, and expected to have 120 normal modes of vibrations under C_1 symmetry. Comparative simulated and experimental IR spectra of DO are plotted in Fig. 3, however, some of the major band peaks along with their approximate assignments are listed in Table 2. In Table 2 and 15 major band peaks of the calculated IR spectra are compared with that of the experimental peaks. Furthermore, these modes (band peaks) are found to be most active in the infra-red absorption. The functional group region of the simulated IR spectra has three peaks including one shoulder peak, consisting of hydroxyl and methyl group stretching.

The O–H band peaks appeared at ca. 3651 and 3120 cm^{-1} and are correlated with the experimental 3548 and 2922 cm^{-1} , respectively. C–H stretching peaked at 2928 cm^{-1} and has good correlation (based on similar assignment) with the observed 2853 cm^{-1} . The most prominent peaks of the finger print region of the calculated IR spectra are situated at 1683 , 1677 , and 1589 cm^{-1} . These peaks have very nice correlation with the observed (experimental) 1666 , 1639 and 1598 cm^{-1} , respectively (see Table 2). Other peaks of this region (simulated) such as 1474 cm^{-1} can be correlated with the experimental 1563 cm^{-1} based on their similar C=C stretching. The simulated band peaked at 1391 cm^{-1} is due to combination of

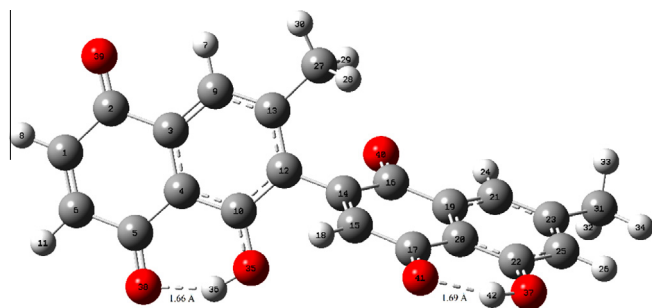


Fig. 2. Optimized geometric structure of DO.

Table 1

Optimized geometric parameters of DO.

Geometrical parameters	B3LYP/6-31G (d,p)	Experimental [23]
Bond length (Å)		
C31–H34, C25–H26	1.09, 1.08	
C15–H18, C6–H11	1.08, 1.08	
O37–H38, O35–H36	0.96, 0.99	
C22–O37, C17–O42, C10–O35	1.35, 1.22, 1.33	1.34, 1.23, 1.33
C2–O40, C5–O39	1.22, 1.48	1.21, 1.47
C31–C23, C23–C25, C25–C22	1.50, 1.39, 1.40	1.50, 1.37, 1.38
C22–C28, C19–C20, C21–C19	1.41, 1.41, 1.39	1.40, 1.40, 1.37
C19–C16, C10–C4, C2–C1	1.48, 1.41, 1.24	1.48, 1.40, 1.23
C15–C14, C14–C12, C12–C10	1.34, 1.49, 1.41	1.33, 1.49, 1.40
C3–C4, C4–C10, C3–C2	1.41, 1.38, 1.49	1.40, 1.37, 1.48
C6–C1, C6–C5	1.34, 1.08, 1.47	1.320, 1.48
Bond angle (°)		
H34–C31–H33	108.0	
C15–C14–C12	122.2	
C1–C2–C3	117.0	
C12–C10–O35	118.6	
C3–C2–O40	122.5	
C2–C1–H8	115.6	
C6–C1–H8	122.3	
Dihedral angle (°)		
H34–C31–H32–C23	–122.5	
O41–C16–C19–C20	–179.0	
C16–C14–C12–C10	111.9	
C15–C14–C12–C13	113.9	
C23–C25–C22–C20	0.04	
C15–C17–C20–C19	0.83	

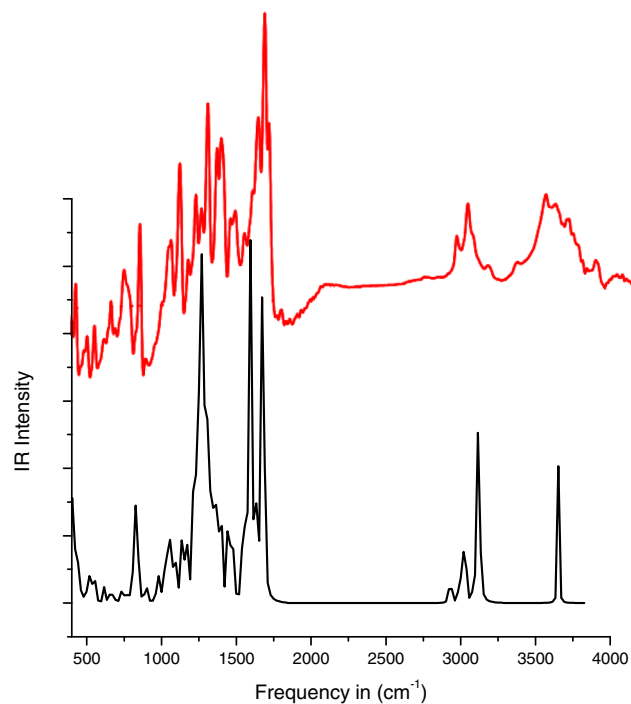


Fig. 3. Experimental (red) and simulated (black) IR Spectra of DO. (For interpretation of the references to color in this figure legend, the reader is referred to the web version of this article.)

C=C stretching and C–H, O–H bending and are correlated with 1453 cm^{-1} of the experimental IR spectra. Other calculated bands such as 1334 cm^{-1} has good correlation with the experimental 1365 cm^{-1} and the band peak at ca. 1266 cm^{-1} can be correlated with the observed 1280 cm^{-1} . The simulated 1258 cm^{-1} is because of C–C stretching and C–H, O–H wagging and has nice correlation

Table 2
Experimental and calculated IR frequencies (in cm^{-1}) of DO.

S. No.	Experimental	Scaled	Unscaled	Approximate assignment
1	3548	3651	3799	ν O–H
2	2922	3120	3246	ν O–H
3	2853	2928	3045	ν C–H (sym)
4	1666	1683	1750	ν C=C, C=O
5	1639	1677	1744	ν C=O, C=C; Wag C–H
6	1598	1589	1652	ν C=C, C–C; Wag C–H
7	1563	1474	1533	ν C=C, β O–H, Wag C–H
8	1453	1391	1447	ν C=C, β C–H, O–H
9	1365	1334	1388	ν C–C, C=C; β O–H, C–H
10	1280	1266	1317	ν C–C; Wag C–H, O–H
11	1245	1258	1309	ν C–C; Wag C–H, O–H
12	1204	1221	1271	ν C–C; Wag C–H, O–H
13	1047	1066	1109	Cis C–H, ring breathing
14	850	836	870	β O–H, C–H
15	444	416	433	β C–H, rings breathing

Note: ν : for stretching, β : out of plan bending, Wag: for wagging, sym: symmetric.

with the experimental 1245 cm^{-1} . C–C stretching and C–H, O–H wagging also produce a peak at 1221 cm^{-1} and has excellent correlation with the observed 1204 cm^{-1} . Simulated 1066 cm^{-1} has C–H scissoring and ring breathing vibration and is about 19 cm^{-1} lower than that of observed 1047 cm^{-1} . The last two peaks of the finger print region at ca. 836 and 416 cm^{-1} , which are because of O–H, C–H, and C–H bending, respectively. The differences between the simulated and observed band peaks is because of gas phase simulation while the experimental IR spectra is that of condensed phase.

UV–vis spectral analysis

Experimental and TD-DFT calculated UV–vis spectra of DO are shown in Figs. 4 and 5, respectively. For comparison reason, UV–vis spectra are simulated both in gas phase and in chloroform media (Fig. 5). In the theoretical UV–vis spectrum vertical excitation energies are plotted against oscillator strength. Three major absorptions are present in the experimental UV–vis spectrum, at ca. 439, 355, and 260 nm. Both of the calculated and observed (experimental) absorbance of the UV–vis spectra of DO along with their transitions are shown in Table 3.

Both theoretical and experimental absorption band peaks have good correlation, observed 439 nm absorption is about 20 nm less than the simulated 459 nm (gas phase). The absorption band peak ca. 439 nm is because of $\pi \rightarrow \pi^*$ transition, the 355 nm is due to

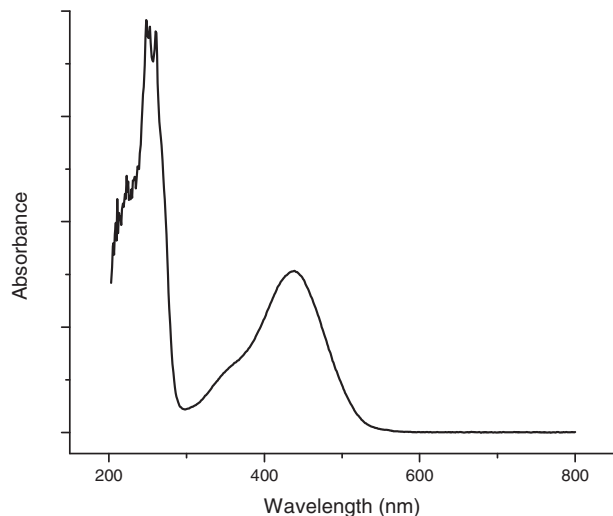


Fig. 4. Experimental UV–vis spectra of DO.

HOMO – 1 to LUMO + 1 transition while the absorbance at ca. 260 nm is a theoretical forbidden transition which is an electronic excitation from HOMO – 8 to LUMO + 2.

Frontier molecular orbitals analysis

The HOMO and LUMO are those orbitals which interact with other species, hence they are called the frontier molecular orbitals. These orbitals are very important in the electric, optical properties, as well as in UV–visible spectra and chemical reactions [24,25]. The energies of HOMO, LUMO and their orbital energy gaps are simulated by using B3LYP/6-31G (d,p) method, while the pictographic design of these frontier molecular orbitals are shown in Fig. 6. Molecular orbitals provide clues into the nature of reactivity, conjugation, aromaticity, lone pairs and some of the structural and physical properties of molecules.

The HOMO energy characterizes the capacity of electron donation and the LUMO energy characterizes the ability to accept electron, and the gaps between HOMO and LUMO characterizes the molecular chemical stability and electrical transport properties [26]. The HOMO and LUMO energy values of DO are estimated to be -6.45 and -3.29 eV , respectively, while the band gap or energy gap is found to be 3.16 eV . The electronic cloud density of HOMO is distributed on the left side of DO, especially on the C=O, O–H, and some C–C bonds, however this electron density is more prominent in LUMO which show its electroactive nature (highly reactive). These HOMO and LUMO lead us to conclude that the most reactive sites of DO is O_{39} (numbering are with ref to Fig. 2).

Mulliken and NBO charge analysis

Charge analysis was performed for the reactive site simulation of DO. Both Mulliken and natural bonding orbital (NBO) analysis were carried out on the optimized geometric structure of DO, shown in Fig. 7. According to NBO charge analysis O_{35} and O_{39} have -0.687 and -0.512 e^- unit of electron charge, respectively. Mulliken charge analyses also confirm this atom to be of highest negative charge (nucleophile), O_{39} has -0.403 e^- unit of electron. This statement is also in line with the frontier molecular orbitals analysis.

Molecular electrostatics potential study

The electrostatic potential (ESP) of DO is calculated and is depicted in Fig. 8. The molecular electrostatic potential (MEP) map predicts the nature of electrophilic attack and nucleophilic reactions of the molecule. MEP has shaped the space around the molecule by its nuclei and electrons. It also provides charge density, delocalization and site of chemical reactivity of the molecules (*vide supra*). MEP map for the DO with color range from -7.31×10^{-2} (deepest red, high electron density) to the 7.31×10^{-2} (deepest blue, high electrophilic region) is simulated. According to the MEP, O_{39} is the regions of highest electron density, which is also in line with frontier molecular orbitals and charge analysis. However, MEP indicates four reactive sites of DO, region around O_{39} (1st highest charge density), region around O_{40} , O_{37} and O_{41} (2nd highest electron density area), the O_{35} and O_{38} regions which are least reactive sites.

Both HOMO/LUMO and the charge analysis (NBO and Mulliken) illustrate the area around O_{39} is the most effective for the non-covalent interactions. We also confirmed the effectiveness of this area from its non-bonding interaction at atmospheric gases. Therefore, O_{39} is used for the interacting study.

Intermolecular interaction of DO with atmospheric gases

Atmospheric gases such as NH_3 , CO_2 , moisture (H_2O), CO, and CO are interacted with DO, near the proximity of O_{39} atom, based

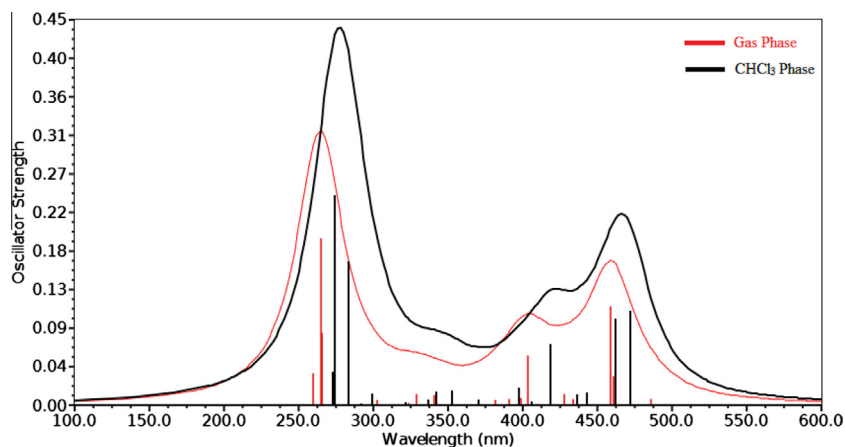


Fig. 5. Simulated UV-vis spectra of DO.

Table 3
Experimental and vertical excitation energy of HDO along with oscillator strength and transition.

Peak	Experimental	Excitation energy (nm)		Oscillator strength		Electronic transition	
		Vacuum	CHCl ₃	Vacuum	CHCl ₃	Vacuum	CHCl ₃
1	439	459	472	0.11	0.11	H → L	H → L
2	355	404	419	0.05	0.07	H ₋₁ → L ₂	H ₋₁ → L ₂
3	260	264	274	0.19	0.24	H ₋₈ → L ₂	H ₈ → L ₂

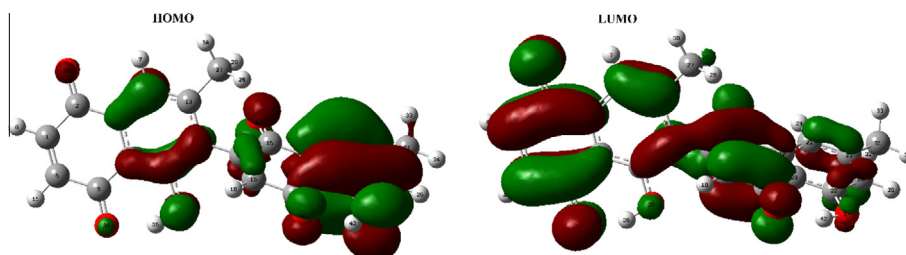


Fig. 6. Frontier molecular orbitals of DO.

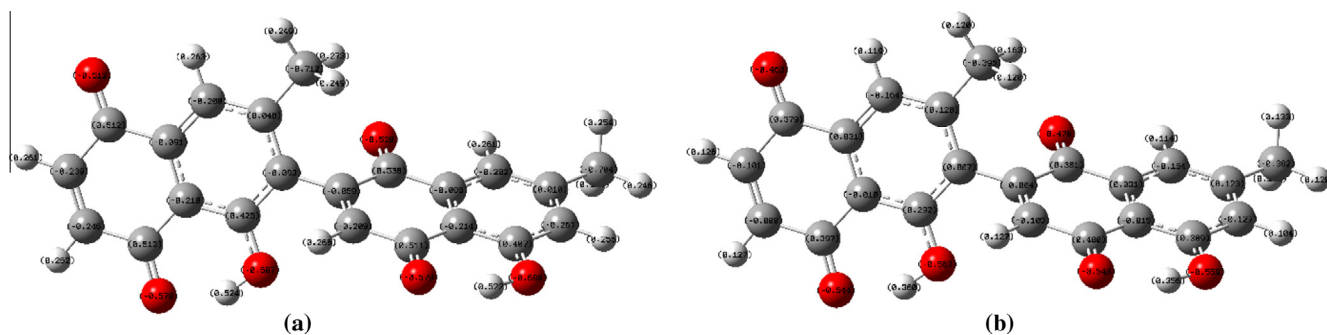


Fig. 7. NBO (a) and Mulliken (b) charge analysis of DO.

on the HOMO, LUMO, NBO, Mulliken charge analysis, and ESP. Although, ESP analysis indicates four reactive sites but the response of other three sites were lower compared to O₃₉ region (*vide supra*). Comparative optimized geometric structures of all these DO–X complexes are given in Fig. 9, along with the important inter- and intra-molecular optimized geometric parameters. Other intermolecular parameters such as ΔE_{int} , $\Delta E_{\text{int,CP}}$, $\Delta E_{\text{gCP-D3}}$, Q_{NBO} and Q_{Mulliken} are listed in Table 4.

DO–NH₃ complex. NH₃ interacts with DO from its H and N to the O₃₉ and H₇ of DO, as depicted in Fig. 9a. The N and H of ammonia form a hydrogen type bonds to the H₇ and O₃₉ of DO. These non-covalent interaction distances are 2.34 Å for N–H₇ and 2.26 Å for H–O₃₉. Ammonia changes the electronic structure properties of DO through charge transfer (NH₃ donates electron) of about 0.006 and 0.007 e⁻ based on both of Q_{NBO} and Q_{Mulliken} analysis, respectively. Although this charge transfer is very small, but yet

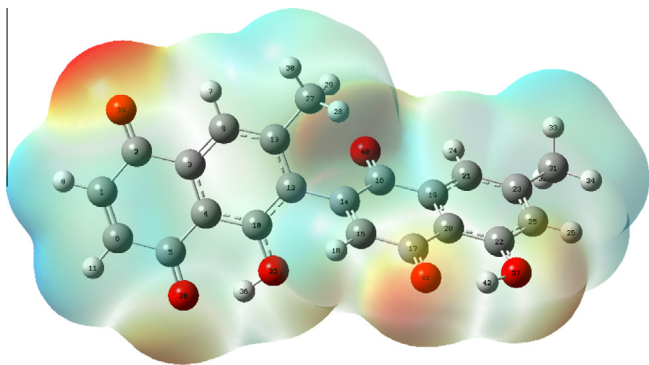


Fig. 8. Molecular electrostatic potential (MEP) of DO.

indicate its alteration in the band gap, λ_{\max} (*vide infra*), and optimized geometric structure of DO. The geometrical parameters especially, near the analytes (NH_3) are found to be effected which is in fact the sensitivity measurements parameter.

The interaction energy of DO– NH_3 complex is about -5.71 and -4.91 kcal mol^{-1} based on ΔE_{int} and $\Delta E_{\text{int,CP}}$, respectively. While the $\Delta E_{\text{gCP-D3}}$ energy is -6.08 kcal mol^{-1} . This is a relatively high energy of interaction which confirmed a hydrogen type of bonding.

DO– H_2O complex. Water donates electrons to DO, and form a DO– H_2O complex which has distorted geometry especially near the adjoining rings (Fig. 9). Highest interaction energy is found in this complex, for which the common interaction energy is -8.47 kcal mol^{-1} whereas the counterpoise corrected energy is -7.80 kcal mol^{-1} . The geometrical counterpoise corrected ($\Delta E_{\text{gCP-D3}}$) is also higher than the DO– NH_3 which is -7.78 kcal mol^{-1} . On the basis of this interaction energy simulation, H_2O interact more

Table 4

ΔE_{int} , $\Delta E_{\text{int,CP}}$, $\Delta E_{\text{gCP-D3}}$, Q_{NBO} and Q_{Mulliken} of DO–X (X = NH_3 , CO_2 , H_2O , CO, and CO).

Species	ΔE_{int}	$\Delta E_{\text{int,CP}}$	$\Delta E_{\text{gCP-D3}}$	Q_{NBO}	Q_{Mulliken}
DO– NH_3	–5.71	–4.91	–6.08	–0.006	–0.007
DO– H_2O	–8.47	–7.80	–7.78	0.003	0.012
DO– CO_2	–2.82	–1.38	–3.07	0	–0.001
DO–CO	–1.38	–0.31	–1.88	–0.001	–0.004

efficiently compared to NH_3 (Table 4). DO donates about 0.003 charge of e^- based on Q_{NBO} , and 0.012 e^- based on Q_{Mulliken} to H_2O molecule. An appreciable amount of non-covalent bond distances for this complex are calculated ca. 1.98 and 2.26 Å, which are lesser than that of DO– NH_3 complex. H_2O also distorts the bond angles of DO (near the proximity of analyte) in small extent.

DO– CO_2 complex. CO_2 gas has little interaction ability with DO, as revealed from intermolecular distances, charge transfer, and interaction energy calculations. A small amount of non-covalent interaction is found to be present in this complex, with Vander Waal types of bonds. These distances are 2.53 Å for $\text{H}_7\text{—O}$ and 2.92 Å for $\text{O}_{39}\text{—C}$, larger than that of NH_3 , and H_2O interacting systems. The Vander Waal electrostatic interaction energy of the DO– CO_2 complex is -2.82 kcal mol^{-1} , counterpoise corrected and $\Delta E_{\text{gCP-D3}}$ energy are -1.38 and 3.07 kcal mol^{-1} , which is much lower than the binding energies for the DO– NH_3 , and DO– H_2O complexes. This low interaction is because of the inertness and zero dipole movement of CO_2 . A negligible amount of charge transferring of about 0.001 e^- based on Mulliken charge analysis is found to be present in the DO– CO_2 complex.

DO–CO complex. Another toxic gas such i.e., Carbon monoxide was also tested by DO with non-bonding interactions and found to have very little interaction as can be seen from the geometric

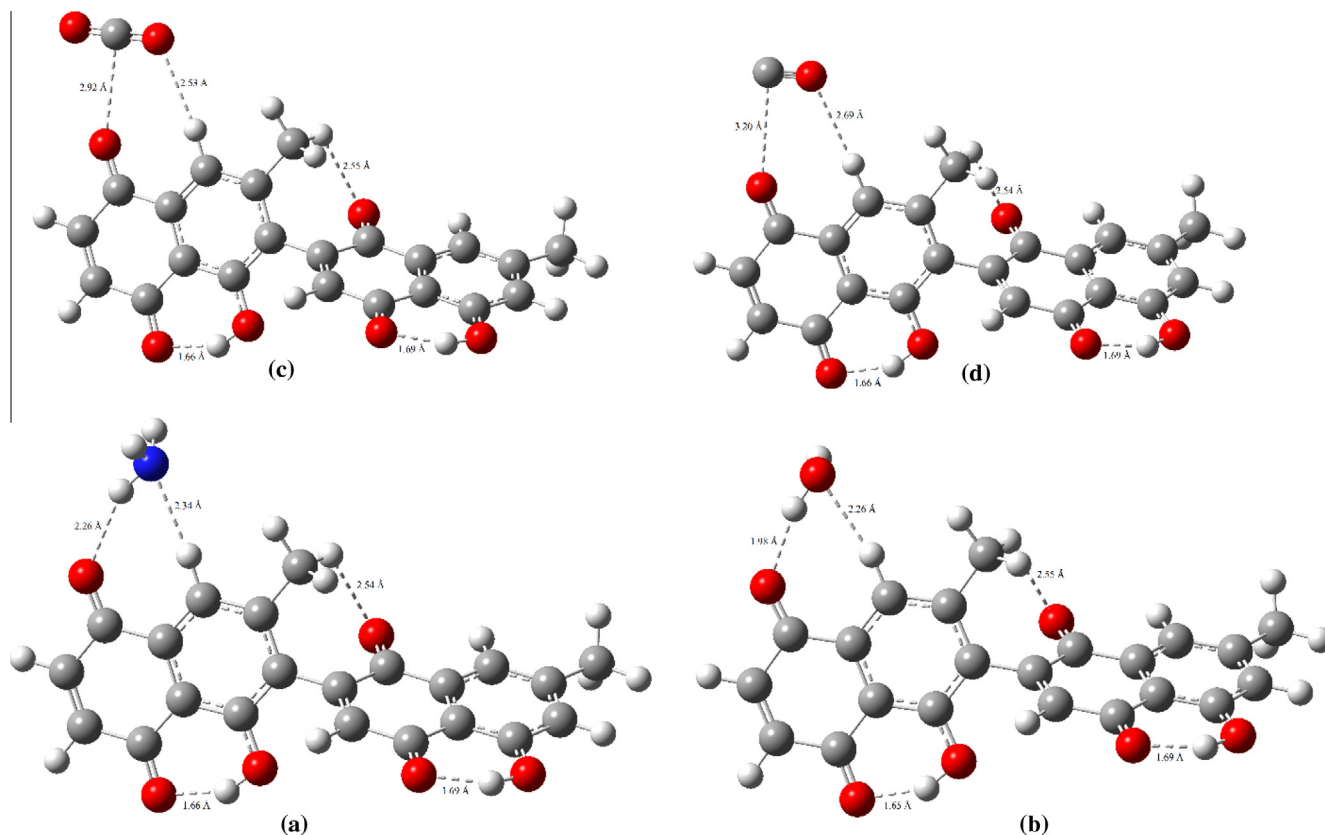


Fig. 9. Optimized geometric structures of DO and DO–X.

Table 5
TD-B3LYP/6-31+G (d,p) calculated electronic excitations of DO and DO-X.

Species	Peak	Excitation energy (nm)	Oscillator strength	Electronic transition
DO	1	459	0.11	S₀ → S₁
DO-NH ₃		457	0.14	S ₀ → S ₁
DO-H ₂ O		458	0.16	S ₀ → S ₁
DO-CO ₂		459	0.15	S ₀ → S ₁
DO-CO		460	0.14	S ₀ → S ₁
DO	2	404	0.05	S₋₁ → S₂
DO-NH ₃		400	0.05	S ₋₁ → S ₂
DO-H ₂ O		408	0.03	S ₋₁ → S ₂
DO-CO ₂		406	0.05	S ₋₁ → S ₂
DO-CO		404	0.05	S ₋₁ → S ₂
DO	3	264	0.19	S₋₈ → S₂
DO-NH ₃		293	0.09	S ₋₈ → S ₂
DO-H ₂ O		264	0.16	S ₋₈ → S ₂
DO-CO ₂		264	0.17	S ₋₈ → S ₂
DO-CO		264	0.17	S ₋₈ → S ₂

parameters; charge exchange and amount of interaction energy (see Table 4). The intermolecular interaction distances at H₇-C and O₃₉-C are found to be 2.69 and 3.20 Å, respectively which are even greater than that of DO-CO₂ complex. Selected bond angles of DO did not change with CO interaction. The amount of charge transfer is also negligible, 0.001 e⁻ based on of NBO and -0.004 e⁻ based on Q_{Mulliken} charge analyses. The charge transfer from CO to DO is much smaller than the charge transfer of the mentioned complexes. This inertness of CO can be attributed to the internal resonance structure of CO ($\text{C}\equiv\text{O}^+$).

UV-vis spectral characteristics

The interaction of atmospheric gases such as NH₃, moisture (H₂O), CO₂, and CO is also simulated with the help of vertical excitation energy's band peaks, oscillator strengths, and orbital transitions. Three prominent band peaks are found for DO and DO-X complexes, as listed in Table 5. Moreover, comparative simulated UV-vis spectra of DO and DO-X complexes are shown in Fig. 10. NH₃ blue-shifts the parent absorptions peaks of DO, except the lower wavelength peak. It also shifts the HOMO-LUMO excitation energy of DO to about 2 nm, with S₀ → S₁ excitation energy from 459 to 457 nm, S₋₁ → S₂ from 404 to 400 nm, and red-shifts the S₋₈ → S₂ from 264 to 293 nm. Optical absorption band peaks of DO-NH₃ complex predict good interaction between NH₃ and DO.

These shifting are very small, but the system is purely vacuum phase and level of theory is also same so, these minute change cannot be ignored.

UV-vis spectra of DO-H₂O complex estimate considerable non-covalent interaction, as can be seen from Fig. 10 and Table 5. Interestingly, moisture blue-shifts the first absorptions of DO from 559 to 558 nm (almost negligible), red-shifts the mid absorption from 404 to 408 nm and have no effect on 264 nm (last peak). The UV-vis spectral data of DO-H₂O complex are also in agreement with discussed characterizations.

UV-vis spectra of DO-CO₂ and DO-CO show very weak type of inter-molecular interaction which can be regarded as Vander Waal bond. The absorption band peaks of DO-CO₂ and DO-CO are quite similar to that of parent DO; red-shifting in the lower excitations energies (1st and 2nd high wavelength peaks) and no shifting in

Table 6
I.P., E.A. and band gap of DO and DO-X.

Species	I.P.	E.A.	Band gap
DO	6.45	3.29	3.16
DO-NH ₃	6.41	3.21	3.20
DO-H ₂ O	6.58	3.42	3.16
DO-CO ₂	6.50	3.35	3.14
DO-CO	6.47	3.32	3.14

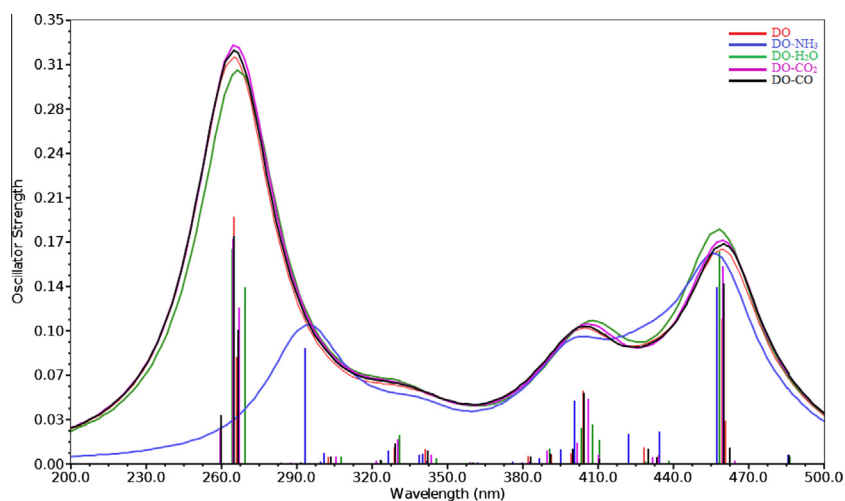


Fig. 10. UV-vis spectra of DO and DO-X.

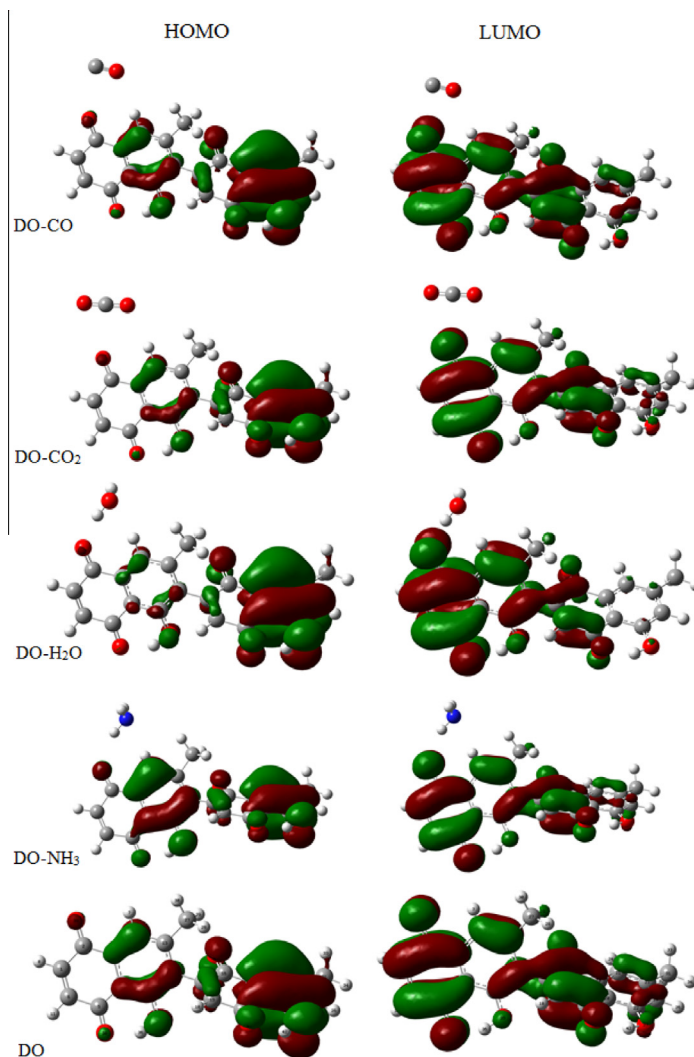


Fig. 11. Frontier molecular orbitals of DO and DO-X.

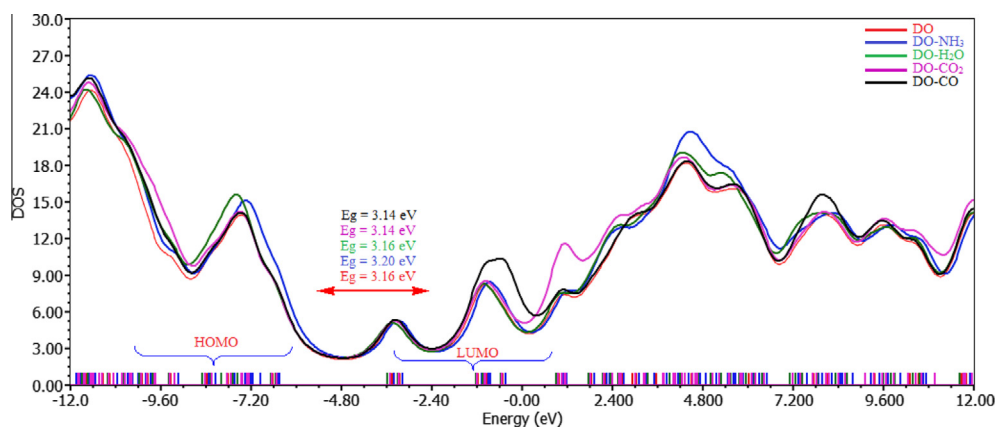


Fig. 12. Total DOS of DO and DO-X.

the last peak (Table 5). Moreover, the molecular orbital transitions (excitation from lower energy orbital to higher orbital) are similar to those of parent molecule (DO). Comparative inter-molecular interaction of DO-CO₂ and DO-CO are lower to that of DO-NH₃ and DO-H₂O complexes.

Electronic properties simulations

Electronic structure properties such as I.P., E.A., HOMO, LUMO, band gap, and DOS of DO are estimated from B3LYP/6-31G (d,p) level of theory. These properties are simulated for the determination of

activity, reactivity and amount of interaction ability of DO with these four different atmospheric gases which are listed in Table 6. The contours of HOMO, LUMO and DOS plots of DO and DO–X are depicted in Figs. 11 and 12. The very important role of the frontier molecular orbitals in the electronic and optical properties are also highlighted here. The results of these electronic properties are quite satisfactory compared to the previous characterizations. The changes in these molecular orbitals reveal a chemical reaction, bond formation (non-covalent), and old bond breaking. The I.P. and E.A. of DO are 6.45 and 3.29 eV which are listed in Table 6. When NH₃ gas is reacted with DO, results non-covalent bonds and lowers both of its I.P. and E.A. which further consequences an enlarge band gap, as can be seen from Table 6, Figs. 11 and 12.

This net lowering in magnitude of I.P. and E.A. consequences decline of ionization and electron affinity of DO–NH₃ complex towards other gases, and also confirm the reduction chemistry of NH₃. Moisture has severe effect on the electronic properties of DO, both I.P. and E.A. increase up to 0.13 eV however, no change is observed in the band gap. This large value of I.P. and E.A. characterize the electroactive nature of DO–H₂O complex, strong ability towards other molecules as compared to parent DO. This behavior can also be seen from the DOS plot as depicted in Fig. 12. This high electroactivity of DO–H₂O complex can be attributed to the electron withdrawing ability of H₂O. Non-bonding interaction of CO₂ and CO with DO also increases its I.P. to about 0.05 and 0.02 eV, respectively. A similar alteration can be found in their E.A.; upon reacting with CO₂ and CO, 0.06 eV increase in the E.A. of DO–CO₂ and 0.03 eV in DO–CO complex.

Conclusion

A comprehensive phytochemical and theoretical study at density functional theory (DFT) was successfully achieved for a natural product, *Diospyrin* (DO). DO was isolated from *D. lotus* plant, and then characterized with different experimental techniques such as NMR, IR, UV–vis, and X-ray crystallography. Proper theoretical protocol was developed by benchmarking, and then from the correlation of experimental and theoretical data. These experimental characterizations were followed by theoretical calculations i.e., optimized geometry, electronic, spectroscopic, inter-molecular interaction and thermodynamic simulations. DFT at hybrid functional (B3LYP) was selected because of the accuracy associated and the 6-31G (d,p) level of theory is employed for all simulations. The molecular structure of DO was confirmed from the experimental NMR, and then from correlation of crystallographic and theoretical optimized geometric structure followed by spectroscopy (IR and UV–vis). Non-covalent interaction of DO is explored with the available atmospheric gases such as NH₃, CO₂, CO, and moisture (H₂O). The experimental and predicted geometrical parameters (bond distances and angles etc), IR and UV–vis spectra [B3LYP/6-31+G (d,p) level of theory] are found to have an excellent correlation. Inter-molecular non-bonding interaction of DO with these gases is investigated through geometrical parameters, electronic properties, thermodynamic simulations, and charge transfer analysis. Electronic properties include I.P., E.A., electrostatic potential, density of states (DOS), HOMO, LUMO, and band gap. The inter-molecular interaction calculations confirmed the presence of non-covalent bonding.

References

- [1] M. Arshad, M. Ahmad, Medico-botanical investigation of medicinally important plants from galliyat areas, NWFP (Pakistan), Ethnobot. Leaflet. 2004 (2004) 6.
- [2] G. Uddin, A. Rauf, T. Rehman, M. Qaisar, Phytochemical screening of *Pistacia chinensis* var. *integerrima*, Middle-East J. Sci. Res. 7 (2011) 707–711.
- [3] P.J. Houghton, The role of plants in traditional medicine and current therapy, J. Altern. Complement. Med. 1 (1995) 131–143.
- [4] S. Bent, R. Ko, Commonly used herbal medicines in the United States: a review, Am. J. Med. 116 (2004) 478–485.
- [5] S. Ganapaty, P. Steve Thomas, G. Karagianis, P.G. Waterman, R. Brun, Antiprotozoal and cytotoxic naphthalene derivatives from *Diospyros assimilis*, Phytochemistry 67 (2006) 1950–1956.
- [6] G. Uddin, A. Rauf, B.S. Siddiqui, N. Muhammad, A. Khan, S.U.A. Shah, Antinociceptive, anti-inflammatory and sedative activities of the extracts and chemical constituents of *Diospyros lotus* L., Phytomedicine 21 (2014) 954–959.
- [7] M.R. Loizzo, F. Menichini, F. Conforti, R. Tundis, M. Bonesi, A.M. Saab, G.A. Statti, B.d. Cindio, P.J. Houghton, F. Menichini, Chemical analysis, antioxidant, antiinflammatory and anticholinesterase activities of *Origanum ehrenbergii* Boiss and *Origanum syriacum* L., Food Chem. 117 (2009) 174–180.
- [8] A. Maiga, K.E. Malterud, D. Diallo, B.S. Paulsen, Antioxidant and 15-lipoxygenase inhibitory activities of the malian medicinal plants *Diospyros abyssinica* (hiern) F. White (Ebenaceae), *lannea velutina* A. Rich (anacardiaceae) and *Crossopteryx febrifuga* (Afzel) Benth. (Rubiaceae), J. Ethnopharmacol. 104 (2006) 132–137.
- [9] A. Nematollahi, N. Aminimoghadamfarouj, C. Wiart, Reviews on 1,4-naphthoquinones from *Diospyros* L., J. Asian Nat. Prod. Res. 14 (2012) 80–88.
- [10] M. Yoshida, K. Mori, Synthesis of diospyrin, a potential agent against leishmaniasis and related parasitic protozoan diseases, Eur. J. Org. Chem. 2000 (2000) 1313–1317.
- [11] E.C. Teeling, M.S. Springer, O. Madsen, P. Bates, S.J. O'Brien, W.J. Murphy, A molecular phylogeny for bats illuminates biogeography and the fossil record, Science 307 (2005) 580–584.
- [12] H. Ullah, A.A. Shah, K. Ayub, S. Bilal, Density functional theory study of poly (o-phenylenediamine) oligomers, J. Phys. Chem. C 117 (2013) 4069–4078.
- [13] H. Ullah, K. Ayub, Z. Ullah, M. Hanif, R. Nawaz, A.A. Shah, S. Bilal, Theoretical insight of polypyrrole ammonia gas sensor, Synth. Met. 172 (2013) 14–20.
- [14] H. Ullah, A. Rauf, Z. Ullah, M. Anwar, A.A. Shah, G. Uddin, K. Ayub, Density functional theory and phytochemical study of Pistagremic acid, Spectrochim. Acta Part A Mol. Biomol. Spectrosc. 118 (2014) 210–214.
- [15] H. Ullah, A.A. Shah, S. Bilal, K. Ayub, DFT study of polyaniline nh₃, co₂, and co gas sensors: comparison with recent experimental data, J. Phys. Chem. C 117 (2013) 23701–23711.
- [16] H. Ullah, A.A. Shah, S. Bilal, K. Ayub, Doping and dedoping processes of polypyrrole: DFT study with hybrid functionals, J. Phys. Chem. C 118 (2014) 17819–17830.
- [17] J.P. Abraham, I.H. Joe, V. George, O. Nielsen, V. Jayakumar, Vibrational spectroscopic studies on the natural product, columbianadin, Spectrochim. Acta Part A Mol. Biomol. Spectrosc. 59 (2003) 193–199.
- [18] R. Withnall, B.Z. Chowdhry, J. Silver, H.G. Edwards, L.F. de Oliveira, Raman spectra of carotenoids in natural products, Spectrochim. Acta Part A Mol. Biomol. Spectrosc. 59 (2003) 2207–2212.
- [19] J.G. Brandenburg, M. Alessio, B. Civalieri, M.F. Peintinger, T. Bredow, S. Grimme, Geometrical correction for the inter- and intramolecular basis set superposition error in periodic density functional theory calculations, J. Phys. Chem. A 117 (2013) 9282–9292.
- [20] H. Kruse, L. Goerigk, S. Grimme, Why the standard B3LYP/6-31g* model chemistry should not be used in DFT calculations of molecular thermochemistry: understanding and correcting the problem, J. Org. Chem. 77 (2012) 10824–10834.
- [21] M.J. Frisch, G.W. Trucks, H.B. Schlegel, G.E. Scuseria, M.A. Robb, J.R. Cheeseman, G. Scalmani, V. Barone, B. Mennucci, G.A. Petersson, Gaussian 09, Revision C. 01, Gaussian, Inc., Wallingford, CT, 2009.
- [22] A.R. Allouche, Gabedit, <http://gabedit.sourceforge.net>, 2011.
- [23] W.T. Harrison, O.C. Musgrave, Diospyrin, Acta Crystallogr. Sect. C: Cryst. Struct. Commun. 60 (2004) 0399–0401.
- [24] M. Jalali-Heravi, A. Khandar, I. Sheikshoae, A theoretical investigation of the structure, electronic properties and second-order nonlinearity of some azo Schiff base ligands and their monoanions, Spectrochim. Acta Part A Mol. Biomol. Spectrosc. 55 (1999) 2537–2544.
- [25] K. Fukui, Role of frontier orbitals in chemical reactions, Science 218 (1982) 747–754.
- [26] D. Yu, R. Cai, Z. Liu, Studies on the photodegradation of Rhodamine dyes on nanometer-sized zinc oxide, Spectrochim. Acta Part A Mol. Biomol. Spectrosc. 60 (2004) 1617–1624.

[Article 17]

Salma Bibi, Salma Bilal, A. A Shah, and Habib Ullah. "*Systematic Analysis of Poly (o-aminophenol) Humidity Sensors.*" *ACS Omega*, 2017, 2 (10), 6380-6390.

Systematic Analysis of Poly(*o*-aminophenol) Humidity Sensors

Salma Bibi,[†] Salma Bilal,^{*†} Anwar-ul-Haq Ali Shah,^{*†} and Habib Ullah[§]

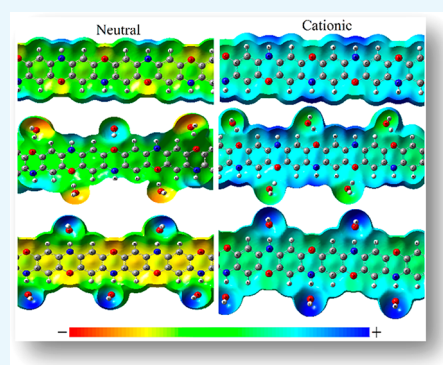
[†]National Centre of Excellence in Physical Chemistry, University of Peshawar, 25120 Peshawar, Pakistan

[‡]Institute of Chemical Sciences, University of Peshawar, 25120 Peshawar, Pakistan

[§]Environment and Sustainability Institute (ESI), University of Exeter, Penryn Campus, Penryn, Cornwall TR10 9FE, United Kingdom

Supporting Information

ABSTRACT: A thin film of poly(*o*-aminophenol), POAP, has been used as a sensor for various types of toxic and nontoxic gases: a gateway between the digital and physical worlds. We have carried out a systematic mechanistic investigation of POAP as a humidity sensor; how does it sense different gases? POAP has several convenient features such as flexibility, transparency, and suitability for large-scale manufacturing. With an appropriate theoretical method, molecular oligomers of POAP, NH and O functional groups and the perpendicular side of the polymeric body, are considered as attacking sites for humidity sensing. It is found that the NH position of the polymer acts as an electrophilic center: able to accept electronic cloud density and energetically more favorable compared to the O site. The O site acts as a nucleophilic center and donates electronic cloud density toward H₂O vap. In conclusion, only these two sites are involved in the sensing process which leads to strong intermolecular hydrogen bonding, having a 1.96 Å bond distance and $\Delta E \sim -35$ kcal mol⁻¹. The results suggest that the sensitivity of the sensor improved with the oxidization state of POAP.



1. INTRODUCTION

Conducting polymers (CPs) are becoming an active field of research which has brought a dynamic revolution in the field of chemistry, physics, and engineering in the last several decades.¹ Electrical conductance along the tailorable structure of CPs, followed by optical and electronic properties, has proven their potential application in a large number of organic electronics such as batteries,² fuel cells,^{3,4} solar cells,⁵ light emitting diodes,⁶ supercapacitors,⁷ and optical displays.^{8,9} The most widely used CPs are polyaniline (PANI),¹⁰ polypyrrole (PPy),¹¹ polythiophene (PT),¹² poly(*o*-phenylenediamine) (POPD),¹³ and poly(*o*-aminophenol) (POAP).¹⁴

Besides these technological applications, CPs are getting a valuable position in the design of gas sensing devices. Humidity control is a grand challenge in various sensitive industries such as packed food, storage of drugs, preventing different antiques and paintings, agricultural uses, and in environmental control.^{15–17} Although humidity sensors are available in the market, based on dew point,¹⁸ catalysis,^{19,20} infrared,²¹ and inorganic semiconductor (Ti, Zn) sensors,^{19,22} most of them require high operation temperature, show deviation from the linear response, and create problems in reversibility. Cost maintenance and high power consumption restrict their viability and versatility.²³ Lots of research is in progress to overcome these drawbacks and develop an effective material for humidity sensing.

One of the best options is to replace other inorganic materials with flexible CPs. CPs are stable and cheap, require low operational temperature, have low weight, and are easily synthesizable with good reversibility and tailorable properties; this make them

prominent compared to other inorganic materials.^{1,24–27} Some of the most commonly used CPs in the field of humidity sensing are PANI,^{28–30} POPD,^{31,32} and PPy,^{33–35} which have been used in different oxidation states. Furthermore, they are either employed in pure, blended, or in composites form with other inorganic materials to enhance their sensitivity, flexibility, and selectivity.³⁶ Scientists are investigating varieties of CPs to be the best humidity sensing materials, but they are facing numerous issues such as formation of a nonuniform, unstable, and adhesive film on the electrode.¹⁷ POAP is a redox conducting polymer with the unique ability to have a uniform, stable, and adhesive film formation besides its other electroactive properties.³⁷ POAP is a substituted derivative of PANI, where the structure has two potentially active sites (NH and O positions) for the interaction of H₂O vap and other related gases. It is recently reported that a modified POAP film has improved sensing properties, compared to other CPs.^{38–40} Although POAP has been experimentally reported as a sensor, no one has paid attention to its mechanistic study; which functional group is more sensitive and how does it attract gas particles?

In this work, we employed density functional theory (DFT) and time-dependent (TD) DFT simulations at various level of theories to find out the best method for precise correlation of theory with the already experimental evidence of POAP. Molecular oligomers of POAP, both reduced and oxidized,

Received: July 19, 2017

Accepted: September 20, 2017

Published: October 5, 2017

with different chain lengths are considered where the NH and O functional groups and perpendicular sides of the polymeric body are considered as attacking sites toward humidity sensing. The sensing phenomenon is investigated from structural distortion (change in geometric parameters), intermolecular interaction energies, natural bonding orbital analysis (NBO), and electronic property simulations such as HOMO, LUMO, density of states, band gap, electrostatic potential, and UV–vis spectral analysis. Moreover, the current theoretical investigation of POAP, combined with the already reported behavior of POAP, will lead to the fabrication of a proficient and competent humidity and other related gas sensor.

2. RESULTS AND DISCUSSIONS

a. Selection of Level of Theory. DFT analysis at various levels of theory is carried on the symmetrical 3PAOP (Figure 1)

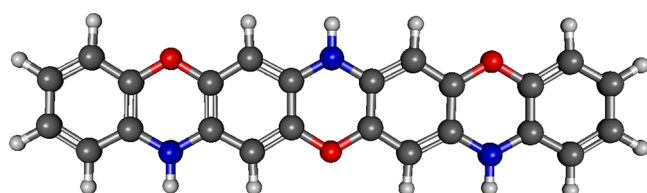


Figure 1. Optimized geometric structure of symmetric 3POAP.

to find the best, inexpensive method for precisely correlating the theory with experiment. Results of ten different levels of theory on the symmetrical 3POAP are listed in Table 1, which led us to conclude that B3LYP/6-31G(d) is the best regarding both the computational time and accuracy points of view.

DFT at the B3LYP/6-31G(d) level of theory not only reproduces the experimental band gap^{41,42} but is very fast and cheap regarding the computational point of view. The difference of 0.28 eV between the experimental and simulated band gap is due to the fact that the observed one was from the thin film while the calculation is that of the gas phase.

b. Selection of Proper Interacting System(s). *i. Optimized Geometric Parameters.* Geometry optimization of all these species has been performed using DFT at the 6-31G(d) level of theory. The sensing potential of *n*POAP toward water vapors (H_2O_{vap}) is estimated from the geometrical distortion of the polymeric backbone, interacting with water vapor(s). These parameters include intermolecular distance, intermolecular bond length, bond angles, and dihedral angles of POAP.

Optimized geometries of 4POAP and their complexes with H_2O at different sides have been shown in Figures 2 and S1–3, while their different geometric parameters are listed in Table 2. We have selected different models to find the best interaction between H_2O and 4POAP, where the H_2O either interacts at NH (Figure 1), O (Figure S1), perpendicular to the backbone (Figure S2), or considering both the NH and O sides of 4POAP (Figure S3). Results and discussion of the latter two interacting systems show that instead of interaction with the polymeric body of 4POAP, water molecules hydrogen bond among themselves, as can be seen from Figures S2 and S3 of the Supporting Information. So, the overall interaction in these species is comparatively low as that of H_2O attached at NH or O functional groups. In case of the 4POAP_NH@ H_2O system, one, two, and three NH sites of 4POAP were alternatively covered with H_2O and it was found that the O of H_2O makes an intermolecular bond of about 1.95 Å with the H of NH in all these complexes.

A similar but less pronounced intermolecular hydrogen bonding is observed in 4POAP_O@ H_2O systems (Figure S1), where the H-bonding is because of the H of H_2O and O of the O site of 4POAP backbone. In summary, both the NH and O sites of 4POAP has a strong interaction with water vapor as can be seen from the strong H-bonding and its distorted geometric structure (Figures 1 and S1).

ii. Interaction Energy, NBO Charge, and Electronic Properties. As a universal solvent, water act as either a proton donor or a proton acceptor which directly depends on the other reactant. In acids/bases, the proton is that of the H^+ ion so, water acts as a proton donor when it reacts with a base; however, it accepts proton when it reacts with an acid. A similar situation is observed, on considering NH and O sites of POAP for water vapor. In the case of $H\cdots O$, where the H of H_2O react with O of POAP oligomer which withdraw the electronic cloud density of 0.012 e^- from its backbone. On considering two H_2O molecules for the O site of 4POAP, water vapor withdraws about 0.014 e^- of charge, and 0.025 e^- in the case of three H_2O . When water vapor was reacted at the NH sites of 4POAP, it donates electronic cloud density toward the polymer as can be seen from Table 2. 4POAP has withdrawn a charge about 3-fold greater than the NBO charge compared to the O site of POAP. On considering the perpendicular attachment of water vapors, a less pronounced situation is observed where H_2O withdraws electronic cloud density of 0.008 e^- . In this interaction, water molecules circulate around the polymeric body and search for either O or NH groups and forms intermolecular H-bonding through self-interaction.

Table 1. Different Levels of Theory and Their Simulated Total Energy (a.u), HOMO, LUMO, Band Gap (eV), and Time Consumed (min)^a

no.	functional	basis set	total energy	HOMO	LUMO	band gap	time
1	B3LYP	6-31G(d)	−953.08	−4.16	−0.34	3.82	15
2	B3LYP	6-31G(d, p)	−953.10	−4.17	−0.35	3.82	16
3	B3PW91	6-31G(d, p)	−952.74	−4.25	−0.45	3.80	18
4	BPV86	6-31G(d, p)	−953.16	−3.60	−1.21	2.39	25
5	CAM-B3LYP	6-31G(d, p)	−952.62	−5.42	+0.92	6.34	34
6	HSEH	6-31G(d, p)	−952.11	−4.00	−0.60	3.40	35
7	LSDA	6-31G(d, p)	−947.86	−4.08	−1.75	2.33	22
8	PBE	6-31G(d, p)	−951.97	−3.49	−1.12	2.37	17
9	TPSS	6-31G(d, p)	−953.27	−3.49	−0.97	2.52	22
10	WB97XD	6-31G(d, p)	−952.79	−6.01	+1.45	7.46	21
11	experimental					3.54 ⁴¹	

^aUsing 3POAP as a model at fixed memory of 10 GB and 4 processors.

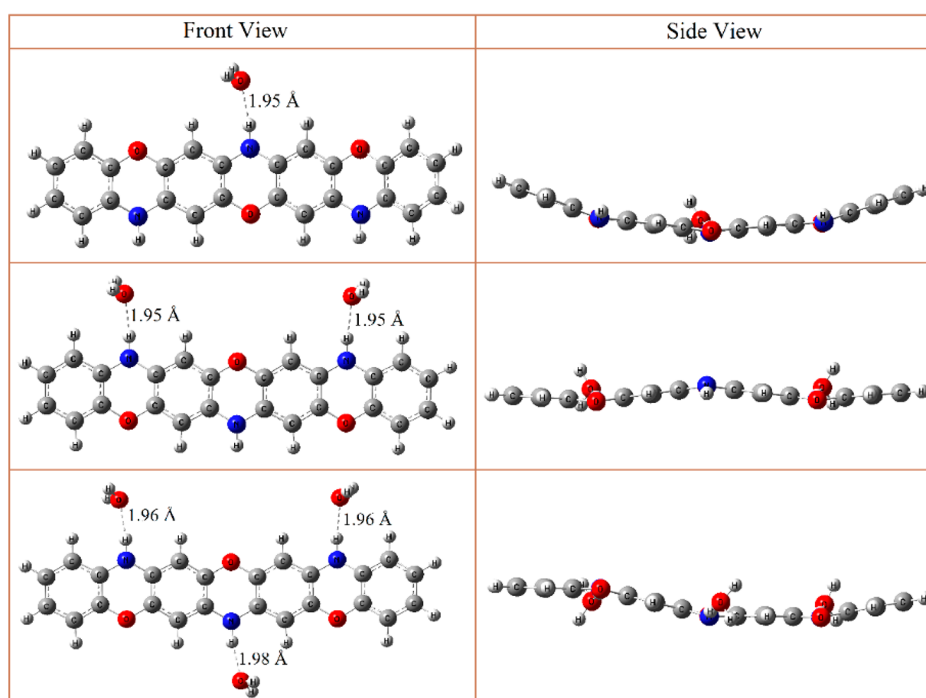


Figure 2. Hydrogen-terminated 4POAP_NH@H₂O.

Table 2. Interaction Energy (kcal mol⁻¹), NBO Charge (e⁻), Band Gap (eV), and First Allowed Excitation Energy of 4POAP and Its Complex with H₂O

no.	species	ΔE_{int}	Q_{NBO}	band gap	E_{excit} (eV)
1	4POAP		0	3.54	3.42 (0.57)
2	4POAP_O@1H ₂ O	-8.22	0.012	3.86	3.63 (0.41)
3	4POAP_O@2H ₂ O	-14.93	0.014	3.81	3.62 (0.48)
4	4POAP_O@3H ₂ O	-21.96	0.025	3.88	3.67 (0.41)
5	4POAP_NH@1H ₂ O	-9.03	-0.032	3.69	3.51 (0.47)
6	4POAP_NH@2H ₂ O	-16.44	-0.064	3.70	3.55 (0.54)
7	4POAP_NH@3H ₂ O	-24.03	-0.095	3.61	3.44 (0.23)
8	4POAP_l@3H ₂ O	-32.00	-0.008	3.87	3.65 (0.42)
9	4POAP@6H ₂ O	-59.05	-0.050	3.73	3.58 (0.30)

Finally, both NH and O sites of 4POAP were covered with H₂O, where water vapors accept electronic cloud density from polymer. This intermolecular charge transfer is inbetween those of the individual O and NH interacting systems but is still a very good interaction. The reason behind this is that one group acts as an electron donator while the other accepts as electronic cloud densities which minimize the net charge exchange.

As discussed earlier, H₂O vapor reacts with POAP backbone via either NH or O sites with strong hydrogen bonding. In the case of 4POAP_O@1H₂O, this intermolecular hydrogen bond distance is -8.22 kcal mol⁻¹, which increases upon increasing the number of water vapors, -14.93 kcal mol⁻¹ in @2H₂O, and -21.96 kcal mol⁻¹ in the case of the 4POAP_O@3H₂O system (Table 2). So, a linear response in interaction energy is observed with number of water vapors. A very similar intermolecular interaction energy is observed in the case of 4POAP_NH@nH₂O systems (Table 2), but here the intermolecular interaction is due to O of H₂O and H of the NH side of the polymer. A -9.03 kcal mol⁻¹ interaction energy is simulated for one water vapor, -16.44 kcal mol⁻¹, for two, and -24.03 kcal mol⁻¹, for three, attached to 4POAP. In contrast to the small charge transfer, a good interaction energy of -32 kcal mol⁻¹ is simulated between the perpendicularly attached water vapors at a backbone

of 4POAP (4POAP_l@3H₂O). On covering all the functional groups (both O and NH) of 4POAP with water vapors, a comparatively higher intermolecular interaction energy of -59.05 kcal mol⁻¹ is observed as can be seen from Table 2. But again, the charge transfer is low and the net behavior is an average of O and NH interacting systems. This comparatively higher interaction energy is because of high number of water vapors while the lower charge exchange (-0.05 e⁻) is due to the self-interaction and intermolecular hydrogen bonding among H₂O vapors. As explained earlier, the perpendicularly attached H₂O vapors tend to minimize themselves near the O and NH functional groups of 4POAP. So, both the O and NH are responsible for the sensing of H₂O vapors. Furthermore, an electrostatic potential map of these four different interacting systems is given in Figure 3, where the electrophilic and nucleophilic sites can be seen as red and blue region, respectively.

We have also carried out UV-vis absorption spectroscopy for all these four-interacting species, which is given in Figure 4 along with the parent 4POAP as a reference. Three distinct absorption band peaks are simulated in the hydrogen terminated 4POAP; at ca. 427, 361, and 251 nm. The broad absorption band peak at ca. 251 nm has a strong correlation with experimentally reported $\lambda = 258 \text{ nm}$ ^{43,44} which can be assigned to the $\pi \rightarrow \pi^*$ transition of

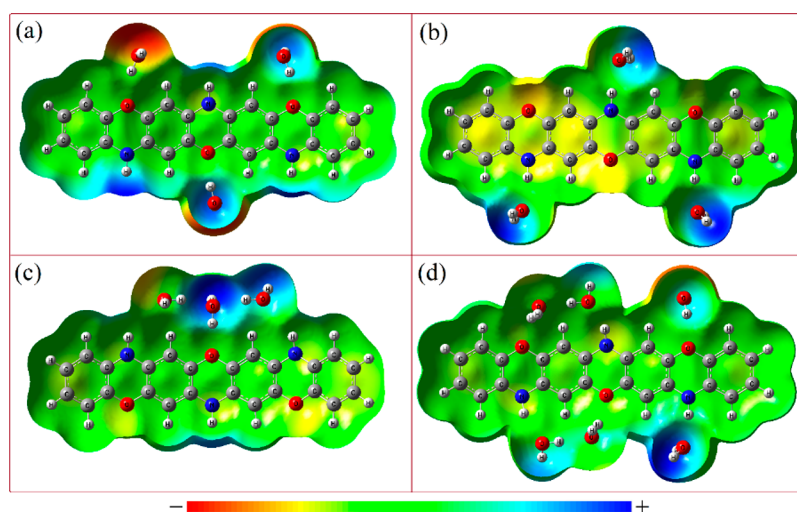


Figure 3. Electrostatic potential map of 4POAP_O@H₂O (a), 4POAP_NH@H₂O (b), 4POAP_l@H₂O (c), and 4POAP@6H₂O (d).

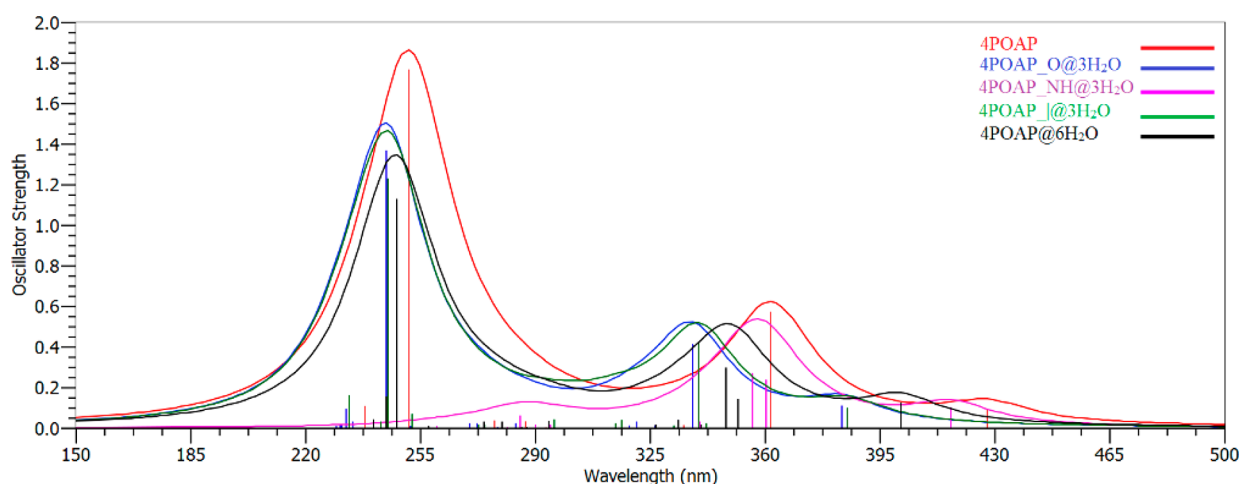


Figure 4. Electronic excitation spectra of 4POAP, where H₂O molecules interact at different sites.

the aromatic benzene unit. On interacting water vapor(s) with 4POAP, all these prominent band peaks are blue-shifted as can be seen from Figure 4 and Table 2. So, water vapor act as a reducing agent which can be seen from the hypsochromic shift in the UV–vis spectra of 4POAP. The HOMO–LUMO band gap of hydrogen terminated 4POAP is 3.54 eV while its first allowed electronic excitation energy is 3.42 eV, as listed in Table 2. The later can be regarded as an optical band gap while the first one is known as electrical band gap. Upon interaction of H₂O vapor at the O side of 4POAP, the band gap elongates and a blue-shifting occurred in the first allowed excitation energy (Table 2). A similar but less pronounced behavior is simulated in case of 4POAP_NH@*n*H₂O systems, where *n* is the number of H₂O vapors. In these four-interaction systems, the trend of band gap elongation and blue shifting of first allowed electronic excitation energy is because of H₂O vapor(s). So, water vapor(s) cause a hypsochromic shift in POAP; attached either at O, NH, l, or all sides of POAP. So, UV–vis absorption spectroscopy will be the best tool in investigating the humidity sensing behavior of POAP and its oligomers.

As reported by Jeffery et al. 2.2–2.5 Å of hydrogen bonding will be “strong or mostly covalent”, 2.5–3.2 Å will be “moderate, mostly electrostatic”, while 3.2–4.0 Å is described as “weak, mostly electrostatic”. The bonding energy for the strong one

should be in the range of –40 to –14 kcal mol^{–1}, for the moderate, –15 to –4 kcal mol^{–1}, and for the weak, <– 4 kcal mol^{–1}.⁴⁵

In summary, POAP senses or reacts to water vapor either at O, NH, or both sites by establishing strong hydrogen (mostly covalent) bonding, although both functional groups have opposite (in term of electron/proton transferring phenomena) but systematic effects. So, the sensing efficiency of the experimentally prepared thin film of POAP and its oligomer will strongly depend on the free availability of O and NH functional groups. Whether the H₂O vapors are in line or perpendicular to its backbone, the reacting sites will be O, NH, or both.

c. Noncovalent Interaction of Water Vapors at the O Site of *n*POAP. After predicting the proper orientation of humidity sensing, different oligomeric chain length of POAP (both reduced and oxidized states) are opted for further simulations. In case of *n*POAP_O@H₂O (where *n* = 2, 4, ..., 10), all available O sites were covered with water vapors. Interaction energy, NBO charge, band gap, and first allowed excitation energy of the respective *n*POAP_O@H₂O systems are listed in Table 3. Analysis of the data of Table 3 led us to conclude that water vapor interaction energy with *n*POAP is about –7 kcal mol^{–1} per water, where the O of *n*POAP donates electronic cloud density toward H₂O. Upon interaction of H₂O vapor with *n*POAP, band gap and first allowed excitation energy of the

Table 3. Interaction Energy (kcal mol⁻¹), NBO Charge (e⁻), Band Gap (eV), and First Allowed Excitation Energy of *n*POAP_O@H₂O Systems

no.	species	ΔE_{int}	Q_{NBO}	band gap	E_{excit} (eV)
1	2POAP			4.45	3.90
2	2POAP_O@H ₂ O	-6.96	0.01	4.49	3.93
3	4POAP			3.76	3.52
4	4POAP_O@H ₂ O	-20.90	0.03	3.83	3.54
5	6POAP			3.29	3.21
6	6POAP_O@H ₂ O	-35.39	0.05	3.69	3.47
7	8POAP			3.26	3.21
8	8POAP_O@H ₂ O	-48.65	0.08	3.28	3.28
9	10POAP			3.22	3.19
10	10POAP_O@H ₂ O	-61.99	0.10	3.23	3.23

resulted complexes increase which is a direct consequence of H₂O adsorption (*vide supra*).

So, along with chain length elongation of POAP, intermolecular interaction energy, NBO charge, band gap, and first allowed electronic excitation energy changes/increases linearly. The HOMO and LUMO energy levels of parent *n*POAP and *n*POAP_O@H₂O are simulated from the density of state (DOS) plots, which are comparatively given in Figure 5. Water vapors change the position of HOMO and LUMO levels of all *n*POAP.

To confirm and elaborate the humidity sensing nature of *n*POAP, UV–vis absorption spectra in the range of 100–600 nm were simulated at the B3LYP/6-31G(d) level of theory. As explained earlier, *n*POAP gives rise to three distinct absorption band peaks. With increasing oligomeric chain length, the third shoulder peak disappears and broadens and shifts the high-energy absorption band peak (~250 nm) toward the visible

range (low energy region). UV–vis absorption spectra of the reduced *n*POAP are given in Figure 6 along with *n*POAP_O@H₂O systems.

Analysis of the results of Figure 6 and Table 3 led us to conclude that all the absorption band peaks of parent *n*POAP are sufficiently blue-shifted upon interaction of water vapors which confirm the strong sensing behavior of POAP. This is further supported by the interaction energy, NBO charge, and band gap alteration.

Generally, COPs are positively charged when experimentally synthesized and the cationic form is more reactive than their counterpart neutral state. So, we considered a monocationic *n*POAP without doping agent using UB3LYP/6-31G(d) level of theory. As expected, *n*POAP⁺ has stronger intermolecular interaction energy with H₂O compared to that of their reduced *n*POAP. The simulated interaction energy is almost double while a similar trend in band gap and first allowed electronic excitation energy is observed. Alteration in band gap and HOMO/LUMO levels of both parent and interacting systems are simulated from DOS, which are given in Figure S4 of the Supporting Information. Interestingly, the charge transferring phenomena is in the opposite direction to that of its reduced form of *n*POAP_O@H₂O systems. All *n*POAP⁺ has withdrawn electronic cloud density from water molecules as can be seen from Figure 7 and Table 4. In Figure 7, an electrostatic potential map (ESP) of the reduced and cationic form of *n*POAP along with water vapors is given. Different colors are used as a symbol for different values of electrostatic potential; red and blue colors show electron rich and electron deficient (high positivity) regions of the species whereas the green color shows the region of zero potential. A neutral electrostatic potential map for *n*POAP, a nucleophilic one for *n*POAP_O@H₂O, and a slightly electrophilic one for

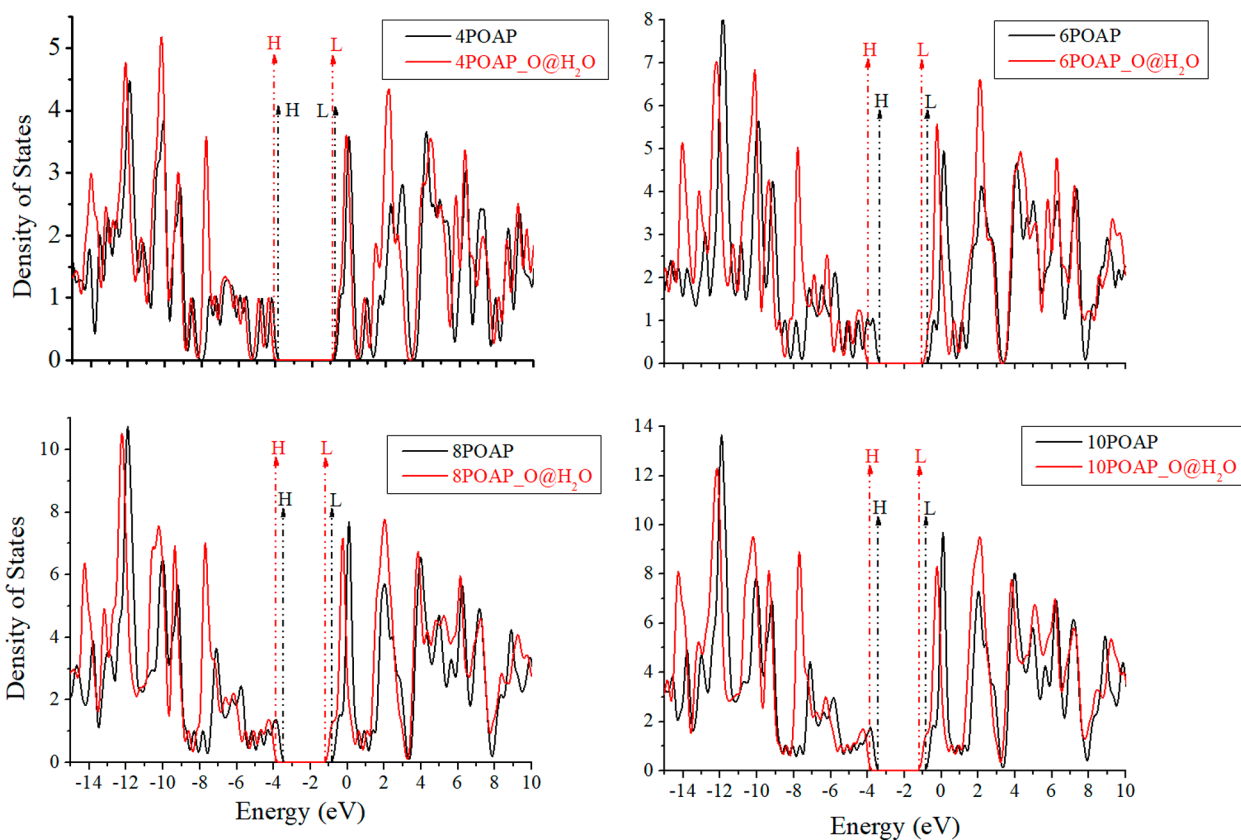


Figure 5. DOS of *n*POAP along with *n*POAP_O@H₂O.

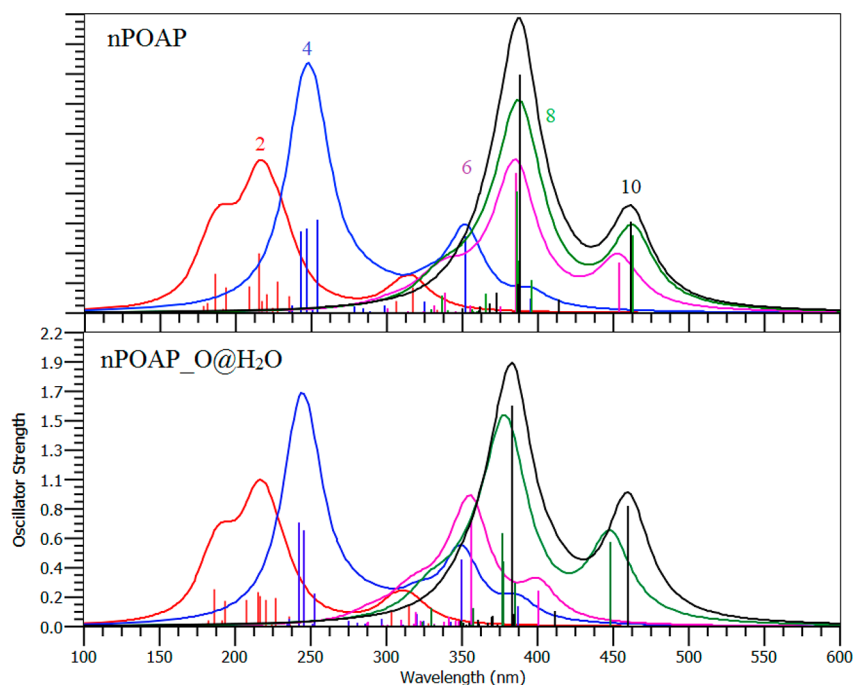


Figure 6. UV-vis absorption spectra of *n*POAP (top) and *n*POAP_O@H₂O (bottom).

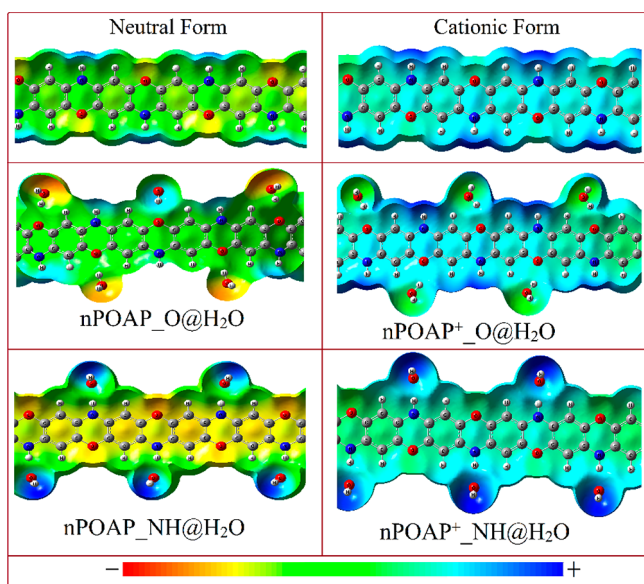


Figure 7. Electrostatic potential map of *n*POAP (both neutral and cationic) along with *n*POAP_{NH}@H₂O and *n*POAP_O@H₂O systems.

*n*POAP_O@H₂O can be clearly seen from the electrostatic potential map (Figure 7). On interacting H₂O vapors with *n*POAP, its backbone becomes more electropositive due to the acceptance of proton from H₂O and the corner (especially H₂O attached sides) turned dark yellow (more electronegative).

The proton acceptance/donating ability of water from *n*POAP and *n*POAP⁺ can also be confirmed from their ESP plots. Both electrostatic potential map and NBO charge analysis strongly corroborate each other (*vide supra*). The UV-vis and UV-vis-near IR spectra of the cationic species along with water vapors are simulated at TD-DFT with UB3LYP/6-31G(d) level of theory. Comparative UV-vis-near IR absorption spectra of *n*POAP_O@H₂O systems are given in Figure 8, along with that of

Table 4. Interaction Energy (kcal mol⁻¹), NBO Charge (e⁻), Band Gap (eV), and First Allowed Excitation Energy of *n*POAP_O@H₂O (at 6-31Gd)

no.	species	ΔE_{int}	Q_{NBO}	band gap	E_{excit} (eV)
1	2POAP ⁺			2.56	2.15
2	2POAP _O @H ₂ O	-13.99	-0.041	2.54	2.21
3	4POAP ⁺			1.03	0.95
4	4POAP _O @H ₂ O	-21.35	-0.076	1.07	0.96
5	6POAP ⁺			0.47	0.56
6	6POAP _O @H ₂ O	-30.12	-0.095	0.51	0.56
7	8POAP ⁺			0.32	0.42
8	8POAP _O @H ₂ O	-41.98	-0.114	0.38	0.46
9	10POAP ⁺			0.21	0.31
10	10POAP _O @H ₂ O	-55.41	-0.270	0.23	0.32

parent *n*POAP⁺. Oxidized *n*POAP has strong UV-vis absorption band peaks in the visible and near IR regions, compared to that of reduced ones. This band shifting to the red or near IR region is because of the formation of a polaronic state, responsible for the high electroactivity. All the absorption band peaks of *n*POAP⁺ blue shift on interacting with water vapors, which are clearly described in Table 4. As discussed in earlier sections, this blue shifting in the absorption band peaks of *n*POAP⁺ is due to the interaction of H₂O.

d. Noncovalent Interaction of Water Vapors at the NH Site of *n*POAP. In order to analyze the sensing behavior of the NH site in *n*POAP (both reduced and oxidized), different oligomers are opted for interaction energy, NBO charge, band gap, ESP, and UV-vis spectral characteristics. A comparatively higher intermolecular interaction energy is estimated in case of *n*POAP_{NH}@H₂O to that of *n*POAP_O@H₂O systems as can be seen from Table 5. The simulated interaction energy for 2POAP_{NH}@H₂O is -7.65 kcal mol⁻¹, -23.03 kcal mol⁻¹ for 4POAP_{NH}@H₂O, 38.34 kcal mol⁻¹ for 6POAP_{NH}@H₂O, -50.46 kcal mol⁻¹ for 8POAP_{NH}@H₂O, and 68.58 kcal mol⁻¹ for 10POAP_{NH}@H₂O systems. In contrast to the O@H₂O

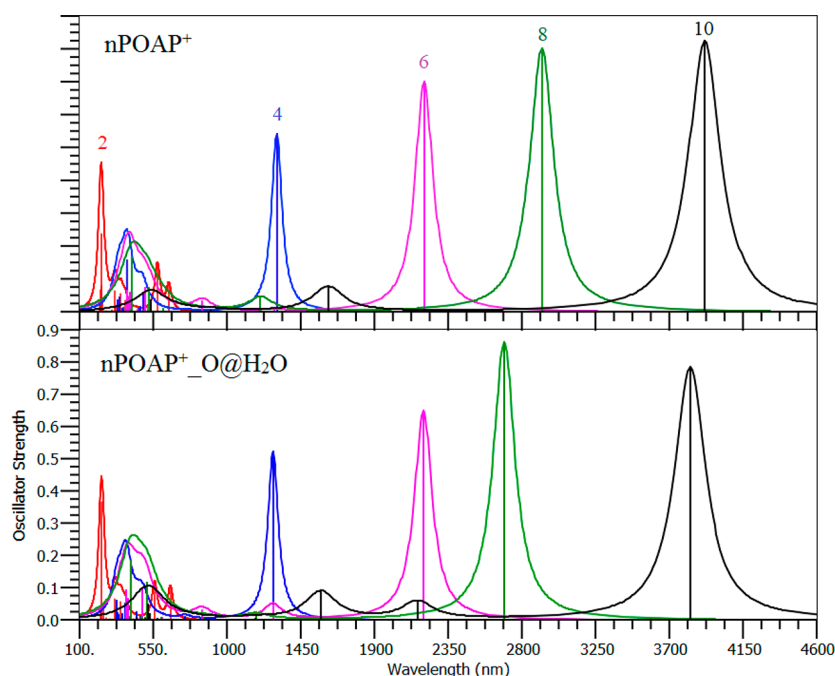


Figure 8. UV–vis–near IR spectra of $n\text{POAP}^+$ (top) and $n\text{POAP}^+_{\text{O@H}_2\text{O}}$ (bottom).

Table 5. Interaction Energy (kcal mol^{-1}), NBO Charge (e^-), Band Gap (eV), and First Allowed Excitation Energy of $n\text{POAP_NH@H}_2\text{O}$

no.	species	ΔE_{int}	Q_{NBO}	band gap	E_{excit} (eV)
1	2POAP			4.45	3.90
2	2POAP_NH@H ₂ O	-7.65	-0.033	4.34	3.84
3	4POAP			3.76	3.52
4	4POAP_NH@H ₂ O	-23.03	-0.095	3.63	3.38
5	6POAP			3.29	3.21
6	6POAP_NH@H ₂ O	-38.34	-0.181	3.21	3.17
7	8POAP			3.26	3.21
8	8POAP_NH@H ₂ O	-50.46	-0.256	3.14	3.14
9	10POAP			3.22	3.19
10	10POAP_NH@H ₂ O	-68.58	-0.330	3.10	3.11

interaction, the nature of NH@H₂O is totally different in the case of proton/electron transferring phenomena. Here the NH side of $n\text{POAP}$ acts as a proton donor, which means the electronic cloud density moves to $n\text{POAP}$ and results an anionic state. This high interaction energy and charge transferring are responsible for strong hydrogen bonding (H–O) between H of NH and O of H₂O in all $n\text{POAP_NH@H}_2\text{O}$ systems. Compared to $n\text{POAP_O@H}_2\text{O}$ systems, here the amount of charge transfer is 3-fold which make the $n\text{POAP}$ backbone more nucleophilic and H₂O vapor more electrophilic. This phenomenon can be clearly seen from the ESP plots (Figure 7) where the yellowish region depicts the electronegative nature and the bluish is that of electropositive character (H₂O sides). This time, the band gap and first allowed electronic excitation energy decrease upon interaction with H₂O vapors as can be seen from Table 5. So, here water act as an oxidizing agent which finally validate the acid/base chemistry of water in different reagents (*vide supra*).

The band gap of 2POAP decreases from 4.45 to 4.34 eV, a decrease of 0.13 eV in 4POAP, 0.08 eV in 6POAP, 0.12 eV in 8POAP, and again a decrease of 0.12 eV in 10POAP is observed upon sensing H₂O vapors. The shifting of HOMO and LUMO energy levels in $n\text{POAP}$ after interacting with H₂O are also very

prominent as can be seen from the DOS plot, given in Figure 9. These band shiftings are clear evidence toward the high sensitivity of $n\text{POAP}$ for H₂O vapors. Moreover, UV–vis absorption spectra of all these interacting species are simulated which are comparatively given in Figure 10 along with isolated $n\text{POAP}$. Absorption band peaks of all $n\text{POAP}$ are red-shifted upon interaction with H₂O, as can be seen from Table 5 and Figure 10. Water vapor has increased the visible light absorption capability of all POAP oligomers (shift the λ_{max} to lower energy region) which further supports and confirms POAP as the best sensor for humidity.

Again, comparatively higher intermolecular interaction energies are observed in all $n\text{POAP}^+_{\text{NH@H}_2\text{O}}$ systems, which are listed in Table 6. In contrast to the reduced state, here water vapors have caused a blue-shifting in all the oxidized oligomers of POAP. This behavior in all POAP^+ oligomers can be analyzed from the blue shifting of UV–vis and UV–vis–near IR absorption band peaks (Figure 11). Being a universal species, water interacts with POAP either in reduced or oxidized state. For clarity reasons, the first allowed electronic excitation band peaks of all these isolated and H₂O interacting $n\text{POAP}^+$ systems are listed in Table 6. However, the charge transferring phenomena is in the same direction as that of $n\text{POAP_NH@H}_2\text{O}$ systems but more prominent. In the case of a reduced state ($n\text{POAP}$), the electronic cloud density was moved to $n\text{POAP}$ due to NH functional groups (electrophilic nature). Here the proton donating nature of $n\text{POAP}^+$ toward H₂O vapors is because of the oxidized state (cationic form). So, upon interaction with H₂O vapors, the oxidized states are reduced as can be visualized from the ESP plot (Figure 7), band gap enlargement, and shifting of HOMO/LUMO levels (Figure S5).

The opposite interacting nature of O and NH functional groups with H₂O vapors can be precisely seen from Figure 12, where the red and blue-shifting of λ_{max} is shown. So, water vapor can be detected at either site (O, NH, or both) of POAP. The strong humidity sensing ability of POAP is stem to the free availability of these two functional groups which simultaneously

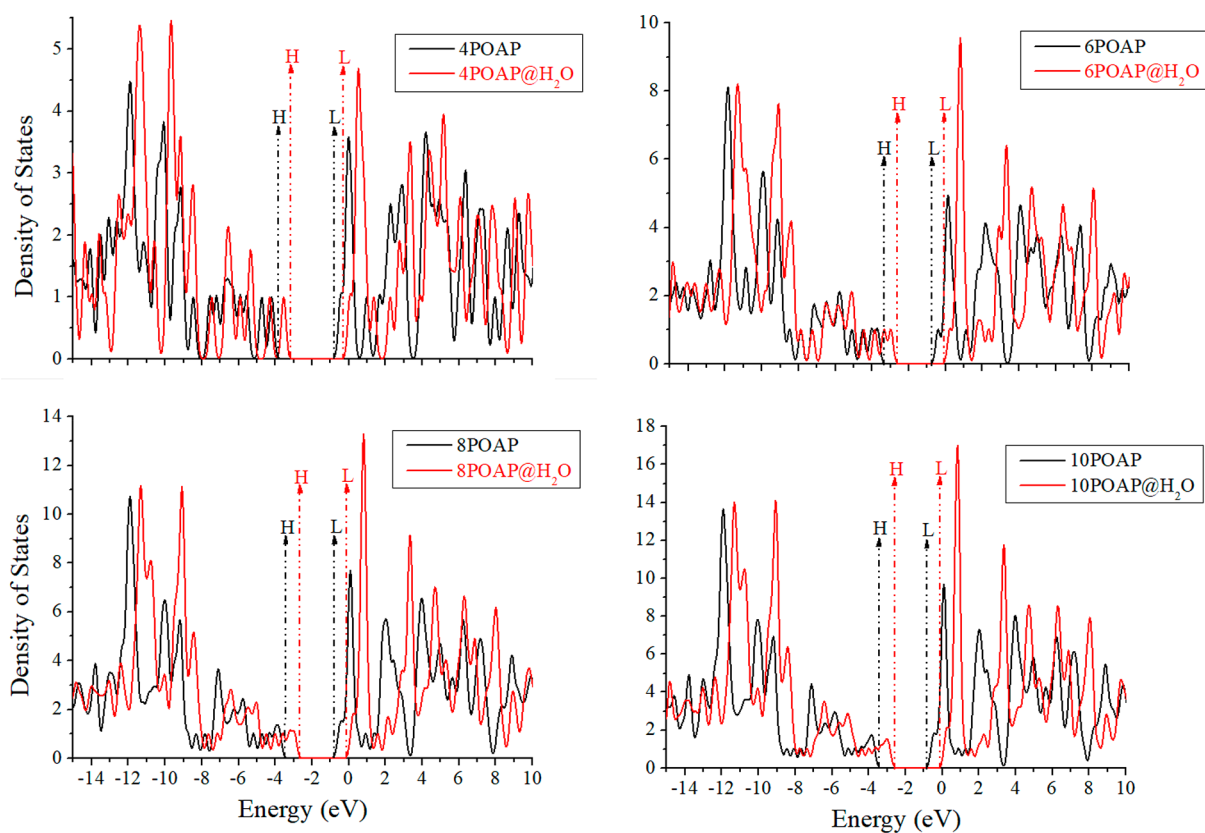


Figure 9. DOS of n POAP along with n POAP_NH@H₂O.

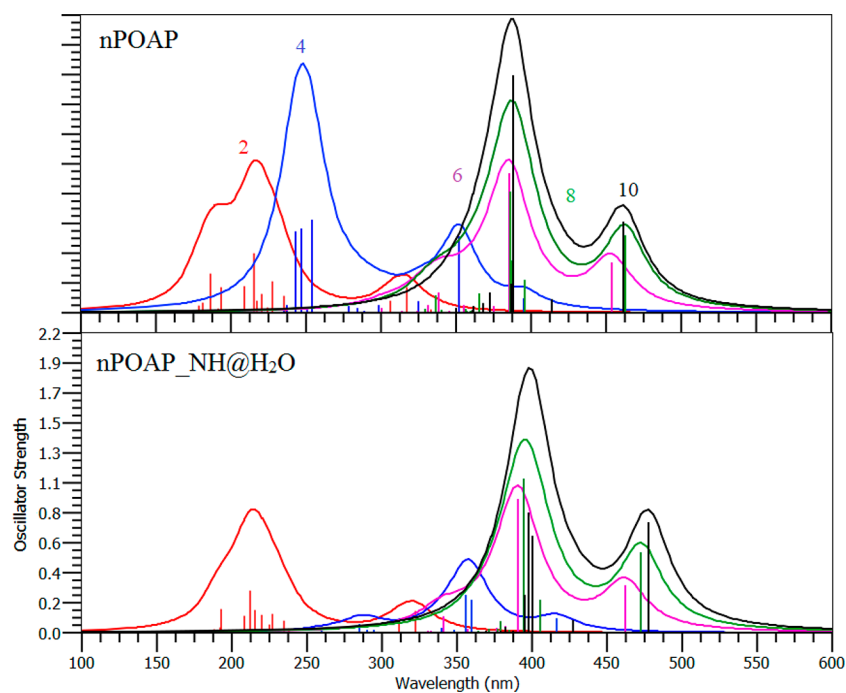


Figure 10. UV-vis absorption spectra of n POAP (top) and n POAB_NH@H₂O (bottom).

act as a proton donor/acceptor agents, followed by redox chemistry of H₂O.

3. CONCLUSION

The prominent nature of poly(*o*-aminophenol) (PAOP) among all CPs is because of its redox conducting nature, ladderlike

molecular structure, and availability of more reactive sites such as O and NH functional groups on its polymeric backbone. Due to the free availability of these functional groups, POAP can be used as a best candidate for gas sensing. We have carried out a systematic theoretical study for a POAP gas sensor; considering its O and NH functional groups as attacking sites for H₂O vapors.

Table 6. Interaction Energy (kcal mol⁻¹), NBO Charge (e⁻), Band Gap (eV), and First Allowed Excitation Energy of *n*POAP⁺_NH@H₂O (6-31/G)

no.	species	ΔE_{int}	Q_{NBO}	band gap	E_{excit} (eV)
1	2POAP ⁺			2.56	2.15
2	2POAP ⁺ _NH@H ₂ O	-20.52	-0.049	2.66	2.18
3	4POAP ⁺			1.03	0.95
4	4POAP ⁺ _NH@H ₂ O	-48.56	-0.117	1.16	1.02
5	6POAP ⁺			0.47	0.56
6	6POAP ⁺ _NH@H ₂ O	-71.60	-0.221	0.60	0.64
7	8POAP ⁺			0.32	0.42
8	8POAP ⁺ _NH@H ₂ O	-94.87	-0.309	0.42	0.49
9	10POAP ⁺			0.21	0.31
10	10POAP ⁺ _NH@H ₂ O	-115.46	-0.380	0.25	0.37

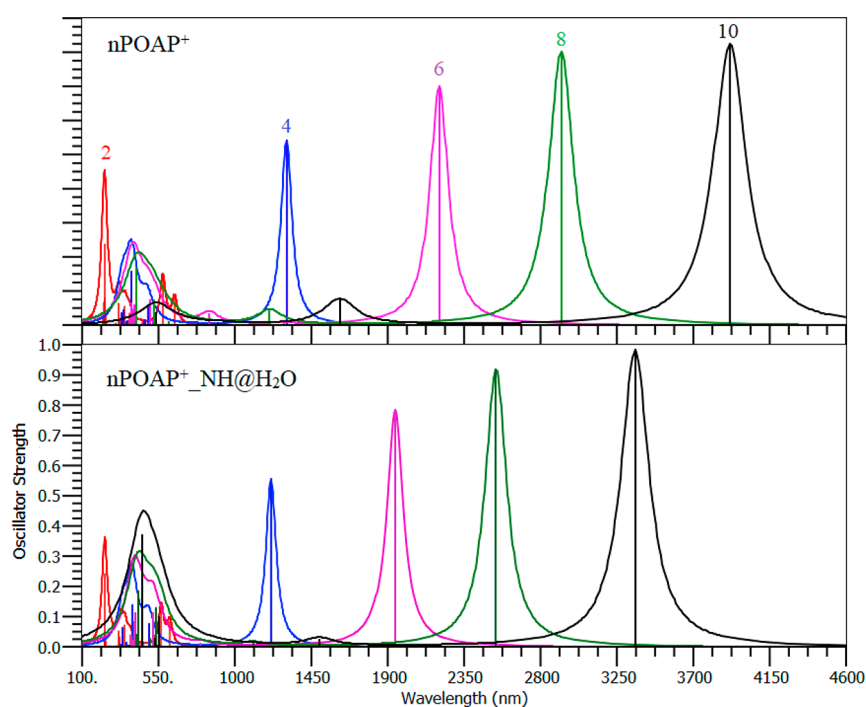


Figure 11. UV-vis-near IR spectra of *n*POAP⁺ (top) and *n*POAP⁺_NH@H₂O (bottom).

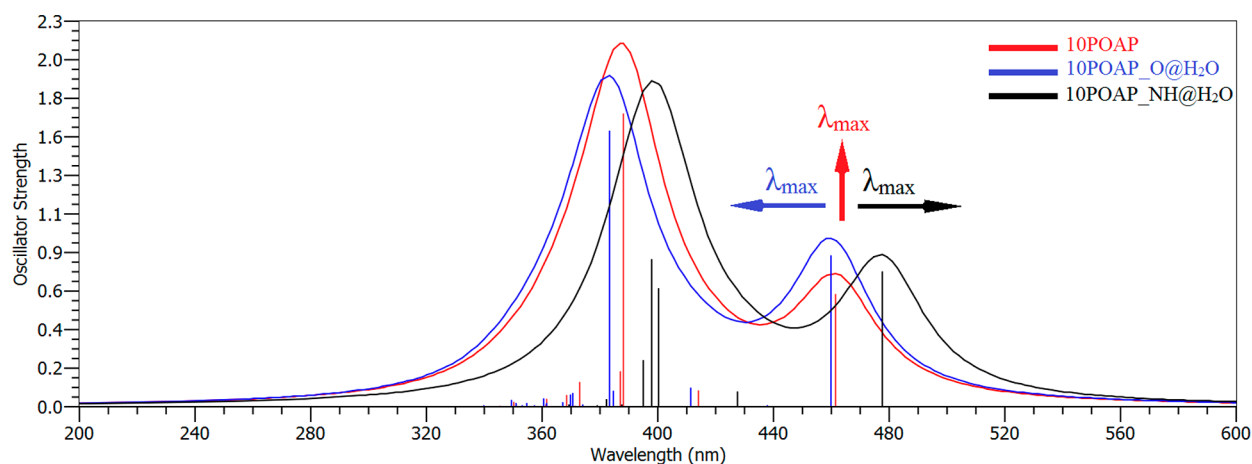


Figure 12. UV-vis spectra of 10POAP@H₂O at O and NH sites.

For theoretical simulations, DFT and time-dependent DFT simulations are performed at the various level of theories. DFT at the B3LYP/6-31G(d) level of theory is found to be the best method for theoretical study of PAOP and its interacting systems

with different analytes. In summary, POAP both in reduced and oxidized states has strong sensing ability toward H₂O vapors which is estimated from good interaction energy, as a consequence the strong hydrogen bonding is more likely covalent.

Furthermore, structural distortion (change in geometric parameters), charge exchange, shifting of HOMO and LUMO levels, band gap alteration, and perturbation in UV–vis spectra absorption band peaks of POAP upon interacting with H₂O validate its sensing ability. Finally, if one side of POAP acts as a proton donor then the other will act as a proton acceptor, which further strengthens its intermolecular interaction; however, the NH position of the polymer is energetically favorable compared to the O site toward H₂O_{vap}. It is concluded that H₂O is responsible for blue-shifting in λ_{max} of POAP UV–vis spectra, so color change in the thin film of POAP may be a direct method for detection.

4. COMPUTATIONAL METHODS

The ground-state geometries of *n*POAP oligomers (where *n* = 2, 4, ..., 10) were simulated using hybrid DFT at the B3LYP functional (Becke three parameter, Lee, Yang, and Parr)⁴⁶ with the 6-31G(d) basis set. B3LYP and its unrestricted formalism, such as UB3LYP, are used for the reduced (POAP) and oxidized (POAP⁺) form of POAP, respectively.⁴⁷ From the last two decades, this level of theory has been proven to accurately describe π -conjugated systems such as CPs and other conjugated materials.^{48–50} All calculations were performed using Gaussian 09,⁵¹ while the results are analyzed through Gabedit⁵² and Gauss view.⁵³ Prior to sensor study of *n*POAP, its symmetrical trimer (hydrogen terminated) is employed for the testing of an appropriate level of theory. Molecular gas phase H₂O is considered as water vapors. Water vapors are interacted at the NH and O sites and perpendicular to the polymeric backbone of 4POAP, considering both reduced and oxidized states. After the systematic study, *n*POAP (*n*POAP and *n*POAP⁺) is interacted with water vapors. POAP⁺ oligomers either isolated or in complex state (*n*POAP⁺@H₂O) are positively charged with doublet spin, and the simulations were performed at the UB3LYP/6-31G(d) level of theory. No symmetry constraint was applied during geometry optimization.⁵⁴ Harmonic frequency calculations were performed to confirm the optimized structures with no negative frequencies. Intermolecular interaction energies were also simulated to study the interaction behavior of polymer with H₂O. This was further confirmed by natural bond orbital (NBO) analysis. Frontier molecular orbitals such as highest occupied molecular orbital (HOMO), lowest unoccupied molecular orbital (LUMO), and their respective band gap calculations were also carried out at the mentioned level of theory. UV–vis absorption spectra are also simulated to understand the sensing behavior of polymers. Both the gas phase and solvent media of acetonitrile using polarized continuum model (PCM) are employed. In case of POAP oligomers, both solvent and gas phase UV–vis spectra were almost similar (see Figure S6), so, in order to reduce the computational cost, the gas phase simulations are considered. Finally, the oligomeric properties were extrapolated to obtain polymeric properties through a second-order polynomial fit equation.⁵⁵

■ ASSOCIATED CONTENT

■ Supporting Information

The Supporting Information is available free of charge on the ACS Publications website at DOI: 10.1021/acsomega.7b01027.

Optimized geometric structures, DOS, and UV–vis spectra of *n*POAP and *n*POAP@H₂O systems (PDF)

■ AUTHOR INFORMATION

Corresponding Authors

*E-mail: anwarulhaqalishah@uop.edu.pk (A.A.S.).

*E-mail: salmabilal@uop.edu.pk. Tel.: +92(091) 9216652, 9216701-20. Fax: +92(091) 9216652 (S.B.).

ORCID

Anwar-ul-Haq Ali Shah: 0000-0002-4991-5194

Habib Ullah: 0000-0001-9290-0265

Notes

The authors declare no competing financial interest.

■ ACKNOWLEDGMENTS

We acknowledge the Higher Education Commission (HEC) Islamabad, Pakistan, for financial support under research grant nos. 20-1647 and 20-3111/NRPU/R&D/HEC.

■ REFERENCES

- (1) Janata, J.; Josowicz, M. Conducting Polymers in Electronic Chemical Sensors. *Nat. Mater.* **2003**, *2*, 19–24.
- (2) Liu, G.; Xun, S.; Vukmirovic, N.; Song, X.; Olalde-Velasco, P.; Zheng, H.; Battaglia, V. S.; Wang, L.; Yang, W. Polymers with Tailored Electronic Structure for High Capacity Lithium Battery Electrodes. *Adv. Mater.* **2011**, *23*, 4679–4683.
- (3) Alberti, G.; Casciola, M.; Massinelli, L.; Bauer, B. Polymeric Proton Conducting Membranes for Medium Temperature Fuel Cells (110–160 °C). *J. Membr. Sci.* **2001**, *185*, 73–81.
- (4) Bae, B.; Yoda, T.; Miyatake, K.; Uchida, H.; Watanabe, M. Proton-Conductive Aromatic Ionomers Containing Highly Sulfonated Blocks for High-Temperature-Operable Fuel Cells. *Angew. Chem., Int. Ed.* **2010**, *49*, 317–320.
- (5) Kim, Y. H.; Sachse, C.; Machala, M. L.; May, C.; Müller-Meskamp, L.; Leo, K. Highly Conductive PEDOT:PSS Electrode with Optimized Solvent and Thermal Post-Treatment for Ito-Free Organic Solar Cells. *Adv. Funct. Mater.* **2011**, *21*, 1076–1081.
- (6) Yu, Z.; Zhang, Q.; Li, L.; Chen, Q.; Niu, X.; Liu, J.; Pei, Q. Highly Flexible Silver Nanowire Electrodes for Shape-Memory Polymer Light-Emitting Diodes. *Adv. Mater.* **2011**, *23*, 664–668.
- (7) Jiang, W.; Yu, D.; Zhang, Q.; Goh, K.; Wei, L.; Yong, Y.; Jiang, R.; Wei, J.; Chen, Y. Ternary Hybrids of Amorphous Nickel Hydroxide–Carbon Nanotube–Conducting Polymer for Supercapacitors with High Energy Density, Excellent Rate Capability, and Long Cycle Life. *Adv. Funct. Mater.* **2015**, *25*, 1063–1073.
- (8) Zeng, X. Y.; Zhang, Q. K.; Yu, R. M.; Lu, C. Z. A New Transparent Conductor: Silver Nanowire Film Buried at the Surface of a Transparent Polymer. *Adv. Mater.* **2010**, *22*, 4484–4488.
- (9) Huang, J.; Virji, S.; Weiller, B. H.; Kaner, R. B. Nanostructured Polyaniline Sensors. *Chem. - Eur. J.* **2004**, *10*, 1314–1319.
- (10) Wang, L. R.; Ran, F.; Tan, Y. T.; Zhao, L.; Kong, L. B.; Kang, L. Coral Reef-Like Polyaniline Nanotubes Prepared by a Reactive Template of Manganese Oxide for Supercapacitor Electrode. *Chin. Chem. Lett.* **2011**, *22*, 964–968.
- (11) Yang, K.; Xu, H.; Cheng, L.; Sun, C.; Wang, J.; Liu, Z. In Vitro and In Vivo Near-Infrared Photothermal Therapy of Cancer Using Polypyrrole Organic Nanoparticles. *Adv. Mater.* **2012**, *24*, 5586–5592.
- (12) Kim, Y.; Cook, S.; Tuladhar, S. M.; Choulis, S. A.; Nelson, J.; Durrant, J. R.; Bradley, D. D.; Giles, M.; McCulloch, I.; Ha, C.-S.; Ree, M. A Strong Regioregularity Effect in Self-Organizing Conjugated Polymer Films and High-Efficiency Polythiophene: Fullerene Solar Cells. *Nat. Mater.* **2006**, *5*, 197–203.
- (13) Behzadi, M.; Noroozian, E.; Mirzaei, M. A Novel Coating Based on Carbon Nanotubes/Poly-Ortho-Phenylenediamine Composite for Headspace Solid-Phase Microextraction of Polycyclic Aromatic Hydrocarbons. *Talanta* **2013**, *108*, 66–73.
- (14) Ehsani, A.; Mahjani, M. G.; Jafarian, M.; Naeemy, A. Influence of Ionic Surfactant on Physio-Electrochemical Properties and Fractal

Dimension of Poly Ortho Aminophenol Film. *Prog. Org. Coat.* **2010**, *69*, 510–516.

(15) Sakai, Y.; Sadaoka, Y.; Matsuguchi, M. Humidity Sensors Based on Polymer Thin Films. *Sens. Actuators, B* **1996**, *35*, 85–90.

(16) Zhu, Z.-T.; Mason, J. T.; Dieckmann, R.; Malliaras, G. G. Humidity Sensors Based on Pentacene Thin-Film Transistors. *Appl. Phys. Lett.* **2002**, *81*, 4643–4645.

(17) Chen, Z.; Lu, C. Humidity Sensors: A Review of Materials and Mechanisms. *Sens. Lett.* **2005**, *3*, 274–295.

(18) Lawrence, M. G. The Relationship between Relative Humidity and the Dewpoint Temperature in Moist Air: A Simple Conversion and Applications. *Bull. Am. Meteorol. Soc.* **2005**, *86*, 225–233.

(19) Kuang, Q.; Lao, C.; Wang, Z. L.; Xie, Z.; Zheng, L. High-Sensitivity Humidity Sensor Based on a Single SnO₂ Nanowire. *J. Am. Chem. Soc.* **2007**, *129*, 6070–6071.

(20) Zhang, Y.; Yu, K.; Jiang, D.; Zhu, Z.; Geng, H.; Luo, L. Zinc Oxide Nanorod and Nanowire for Humidity Sensor. *Appl. Surf. Sci.* **2005**, *242*, 212–217.

(21) Gradon, L.; Clark, A. B.; Seakins, P. J. Infrared gas analyser and humidity sensor. US Patent US 5468961 A, 1995.

(22) Romain, A.-C.; Nicolas, J.; Andre, P. In *Seminars in Food Analysis* **1997**; Vol. 2, p 283–296.

(23) Bai, H.; Shi, G. Gas Sensors Based on Conducting Polymers. *Sensors* **2007**, *7*, 267–307.

(24) Hwang, L.; Ko, J.; Rhee, H.; Kim, C. A Polymer Humidity Sensor. *Synth. Met.* **1993**, *57*, 3671–3676.

(25) Ullah, H.; Shah, A. A.; Bilal, S.; Ayub, K. DFT Study of Polyaniline NH₃, CO₂, and CO Gas Sensors: Comparison with Recent Experimental Data. *J. Phys. Chem. C* **2013**, *117*, 23701–23711.

(26) Bibi, S.; Ullah, H.; Ahmad, S. M.; Ali Shah, A. A.; Bilal, S.; Tahir, A. A.; Ayub, K. Molecular and Electronic Structure Elucidation of Polypyrrole Gas Sensors. *J. Phys. Chem. C* **2015**, *119*, 15994–16003.

(27) Ullah, H.; Ayub, K.; Ullah, Z.; Hanif, M.; Nawaz, R.; Bilal, S.; Shah, A. H. A. Theoretical Insight of Polypyrrole Ammonia Gas Sensor. *Synth. Met.* **2013**, *172*, 14–20.

(28) Nohria, R.; Khillan, R. K.; Su, Y.; Dikshit, R.; Lvov, Y.; Varahramyan, K. Humidity Sensor Based on Ultrathin Polyaniline Film Deposited Using Layer-by-Layer Nano-Assembly. *Sens. Actuators, B* **2006**, *114*, 218–222.

(29) Lin, Q.; Li, Y.; Yang, M. Polyaniline Nanofiber Humidity Sensor Prepared by Electrospinning. *Sens. Actuators, B* **2012**, *161*, 967–972.

(30) Jain, S.; Chakane, S.; Samui, A.; Krishnamurthy, V.; Bhoraskar, S. Humidity Sensing with Weak Acid-Doped Polyaniline and Its Composites. *Sens. Actuators, B* **2003**, *96*, 124–129.

(31) Tonosaki, T.; Oho, T.; Isomura, K.; Ogura, K. Effect of the Protonation Level of Poly (*O*-Phenylenediamine) (POPD) on the Ac Impedance of Humidity-Sensitive POPD/Poly (Vinyl Alcohol) Composite Film. *J. Electroanal. Chem.* **2002**, *520*, 89–93.

(32) Ogura, K.; Tonosaki, T.; Shiigi, H. Ac Impedance Spectroscopy of Humidity Sensor Using Poly (*O*-Phenylenediamine)/Poly (Vinyl Alcohol) Composite Film. *J. Electrochem. Soc.* **2001**, *148*, H21–H27.

(33) Suri, K.; Annapoorni, S.; Sarkar, A.; Tandon, R. Gas and Humidity Sensors Based on Iron Oxide–Polypyrrole Nanocomposites. *Sens. Actuators, B* **2002**, *81*, 277–282.

(34) Zhang, T.; He, Y.; Wang, R.; Geng, W.; Wang, L.; Niu, L.; Li, X. Analysis of DC and AC Properties of Humidity Sensor Based on Polypyrrole Materials. *Sens. Actuators, B* **2008**, *131*, 687–691.

(35) Geng, W.; Li, N.; Li, X.; Wang, R.; Tu, J.; Zhang, T. Effect of Polymerization Time on the Humidity Sensing Properties of Polypyrrole. *Sens. Actuators, B* **2007**, *125*, 114–119.

(36) Parvatikar, N.; Jain, S.; Khasim, S.; Revansiddappa, M.; Bhoraskar, S.; Prasad, M. A. Electrical and Humidity Sensing Properties of Polyaniline/WO₃ Composites. *Sens. Actuators, B* **2006**, *114*, 599–603.

(37) Salavagione, H. J.; Arias-Pardilla, J.; Pérez, J.; Vázquez, J.; Morallón, E.; Miras, M. C.; Barbero, C. Study of Redox Mechanism of Poly (*O*-Aminophenol) Using in Situ Techniques: Evidence of Two Redox Processes. *J. Electroanal. Chem.* **2005**, *576*, 139–145.

(38) Bilal, S.; Bibi, S.; Ahmad, S. M.; Shah, A. H. A. Counterpoise-Corrected Energies, NBO, HOMO–LUMO and Interaction Energies

of Poly (*O*-Aminophenol) for Ammonia Sensing by DFT Methods. *Synth. Met.* **2015**, *209*, 143–149.

(39) Valdes García, M. a. A. V.; Tunon Blanco, P. T.; Ivaska, A. A Poly (*O*-Aminophenol) Modified Electrode as an Amperometric Hydrogen Peroxide Biosensor. *Electrochim. Acta* **1998**, *43*, 3533–3539.

(40) Li, J.; Zhao, J.; Wei, X. A Sensitive and Selective Sensor for Dopamine Determination Based on a Molecularly Imprinted Electropolymer of *O*-Aminophenol. *Sens. Actuators, B* **2009**, *140*, 663–669.

(41) Tucceri, R.; Arnal, P. M.; Scian, A. N. Spectroscopic Characterization of Poly (Ortho-Aminophenol) Film Electrodes: A Review Article. *ISRN Polym. Sci.* **2012**, *2012*, 1–26.

(42) Shah, A. H. A.; Holze, R. Poly (*O*-Aminophenol) with Two Redox Processes: A Spectroelectrochemical Study. *J. Electroanal. Chem.* **2006**, *597*, 95–102.

(43) Zhang, A.; Cui, C.; Chen, Y.; Lee, J. Synthesis and Electrochromic Properties of Poly-*O*-Aminophenol. *J. Electroanal. Chem.* **1994**, *373*, 115–121.

(44) Tucceri, R.; Barbero, C.; Silber, J.; Sereno, L.; Posadas, D. Spectroelectrochemical Study of Poly-*O*-Aminophenol. *Electrochim. Acta* **1997**, *42*, 919–927.

(45) Jeffrey, G. A. *An Introduction to Hydrogen Bonding*; Oxford University Press: New York, 1997; pp 1–303.

(46) Becke, A. D. Density-Functional Exchange-Energy Approximation with Correct Asymptotic Behavior. *Phys. Rev. A: At., Mol., Opt. Phys.* **1988**, *38*, 3098.

(47) Alemán, C.; Ferreira, C. A.; Torras, J.; Meneguzzi, A.; Canales, M.; Rodrigues, M. A.; Casanovas, J. On the Molecular Properties of Polyaniline: A Comprehensive Theoretical Study. *Polymer* **2008**, *49*, 5169–5176.

(48) Ullah, H.; Shah, A.-u.-H. A.; Bilal, S.; Ayub, K. Doping and Dedoping Processes of Polypyrrole: DFT Study with Hybrid Functionals. *J. Phys. Chem. C* **2014**, *118*, 17819–17830.

(49) Ullah, H.; Shah, A. A.; Ayub, K.; Bilal, S. Density Functional Theory Study of Poly (*O*-Phenylenediamine) Oligomers. *J. Phys. Chem. C* **2013**, *117*, 4069–4078.

(50) Zade, S. S.; Bendikov, M. From Oligomers to Polymer: Convergence in the Homo–Lumo Gaps of Conjugated Oligomers. *Org. Lett.* **2006**, *8*, 5243–5246.

(51) (a) Frisch, M. J.; Trucks, G. W.; Schlegel, H. B.; Scuseria, G. E.; Robb, M. A.; Cheeseman, J. R.; Scalmani, G.; Barone, V.; Mennucci, B.; Petersson, G. A.; et al. *Gaussian 09*, Rev. D. 0.1; Gaussian, Inc.: Wallingford, CT, 2013. (b) *Gaussian 09*, Rev. A. 02, Gaussian, Inc.: Wallingford, CT, 2013; 200.

(52) Allouche, A. R. Gabedit—A Graphical User Interface for Computational Chemistry Softwares. *J. Comput. Chem.* **2011**, *32*, 174–182.

(53) Dennington, R. D.; Keith, T. A.; Millam, J. M. *Gaussview 5.0.8*; Gaussian Inc, 2008.

(54) Yanai, T.; Tew, D. P.; Handy, N. C. A New Hybrid Exchange–Correlation Functional Using the Coulomb-Attenuating Method (CAM-B3LYP). *Chem. Phys. Lett.* **2004**, *393*, 51–57.

(55) Zade, S. S.; Bendikov, M. From Oligomers to Polymer: Convergence in the HOMO-LUMO Gaps of Conjugated Oligomers. *Org. Lett.* **2006**, *8*, 5243–5246.

[Article 18]

H Ullah, Tahir. A “*Metal Ferrites: Prospective Materials for Solar Energy Conversion and Environment Applications*” *Review Article*. Under Review in *Progress in Materials Science*. 2018.

[Article 19]

Hyeong Pil Kim, Anil Kanwat, Habib Ullah, D.G, Xiuling Li, Jeongmo Kim, W. J. Silva, F.K. Schneider, Abd. Rashid bin Mohd Yusoff, Jin Jang, Deji Akinwande, A. A. Tahir, and Mohammad Khaja Nazeeruddin. *“Improving Charge Transport and Stability of Perovskite Thin Film Transistors by Crosslinking with Diethyl-(12-phosphonododecyl)phosphonate”* Ready to submit to Nature Chemistry. 2018.

[Article 20]

H Ullah, M. Sookhajian, W. J. Basirun, A. A. Tahir, M. A. Mat Teridi^{4*} *"ITO free of 10.73% efficiency visibly transparent triple-junction polymer solar cell"*

Ready to Submit to *Advanced Functional Materials*. 2018.

Dr. Habib Ullah Yousaf Z ai

Hu203@exeter.ac.uk

habibullah@uop.edu.pk

habib_chemist@yahoo.com



- 23.04.1986* LundKhawar, Takht Bhai, Mardan
(Khyber Pakhtunkhwa), Pakistan.
- 1992-1999* Primary and Middle Schools (Mardan).
- 1999-2002* Secondary School (Mardan).
- 2002* Secondary School Certificate (Matriculation), BISE Peshawar.
- 2002-2005* Intermediate at Govt. Superior Science College Peshawar.
- 2005* Higher Secondary School Certificate (**F.Sc**), BISE Peshawar.
- 2005-2007* Study of Chemistry, Zoology and Geography at Govt. Superior Science College Peshawar.
- 2007* Bachelor of Science (**B.Sc**), University of Peshawar.
- 2007-2009* Master of Science (**M.Sc**) in Physical Chemistry, Hazara University, Mansehra.
- 2009-2010* Scientific fellow at Chemistry Department, Hazara University, Mansehra.
- 2010* Master of Philosophy (**M.Phil**) in Physical Chemistry, University of Peshawar.
- 2010-2013* Scientific fellow at Institute of Chemical Sciences, University of Peshawar.
- 2011-2014* Teaching Assistant at Institute of Chemical Sciences, University of Peshawar.
- 2014-2017* Teaching Assistant at Renewable Energy, University of Exeter, UK.
- 2014-2018* Doctor of Philosophy (**Ph.D**) in Renewable Energy, University of Exeter, UK.

Selected Publications

1. Hyeong Pil Kim, Anil Kanwat, **Habib Ullah**, D.G, Xiuling Li, A. A. Tahir, and Mohammad Khaja Nazeeruddin. "Improving Charge Transport and Stability of Perovskite Thin Film Transistors by Crosslinking with Diethyl-(12-phosphonododecyl)phosphonate" Ready to submit **Nature Chemistry**, 2018.
2. **Habib Ullah**,* M. Sookhajian, W. J. Basirun, A. A. Tahir, M. A. Mat Teridi* "ITO free of 10.73% efficiency visibly transparent triple-junction polymer solar cell" Ready to Submit to **Advanced Functional Materials** 2018.
3. **Habib Ullah**,* Tahir. A "Metal Ferrites: Prospective Materials for Solar Energy Conversion and Environment Applications" **Review Article**. Under Review in **Progress in Materials Science** 2018.
4. **Habib Ullah**,* Tahir. A A, Salma Bibi, Mallick. T, and Karazhanov, S. "Electronic Properties of γ -TaON and Its Surfaces for Solar Water Splitting" **Appl. Catal., B: Environ.** 2018, (229), 24-31.
5. **Habib Ullah**,* Tahir. A, and Mallick. T "Structural and Electronic Properties of Oxygen Defective and Se-Doped p-Type $\text{BiVO}_4(001)$ Thin Film for the Applications of Photocatalysis" **Appl. Catal., B: Environ.** 2018, (224), 895-903.
6. J. Safaei, **Habib Ullah**,* N. A. Mohamed, M. F. M. Noh, M. F. Soh, A. A. Tahir, N. A. Ludin, M. A. Ibrahim, W. N. R. W. Isahak, M. A. M. Teridi, "Enhanced photoelectrochemical performance of Z-scheme $g\text{-C}_3\text{N}_4/\text{BiVO}_4$ photocatalyst." **Appl. Catal., B: Environ.**, vol. 234, pp. 296-310, Oct. 2018.
7. Salma Bibi, Salma Bilal, A. A Shah, and **Habib Ullah**. "Systematic Analysis of Poly (*o*-aminophenol) Humidity Sensors." **ACS Omega**, 2017, 2 (10), 6380-6390.
8. Siti M. Nasir, **Habib Ullah**,* Asif A. Tahir, Mehdi Ebadi, Jagdeep S. Sagu, and M. Asri Teridi* "New Insights into Se/BiVO_4 Heterostructure for Photoelectrochemical Water Splitting: A Combined Experimental and DFT Study" **Journal of Physical Chemistry C**, 2017, 121 (11), 6218-6228.
9. **Habib Ullah**,* A. A. Tahir, and T. K. Mallick, *Polypyrrole/TiO₂ Composites for the Application of Photocatalysis Sens Actuators*, B241 (2017) 1161-1169.
10. **Habib Ullah**,* S. Bibi, A. A. Tahir, and T. K. Mallick, *Donor-acceptor polymer for the design of All-Solid-State dye-sensitized solar cells* **J. Alloys Compd.** 696 (2017) 914-922.
11. **Habib Ullah**,* S. Bibi, A. A. Tahir, and T. K. Mallick, Density Functional Theory Study of Selenium-Substituted Low-Bandgap Donor-Acceptor-Donor Polymer **Journal of Physical Chemistry C** 120 (2016) 27200-27211.
12. Asif Ali Tahir, **Habib Ullah**, Sudha, Mohd Asri Mat Teridi, *Senthilarasu Sundaram, *Anitha Devadoss "Energy Conversion, Storage, Environmental and Biosensing Application of Graphene and Its Derivatives" **The Chemical Record**. 16 (2016) 1591-1634.
13. Muhammad Kamran, **Habib Ullah**,* A. A. Shah, Asif Ali Tahir, Khurshid Ayub. "Density Functional Theory and Experimental Study of Poly (Aniline-*co*-Pyrrole)" **Polymer**, 2015, 72, 30-39.
14. Salma Bibi, **Habib Ullah**, Asif Ali Tahir. "Molecular and Electronic Structure Understanding of Polypyrrole Gas Sensors." **Journal of Physical Chemistry C**, 2015, 119, 15994-16003.
15. **Habib Ullah**.; Shah, A. A.; Bilal, S.; Ayub, K. Doping and Dedoping Processes of Polypyrrole: DFT Study with Hybrid Functionals. **Journal of Physical Chemistry C** 2014, 118, 17819.
16. **Habib Ullah**.; Shah, A. A.; Ayub, K.; Bilal, S. Density Functional Theory Study of Poly (*o*-phenylenediamine) Oligomers. **Journal of Physical Chemistry C** 2013, 117, 4069.
17. **Habib Ullah**.; Shah, A. A.; Bilal, S.; Ayub, K. DFT Study of Polyaniline NH₃, CO₂, and CO Gas Sensors: Comparison with Recent Experimental Data. **Journal of Physical Chemistry C** 2013, 117, 23701.